Hailiang Yu
Haitao Gao
Zhou Li

High-Performance Metallic Composites Fabricated by Advanced Rolling Techniques

Springer

Hailiang Yu, Haitao Gao and Zhou Li

High-Performance Metallic Composites Fabricated by Advanced Rolling Techniques



Hailiang Yu
Central South University, Changsha, China

Haitao Gao
Central South University, Changsha, China

Zhou Li
Central South University, Changsha, China

ISBN 978-981-97-4330-8 e-ISBN 978-981-97-4331-5
https://doi.org/10.1007/978-981-97-4331-5

© The Editor(s) (if applicable) and The Author(s), under exclusive license to Springer Nature Singapore Pte Ltd. 2024

This work is subject to copyright. All rights are solely and exclusively licensed by the Publisher, whether the whole or part of the material is concerned, specifically the rights of translation, reprinting, reuse of illustrations, recitation, broadcasting, reproduction on microfilms or in any other physical way, and transmission or information storage and retrieval, electronic adaptation, computer software, or by similar or dissimilar methodology now known or hereafter developed.

The use of general descriptive names, registered names, trademarks, service marks, etc. in this publication does not imply, even in the absence of a specific statement, that such names are exempt from the relevant protective laws and regulations and therefore free for general use.

The publisher, the authors and the editors are safe to assume that the advice and information in this book are believed to be true and accurate at the date of publication. Neither the publisher nor the authors or the editors give a warranty, expressed or implied, with respect to the material contained herein or for any errors or omissions that may have

been made. The publisher remains neutral with regard to jurisdictional claims in published maps and institutional affiliations.

This Springer imprint is published by the registered company Springer Nature Singapore Pte Ltd.
The registered company address is: 152 Beach Road, #21-01/04 Gateway East, Singapore 189721, Singapore

Contents

1 Introduction of Fabrication of Metallic Composites

References

2 Fabricated Metal Laminates via Hot Roll Bonding Techniques

2.1 Introduction of Hot Roll Bonding Technique

2.2 Interface Bonding Behavior During Hot Deformation

2.2.1 Interface Bonding Behavior Affected by Heating Temperature

2.2.2 Interface Bonding Behavior Affected by Reduction Ratio

2.2.3 Interface Bonding Behavior Affected by Deformation Pass Number

2.2.4 Interface Bonding Behavior Affected by Strain Rate

2.2.5 Interface Bonding Behavior Affected by Holding Time

2.3 Shear Strength of Hot-Rolled Laminates

2.4 Interface Bonding Mechanism of Laminates During Hot Roll Bonding

2.5 Cu/Al Laminates with Thin SUS304 Interlayer via Hot Roll Bonding

2.6 Cu/Al/Cu Laminates with SUS304 Interlayer Subjected to Annealing

2.7 Cu/Al Laminates Subjected to High-Temperature Accumulative Roll Bonding

2.7.1 Mechanical Properties and Microstructure of Cu/Al Laminates During ARB

2.7.2 Strengthening Mechanism of Cu/Al Laminates During ARB

References

3 Fabricated Metal Laminates via Cold Roll Bonding Techniques
3.1 Al/Ti Laminates Subjected to Cold Roll Bonding and Annealing
3.1.1 Microstructure Evolution of Al/Ti Laminate During Processing
3.1.2 Mechanical Properties Al/Ti Laminate After Processing
3.1.3 Microstructure Evolution Mechanism of Al/Ti Laminate During Annealing
3.1.4 Deformation Mechanism of Annealed Al/Ti Laminates
3.1.5 Abnormal High Dislocation Density in Annealed Al/Ti Laminates
3.2 Cu/Ti Laminates Subjected to Cold Roll Bonding
3.2.1 Microstructure Evolution of Cu/Ti Laminate During Cold Roll Bonding
3.2.2 Deformation Mechanism of Cu/Ti Laminate During Cold Roll Bonding
3.3 Cu/Al Laminates Subjected to Cold Roll Bonding
3.3.1 Development of Porous Cu/Al/Cu Laminate Foils
3.3.2 Development of Cu/Al/Cu Laminates via Powder-In-Tube Method
3.3.3 Mechanism of Enhanced Bonding Strength of Cu/Al Laminates with SUS304 Interlayer
References
4 Fabricated Metal Laminates via Cryorolling
4.1 AA1050/AA5052 Laminates via Cryorolling
4.1.1 Mechanical Properties of AA1050/AA5052 Laminates
4.1.2 Microstructure Evolution of AA1050/AA5052 Laminates

4.1.3 Fracture Morphology of AA1050/AA5052 Laminates After Tensile Testing

4.2 AA1050/AA6061 Laminates via Cryorolling

4.2.1 Mechanical Properties of AA1050/AA5061 Laminates

4.2.2 Microstructure Evolution of AA1050/AA5061 Laminates

4.2.3 Fracture Morphology of AA1050/AA5061 Laminates After Tensile Testing

4.2.4 Effect of Aging on Mechanical Properties of AA1050/AA5052 Laminates

4.2.5 Microstructural Evolution Mechanism of AA1050/AA6061 Laminate During Aging

4.3 Al/Ti/Al Laminates via Cryorolling

4.3.1 Edge Crack-Free Al/Ti/Al Laminates via Cryorolling

4.3.2 Mechanical Properties of Cryorolled Al/Ti/Al Laminates

4.3.3 Microstructure Evolution of Al/Ti/Al Laminates

4.3.4 Interface Bonding Mechanism of Al/Ti/Al Laminates During Cryorolling

4.3.5 Effect of Cryorolling Temperatures on Peeling Strength of Al/Ti/Al Laminates

4.3.6 Mechanism of Enhanced Peeling Strength of Al/Ti/Al Laminates via Cryorolling

4.4 Al/Mg/Al Laminates via Cryorolling

4.4.1 Microstructure Evolution of the Al/Mg/Al Laminates During Rolling

4.4.2 Mechanical Properties of the Al/Mg/Al Laminates During Rolling

4.4.3 Microstructure Evolution Mechanism of the Mg-Li Layer During Cryorolling

4.5 Cu/Al/Cu Laminates Subjected to Cryorolling

4.5.1 Microstructure and Mechanical Properties of Cu/Al/Cu Laminates

4.5.2 Fracture Mechanism of Cryorolled Cu/Al/Cu Laminates

4.5.3 Microstructure Evolution of Cu/Al Laminates Subjected to ARB and Cryorolling

4.5.4 Tensile Properties of Cu/Al Laminates Subjected to ARB and Cryorolling

4.5.5 Thermal Stability of Cu/Al Laminates Subjected to ARB and Cryorolling

4.6 Cu/Nb Laminates Subjected to Cryorolling and Annealing

4.6.1 Mechanical Properties of Cu/Nb Laminates

4.6.2 Microstructural Evolution of Cu/Nb Laminates

4.7 Cu/Brass Laminates Subjected to Cryorolling

4.7.1 Microstructural Evolution of Cu/Brass Laminates

4.7.2 Mechanical Properties of Cu/Brass Laminates

References

5 Fabricated Al/Particle Composites via Cryorolling

5.1 Fabrication of AA1050/HEAp MMCs via Cryorolling

5.1.1 Microstructure Evolution of AA1050/HEAp Composites

5.1.2 Mechanical Properties of AA1050/HEAp MMCs

5.1.3 Mechanism of Suppression of Microvoid and Fracture in AA1050/HEAp MMCs During Cryorolling

5.1.4 Mechanism of Cryorolling on Enhanced Mechanical Property of AA1050/HEAp MMCs

5.2 Fabrication of AA2024/HEAp MMCs via Cryorolling

5.2.1 Microstructure Evolution of AA2024/HEAp MMCs

5.2.2 Mechanical Properties of AA2024/HEAp MMCs

5.2.3 Mechanism of Enhanced Mechanical Properties of AA2024/HEAp MMCs

5.3 Fabrication of AA5083/HEAp MMCs During Cryorolling

5.3.1 Microstructure Evolution of AA5083/HEAp MMCs

5.3.2 Mechanical Properties of AA5083/HEAp MMCs

5.3.3 Mechanism of Enhanced Mechanical Properties of AA5083/HEAp MMCs During Cryorolling

5.4 Fabrication of AA1050/HEAp Composites Subjected to Asymmetric Cryorolling

5.4.1 Microstructure Evolution of AA1050/HEAp Composites During Asymmetric Cryorolling

5.4.2 Mechanical Properties of Asymmetrical Cryorolled AA1050/HEAp Composites

5.4.3 Mechanism of Enhanced Mechanical Properties of AA1050/HEAp Composites via Asymmetric Cryorolling

5.5 Mechanical Properties of Al/HEAp Composites at Extreme Environments

5.5.1 Mechanical Properties of Al/HEAp MMCs in a Cryogenic Environment

5.5.2 Microstructure Evolution of Al/HEAp MMCs During Cryogenic Tensile Testing

5.5.3 Mechanism of Al/HEAp MMCs Strength Enhancement in a Cryogenic Environment

5.5.4 Mechanism of Al/HEAp MMCs Elongation Enhancement in Cryogenic Environment

5.6 Al/TiC Composites via ARB and Cryorolling

5.6.1 Microstructural Evolution of Al/TiC AMCs During ARB

5.6.2 Mechanical Properties of ARB-Processed Al/TiC AMCs

5.6.3 Various Ceramic Nano-particles Reinforced AMCs via ARB

References

6 Future Applications of High-Performance Metallic Composites

6.1 Aerospace and Aviation

6.2 Defense and Military

6.3 Energy Applications

References

About the Authors



Dr. Hailiang Yu is a full professor at Central South University. He has been engaged in advanced non-ferrous metals and alloy forming and processing. He has published 230 papers and two monographs. He also contributed to two edited books and two chapters. He is currently a member of the Board of Directors of the Nonferrous Metals Society of China, and the Composites Committee of the Nonferrous Metals Society of China. He serves as a key reader of *Metallurgical and Materials Transactions A*, and the editorial board of *Chinese Journal of Mechanical Engineering*, *Journal of Plastics Engineering*, and *Scientific Reports*, and young expert of *Engineering*.



Dr. Haitao Gao is a lecturer at Central South University specializing in the research fields of metal matrix composites and advanced forming technologies for new energy vehicles. Currently, he is in charge of the projects supported by National Natural Science Foundation and the Hunan Provincial Natural Science Foundation. He has filed more than 10 patent applications and published over 30 high-level SCI journal papers. He has been awarded the Second Prize of the China Nonferrous Metal Industry Science and Technology Award.

Dr. Zhou Li is an Associate Professor at Central South University. His research interests include automotive body new materials and advanced forming technology, new energy pure electric vehicle gearbox design and manufacturing. He has also participated in national projects in Australia as a chief investigator, applied for 10 patents, and published 20 papers in high-level journals. He has won the second prize of China Machinery Industry Science and Technology Award, the third prize of “Double Creation” Competition of the European and American Alumni Association.



© The Author(s), under exclusive license to Springer Nature Singapore Pte Ltd. 2024
H. Yu et al., *High-Performance Metallic Composites Fabricated by Advanced Rolling Techniques*
https://doi.org/10.1007/978-981-97-4331-5_1

1. Introduction of Fabrication of Metallic Composites

Hailiang Yu[1] ✉, Haitao Gao[1] ✉ and Zhou Li[1]
(1) Central South University, Changsha, China

✉ **Hailiang Yu (Corresponding author)**
Email: yuhailiang@csu.edu.cn

✉ **Haitao Gao**
Email: gaohaitao@csu.edu.cn

With the rapid development of science and technology, many new requirements for metallic materials are put forward, such as low density, high strength, high wear resistance and corrosion resistance. Under this situation, the unitary metallic material is difficult to meet the needs of industrial production and metallic laminates come into being, which have attracted much attention because of their unique physical and chemical properties [1]. There are many species of metal laminates [2–5], such as Cu/Al, Mg/Al, Al/steel, Cu/invar, and Al/Ti laminates. They have been widely applied in the fields of automobile, aviation, shipbuilding, electronics and chemical industry, such as heat exchanger for automobile [6], aircraft parts [7], ship hull [8], electronic components [9], grounding wire for petrochemical enterprises [10]. The promotion and application of metal laminates are of great significance to solve the outstanding problems of current energy structure and industrial structure [11].

Currently, the preparation technologies of metallic composites have made great progress, which can be divided as liquid–liquid bonding,

solid–liquid bonding and solid–solid bonding according to the physical state of matrix metal, as shown in Fig. 1.1. The typical liquid–liquid bonding method is the core filling continuous casting technique. In the fabrication process of metal laminates, the solidification of matrix metal and formation of bonding interface can be simultaneously carried out, which obviously shortens the production process [12]. Nevertheless, core filling continuous casting technique requires very high control precision on the process variables and exhibits the low yield of finial products [13].

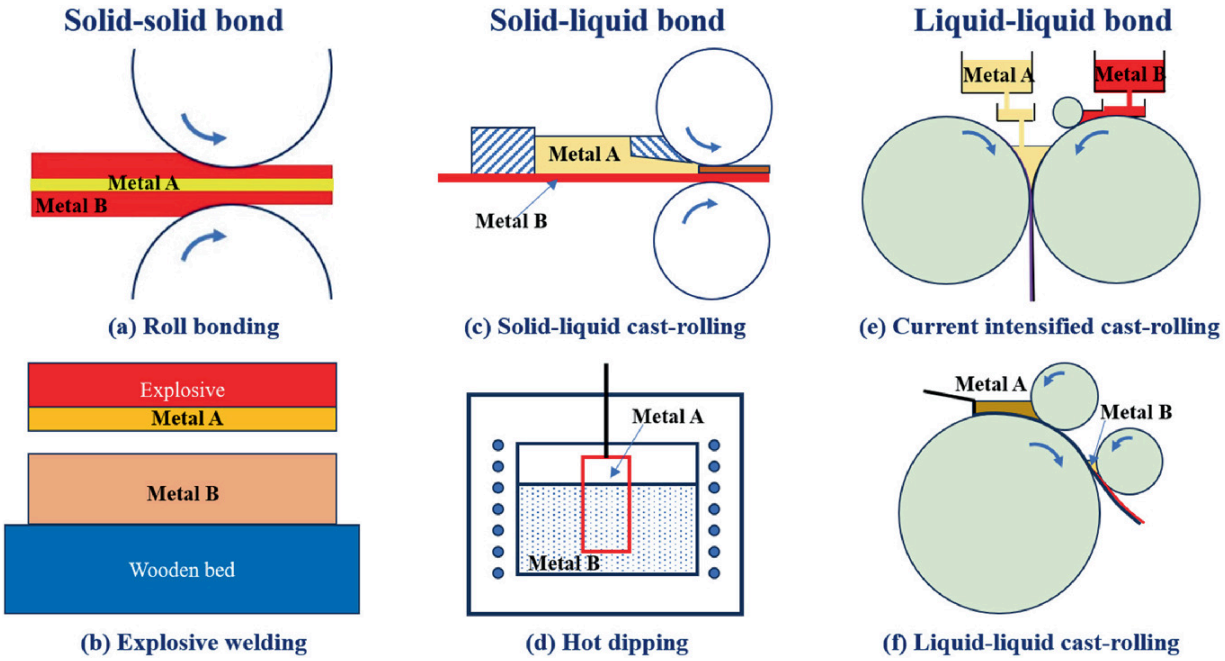


Fig. 1.1 Illustration of techniques for fabrication of metallic composites

Roll-casting technique is regarded as the representative of solid–liquid bonding of metal laminates [14]. Compared with the core filling continuous casting technique, the obvious advantages of roll-casting technique are high production efficiency and low production costs. Moreover, high interfacial bonding strength can be easily obtained under the dual effect of high temperature and rolling pressure [15]. However, the high temperature of liquid metal from another perspective, also leads to the high energy consumption.

Nowadays, the solid–solid method is used for the widest range of industrial application due to its process controllability, which mainly including roll bonding technique [16], extrusion bonding technique [17], and explosive welding technique [18]. Compared with other

techniques, the less pollution, stable production process and high production efficiency of roll bonding technique make obvious advantages. In the roll bonding process, the oxidation film on the surface of matrix metal is broken and obvious plastic flow occurs under the action of huge rolling pressure. And then, close contact for these atoms around the bonding interface are carried out. Finally, metallurgical bonding interface can be formed through the heat input and atomic diffusion. Before roll bonding, surface treatment is usually adopted to remove the grease or dirt and expose the fresh matrix metal. Moreover, the annealing process is also necessary to regulate the thickness of intermetallic compound (IMC) layer [19].

In this book, the recent efforts and advances in the roll bonding of metal laminates are summarized to reveal the potential mechanism. Based on the comprehensive understanding and our numerous original works, some important issues about the fabrication method, evolution mechanism of bonding interface and reinforcement factors of roll-bonded metal laminates are introduced.

References

1. Gao HT, Kong C, Yu HL (2023) Lightweight metal laminated plates produced via (hot, cold and cryogenic) roll bonding: a review. Trans Nonfer Met Soc China 33:337–356 [Crossref]
2. Khojastehnezhad VM, Pourasl HH (2018) Microstructural characterization and mechanical properties of aluminum 6061–T6 plates welded with copper insert plate (Al/Cu/Al) using friction stir welding. Trans Nonfer Met Soc China 28:415–426 [Crossref]
3. Ding YL, Wang JG, Zhao M, Ju DY (2018) Effect of annealing temperature on joints of diffusion bonded Mg/Al alloys. Trans Nonfer Met Soc China 28:251–258 [Crossref]
4. Li CL, Fan D, Yu XQ, Huang JK (2019) Residual stress and welding distortion of Al/steel butt joint by arc–assisted laser welding–brazing. Trans Nonfer Met Soc China 29:692–700 [Crossref]
5. Nie QQ, Chen GH, Wang B, Yang L, Tang WM (2021) Process optimization, microstructures and mechanical/thermal properties of Cu/Invar bi–metal matrix composites fabricated by spark plasma sintering. Trans Nonfer Met Soc China 31:3050–3062 [Crossref]

6. Zu GY, Wang N, Yu JM, Wen JL (2003) Application of composite brazing aluminum foil technology in automotive heat exchanger production. Autom Tech Mater 12:37–38
7. Wang XL, Wei YH (2016) Application and development of metal matrix composites in the aerospace field. Sci Tech Innov Herald 6:16–18
8. Chen YL (1990) New technology of composite materials for shipbuilding. Fiber Reinforced Plastics/Compos 3:17
9. Hartley WD, Garcia D, Yoder JK, Poczatek E, Forsmark JH, Luckey SG, Dillard DA, Yu HZ (2021) Solid–state cladding on thin automotive sheet metals enabled by additive friction stir deposition. J Mater Process Tech 291:117045
[Crossref]
10. Liu B (2011) Application of copper–steel composites and exothermic welding technology in the grounding system of petrochemical enterprises. China New Tech Prod 8:14
11. Wang T, Qi YY, Liu JL, Han JC, Ren ZK, Huang QX (2020) Research progress of metal laminates roll bonding process at home and abroad. J Harbin Inst Tech 52(6):42–56
12. Xue ZY, Liang H, Yu WH, Wu CJ (2013) Orthogonal tests of copper–clad aluminum bimetal continuous casting by nitrogen pressure core–filling. China Foundry 10(6):385–390
13. Su YJ, Liu XH, Huang HY, Liu XF, Xie JX (2011) Interfacial microstructure and bonding strength of copper cladding aluminum rods fabricated by horizontal core–filling continuous casting. Metall Mater Trans A 42:4088–4099
[Crossref]
14. Liu SY, Wang AQ, Lu SJ, Xie JP (2018) High–performance Cu/Al laminated composites fabricated by horizontal twin–roll casting. Materialwiss Werkstofftech 49:1213–1223
[Crossref]
15. Wang ZJ, Li YW, Zhang WN, Wang GD, Liu HT (2021) Microstructural evolution and mechanical properties of titanium–alloying high borated steel sheets fabricated by twin–roll strip casting. Mater Sci Eng A 811:141067
[Crossref]
16. Kim IK, Hong SI (2013) Effect of heat treatment on the bending behavior of tri–layered Cu/Al/Cu composite plates. Mater Des 47:590–598
[Crossref]
17. Rhee KY, Han WY, Park HJ, Kim SS (2004) Fabrication of aluminum/copper clad composite using hot hydrostatic extrusion process and its material characteristics. Mater Sci Eng A 384:70–76
[Crossref]
18. Loureiro A, Mendes R, Ribeiro JB, Leal RM, Galvão I (2016) Effect of explosive mixture on quality of explosive welds of copper to aluminum. Mater Des 95:256–267
[Crossref]

19. Yu Y, Song HW, Chen Y, Xu Y, Zhang SH, Wang SD (2014) Investigation on fabrication and mechanical property of ultra–thin Cu/Al clad strip used for coax. Mater Sci Tech 22(5):13–18

© The Author(s), under exclusive license to Springer Nature Singapore Pte Ltd. 2024
H. Yu et al., *High-Performance Metallic Composites Fabricated by Advanced Rolling Techniques*
https://doi.org/10.1007/978-981-97-4331-5_2

2. Fabricated Metal Laminates via Hot Roll Bonding Techniques

Hailiang Yu[1] ✉, Haitao Gao[1] ✉ and Zhou Li[1]
(1) Central South University, Changsha, China

✉ **Hailiang Yu (Corresponding author)**
Email: yuhailiang@csu.edu.cn

✉ **Haitao Gao**
Email: gaohaitao@csu.edu.cn

2.1 Introduction of Hot Roll Bonding Technique

The hot roll bonding technique of metal laminates initially appeared in the 1940s, which is usually applied in the fabrication of thick plate. The hot roll bonding technique can reduce the rolling force but with weak production stability. Before hot roll bonding, matrix metals are preheated to a certain temperature, which will significantly affect the comprehensive properties of metal laminates. Low preheated temperature may lead to the high resistance to deformation and insufficient atomic diffusion around the bonding interface. Nevertheless, the formation of thick IMC layer, even the interfacial cracks, is easily induced by the high preheated temperature. Moreover, protective atmosphere is generally adopted in the hot roll bonding process to avoid the oxidation of interfacial metal [1].

Numerous works about hot roll bonding of metal laminates have been carried out. Menon and Chen [2] used hot roll bonding and

annealing to fabricate crack-free laminate s of Al_2O_3 and ZrO_2 with a layer thickness of 4–60 μm. Ag/Cu laminates were fabricated by roll bonding at different temperatures and annealing for different periods at 673 K and 1073 K by Zhang et al. [3]. They found that the speed of Cu atoms moving into the Ag side was faster than that of Ag atoms moving into Cu side. Peng et al. [4] fabricated Cu/Al laminates by hot roll bonding at 703 K with a 60% reduction ratio in a single pass. At lower sintering temperature, $CuAl_2$ appeared at the interface. As the temperature increased, Cu_9Al_4 phase increased. Luo et al. [5] found that the growth rate of IMCs at the bonding interface of the hot-rolled Al/Mg laminate increased with the rising of annealing temperature and the mathematical relationship between the IMCs thickness, annealing temperature and annealing time was built as Eq. (2.1):

$$y^2 = 1.98 \times 10^6 \exp\left(-\frac{83418}{RT}\right)\left(t - 0.78 \exp\frac{29770}{RT}\right) \tag{2.1}$$

where y was the thickness of IMCs layer (μm), T was the annealing temperature (K), R was the Boltzmanns constant (8.314 J/(mol·K)), t was the annealing time (min). Cui et al. [6] thought that roll bonding and subsequent reaction annealing laminates were a feasible near-net-shape processing method for the production of Ti/(TiB_2/Al) laminates.

2.2 Interface Bonding Behavior During Hot Deformation

A series of experiments on interface bonding in a low-carbon steel under hot plastic deformation were carried out using the thermo-mechanical simulator. The main influence factors such as the heating temperature, holding time, reduction ratio, strain rate and number of deformation passes on the interface bonding behavior in the laminates were analyzed using SEM imaging. The results provide sufficient basis for further research on interface bonding and propagating in steel during plastic deformation, and also on quality control in roll bonded products [7].

2.2.1 Interface Bonding Behavior Affected by Heating Temperature

Figure 2.1 gives SEM micrographs of the interface bonding zone for different heating temperatures. There is an obvious commencement of interface bonding when the heating temperature is 1173 K. At this stage, the macro-debonding regions disappear, but there are still many small holes and small grains of size less than 10 μm in the interface zone, and the microstructure is only ferrite compared with that of the overall matrix. When the heating temperature reaches 1273 K, the interface bonding is clearly better, and fewer and smaller holes remain in the transitional zone where the grain size increases and the microstructure is still ferrite. When the heating temperature reaches 1373 K, the holes undergo further reduction in size and the microstructure is similar to the matrix of some pearlite. There are no holes in the entire interface zone, and the microstructure around the interface zone is similar to that of the matrix when the heating temperature reaches 1473 K. The figures show that the degree of interface bonding quality increases progressively and the transitional zone of residual voids gradually disappears with increasing the heating temperatures.

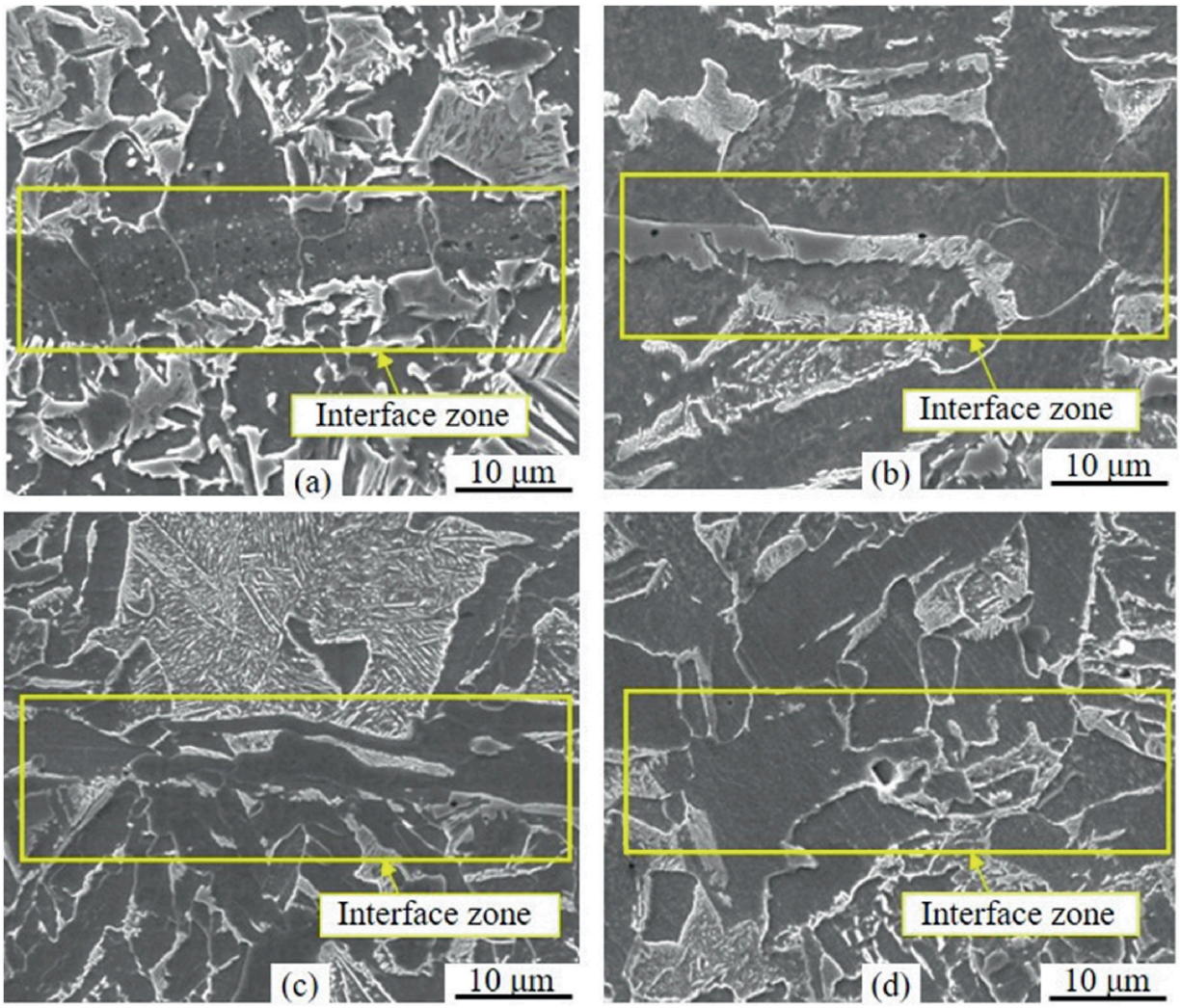


Fig. 2.1 SEM micrographs of interface bonding zone after deformation for various heating temperatures. **a** 1173 K, **b** 1273 K, **c** 1373 K, and **d** 1473 K

The relationship between the number of residual holes and the heating temperature (T_H) is shown in Fig. 2.2. Curve-fitting yields the following equation:

$$y = 5.04 \times 10^{13} \exp(-T_H/42.16) + 1.23 \tag{2.2}$$

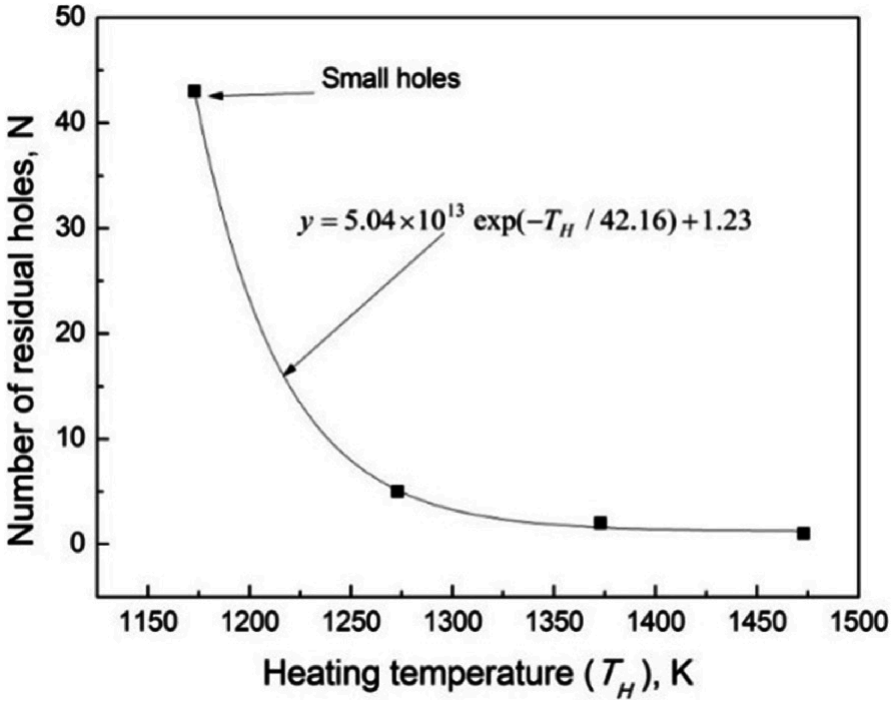


Fig. 2.2 Number of residual holes in the interface bonding zone after deformation as a function of heating temperatures

The deformation resistance of the samples decreases as the heating temperature increases. Thus, the protrusions on the interfaces will deform more easily under compression. When the contact surface increases, the density of residual holes around the interface bonding zone decreases. The relationship between the diffusion coefficient and the heating temperature can be calculated by Arrhenius formula,

$$D = D_0 \exp(-Q/RT) \tag{2.3}$$

where D is the diffusion coefficient, D_0 is the diffusion constant, Q is the molar activation energy of diffusion, R is the universal molar gas constant, and T is the thermodynamic temperature.

With increasing the heating temperature, the atoms on the interfaces can migrate more easily, corresponding to the higher diffusion coefficient. This leads to enhanced interface bonding quality. Simultaneously, the higher the heating temperature is, the more easily the grains around the interface zone grow, which accelerates the migration of defects, and results in narrowing the bonding transitional zone.

2.2.2 Interface Bonding Behavior Affected by Reduction Ratio

Figure 2.3 shows SEM micrographs of the center of the interface bonding zone of specimens after compressive deformation for various reduction ratios. In Fig. 2.3a, the majority of interface zone is still in a disconnected state when the reduction ratio is zero. Although the reduction ratio is set to zero, a very small reduction occurs in the holding process. The temperature around interfaces is not uniform due to the non-uniform thermal resistance in the interface zone with the current power heating. This induces bonding in parts of the interface zone. Bonding is not seen in the other zones because the normal distance between interfaces is too large and the atoms cannot jump directly across the gap. When the reduction ratio is 10%, the bonding area in the interface zone increases, and most parts of interface zones bond together. However, the degree of interface bonding is not high, and a number of large holes can be seen in the interface zone, as shown in Fig. 2.3b. During the compressive deforming, the protrusions on the interfaces come into contact first, which enlarge the contact surface in the bonding zone, so that the interfaces bond due to a combination of atomic diffusion under the stress and thermal gradients. The interfaces do not come into full contact for this reduction ratio, leaving some residual holes. SEM micrographs of the interface bonding zone shown in Fig. 2.3c and d correspond to an increased reduction ratio of 20% and 30% respectively. Here, the hole size decreases significantly compared to that in Fig. 2.3b. It is also seen from Fig. 2.3a–d that the microstructure in the interface bonding transitional zone consists of only ferrite [8]. When the reduction ratio is 40%, it is difficult to detect holes remaining in the interface zone after deformation. But there is still an obvious transitional zone whose microstructure is different from that of the overall matrix. The grain size in the bonding transitional zone is smaller than that of the matrix, as shown in Fig. 2.3e. When the reduction ratio increases to 50%, the grains in the interface bonding zone are similar to those in the matrix, whose microstructure is no longer only ferrite, as shown in Fig. 2.3f.

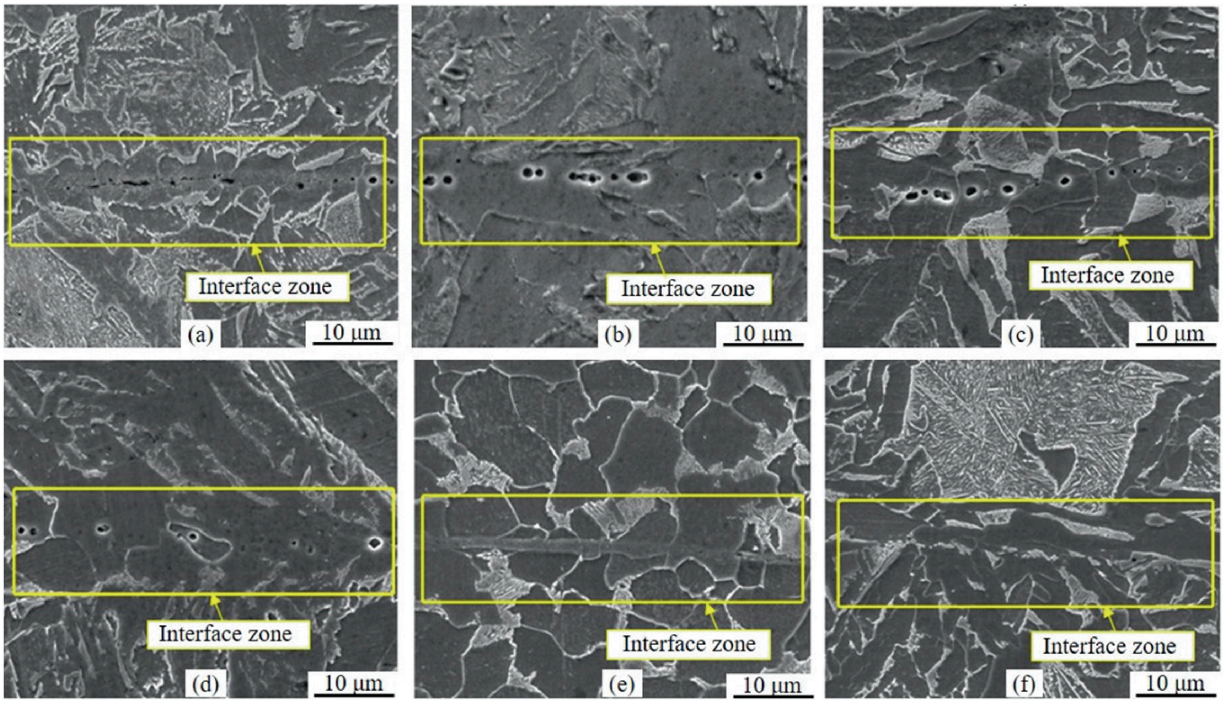


Fig. 2.3 SEM micrographs of interface bonding zone for different reduction ratios. **a** 0%, **b** 10%, **c** 20%, **d** 30%, **e** 40% and **f** 50%

Figure 2.4 shows the relationship between the number of residual holes in the interface bonding zone and reduction ratio (R), which is fitted well by Eq. (2.4).

$$y = 23.07 - 0.88R + 0.01R^2 \tag{2.4}$$

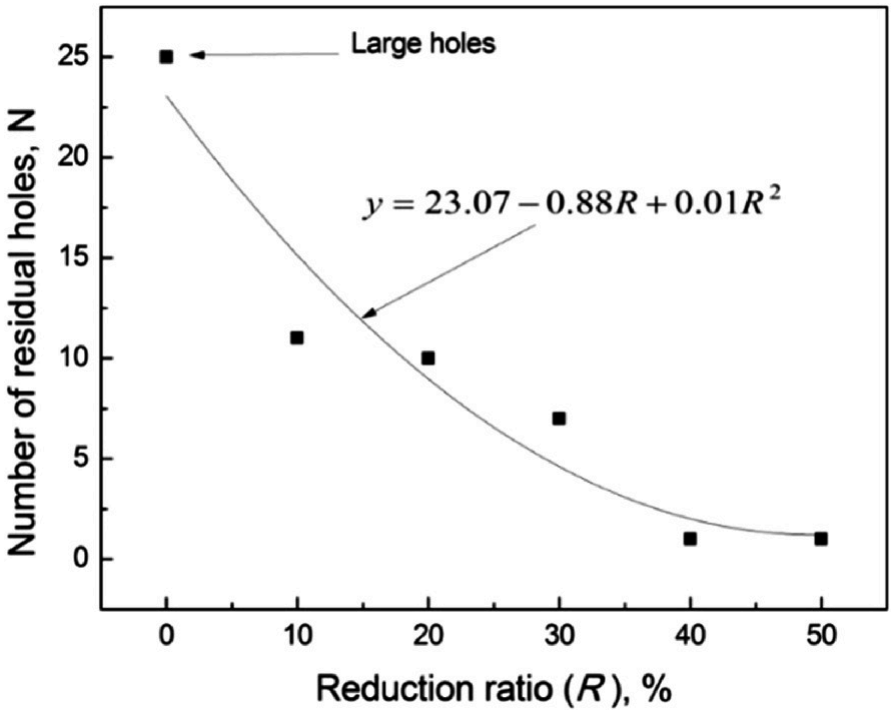


Fig. 2.4 Number of residual holes in the interface bonding zone after deformation as a function of reduction ratios

It is seen that as the reduction ratio increases, the interface bonding degree in the interface zone increases, the interface bonding transitional zone gradually narrows, and the difference in the microstructure between the transitional zone and the matrix also reduces. With greater reduction ratio, the deformation of the protrusions on the interfaces increases, increasing the contact surface. For a given deformation temperature, the diffusion driving force caused by the temperature is unchanged. With increasing deformation, the stress gradient increases, so that the diffusion driving force for atomic diffusion on the interfaces increases. This accelerates the formation of bonds across the interfaces. At the same time, as the reduction ratio increases, the driving force of atomic diffusion also increases, increasing the energy of the lattice distortion.

2.2.3 Interface Bonding Behavior Affected by Deformation Pass Number

Figure 2.5 shows SEM micrographs of the interface bonding zone after compressive deformation for different number of deformation passes, with the total reduction ratio held constant value of 50%. There are

some residual small holes in the interface bonding transitional zone after the fifth deformation pass with 10% reduction per pass. When the number of deformation passes is three (reduction schedule 20 + 20 + 10%), there are still small holes in the interface bonding transitional zone, and the microstructure in the interface bonding transitional zone becomes more uniform in the matrix. When the schedule of the deformation is 30 + 20% (two passes), the holes decrease further in size/number. When the reduction ratio is 50% in one pass, there are very few holes which remain in the interface zone after deformation.

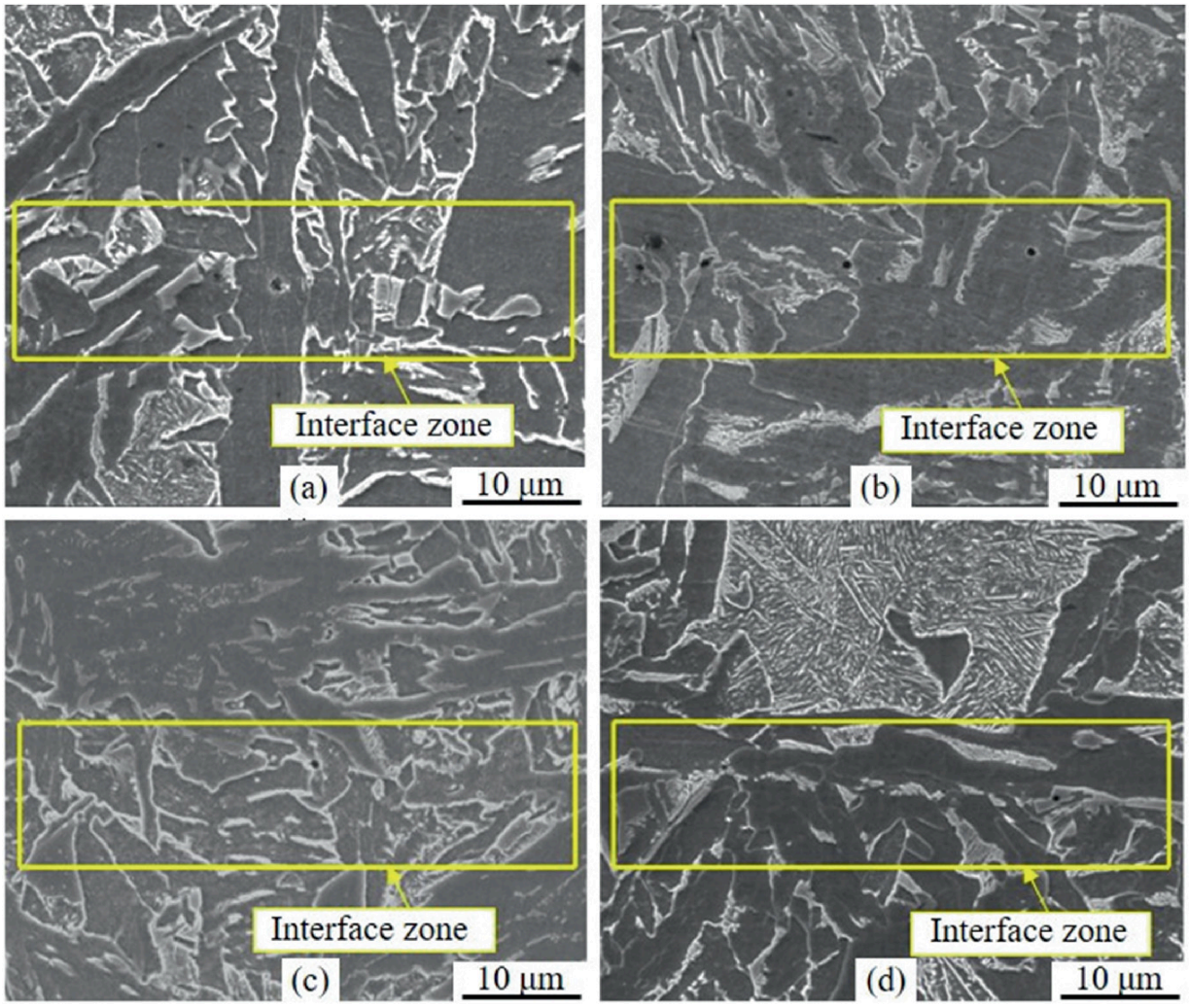


Fig. 2.5 SEM micrographs of interface bonding zone for various deformation passes with identical total reduction ratio. **a** Five passes, **b** Three passes, **c** Two passes, and **d** One pass

It is seen that the number of residual holes in the interface zone after deformation decreases as the number of deformation pass decreases when the total reduction ratio is constant, so that the

interface bonding degree improves. The relationship between the number of residual holes and the number of deformation pass is approximate linear relationship, as shown in Fig. 2.6. For the same total reduction ratio, the deformation in every pass can be specified; as the number of the deformation pass increases, the deformation in every pass decreases. Due to the short-range Van der Waals forces, the deformation in every pass will just occur at the sample surface when the number of deformation pass is large enough. The total deformation reaches the set reduction ratio after multi-pass deformation, and the deformation at the center of sample will be still small, which will result in lots of residual holes in the interface zone, thus the interface bonding degree decreases.

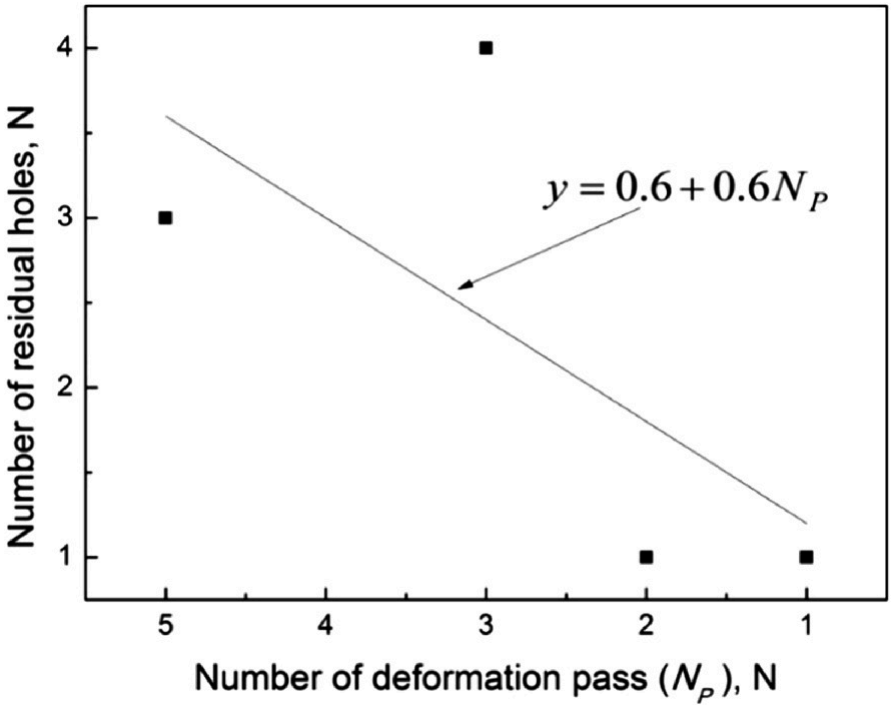


Fig. 2.6 Number of residual holes in the interface bonding zone after deformation as a function of number of deformation passes with the same total reduction ratio constant value

2.2.4 Interface Bonding Behavior Affected by Strain Rate

Figure 2.7 shows SEM micrographs of the interface bonding zone after compressive deformation at various strain rates. When the strain rate is 15 s^{-1}, there are holes which are distributed linearly at the interface zone and the size of holes is large. When the strain rate is 5 s^{-1}, the number of small holes decreases, and interface bonding improves.

When the strain rate is 1 s^{-1}, the interface bonding degree in the interface zone improves further. It is difficult to detect the holes visually in Fig. 2.7c. When the strain rate is 0.01 s^{-1}, the interface bonding degree is the highest, and the transitional zone cannot be visually identified.

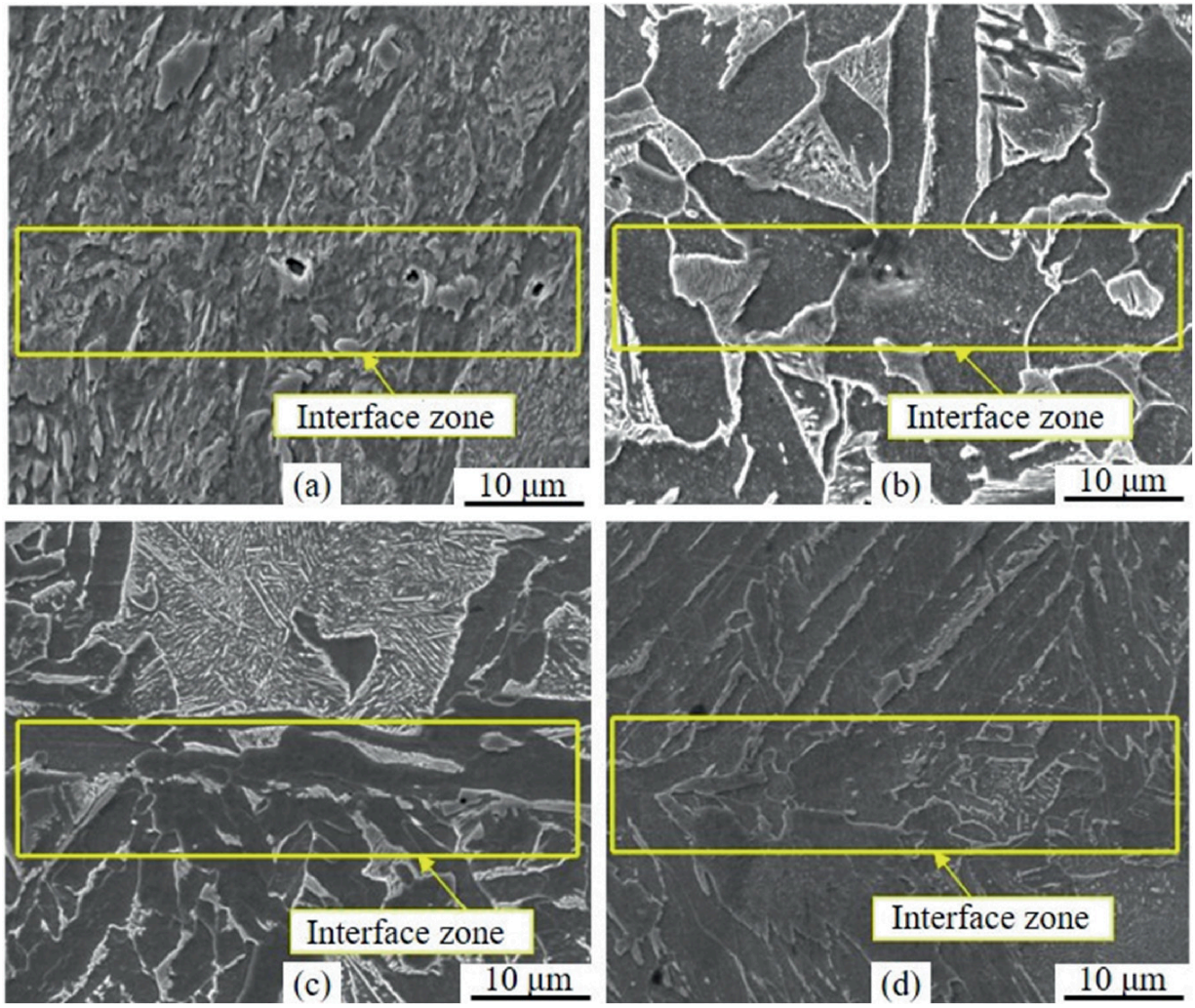


Fig. 2.7 SEM micrographs of interface bonding for various strain rates. **a** 15 s^{-1}, **b** 5 s^{-1}, **c** 1 s^{-1}, and **d** 0.01 s^{-1}

The relationship between the number of residual holes and the strain rate is shown in Fig. 2.8. With decreasing in the strain rate, the number of residual holes in the interface zone obviously decreases, and the interface bonding quality increases. The atomic diffusion coefficient on the interfaces and recrystallization around the interface zone are affected by the strain rate. Elimination of the gap between interfaces is

affected by recrystallization in the interface zone. Firstly, the nucleus deforms, and then the grain grows. With increasing in grain size, the necessary material is moved by diffusion from the matrix. So, a new weak zone might emerge near the interface. If the recrystallization occurs rapidly, and the atoms far away from the interfaces cannot diffuse immediately. So, some holes will remain in the interface zone. As the strain rate increases, the holes increase in size/number and the interface bonding quality decreases. In addition, with increasing strain rate, the holding time for interface bonding will decrease. As seen in the following section, the holding time is one of the main factors influencing interface bonding quality. The shorter the holding time, the less adequate is the atomic diffusion. The average distance between atoms is directly proportional to the square root of diffusion time, as shown in Eq. (2.5):

$$X = K\sqrt{\tau} \tag{2.5}$$

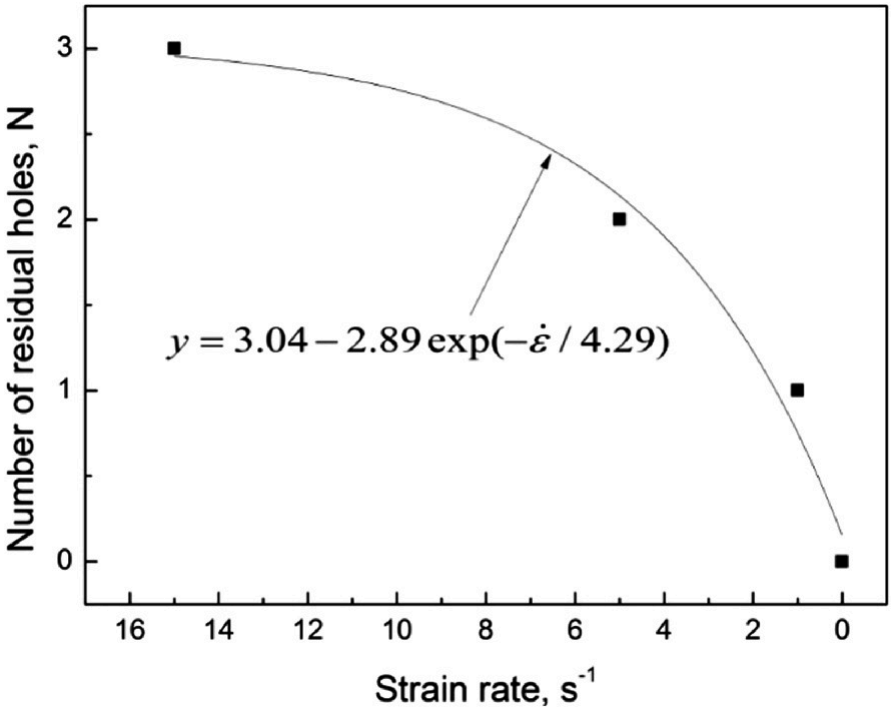


Fig. 2.8 Number of residual holes in the interface bonding zone after deformation as a function of strain rates

where X is the average migration distance of the atomic diffusion (mm); τ is the diffusion time (s); K is the constant related to material

($mm \cdot s^{-1/2}$).

2.2.5 Interface Bonding Behavior Affected by Holding Time

Figure 2.9 shows SEM micrographs of the interface bonding zone after compressive deformation for different holding time durations. When the holding time is 1 min, some residual holes linearly distribute in the interface zone. When the holding time is 5 min, there are new grains formed in the interface zone, but there still is an obvious transitional zone of interface bonding. When the holding time is 10 min, the transitional zone becomes unclear, and the size of the holes decreases. When the holding time reaches 20 min, the grain size in the interface zone is similar to that of the matrix, and the interface bonds quite well. These results show that the interface bonding quality improves with extension of the holding time.

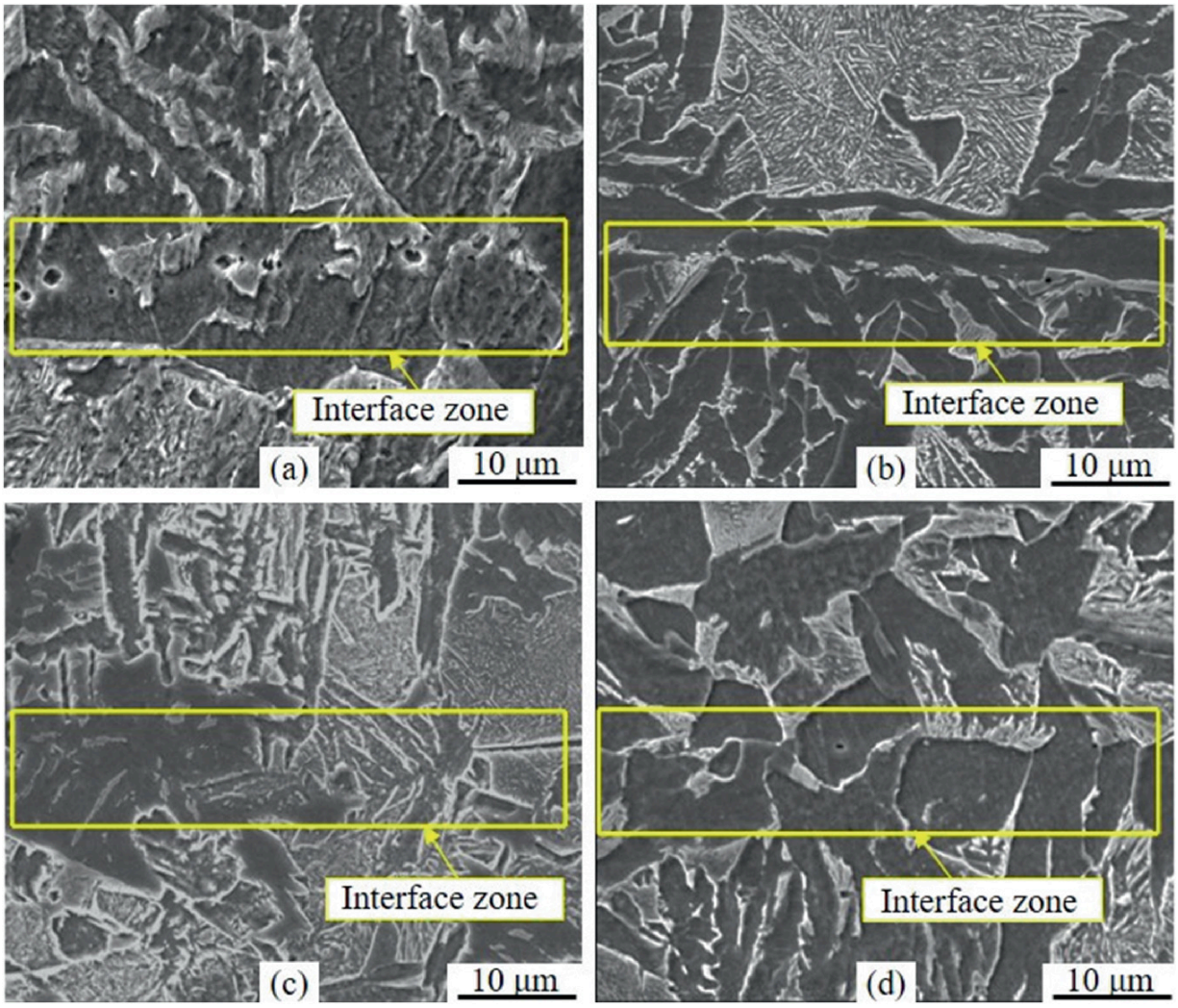


Fig. 2.9 SEM micrographs of interface bonding zone for various holding time durations. **a** 1 min, **b** 5 min, **c** 10 min, and **d** 20 min

Figure 2.10 shows the relationship between the number of residual holes and the holding time. With longer holding time durations, the number of residual holes reduces greatly.

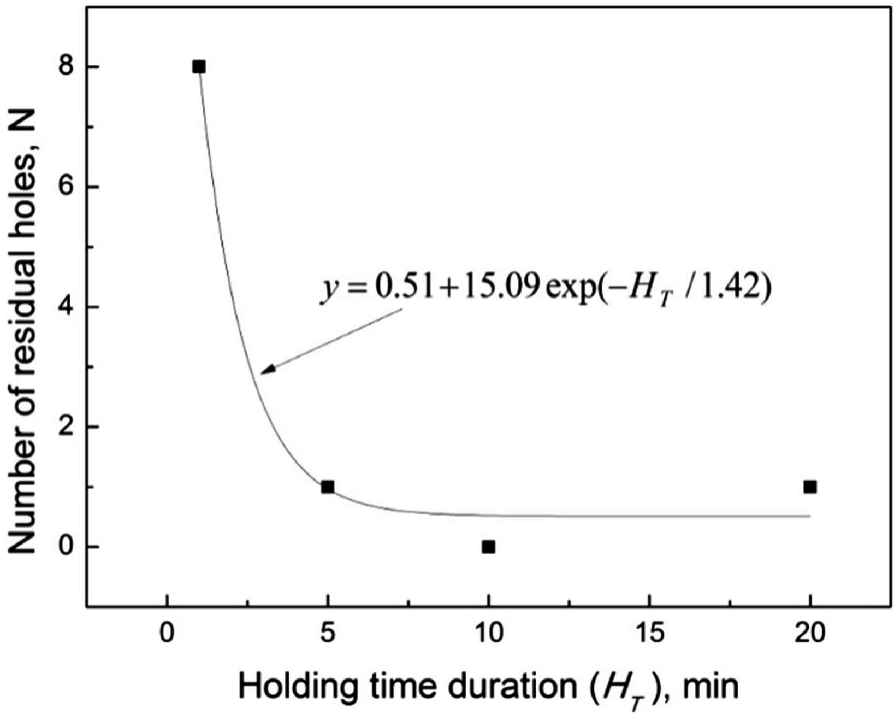


Fig. 2.10 Number of residual holes in the interface bonding zone after deformation as a function of holding time durations

With extension of holding time, there is sufficient opportunity for atomic diffusion to occur around the interface zone, contributing to interface bonding, and uniformity in the microstructure. According to the Fick's second law of diffusion,

$$\frac{\partial C}{\partial t} = D\frac{\partial^2 C}{\partial x^2} \tag{2.6}$$

where, the atomic concentration C is a function of the diffusion distance x and the diffusion time t. The diffusion distance is directly proportional to the square root of the diffusion time, as shown in Eq. (2.6). The holding time plays a key role at the beginning of bonding processes, and its effect gradually decreases with extension of the holding time. As far as its contribution to atomic diffusion is concerned, the effect of holding time is just less than that of heating temperature. The heating time impacts the bonding quality at the beginning and the interfaces can bond completely when the heating time is long enough.

2.3 Shear Strength of Hot-Rolled Laminates

According to the designed shape shown in Fig. 2.11, the samples are machined through the wire-cut machine, which are used for measuring the bonding strength by using the tensile testing machine [9].

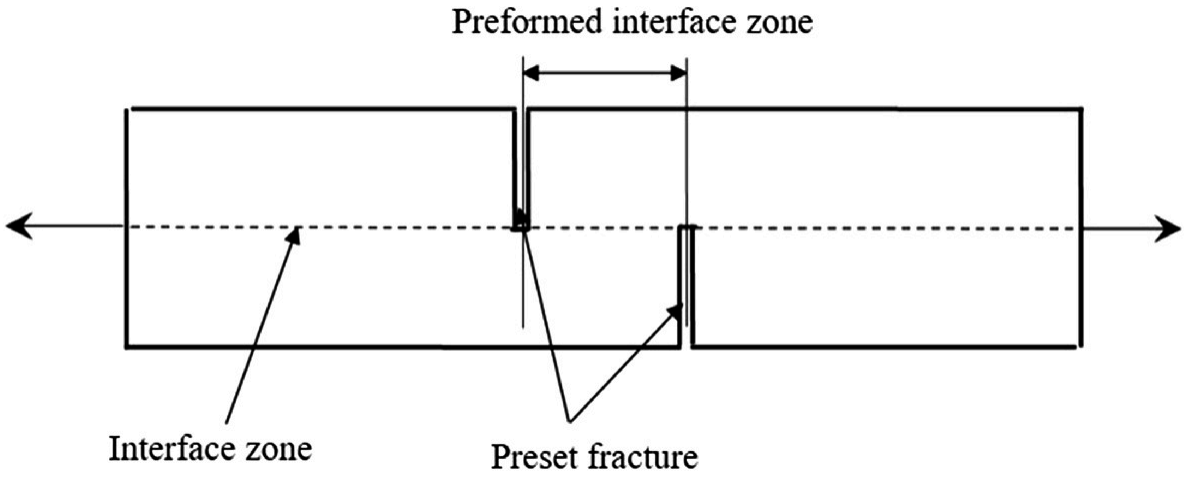


Fig. 2.11 Schematic drawing of tensile sample for measuring bonding strength

Figure 2.12 shows the fracture form of the samples. For the samples subjected to 5% reduction ratio, the sample fractures along the bonding interface, as shown in Fig. 2.12a; for the samples subjected to the 50% reduction ratio (Fig. 2.12b), the sample fractures along the sample matrix, which means that the strength of bonding zone approximately equals that of the matrix and the bonding is quite well.

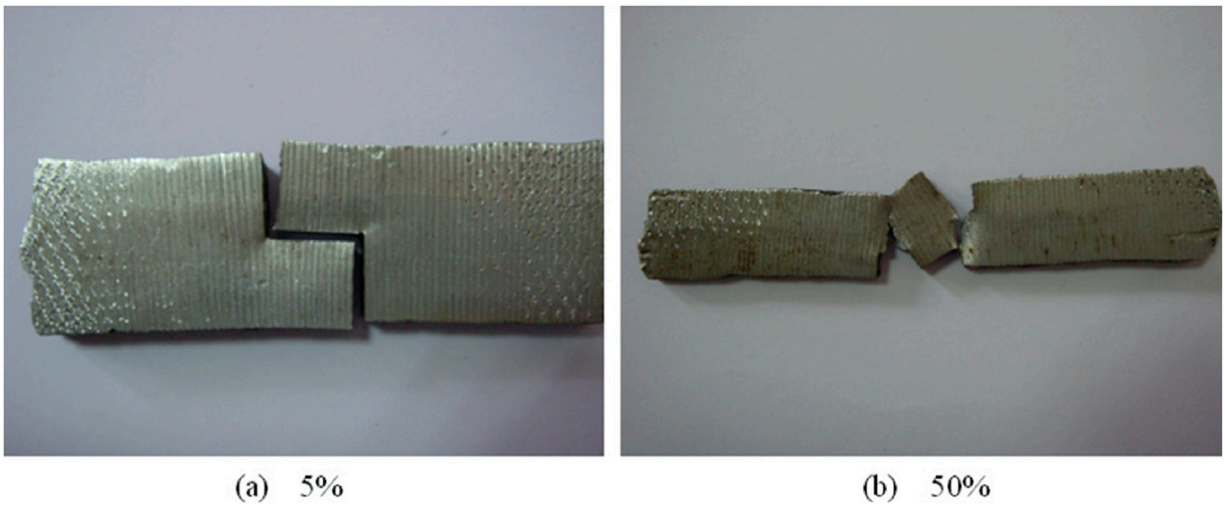


Fig. 2.12 Tensile fracture of roll bonded samples

Figure 2.13 shows the curve of load versus displacement during stretching. When the reduction ratio is 5%, the maximum extension of length is 1 mm, and the maximum tension is 100 MPa. When the reduction ratio reaches 50%, the maximum extension of length is 5 mm, and the maximum tension reaches 240 MPa. In order to compare the effects of rolling reduction ratio on bonding quality, the maximum shear strength is employed in the following, which equals the maximum tension versus the area of preformed bonding zone.

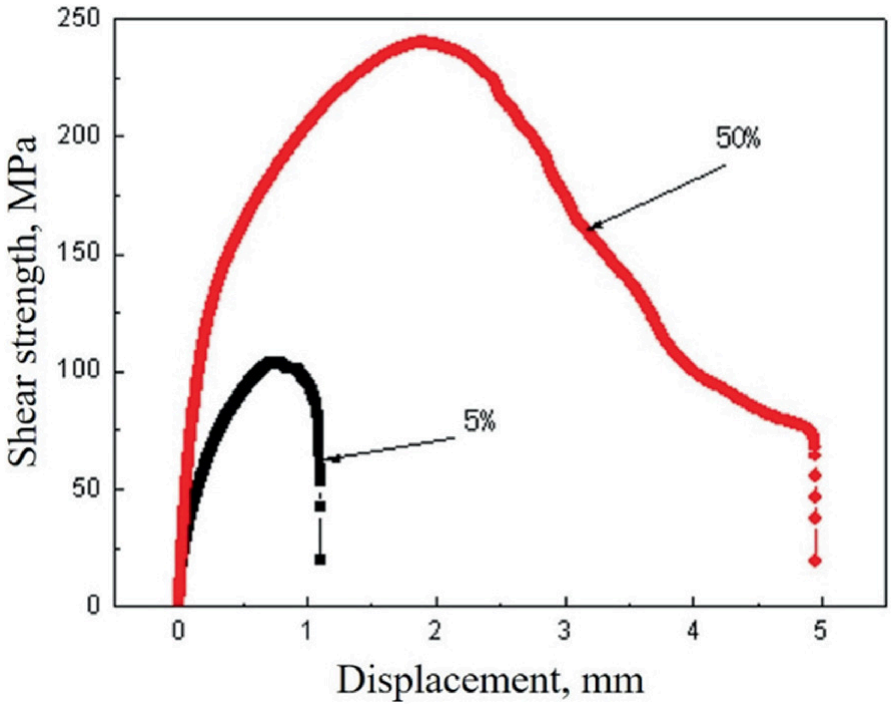


Fig. 2.13 Curve of load to dislocation during stretching

Figure 2.14 shows the shear strength of the preset bonding zone after hot rolling under a variety of reduction ratios. When the reduction ratio is less than 10%, the shear strength of bonding zone linearly increases from 0 to 160 MPa with increasing the rolling reduction ratios. As the reduction ratio further increases, the shear strength of the bonding zone also gradually increases, but the amplification gradually decreases. When the reduction ratio reaches 40%, the shear strength of bonding zone reaches 200 MPa. In Fig. 2.14, when the reduction ratio is 50%, the samples break along the matrix and the tensional stress reaches 240 MPa, the strength of slab matrix. Equation (2.7) can be

used to calculate the shear strength of bonding surface under a variety of reduction ratios during rolling.

$$\sigma_{\mathrm{T}} = -0.45179 + 28.01148\varepsilon - 1.60209\ \varepsilon^2 + 0.04544\varepsilon^3 - 6.55158 \times 10^{-4}\ \varepsilon^4 + 4.0331 \times 10^{-6}\varepsilon^5 \tag{2.7}$$

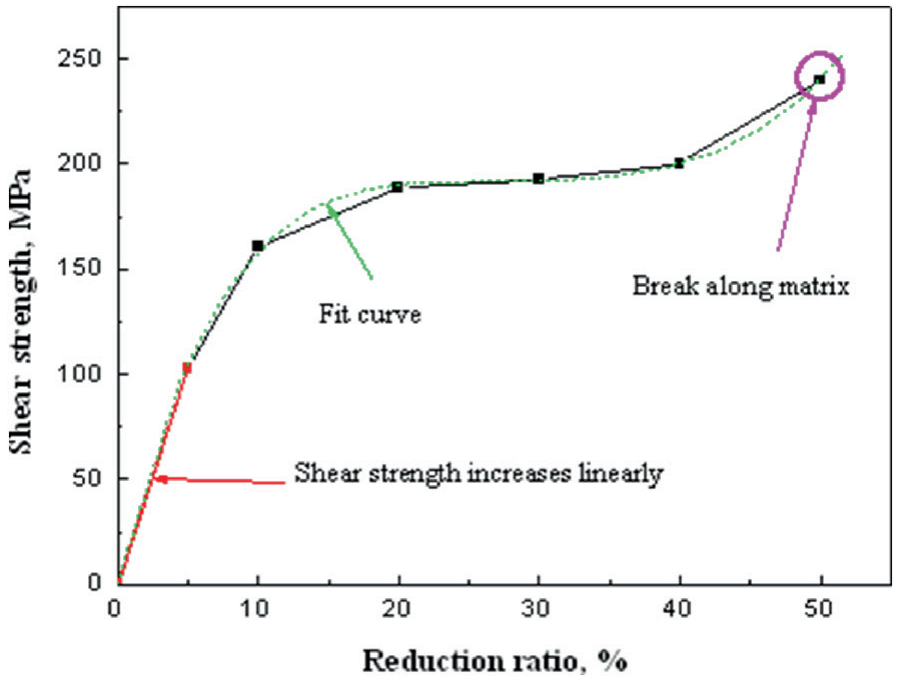


Fig. 2.14 Shear strength of bonding zones for various reduction ratios

where, σ_{T} is the shear strength, ε is the reduction ratio.

Figure 2.15 shows the fracture morphology of bonding zones under various reduction ratios during hot roll bonding, where the reduction ratio in (a)–(f) is 5%, 10%, 20%, 30%, 40% and 50% separately. When the reduction ratio is 5%, in the whole view of fracture surface, a small number of zones are dimple fracture which means that these zones can achieve good bonding, but most zones are cleavage fracture where the interface does not bond well (Fig. 2.15a). When the reduction ratio is 10%, the dimple fracture zone increases clearly (Fig. 2.15b) and this means that the bonding quality increases. When the reduction ratio reaches 20–30%, as the reduction ratio further increases, the size and the number of dimple fracture zones increase greatly (Fig. 2.15c and d). However, the dimple fracture zones do not connect with each other. When the reduction ratio is 40%, the fracture type of samples is

completely dimpling fracture (Fig. 2.15e), which implies the interface bonding excellent, which is similar to that in Fig. 2.15f, which fractures along the sample matrix.

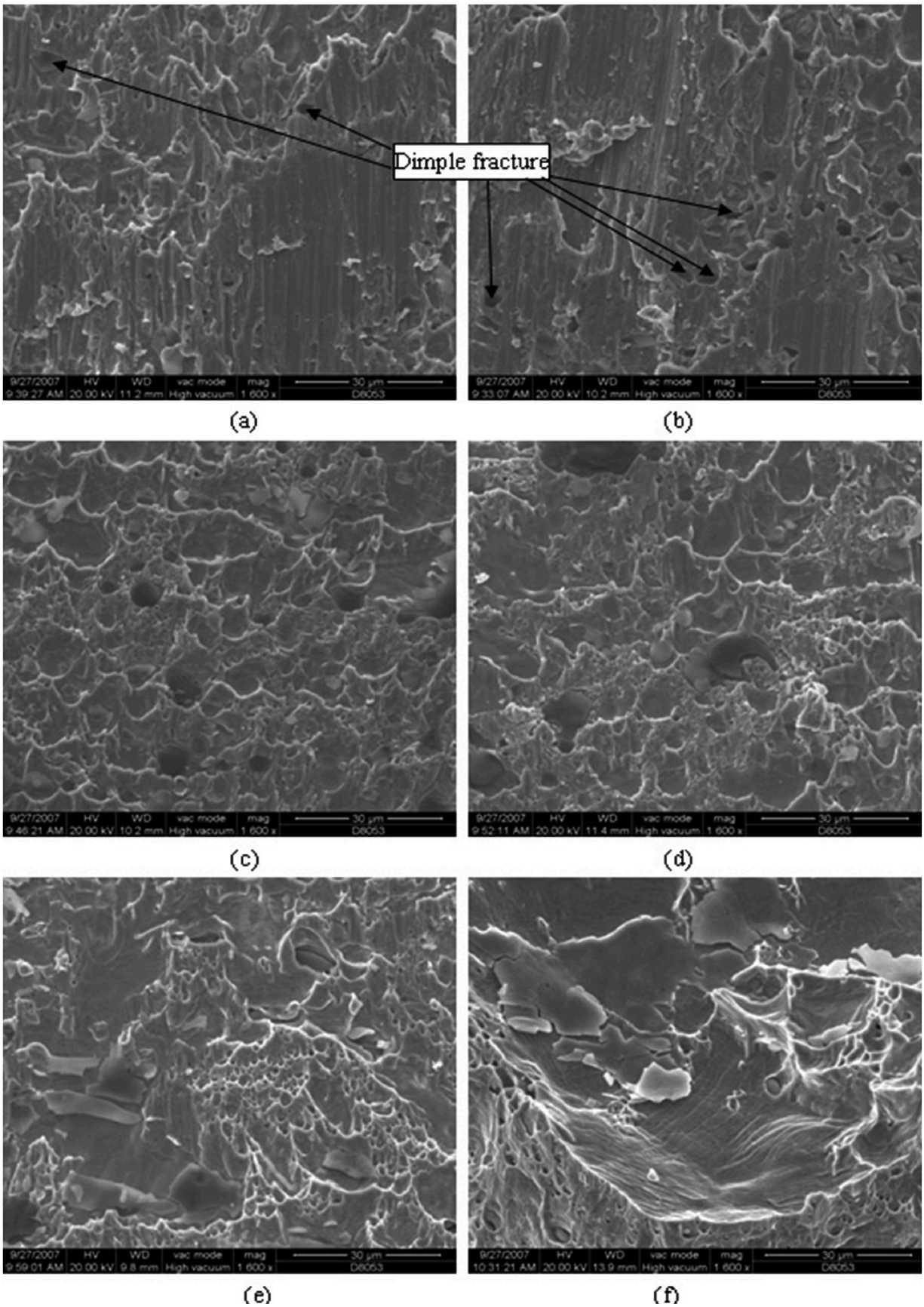

Dimple fracture
(a)
(b)
(c)
(d)
(e)
(f)

Fig. 2.15 Fracture morphology of bonding zones under the reduction ratio of **a** 5%, **b** 10%, **c** 20%, **d** 30%, **e** 40%, and **f** 50% during hot roll bonding

2.4 Interface Bonding Mechanism of Laminates During Hot Roll Bonding

The recrystallization in the ferrite and the grain growth during the process of interface bonding are shown schematically in Fig. 2.16 [10]. In the process of hot roll bonding, high temperature combined with severe plastic deformation can induce interface bonding. At high temperature, recrystallization can occur at the free interfaces, as shown in Fig. 2.16a. With increasing the energy input by severe plastic deformation, an uneven distribution of energy on the interface can lead to different deformation intensity on the interfaces. Tiny grains will appear and grow towards the gap, resulting in shrinking the gap gradually, shown in Fig. 2.16b. Usually, surfaces in materials are uneven and the convex surfaces come into contact firstly. In other words, interface bonding is initiated at such points of contact. The interfaces can only be partially joined or welded to reach the threshold of atomic interactions under the rolling pressure, the remaining regions can be bonded through the atomic movement, as shown in Fig. 2.16c. Thus, the original long interface is divided into several discontinuous shorter holes. When the atoms on both sides of interfaces come within the range of atomic interactions, intermittent partial interface bonding will take place, and the interface bonding area appears as a distribution of porosity defects, as shown in Fig. 2.16d. The existence of interface can increase the system energy, leaving the system in an unstable state. However, new grain nucleation and growth can utilize this excess energy. New grains will form around these gaps. The new grains nucleate and grow or near the defect free surface during slow cooling which can be called the repair recrystallization, and then the bonding area extends. Tiny grains, which appear in local bonding areas, whose growth regions will continue to grow until their sizes are close to matrix grains, shown in Fig. 2.16e.

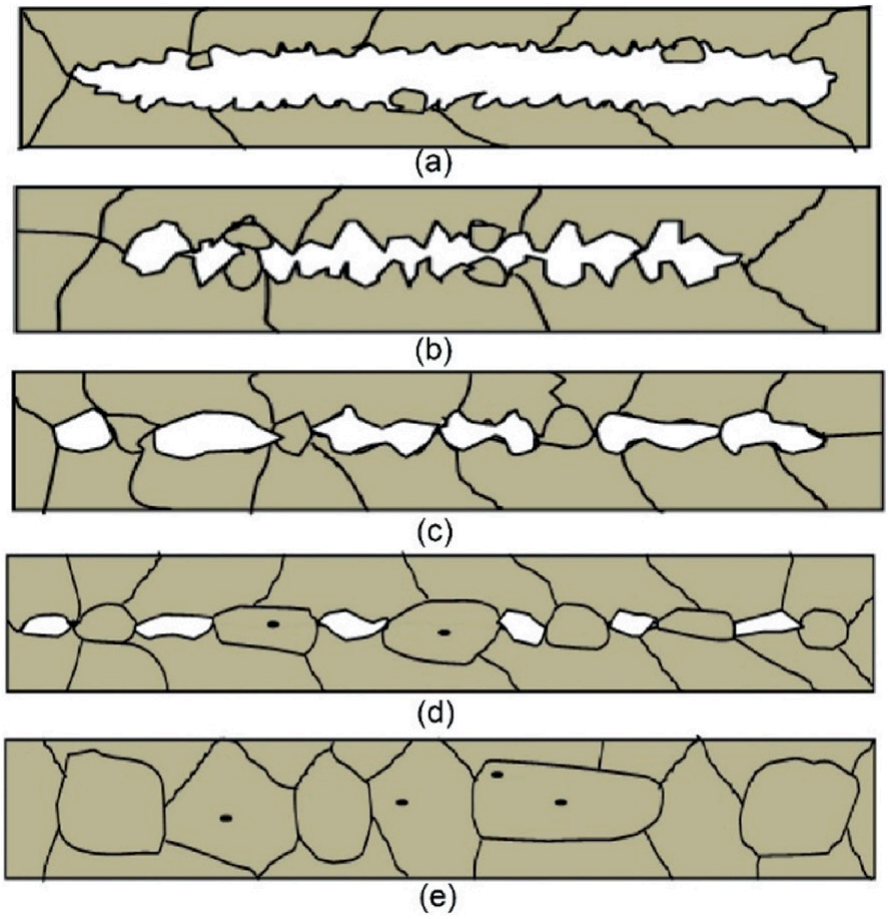


Fig. 2.16 Interface bonding mechanism of laminates subject hot roll bonding

2.5 Cu/Al Laminates with Thin SUS304 Interlayer via Hot Roll Bonding

Cu/Al/Cu laminates with thin SUS304 interlayer of 30 μm were fabricated by hot roll bonding. The T2 Cu and AA1060 sheets were used as start materials. The Cu and Al sheets were annealed at 873 K and 673 K for 2 h respectively to obtain a fully homogeneous coarse grain structure, and then cut into a same size of 100 × 50 × 1 mm. Before roll bonding, the Cu and Al sheets were wire brushed to remove the surface oxide layer and contamination. Then the Cu, Al and SUS304 sheets were stacked together and fixed by aluminum rivets. The stacked sheets were preheated at 723 K for 1 min and then rolled at a speed of 1 m/min. Table 2.1 illustrates roll bonded Cu/Al/Cu clad sheets under different condition.

Table 2.1 Illustration of roll bonded Cu/Al/Cu clad sheets

Sample (%)	Rolling reduction (%)	Condition
W-50	50	With SUS304 interlayer
W-70	70	With SUS304 interlayer
W-80	80	With SUS304 interlayer
WO-50	50	Without interlayer
WO-70	70	Without interlayer
WO-80	80	Without interlayer

The ordinary laminate rolling bonding is an effective and efficient process to manufact large volume laminates continuously, which also avoid the additional welding process. In this study, the SUS304 interlayer was introduced in Cu/Al/Cu laminates by using rolling bonding. The peeling strength, morphologies of peeling surface, element diffusions and microstructure were examined, then the enhancement mechanism of SUS304 interlayer on the interfacial bonding strength of Cu/Al laminates was systematically discussed by combining the regulation of IMCs, mechanical joggle and shear deformation [11].

Figure 2.17 displays the peeling strength of Cu/Al/Cu laminates with or without SUS304 interlayer subjected to different rolling reduction. The peeling strength increased with the rolling reduction. When the rolling reduction was relatively low of 50%, both W-50% and WO-50% presented the same trend that peeling strength was almost parallel to the X-axis at value close to 0, which meant the dissimilar metals were not bonded well. When the rolling reduction increased to 70%, the peeling strength curves of W-70% and WO-70% became totally different. The peeling strength of WO-70% kept the origin trend and had a slight improvement to 2.9 N/mm, whereas, the peeling strength of W-70% presented a peak-valley shape. The peak value of peeling strength of W-70% was about 15.5 N/mm, which was 5 times higher than that of WO-70%. The valley value of peeling strength of W-70% was about 4.1 N/mm, which was comparative with that of WO-70%. When rolling reduction further increased to 80%, the peeling strength curves of WO-80% increased to 8.3 N/mm. The peak value and valley value of peeling strength W-80% increased to 17.8 N/mm and 4.8 N/mm respectively.

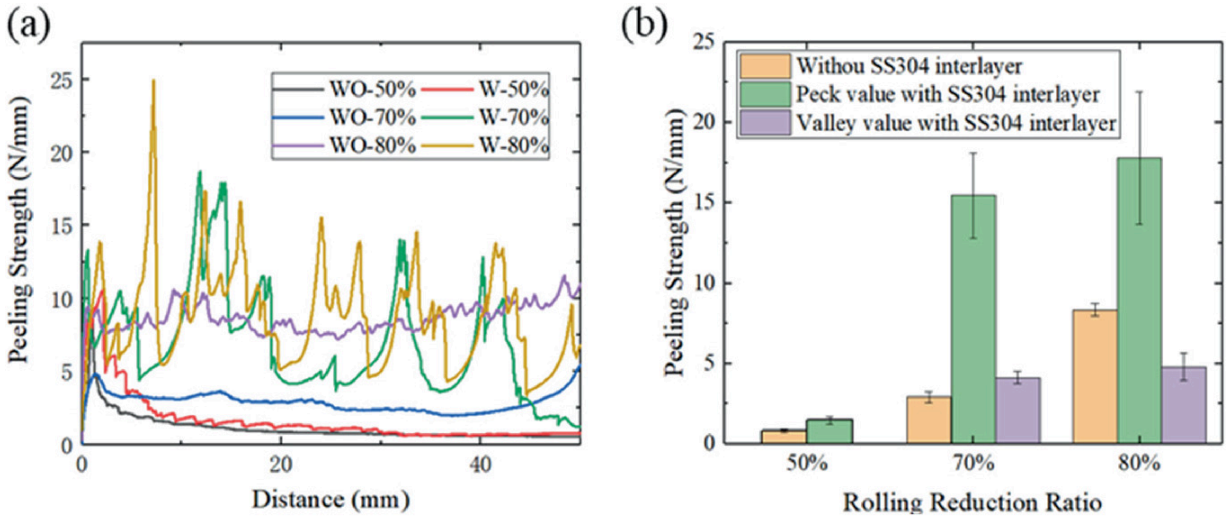


Fig. 2.17 **a** Peeling strength of Cu/Al/Cu laminates with or without SUS304 interlayer subjected to different rolling reduction; **b** Peeling strength versus the rolling reduction ratio

Figure 2.18a–c show the OM images of Cu/Al/Cu laminates without SUS304 interlayer in RD-ND plane. Obviously, a straight and continuous interface was formed in the roll cladding process. With the increasing in the rolling reduction, no cracks or voids were detected. Figure 2.18d–f show the OM images of Cu/Al/Cu laminates with SUS304 interlayer in RD-ND plane. During roll bonding, the SUS304 foil cracked into small fragments, embedded in the Cu/Al matrix and distributed discretely in the Cu/Al interface, due to the limited deformability of the SUS304 foil.

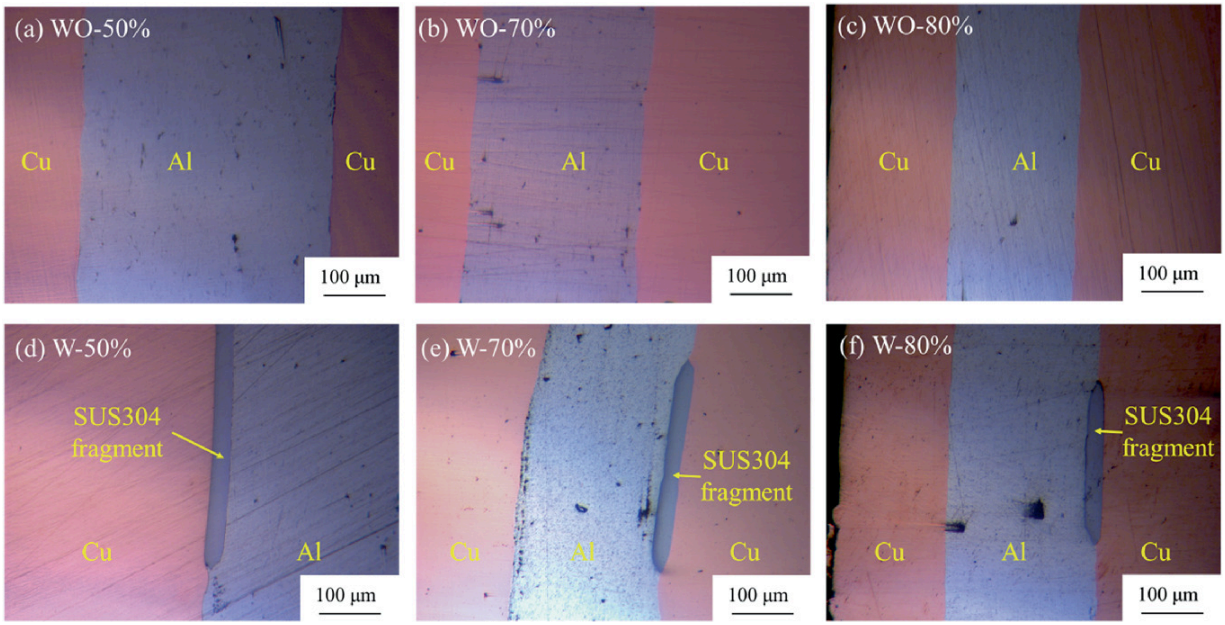


Fig. 2.18 OM images of Cu/Al/Cu laminates in RD-ND plane

The thickness variation of SUS304 interlayer under different rolling reduction is illustrated in Fig. 2.19a. There is an inflection point of SUS304 interlayer thickness curve, and then the interlayer thickness is linearly dependent on rolling reduction approximately. In the beginning stage, the interlayer thickness only reduced a little, which did not elevate the peeling strength of Cu/Al/Cu laminates effectively. This result was also reflected in Fig. 2.17a. When the rolling reduction accessed 70% and 80%, the interlayer thickness reduced to 22.8 mm and 19.5 mm respectively. The mismatching deformability of dissimilar metals caused shear deformation in Cu/Al interface, causing SUS304 interlayer necking and cracking. The degree of shear band angle both near Cu side (φ_1) and Al side (φ_2) decreased while the rolling reduction increased (Fig. 2.19b). The φ_1 decreased from 25.8 to 16.9° and 15.7° and the φ_2 decreased from 32.8 to 22.9° and 16.5° when rolling reduction increased from 50 to 70% and 80%. The decrement of φ_1 and φ_2 indicated that SUS304 subjected severe deformation. It's also notable that the difference between φ_1 and φ_2 decreased, which indicated uniformity of deformation increased.

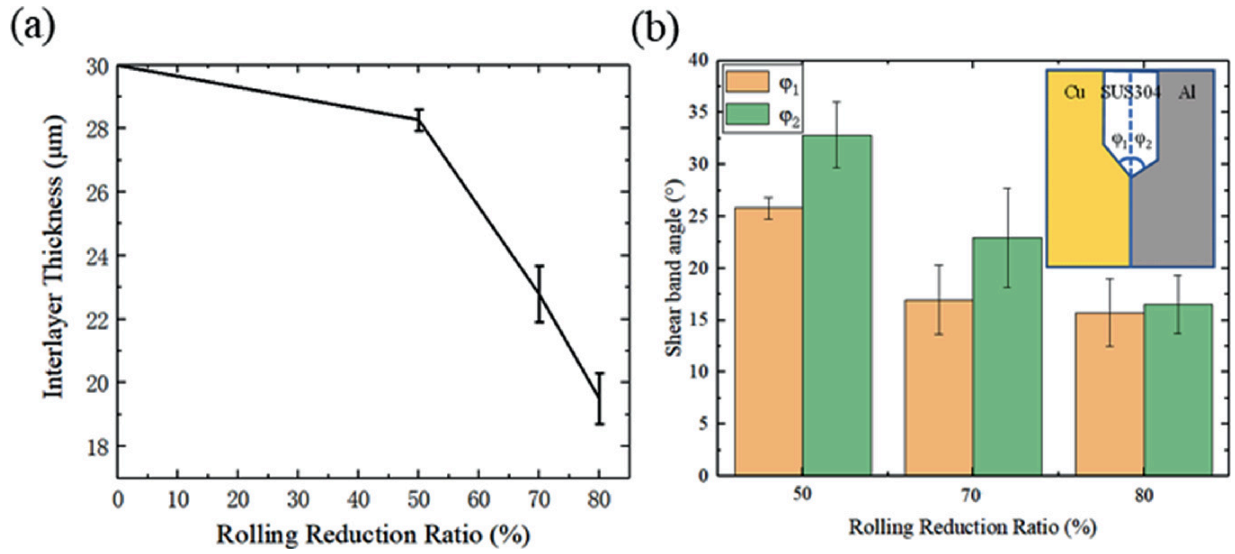
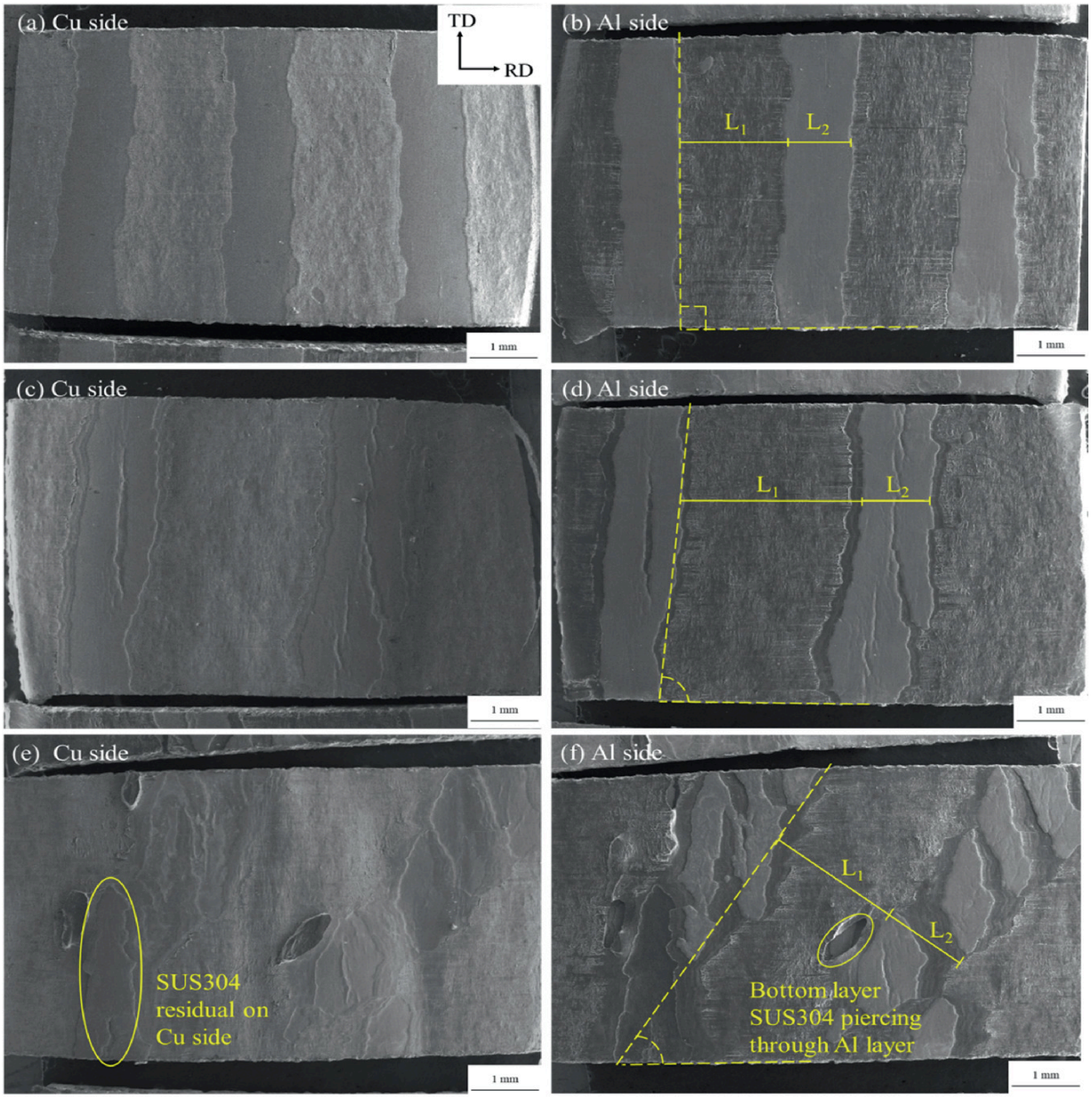


Fig. 2.19 **a** Interlayer thickness-rolling reduction ratio curve; **b** Shear band angle-rolling reduction ratio curves, the insert picture illustrates the shear band angle near Cu side and Al side

Figure 2.20 gives the peeling surface of Cu/Al/Cu laminates with SUS304 interlayer after 50, 70 and 80% rolling reduction. The SUS304

cracked perpendicular along the rolling direction at beginning, and the degree between SUS304 fragments and rolling direction (φ_1 and φ_2) decreased with the increasement of rolling reduction. The mean distance between adjacent SUS304 fragments increased from 1.54 to 2.59 mm, 2.31 mm and the mean length of SUS304 fragments increased from 0.91 to 1.03 mm, 1.32 mm, when rolling reduction increased from 50 to 70% and 80% respectively (Fig. 2.20g). There were only few cracks detected near the edge of SUS304 fragments when rolling reduction was 50%, while internal cracks were detected when rolling reduction increased to 70%. The Cu/Al matrix were extruded into these crack regions and caused local strain concentration, which changed the degree between SUS304 fragments and rolling direction. When rolling reduction further increased to 80%, SUS304 fragments broken up again and turned into small blocks. Besides, the combination of thickness reduction of Al layer, elevated bonding strength and local strain caused the bottom layer SUS304 piercing through Al layer and some SUS304 residual remaining on Cu side.


(a) Cu side
TD
RD
1 mm
(b) Al side
L1
L2
1 mm
(c) Cu side
1 mm
(d) Al side
L1
L2
1 mm
(e) Cu side
SUS304
residual on
Cu side
1 mm
(f) Al side
L1
L2
Bottom layer
SUS304 piercing
through Al layer
1 mm

(g)

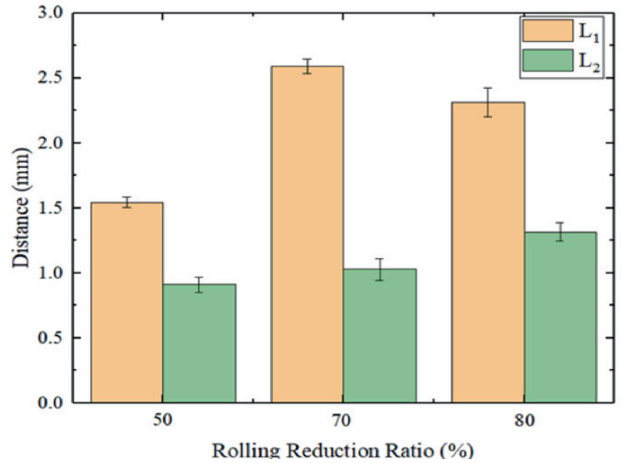

3.0
2.5
2.0
1.5
1.0
0.5
0.0
Distance (mm)
L1
L2
50
70
80
Rolling Reduction Ratio (%)

Fig. 2.20 Peeling surface of **a**, **b** W-50%, **c**, **d** W-70% and **e**, **f** W-80% samples; **g** Space and length of SUS304 interlayer versus rolling reduction ratio

In order to reveal the corresponding relationship between peeling strength curve and peeling surface, the videos were taken with the peeling strength experiment simultaneously. As shown in Fig. 2.21a–c, the peak value of W-70% sample corresponded to the area near the edge of SUS304 fragments, while the valley value of W-70% samples corresponded to the Cu/Al direct bonding area. For the samples subjected to 80% rolling reduction, it's hard to tell a distinct difference of corresponding area between peak value and valley value because of the size and distribution of small SUS304 blocks (Fig. 2.21d–f). When peeling strength reached peak values, less Cu/Al direct bonding area exposed in the split line comparing with valley values, which revealed the similar relationship with W-70% sample.

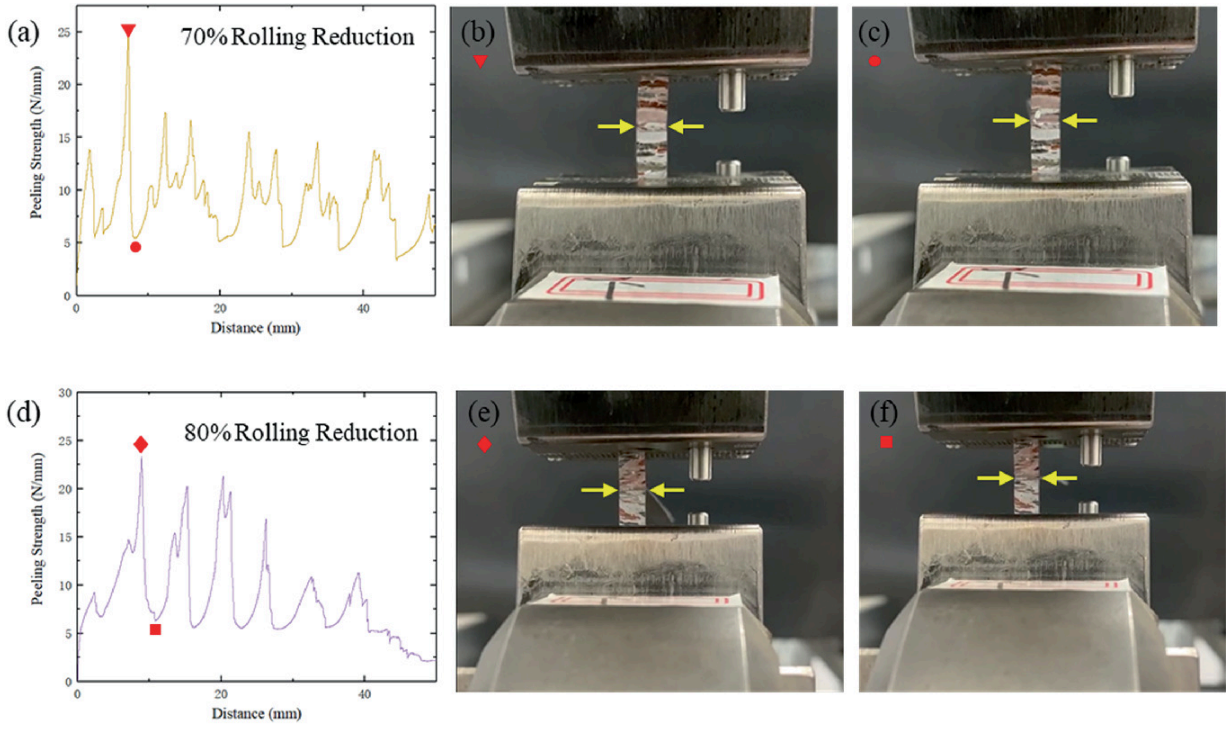


Fig. 2.21 The corresponding relationship between peeling strength curve and peeling surface; **a** The peeling strength curve of W-70% sample; corresponding photos of **b** peak value and **c** valley value of peeling strength marked in (**a**); **d** The peeling strength curve of W-80% sample; corresponding photo of **e** peak value and **f** valley value of peeling strength marked in (**d**). The arrow marked in (**b**, **c**, **e**, **f**) pointed the split line of Cu and Al layers

Figure 2.22 presents the local morphologies of peeling surface of W-50% samples. In the Cu side, a bulge rectangle in Fig. 2.22a divided the image into two parts, the left part is SUS304 fragments edge area and the right part is SUS304 interlayer contacted area. The SUS304 fragments edge area contained large amounts of ridges (point A) and some chips (point B). The corresponding backscattered electron image and EDS results show that the ridges were mainly formed by the strong bonding of Cu/Al and the chips are formed by the weak bonding of Cu/Al where Cu matrix were pressed by Al layer. However, the SUS304 interlayer contacted area was flat and only few slit-like ridges were detected within this area, which was mainly caused by the crack of SUS304 that also illustrated in Fig. 2.20b. In the Al side, the morphology of peeling surface was similar with that in the Cu side. The SUS304 fragments were embedded in Al matrix and some Cu residual remained near Al ridges.

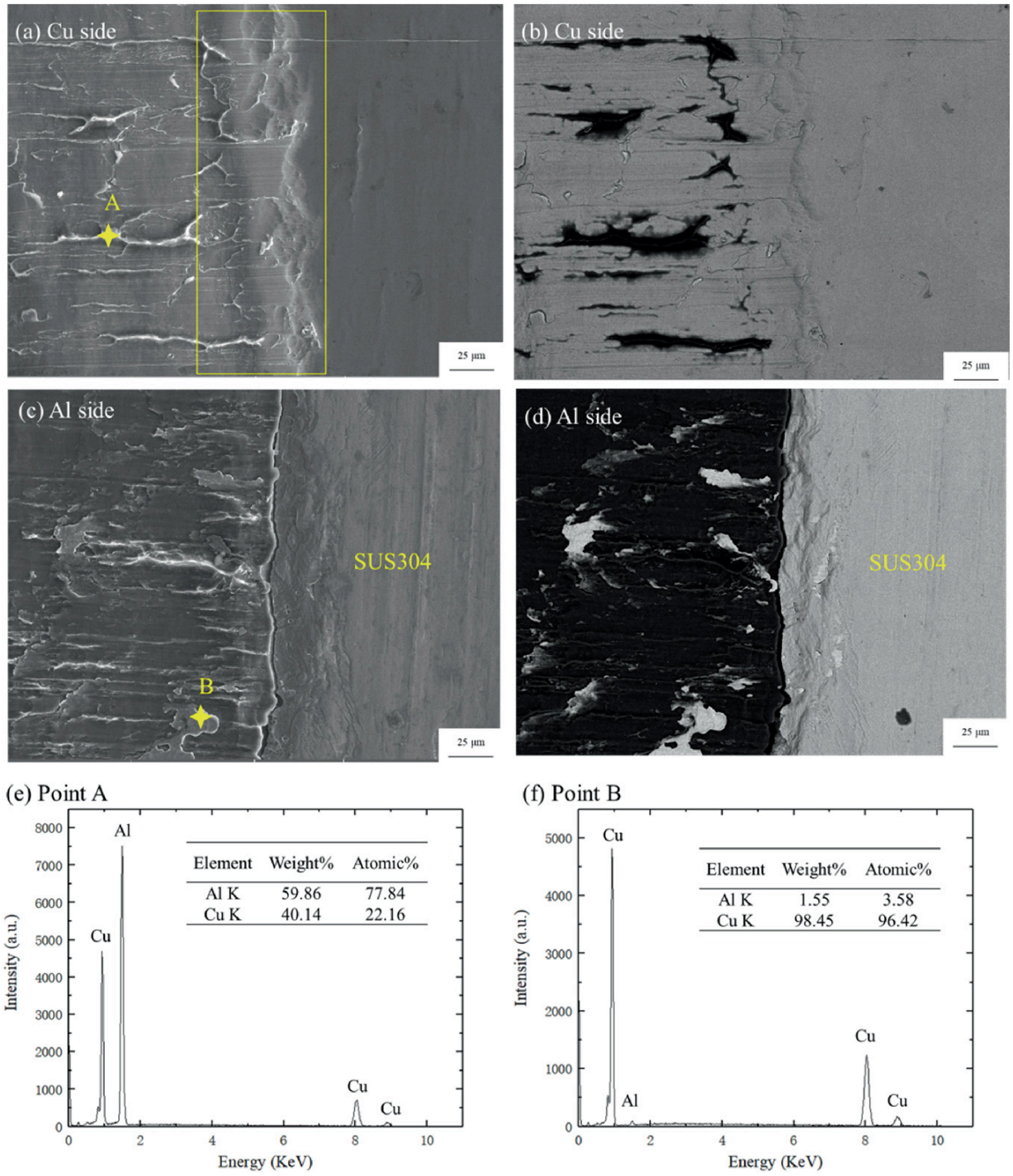


Fig. 2.22 Peeling surface of W-50% samples. **a** Cu side near the edge of SUS304 fragments and **b** corresponding backscattered electron image; **c** Al side near the edge of SUS304 fragments and **d** corresponding backscattered electron image; **e**, **f** EDS results of point A and B marked in (**a**) and (**c**)

Figure 2.23 shows the local morphologies of peeling surface of W-70% samples. The Cu/Al direct contacted area in the Cu side is shown in Fig. 2.23a. Many ridges were detected which indicated the improved

valley value of peeling strength. The bulge was also found near the edge of SUS304 fragment in the Cu side, indicating the SUS304 fragments restricted the plastic deformation of Cu layer and the local strain concentrated, which further enhanced the bonding effect. In the Al side, the ridges became denser and some dimples were detected, indicating the well bonded interface. The flat area closed to SUS304 fragments was the gap between SUS304 fragments and Cu/Al bonded area, indicating the SUS304 fragments were already embedded in Al matrix deeply, thus improved the mechanical joggle. The higher rolling reduction caused higher rolling pressure and surface expansion, thus more interface microcracks formation and bonding area, benefiting the increasement of bonding strength. Naseri et al. [12] pointed out that the number of cracks on the surface layers increases with the amount of plastic deformation, providing further channels for virgin metals to be exposed.

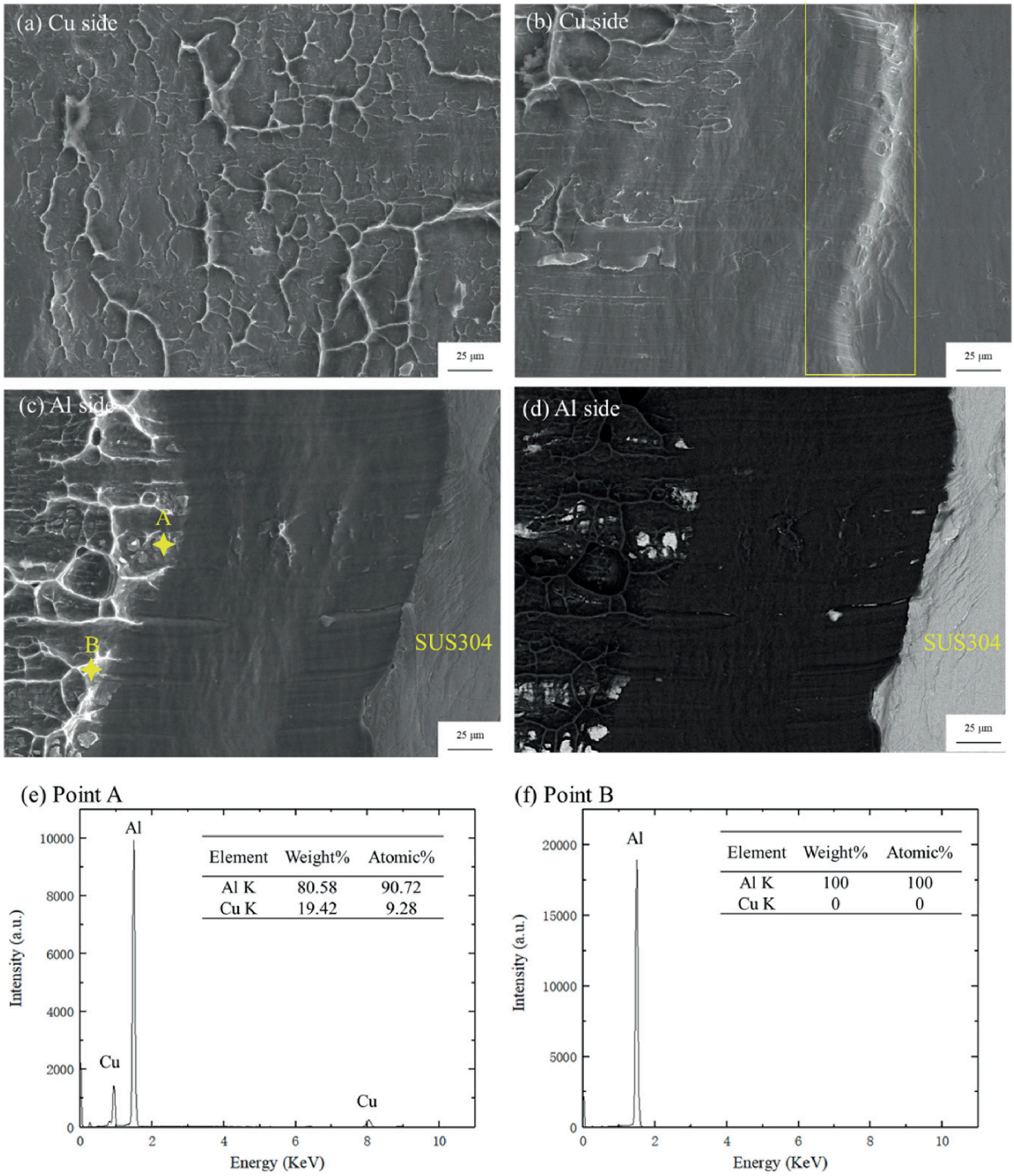


Fig. 2.23 Peeling surface of W-70% samples; **a** Cu side near Cu/Al direct bonding area; **b** Cu side near the edge of SUS304 fragments; **c** Al side near the edge of SUS304 fragments and **d** corresponding backscattered electron image; **e**, **f** EDS results of point A and B marked in (**c**)

Figure 2.24 displays the local morphologies of peeling surface of W-80% samples. The obvious difference of morphology of peeling surface was that blocky Al remained on the Cu surface after the peeling test,

comparing with that after 50% and 70% rolling reduction. The backscattered electron image (Fig. 2.24b) shows the dense Al ridges distributed near Al residual block, indicating tight bonding was formed, which conformed to the peeling strength results in Fig. 2.17.

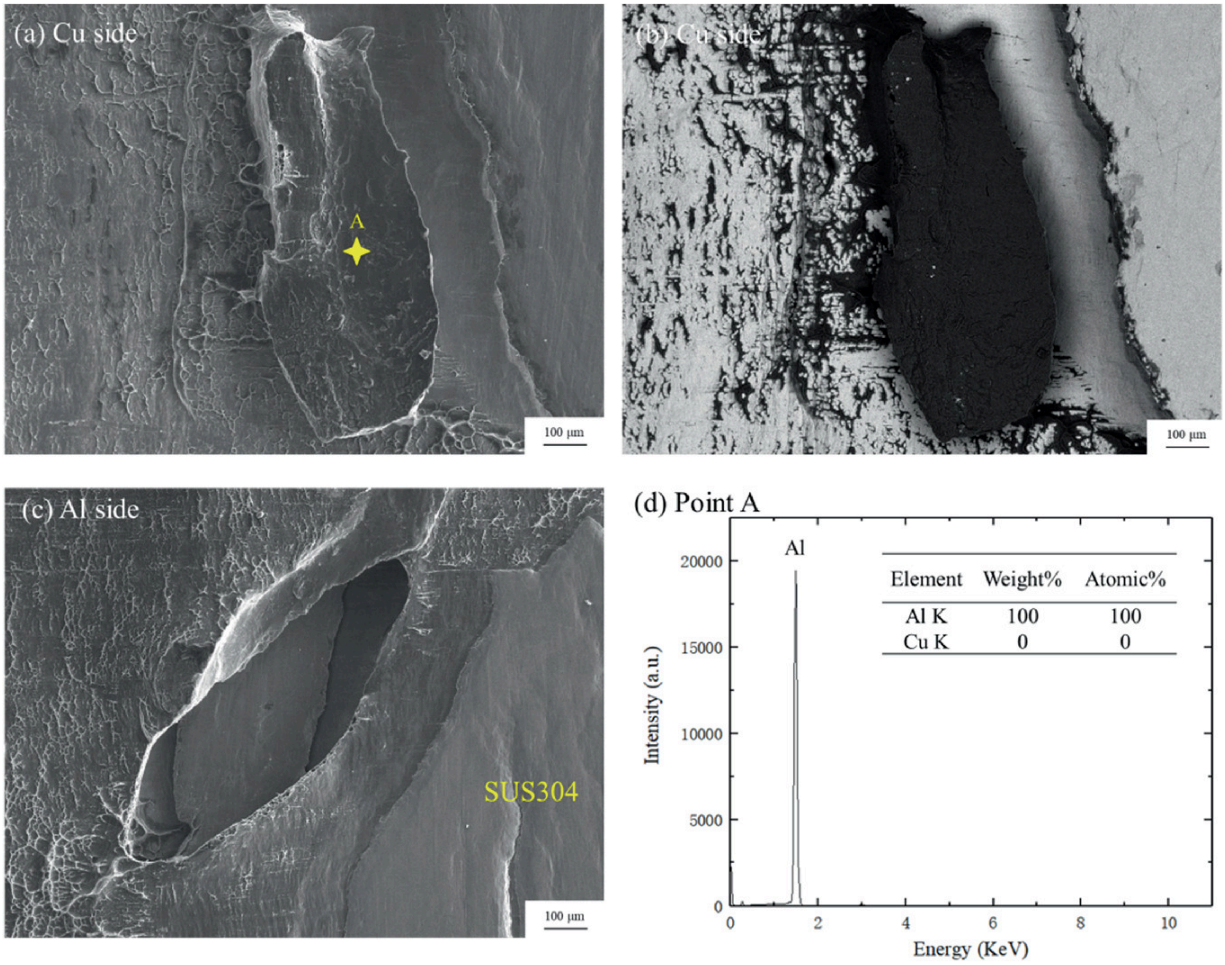


Fig. 2.24 Peeling surface of W-80% samples; **a** Cu side near Cu/Al direct bonding area and **b** corresponding backscattered electron image; **c** Al side near the edge of SUS304 fragments; **d** EDS result of point A marked in (**a**)

The 3D morphology scanning results of peeling surface after 50% rolling reduction are shown in Fig. 2.25a and c. Obviously, the WO-50% samples show flat morphology and only few waves were detected because of the mismatch of plasticity between Cu/Al dissimilar metals, which meant the preliminary mechanical joggle formed. Figure 2.25b and d display the height distribution along rolling direction of peeling surface. The incline of curves in Fig. 2.25b was caused by the gap between the samples and testbed. The red line marked in Fig. 2.25b and d represented the Cu/Al interface. The bonding depth of the WO-50%

samples was less than 4.5 μm. Benefit by inducing the SUS304 interlayer, the bonding depth of the W-50% samples increased to 8.9 μm.

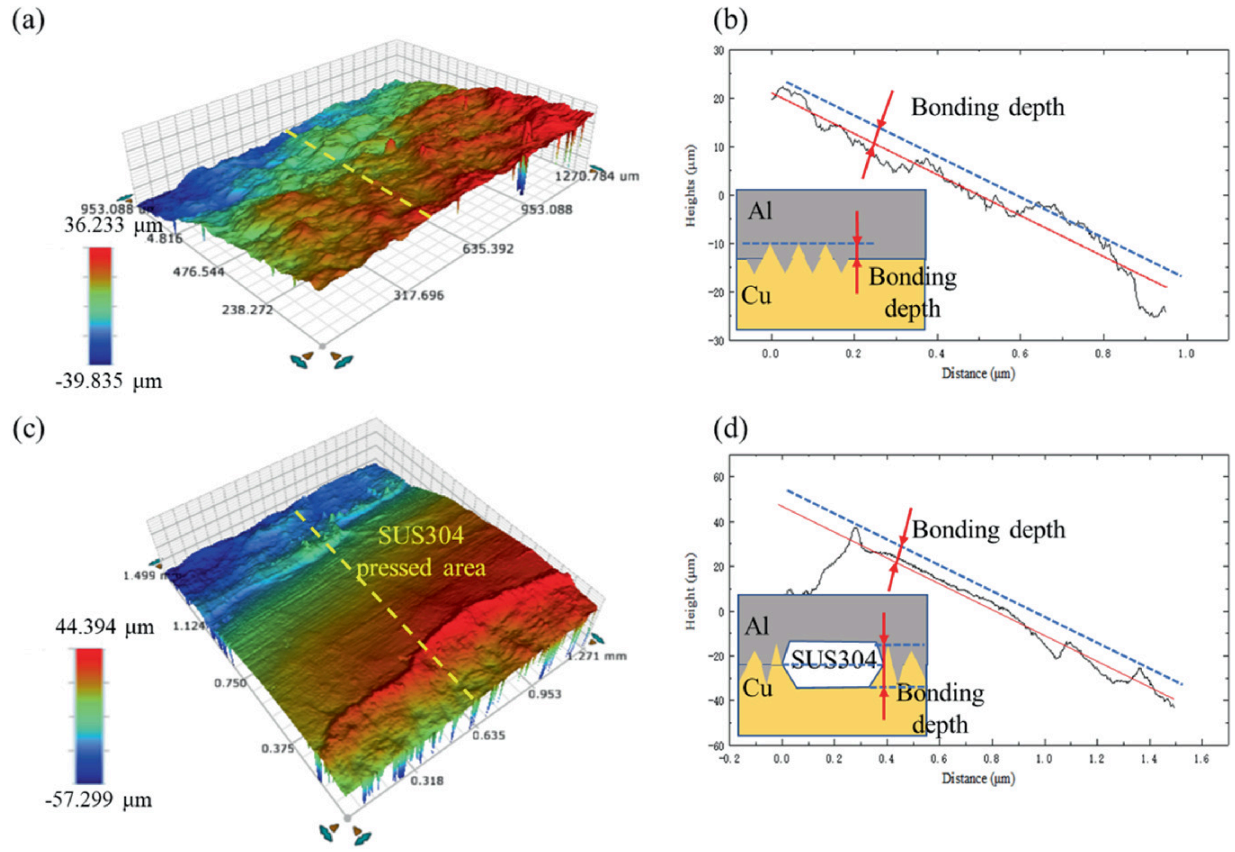


Fig. 2.25 3D morphology scanning results of peeling surface in Cu side after 50% rolling reduction; **a** WO-50% sample; **b** Corresponding height distribution of (**a**); **c** W-50% sample; **d** Corresponding height distribution of (**c**). The dash line marked in (**a**, **c**) is the height distribution scanning line. The insert map in (**b**, **d**) illustrate the bonding depth

The 3D morphology scanning results of peeling surface after 70% rolling reduction are shown in Fig. 2.26a and c. The WO-70% samples kept the similar 3D morphology with that in the WO-50% samples. The peeling surface of W-70% samples became curving because the SUS304 fragments hindered the plastic flow strain and intensified the mismatching deformation of dissimilar metals. In Fig. 2.26b and d, the bonding depth of WO-70% samples slightly increased to 4.7 μm, matching the minor increasement of peeling strength illustrated in Fig. 2.17. However, the bonding depth of W-70% samples increased to 18 μm sharply. The high bonding depth made high mechanical joggle, thus made high bonding strength.

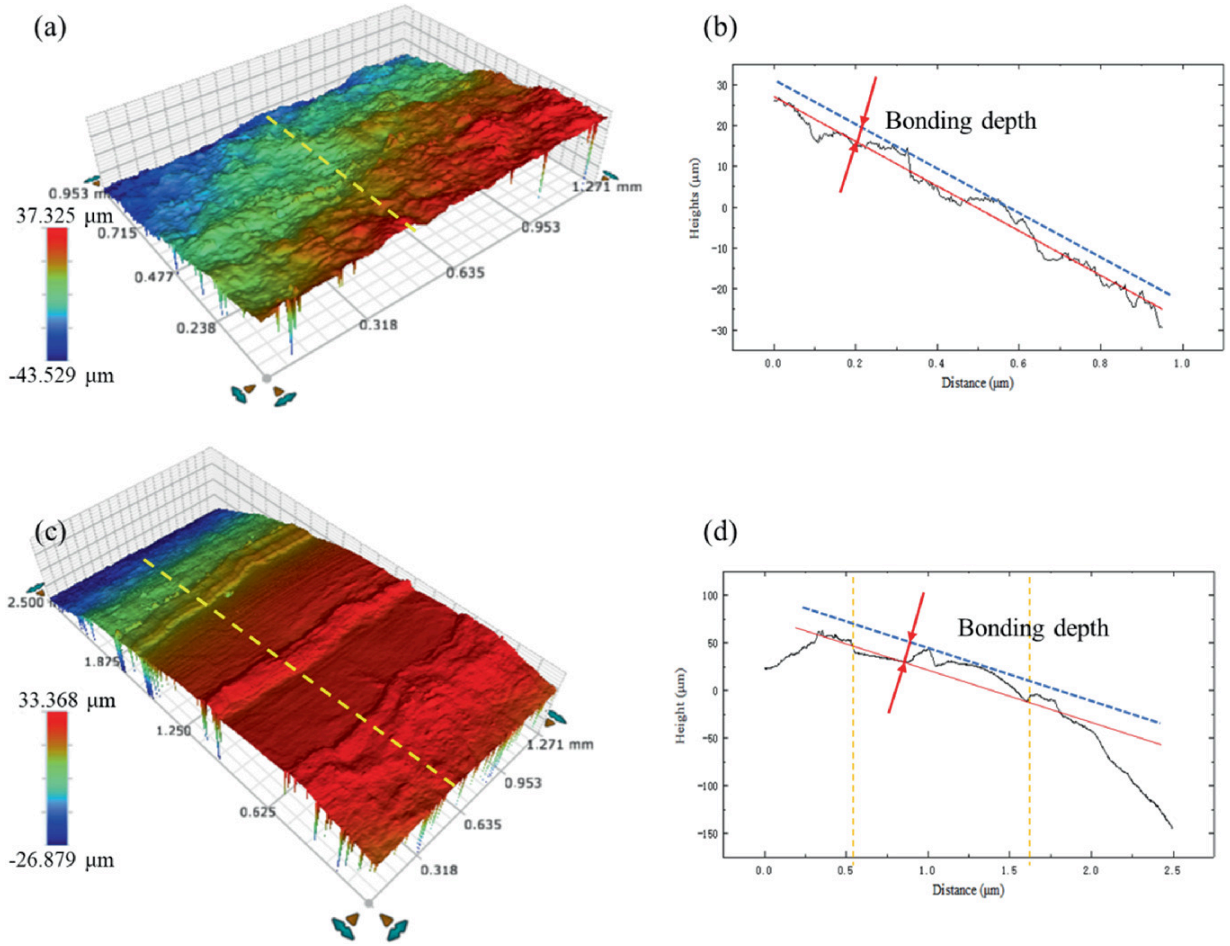


Fig. 2.26 3D morphology scanning results of peeling surface in Cu side after 70% rolling reduction; **a** WO-70% sample and **b** corresponding height distribution; **c** W-70% sample and **d** corresponding height distribution. The dash line in (**a**, **c**) is the height distribution scanning line

The 3D morphology scanning results of peeling surface after 80% rolling reduction are shown in Fig. 2.27a and c. The roughness of peeling surface of the WO-80% samples increased and some cuspidal points distributed in the peeling surface, indicating the bonding effect improved. For the W-80% samples, the improved bonding strength made some SUS304 and Al residual in the Cu side. In Fig. 2.27b and d, the bonding depth of WO-80% samples increased to 7.7 μm. A upwarp was also detected in the Cu side, as shown in Fig. 2.26b, which caused by the peeling test for its improved peeling strength. The bonding depth of W-80% samples increased to 24 μm, thus the peeling strength increased further as illustrated in Fig. 2.17. It's also noticeable that the bonding depth is not strictly related to the thickness of SUS304 interlayer, because of the extrusion of matrix metals as indicated as the bulge in Figs. 2.22a and 2.23b, the small gap or voids in the interface

and the measurement accuracy affected by the curving of the curves. The bonding depth of with SUS304 interlayer samples was much higher than that of without SUS304 interlayer samples, indicating the mechanical joggle was introduced by the SUS304 interlayer.

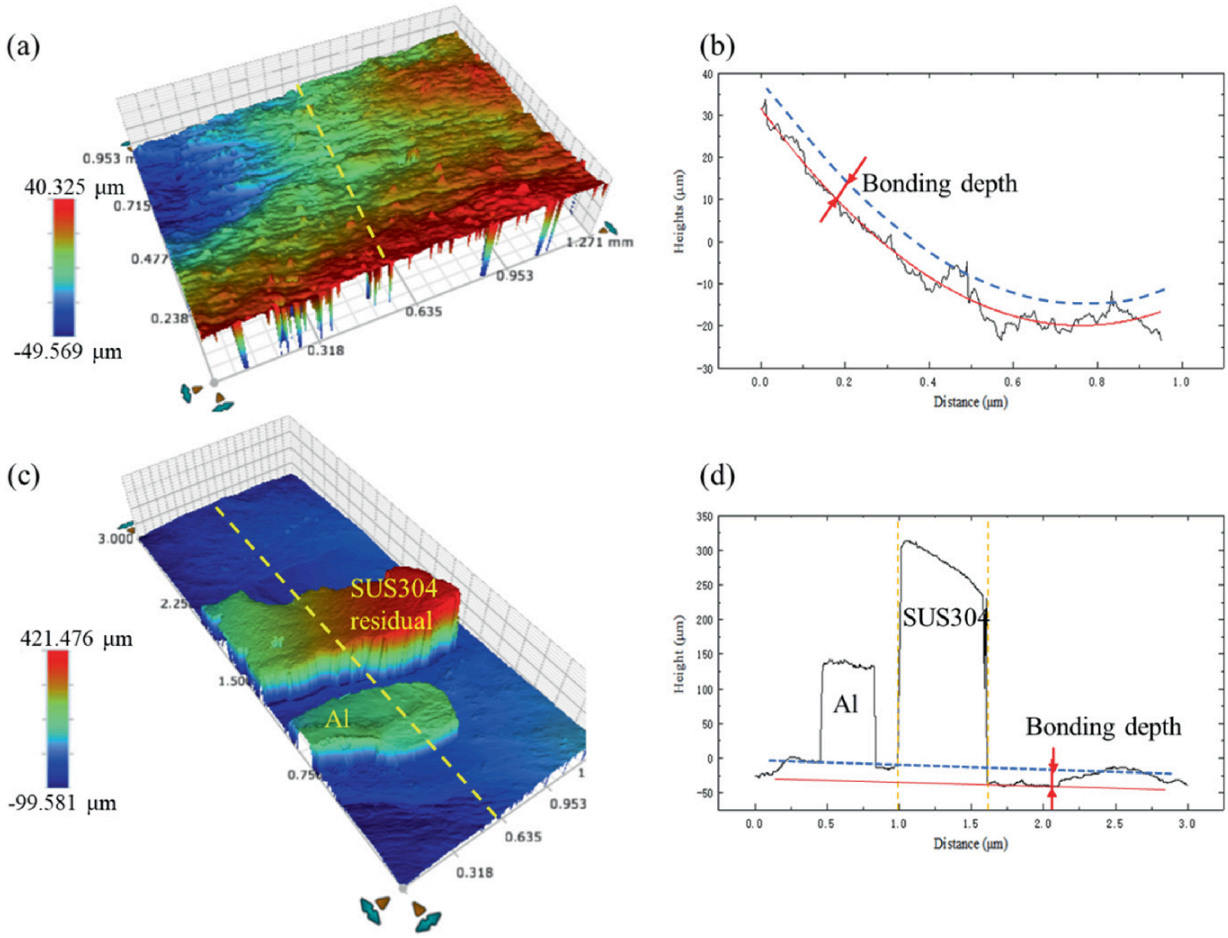


Fig. 2.27 3D morphology scanning results of peeling surface in Cu side after 80% rolling reduction. **a** WO-80% sample and **b** corresponding height distribution; **c** W-80% sample and **d** corresponding height distribution. The dash line in (**a**, **c**) is the height distribution scanning line

Figure 2.28 displays the EDS line scan analysis across the interface of Cu/Al/Cu laminates and the diffusion distance of different elements are calculated in Table 2.2. The results show that the diffusion distance of Al element in WO-50%, WO-70% and WO-80% samples were 4.72 μm, 5.30 μm and 5.55 μm respectively. The diffusion distance of Al element in W-50%, W-70% and W-80% samples were 6.20 μm, 7.06 μm and 6.58 μm respectively. The former rolling deformation created large quantities of defects in the SUS304, promoting the interaction of defects and vacancies. The impurity of other solid solution elements lowered

jumping energy for atom movement comparing with Cu. Therefore, the SUS304 interlayer promoted the diffusion of Al element, which explained the morphology of peeling surface that SUS304 fragment mainly attached in the Al side. The diffusion distance of Cu element is basically same either in the samples with or without SUS304 interlayer, thus the effect of SUS304 interlayer changed the peeling path of Cu/Al interface to Cu/SUS304 interface. The results also approved that the SUS304 interlayer hinder the formation of Cu/Al IMCs without sacrificing the elements diffusion.

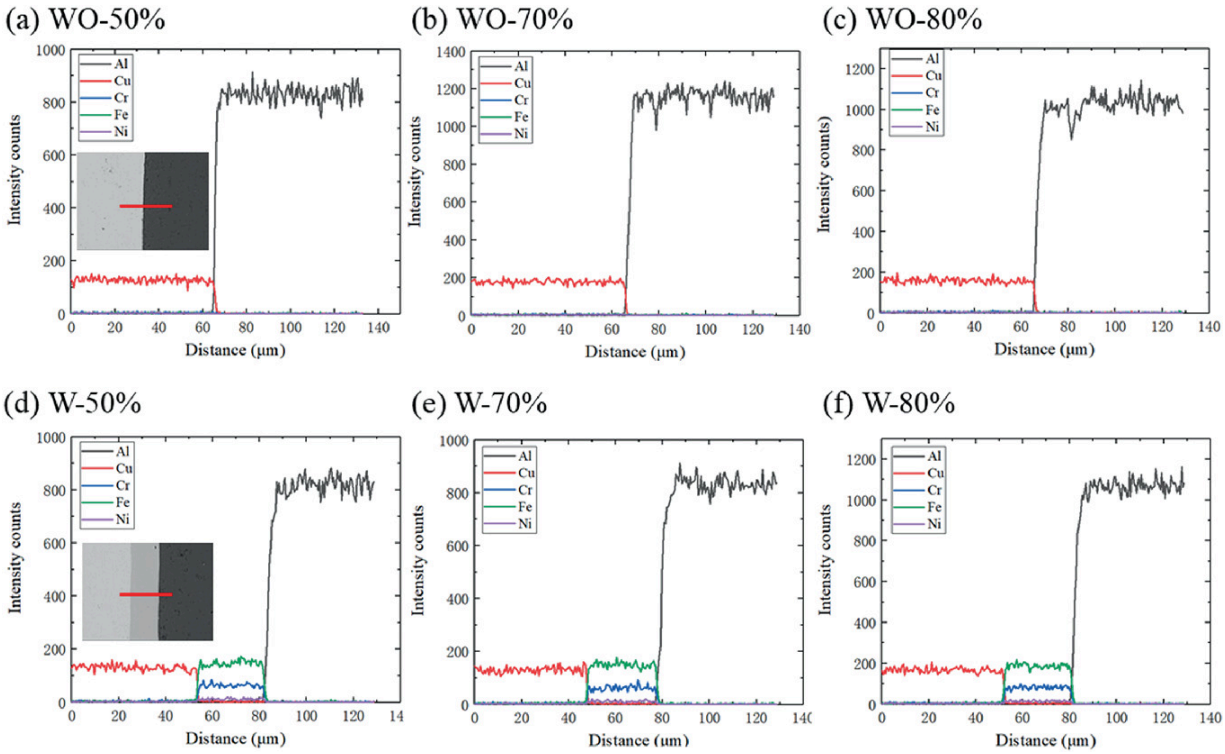


Fig. 2.28 EDS line scan analysis across the interface of Cu/Al/Cu laminates **a**–**c** without SUS304 samples subjected 50, 70 and 80% rolling reduction, **d**–**f** with SUS304 samples subjected 50, 70 and 80% rolling reduction

Table 2.2 Diffusion distance of different elements

Sample	Diffusion distance (μm)				
	Al	Cu	Cr	Fe	Ni
WO-50%	4.72	3.14			
WO-70%	5.30	2.81			
WO-80%	5.55	2.04			

Sample		Diffusion distance (μm)				
		Al	Cu	Cr	Fe	Ni
W-50%	Al side	6.20		2.62	3.23	1.25
	Cu side		3.16	2.26	2.26	0.77
W-70%	Al side	7.06		2.78	3.30	1.34
	Cu side		2.16	1.64	2.87	1.18
W-80%	Al side	6.58		2.10	3.16	0.76
	Cu side		2.07	1.34	2.84	0.74

The mechanism of roll bonding is proposed as the SUS304 interlayer, which induced strain hardening layer near it by shear strain, will fracture by deformation. The Cu/Al matrix metals exposed in the cracks will be extruded by pressure, and contact and then bonding is established between the dissimilar metals. This mechanism is schematically outlined in Fig. 2.29.

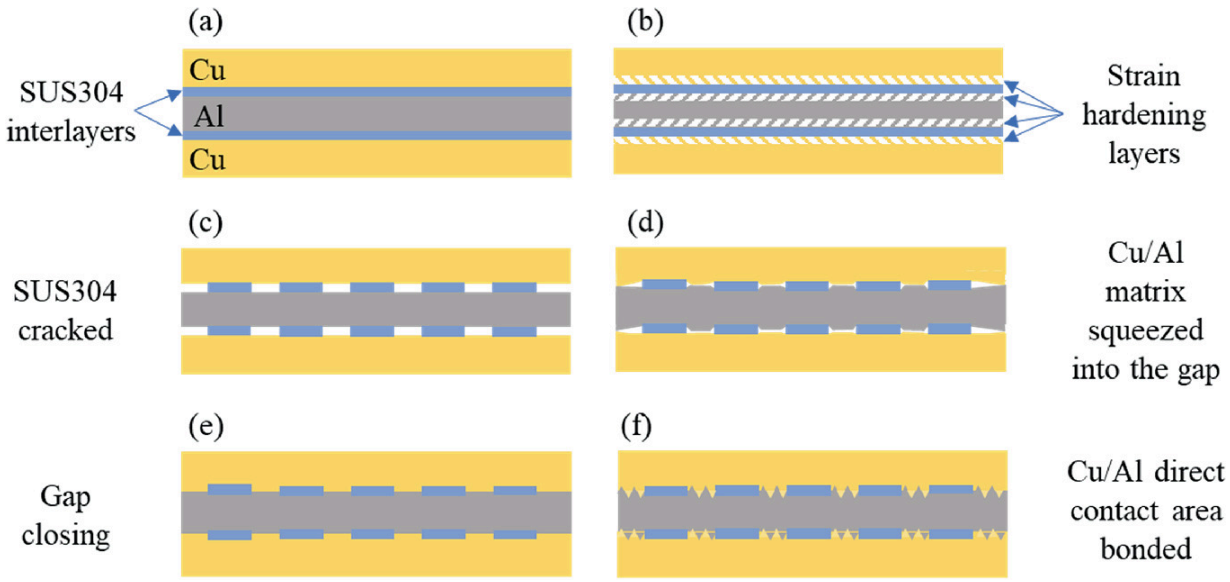


Fig. 2.29 Schematic outline of interface bonding process

From the experimental results above, by introducing SUS304 interlayer, the enhancement of bonding strength mainly includes three parts: (1) the prohibition of IMCs' formation without sacrificing the elements diffusion, (2) the mechanical joggle which SUS304 fragment provided itself, and (3) SUS304 interlayer elongated the deformation path of strain hardening layer to improve bonding strength of matrix

metals. The mechanical joggle is related to the volume of bonding area, and improvement of bonding strength in the matrix metals is related to the expansion ratio of the strain hardening layer. These two enhancement parts are discussed in details as follow.

In a certain length of Cu/Al/Cu laminates enhanced by SUS304 interlayer, the bonding area includes two parts. One is the Cu/Al direct contact area, and the other is SUS304 fragments. The bonding interface is illustrated in Fig. 2.30. The bonding area is the embedded volume of dissimilar metals in the Cu or Al matrix, which has the effect of hinder the relative movements of dissimilar metals, thus improve the bonding strength of interface.

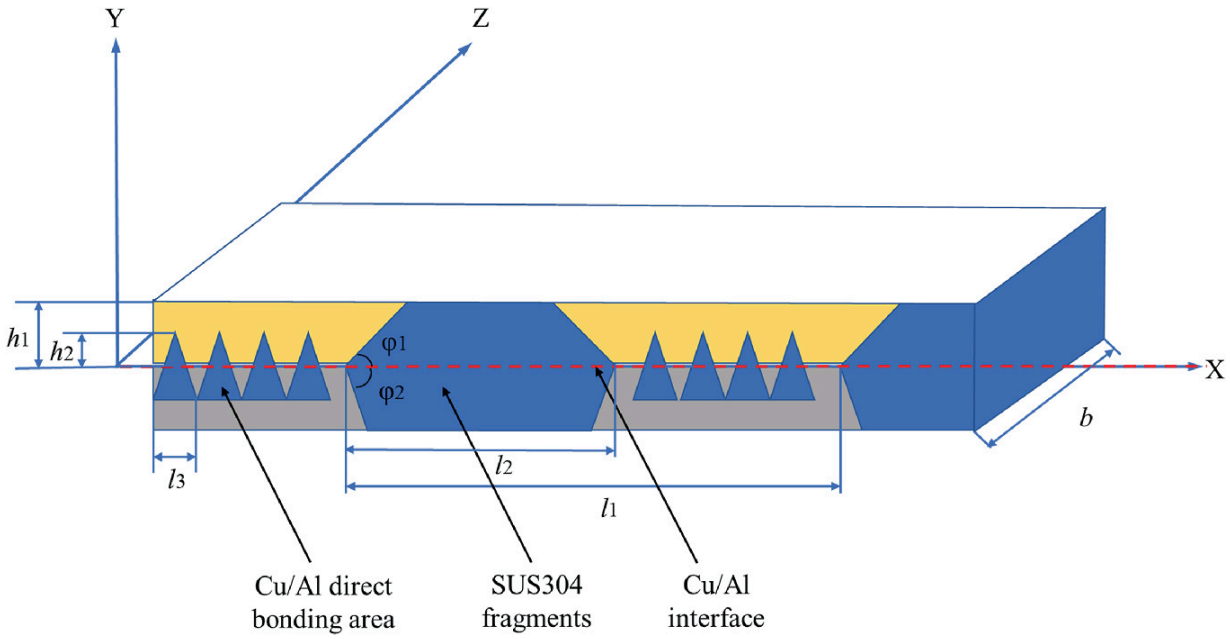


Fig. 2.30 Schema of bonding surface in Cu/Al laminate with SUS304 interlayer after rolling

In Fig. 2.30, the volume of one piece of SUS304 in bonding interface can be calculated by Eq. (2.8):

$$V_{SS304piece} = \left[\left(l_2 - \frac{h_1}{\tan\varphi}\right) h_1\right] b \tag{2.8}$$

Thus, the total volume of SUS304 in a unit length *x* is,

$$V_{SS304} = \left[\left(l_2 - \frac{h_1}{\tan\varphi}\right) h_1\right] b\frac{x}{l_1} \tag{2.9}$$

The total volume of Cu/Al direct contact area is,

$$V_{Cu/Al} = \frac{1}{2} h_2 \frac{l_3}{2} b \frac{x - \frac{x}{l_1} l_2}{l_3} = \frac{h_2 x b (l_1 - l_2)}{4 l_1} \tag{2.10}$$

The total volume of bonding area is,

$$V = V_{SS304} + V_{Cu/Al} = \left[\left(l_2 - \frac{h_1}{\tan \varphi} \right) h_1 + \frac{h_2 (l_1 - l_2)}{4} \right] \frac{xb}{l_1} \tag{2.11}$$

According to Eq. (2.11), we can obtain Eqs. (2.12) and (2.13):

$$\frac{\partial V}{\partial l_1} = \left[\frac{h_2 l_2}{4} - \left(l_2 - \frac{h_1}{\tan \varphi} \right) h_1 \right] \frac{xb}{l_1^2} \tag{2.12}$$

$$\frac{\partial V}{\partial l_2} = \left(h_1 - \frac{h_2}{4} \right) \frac{xb}{l_1} \tag{2.13}$$

where h_1 and h_2 is bonding depth of SUS304 fragments and Cu/Al direct bonding area respectively, l_1 is distance of distribution of adjacent SUS304 fragments, l_2 is the length of the SUS304 fragments, l_3 is the length of ridges in the Cu/Al direct bonding area, φ is the degree of shear band angle. b is the width of Cu/Al/Cu laminates, x is the length of the laminates. From the Eqs. (2.11)–(2.13) and experiment results, h_1 is much larger than h_2, the total volume of bonding area is negative related to l_1 but positive related to l_2. When the rolling reduction increased, l_2 increased but l_1 (l_1=L_1 + L_2 in Fig. 2.20) almost kept as a constant, which explained the improved the bonding strength. It's also noticeable that the calculation of bonding area ignored the gap between SUS304 fragments edges and Cu/Al matrix. The degree of increasement of the bonding strength was not significant when rolling reduction increased.

During roll bonding, a strain-hardening layer was produced in the contacting surface, which would expand, crack and form bonding area. The bonding strength related to the ductility and expansion ratio of contacting surface and the effective normal pressure is defined as Eq. (2.14).

$$\sigma_B = (1 - G)\, Y p_b \tag{2.14}$$

where G is a parameter representing the ductility of the contacting surface, when the contacting surface is completely ductile, the $G = 1$, and when the contacting surface is completely brittle, the $G = 0$. p_b is the effective normal pressure. Govindaraj et al. [13] pointed out that the size of micro-cracks increased with the increasement of rolling reduction, the part of the normal pressure related to the extraction into narrow cracks became small, and $p_b \approx \sigma_{vM}$ can be taken as a rough estimate of the normal pressure, where σ_{vM} is the yield of the matrix materials. Y is the expansion ratio of contacting surface,

$$Y = \frac{S_1 - S_0}{S_1} \tag{2.15}$$

where S_1 is the area of contacting surface after deformation, and S_0 is that before deformation. The original area of contacting surface is,

$$S_0 = x_0 b \tag{2.16}$$

where x_0 is the original length of the laminates.

The total area of contacting surface (with SUS304) after deformation is,

$$\begin{aligned} S_1 &= \left[\left(l_2 + 2h_1 \frac{1 - \cos\varphi}{\sin\varphi} \right) + (l_1 - l_2) \right] \frac{xb}{l_1} \\ &= \left(l_1 + 2h_1 \frac{1 - \cos\varphi}{\sin\varphi} \right) \frac{xb}{l_1} \end{aligned} \tag{2.17}$$

The total area of contacting surface (without SUS304) after deformation is,

$$S_1' = xb \tag{2.18}$$

Hence the expansion ratio of contacting surface with or without SUS304 interlayer can be calculated as follow,

$$Y = \frac{\left(l_1 + 2h_1\frac{1-\cos\varphi}{\sin\varphi}\right)\frac{xb}{l_1} - x_0 b}{\left(l_1 + 2h_1\frac{1-\cos\varphi}{\sin\varphi}\right)\frac{xb}{l_1}} = \frac{l_1(x-x_0) + 2h_1 x\frac{1-\cos\varphi}{\sin\varphi}}{l_1 x + 2h_1 x\frac{1-\cos\varphi}{\sin\varphi}} \tag{2.19}$$

$$Y' = \frac{xb - x_0 b}{xb} = \frac{x - x_0}{x} \tag{2.20}$$

Define the $\triangle$ as the difference of the area of contacting surface between with SUS304 interlayer samples S_1 and without SUS304 interlayer samples S_1', then the difference between Y and Y' can be calculated as

$$\Delta = S_1 - S_1' = \left(l_1 + 2h_1\frac{1-\cos\varphi}{\sin\varphi}\right)\frac{xb}{l_1} - xb = \frac{2h_1}{l_1}\frac{1-\cos\varphi}{\sin\varphi}xb \tag{2.21}$$

$$Y - Y' = \frac{S_0\Delta}{(S'+\Delta)S'} = \frac{2x_0 h_1(1-\cos\varphi)}{x[l_1\sin\varphi + 2h_1(1-\cos\varphi)]} \tag{2.22}$$

Combine the Eq. (2.22) and the experimental results, the Cu/Al/Cu laminates with SUS304 interlayer have a higher surface expansion ratio (Y), benefitting from introducing the SUS304 interlayer, which significantly elongated the deformation path of contacting surface. This high surface expansion ratio causing cracking in the contacting surface and extrusion of virgin matrix materials, resulting high bonding strength between dissimilar materials.

Figure 2.31 shows the EBSD results of Cu/Al/Cu laminates subjected to 50% rolling reduction. In the WO-50% samples, the Cu and Al matrix subjected comparable deformation and elongated simultaneously. The gap between the Cu and Al was caused by the formation of IMCs, which was harmful to the bonding strength. Meanwhile, in W-50% samples, the grains near SUS304 interlayer have been significantly refined compared with that far from the interlayer. The higher grain refinement efficiency in the W-50% samples is attributed to the higher shear strain by introducing hard SUS304

interlayer, which is illustrated in the KAM results (Fig. 2.31c and d). The strain hardening layers benefits the bonding effect in further deformation process. Besides, some small voids were also detected in W-50% samples, indicating a low bonding strength.

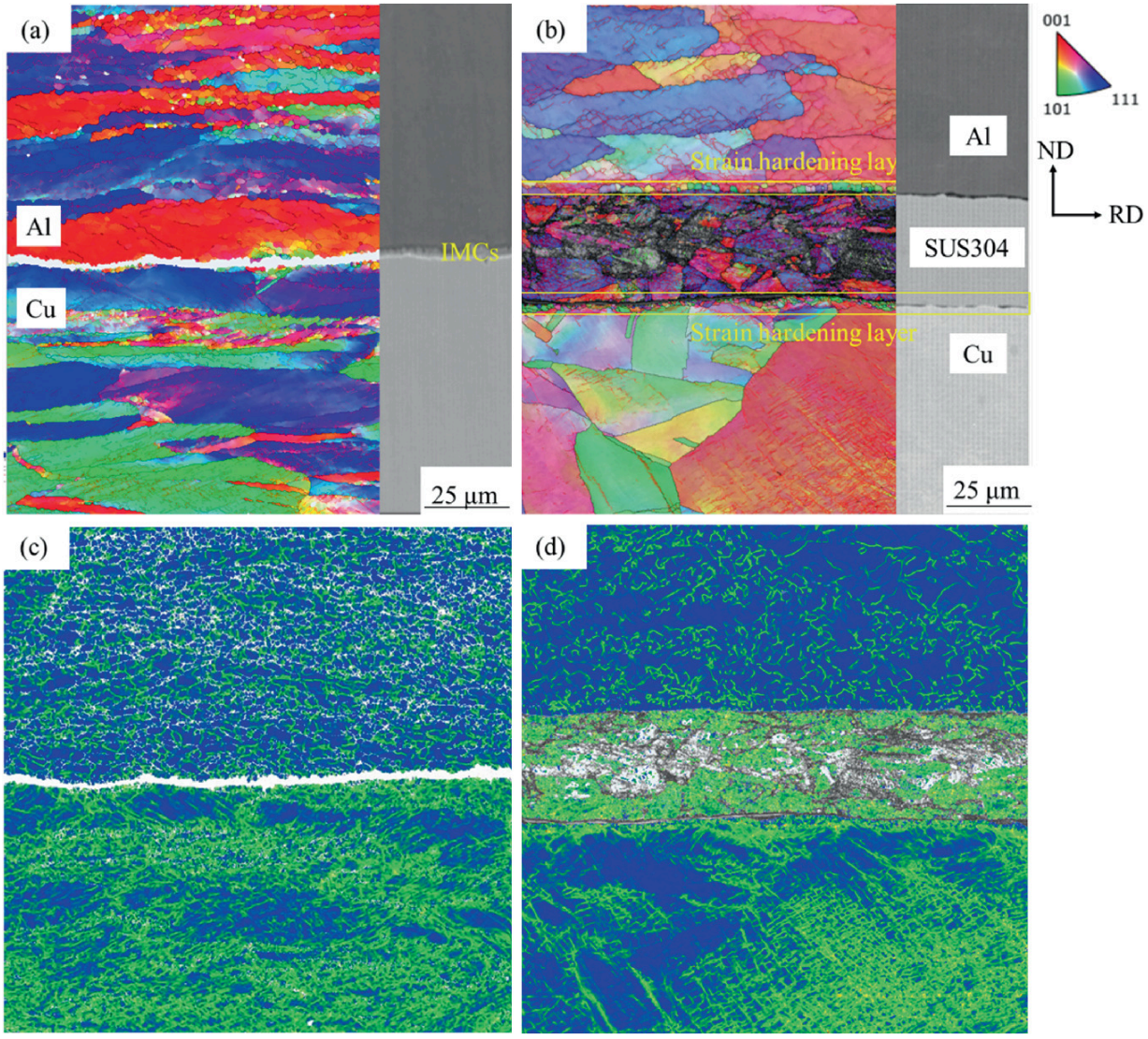


Fig. 2.31 EBSD results of **a** WO-50% sample, **b** W-50% sample, and **c**, **d** their corresponding KAM results

Figure 2.32 gives the EBSD results of Cu/Al/Cu laminates subjected to 70% rolling reduction. The dash line marked in Fig. 2.32a and b is the interface of dissimilar metals. Either in the WO-70% samples or in the W-70% samples, all obvious gaps in the interface were closed, and tight bonding formed. In the WO-70% samples, the Cu and Al matrix both severe deformed, which was corroborated with the detection of

dense low angle grain boundaries (LAGBs) and homogeneous strain distribution. In the W-70% samples, the Cu and Al matrix showed a significantly different deformation path. The Al deformed severely and turned into traditional rolled lath microstructure as similar as that in WO-50% samples, while the deformation of Cu was relatively low, the strain was mainly concentrated in the Cu/SUS304 and Al/SUS304 interfaces. A finer grain layer was located in these interfaces, which was contributed to a higher bonding strength.

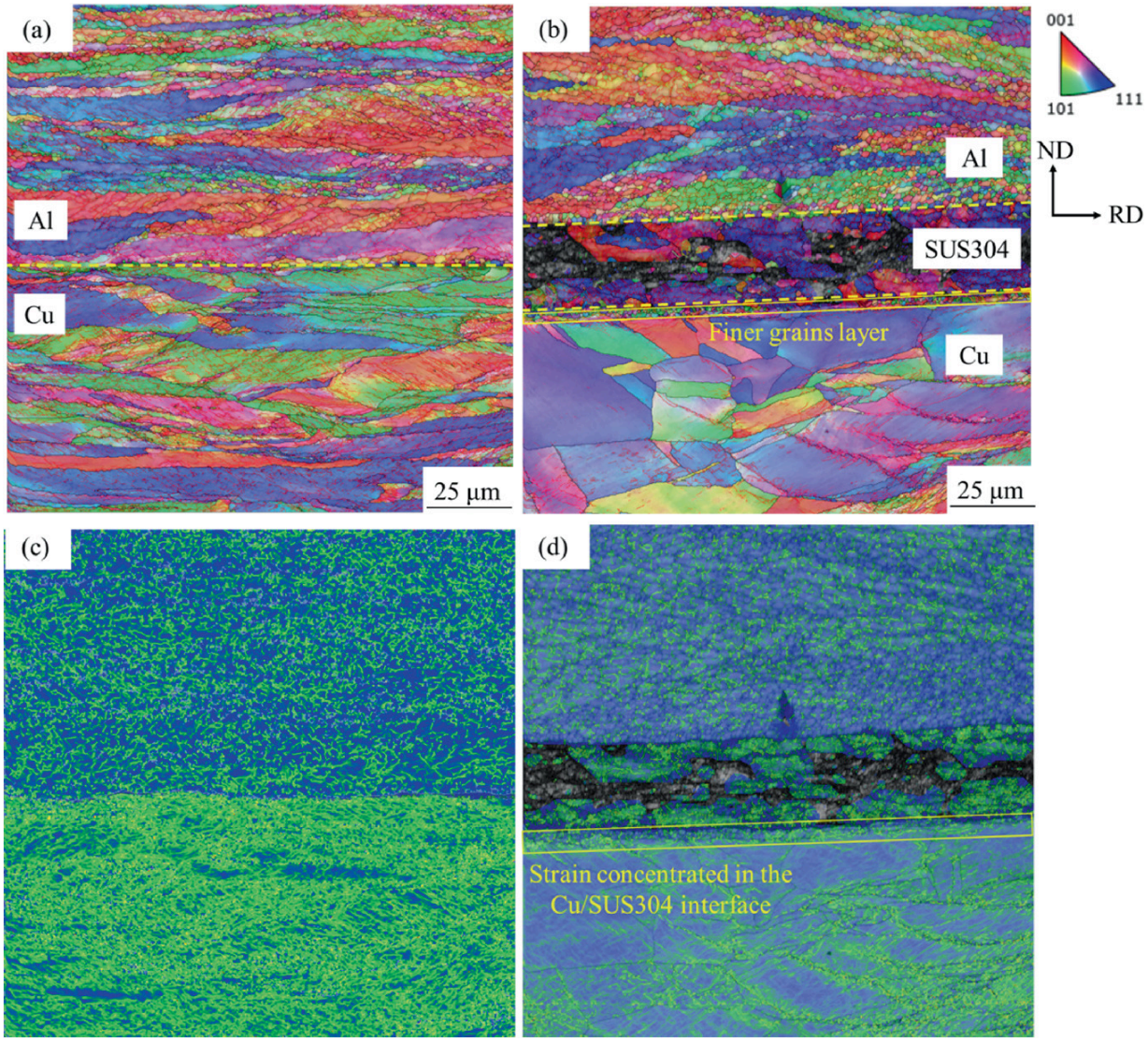


Fig. 2.32 EBSD results of **a** WO-70% sample, **b** W-70% sample, and **c**, **d** their corresponding KAM results

Figure 2.33 presents the EBSD results of Cu/Al/Cu laminates subjected to 80% rolling reduction. With the increasement of rolling

reduction, the degree of deformation increased and the grains size got finer. In the WO-80% samples, the interface between the Cu and Al matrix became fuzzy. The grain size further refined and the strain further increased. In the W-80% samples, there's a conspicuous area where the grains were relatively coarse and the strain was relatively low. On the one hand, these coarse grains indicated the shear deformation between the SUS304 interlayer and the matrix metals; on the other hand, these coarse grains may retain some strain hardening capacity, which will benefit their deformability of the Cu/Al/Cu laminates. Besides, either in the Cu side or in the Al side, the shear bands distributed along the edge of the SUS304 fragments. The degrees between the shear band and the rolling direction were consistent with the above results in Fig. 2.19. The appearance of these shear bands contributed the change of deformation mode from uniform deformation to shear localization deformation and further grain refinement which was benefit to the bonding strength.

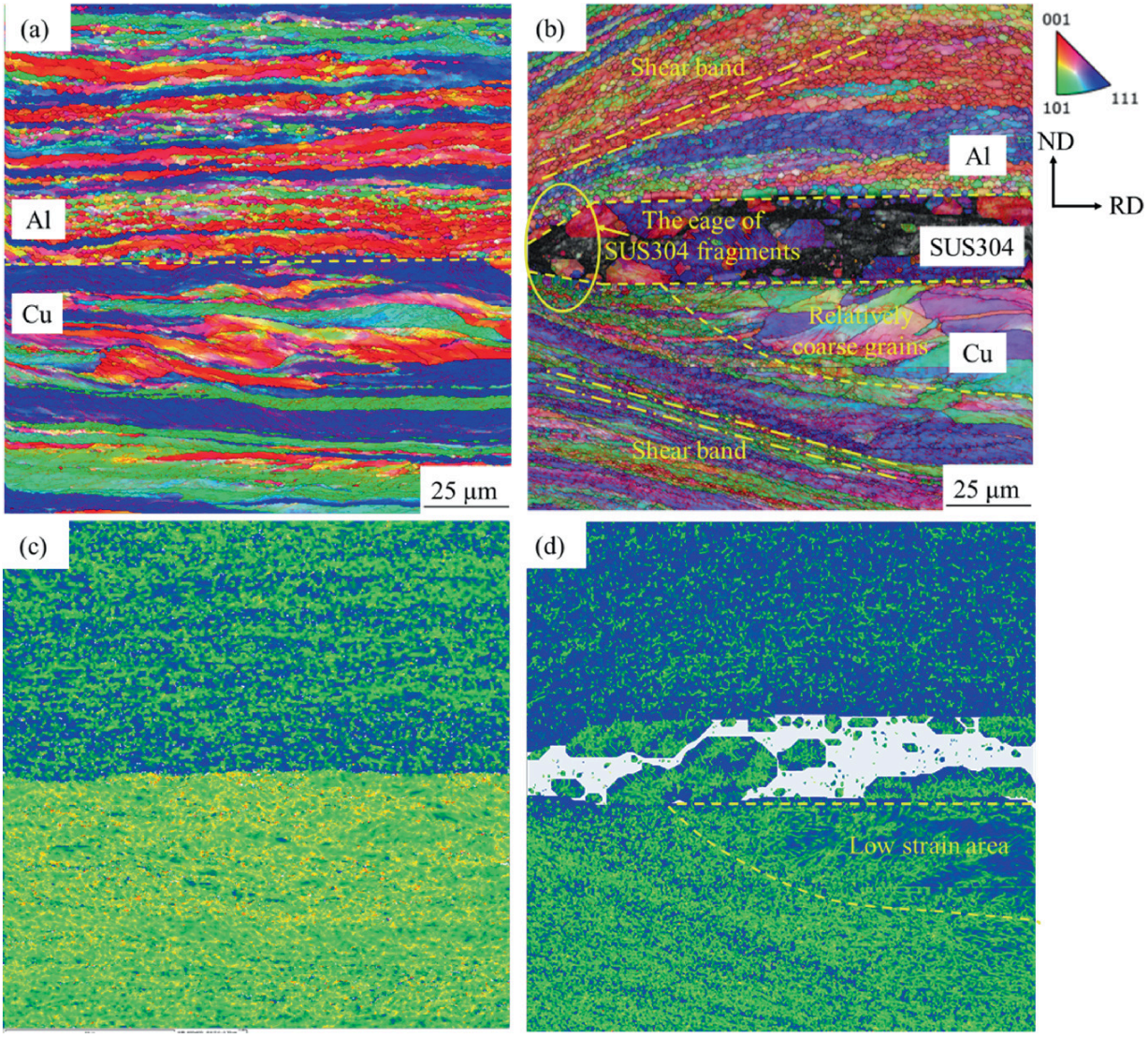


Fig. 2.33 EBSD results of **a** WO-80% sample, **b** W-80% sample, and **c**, **d** their corresponding KAM results

As shown in Figs. 2.31, 2.32 and 2.33, there were two shear deformation regions induced by the SUS304 interlayer, one is located in the Cu/SUS304 and Al/SUS304 interface where SUS304 interlayer promoted the mismatch of metal flow, another one distributed near the edges of SUS304 fragments which significantly changed the direction of metal flow. The shear deformation not only benefited the formation of strain hardening layers, but also had a significant influence on the closure of holes. Besides, shear deformation was also conducive to improving the bond energy of dissimilar metal atoms. The interface bond energy increased with the degree of shear deformation. As described in Eq. (2.23), the total energy almost kept unchanged, while

the sum of potential energy increased with shear deformation. This results also provide a micro scale investigation to the bonding mechanism.

$$E_{Interface} = E_T - (E_{Matrix1} - E_{Matrix2}) \tag{2.23}$$

where, $E_{Interface}$ is the interface bond energy, E_T is the total energy of the molecular system, $E_{Matrix1}$ and $E_{Matrix2}$ are potential energy of matrix atoms.

The total bonding strength of Cu/Al/Cu laminates with SUS304 interlayer can be described as Eq. (2.24).

$$\sigma_{B-total} = \sigma_{Joggle} + \sigma_{Matrix} + (\sigma_{Shear} + \sigma_{Diffusion} - \sigma_{IMCs}) \tag{2.24}$$

where $\sigma_{B\text{-}total}$ is the total bonding strength of the laminates, σ_{Joggle} is the bonding strength attributed to the mechanical joggle, σ_{Matrix} is the bonding strength attributed to the bonding effect of matrix metals, σ_{Shear} is the bonding strength attributed to the shear deformation, $\sigma_{Diffusion}$ is the bonding strength attributed to the element's diffusion across the interface, and σ_{IMCs} is the bonding strength reduction caused the formation of IMCs. Substituting parameters *V* and *Y* into Eq. (2.24), then the total bonding strength can be described as Eq. (2.25).

$$\sigma_{B-total} = K_1 V + K_2(1 - G)Y + C \tag{2.25}$$

where K_1 and K_2 are constants related to *V* and *Y* respectively, *C* is the combination of σ_{Shear}, $\sigma_{Diffusion}$ and σ_{IMCs}.

Table 2.3 lists the calculation results of bonding area and expansion ratio of the strain hardening layer. Considering the characteristic of T-type peeling test, *x* and *b* were not taken into calculation, which represented a unit length and the width of samples respectively.

Table 2.3 Calculation of bonding area and expansion ratio of the strain hardening layer

	With SUS304	**Without SUS304**	**Difference**
V (50%)	5.572*xb*	1.125*xb*	4.447*xb*
Y (50%)	0.335*x*	0.333*x*	0.002*x*
V (70%)	3.961*xb*	1.175*xb*	2.786*xb*
Y (70%)	0.412*x*	0.411*x*	0.001*x*

	With SUS304	Without SUS304	Difference
V (80%)	4.674*xb*	1.925*xb*	2.749*xb*
Y (80%)	0.446*x*	0.444*x*	0.002*x*

Figure 2.34 shows the calculation results varying with the rolling reduction. It's clearly showed that the bonding area of with SUS304 samples is much larger than that without SUS304 samples, indication mechanical joggle plays an important role in improving the bonding strength of Cu/Al/Cu laminates. The decrease of bonding area at 70% rolling reduction attributed to the widening of space between adjacent SUS304 fragments, as indicated in Fig. 2.20g**.** The difference of the strain hardening layers' expansion ration is minute because of the limited thickness of SUS304 interlayer. It's assumed that the strain hardening layer got more brittle with the increasement of rolling reduction, hence a smaller *G* value and a higher matrix bonding effect.

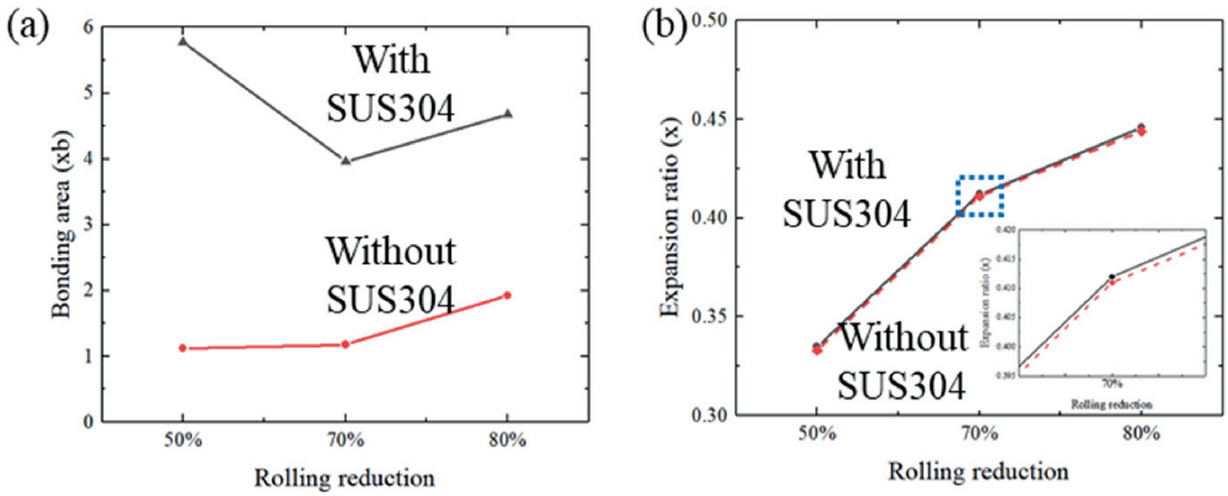


Fig. 2.34 **a** Calculation of bonding area; **b** Expansion ratio of the strain hardening layer. The insert map in (**b**) illustrates expansion ratio of the strain hardening layer at 70% rolling reduction

2.6 Cu/Al/Cu Laminates with SUS304 Interlayer Subjected to Annealing

Cu/Al laminates with an SUS304 interlayer are fabricated by hot rolling and then annealed at different temperature [14]. The effect of annealing temperature on the comprehensive properties, interfacial structure, and crack propagation of the laminates is investigated. Figure 2.35a

shows the tensile curves of annealed Cu/Al laminates with a SUS304 interlayer. The overall trend shows a decrease in tensile strength and an increase in elongation as increasing the annealing temperature, as shown in Fig. 2.35b. Specifically, the unannealed sample exhibits a tensile strength of 267 MPa and a fracture elongation of 3.82%. After annealing at 200 °C (473 K), the strength decreases to 219 MPa while the fracture elongation recovers to 7.2%. Upon annealing at 300 °C, the tensile strength and fracture elongation of the sample are 158 MPa and 24.1%, respectively. As the annealing temperature increases to 400 °C (673 K), the tensile strength and fracture elongation of the sample become 162 MPa and 31.84%, respectively.

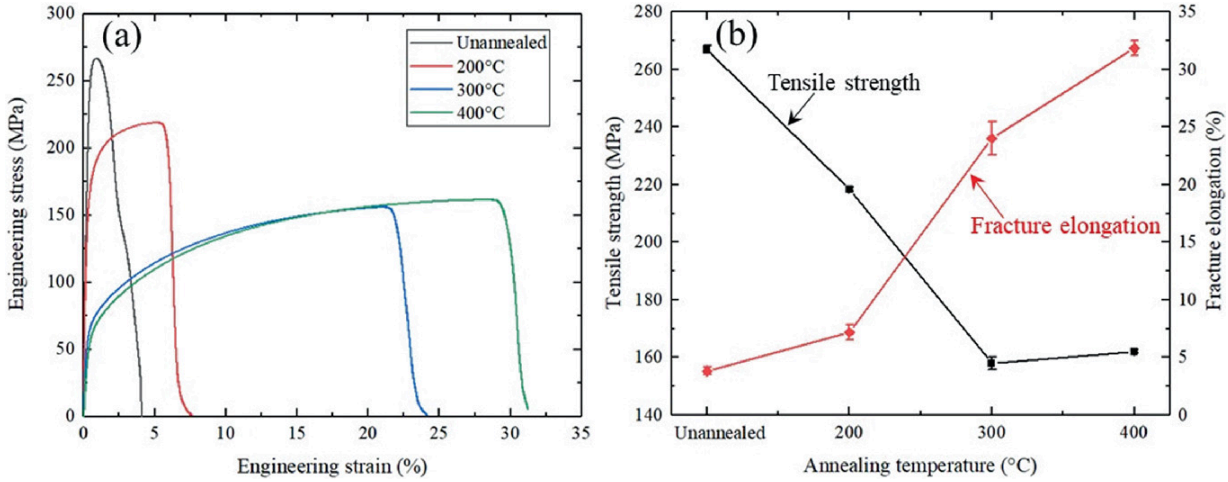


Fig. 2.35 **a** Tensile curves and **b** variation trend in strength and elongation of Cu/Al/Cu laminates with a SUS304 interlayer annealed at different temperature

The peeling curves of annealed Cu/Al/Cu laminates with a SUS304 interlayer is provided as Fig. 2.36a. The peel curves of the laminates exhibit a discontinuous distribution of peaks and valleys, and the peel strength firstly increases and then decreases with the increase of annealing temperature. The average peeling strengths of the unannealed sample, as well as those annealed at 200 °C, 300 °C, and 400 °C, are 6.2 N/mm, 19.6 N/mm, 10.6 N/mm, and 2.4 N/mm, respectively. For the unannealed sample, the peak and valley peeling strengths are 15.5 and 4.1 N/mm. At an annealing temperature of 200 °C, the peak and valley peel strengths are improved to 27.9 and 18.9 N/mm. As the annealing temperature increases to 300 °C, the peak and valley peeling strengths are reduced to 14.0 N/mm and 8.6 N/mm. When the annealing temperature further increases to 400 °C, the

peeling strength is sharply decreased to 2.4 N/mm (Fig. 2.36b). Moreover, the initial discontinuous distribution of peaks and valleys is replaced by the curves with a ripple shape.

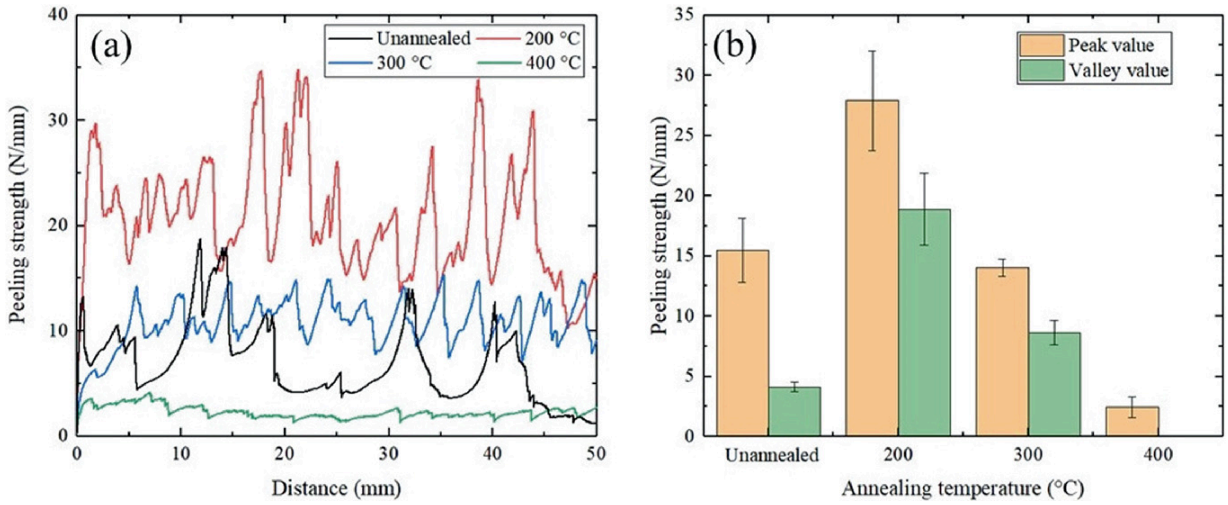


Fig. 2.36 **a** Peeling curves of Cu/Al/Cu laminates with a SUS304 interlayer subjected to annealing under different temperature, **b** peeling strength varies with annealing temperature

Figure 2.37 shows the interfacial morphologies of annealed Cu/Al/Cu laminates with a SUS304 interlayer. It can be seen that no IMCs are formed at the interface after annealing at 200 °C (Fig. 2.37a and b). When the annealing temperature reaches 300 °C, the formation of IMCs can be observed in the direct contact area between Cu matrix and Al matrix. While no IMCs are generated in these regions containing the SUS304 interlayer (Fig. 2.37c and d). With the further increase of annealing temperature to 400 °C, the formation of IMCs between Cu matrix and Al matrix becomes evident. Additionally, the thickness of the IMC layer is significantly increased. However, it is worth noting that there are still no IMCs are observed between Cu/Al matrix and SUS304 interlayer (Fig. 2.37e and f). The above results suggests that the presence of SUS304 interlayer effectively hinders the formation of interfacial IMCs.

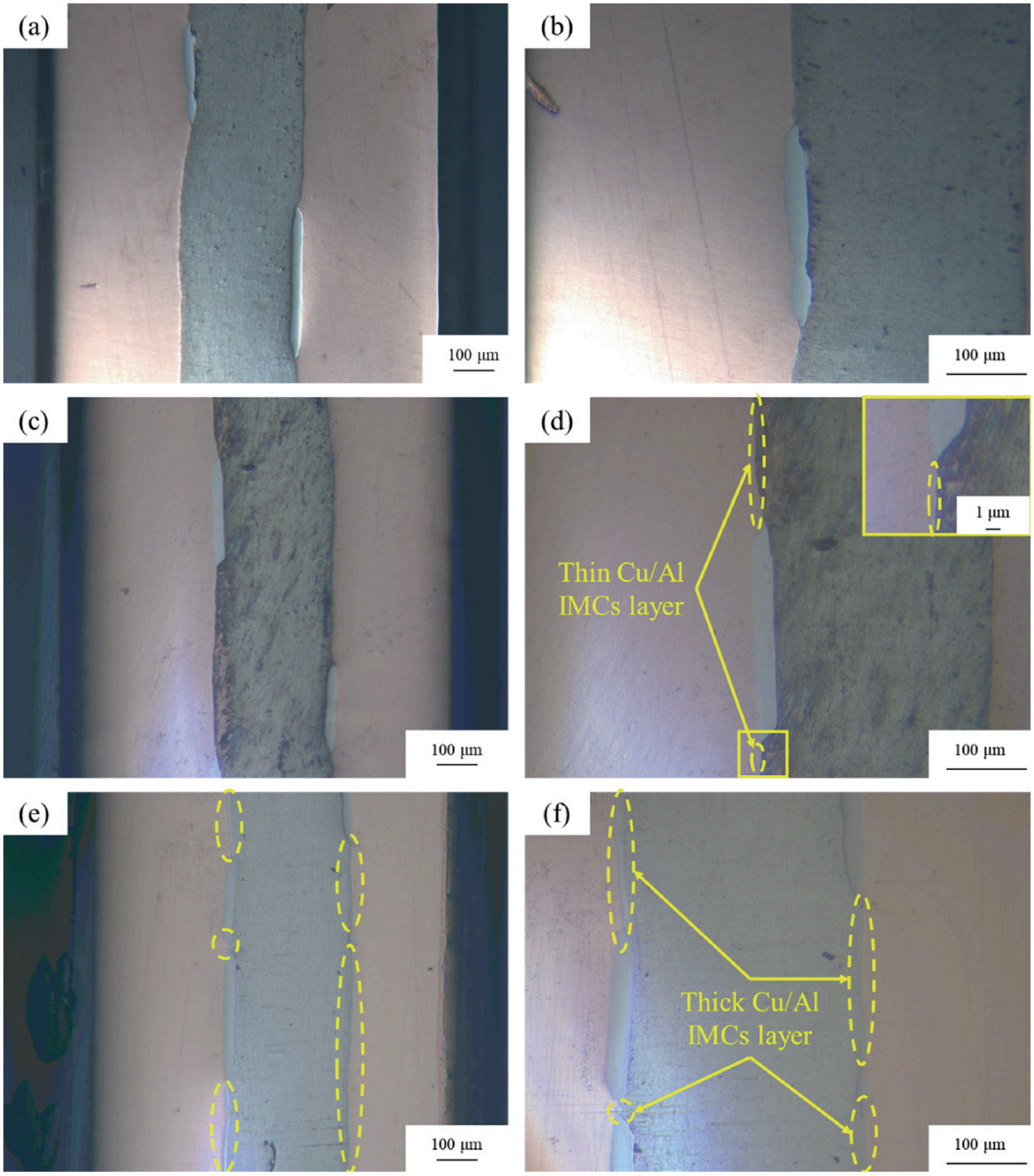


Fig. 2.37 Morphologies of Cu/Al/Cu laminates with a SUS304 interlayer subjected to annealing under different temperature: **a**, **b** 200 °C, **c**, **d** 300 °C, **e**, **f** 400 °C

To observe the formation and distribution of IMCs at the interface in more detail, the edge region of SUS304 fragments is examined by SEM, as shown in Fig. 2.38. A well-bonded Cu/Al interface is present regardless of whether the specimens have undergone annealing treatment. Additionally, a Cu/SUS304 interface with gaps can be

observed. Under the given rolling pressure and thermal input conditions, it is insufficient to form a robust bonding interface between Cu matrix and SUS304.

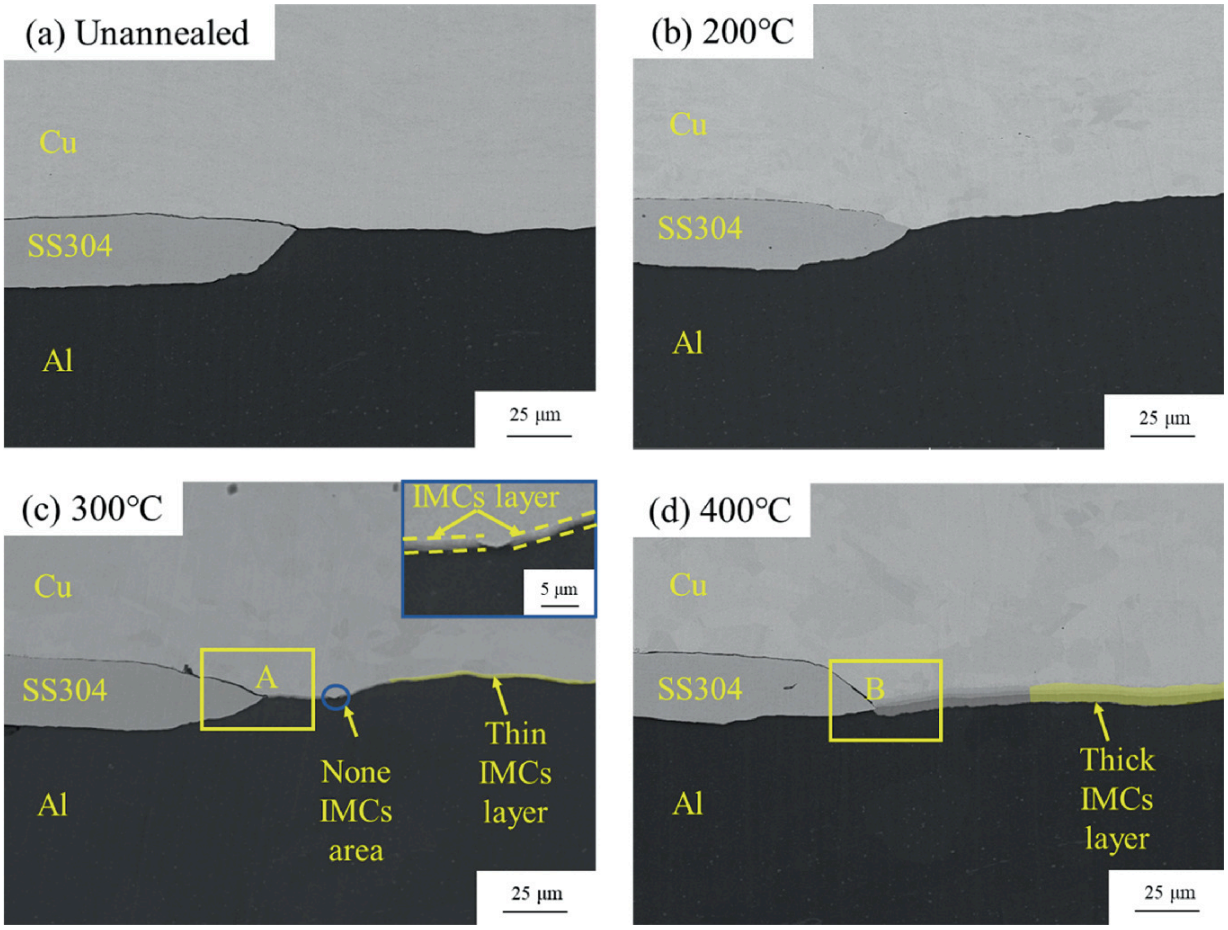


Fig. 2.38 Micro-morphology near the edges of SUS304 fragments for **a** unannealed sample and annealed samples at **b** 200 °C, **c** 300 °C, **d** 400 °C

For the unannealed and low-temperature annealed samples (200 °C), no IMCs are detected in these regions containing SUS304 fragments and the direct contact area between Cu matrix and Al matrix (Fig. 2.38a and b). For the sample annealed at 300 °C, a thin layer of IMCs growing at the Cu/Al interface can be observed. Local magnification shows that the IMCs don't completely cover the entire Cu/Al interface, and there are still some areas without the generation of IMC (Fig. 2.38c). This can be attributed to the relatively low annealing temperature, which is not high enough to facilitate the bonding in the micro-gap regions through atomic diffusion, thereby impeding the generation of IMCs. When the annealing temperature is increased to

400 °C, a significantly thicker layer of IMCs has formed on the Cu/Al interface, effectively covering the majority of the interface (Fig. 2.38d).

In Fig. 2.38c and d, it can be observed that multiple layers of IMCs are formed at the Cu/Al interface after annealing. The composition and dimensions of these IMCs at the interface of these samples annealed at 300 °C and 400 °C is determined by Fig. 2.39, corresponding to regions A and B in Fig. 2.38c and d, respectively. For the sample annealed at 300 °C, a gap is observed between SUS304 fragments and the IMCs, indicating incomplete formation of IMCs. Only a small amount of IMCs are observed to grow on the Al side within the gaps. Additionally, the IMCs can be divided into three layers, with the layer close to Cu/Al matrix being the thicker, and the middle layer being thinner Fig. 2.39a. For the sample annealed at 400 °C, the gap between SUS304 fragments and the IMCs is almost eliminated. The IMCs have fully grown along the Cu/Al interface and effectively filled the gaps at the Cu/SUS304 interface.

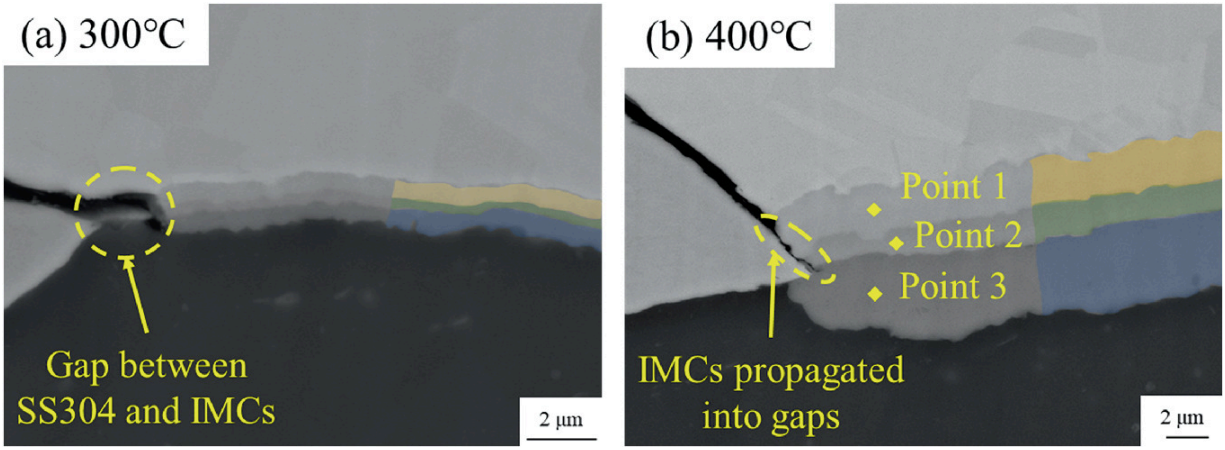


Fig. 2.39 Growth of IMCs at the interface of Cu/Al/Cu laminates after annealing: **a** 300 °C and **b** 400 °C

The thickness of the IMC layer in these metal laminates annealed at 300 and 400 °C is statistically analyzed, are shown in Table 2.4. For the sample annealed at 300 °C, the total thickness of the IMC layer is determined to be 1.36 μm, with a thickness of 0.56 μm for the layer closer to the Al side, 0.28 μm for the middle layer, and 0.52 μm for the layer closer to the Cu side. Under the annealing condition of 400 °C, the total thickness of the IMC layer is 6.71 μm, with a thickness of 2.24 μm

for the layer closer to the Al side, 1.18 μm for the middle layer, and 1.99 μm for the layer closer to the Cu side.

Table 2.4 Thickness of each IMC layer after annealing at 300 and 400 °C

IMC layer	300 °C/μm	400 °C/μm
Cu side	0.52	1.99
Middle layer	0.28	1.18
Al side	0.56	2.24
Total thickness	1.36	6.71

The specific phase composition of each IMC layer in the sample annealed at 400 °C is analyzed using EDS. The positions of the points are shown in Fig. 2.39b, and the results are presented in Table 2.5. It can be inferred that the crystalline phase of the IMC layer close to the Al side, with the highest thickness, is Al_2Cu. The crystalline phase in the middle layer is AlCu, with an atomic ratio of Al to Cu close to 1:1. The crystalline phase of the IMC layer close to the Cu side is Al_4Cu_9, with the highest content of Cu element.

Table 2.5 Composition of Cu and Al elements at each point in the IMCs layer (atomic %)

Position	Al	Cu	Phase
1	39.86	60.14	Al_4Cu_9
2	55.74	44.26	AlCu
3	68.98	31.02	Al_2Cu

In order to ascertain the distribution of the elements in SUS304 interlayer after annealing at 300 and 400 °C and their influence on the formation of IMCs, EDS mapping and line scanning are performed at the interface of Cu/Al laminates, as shown in Fig. 2.40. For the sample annealed at 300 °C, only trace amounts of Al and Cu elements diffuse across the bonding interface. The elements of Fe, Cr, and Ni in SUS304 interlayer exhibit the negligible diffusion. According to the line scanning results, only Al and Cu elements are present and the diffusion profile shows a smooth transition (Fig. 2.40a). For the sample annealed at 400 °C, noticeable diffusion of both Al and Cu elements can be observed. The distribution of these elements extends beyond their

respective matrices, forming densely distributed regions. This indicates that both Al and Cu elements have undergone significant diffusion after annealing at 400 °C, resulting in the formation of relatively thick IMCs layers. On the other hand, there is no evident diffusion of Fe, Cr, Ni, and other elements in SUS304 interlayer. The distribution of these elements in IMC layer is mainly confined to the region overlapping with SUS304 interlayer in the line scan results across the IMC layer. The primary elements present are still Al and Cu. At this point, the diffusion profiles of both elements exhibit noticeable changes. The diffusion of Al element decreases linearly with increasing distance from the Al matrix, while the diffusion profile remains relatively smooth. In contrast, the diffusion of Cu element shows distinct breakpoints.

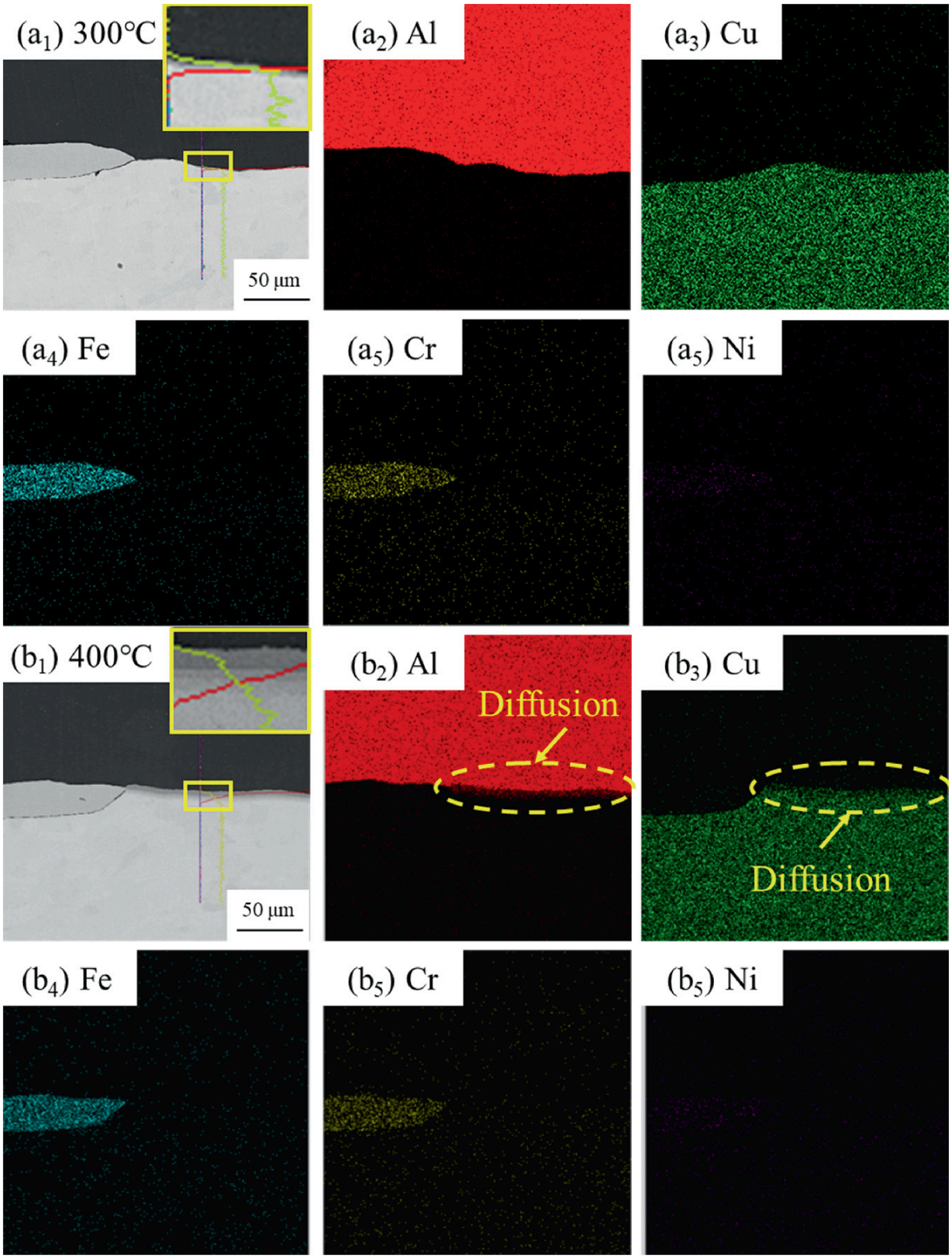


Fig. 2.40 EDS mapping and line scanning near the Cu/Al interface of annealed samples at **a** 300 °C and **b** 400 °C

Therefore, on one hand, there is a significant mutual diffusion area between Al and Cu elements, corresponding to the thicker layer of metal IMCs formed after annealing at 400 °C. On the other hand, the almost stepwise diffusion profile of Cu element at the Cu-Al interface indicates the generation of various metal IMCs at this interface, with different proportions of Al and Cu elements. This finding validates the conclusions presented in Table 2.5.

In order to investigate the detailed effects of annealing on the bonding interface of Cu-Al laminates with SUS304 interlayers and the role of IMCs in the bonding strength, the morphology of the peeling surface of the annealed Cu-Al laminate with a SUS304 was studied using SEM. Figure 2.41 shows the morphology of the peeling surface of the Cu-Al laminate with a SUS304 interlayer after annealing at 200 °C. On the Cu side (Fig. 2.41a), large undulations can be observed on the peeling surface. This is because the interface has a high bonding strength at this stage, and the peeling path passes through the Al layer in the middle of the Cu-Al laminate to reach the other Cu layer at the bottom. In the enlarged region in Fig. 2.41c, some ductile dimples with a diameter of about 100 μm and numerous slightly smaller dimples can be observed. Residual Al matrix can also be observed in some of the dimples. In the enlarged region in Fig. 2.41e, the underlying Cu matrix has been fully squeezed into the cracks of the fractured SUS304 interlayer, and numerous ridge-like morphologies can be observed. On the Al side (Fig. 2.41b), a similar morphology to the Cu side can be observed in the locally enlarged image of the direct Cu-Al contact region (Fig. 2.41d). This region is densely covered with dimples and ridge-like morphologies. In the region embedded by the fragments of the SUS304 interlayer (Fig. 2.41f), there are “ridges” with corresponding shapes and higher heights distributed along the edges of the SUS304 interlayer fragments, and numerous dimples are present around them.

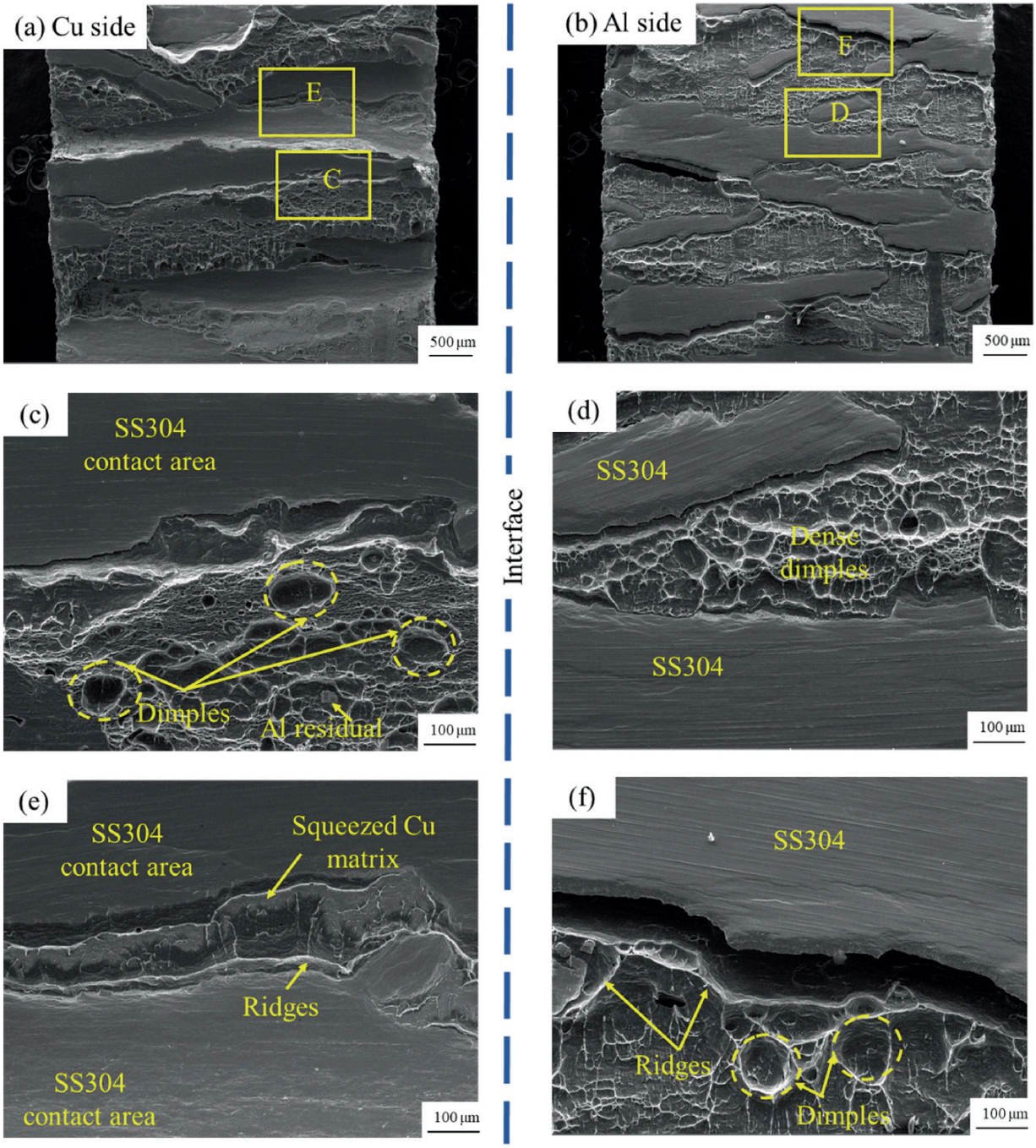


Fig. 2.41 The peeling surface of Cu/Al/Cu laminates with SUS304 interlayer after 200 °C annealing; **a**, **c**, **e** Cu side, **b**, **d**, **f** Al side

Based on the analysis of the morphology of the peeling surface on the Cu and Al sides, it can be concluded that apart from the region in contact with the SUS304 interlayer, the dominant features on the peeling surface are dimples and ridge-like morphologies. The peeling path mainly occurs at the Cu/Al interface and the Cu/SUS304 interface. It can be inferred that after annealing at 200 °C, the bonding strength at

the Cu/Al interface is high, and the plasticity of the Cu and Al matrices has recovered to a certain extent.

Figure 2.42 displays the morphology of the peeling surface of the Cu-Al laminate with a SUS304 interlayer after annealing at 300 °C. At this temperature, IMCs have formed at the interface, leading to a significant change in the peeling surface morphology. In the locally enlarged image on the Cu side (Fig. 2.42c), the morphology in the region in contact with SUS304 is similar to that of the sample annealed at 200 °C, appearing as a smooth surface without dimples or ridge-like morphologies. Near the edge of the SUS304 contact region, numerous densely arranged and almost parallel ridge-like morphologies can be observed, with some smooth peeling surfaces visible between adjacent ridges. In the locally enlarged image on the Cu side (Fig. 2.42e), the region in direct contact with Al exhibits a dominance of smooth peeling surfaces, along with the presence of densely distributed ridge-like morphologies. On the Al side, the overall morphology is consistent with that on the Cu side. In the locally enlarged image in the region adjacent to the fragments of the SUS304 interlayer (Fig. 2.42d), ridge-like morphologies are distributed along the edges of the SUS304 interlayer, accompanied by smooth peeling fracture surfaces. Far from the fragments of the SUS304 interlayer, there is a large population of almost parallel ridge-like morphologies. In Fig. 2.42f, a larger area of smooth peeling fracture surfaces is observed in the region where Cu and Al are in direct contact, while the remaining areas are densely populated with ridge-like morphologies.

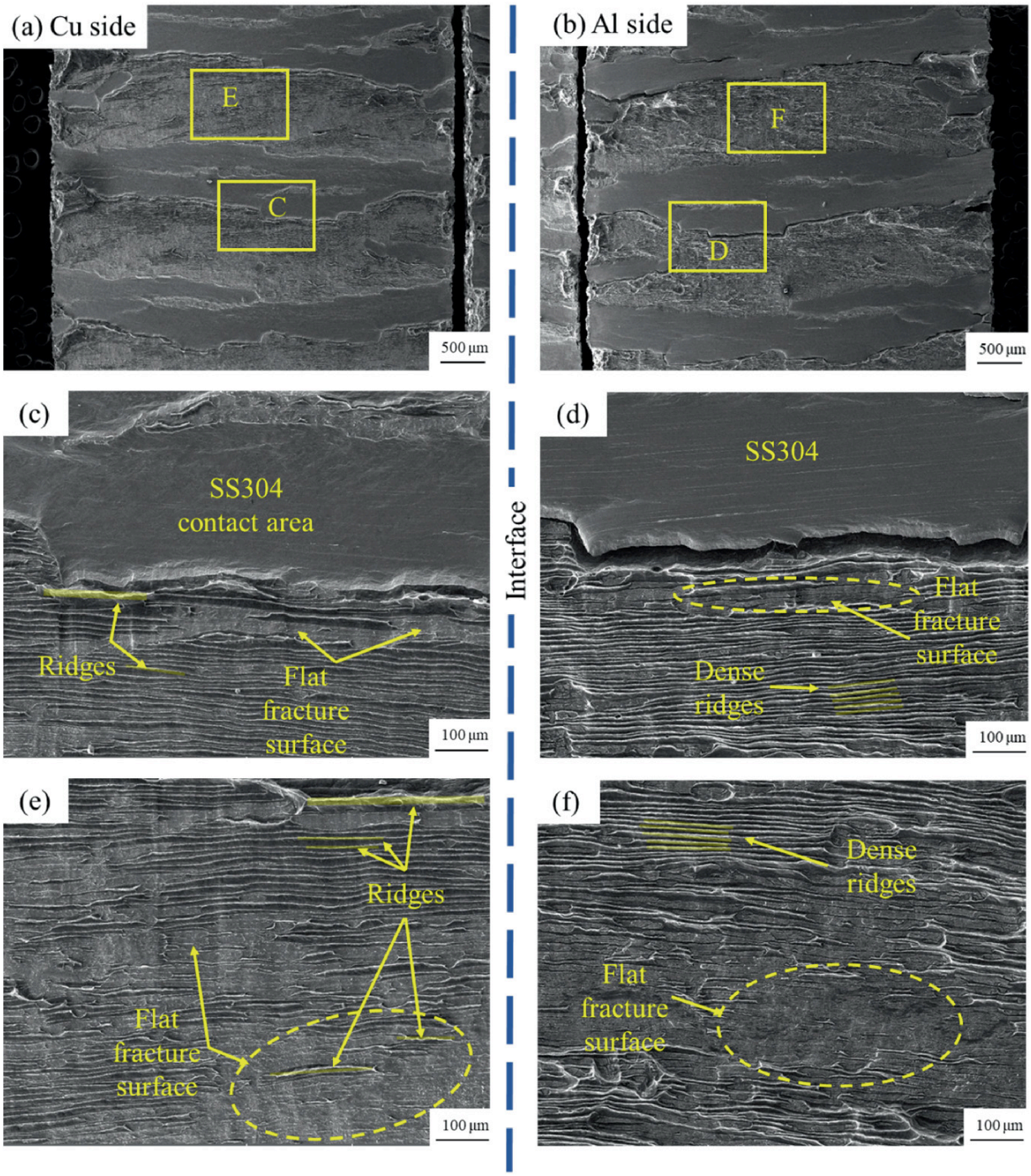


Fig. 2.42 The peeling surface of Cu/Al/Cu laminates with SUS304 interlayer after 300 °C annealing; **a**, **c**, **e** Cu side, **b**, **d**, **f** Al side

In the analysis of the peeling surface morphology of the sample annealed at 300 °C, a significant presence of smooth peeling fracture surfaces and parallel ridge-like morphologies was observed. To determine the specific phases of these morphologies, EDS analysis was performed, as shown in Fig. 2.43. The EDS results of six points in

Fig. 2.43 were analyzed to determine the atomic ratio of Cu and Al elements at each point, leading to conclusions about the main phases at each point, as summarized in Table 2.6.

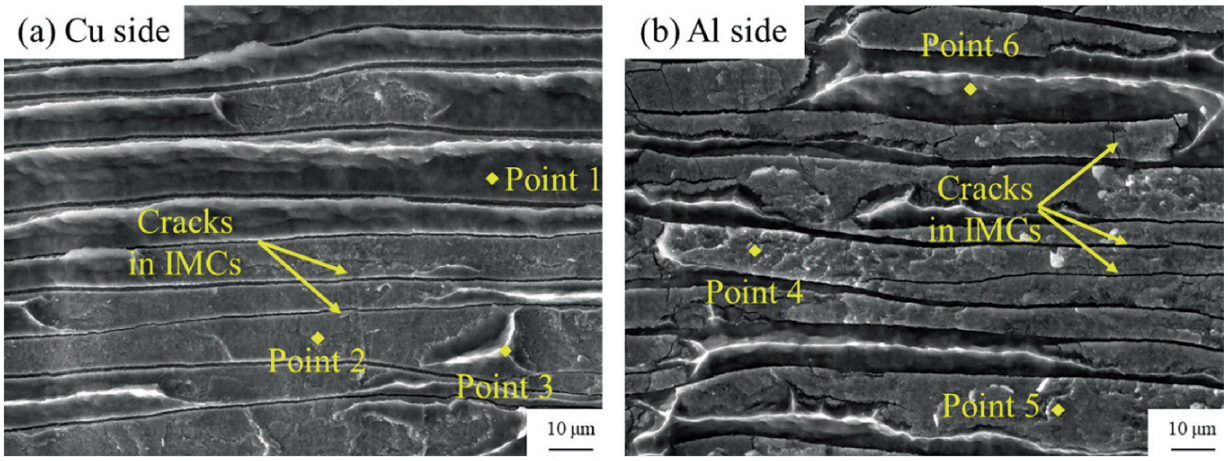


Fig. 2.43 The EDS results of peeling surface in 300 °C annealed samples. **a** Cu side, **b** Al side

Table 2.6 Composition of Cu and Al elements at each point in the peeling surface of the samples subjected to 300 °C annealing (atomic %)

Position	Al	Cu	Phase
1	97.52	2.48	Al
2	36.62	63.38	Al_4Cu_9
3	98.17	1.83	Al
4	55.18	44.82	Al_2Cu + AlCu
5	64.76	35.24	Al_2Cu
6	99.64	0.36	Al

The EDS results indicate that the ridge-like morphologies and the region between adjacent ridges on the peeling surface of the sample annealed at 300 °C are mainly composed of Al matrix. The smooth peeling fracture surfaces are primarily composed of IMCs Al_2Cu and AlCu, with the presence of the Al_4Cu_9 phase in some areas. Additionally, numerous cracks were observed in the IMCs on both the Cu and Al sides. These cracks mainly run parallel to the direction of the ridge-like morphologies, which is perpendicular to the rolling direction. Furthermore, some randomly oriented smaller cracks were also

present. These cracks within the IMCs significantly weaken the bonding effect at the interface.

Figure 2.44 depicts the morphology of the peeling surface of the Cu-Al laminate with a SUS304 interlayer after annealing at 400 °C. As the thickness of the IMC layer increases, the peeling surface becomes smoother overall. Even in the region embedded with the SUS304 interlayer, there is no significant elevation compared to other areas. Moreover, the ridge-like morphologies in the interface morphology are practically absent. On both the Cu and Al sides, except for the region in contact with SUS304, the IMCs exhibit brittle fracture characteristics. Numerous cracks, oriented perpendicular to the rolling direction, can be observed within the brittle IMCs. The IMCs, which cover the entire interface, essentially prevent direct contact between the Cu and Al matrices. The significant presence of cracks within these IMCs leads to a drastic reduction in the bonding strength of the interface after annealing at 400 °C.

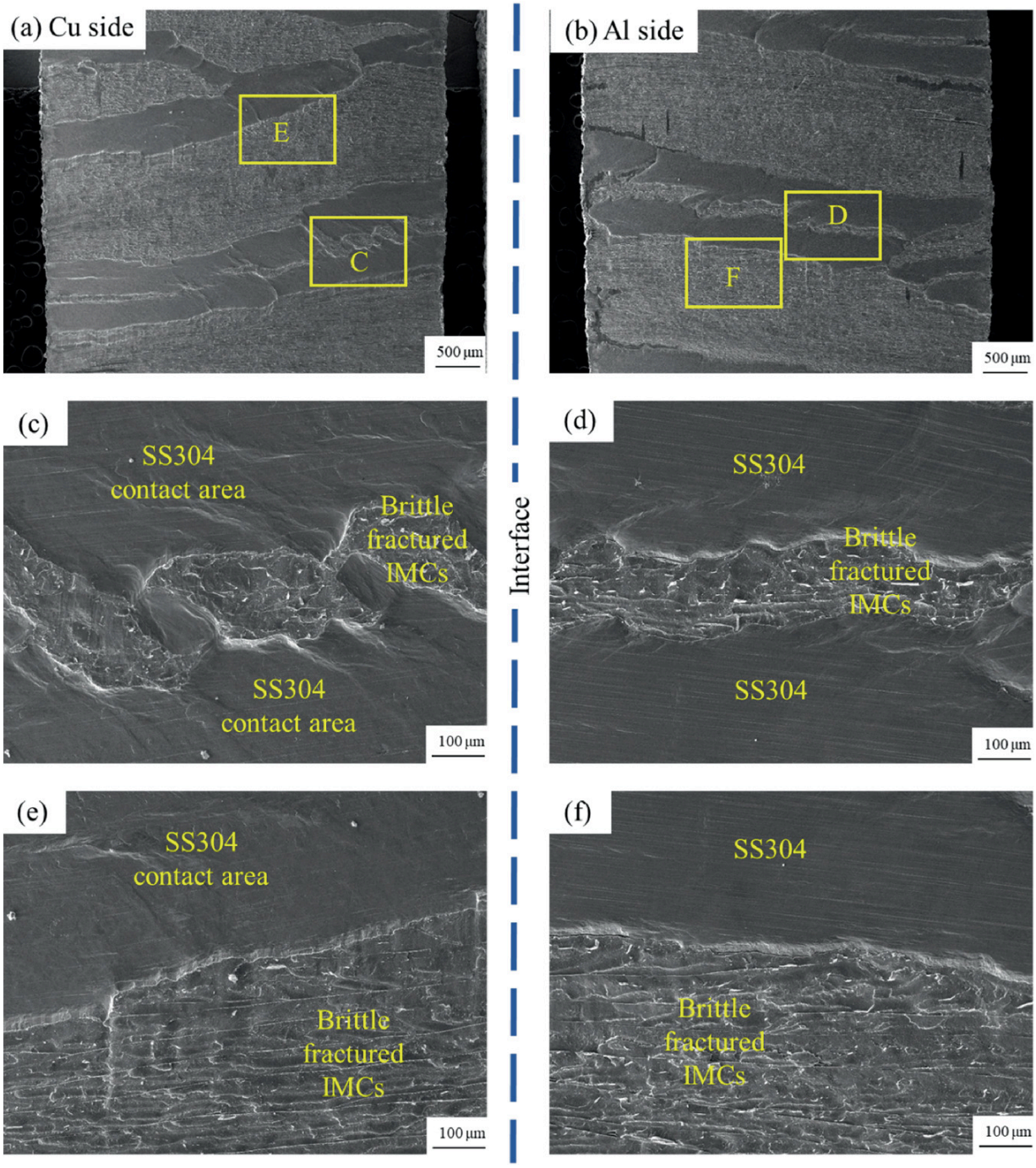


Fig. 2.44 Peeling surface of Cu/Al/Cu laminates with SUS304 interlayer after 400 °C annealing; **a**, **c**, **e** Cu side, **b**, **d**, **f** Al side

To further determine the distribution and phase composition of the brittle fractured IMCs in the morphology of the peeling surface after annealing at 400 °C, SEM and EDS analyses were conducted on the selected region. The results are shown in Fig. 2.45 and Table 2.7,

respectively. It can be observed that the brittle fractured IMCs consist of Al_2Cu and AlCu, indicating that the fractures occur within the IMC layer.

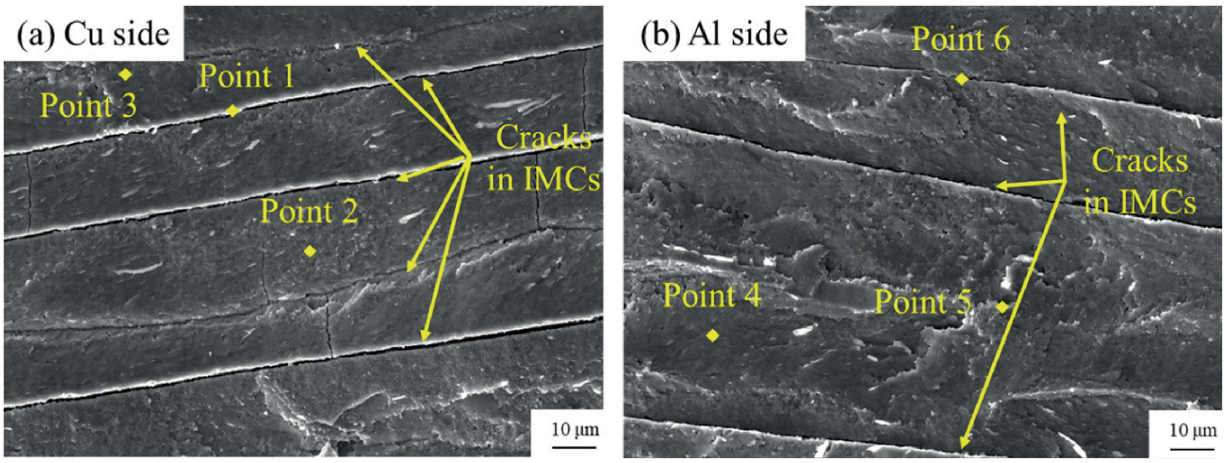


Fig. 2.45 The EDS results of peeling surface in 400 °C annealed samples. **a** Cu side, **b** Al side

Table 2.7 Composition of Cu and Al elements at each point in the peeling surface of the samples subjected to 400 °C annealing (atomic %)

Position	Al	Cu	Phase
1	70.38	29.62	Al_2Cu
2	54.83	45.17	Al_2Cu + AlCu
3	67.15	32.85	Al_2Cu
4	68.82	31.18	Al_2Cu
5	65.09	34.91	Al_2Cu
6	57.94	42.06	Al_2Cu + AlCu

Figure 2.46 presents the distribution of microstructures and the level of recrystallization in the as-annealed sample. From Fig. 2.46c, it can be observed that the majority of the sample is comprised of deformed grains. In the Cu matrix, a small amount of substructure can be observed. This is mainly attributed to the fact that the presence of a SUS304 interlayer in the Cu-Al laminate promotes plastic deformation concentration at the interface. As a result, the degree of deformation in the Cu matrix is relatively lower, leading to some grains exhibiting lower deformation levels compared to the overall deformation. Additionally, a layer of fine recrystallized grains can be observed at the

Cu/SUS304 interface, which is a result of dynamic recrystallization during the plastic deformation and grain refinement process.

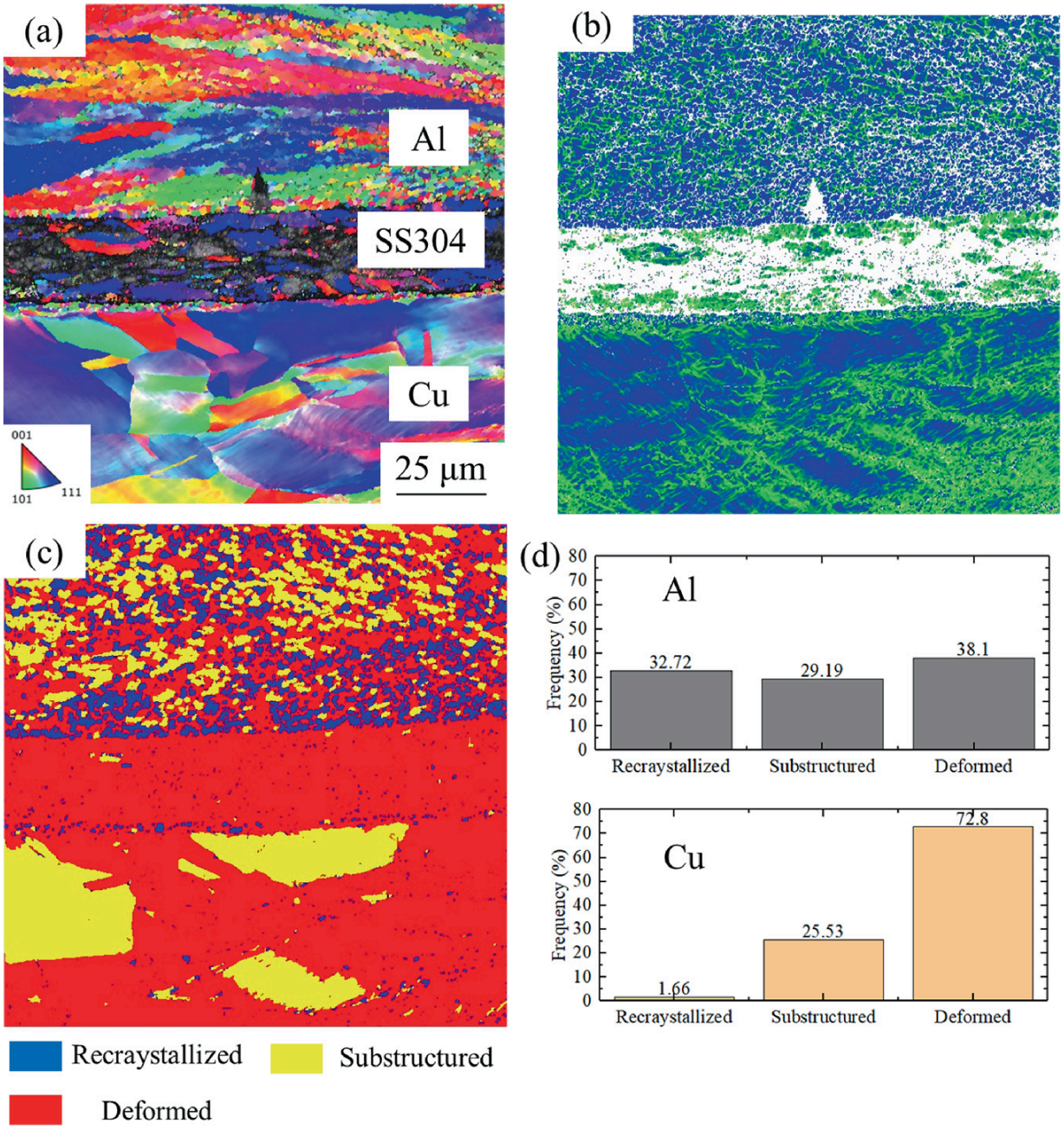


Fig. 2.46 Unannealed sample, **a** IPF map, **b** corresponding KAM result, **c** distribution of recrystallization, **d** fraction of recrystallized grains, substructured grains and deformed grains in Al side and Cu side respectively

On the Al side, a uniform distribution of recrystallized grains, substructures, and deformed grains can be observed. This is because the Al matrix is relatively soft, and a significant level of plastic

deformation occurs throughout the Al matrix. During the process of grain refinement caused by plastic deformation, dynamic recovery and dynamic recrystallization occur simultaneously. Furthermore, a similar phenomenon can be observed on the Al/SUS304 interface, where a densely distributed region of recrystallized grains can be observed. This is also attributed to the alteration of stress and strain distribution in the Al matrix due to the presence of the SUS304 interlayer.

Figure 2.46d illustrates the proportions of three different types of grain structures, namely recrystallized grains, substructures, and deformed grains, in the Al and Cu matrices. In the Al matrix, the proportion of recrystallized grains is 32.72%, the proportion of substructures is 29.19%, and the proportion of deformed grains is 38.1%. The proportions of these three types of grains are relatively equal, with a slightly higher proportion of deformed grains. In the Cu matrix, the proportion of recrystallized grains is 1.66%, the proportion of substructures is 25.53%, and the proportion of deformed grains is 72.8%.

Figure 2.47 presents the distribution of microstructures and the level of recrystallization in the sample annealed at 200 °C. In the IPF map (Fig. 2.47a), the grains in the sample annealed at 200 °C did not exhibit significant growth. On the Al side, the characteristic rolling texture is still retained, with numerous grain boundaries dispersed throughout. On the Cu side, the grains near the Al/Cu interface and the Cu/SUS304 interface are relatively small, while the grains further away from the interface are coarser. Furthermore, it can be observed that, compared to the as-annealed sample, the grains on the Cu side of the sample annealed at 200 °C are actually smaller. This is primarily due to the presence of shear bands along the edges of the SUS304 interlayer, which further promotes microstructure refinement.

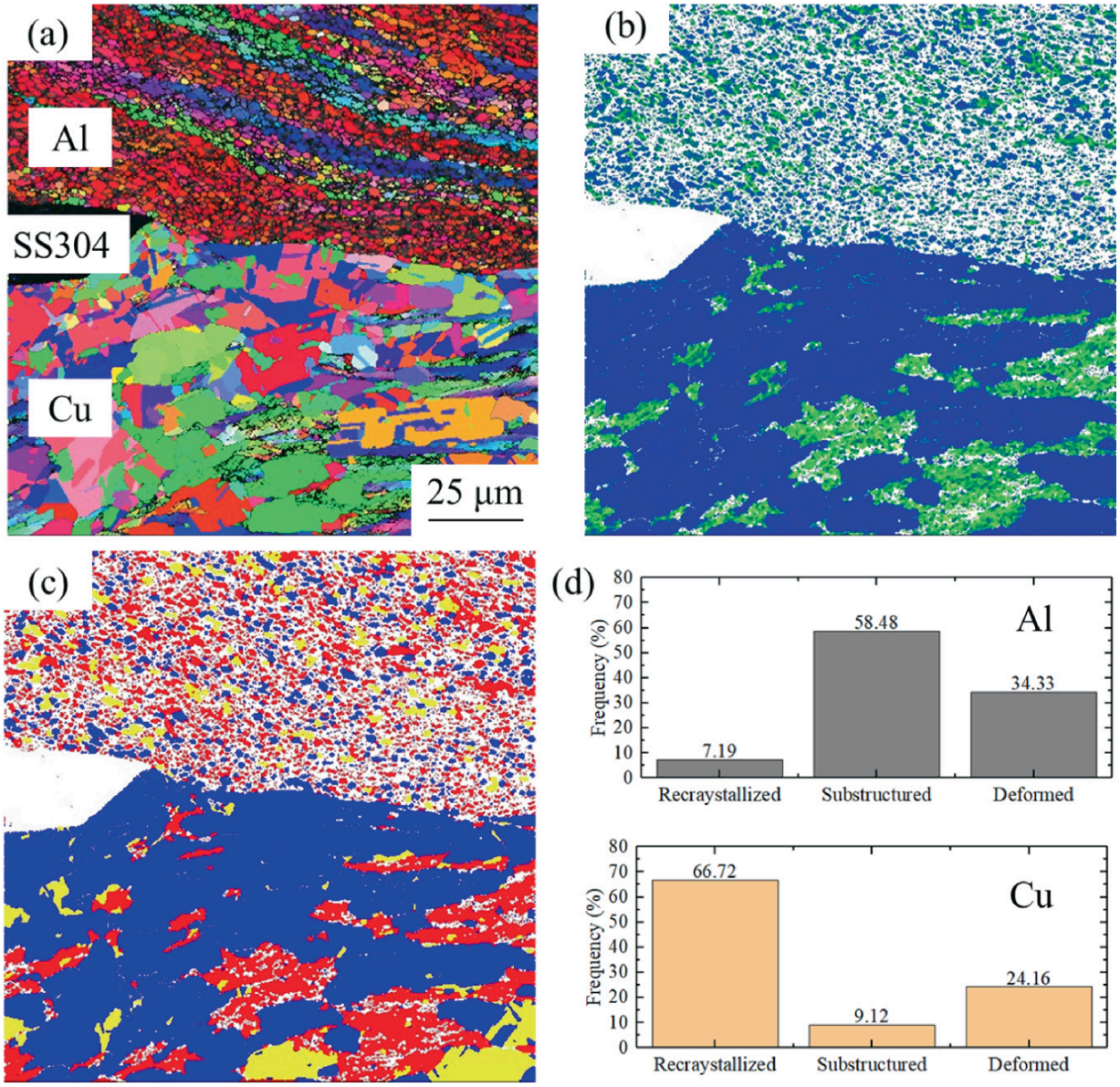


Fig. 2.47 200 °C annealed sample, **a** IPF map, **b** corresponding KAM result, **c** distribution of recrystallization, **d** fraction of recrystallized grains, substructured grains and deformed grains

In the KAM results shown in Fig. 2.47b, the Al side exhibits regions with higher strain and regions with lower strain. On the Cu side, a large portion of the regions reflects strain relief, with only some grains showing higher strain levels. By analyzing the recrystallization distribution map (Fig. 2.47c), it can be observed that the Al matrix consists of randomly distributed partially recrystallized grains and a significant amount of substructures. On the Cu side, most of the grains along the interface have undergone recrystallization, while the grains corresponding to higher strain levels in the KAM map still remain as

deformed grains. The primary reason for the occurrence of recrystallization in the grains adjacent to the interface is the significant plastic deformation experienced by these grains during the rolling and bonding process, with the introduction of shear deformation by the SUS304 interlayer. These areas of grains suffer a high degree of grain refinement and accumulate numerous defects, reducing the energy required for recrystallization nucleation. The presence of a considerable proportion of deformed grains is attributed to the relatively low annealing temperature, where the limited heat input is insufficient to ensure recrystallization nucleation in the majority of the grains.

The proportions of three different types of grain structures, namely recrystallized grains, substructures, and deformed grains, in the Al and Cu matrices were measured and are shown in Fig. 2.47d. In the Al matrix, the proportion of recrystallized grains is 7.19%, the proportion of substructures is 58.48%, and the proportion of deformed grains is 34.33%. In the Cu matrix, the proportion of recrystallized grains is 66.72%, the proportion of substructures is 9.12%, and the proportion of deformed grains is 24.16%.

Figure 2.48 presents the distribution of microstructures and the level of recrystallization in the sample annealed at 300 °C. In the IPF map shown in Fig. 2.48a, it can be observed that the grain size of the Cu-Al matrix has increased to some extent, and the characteristic rolling texture has been almost completely eliminated. The grains exhibit a random orientation typical of recrystallization. At the interface of the laminate, in the region of direct contact between the Cu and Al matrices, the refined grain structure has essentially disappeared. It has been replaced by IMCs formed by the diffusion of Cu and Al elements. In the region where the fragments of the SUS304 interlayer contact the Cu-Al matrix, a portion of the refined grain structure is retained. This is primarily because the SUS304 interlayer suppresses the formation of Cu-Al IMCs, and therefore, the grain recovery and recrystallization in this region are incomplete. The KAM results in Fig. 2.48b show that after annealing at 300 °C, the stress in the Cu-Al matrix has been relieved. Particularly for the Cu matrix, there are no significant regions of stress concentration. The release of stress also affects the mechanical interlocking effect at the interface of the Cu-Al

laminate. Additionally, it can be observed from Fig. 2.48c that the sample annealed at 300 °C no longer retains deformed structures. The Cu and Al matrices consist primarily of recrystallized grains and substructures. Figure 2.48d provides a statistical analysis of the proportions of recrystallized grains, substructures, and deformed grains in the Cu-Al matrix. The results show that in the Al matrix, the proportion of recrystallized grains is 4.59%, the proportion of substructures is 92.16%, and the proportion of deformed grains is 3.24%. The predominant grain structure is substructures. This is mainly attributed to the relatively low annealing temperature and short annealing time, which result in incomplete recrystallization in the Al matrix. In the Cu matrix, the proportion of recrystallized grains is 67.85%, the proportion of substructures is 30.94%, and the proportion of deformed grains is 1.21%.

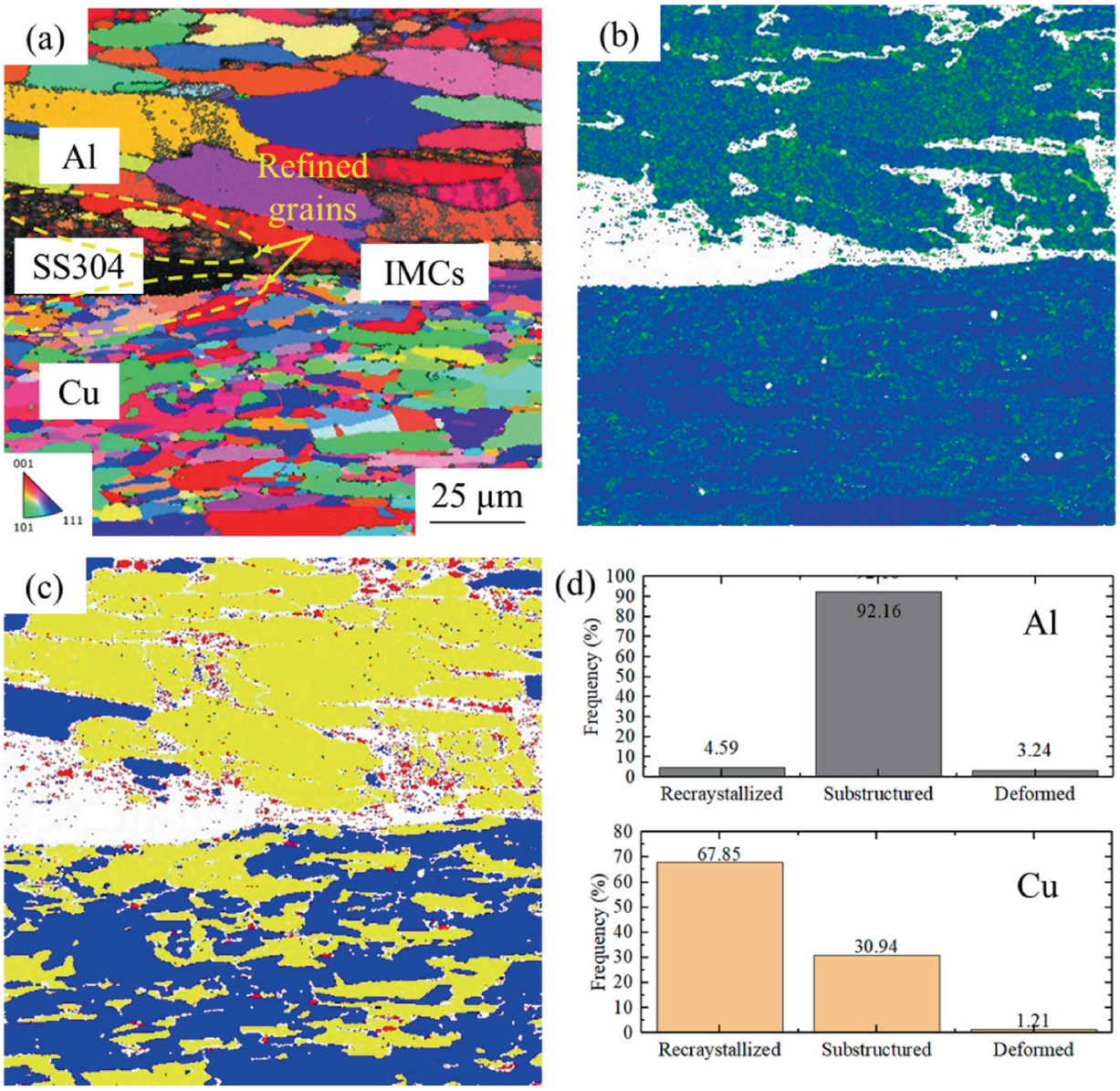


Fig. 2.48 300 °C annealed sample, **a** IPF map, **b** corresponding KAM result, **c** distribution of recrystallization, **d** fraction of recrystallized grains, substructured grains and deformed grains

Figure 2.49 displays the distribution of microstructures and the level of recrystallization in the sample annealed at 400 °C. In Fig. 2.49a, it can be observed that the grains on the Al side are predominantly equiaxed with random orientations. On the Cu side, the grains have grown larger, and there are numerous annealing twins. At the interface of the Cu/Al laminate, a significantly thickened layer of IMCs can be observed in the region of direct Cu-Al bonding. The refined grains around the fragments of the SUS304 interlayer have essentially disappeared. After annealing at the higher temperature of 400 °C, the

accumulation of dislocations resulting from the rolling and composite processes leads to their merging and release. This reduces the obstruction effect on the diffusion and migration of Cu and Al atoms into the opposite matrix metal. Diffusion is enhanced, resulting in a significant increase in the thickness of the IMC layer. These results indicate that the Cu-Al matrix has undergone complete recovery after annealing at 400 °C. In the KAM results shown in Fig. 2.49b, the stress is further relieved in the sample annealed at 400 °C. Only in some regions where complete recovery has not occurred or at grain boundaries can a denser distribution of stress be observed. The statistical results in Fig. 2.49d show that in the Al matrix, the proportion of recrystallized grains is 2.12%, the proportion of substructures is 90.87%, and the proportion of deformed grains is 7.02%. In the Cu matrix, the proportion of recrystallized grains is 32.97%, the proportion of substructures is 60.32%, and the proportion of deformed grains is 2.72%.

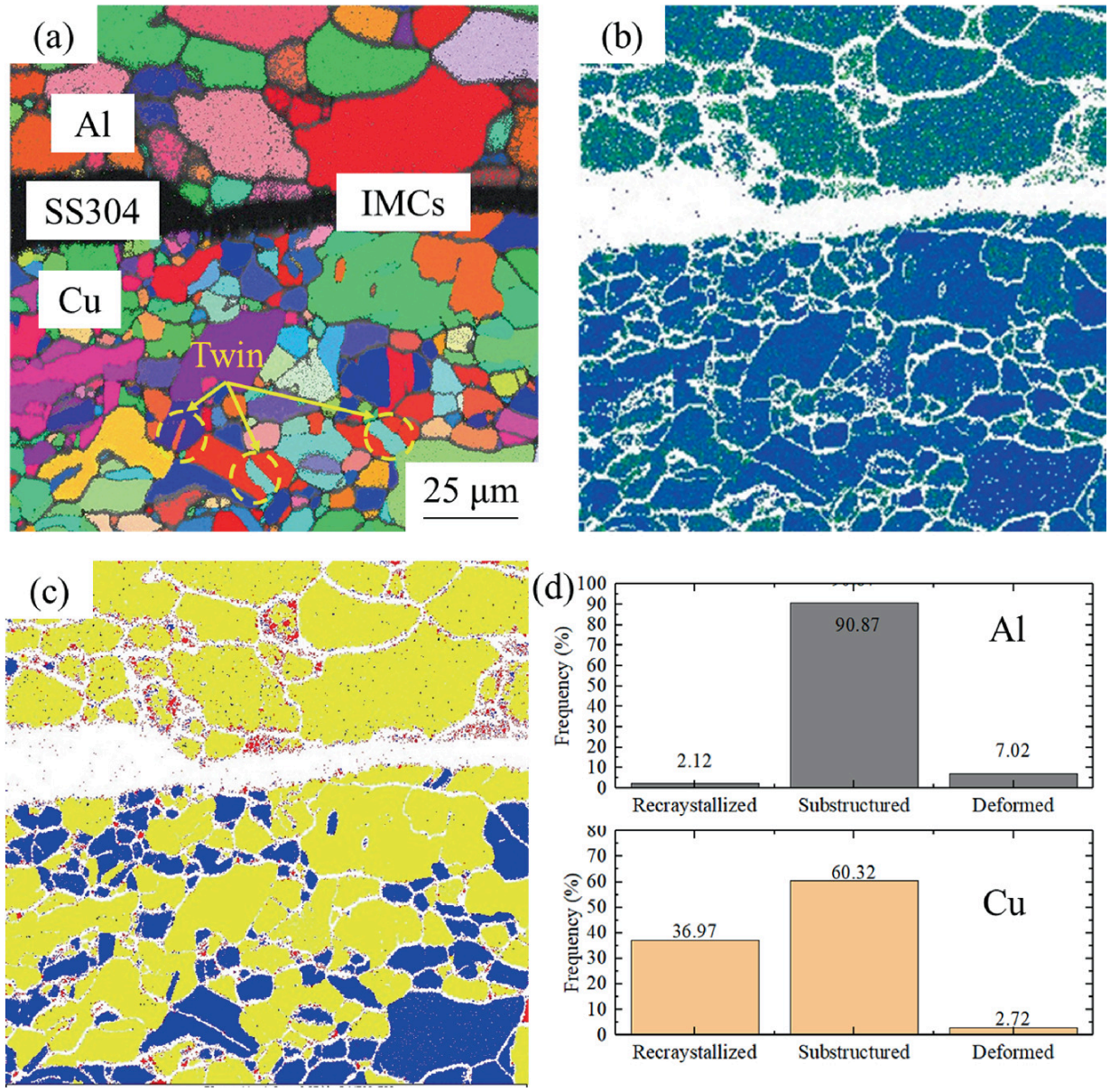


Fig. 2.49 400 °C annealed sample, **a** IPF map, **b** corresponding KAM result, **c** distribution of recrystallization, **d** fraction of recrystallized grains, substructured grains and deformed grain

Figure 2.50 illustrates the fracture surface morphology of the Cu/Al laminate with a SUS304 interlayer. For the as-received sample, as shown in Fig. 2.50a, the fracture surface appears relatively flat. The SUS304 layer can be observed at the interface between the Cu and Al matrices. Upon further magnification of the localized region at the interface, as shown in Fig. 2.50b, features such as dimples and cleavage planes can be observed on the fracture surface. This fracture pattern is indicative of quasi-cleavage fracture. Meanwhile, at the interface, the Cu and Al matrices can be seen to be tightly connected, suggesting that the

interface of the as-received sample can withstand deformation along the rolling direction without separation due to its high bonding strength. Additionally, the early fracture occurrence on one side of the Cu matrix, as observed in Fig. 2.50a, is mainly due to the incomplete symmetry of the SUS304 interlayer during the rolling and bonding process. During tensile testing, the stress concentration near the fragments of the SUS304 interlayer leads to the early fracture of one side of the Cu matrix compared to the other matrix materials. After annealing at 200 °C, the plasticity of the Cu-Al matrix has undergone partial recovery. The presence of necking phenomena in the fracture surface of the sample, as shown in Fig. 2.50c, is evident. The fragments of the SUS304 interlayer are embedded at the interface of the Cu-Al matrix. After annealing at 300 °C, as the plasticity of the Cu-Al matrix further recovers, the sharpness of the necking angle increases. Another notable feature is the appearance of intact fragments of the SUS304 interlayer on the fracture surface with a significantly wider width than that of the necked Cu-Al matrix, as shown in Fig. 2.50e. This is mainly because during stretching, the SUS304 fragments, with their higher strength compared to the annealed Cu-Al matrix, undergo deformation primarily concentrated in the Cu-Al matrix. Furthermore, the SUS304 interlayer has tightly bonded to the matrix. On the fracture surface, the Al matrix appears to be “torn” as the layers separate due to necking, and some fragments of the SUS304 interlayer remain tightly bonded to the Al matrix. In the locally enlarged region at the interface of the fracture surface in Fig. 2.50f, numerous densely distributed dimples can be observed in the matrix, indicating good plasticity of the matrix after annealing at 300 °C. Additionally, in the region of direct contact between Cu and aluminum, partial strip-like fractures of the Cu-Al IMCs can be observed on the fracture surface, with the fracture direction parallel to the direction of tension. As the annealing temperature increases to 400 °C, the Cu-Al matrix exhibits good plasticity. The fracture surface still displays the necking morphology of the Cu-Al matrix, but at this point, the fragments of the SUS304 interlayer are no longer visible on the fracture surface (Fig. 2.50g). In the magnified image of the interface (Fig. 2.50h), numerous Cu-Al IMCs IMCs can be observed in the region of direct contact between Cu and Al. The fractures of the Cu-Al IMCs can occur both parallel and perpendicular to

the rolling direction, with the fractures perpendicular to the rolling direction being predominant.

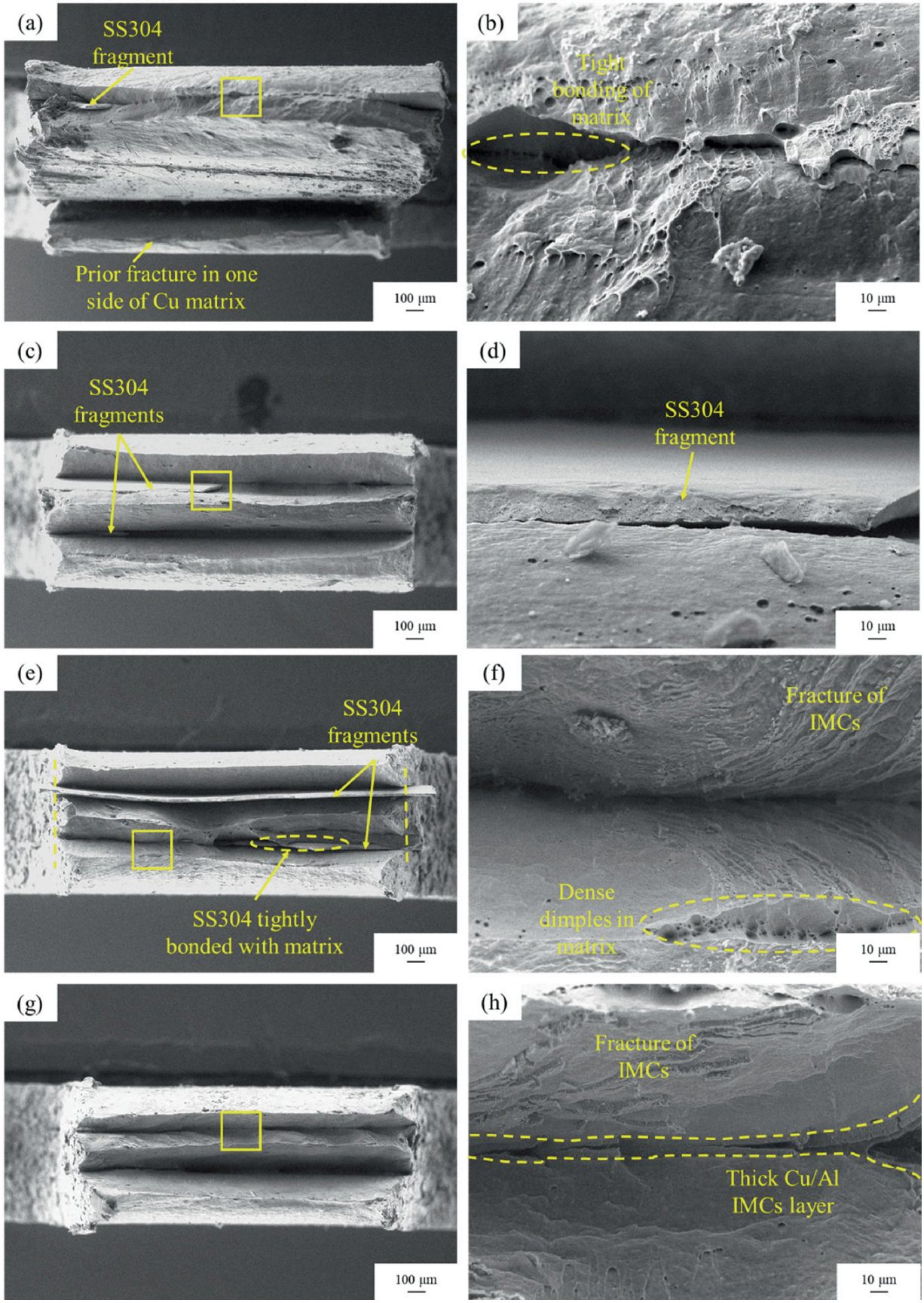

(a)
SS304 fragment
Prior fracture in one side of Cu matrix
100 μm
(b)
Tight bonding of matrix
10 μm
(c)
SS304 fragments
100 μm
(d)
SS304 fragment
10 μm
(e)
SS304 fragments
SS304 tightly bonded with matrix
100 μm
(f)
Fracture of IMCs
Dense dimples in matrix
10 μm
(g)
100 μm
(h)
Fracture of IMCs
Thick Cu/Al IMCs layer
10 μm

Fig. 2.50 Tensile fracture morphology of Cu/Al/Cu laminates with SUS304 interlayer subjected to annealing under different temperature. **a**, **b** Unannealed, **c**, **d** 200 °C, **e**, **f** 300 °C, **g**, **h** 400 °C

2.7 Cu/Al Laminates Subjected to High-Temperature Accumulative Roll Bonding

We investigated the influence of temperature on the mechanical behavior of Cu/Al laminates [15]. The rolling temperature affected the structural evolution of diffusion layer between Cu layers and Al layers. We found that the microstructure of diffusion layers in Cu/Al laminates processed by accumulative roll bonding (ARB) at high temperatures can be controlled to enhance their mechanical properties.

2.7.1 Mechanical Properties and Microstructure of Cu/Al Laminates During ARB

Figure 2.51 shows the mechanical properties of ARB-processed Cu/Al laminates at different rolling temperatures. When the rolling temperature is 350 °C, the Cu/Al laminates show a high yield stress, but the fracture engineering strain is the lowest among the four rolling temperatures. When the rolling temperature increases to 400 °C, the yield stress of the Cu/Al laminates decreases remarkably. However, with further increasing the rolling temperature to 450 and 500 °C, the yield stress of laminates changes to increase while their ductility reduces slightly. Figure 2.51b shows that the ultimate tensile stress of laminates increases with higher rolling temperature, and also shows that the laminates subjected to rolling temperature of 400 °C have the best ductility. The mechanical properties of the ARB-processed Cu/Al laminates when the rolling temperature is higher than 400 °C is unexpected and we will explain these feathers from the microstructural evolution in the following.

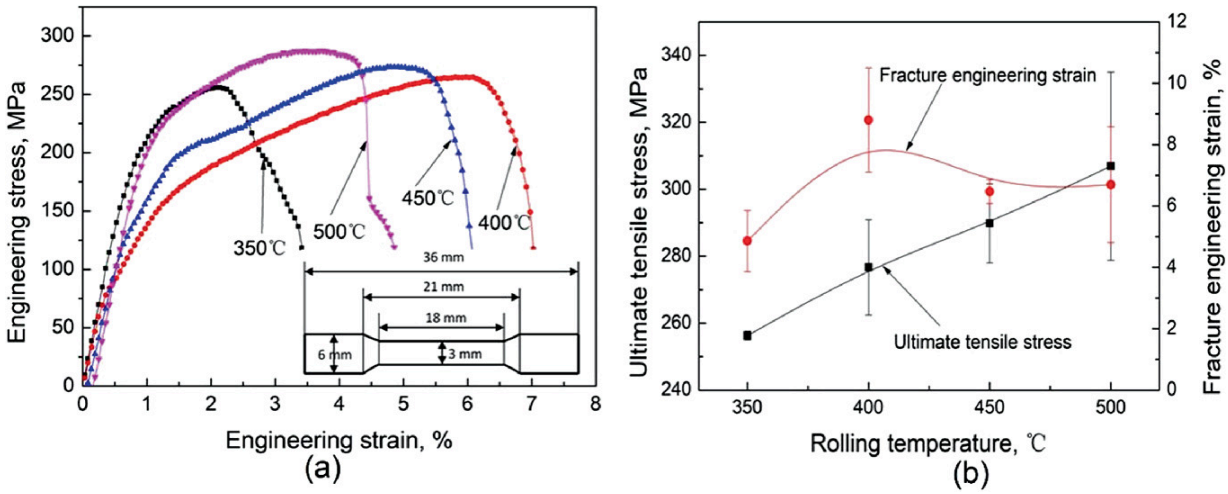


Fig. 2.51 Mechanical properties of Cu/Al laminates. **a** Engineering stress–strain curves. **b** Ultimate tensile stress as a function of rolling temperature, and fracture engineering strain as a function of rolling temperature

Figure 2.52 shows the macro-distribution of Cu layer and Al layer after three ARB passes. Deformation of Cu layers and Al layers during ARB are relatively uniform. In addition, the interface between Cu layer and Al layer are bonded well. Figures 2.53 and 2.54 shows the optical microscopy images and SEM images of the microstructure of Al and Cu layers after ARB processing at different temperatures. The ARB-process at low temperature of 350 °C refined the grain size and the resulting composites show high yield stress and low ductility. With increasing the rolling temperature, the grain size increases obviously. The mean thickness of grains increases from 9.4 to 13.5 μm when the rolling temperature increases from 350 to 500 °C (Fig. 2.53). After the ARB processing, the microstructure morphed into a laminated structure (Fig. 2.54). In Fig. 2.54, when the rolling temperature is 350ºC, the mean thickness of laminated structures is 3.1 μm and increases to 7.5 μm when the rolling temperature increases to 500 °C.

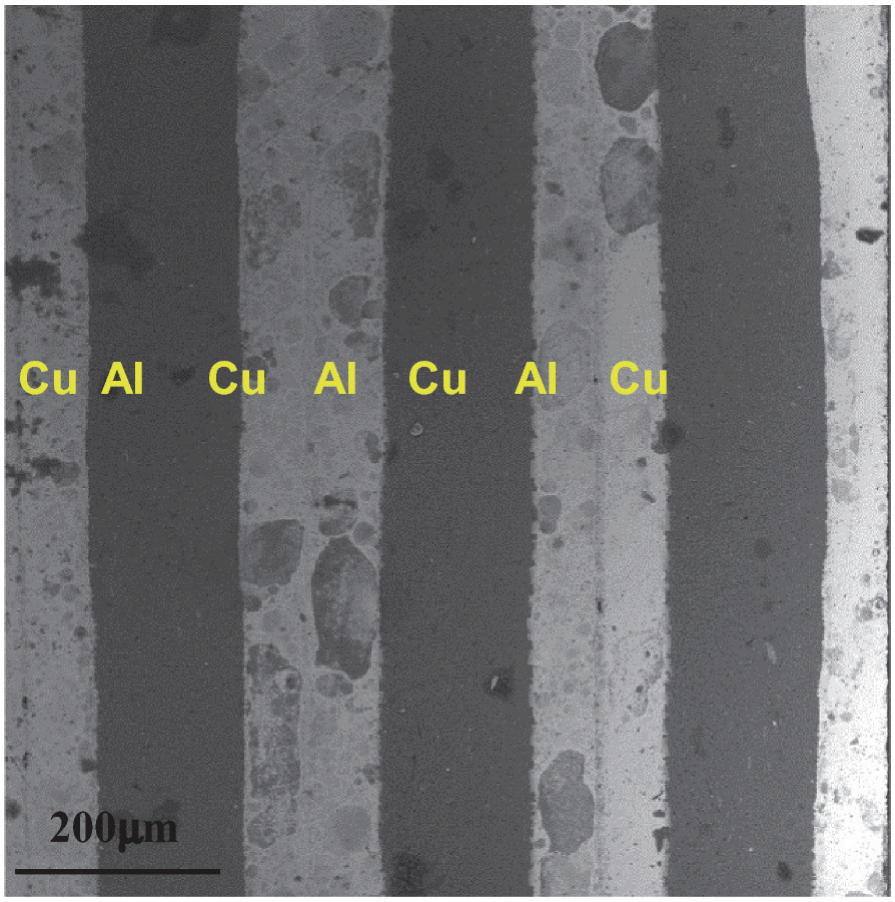


Fig. 2.52 SEM image of ARB processed Cu/Al laminate

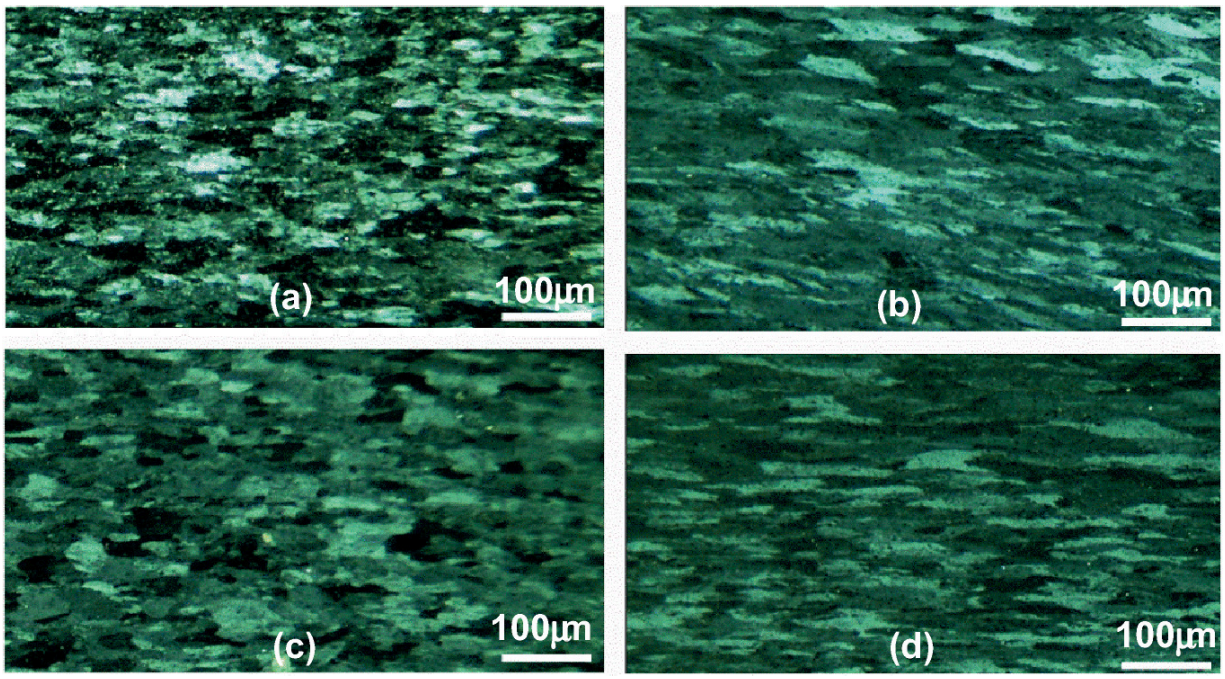


Fig. 2.53 Optical microscopy images of the microstructure in Al layer after ARB processing at different rolling temperatures, **a** 350 °C; **b** 400 °C; **c** 450 °C; **d** 500 °C

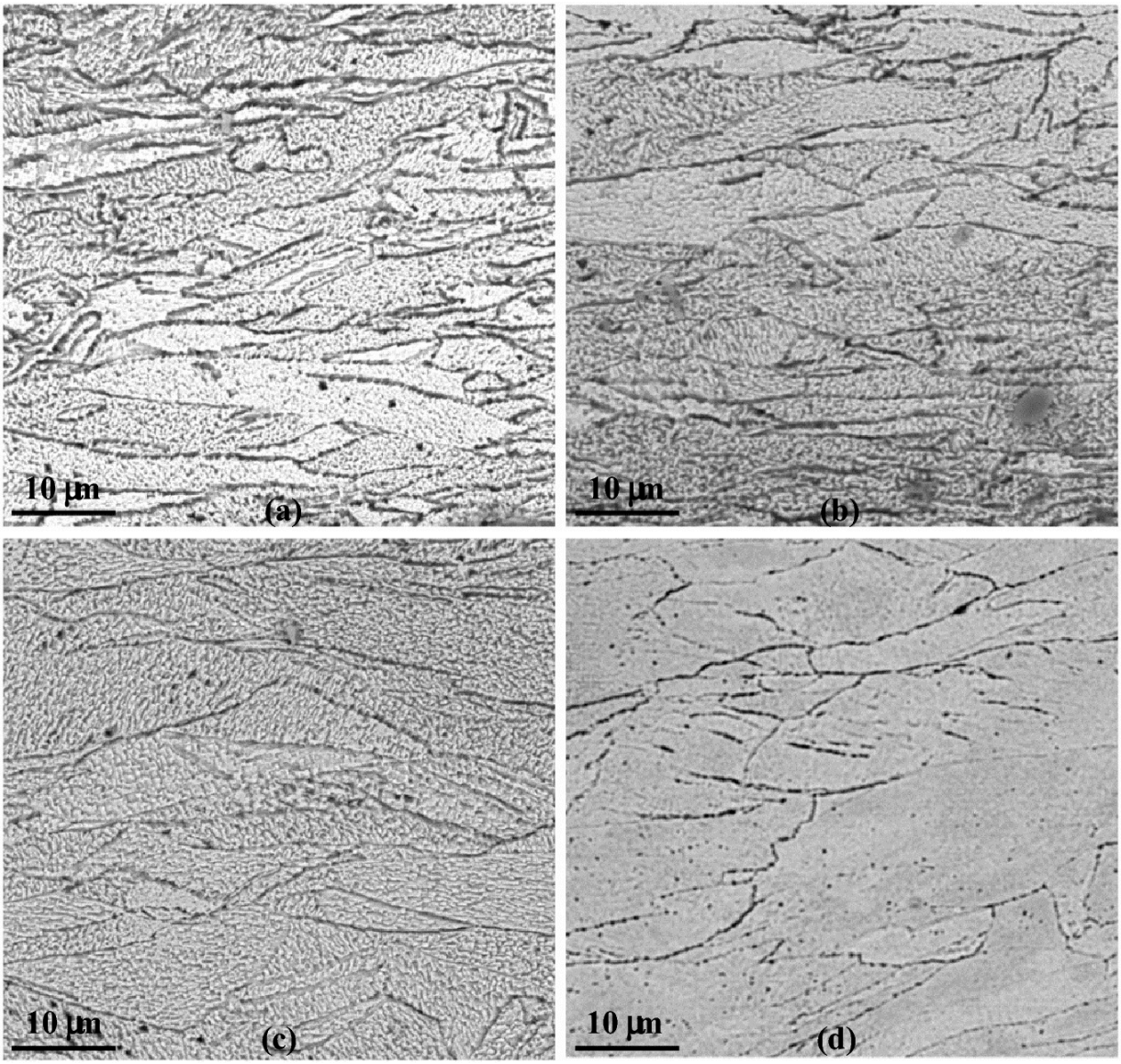


Fig. 2.54 SEM images of the microstructure in Cu layer after ARB processing at different rolling temperatures, **a** 350 °C; **b** 400 °C; **c** 450 °C; **d** 500 °C

Figure 2.55a–d show the SEM images of the microstructure near the interface between Cu layer and Al layer. When the rolling temperature is 350 °C, it is difficult to detect the Al/Cu IMC layer in the laminate after three- ARB passes. However, when the rolling temperature increases to 400 °C, intermetallic layers appear near the interface. As the rolling temperature increases, the thickness of intermetallic layer between Cu layer and Al layer increases. Figure 2.55d shows that the intermetallic layer becomes serrated after ARB processing at 500ºC,

which is a common feature of bimetallic composites after high-temperature rolling.

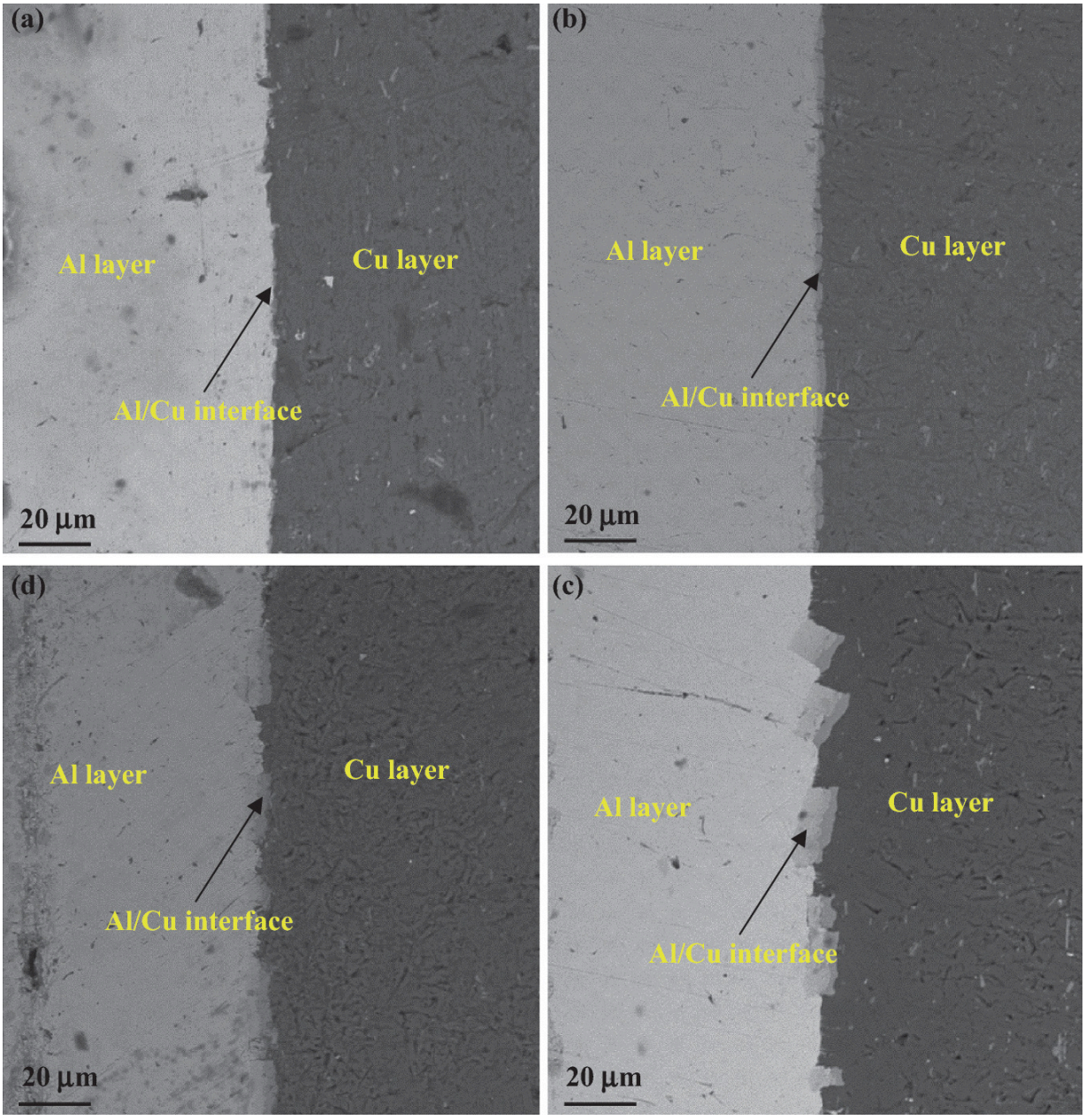


Fig. 2.55 SEM images of structure near the interface between Cu layer and Al layer after three ARB passes, **a** 350 °C; **b** 400 °C; **c** 450 °C; **d** 500 °C

Figure 2.56a–d show the EDS mapping of Al and Cu element distribution near the interface between Cu layer and Al layer. With increasing the rolling temperature, the thickness of diffusion zone between Cu layer and Al layer increases significantly and four tests were taken at random places for each sample. The average thickness of

diffusion layer is only 1.79 μm at rolling temperature of 350 °C and increases to 27.87 μm at 500 °C. Here, we assume that the thickness of diffusion layer is zero for the Cu/Al laminate processed by ARB at room temperature. The relationship between the mean thickness of diffusion layer ($t_{diffusion_layer}$) and the rolling temperature (T) is shown in Fig. 2.56e, which can be fitted by Eq. (2.26),

$$t_{diffusion_layer} = 1997.1\left(\frac{T}{1000}\right)^{6.11688} \tag{2.26}$$

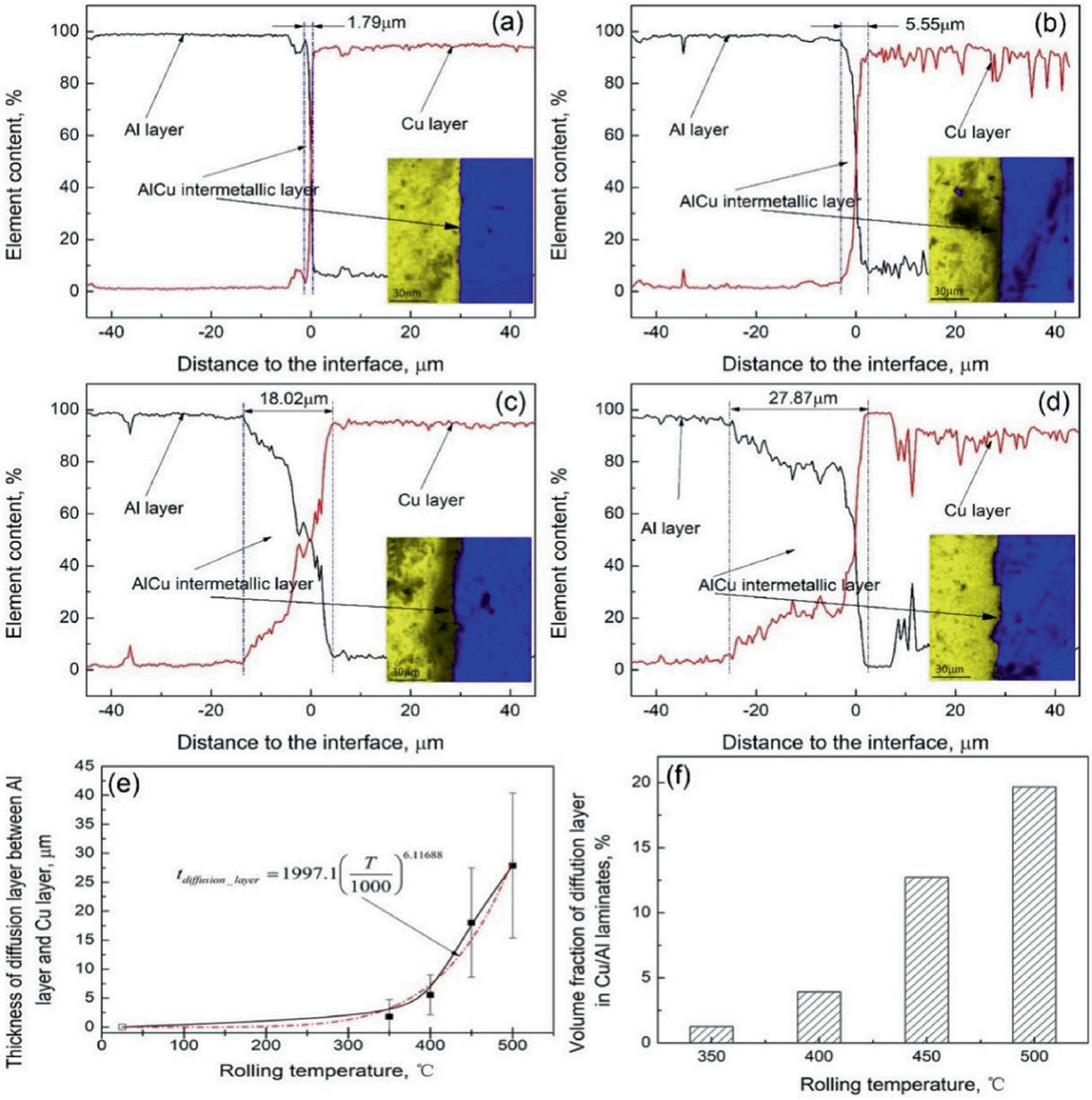


Fig. 2.56 Cu and Al element distribution near Cu/Al interface after three ARB passes for rolling temperature at **a** 350 °C, **b** 400 °C, **c** 450 °C and **d** 500 °C; **e** The mean thickness of diffusion layer between Al layer and Cu layer vs rolling temperature; **f** Volume fraction of diffusion layer versus rolling temperature

Equation (2.26) is fitted by the allometry model, and the thickness of diffusion layer and rolling temperature is exponentially related, with the scaling exponent of the equation being 6.11688. It is obvious that the mean thickness of diffusion layer between Cu layer and Al layer increases quickly with raising rolling temperature. We further assume that the thicknesses of diffusion layer are the same in the laminates, and since there are six Cu/Al interfaces in the laminates, thus the volume fraction of diffusion layer in the laminates can be obtained, as shown in Fig. 2.56f. When the rolling temperature is 400 °C, the volume fraction of diffusion layer is 3.9%. When the rolling temperature increases to 450 °C, the volume fraction of diffusion layer is 12.7%. The change in the thickness of the diffusion layer is related with the mechanical properties well. It is obvious that the effect of diffusion layer on the mechanical behavior of the laminates cannot be neglected when the rolling temperature is higher than 450 °C, despite that the influence is slight when the rolling temperature is lower than 400 °C.

Figure 2.57 shows the SEM images of fracture surface of Al/Cu laminates after tensile tests. In Fig. 2.57b, the dimples are deeper and the number of dimples is more compared with other samples, which implies the higher ductility of samples when the rolling temperature is 400 °C. In addition, the debonding between layers is very clearly when the rolling temperature is 350 °C (Fig. 2.57a), and the debonding between layers is slightly when the rolling temperature is 500 °C (Fig. 2.57d). These results mean that the bonding strength increases with rolling temperature.

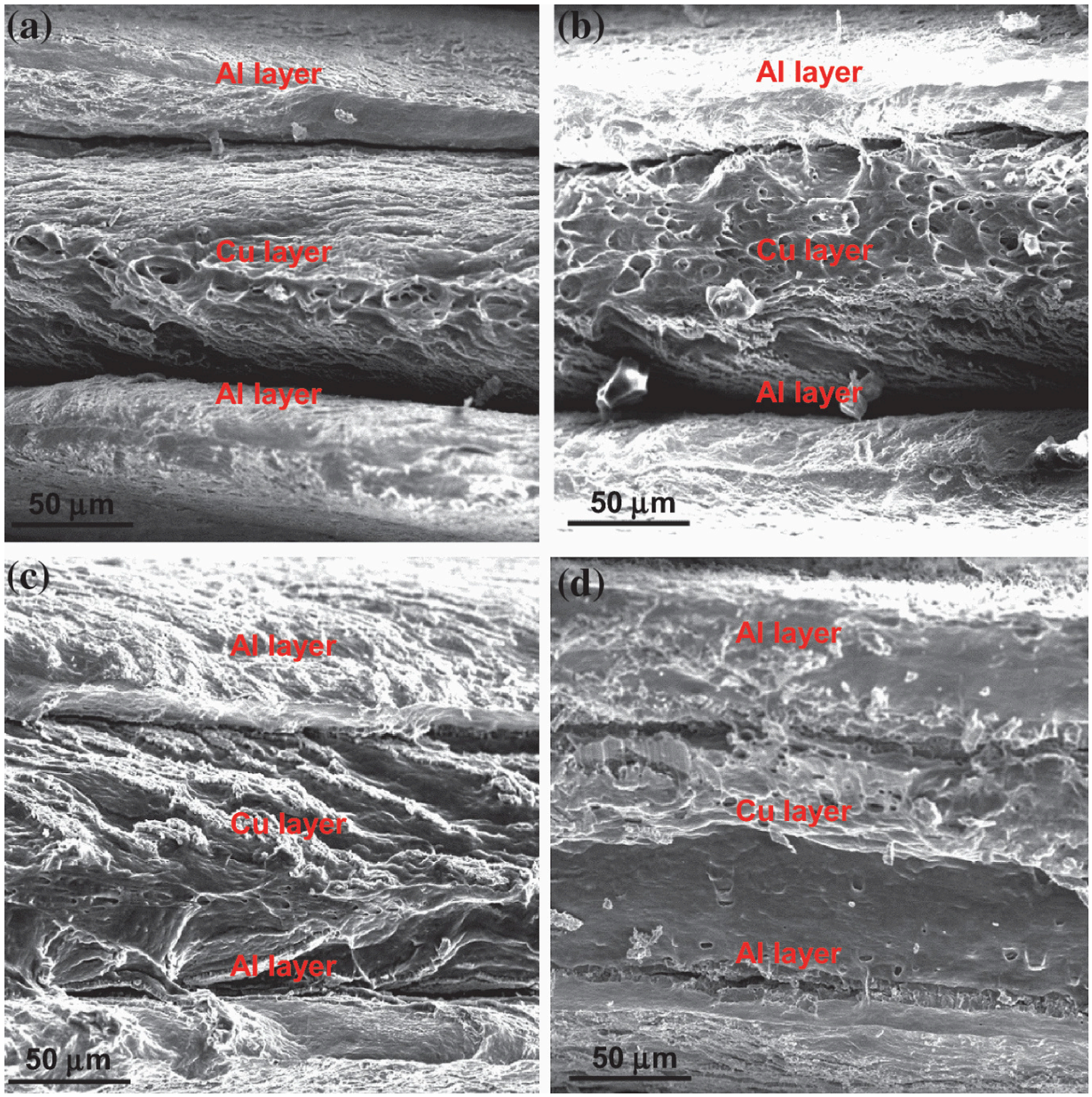


Fig. 2.57 SEM images of fracture surface of laminates for rolling temperature at **a** 350 °C, **b** 400 °C, **c** 450 °C and **d** 500 °C

2.7.2 Strengthening Mechanism of Cu/Al Laminates During ARB

In Fig. 2.51, the Cu/Al laminates processed by ARB at 500 °C show the highest yield strength and tensile strength among all samples. In this study, the ARB processing parameters are the same except for the rolling temperatures. It is obvious that the rolling temperatures affect the grain sizes of Cu layer and Al layer in laminates which affects the

mechanical properties of the laminates. Generally, with finer grain size, the yield stress of the composites increases. Under plastic deformation, the grain size in metals is related to dislocation cell thickness and dislocation density, which can be described in Eqs. (2.27)–(2.29),

$$\rho_c = \gamma \left(\alpha^* \frac{1}{\sqrt{3}b} \sqrt{\rho_{ws}+\rho_{wg}} - \beta^* \frac{6}{bd(1-f)^{1/3}} - k_0 \left(\frac{\gamma}{\gamma_0} \right)^{-1/n} \rho_c \right) \quad (2.27)$$

$$\rho_{ws} = \gamma \left(\beta^* \frac{\sqrt{3}(1-f)}{fb} \sqrt{\rho_{ws}+\rho_{wg}} + (1-\xi)\beta^* \frac{6(1-f)^{2/3}}{bdf} - k_0 \left(\frac{\gamma}{\gamma_0} \right)^{-1/n} \rho_{ws} \right) \quad (2.28)$$

$$\rho_{wg} = \gamma \xi \beta^* \frac{6(1-f)^{2/3}}{bdf} \quad (2.29)$$

where ρ_c is dislocation cell wall; ρ_{ws} is statistical dislocation density; ρ_{wg} is geometrically necessary dislocation density; γ is shear strain rate; α^* and β^*-are dislocation evolution rate control parameters for the materials; n is temperature sensitivity parameter, $n = \frac{B}{T}$, B is a materials parameter; T is temperature; f is the volume fraction of dislocation cell wall; b is the magnitude of the Burgers vector of the material; d is dislocation cell size; ξ is fraction of the dislocations incoming into cell walls from the cell interiors; k_0 is the dislocation annihilation rate parameter,

$$k_0 = 1.334 \times 10^{-5} T^2 - 1.176 \times 10^{-3} T + 6.14 \quad (2.30)$$

From Eqs. (2.28)–(2.30), when the temperature is higher than the room temperature, the dislocation density will reduce with increasing the temperature. Especially, grain growth occurs in sheets at higher temperature during deformation, which will result in coarse grain in the rolled sheets. As shown in Figs. 2.53 and 2.54, after three ARB passes, the grain size in pure Al and pure Cu increases dramatically as the rolling temperature increases from 350 to 500 °C. According to the Hall–Petch equation, the yield stress reduces with increasing grain size in crystalline materials. This can explain the decrease of yield stress of the Cu/Al laminates subjected to ARB at the rolling temperature of 350

and 400 °C. But, the yield stress of laminates increases as the rolling temperature increases from 400 to 500 °C although the grain size of laminates increases.

Increasing the rolling temperature might lead to higher bonding strength. In Fig. 2.57, the bonding quality between Cu layer and Al layer is the best when the Cu/Al laminates is fabricated by ARB at 500 °C. Peng et al. [6] studied the effect of rolling temperature on the bonding strength of Cu/Al laminates from 350 to 500 °C and found the bonding strength reaches the largest value when the rolling temperature is 430 °C. However, the relationship between bonding strength and mechanical properties of laminates is still under debate. Heydari and Sedighi [7] reported that the tensile strength of AA1050/AA5083 laminates processed by warm ARB increases with increasing rolling passes, but the bonding strength and elongation first decreases if the number of laminated layers is less than 8 and then increases by further increasing the number of laminated layers. Thus, the bonding strength between layers also cannot explain the change of mechanical properties of laminates subjected to ARB when the temperature is higher than 400 °C.

In Figs. 2.55 and 2.56e, the thickness of diffusion layer in laminates changes as rolling temperature varies, which affects the mechanical properties of laminates. Li et al. [8] reported Al/Cu laminates have the highest tensile strength after annealing at 300 °C for 1 h compared with cold rolled sheets. In Cu/Al laminates, the intermetallic diffusion layer contains Al_2Cu, AlCu, Al_3Cu_4 and Al_4Cu_9. The microhardness of AlCu intermetallic is larger than that of the Al layer and the Cu layer, which may reach nine times of the microhardness of pure Cu when the Cu concentration in the as-solidified Al-Cu alloys is between 80 and 90% (at%). Thus, increasing the thickness of diffusion layer will increase the tensile strength. The interface diffusion happens during both the heating and rolling process. The diffusion is determined by the rolling processes which play an important role in bonding the two layers together and lead to the formation of bonded interface. In Fig. 2.56f, the volume fractions of diffusion layer in the laminates are 1.2%, 3.9%, 12.7% and 19.7% for the rolling temperature at 350 °C, 400 °C, 450 °C and 500 °C respectively. When the rolling temperature is 350 and 400 °C, the strength contribution from diffusion layer on the mechanical

properties is less than 3.9% of the total volume, which is much less than the effect of grain size in Cu layer and Al layer. However, when the rolling temperature is 450 and 500 °C, the effect of diffusion layer on the mechanical properties is larger than 12%, which plays a key role on the mechanical properties of laminates compared to the coarser grains at higher rolling temperature. Thus, the yield strength of Cu/Al composites increases due to the high fractions of diffusion layer, although the coarser grains reduce yield strength slightly. In addition, the ultimate tensile strength is also affected by the diffusion layer in composites. As the diffusion layer thickness increases, the ultimate tensile strength increases.

References

1. Jing YA, Qin Y, Zang XM, Li YH (2014) The bonding properties and interfacial morphologies of clad plate prepared by multiple passes hot rolling in a protective atmosphere. J Mater Process Tech 214:1686–1695
[Crossref]
2. Menon M, Chen IW (1999) Bimaterial composites via colloidal rolling techniques: I, microstructure evolution during rolling. J Am Ceram Soc 82:3413–3421
[Crossref]
3. Zhang L, Meng L, Zhou SP, Yang FT (2004) Behaviors of the interface and matrix for the Al/Cu bimetallic laminates prepared by roll bonding and diffusion annealing. Mater Sci Eng A 371:65–71
[Crossref]
4. Peng XK, Wuhrer R, Heness G, Yeung WY (1999) On the interface development and fracture behavior of roll bonded copper/aluminum metal laminates. J Mater Sci 34:2029–2038
[Crossref]
5. Luo CZ, Liang W, Chen ZQ, Zhang JJ, Chi CZ, Yang FQ (2013) Effect of high temperature annealing and subsequent hot rolling on microstructural evolution at the bond–interface of Al/Mg/Al alloy laminated composites. Mater Charact 84:34–40
[Crossref]
6. Cui XP, Fan GH, Geng L, Wu H, Pang JC, Gong JX (2014) Influence of raw material selection and fabrication parameters on microstructure and properties of micro–laminated TiB2–TiAl composite sheets. Mater Sci Eng A 589:83–88
[Crossref]
7. Yu HL, Liu XH, Li XW, Godbole A (2014) Crack healing in a low–carbon steel under hot plastic deformation. Metall Mater Trans A 45:1001–1009
[Crossref]

8. Wei D, Han J, Jiang Z, Lu C, Tieu K (2006) A study on crack healing in 1045 steel. J Mater Process Tech 177:233–237
[Crossref]
9. Yu HL, Liu XH (2011) Research on crack healing in slab during hot rolling. Adv Mater Res 264–265:439–444
[Crossref]
10. Gao HT, Ai ZR, Yu HL, Wu HY, Liu XH (2014) Analysis of internal crack healing mechanism under rolling deformation. PLoS ONE 9:e101907
[Crossref][PubMed][PubMedCentral]
11. Li J, Gao HT, Kong C, Yu HL (2022) Insight into the bonding mechanism in Cu/Al/Cu clad sheets via introduction of thin SUS304 interlayer. J Mater Res Tech 21:4619–4635
[Crossref]
12. Naseri M, Reihanian M, Borhani E (2016) Bonding behavior during cold roll–cladding of tri–layered Al/brass/Al composite. J Manuf Process 24:125–137
[Crossref]
13. Govindaraj NV, Lauvdal S, Holmedal B (2013) Tensile bond strength of cold roll bonded aluminum sheets. J Mater Process Tech 213:955–960
[Crossref]
14. Gao HT, Li J, Kong C, Yu HL (2023) Effect of annealing on mechanical properties and interfacial microstructure of Cu/Al/Cu clad sheets with a SUS304 interlayer. Under consideration
15. Wang L, Du QL, Li C, Cui XH, Zhao X, Yu HL (2019) Enhanced mechanical properties of lamellar Cu/Al composites processed via high–temperature accumulative roll bonding. Trans Nonfer Met Soc China 29:1621–1630
[Crossref]

© The Author(s), under exclusive license to Springer Nature Singapore Pte Ltd. 2024
H. Yu et al., *High-Performance Metallic Composites Fabricated by Advanced Rolling Techniques*
https://doi.org/10.1007/978-981-97-4331-5_3

3. Fabricated Metal Laminates via Cold Roll Bonding Techniques

Hailiang Yu[1] ✉, Haitao Gao[1] ✉ and Zhou Li[1]
(1) Central South University, Changsha, China

✉ **Hailiang Yu (Corresponding author)**
Email: yuhailiang@csu.edu.cn

✉ **Haitao Gao**
Email: gaohaitao@csu.edu.cn

Different from the hot roll bonding technique, cold roll bonding is completed at room temperature. Moreover, more than 60% reduction in the first rolling pass accompanied by the high-level equipment is necessary to obtain the high bonding quality. The significant advantages of cold roll bonding techniques are that the flexible regulation of IMCs thickness can be easily achieved through adjusting the heat treatment and the oxidation of matrix around the bonding interface can be avoided. From another perspective, serious edge cracks may appear in the metal laminates with hard and brittle matrix metals.

3.1 Al/Ti Laminates Subjected to Cold Roll Bonding and Annealing

Yu et al. [1] investigated the microstructure and mechanical properties of an Al/Ti/Al laminate resulting from different annealing times. We found that the technique of roll bonding combined with annealing of Al/Ti/Al laminates can be used to fabricate trimodal metallic sheets,

consisting of coarse-grained Al, ultrafine-grained Ti and $TiAl_3$ particles. When annealed for 24 h, the laminate shows the highest yield strength and good ductility.

In order to study the deformation mechanism of the Al/Ti/Al laminate after annealing for different time durations, we carried out two-dimensional finite element (FE) simulations of the tensile tests on the LS-DYNA platform. Figure 3.1 shows details of the geometry and mesh of the tensile test samples for annealing at 873 K for 6, 12, 24, 48 and 168 h at a local zone. The models were meshed with four-node elements, assuming a zero plain strain along the thickness direction. The mesh consisted of 94,519 nodes and 94,244 elements. We assumed that the voids are uniformly distributed at the frontier of the $TiAl_3$ particles and that the $TiAl_3$ particles are uniformly distributed in the Al matrix apart from the regions adjacent to the Ti layer. In addition, we also assumed that the number of voids and the number of $TiAl_3$ particles are related to the annealing period. With increasing annealing time, the $TiAl_3$ layer thickness increases and the number of voids gradually reduces. After annealing for 6 h, the voids take up half of the interfaces between the $TiAl_3$ particles and the Al matrix, as shown in Fig. 3.1a. For the 12 h annealing model, fewer voids are set at the frontier of the $TiAl_3$ layer. There are no visible voids at the $TiAl_3$ layer edge after annealing for 24, 48 and 168 h. In the foils annealed for 48 h, there is no pure Ti residue that transform into $TiAl_3$, as shown in Fig. 3.1d. In the FE models, the Al and Ti layers were assumed to be plastic kinematic materials, with yield stresses of 80 MPa and 515 MPa, respectively. The $TiAl_3$ is considered elastic with an elastic modulus of 216 GPa. In the models, tensile loading along the laminate rolling direction was applied to study the deformation features.

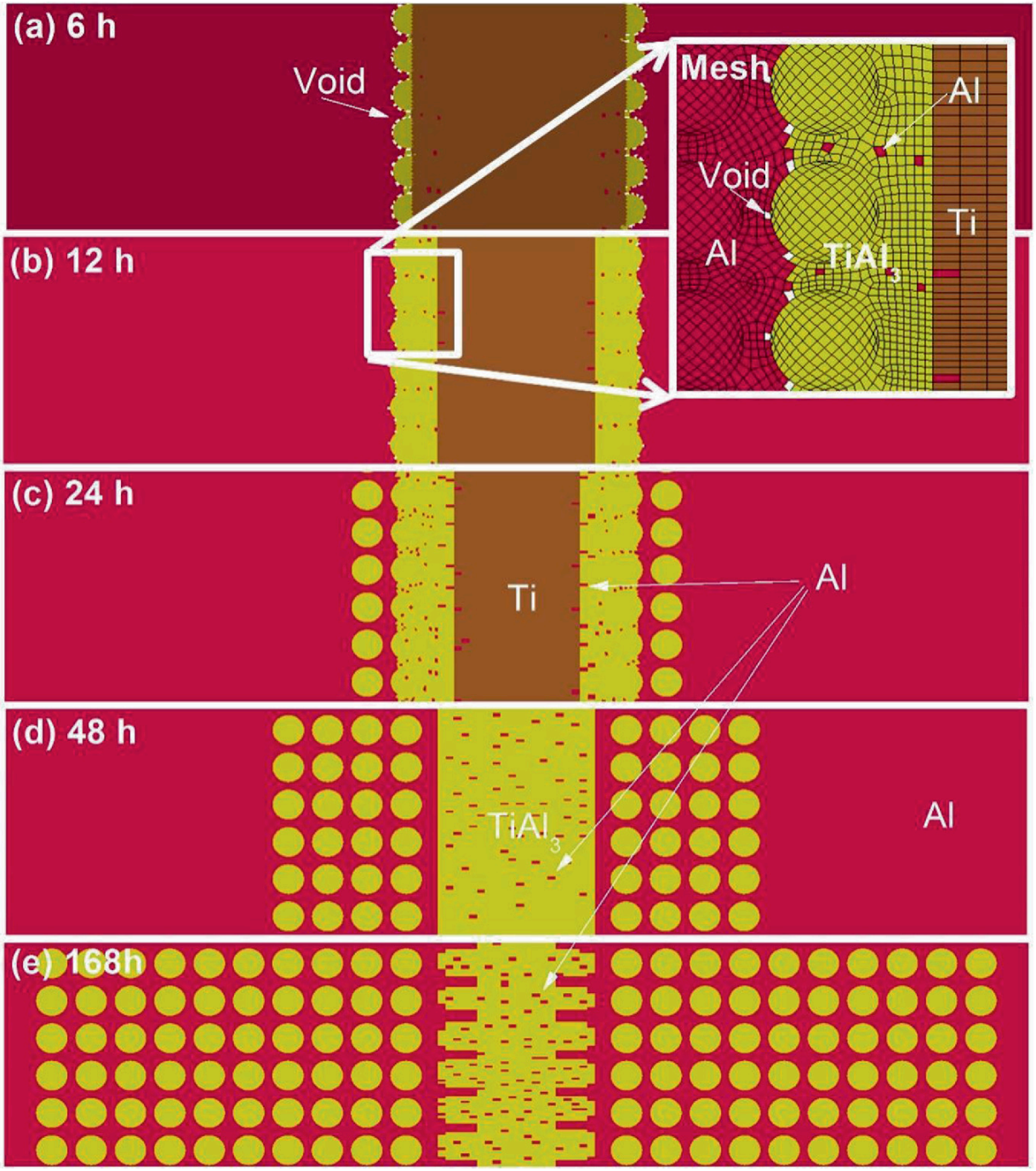


Fig. 3.1 Geometry and FE mesh of Al/Ti laminates after annealing at 873 K for **a** 6 h, **b** 12 h, **c** 24 h, **d** 48 h and **e** 168 h

3.1.1 Microstructure Evolution of Al/Ti Laminate During Processing

Figure 3.2 shows a sequence of SEM–EDS mapping images around the Ti zone after processing. After the rolling process, the Ti layers are

fractured and dispersed in the Al layers, as shown in Fig. 3.2a. For high reduction in thickness of the metal laminates with different mechanical properties, a plastic instability develops and the harder phase starts necking, gets separated and finally fractures to oval-shaped or concave-shaped segments. After cold roll bonding, there is no obvious intermetallic at the Ti and Al interface. When the rolled laminates are annealed, the intermetallic is found to develop at the Ti/Al interface. As the annealing time increases, the intermetallic zone is found to spread, as shown in Fig. 3.2b–f. In Fig. 3.2b, after annealing at 873 K for 6 h, $TiAl_3$ is the only phase that can form and grow at the Ti/Al interface. As the annealing time increases to 12 h, the thickness of the $TiAl_3$ layer increases, as shown in Fig. 3.2c. In addition, the growth of the $TiAl_3$ layer occurs mainly on the Al foil side. When the annealing time increases to 24 h, the continuous Ti layer is broken up into a number of islands surrounded by a $TiAl_3$ layer, as shown in Fig. 3.2d. The residual thickness of the Ti layer after annealing for 24 h is 10 μm, and 17.5 μm after annealing for 6 h. When the annealing time increases to 48 h, we cannot observe any residual pure Ti layers. The intermetallic layer growth can be described by two different mechanisms: reaction control and diffusion control. Initially, when the intermetallic layer is very thin, the reactivity of the Ti surface is realized to the full extent because that the supply of the Al atoms is almost instantaneous due to the negligibly short diffusion paths. In such a case, the reaction controls the intermetallic formation. This mechanism will dominate for short annealing times. Here, we focus on the second mechanism. After sufficient growth in the intermetallic layer, diffusion becomes more difficult and will be the controlling step. Figure 3.3a shows the thickness of the residual Ti layer (T_{Ti}) as a function of the annealing time (t) between 6 and 48 h. The residual thickness changes linearly, as shown in Eq. (3.1):

$$T_{Ti} = 19.5 - 0.4t \tag{3.1}$$

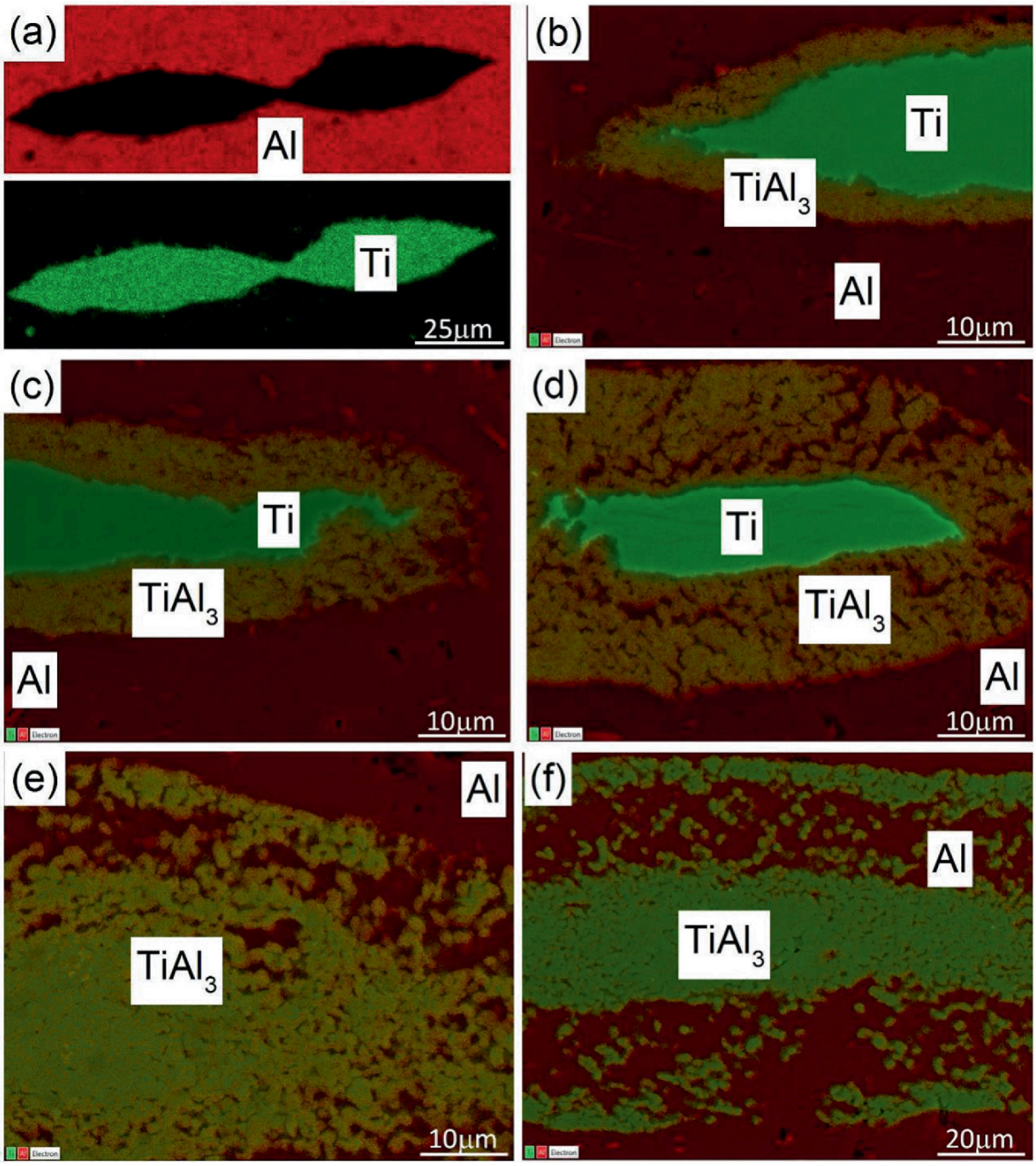


Fig. 3.2 SEM–EDS mapping images of **a** cold roll bonded Al/Ti/Al laminate, and Al/Ti/Al laminate samples for annealing at 873 K for **b** 6 h, **c** 12 h, **d** 24 h, **e** 48 h and **f** 168 h

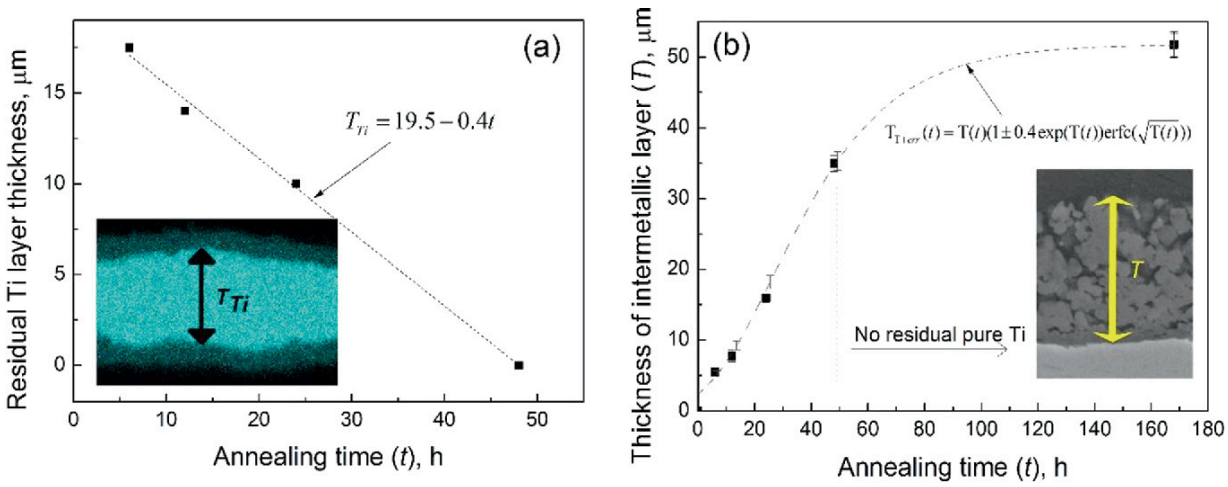


Fig. 3.3 Curves of annealing time versus **a** residual Ti layer thickness, and versus **b** thickness of $TiAl_3$ intermetallic layer

From the equation, the diffusion reaction speed of Ti atoms changes slightly after long annealing time. In addition, as shown in Fig. 3.2e, the $TiAl_3$ layer distributed with two zones. With further increasing in the annealing time, there is no pure Ti layer in the laminate, and the $TiAl_3$ is distributed in the form of distinct particles, as shown in Fig. 3.2f. However, the thickening of the $TiAl_3$ is slowed down, as shown in Fig. 3.3b. Figure 3.3b shows the thickness of the intermetallic layer (T) as a function of the annealing time (t). The time-dependence of the thickness of the intermetallic layer involving the complementary error function can be described by:

$$\mathrm{T}_{\mathrm{T}+err}(t) = \mathrm{T}(t)(1 \pm 0.4\exp(\mathrm{T}(t))\mathrm{erfc}(\sqrt{\mathrm{T}(t)})) \tag{3.2}$$

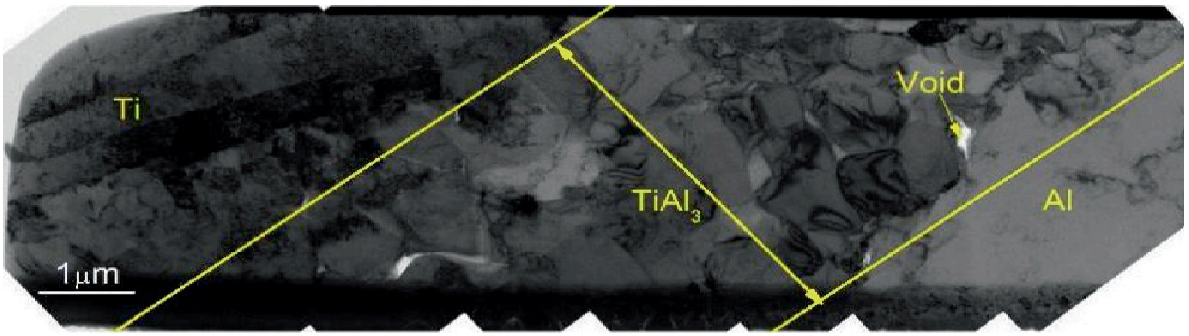
where,

$$\mathrm{T}(t) = 51.8\exp(-\exp(-0.042(t-26.5))) \tag{3.3}$$

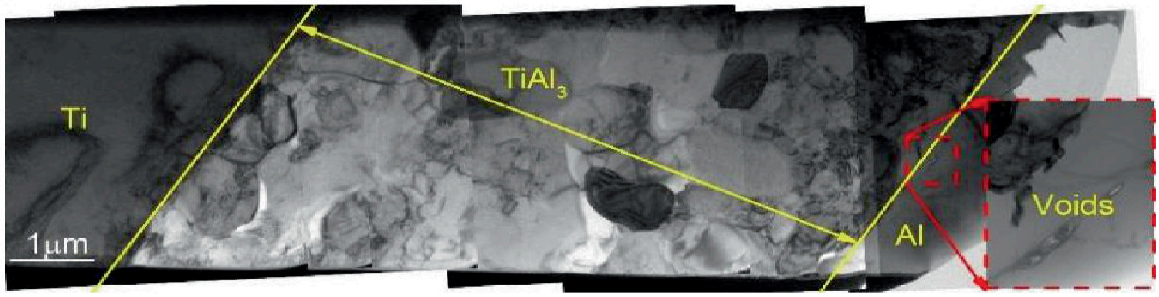
According to Eqs. (3.2) and (3.3), the change in the thickness of the intermetallic layer varies with the annealing time in the form of a double exponential. When the annealing time is less than 48 h, there are some residual zones of pure Ti in the laminates, and the thickness of the intermetallic layer increases rapidly with the annealing time. However, with further increase in the annealing time, the growth is slower.

In order to further study the details of the evolution of the $TiAl_3$ layer, TEM images of intermetallic layer for different annealing times

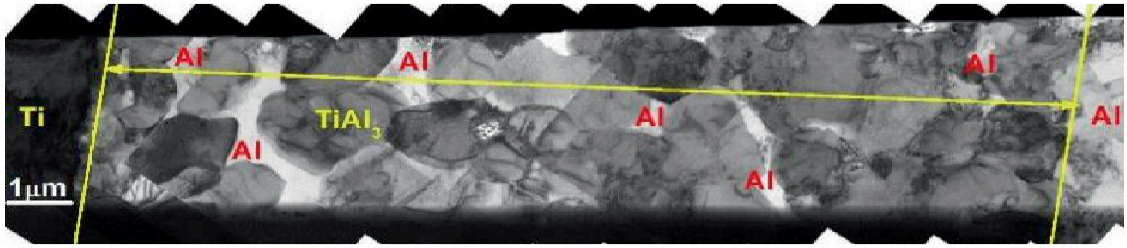
are shown in Fig. 3.4. Figure 3.4a shows the sample after annealing for 6 h. In the figure, we can observe some voids near the Ti and Al matrices. In addition, the $TiAl_3$ layer is seen to consist of distinct particles in the Al. Simultaneously, voids are formed due to the great difference in diffusion between Ti and Al atoms in the intermediate phases such as $TiAl_3$. This is the so-called 'Kirkendall effect', which has been found in several IMCs, and has been applied in the fabrication of porous Ti–Al alloys. When the annealing time increases to 12 h, the $TiAl_3$ layer thickens, and the separation between the $TiAl_3$ particles increases, as shown in Fig. 3.4b. In addition, the void size decreases greatly compared with that after annealing for 6 h. In Fig. 3.4c, we can observe that the $TiAl_3$ particles are distributed in the Al matrix without voids surrounding the $TiAl_3$ particles. At this stage, the laminate is a kind of trimodal material consisting of the coarse-grained Al, individual $TiAl_3$ particles and an ultrafine-grained Ti layer. As the annealing time increases to 48 h, there is no pure Ti residue in the laminate, because all the Ti is transformed into $TiAl_3$ particles, as shown in Fig. 3.4d. When the annealing time is increased to 7 days, the separation between $TiAl_3$ particles increases greatly, as shown in Fig. 3.4e.



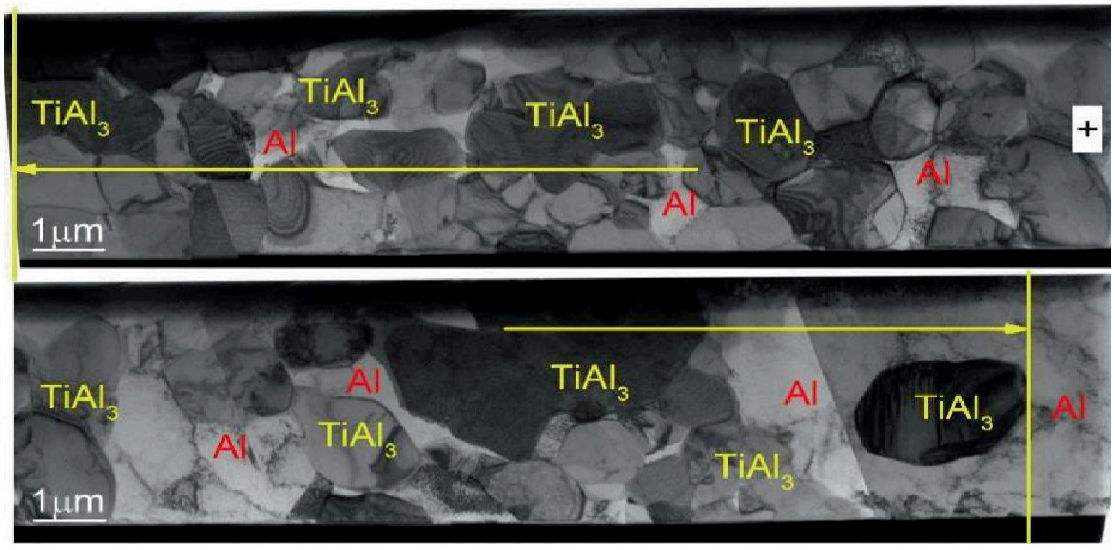
(a) Annealing for 6 hours



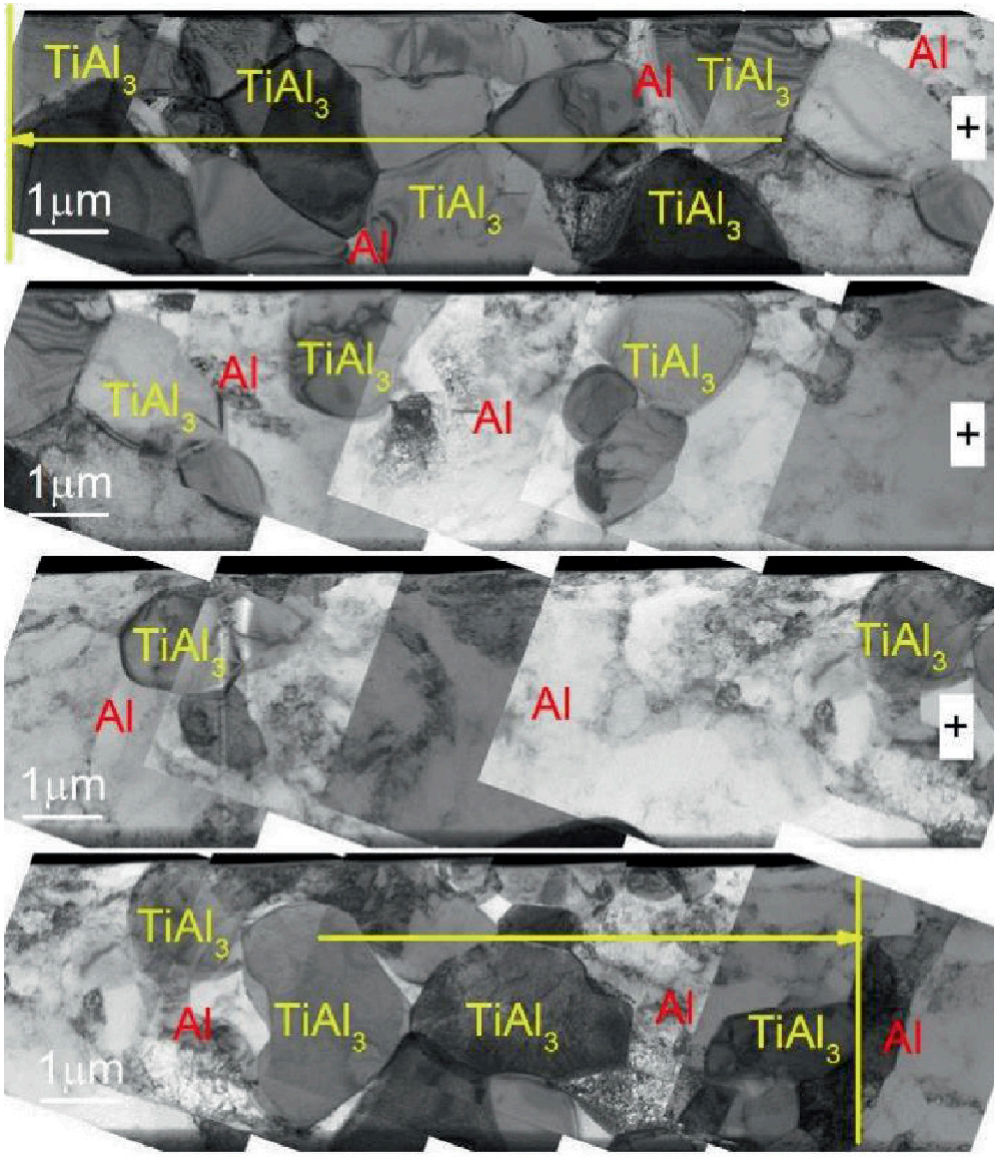
(b) Annealing for 12 hours



(c) Annealing for 24 hours



(d) Annealing for 48 hours



(e) Annealing for 168 hours

Fig. 3.4 TEM images of interface zone of Ti/Al laminates annealed at 873 K for **a** 6 h, **b** 12 h, **c** 24 h, **d** 48 h and **e** 168 h

3.1.2 Mechanical Properties Al/Ti Laminate After Processing

Figure 3.5 shows the engineering stress vs elongation curves of the samples after different annealing times. After cold roll bonding, the Al/Ti/Al laminate shows improved strength, but its elongation during tensile testing (ductility) is low. For the ultrafine-grained AA1235

sheets, the yield strength ranges from 135 to 140 MPa, as a result of the ARB technique. With the addition of a Ti foil during rolling, the yield strength of the laminate increases to 210 MPa although with a reduced ductility. After annealing at 873 K for 6 h, the yield strength reduces greatly and the ductility is limited. Generally, annealing makes the materials softer but more ductile. In addition, the limited ductility may be due to the effect of the voids at the interface between the $TiAl_3$ and the Al and Ti matrices as shown in Fig. 3.4a. After annealing at 873 K for 12 h, the yield strength increases to 100 MPa, and the uniform elongation increases to 0.4 mm. The low strength should still be affected by the residual voids in the laminate after annealing, as shown in Fig. 3.4b. After annealing at 873 K for 24 h, the laminate has a higher yield strength (135 MPa). The increase of the yield strength in these samples may be related to the increase in the $TiAl_3$ phase fraction resulting from prolonged annealing. As the annealing time increases to 48 h, the yield strength reduces slightly. However, there is larger strain hardening during the tensile process, and the tensile strength is relatively greater than that of laminates after annealing at 873 K for 24 h. At this stage, there is no residual Ti layer in the laminate, and the $TiAl_3$ accelerates the strain hardening during the deformation. When the annealing time reaches 168 h, both the yield strength and the elongation rate of the samples reduce. The drop in the yield strength for longer annealing time may be related to the reduction of defect concentration, grain growth, or recovery of the deformed crystal structure of the Al matrix. The difference in the deformation of $TiAl_3$ grain and Al matrix may cause the poor ductility for the samples after annealing 168 h.

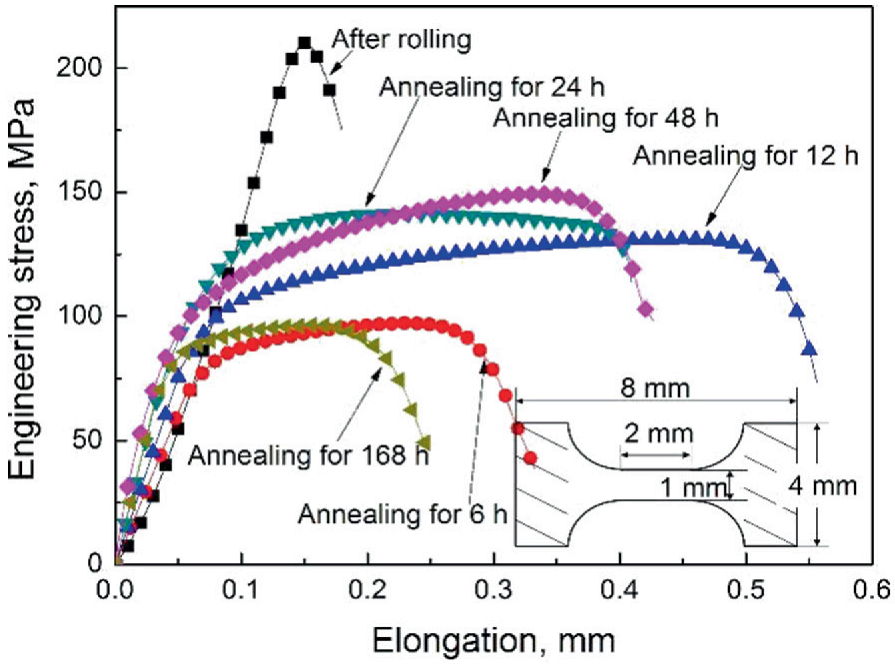


Fig. 3.5 Engineering stress versus elongation curves of Al/Ti laminates after rolling and different heat treatments

Figure 3.6 shows SEM images of fracture surface of the tensile tested samples subjected to different annealing times. After annealing for 6 h, the fracture surface is large, as shown in Fig. 3.6a. For an annealing time of 12–48 h, we can observe extensive necking during tensile testing, compared to the samples with the annealing times 6 h and 168 h. The necking is minimum when the annealing time reaches 168 h, as shown in Fig. 3.6e. The area reduction ratio has been suggested as a measure of foil ductility. Assuming volume conservation, the final cross-sectional area (A_{final}) can be related to a true fracture strain, as shown in Eq. (3.4),

$$\varepsilon_{axial} = \ln(A_{initial}/A_{final}) = \ln\left(\frac{1}{1-q}\right) \tag{3.4}$$

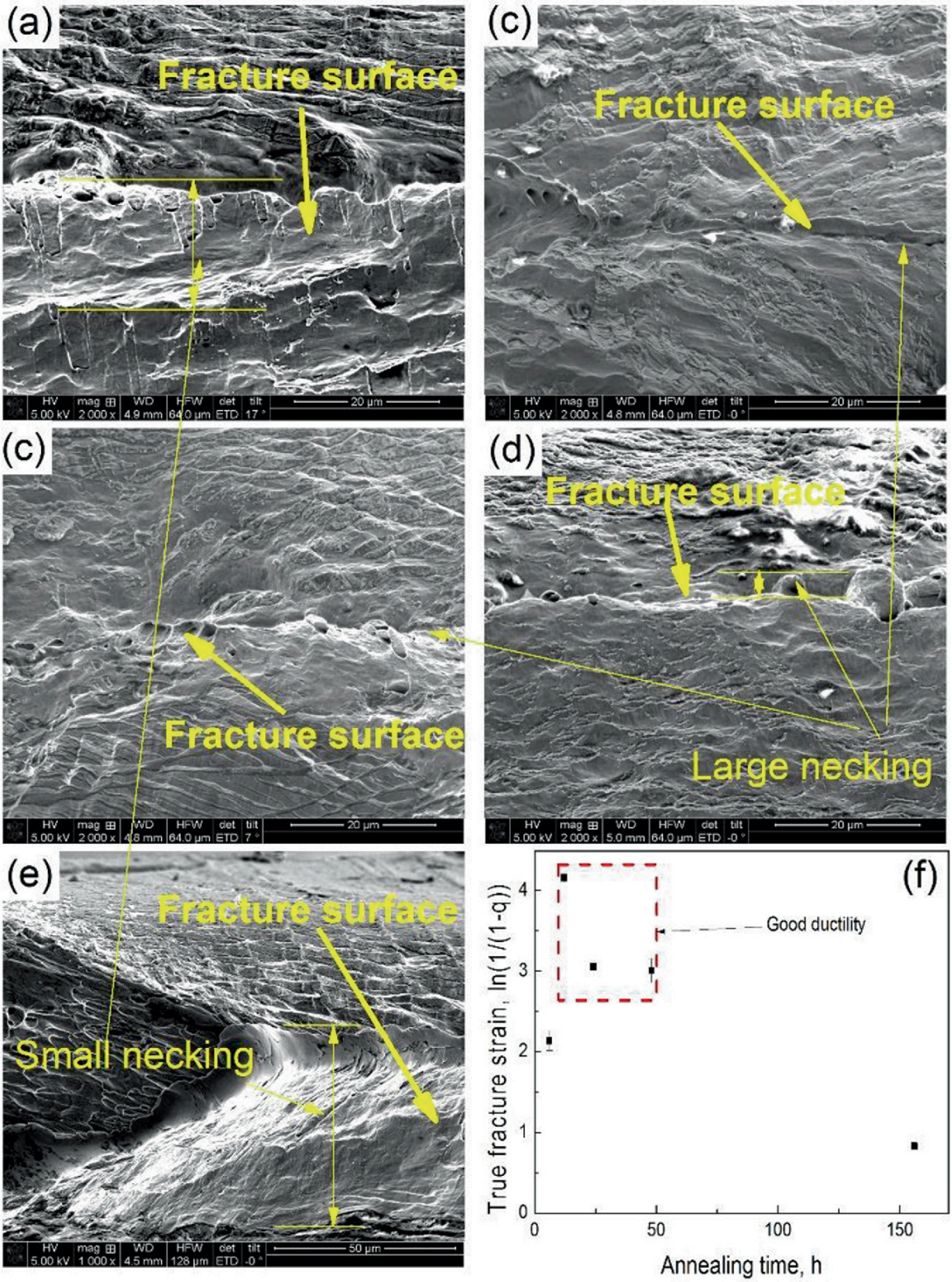

(a)
Fracture surface
(c)
Fracture surface
(c)
Fracture surface
(d)
Fracture surface
Large necking
(e)
Fracture surface
Small necking
(f)
Good ductility
True fracture strain, ln(1/(1-q))
Annealing time, h
0
1
2
3
4
0
50
100
150

Fig. 3.6 SEM images of fracture surfaces of tensile tested samples after annealing at 873 K for **a** 6 h, **b** 12 h, **c** 24 h, **d** 48 h and **e** 168 h. **f** true fracture strain versus annealing time

where $A_{initial}$ is the cross-section area before the tensile testing, and q is the area reduction ratio. Equation (3.4) gives the true fracture strain, as shown in Fig. 3.6f. In Fig. 3.6f, the true fracture strain increases with increasing the annealing time from 6 to 12 h. However, it gradually reduces with longer annealing time. When the annealing time reaches 168 h, the sample has the lowest fracture strain.

3.1.3 Microstructure Evolution Mechanism of Al/Ti Laminate During Annealing

As shown in Fig. 3.4, the laminate can be a typical trimodal laminate, consisting of a matrix of coarse-grained Al layer, ultrafine-grained Ti and $TiAl_3$ particles. Figure 3.7 illustrates this kind of trimodal structure, in which the grain size of Ti is 500 nm and the size of $TiAl_3$ particles is <3 μm. It is interesting that the distribution of $TiAl_3$ particles is neither uniform nor with a uniform gradient. Instead, the $TiAl_3$ particles are concentrated near both the original Ti layer and most of the $TiAl_3$ particle frontiers. According to Fick's second law of diffusion, it is:

$$\frac{\partial C}{\partial t} = D\frac{\partial^2 C}{\partial x^2} \tag{3.5}$$

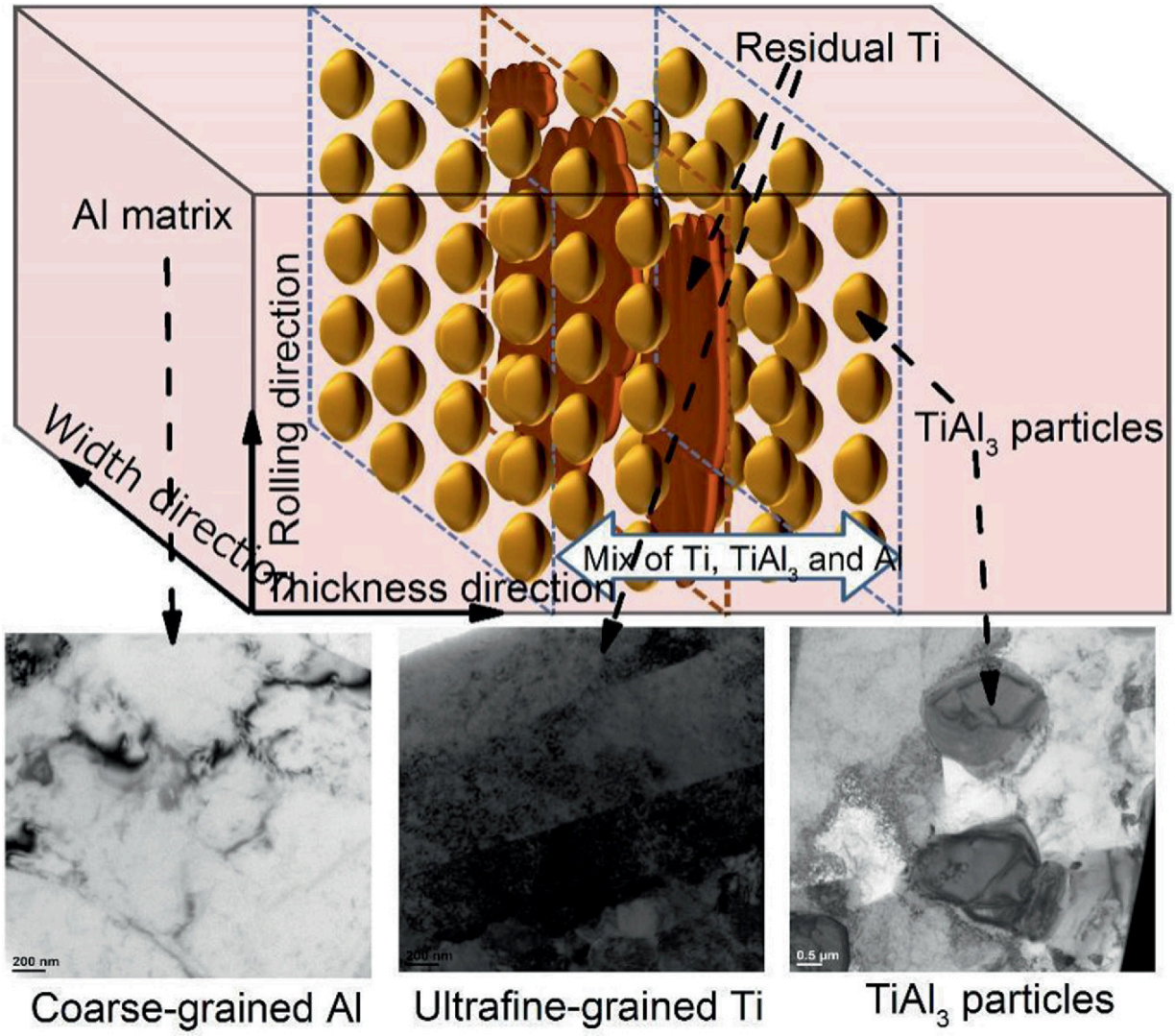


Fig. 3.7 Illustration of the new trimodal laminates combined with coarse Al matrix, nanograined Ti and $TiAl_3$ particles

here, the atomic concentration C is a function of the diffusion distance x (thickness of the intermetallic layer in this study) and the diffusion time t (annealing time in this study). For the Ti–Al system, Luo and Acoff [2] proposed the following formula for the diffusion coefficient D:

$$D = -\frac{1}{2t}\left[\frac{\partial N_A}{\partial x}\right]^{-1}\int_{N_{A1}}^{N_A} x dN_A \tag{3.6}$$

where N_A is the composition or atomic fraction at a distance x from the Matno interface, N_{A1} is the concentration of one side on the diffusion

couple at a point away from the interface where the composition is constant, $\left[\frac{\partial N_A}{\partial x}\right]^{-1}$ is the inverse of the concentration gradient, and $\int_{N_{A1}}^{N_A} x dN_A$ is the integral. For short time annealing, Eqs. (3.5) and (3.6) can be used to explain the evolution at the interface between Ti and Al layers. As shown in Fig. 3.4a and b, the $TiAl_3$ is uniformly distributed between the Ti and Al layers. However, these two equations cannot explain the large space between $TiAl_3$ particles and their distribution in Fig. 3.4d and e in terms of a diffusion mechanism. In studies of Ti/Al diffusion bonding, the influence of the intermetallic on the diffusion is generally neglected. In the present study, we assume that the effect of annealing on the Ti/Al laminate can be explained in terms of the following sequence of steps: (1) Nucleation of $TiAl_3$: chemical reaction between Ti and Al at the Ti/Al interface is energy favorable, so that Ti + 3Al = >$TiAl_3$. In the initial period the rate of the $TiAl_3$ formation process at the interface between Ti and Al is constant with time in the solid-phase reaction; (2) The $TiAl_3$ grains grow and so the number of Al atoms at the interface of Ti/$TiAl_3$ reduces; (3) The Al atoms diffuse through the interstices between the $TiAl_3$ particles, leading to break down of the $TiAl_3$ particles on the Ti surface, as shown in Fig. 3.4b. If the Al diffusion is faster in the $TiAl_3$ phase, it will form a continuous film of $TiAl_3$ on the surface of Ti. (4) The driving force for the Al diffusion is the concentration gradient and recrystallization of the deformed microstructure following rolling; (5) Enough Al atoms are supplied to the fresh surface of Ti, and these react with Ti to form new $TiAl_3$ particles. In this study, the Al layer is much thicker than the Ti layer. (6) There is no evidence that particulate pure Ti separated from the Ti core in SEM and TEM analysis (Figs. 3.2 and 3.4), and there is also no evidence of the formation of the buffer zone between Ti and $TiAl_3$, which indicates that the Ti atoms diffuse into Al slower than the other way around. (7) The formation of the new particles will push the previously formed $TiAl_3$ particles into the pure Al region. (8) All pure Ti reacts with Al and forms $TiAl_3$ in the prolonged annealing process, and

forms the $TiAl_3$ ring feature. In Fig. 3.4e, we find that the $TiAl_3$ particles are larger, and farther apart.

3.1.4 Deformation Mechanism of Annealed Al/Ti Laminates

In the annealing process, the appearance of intermetallic particles can improve both the ductility and the strength of the Al/Ti laminates. In order to understand the deformation mechanism of the laminates for different annealing times, finite element simulations were carried out. Figure 3.8 shows the equivalent strain in the laminate after different annealing times. The line of symmetry is shown in red. In Fig. 3.8a (annealing time 6 h), although the maximum strain at this stage is very small, cracks can occur very easily at the interface between Ti and $TiAl_3$ due to the voids. In this case, the sample has a lower elongation, strength and fracture strain, as shown in Figs. 3.5 and 3.6f. Figure 3.8b (annealing time 12 h) shows a reduced number of voids, improving the yield stress and elongation. For the same elongation, the sample has minimum equivalent strain compared with other samples. This results in the maximum fracture strain, as shown in Fig. 3.6f. Figure 3.8c shows the strain distribution in the laminate after annealing for 24 h. The yield stress of the laminate improves further due to the elimination of voids at the $TiAl_3$/Al and $TiAl_3$/Ti interfaces. In addition, as shown in the figure, the deformation of the Al matrix assumes a web pattern, resulting in a bimodal grain distribution during tensile testing and improved the uniform elongation of the laminate. For longer annealing times, the maximum equivalent strain increases. When the annealing time is 168 h, the maximum equivalent strain reaches 0.175 (Fig. 3.8e), while it is less than 0.088 for the other samples. In addition, there is no strain hardening in the Al matrix of the laminate, which results in reduced tensile strength (Fig. 3.5) and reduced true fracture strain (Fig. 3.6f).

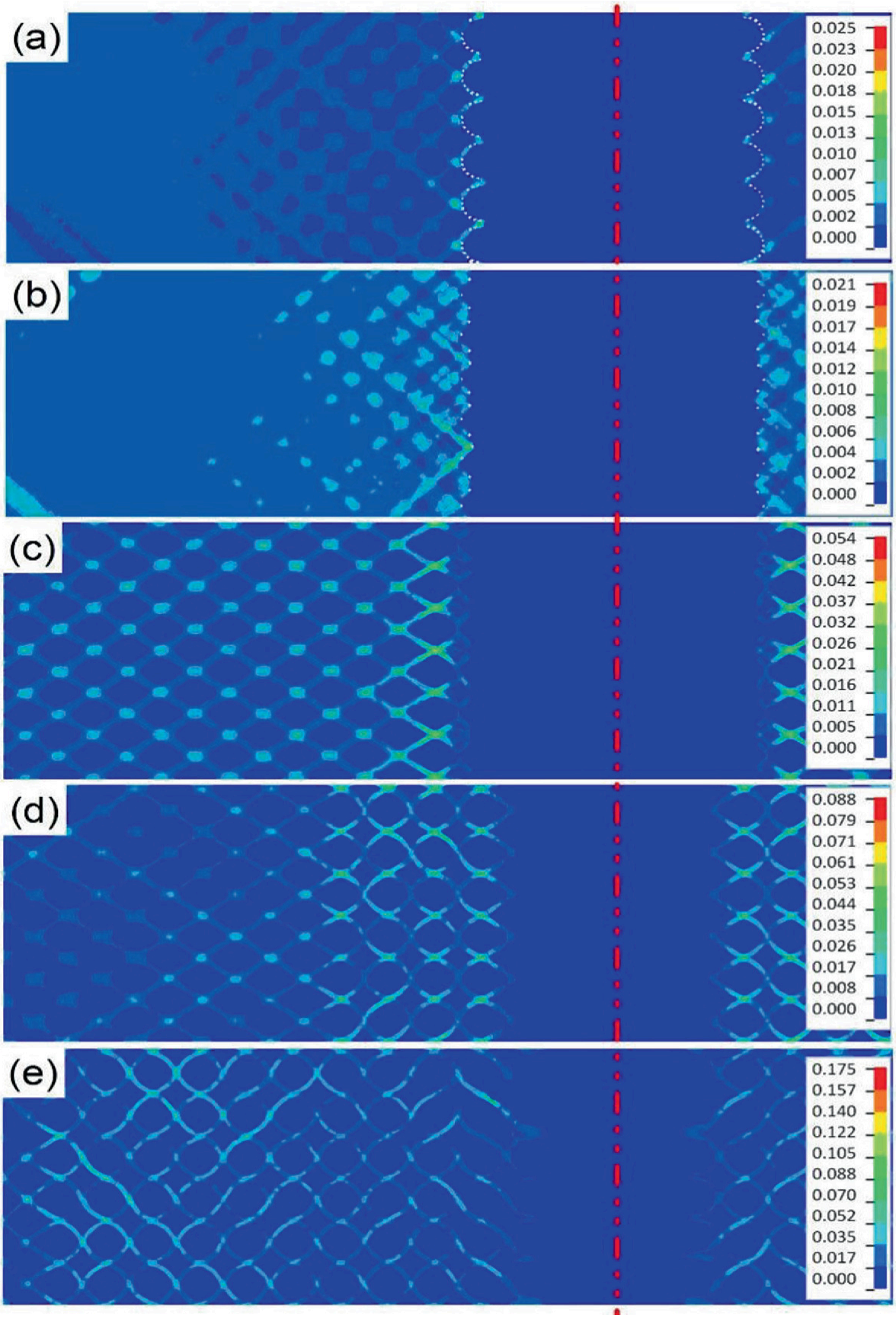

(a)
0.025
0.023
0.020
0.018
0.015
0.013
0.010
0.007
0.005
0.002
0.000
(b)
0.021
0.019
0.017
0.014
0.012
0.010
0.008
0.006
0.004
0.002
0.000
(c)
0.054
0.048
0.042
0.037
0.032
0.026
0.021
0.016
0.011
0.005
0.000
(d)
0.088
0.079
0.071
0.061
0.053
0.044
0.035
0.026
0.017
0.008
0.000
(e)
0.175
0.157
0.140
0.122
0.105
0.088
0.070
0.052
0.035
0.017
0.000

Fig. 3.8 Equivalent strain distribution of samples with the same elongation, **a** after annealing at 873 K for 6 h, **b** 12 h, **c** 24 h, **d** 48 h and **e** 168 h

Figure 3.9 shows the local fracture model of the samples during tensile testing for samples subjected to annealing at 873 K for (a) 6 h, (b) 12 h, (c) 24 h, (d) 48 h, and (e) 168 h. When the annealing time is 6 h, the fracture angle is 43°, as shown in Fig. 3.9a. Equation (3.7) shows the Tresca criterion based on the maximum shear stress:

$$\tau_{\max} = \frac{\sigma_1 - \sigma_3}{2} = C_2 \tag{3.7}$$

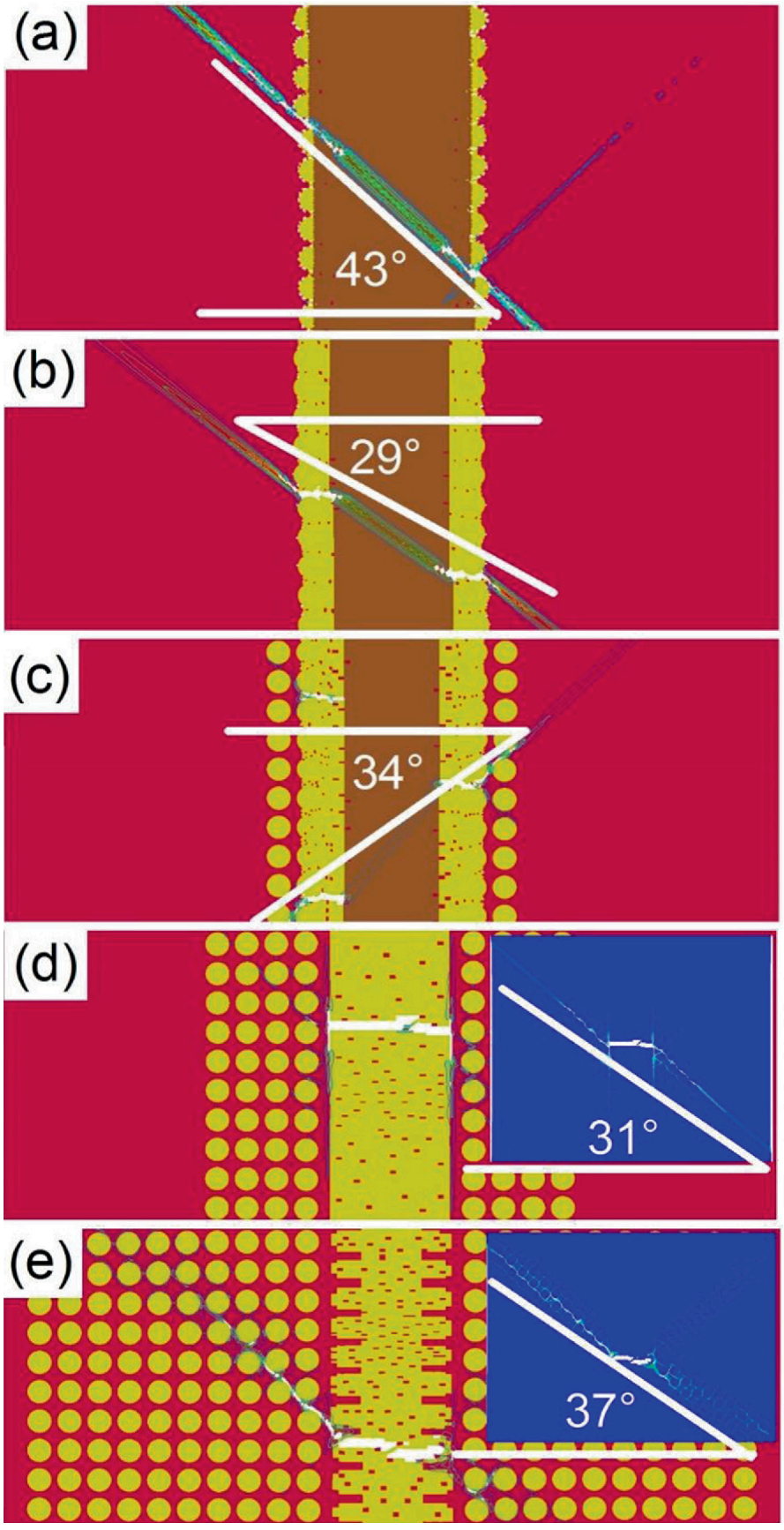

(a)
43°
(b)
29°
(c)
34°
(d)
31°
(e)
37°

Fig. 3.9 Fracture model at a local zone for the Al/Ti laminates after annealing at 873 K for **a** 6 h, **b** 12 h, **c** 24 h, **d** 48 h, and **e** 168 h

In the tensile process, the maximum shear stress ($\tau_{\max}$) is generally at 45° to the loading direction. According to the criterion, the laminates annealed for 6 h will be easy to fracture because the fracture direction is oriented along the maximum shear stress. When the annealing time is 12 h, the shear fracture angle is reduced to 29°, as shown in Fig. 3.9b. In this case, when the crack propagates to the Al matrix, the crack tip will be blunted, leading to a fracture delay and a higher ductility. The fracture strain is therefore improved, as shown in Fig. 3.6f. For annealing times of 24 and 48 h, the shear fracture angle increases slightly, leading to a slight reduction in ductility as shown in Fig. 3.6f. When the annealing time increases to 168 h, the shear fracture angle increases to 37°, as shown in Fig. 3.9e. In addition, the cracks can propagate quickly between the $TiAl_3$ particles and there is no coarse-grained Al to stop the crack propagation near the laminate surface. This results in reduced ductility, as shown in Fig. 3.6e and f.

3.1.5 Abnormal High Dislocation Density in Annealed Al/Ti Laminates

Furthermore, the asymmetric rolled Al/Ti/Al laminate foils were annealed at 873 K for up to seven days [3]. We found an abnormally high residual dislocation density in the pure Al zone. The residual dislocation density was found to reach 7.5×10^{14} m^{-2}, higher than that in Al after being subjected to some kinds of severe plastic deformation processes.

Figure 3.10 shows an FIB sample and TEM micrographs at the frontiers of the $TiAl_3$ particles region near the Al layer under a range of annealing times. Upon annealing, the Ti and Al diffuse at the interfaces, and some of Ti and Al atoms react to form intermetallic. Initially, a number of voids are observed in the annealed structures. These are caused by the Kirkendall effect and by the difference in molar volumes between the reactants, as shown in Fig. 3.10b. As the annealing time increases, the voids at the $TiAl_3$/Al interface decrease, (Fig. 3.10c), leaving a number of smaller voids at the $TiAl_3$ particle frontier. After annealing for 48 h, voids at the frontier of $TiAl_3$ are hardly noticeable

(Fig. 3.10d). However, after 168 h of annealing, an abnormally high residual dislocation density can be found in the Al zone approaching the $TiAl_3$ particle, (Fig. 3.10e). Figure 3.10f shows a detail of Fig. 3.10e. In the Al zone approaching the $TiAl_3$ particle, the residual dislocation density is about 7.5×10^{14} m^{-2}. The low-density region should have a residual dislocation density of 3.6×10^{13} m^{-2}, and the "dislocation-free" region a residual dislocation density up to 1.8×10^{12} m^{-2}. Generally, dislocations can be piled up neatly at the frontiers of a particle. However, a random distributed mass of dislocations within the whole grain is observed, as shown in Fig. 3.10e. Ti and Al alloys can be synthesized as different intermetallics such as Ti_3Al, TiAl, $TiAl_2$, and $TiAl_3$ when processed at different temperatures. Generally, when the annealing temperature is less than 923 K, the titanium aluminide forms $TiAl_3$ at fairly low temperatures in the prior Al-rich layer after just a few hours. The element distribution in a local zone of Fig. 3.10e is shown in Fig. 3.11. In Fig. 3.11a–d, the intermetallic particle is seen surrounded by pure Al. In Fig. 3.11e, the particle is $TiAl_3$. In Fig. 3.11f, it is seen that the high dislocation density zone is Al with about 0.5% Ti. The particle size of the Region of Interest (ROI) is about 500 nm. Referring to the profiles of previous EDS line scan study in similar working conditions, the distance of affected region due to the X-ray generated from the neighbouring grain is less than 100 nm for a vertical grain boundary. So, we believe that a few Ti atoms exist in the ROI.

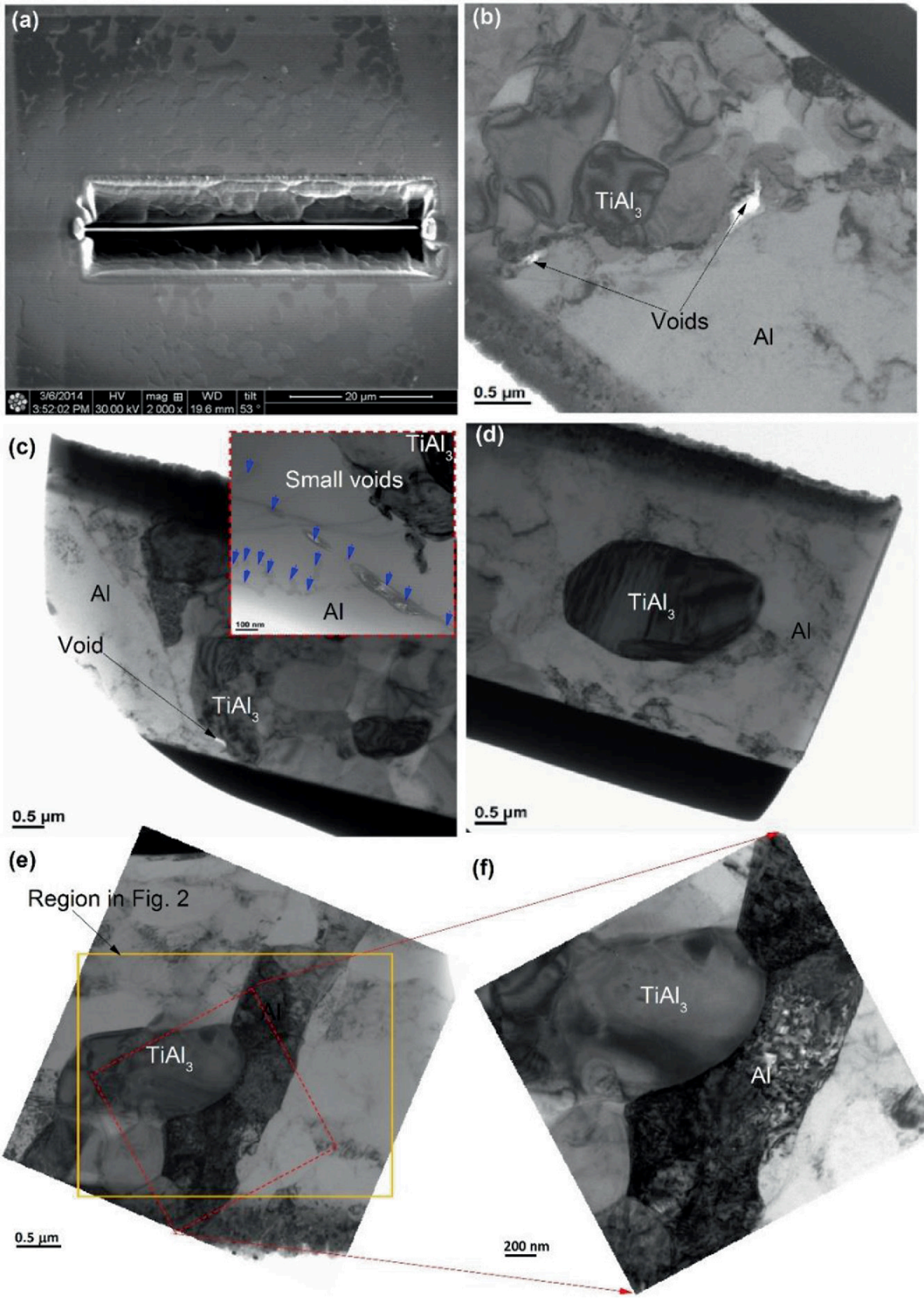

(a)
3/6/2014 3:52:02 PM
HV 30.00 kV
mag 2 000 x
WD 19.6 mm
tilt 53 °
20 µm
(b)
TiAl3
Voids
Al
0.5 µm
(c)
TiAl3
Small voids
Al
100 nm
Al
Void
TiAl3
0.5 µm
(d)
TiAl3
Al
0.5 µm
(e)
Region in Fig. 2
Al
TiAl3
0.5 µm
(f)
TiAl3
Al
200 nm

Fig. 3.10 **a** FIB image of Al/Ti/Al laminate for annealed 168 h. TEM images of annealed Al/Ti/Al laminates in $TiAl_3$ particle frontier for 6 h, **b** 12 h, **c**, 48 h, **d** and 168 h, **e**, **f** is a detail of (**e**)

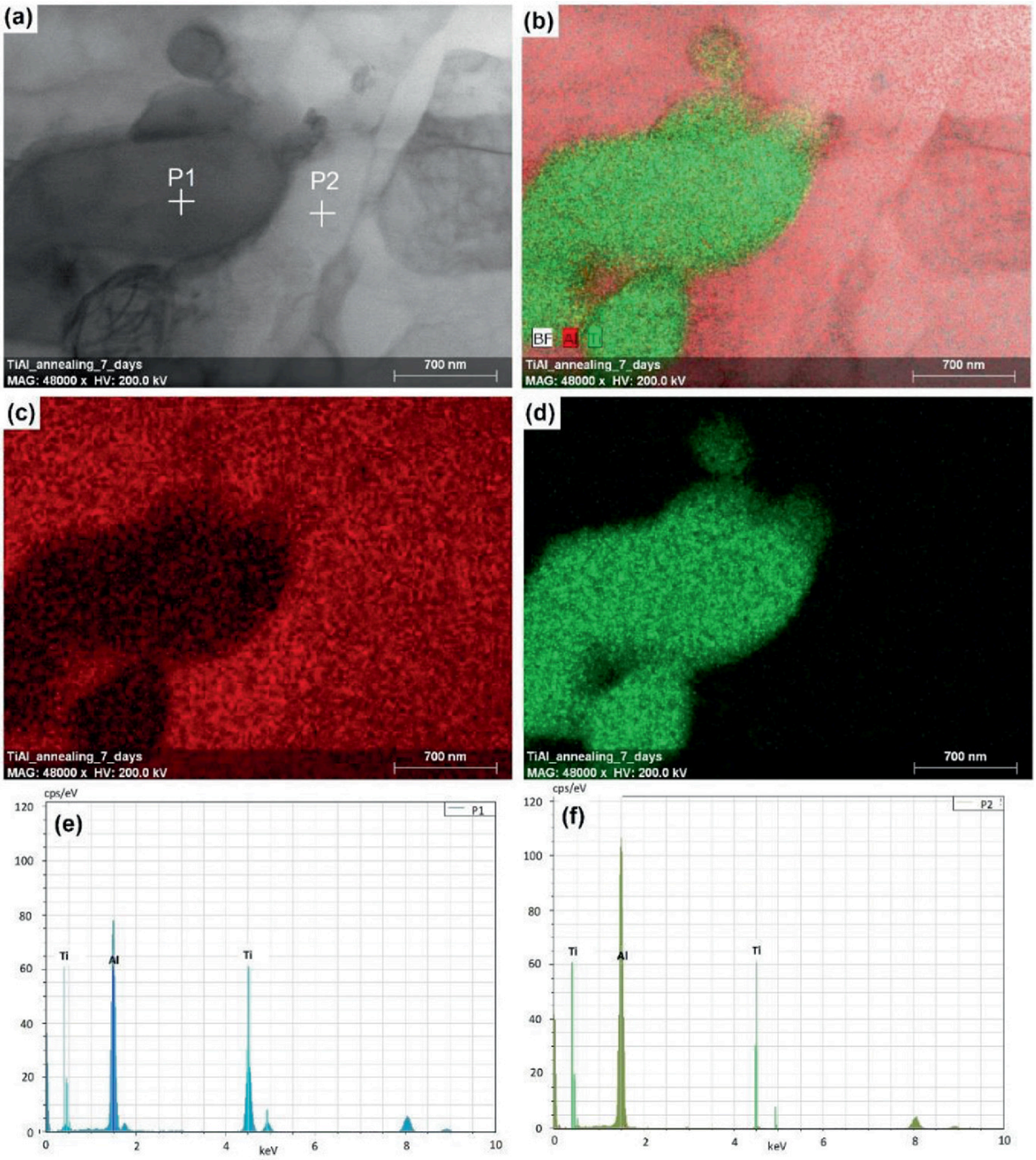


Fig. 3.11 Element distribution at the local zone in Fig. 3.10e. **a** Image of local zone in $TiAl_3$ particle frontier, **b** Combined Ti and Al distribution, **c** Al distribution, **d** Ti distribution, element composition at **e** P1 and **f** P2 in Fig. 3.11a

Figure 3.12 shows the residual dislocation density in Al subjected to different processes. For pure Al, the residual dislocation density is very low after annealing. As the proportion of other elements increases, the residual dislocation density increases gradually. For an Al single crystal, the residual dislocation density is only 1×10^{7} m^{-2}. With 20% whisker in pure Al, the residual dislocation density increases to 10^{13} m^{-2}, and 4×10^{14} m^{-2} for AA6061 with SiC particles. For Al and SiC, the thermal expansion ratio is 10:1. When the composite is cooled from elevated temperatures, uneven strains occur due to differential thermal contraction at the Al/SiC interface, which can generate dislocations. Table 3.1 lists the thermal expansion coefficients of Al and $TiAl_3$ from 300 to 900 K. In this temperature range, the ratio of thermal expansion coefficients between Al and $TiAl_3$ varies from 0.95 and 1.2. In addition, the residual dislocation density in pure Al has been found to increase greatly under SPD. The residual dislocation density of highly strained Al can reach 3.46×10^{14} m^{-2} and 7.07×10^{14} m^{-2} after HPT and ECAP processing respectively. Miyajima et al. [4] found that the residual dislocation density was around 10^{14} m^{-2} in commercial pure Al samples when the equivalent strain is about 10 in samples subjected to ARB. However, all these values are less than the value found in the current study, which is 7.5×10^{14} m^{-2}.

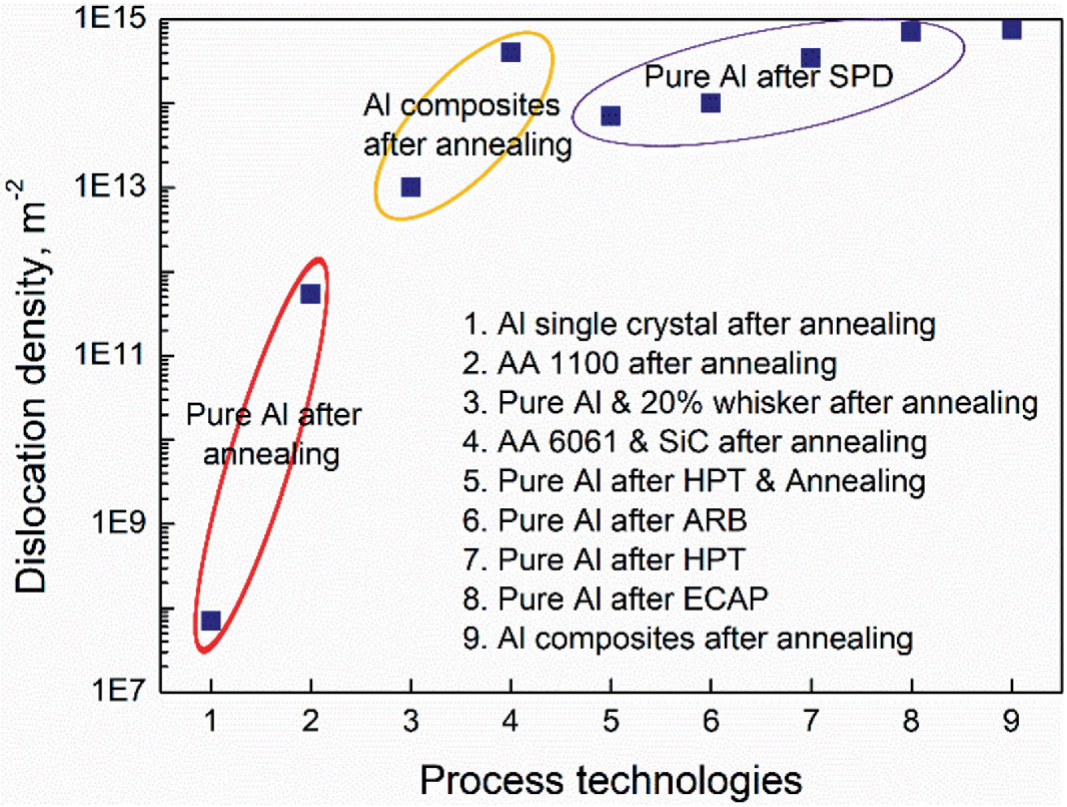


Fig. 3.12 Dislocation density in Al subjected to different processes

Table 3.1 Thermal expansion coefficient of Al and $TiAl_3$ at different temperatures

Temperature, K	**300**	**450**	**600**	**750**	**900**
Al, 10^{-6} /K	23.2	24.5	25.1	25.2	25.6
$TiAl_3$, 10^{-6} /K	19.5	22.5	24.3	25.8	26.9

In the current study, Al/Ti/Al laminates underwent severe plastic deformation during rolling, causing dislocations that were annihilated during annealing at the first stage. Figure 3.10b shows low residual dislocation density and some voids in the pure Al zone. The above discussion suggests that the high residual dislocation density in the pure Al zone is caused neither by the difference in thermal expansion coefficients nor by severe plastic deformation, but by a new mechanism.

It is well known that the annihilation of the dislocations may result in vacancies and voids. Seitz [5] reported the mechanism of vacancy generation by moving dislocations. He proposed four mechanisms by which vacant lattice sites could conceivably be generated during plastic

flow: (1) by local heating of the lattice in the immediate vicinity of the dislocation as it moves through the lattice and absorbs energy from the applied stress field; (2) by geometrical means in which dislocations of opposite sign moving in neighbouring planes annihilate one another and produce a row of vacancies; (3) as a result of instability of the in-phase motion of atoms during passage of a dislocation; (4) as a result of large, transient thermal pulses in regions where dislocations annihilate one another and produce a large lattice disturbance. The theory of vacancies and voids caused by the movement of dislocations is widely used in fracture analysis. However, there has never been any report on the vacancies and voids transferring into dislocations during annealing.

Here, we propose that the high residual dislocation density in the Al zone is related to the evolution of voids and the diffusion of Ti atoms. The diffusion between Ti and Al and formation of IMCs during the long-time annealing of severely deformed material makes it possible for some Ti atoms to move beyond the boundary of the stoichiometric $TiAl_3$ region and form a buffer zone of a low-concentration solid solution of Ti in Al at the frontier region of $TiAl_3$ particle, as shown in Fig. 3.11f. Figure 3.13 illustrates the generation of high dislocation density in the Al matrix. Voids are caused by the difference in speeds in which the Al and Ti atoms move in the initial stages of diffusion (Fig. 3.13a). As the annealing time increases, large Kirkendall voids are divided into smaller voids and distributed in the Al matrix (Fig. 3.13b). For metallic materials, the number and size of voids could be reduced by increasing the time of exposure to high temperature. According to Fick's second law of diffusion, with an increase in time, there is sufficient opportunity for atomic diffusion to occur around the voids. Pines and Syrenko [6] believed that when the microcracks are healed, dislocations begin to act as vacancy sources. This results in an acceleration of their climb and consequential annihilation. As the annealing time increases, irregularly shape voids will gradually change into spherical voids to minimize the surface energy. In addition, some of the Ti atoms will move and be adsorbed at the void surface (Fig. 3.13c). When $TiAl_3$ particles meet a grain boundary, this will stop further movement of the $TiAl_3$ particles. Only a few Ti atoms pass through the grain boundary. With the movement of atoms at high temperature, the

size of the spherical voids will gradually decrease and become vacancies. In addition, the distributed Ti atoms will assemble at the vacancies to minimize the free energy (Fig. 3.13d). Vacancies have a tendency to cluster at the boundary. As clusters increase in size, they eventually change to other configurations which can be interpreted as nucleation of dislocation loops. At such conditions, the laminates was cooled from 873 K to room temperature, and dislocations are generated and pinned by the Ti atoms or clusters yielding a dislocation density of 7.5×10^{14} m^{-2} (Fig. 3.10e).

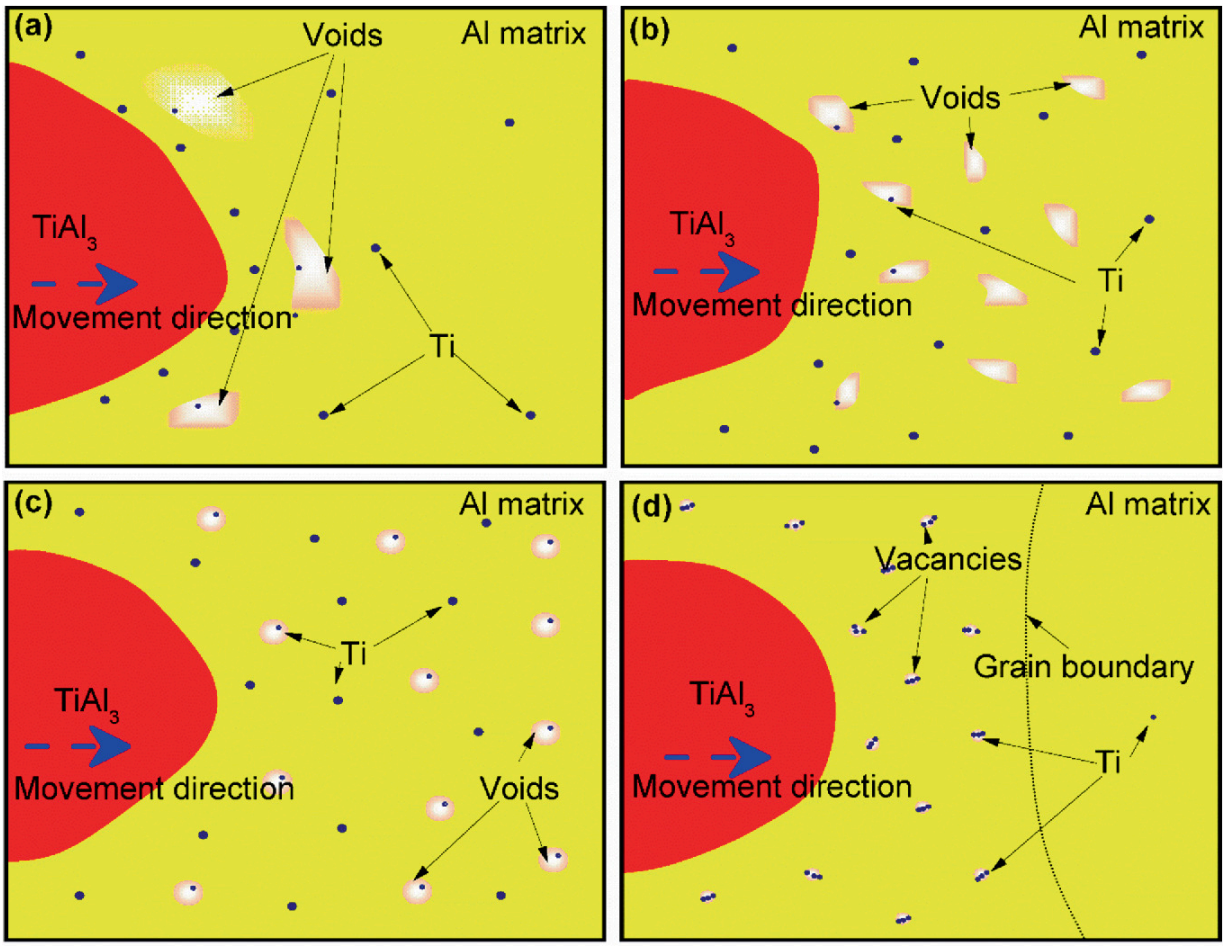


Fig. 3.13 Schematic illustration of dislocation generation processing in Al after annealing of Al/Ti/Al laminates. **a** large Kirkendall voids at fronter of $TiAl_3$, **b** large voids divided into smaller voids, **c** voids with irregular shape changes into circular voids and Ti absorbed into the voids, **d** voids change into vacancies and most of Ti is adsorbed at the surfaces of vacancies, generating a high density of dislocations

3.2 Cu/Ti Laminates Subjected to Cold Roll Bonding

We have applied the cold roll-bonding technique to produce nanocomposite Cu/Ti laminates which can be used to fabricate smarter micro parts with high strength, good thermal conductivity and sound absorption properties [7]. From the experimental results, we found that the hard Ti foil material fractures and is distributed in the Cu matrix during rolling. We also propose a deformation mechanism of the hard layer surrounded by soft materials during rolling which is different to that shown in Fig. 3.14.

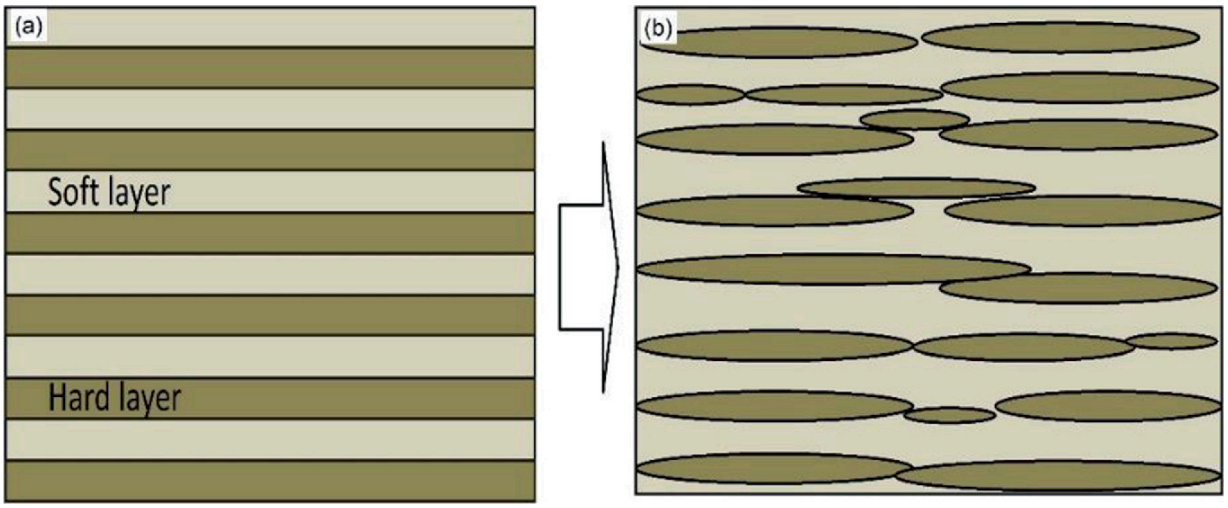


Fig. 3.14 Illustration of deformation feature of laminate with increasing strain during rolling, **a** after the first pass, **b** after multi passes

3.2.1 Microstructure Evolution of Cu/Ti Laminate During Cold Roll Bonding

Figure 3.15 shows SEM images of a section of Cu/Ti laminates with different foil thicknesses. Figure 3.15a shows the Cu/Ti/Cu foil, Fig. 3.15b for Cu/Ti/Cu/Ti/Cu foil, Fig. 3.15c for Cu/Ti/Cu/Ti/Cu/Ti/Cu foil and Fig. 3.15d for Cu/Ti/Cu/Ti/Cu/Ti/Cu/Ti/Cu foil. As seen in the figure, the Ti layers become increasingly discontinuous in the Cu matrix as the laminate foil thickness reduces. In the case of annealed Cu and Ti foils, the yield strength of the Ti layer is higher than that of the Cu layer. However,

there has been no analysis of the mechanism of the phenomenon to date. We generally would expect the hard material to break the softer material, when they undergo deformation together. However, the experimental observations are contrary to this expectation. We need to explain why the hard materials fractured in rolling when surrounded by soft material.

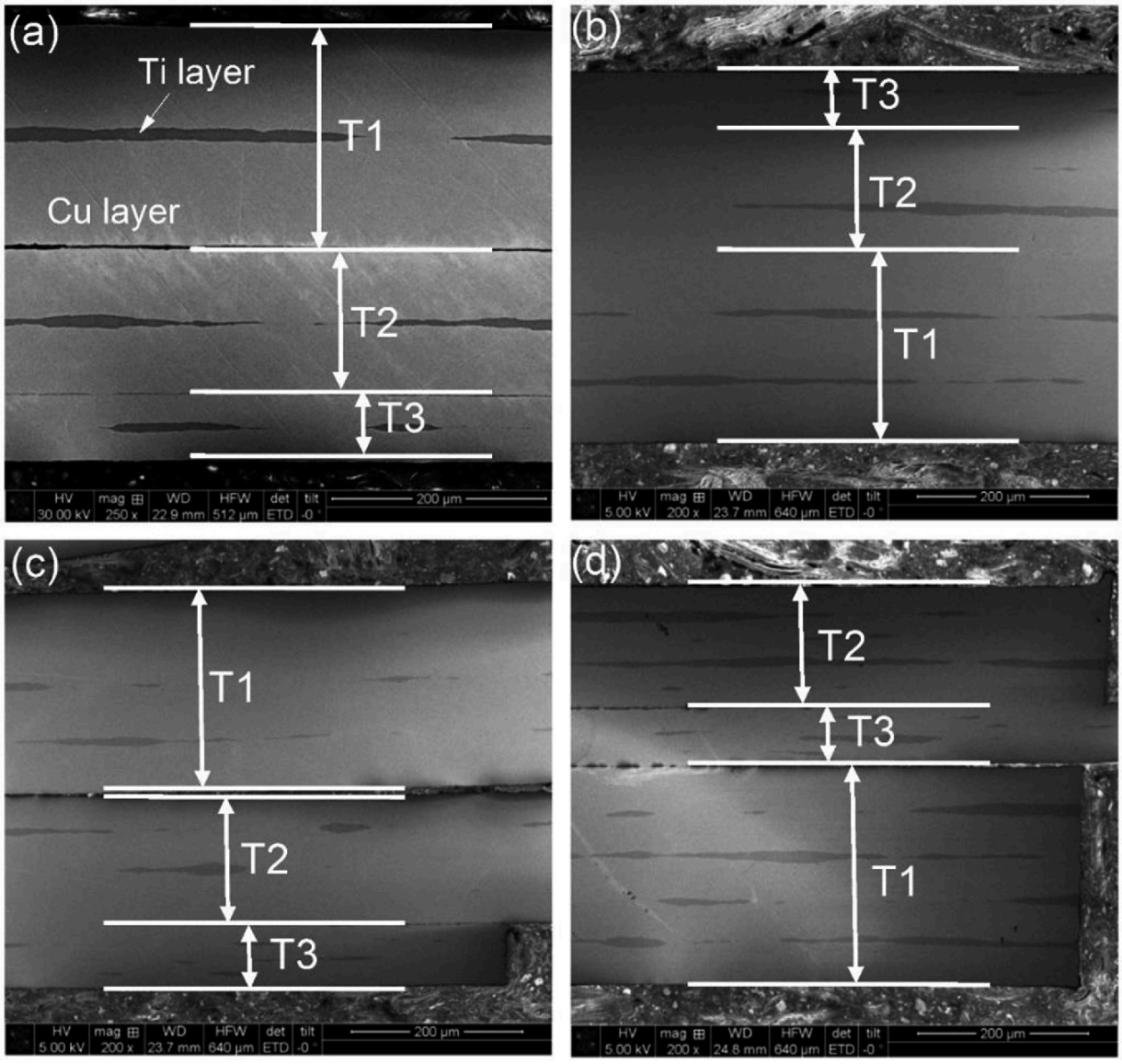


Fig. 3.15 SEM image of the section of Cu/Ti laminates with different thickness for **a** one layer, **b** two layers, **c** three layers and **d** four layers Ti foils

Figure 3.16 shows TEM images of different sections around the fracture end of Ti layer for rolled foils. It can be seen that all the Cu/Ti interfaces are 'concave' when observed from the Ti side, in which the

Cu layers are recessed into the Ti layers. It is obvious that this is different from Fig. 3.14, in which the interfaces are convex when observed from the hard metal side.

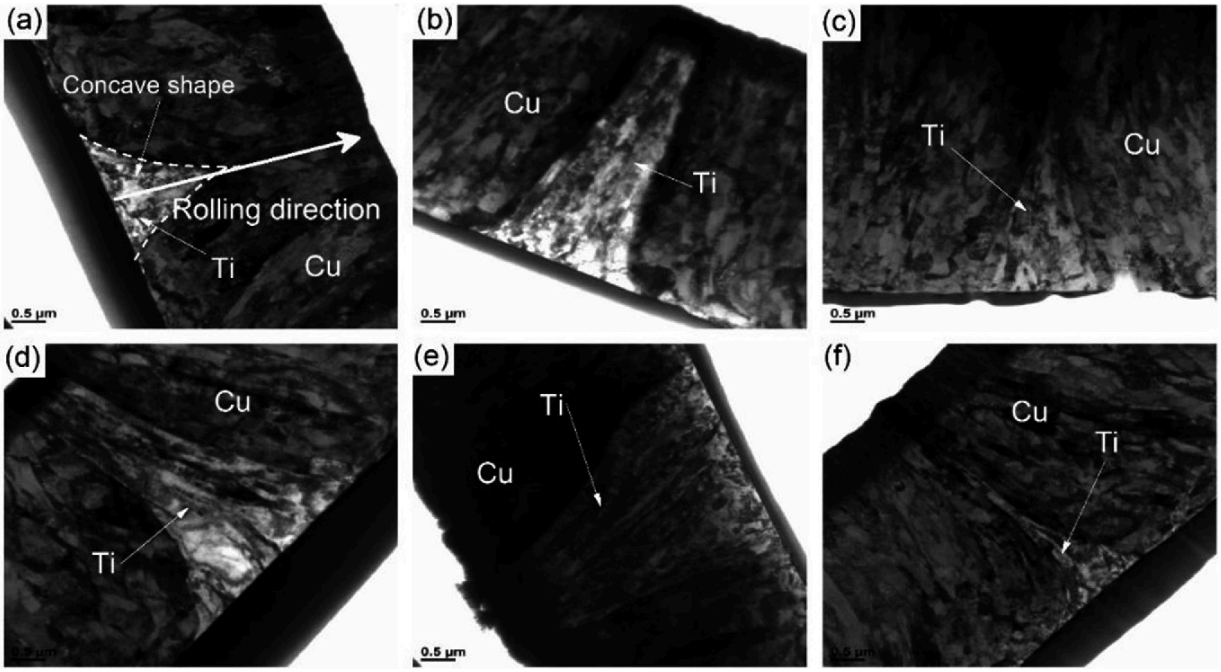


Fig. 3.16 TEM graph of Ti layer shape along the rolling direction

Figure 3.17 shows TEM images of the microstructure of Cu near the interface with different laminate foil thickness with one layer Ti foil. When the laminate foil thickness is reduced to 220 μm, the grain size near the Ti layer is much finer than elsewhere. This implies severe shear friction deformation between the Ti layer and the Cu layer during rolling, as shown in Fig. 3.17a. With further reduction in the foil thickness, the strain in the foil increases and the microstructure of Cu layer is nearly uniform, as shown in Fig. 3.17c. The strength of nanostructured metal materials is usually related to the grain size by the well-known Hall–Petch relationship:

$$\sigma_y = \sigma_0 + kd^{-0.5} \tag{3.8}$$

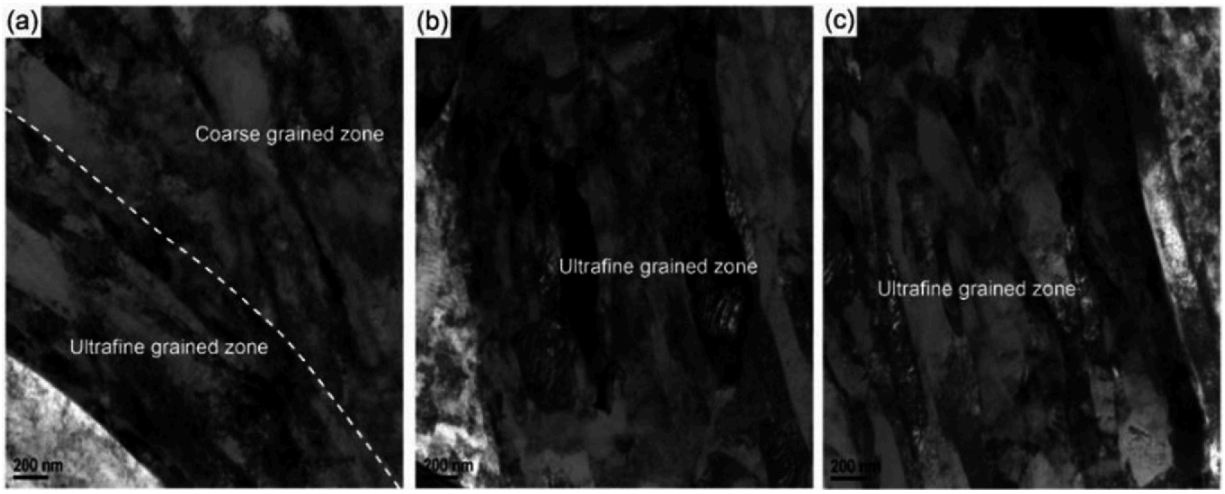


Fig. 3.17 TEM graph of microstructure of Cu layer near interface with the laminate foil thickness 220 mm (**a**), 140 mm (**b**) and 62 mm (**c**)

where σ_y is yield stress, σ_0 and k are constants for the material, and d is the grain size. With reduced grain size of Cu near the Ti layer, the strength of the Cu in this zone will be higher than elsewhere. As the number of rolling passes increases, the thickness of the refined layer gradually increases and finally becomes uniform. This may be one of the main grain refinement mechanisms of nanocomposite foil materials fabricated by the rolling technique.

3.2.2 Deformation Mechanism of Cu/Ti Laminate During Cold Roll Bonding

For fabrication of high-quality nanocomposite foils, deformation of the harder material is very important for grain refinement. We used a Ti foil to enhance the Cu matrix. The thickness of Ti foil is 1/12 of the thickness of the Cu foil. Generally, we would expect the Cu and Ti layers to deform uniformly in the rolling process, eventually resulting in a laminate structure. Under ideal conditions, for two layers with the same mechanical properties, we expect the interface to be a straight line, as shown in Fig. 3.18a. However, this may not be true in the case of Cu and Ti foils, due to different mechanical properties of Cu and Ti. Some researchers have investigated the conditions under which thicknesses of the hard layer and the soft layer are the same or similar. Mozaffari et al. [8] studied the structure of multilayered Al/Ni laminate during ARB. They observed that after the first cycle of sandwich production, the

nickel layers were bonded with the Al layer. Then they started to neck and fractured locally. After six cycles, the nickel layer broke up and was homogenously distributed in the Al matrix. During the first three cycles, the hard layers were able to deform in the same way as the soft layers. The deformation became inhomogeneous and the thickness of hard layers starts to vary along the rolling direction after subsequent ARB cycles. The hard layers started to neck with further deformation and the adjacent soft material then protruded and filled the necked and fractured regions. In the results of Mozaffari et al., the interface shape of hard layer was seen to be similar to that in Fig. 3.18b. However, in this study, it was found that when the thickness of the hard layer is much thinner than that of the soft layer, new deformation pattern develops, where the hard layer assumes a concave shape, as shown in Figs. 3.16 and 3.18c.

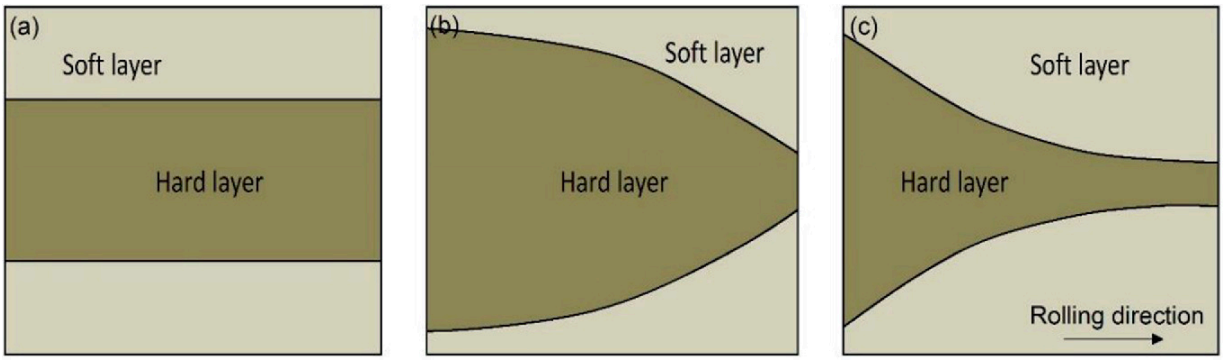


Fig. 3.18 Illustration of interface shapes between hard and soft layers. **a** uniform deformation; **b** convex shape; **c** concave shape

Usually, the thickness of the soft layers is the same as that of the hard layers. In the deformation process, the hard layer plays a key role which results in the soft layer surrounding the hard layer material. However, in the present study, the thickness of the Ti layer is only 25 μm, and the thickness of Cu layer is 300 μm. In the deformation process, the thicker Cu layer plays the key role. In recent years, size effects on the plasticity of materials have attracted increasing attention. Figure 3.19 shows FE-simulation results of the Ti layer shape for different thicknesses of the Ti layer. It is seen that when the thickness of Ti layer is 200, 100 or 50 μm, the interface shape of the Ti layer is convex. When the thickness of the Ti layer is reduced to 25 μm, the interface of the Ti layer adopts a concave shape.

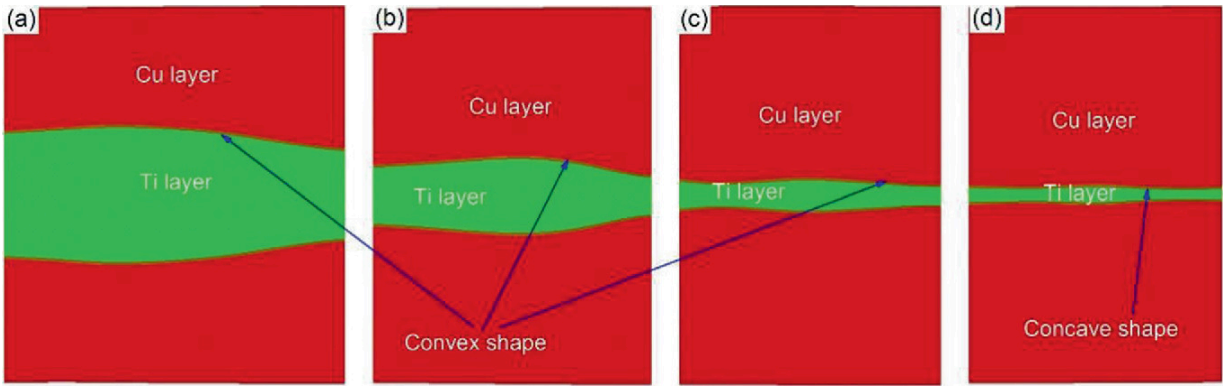


Fig. 3.19 FE simulation of Ti layer shape after rolling processing for Ti layer thickness **a** 200 mm, **b** 100 mm, **c** 50 mm, and **d** 25 mm

Figure 3.20 shows the equivalent stress and strain distribution in the Cu/Ti laminate with one layer Ti foil in the rolling deformation zone simulated by FEM. In Fig. 3.20a and b, it is seen that we can associate a wavelength to the deformation of the laminate. The fluctuation wavelength of laminate layers under instability deformation conditions studied by Junqua and Grilhé [9, 10], was affected by the elastic modulus, yield stress, thickness, and surface energy, as shown in Eqs. (3.9)–(3.15).

$$F(hK)/hK \geq \gamma/4Ch \tag{3.9}$$

$$F(hK) = (1-\Gamma)(1+K)\frac{K(1-\Gamma^2)+\exp(-2hK)[D+4hK\Gamma(\Gamma-1)]+\exp(-4hK)(D+\Gamma^2K)}{(\Gamma+K)(1+\Gamma K)+4hK\exp(-2hK)(\Gamma+K)(1-\Gamma)-\exp(-4hK)K(1-\Gamma)^2} \tag{3.10}$$

$$\Gamma = E_B/E_A \tag{3.11}$$

$$K = \frac{2\pi}{\lambda} \tag{3.12}$$

$$D = 4\Gamma + 2K + 2\Gamma K \tag{3.13}$$

$$C = \frac{E_A}{E_B}\left(\frac{7-K}{1+K}\right)^2\left(\frac{\delta a}{a}\right)^2 \tag{3.14}$$

$$\frac{\delta a}{a} = (\sigma_B - \sigma_A)\frac{E_A + E_B}{2E_A E_B} \tag{3.15}$$

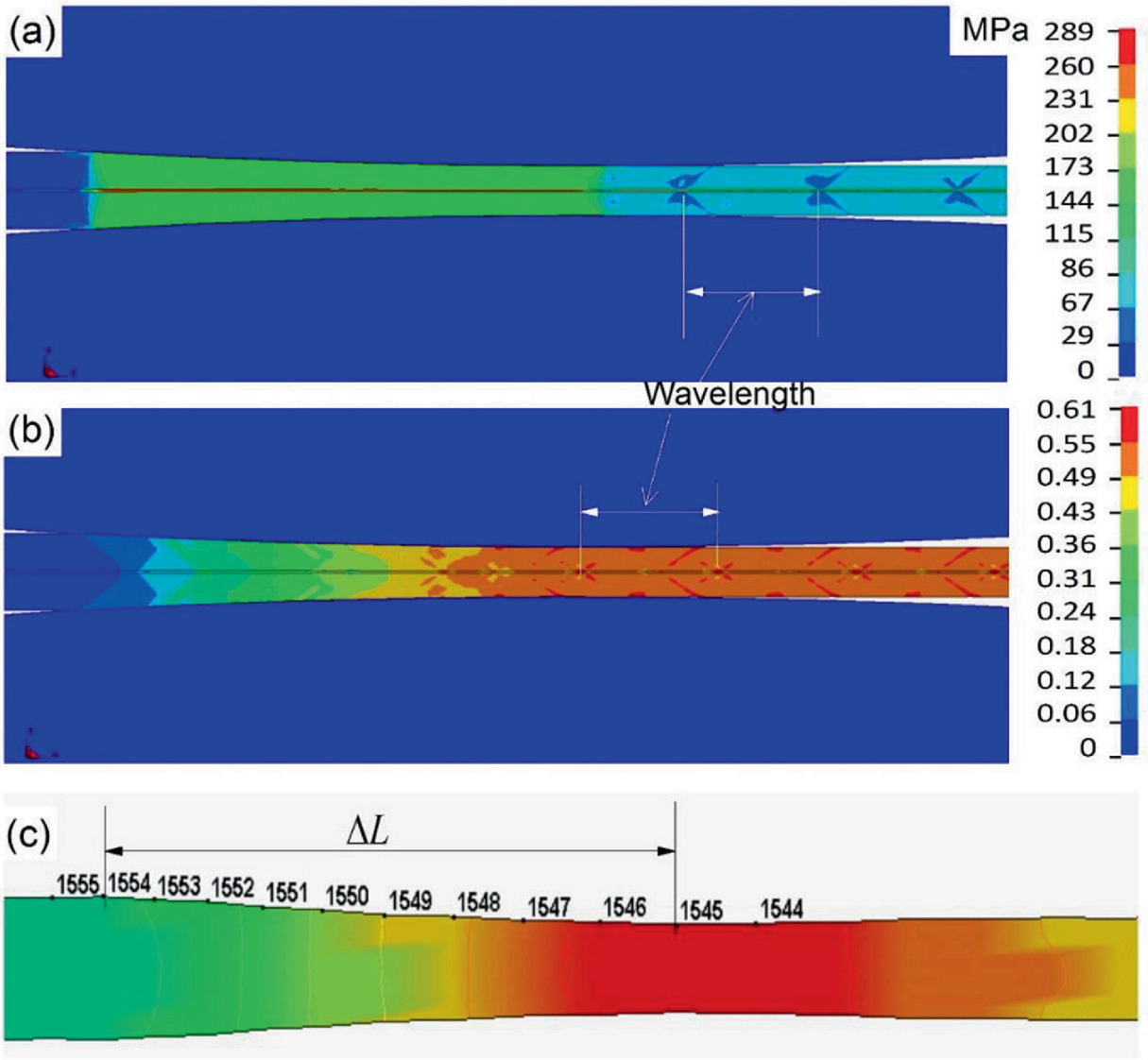


Fig. 3.20 Equivalent stress (**a**), strain (**b**) distribution of the laminate foil in the rolling deformation zone, and sectioned wavelength (**c**)

where λ is the fluctuation wavelength, h is the thickness of Ti layer, E_A is the elastic modulus of the Ti layer, E_B is the elastic modulus of the Cu layer, γ is the isotropic surface energy per unit area (207 mJ/m^2 for pure Ti), σ_A is the yield stress of the Ti layer, and σ_B is the yield stress of the Cu layer. Using the same material parameters in the FE models, the

$F(hK)/hK$ vs hK curve for the 25 μm thick Ti layer is shown in Fig. 3.21. From Eq. (3.12), the fluctuation wavelength (λ) is about 525 μm, which is close to the FEM-calculated value of 660 μm in Fig. 3.20. This also corresponds to the length of the Ti layer after the first rolling pass of the Cu/Ti laminate shown in Fig. 15a. The difference between the analytical result and the FEM result may be due to the assumptions of the analytical models which do not consider the thickness effect of the Cu layer. As shown in Fig. 3.20c, when the Ti layer thickness is 25 μm, the Ti layer has a wavy 'dog-bone' shape, with a large reduction in thickness at some locations. If the reduction of thickness of the Ti layer is caused by compression between Cu layers, the thickness of the Ti layer is seen to be uniform. Thus, it is obvious that the tensile stress along the rolling direction in the deformation zone plays an important role in the deformation mechanism of the Ti layer.

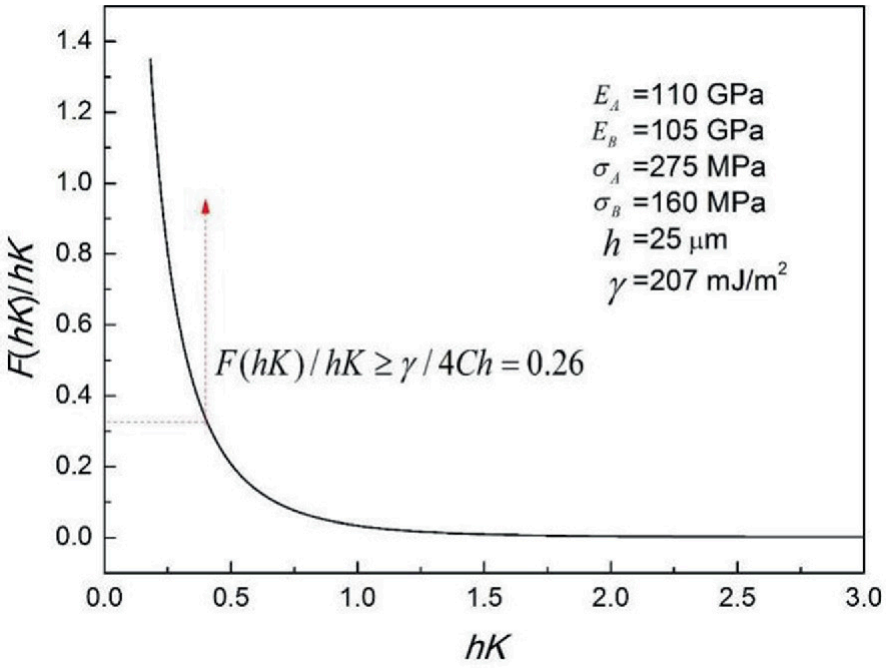


Fig. 3.21 Representation of F(hK)/hK versus hK curve for h = 25 μm and Γ = 105:110

Figure 3.22 shows the evolution of the interface shape in the rolling process. At the "P0" position (entry point), there is no difference in the foil thicknesses. At the "P1" position, the Ti layer begins to deform, but assumes a convex shape. With increased deformation, the convex shape gradually changes to concave, as at "P2". With further deformation to

"P3" and "P4", the interface shape totally transforms into a concave shape.

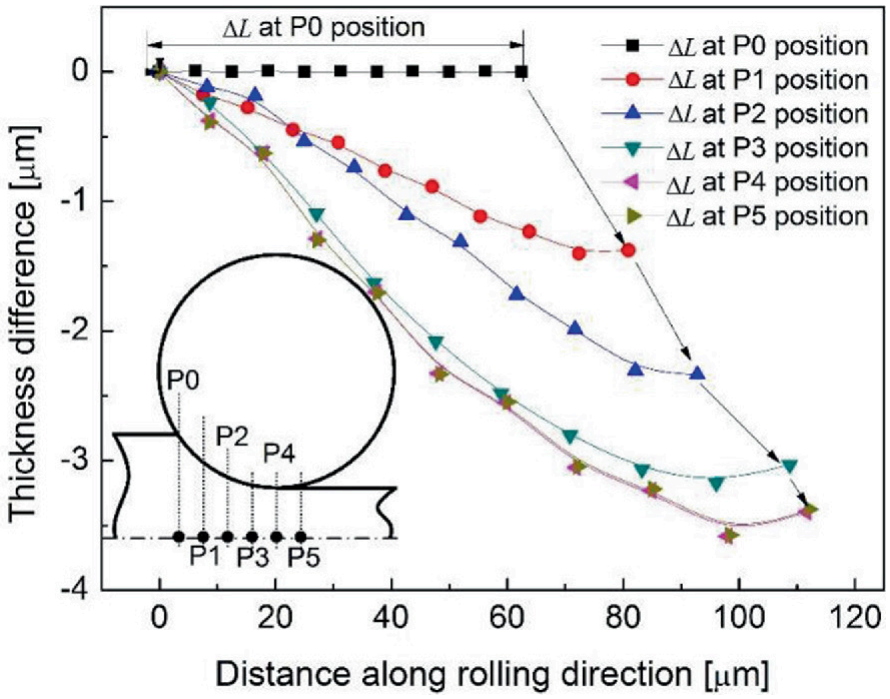


Fig. 3.22 Evolution of interface of nodes (DL) in Fig. 3.20c in the rolling deformation zone

Figure 3.23 shows the σ_X (stress) distribution in the Cu/Ti laminate in the rolling deformation zone. At the entry and exit zones, the Ti layer experiences tensile stress because the Cu layers are relatively soft compared with the Ti layer. In the deformation process, the soft Cu foil is more elongated along the rolling direction compared to the hard Ti foil, which develops shear friction force (f_s). The shear stress acting on the Ti layer surfaces makes the Ti layer behave like tensile test samples. When the shear stress is larger than a certain value, the Ti layer undergoes necking. As the number of rolling passes increases, the Ti layer may fracture and become discontinuous as shown in Fig. 3.15. In addition, this deformation feature also results in severe shear strain at the interface of Cu layers and brings about grain refinement, as shown in Fig. 3.17a. In the Cu layer, there is a gradient of grain size, with the maximum refinement near the interface of Ti layer/Cu layer. With further rolling deformation, the ultrafine grained zone gradually increases in size. For the rolling process of laminates with a hard metal surrounding soft metals, grain refinement occurs firstly inside the

laminates and gradually extends to the laminate surface, as illustrated in Fig. 3.24.

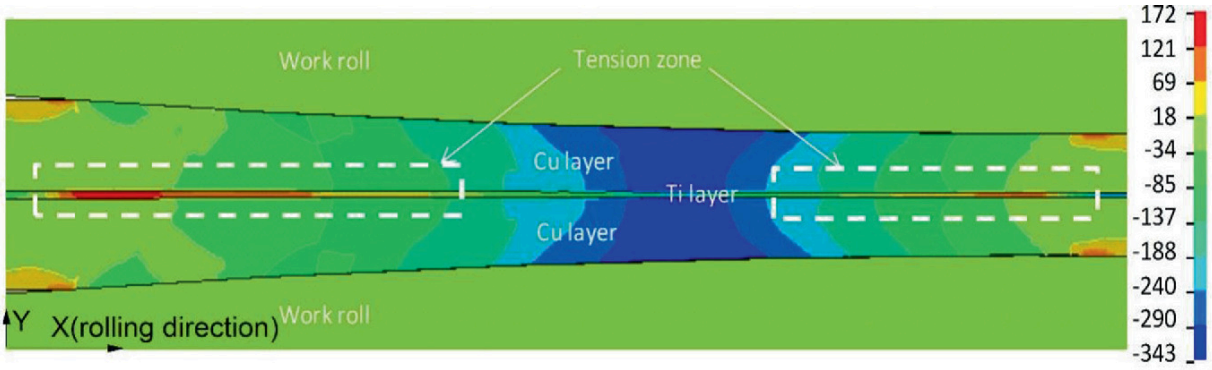


Fig. 3.23 σ_X distribution in the rolling deformation zone [MPa]

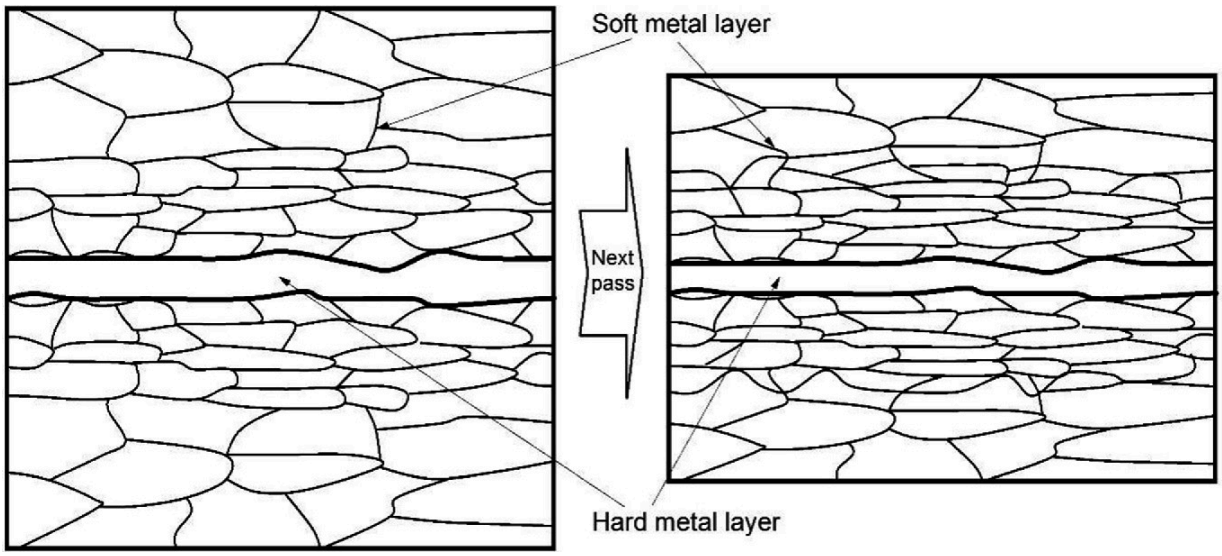


Fig. 3.24 Illustration of grain refinement for the hard metal surrounded by soft metal during roll bonding

To fabricate nanocomposite Cu/Ti laminate, it is desirable that the Ti layers are uniformly distributed between the Cu layers. A suitable process should be designed to achieve this. From the experimental results, we also found that the Ti layer may have a larger plasticity under the rolling conditions, as shown in Fig. 3.25. During rolling, the Ti foil is acted upon by two compressive stresses and one tensile stress. Under such conditions, the thickness of Ti layer was reduced from 25 μm to about 200 nm. This suggests a significant enhancement in plasticity, which was 125 times the normal elongation under similar rolling conditions.

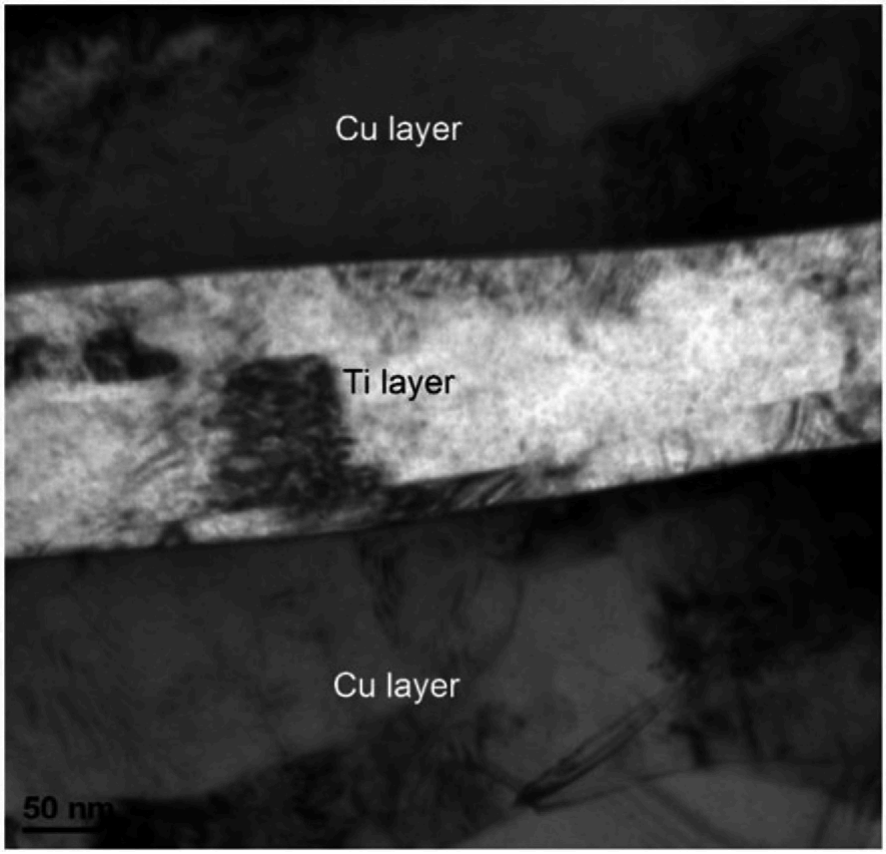


Fig. 3.25 TEM micrograph of Ti layer in Cu/Ti laminate

3.3 Cu/Al Laminates Subjected to Cold Roll Bonding

3.3.1 Development of Porous Cu/Al/Cu Laminate Foils

We report a special deformation phenomenon: porosity in the Al layer during Cu/Al/Cu laminate rolling with different Al thicknesses [11]. This discovery points the way to a new approach to fabricate porous Al laminates. Such foils can conceivably be used in manufacturing micro-parts capable of shielding electrical devices or buildings from electromagnetic noise.

Figure 3.26 shows the microstructure of the annealed samples for the aluminium sheets with thicknesses 130 μm and 40 μm respectively. Both are seen to have a similar microstructure. The mean grain size in the 130 μm aluminium layer is larger than 2.0 μm, and that in the 40 μm aluminium layer, larger than 2.2 μm. Thus, it is seen that the

occurrence of pores is not irrelevant to the grain size. In addition, we did not find any pores in these two samples.

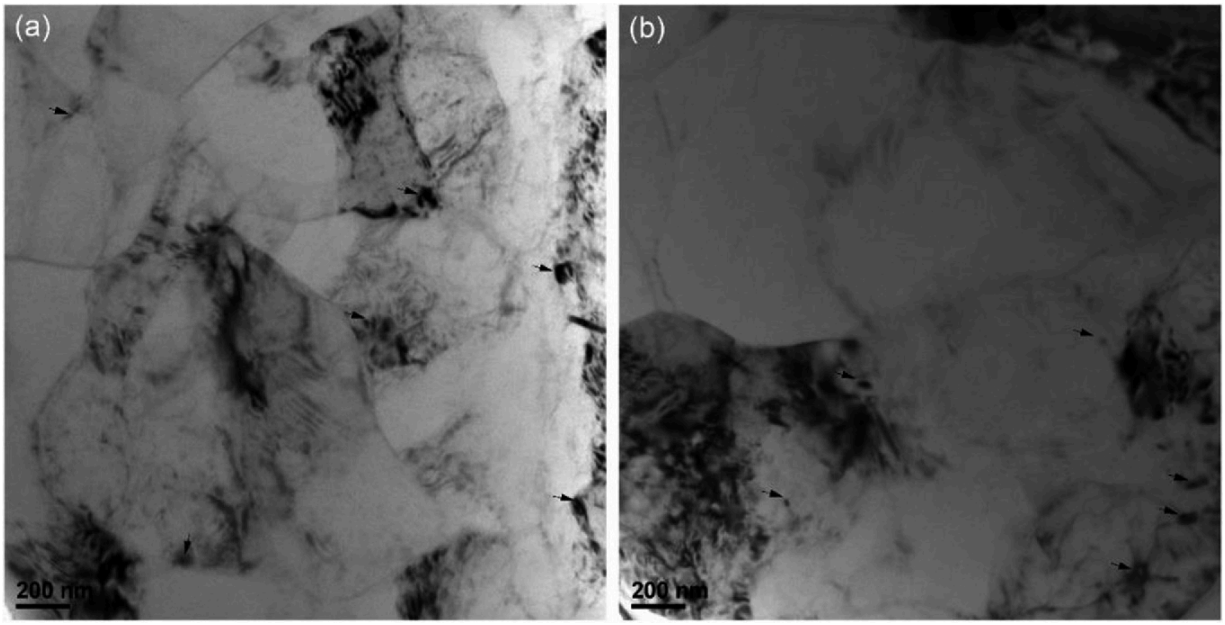


Fig. 3.26 TEM images of annealed samples for **a** 130 μm and **b** 40 μm. Inclusions are shown by arrows

Figure 3.27a shows the TEM sample prepared with the focused ion beam (FIB) technique. The FIB technique makes it possible to reveal the micro-defects in the samples without damage. Figure 3.27b–d show a typical interface between the Cu and Al layers corresponding to Al layer thickness 16 μm, 40 μm and 130 μm respectively. For roll bonding between the Cu and Al layers, the reduction ratio determines the quality of interface bonding. After rolling, the interface between the Cu and Al layers shows good bonding, with no discernible residual holes or cracks. In this study, the rolling reduction ratio during the first pass is larger than 50%, which results in good bonding at the interface. In addition, in Fig. 3.27b–d, there are no pores observed in the Cu layer, however, there are some nanoscale pores seen in the Al layer.

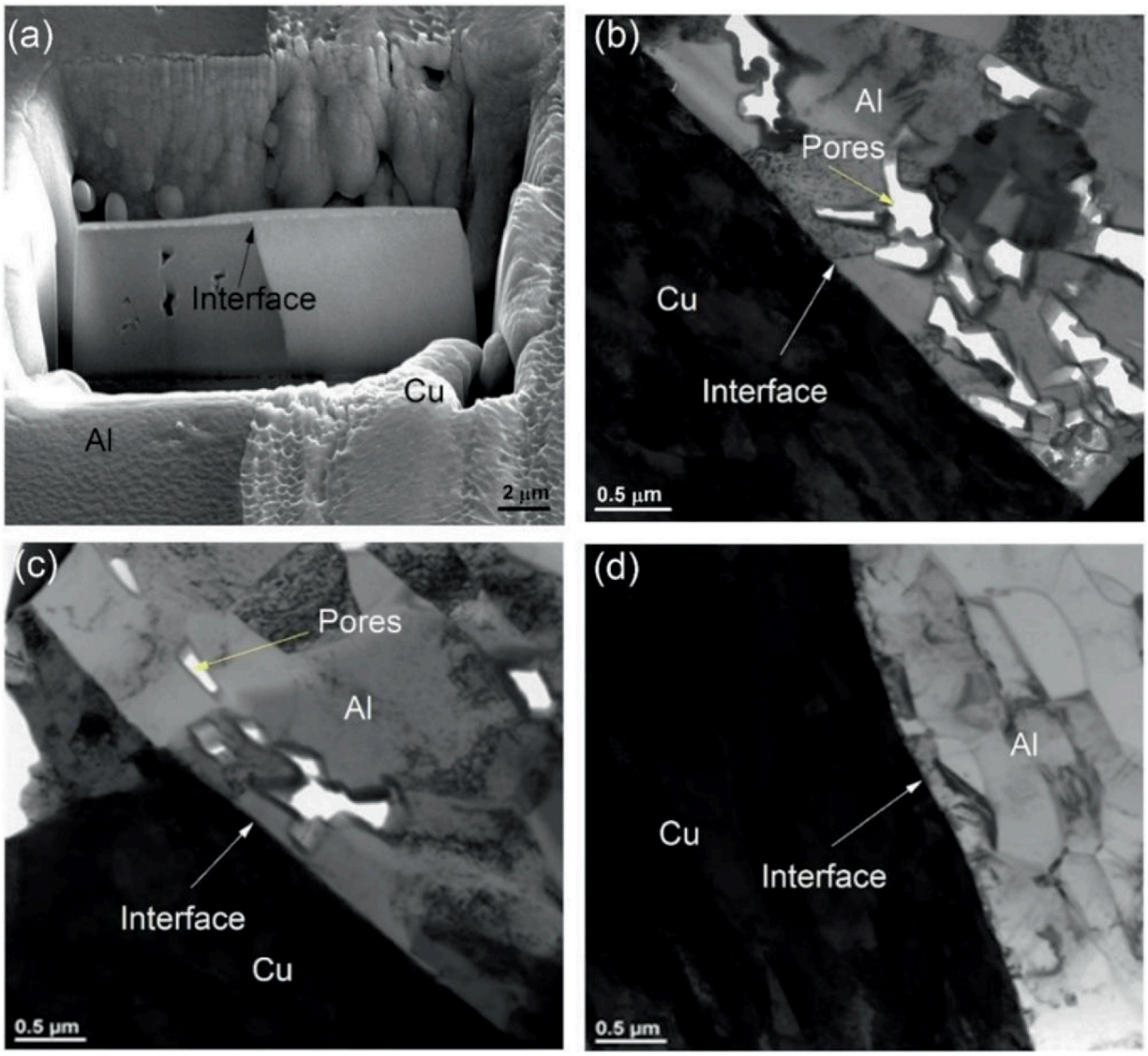


Fig. 3.27 FIB sample (**a**), and TEM images for (**b**) interface between Al/Cu for Al sheet thickness 16 μm, **c** 40 μm and **d** 130 μm

Figure 3.28 shows the TEM images of the Al layer after rolling. There are a large number of pores in the Al layer both near the grain boundaries and inside the grains. In Fig. 3.28a–d, it appears that the density of nano-scale pores in the Al layer increases with reducing thickness of the Al layer. When the thickness of the Al layer is 130 μm, there are only a few pores visible. The fraction of the nanoscale pores in the image was found to be about 10%. However, when the thickness of the Al layer is 16 μm, about half of the image is taken up by pores. This results in a good Al foam structure in the multilayer laminate.

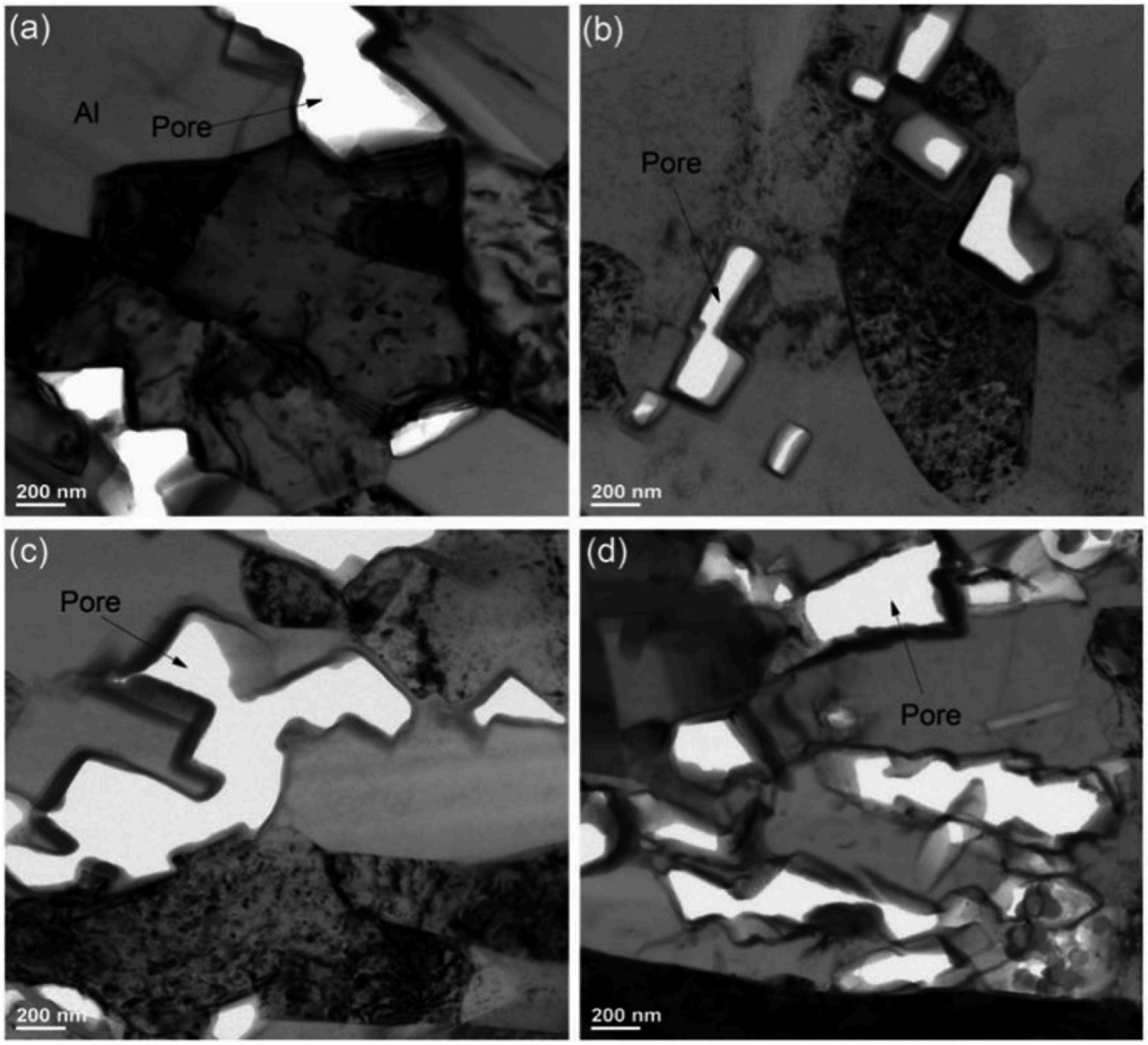


Fig. 3.28 TEM images for Al layer in Cu/Al/Cu laminate for Al sheet thickness **a** 130 μm, **b** 70 μm, **c** 40 μm and **d** 16 μm

Figure 3.29a–c show the section profile after the second rolling pass. During Cu/Al/Cu laminate rolling, Al sheets with all three thicknesses deform uniformly without severe necking and fracture. For bimetal laminates, fracture of the layers often occurs due to different yield stresses and deformation flow. In some previous studies, it has been observed that during rolling of metal laminates with different mechanical properties and involving high reduction in thickness, a plastic instability develops, the harder phase starts necking and eventually gets separated into small pieces. The absence of necking implies that the Cu and Al layers undergo equal elongation during rolling. However, there are large differences in thickness reduction

ratios for the different Al layer thicknesses, as shown in Fig. 3.29d. For the annealed CP Cu sheet and CP Al sheet, the yield stress of Al sheet is lower than that of Cu sheet. Thus, the reduction ratio of Al layer is larger than that of Cu layer in a rolling pass. In this study, the side and end of Cu/Al/Cu laminate were welded, thus, their elongations after rolling are the same. If there are no pores in the Al layer, the thickness reduction ratio $((T_{Al0}\text{-}T_{Al1})/T_{Al0})/((T_{Cu0}\text{-}T_{Cu1})/T_{Cu0})$ (where T_{Al0} and T_{Al1} are the thickness of the Al layer before and after rolling respectively, and T_{Cu0} and T_{Cu1} are the thickness of Cu layer before and after rolling respectively) should be equal to 1. If there are some pores in the Al layer, the density of pores would increase as the value of $((T_{Al0}\text{-}T_{Al1})/T_{Al0})/((T_{Cu0}\text{-}T_{Cu1})/T_{Cu0})$ deceases. In the experiments in the present study, with reduction in the Al sheet thickness, the thickness reduction ratio of Al sheets before and after rolling become less than that of Cu sheets. When the initial thickness of Al layer is 130 μm, the thickness reduction ratio of Al and Cu sheets after rolling $((T_{Al0}\text{-}T_{Al1})/T_{Al0})/((T_{Cu0}\text{-}T_{Cu1})/T_{Cu0})$ is approximately 1. However, when the initial thickness of the Al layer is 16 μm, the thickness reduction ratio of Al and Cu sheets after rolling $((T_{Al0}\text{-}T_{Al1})/T_{Al0})/((T_{Cu0}\text{-}T_{Cu1})/T_{Cu0})$ is only 0.85, which means that more than 15% of the Al layer volume consists of nano-scale pores. This is in good agreement in the observation of pore density in Fig. 3.28, in which the nano-pore density increases as the thickness of Al layer reduces.

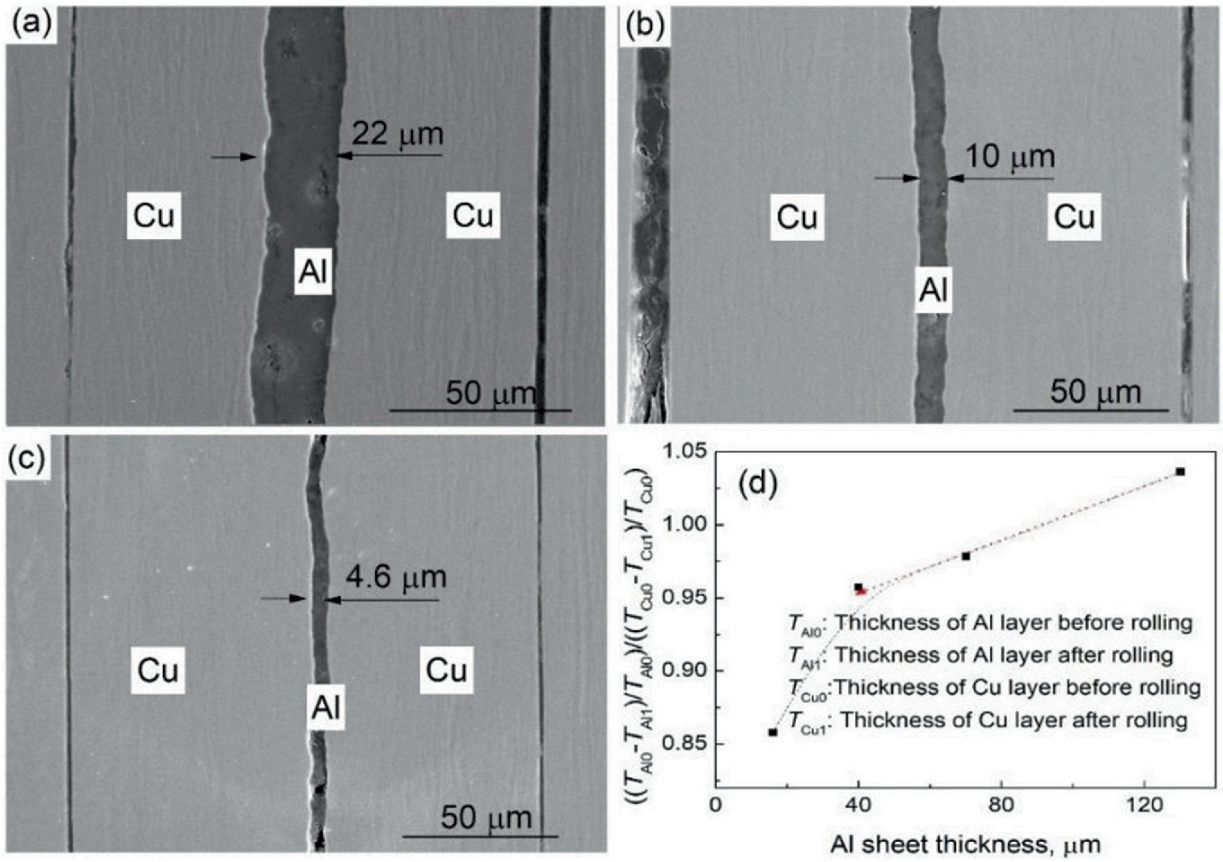


Fig. 3.29 SEM images of laminate section for initial Al thickness **a** 130 μm, **b** 40 μm and **c** 16 μm. **d** Thickness reduction ratio as a function of Al layer thickness

Figure 3.30a shows that the stress changes in the roll bite. At the point of entrance of the roll bite, the Al layer is under compressive stress, which would not result in the formation of pores in the Al layer. However, in the exit zone, the tensile stress become predominant, which might lead to the formation of pores in the material. The roll bite can be divided into the 'forward slip zone' and the 'backward slip zone'. In the forward slip zone, both the Cu and the Al layers are under compression and their thicknesses reduce. In the backward slip zone, the direction of the friction force on the surface of the Cu layers is opposite to the rolling direction. In addition, due to the spring-back of laminate in the exit zone, the surface of the laminate is under tension, which results in tension in the Al layer in the exit zone. Figure 3.30b shows the maximum tensile stress in the Al layer as a function of the thickness ratio $T_{\mathrm{Al0}}/T_{\mathrm{Cu0}}$. It can be described by Eq. (3.16):

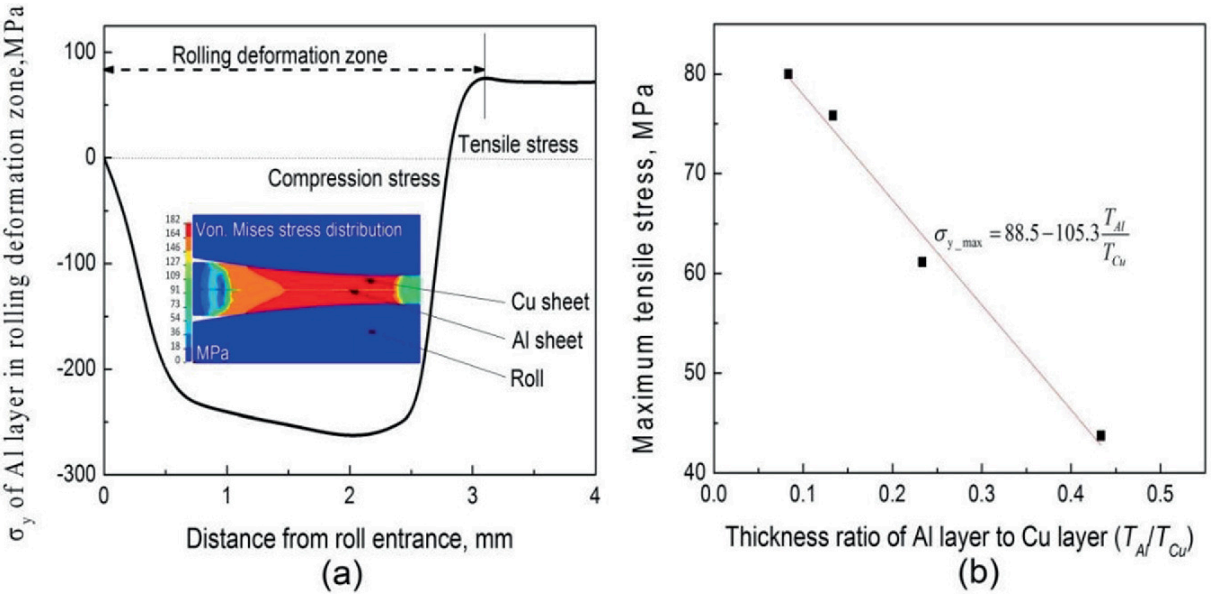


Fig. 3.30 Stress value versus foil thickness calculated by FEM

$$\sigma_{y_\max} = 88.5 - 105.3\frac{T_{\mathrm{Al0}}}{T_{\mathrm{Cu0}}} \tag{3.16}$$

From Eq. (3.16), it is obvious that the tensile stress of the Al layer increases with reducing thickness of the Al layer, which directly results in the nano-porous structure in the Cu/Al/Cu laminate after rolling.

In general, the failure of homogeneous or heterogeneous material is caused by the nucleation and growth of pore and/or microcracks in the week point of the work pieces. The breakdown of a severely deformed material occurs due to local stress concentrations. The weekly bonded interface between hard inclusions and soft matrix, or dirty interface and grain boundaries are usually responsible for both stress concentrations and pore nucleation. In this study, AA1230 sheets have been used, in which there are some alloying elements such as Fe + Si (0.7%) and Cu (0.1%), and these elements are harder to deform compared to the Al matrix. In Fig. 3.31, the nanoscale inclusions are shown by arrows. Under severe plastic deformation, the assembled alloying elements will result in stress concentration and lead to the formation of nano-scale pores. Ervasti and Ståhlberg [12] found evidence of void initiation close to a macro-inclusion during hot rolling when the inclusions are hard materials. However, in current study, no voids were observed at the interface of Cu and Al, but large amounts of faceted voids were found near the center of Al layer. The nucleation of

the voids under local stress concentrations may partly be attributed to the residual impurities in the starting material of Al, such as minor Si and Fe, which might not be responsible for the formation of the interlinked large pores. It is more likely that the formation of the majority of the pores might be caused by the surface oxidation between Al sub-layers introduced during the multi-pass rolling process. The separation might occur at the interphase of $Al/Al_2O_3|Al_2O_3/Al$, where should be the weakest point under tensile tension in exit side of the rolling process, thus promoting the initiation and growth of the voids. This type of decohesion phenomena between Al grains on basal plane to form the foam structure with faceted sidewalls during rolling process should be suppressed by the ductile deformation with multiple slip systems, which promoted the dimple fracture morphology of Al in tensile testing. Kadkhodapour et al. [13] investigate the nucleation, growth and coalescence of voids in a dual-phase steel material. They found that void nucleation may occur through interphase grain-boundary decohesion between ferrite and the neighbouring martensite grains, which may be influenced by deformation localization due to microstructural inhomogeneity. Langdon [14] studied voids formation in superplastic materials, including Al alloys, and pointed out that the size and shape of internal voids were controlled by both the properties of the material and testing conditions. Large amounts of voids were observed near the fracture tip of the specimen aligned along the tensile axis. There also was evidence for void interlinkage. Srivatsan et al. [15] studied tensile deformation and fracture behavior of AA7055. Based upon their observation during the tensile to fracture experiments, they suggested that macroscopic fracture of the alloy was by shear, while microscopic fracture revealed features reminiscent of both brittle and locally ductile mechanisms, that is, combination of cracking along the grain and sub-grain boundaries coupled with ductile micro-void formation, growth and coalescence. In addition, strain concentrations during plastic deformation can occur and cause the formation of voids and microcracks. The origin of the decohesion separation occurred under the tensile tension in the normal direction may also be related to the residual air bubble or surface contamination species trapped between Al sub-layers. The premature failure of the material in Al layer in this direction could be related with work hardening during the

rolling process, which mainly accelerate the elongation development of material in rolling direction. The mechanism behind this observation is still not fully understood. Further study is needed to establish the new model to cope with the dynamic process of multi-layer heterogeneous materials in rolling fabrication of new advanced materials. From the discussion above, we conclude that a combination of tensile stress, nanoscale inclusions and severe plastic deformation in the Al layer leads to the initiation of nano-scale pores in the Al layer.

In Fig. 3.28, it is seen that a number of pores have sidewalls characterized by 90° turns. This can be seen as the effect of the neighboring grain orientation during deformation. The crystal structure of Al is face-centered cubic (FCC) structure. The slip system of this type of material is {111} <110>, which is the root cause of the ductile plastic deformation and the formation of dimple shaped fracture surface during tensile testing of Al. However, the origin of the observed faceted pores with perpendicular sidewalls seems to be related to the cold work hardening and localized high stress concentration on some weak points along the grain boundaries within the deformed Al layer. This process may provide enough activation energy for nucleation of this type of pores along specific crystallographic orientations. The tensile stress on the exit side of rolling may enhance the displacement of material along the coalesced pores. Figure 3.31 shows that the longitudinal axis of an observed rectangular pore was found to be parallel to the [100] direction of the neighboring grain. This implies that the sidewalls of the observed pore coincide with the {001} planes of this grain, which should not be associated with the transgranular dislocation glide on the slip system of {111} <110>. It is more likely for this type of faceted pores to be nucleated on the intergranular boundaries with the preferred crystallographic habit plane, such as {001}, and grow up to form the foam structure with the strong tensile stress during the rolling process. It is interesting to note that the phase interface between the Cu and the Al is much stronger than the internal intergranular structure of Al. This also directly leads to the formation of such a sandwich foam structure without signification defects on the binding region between the Cu and Al layers.

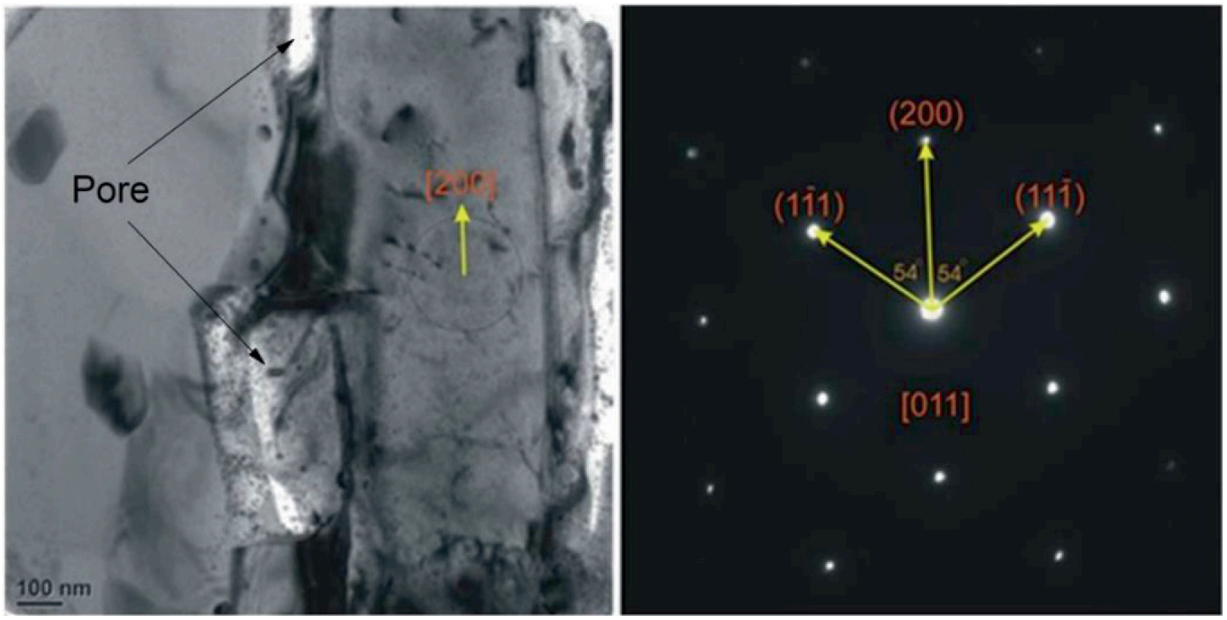


Fig. 3.31 The TEM micrograph and associated SAD pattern with the beam direction on [011] show the observed faceted void with the sidewalls on {001} plane of the neighboring grain in the Al layer

3.3.2 Development of Cu/Al/Cu Laminates via Powder-In-Tube Method

Cu/Al/Cu laminates were successfully fabricated by using the powder-in-tube method [16]. To remove the oxide and other impurities, the inner wall of the Cu tube was cleaned using a wire brush and acetone. This process could also increase the surface roughness and expose fresh metal, which is beneficial for the bonding of two metals. Al powder (99.99% in purity) was packed into the pure Cu tubes (99.5% in purity) with an outer diameter of 10 mm and an inner diameter of 8 mm. Then, these composite tubes were sealed and cold worked into tapes (1.5 mm thickness) by flat rolling. The as-rolled tapes were cut into pieces, which were annealed in a resistance furnace, followed by further cold rolling. To explore the influence of annealing temperature and reduction rate on the microstructure and mechanical properties of the Cu/Al/Cu laminates, these tapes were first annealed at 350 °C, 450 °C and 550 °C for 40 min, respectively. For comparison, half of these samples were subsequently rolled to a thickness of 0.5 mm. Only three rolling passes for laminates from 10 to 0.5 mm are needed (10 mm–4 mm–1.5 mm–0.5 mm). Moreover, the edges of samples are trim without obvious cracks, which can guarantee high yield of the

laminates. Figure 3.32 illustrates the fabrication procedures of the Cu/Al/Cu laminates used in this investigation.

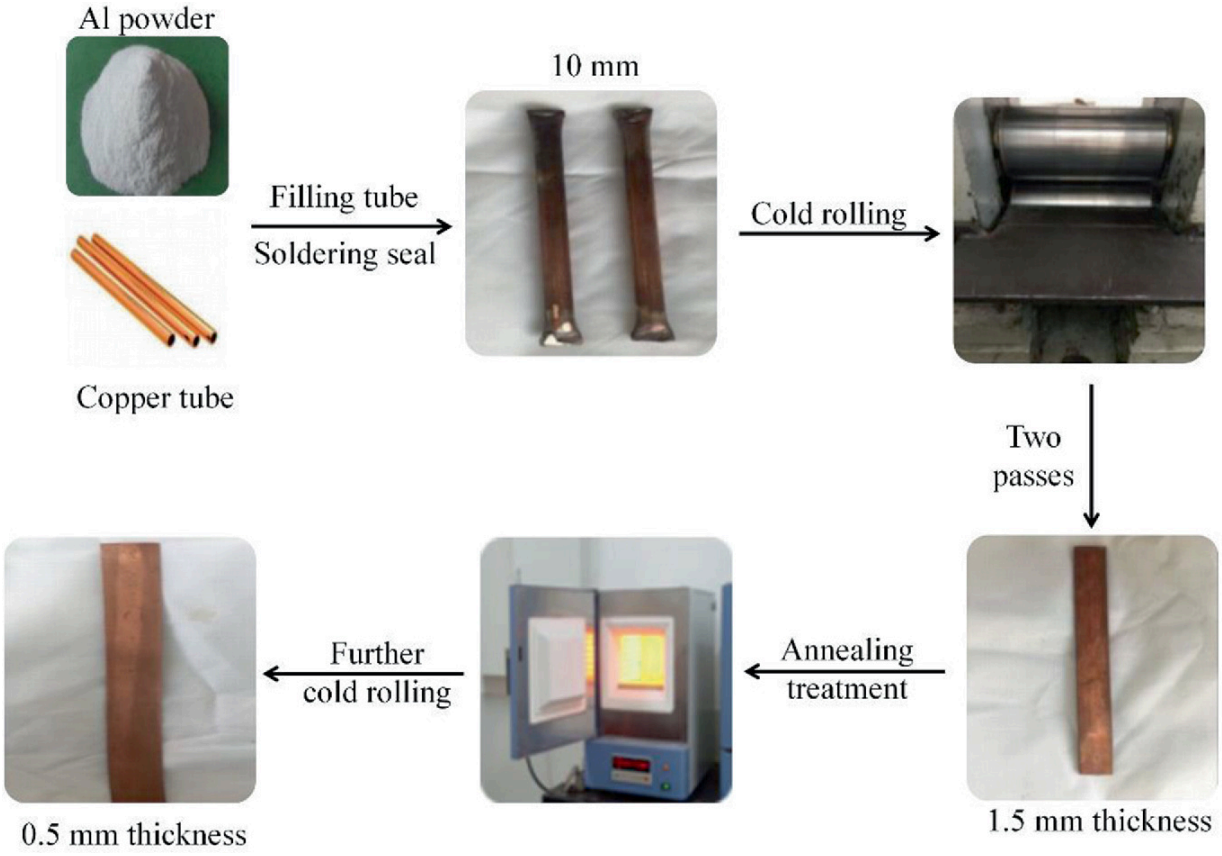


Fig. 3.32 Illustration of fabrication process of Cu/Al/Cu laminates via in-tube method

Figure 3.33a–c show the SEM images close to the bonding interface of the samples (1.5 mm thickness) annealed at different temperatures. Cu and Al are tightly bonded and obvious interfacial intermetallic layers can be observed. In addition, the thickness of the reaction layer will continue to increase with the rise of heat treatment temperature. At a low annealing temperature, most of the interfacial atoms are bound by surface energy. Thus, interface diffusion is faintly characterized by a narrow intermetallic layer (Fig. 3.33a). When the annealing temperature rises, thermal energy obtained by Cu atoms and Al atoms can exceed the diffusion barrier and promote the formation of more IMCs. The range of atomic diffusion is enlarged, and a wider diffusion layer is achieved (Fig. 3.33b and c). It is interesting that the bonding interface after annealing becomes wavelike and the wave amplitude will become larger with the increase of annealing temperature

(Fig. 3.33a–c). The bonding interfaces of the 350, 450 and 550 °C annealed laminates suffering 95% cold rolling reduction (0.5 mm thickness) are shown in Fig. 3.33d–f, respectively. Compared with the interfaces of the annealed laminates, the diffusion layer after further cold rolling becomes thin and discontinuous (Fig. 3.33d–f), which results from the cracking of brittle diffusional layer. Especially, for the 550 °C annealed laminates with a thick diffusional layer, further cold rolling even causes visible diffusional layer fracture as a result of the large rolling force penetrating the thickness of the laminates. Some fragments of IMCs are squeezed into the Al substrate, as shown in Fig. 3.33f.

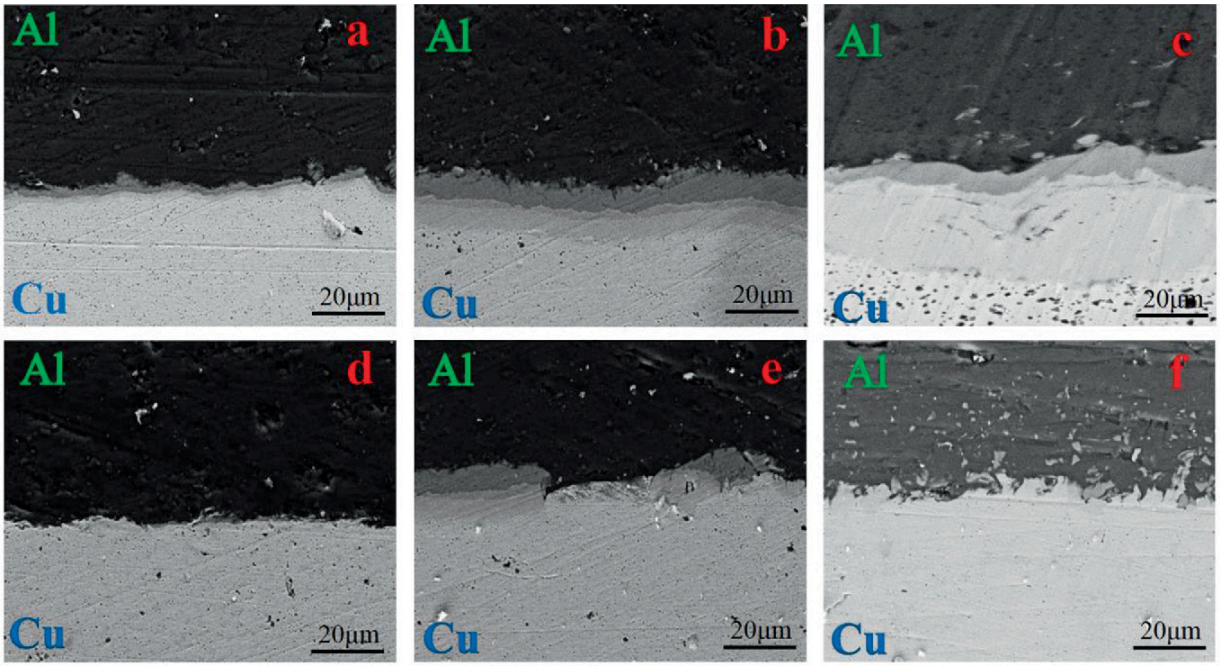


Fig. 3.33 Cu/Al bonding interfaces by SEM: samples of 1.5 mm thickness annealed at **a** 350 °C, **b** 450 °C, **c** 550 °C and further cold rolled to 0.5 mm thickness **d** after 350 °C annealing, **e** after 450 °C annealing, **f** after 550 °C annealing

Figure 3.34 shows the line scans across the Cu/ Al interface. In the annealed laminates, the diffusional width increases from 5.8 μm at 350 °C (Fig. 3.34a) to 35.1 μm at 550 °C (Fig. 3.34c). After further cold rolling, the diffusional width at the bonding interface significantly decreases, from 2.6 μm for the 350 °C annealed strip (Fig. 3.34d) to 8.3 μm for the 550 °C annealed strip (Fig. 3.34f). Moreover, it can be observed that the degree of atomic diffusion at the bonding interface for Cu is stronger than that for Al. For the intermediate annealing

process, the diffusion coefficient of Cu on Al is higher than that of Al on Cu. For example, D_{Cu-Al} is 9.2×10^{-21} m^2/s and D_{Al-Cu} is 3.4×10^{-21} m^2/s for T = 110 °C. Besides, this difference will become more marked when the temperature increases. As for the further cold rolling process, the lattice constants for Cu and Al are α_{Cu} = 0.3615 nm and α_{Al} = 0.4082 nm, respectively. Thus, Cu atoms enter the interstitial site of Al lattice easier than that for Al atoms, which has been proven by the accumulative roll bonding process of multi-layered Al/Cu composites.

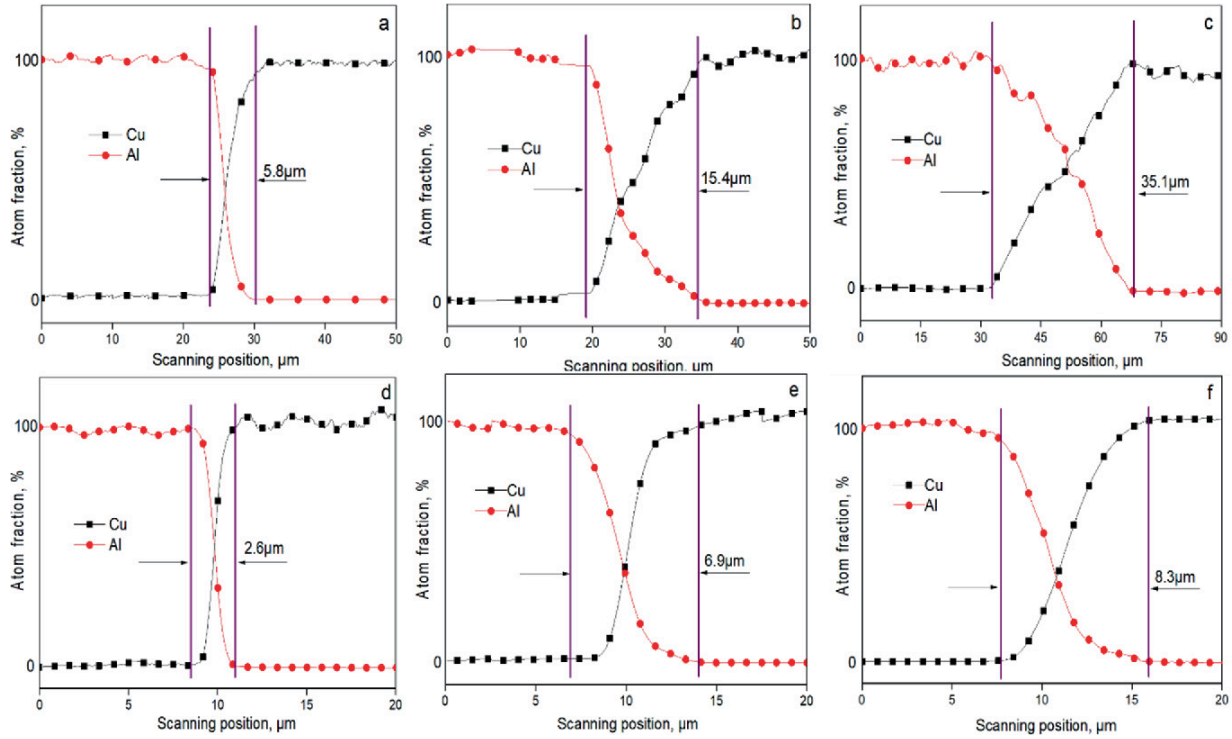


Fig. 3.34 Contents of Cu and Al across the bonding interface: samples with 1.5 mm thickness annealed at **a** 350 °C, **b** 450 °C, **c** 550 °C and cold rolled to 0.5 mm thickness **d** after 350 °C annealing, **e** after 450 °C annealing, **f** after 550 °C annealing

To make the difference of inter-diffusion zone more apparent, the width values under different conditions are plotted in Fig. 3.35. It is interesting that the higher intermediate annealing temperature, the larger the reduction of diffusional width that is achieved. The reductions of diffusional width for the laminates annealed at different temperatures are 3.2 μm (350 °C), 8.5 μm (450 °C) and 25.8 μm (550 °C), respectively. After high-temperature (above 300 °C) annealing, the interfacial reaction layers include Cu_9Al_4, CuAl (Cu_4Al_3) and $CuAl_2$. All of these chemical compounds are brittle and of low

plasticity. The varieties and changes of the Cu/Al IMCs on the peeling surfaces of the laminates will be discussed in the following sections in detail.

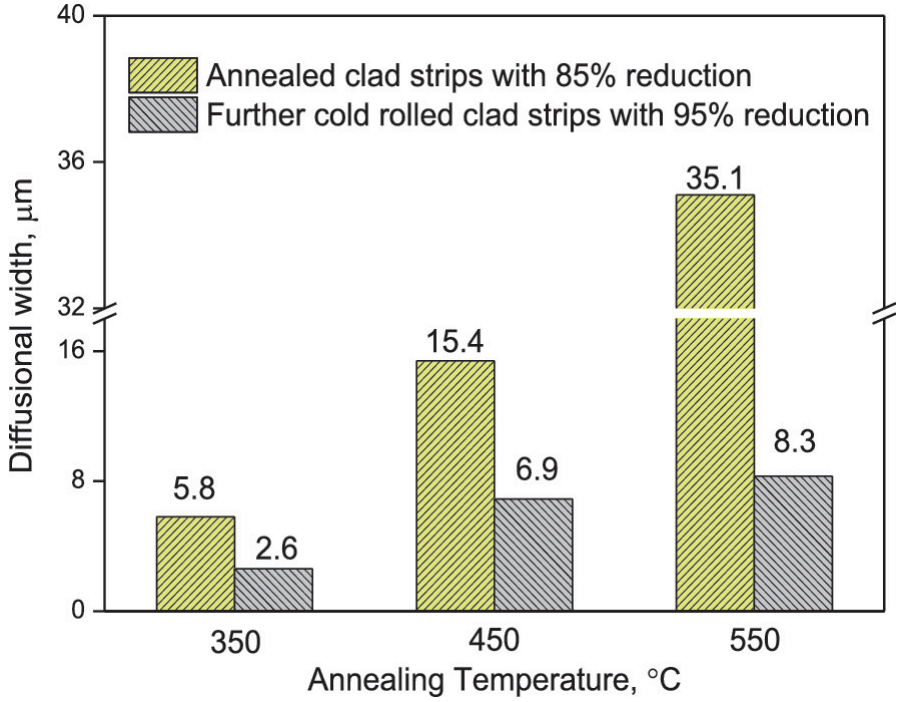


Fig. 3.35 The diffusional width of the Cu/Al/Cu laminates under different annealing temperatures and reductions

The peeling strength curves and the average peeling strength of the Cu/Al/Cu laminates after annealing and further cold rolling are shown in Fig. 3.36. The experimental results show that the Cu/Al/Cu laminates processed by the powder-in-tube method have a relatively steady performance (Fig. 3.36a). With the increase of annealing temperature, the average peeling strength of the laminates (1.5 mm thickness) increases first and then decreases, from 3.1 N/mm at 350 °C to 5.2 N/mm at 450 °C to 2.9 N/mm at 550 °C. The average peeling strengths of the corresponding further cold-rolled laminates (0.5 mm thickness) are 10.6 N/mm, 17.8 N/mm and 3.2 N/mm (Fig. 3.36b), respectively. Obviously, further cold rolling process will markedly increase the peeling strength of the Cu/Al/Cu laminates except for those annealed at 550 °C. For the laminates annealed at 350 and 450 °C, further cold rolling process can break the brittle Cu/Al IMCs and promote the formation of high-strength intermetallic layers. The thick intermetallic layer (i.e., 35.1 μm in laminates annealed at 550 °C) can only be broken

up, rather than reform high-strength IMCs, which can also be proven by Fig. 3.33f.

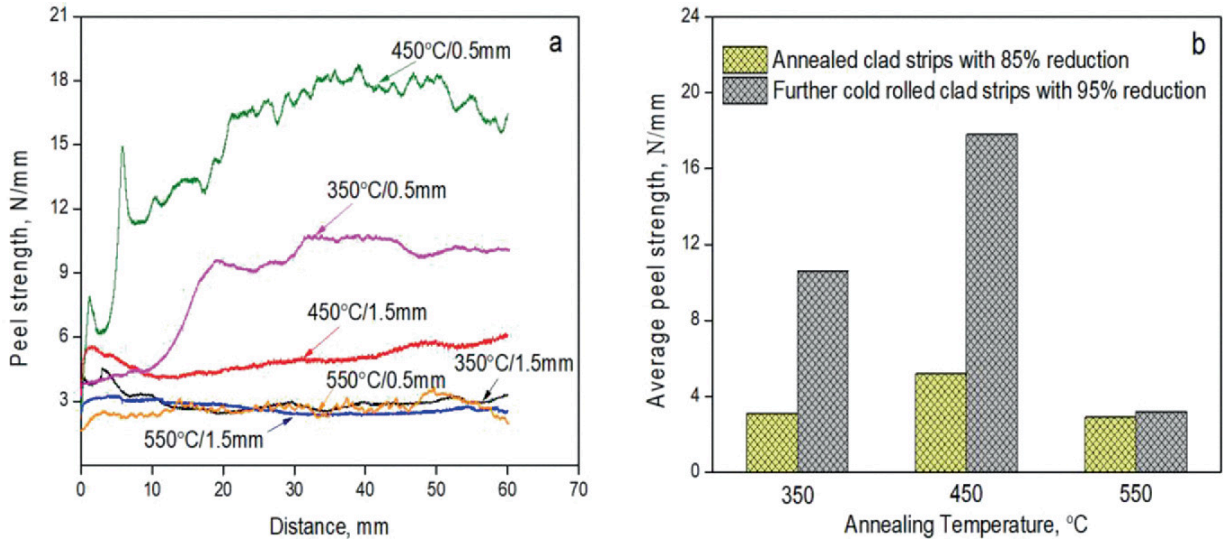


Fig. 3.36 The peeling strength of Cu/Al/Cu laminates: **a** peeling strength curves and **b** average peeling strength under different annealing temperatures and reductions

The Kirkendall effect of void formation near the Cu substrate would be promoted in the annealing process. The agglomeration of voids in the solid solution of Cu leads to the formation of a weak layer in the interface region, which greatly reduces the bonding strength of the laminates. Thus, to make our analysis more targeted and concise, only the Cu surface morphologies of the laminates after peeling are provided. The mechanical performance of laminates is tightly related to the compactness and continuity of the IMC on the peeling surface. In addition, the roughness of the peeling surface can directly reflect the reaction degrees of Cu atoms and Al atoms. These laminates with excellent properties usually possess a rough peeling surface, and their IMCs are relatively compact, continuous and thin, which can be proven in the following analysis. The morphology and compounds of 350 °C annealed and further cold-rolled laminates after peeling are shown in Fig. 3.37. The peeling surface is smooth, and some small cracks and voids can be observed (Fig. 3.37a). The EDS results indicate that the compounds on the Cu surface are Cu_9Al_4 and α-Cu, as shown in Fig. 3.37c and d. The phase of Cu_9Al_4 on the peeling surface is bumpy while α-Cu has a smooth surface, which can be seen in Fig. 3.37b. The existence of fresh Cu proves that further energy input is necessary for

the close integration of the Cu/Al/Cu laminates. The peeling surfaces of the further cold rolled laminates are shown in Fig. 3.37e. It can be seen that their peeling surfaces are much more rugged than those of the annealed strips. The increment of the surface roughness is in accordance with the enhancement of peeling strength (Fig. 3.36). The compounds on the peeling surface are mainly divided into two shapes: rice dough and salient (Fig. 3.37f), which are seldom observed on the peeling surfaces of the annealed strips. The chemical components of "rice dough" and "salient" are CuAl and Al, respectively, as shown in Fig. 3.37g and h. Both the disappearance of α-Cu and existence of CuAl and Al on the peeling surface (Cu surface) prove that further cold rolling process can promote the combination of Cu and Al atoms and the formation of metallic bonds.

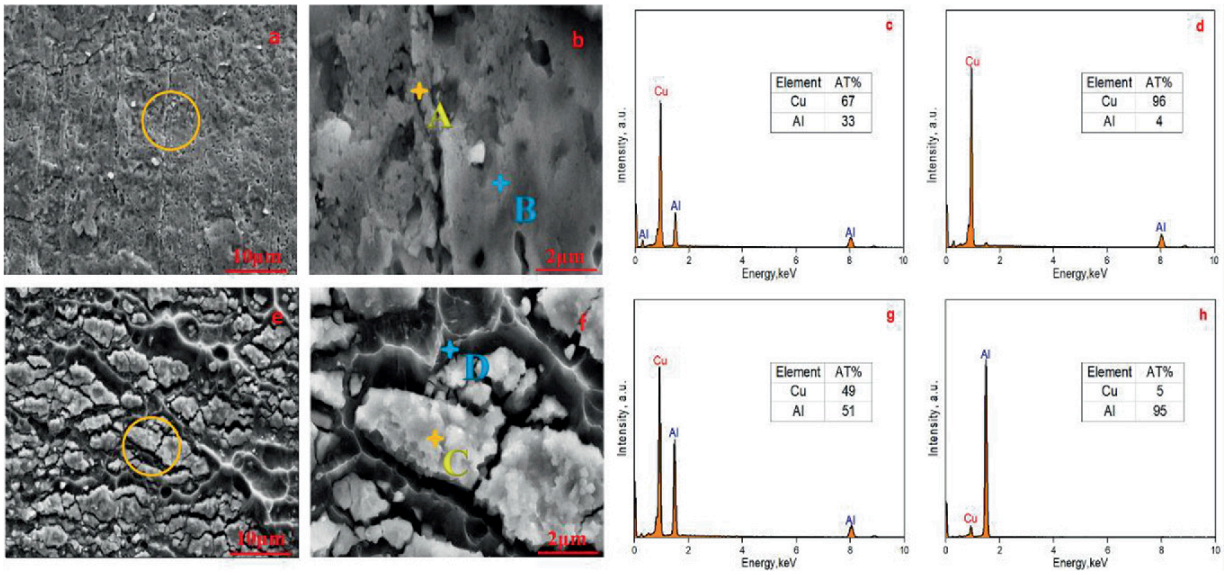


Fig. 3.37 Peeling surfaces of 350 °C annealed laminates: **a** Cu surface, **b** an enlarged image of the yellow circle zone in this figure (**a**), (**c**) (**d**) composition of point A and B in this figure (**b**) and further cold rolled to 0.5 mm: **e** Cu surface, **f** an enlarged image of the yellow circle zone in this figure (**e**), (**g**) (**h**) composition of point C and D in this figure (**f**)

The morphology and compounds of 450 °C annealed and further cold-rolled laminates after peeling are shown in Fig. 3.38. With the increase of annealing temperature, fresh Cu cannot be observed any more, which indicates that the bonding zones have been expanded (Fig. 3.38a). The mechanism of an increment in the peeling strength induced by higher annealing temperature is the enhancement of bonding strength through microstructure evolvement of the bonding

interface, i.e., the disappearance of the residual voids and the increase of the roughness of the peeling surface. The main compound in the peeling surface is $CuAl_2$, mixed with a small quantity of Cu_9Al_4 and Al (Fig. 3.38b, c and d). After further cold rolling, the diffusional width of the 450 °C annealed laminates shows an obvious decrease (Fig. 3.34b and e). There are many compact and uniform chunks embedded on the peeling surface, as shown in Fig. 3.38e and f. The type of compounds shows almost no change: the main phase is still $CuAl_2$ and the content of Al increases slightly. Nevertheless, the peeling strength of the laminates is markedly enhanced (Fig. 3.33b). The above results can indicate that the phase of $CuAl_2$ can be strengthened under a large rolling force penetrating the thickness of the strip.

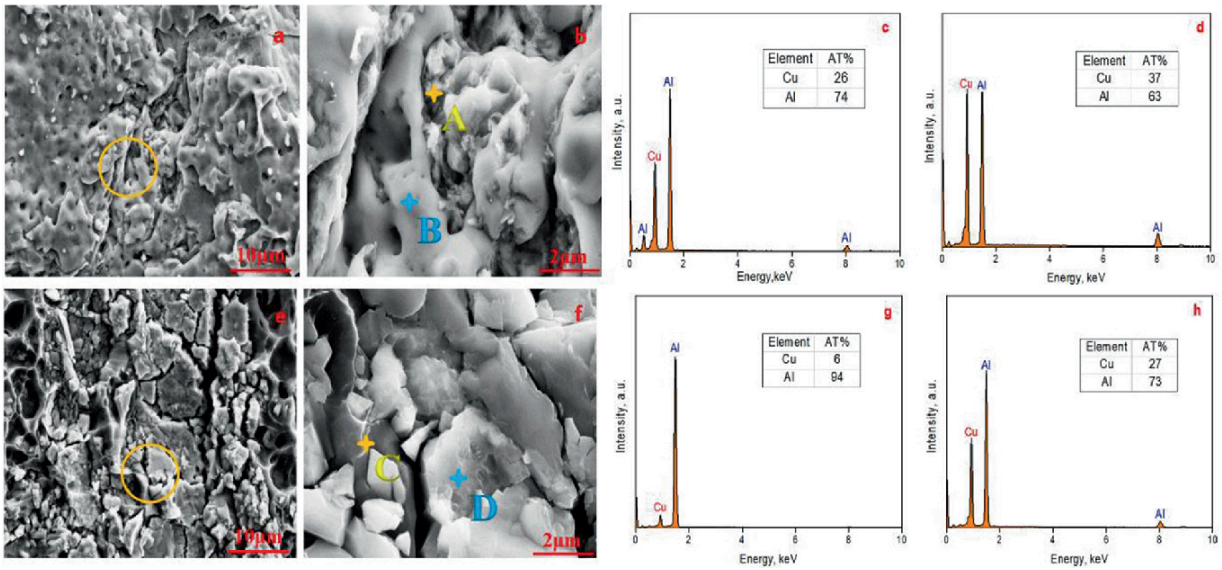


Fig. 3.38 Peeling surfaces of 450 °C annealed laminates: **a** Cu surface, **b** an enlarged image of the yellow circle zone in this figure (**a**), (**c**) (**d**) composition of point A and B in this figure (**b**) and further cold rolled to 0.5 mm: **e** Cu surface, **f** an enlarged image of the yellow circle zone in this figure (**e**), (**g**) (**h**) composition of point C and D in this figure (**f**)

The morphology and compounds of 550 °C annealed and further cold rolled laminates after peeling are shown in Fig. 3.39. Many salients can be observed on the peeling surface, as shown in Fig. 3.39a and b, and the main compound is CuAl (Fig. 3.39c and d). After annealing at 550 °C, wider diffusional layers are formed, but the peeling strength of the laminates decreases sharply. The probable reason is the existence of large amounts of intermetallic phase CuAl. The CuAl phase is hard and brittle and impairs the bonding strength when the percentage is high.

Even if the further cold rolling process can visibly reduce the width of the diffusion layer and promote the phase transformation on the peeling surface from CuAl to $CuAl_2$ (Fig. 3.39g and h), large amounts of fragmental $CuAl_2$ phase. Figure 3.39e and f will hinder the formation of high-strength metallic bonds between Cu and Al atoms and cannot provide high mechanical performance for the Cu/Al/Cu laminates. Based on above experimental results, there exists an optimal intermediate annealing temperature (approximately 450 °C) for a Cu/Al/Cu laminate processed by the powder-in-tube method that will promote the formation of a modest intermetallic layer (neither too thin nor thick). The laminates can exhibit excellent performance only with a moderate diffusional thickness, which can also be proven in the tensile test.

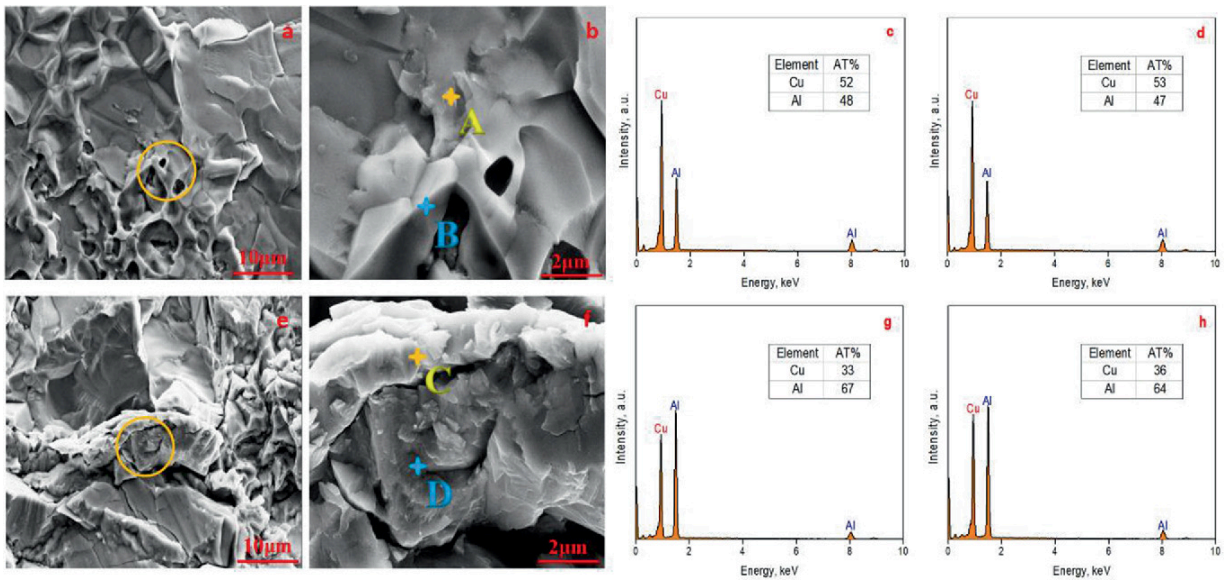


Fig. 3.39 Peeling surfaces of 550 °C annealed laminates: **a** Cu surface, **b** an enlarged image of the yellow circle zone in this figure (**a**), (**c**) (**d**) composition of point A and B in this figure (**b**) and further cold rolled to 0.5 mm: **e** Cu surface, **f** an enlarged image of the yellow circle zone in this figure (**e**), (**g**) (**h**) composition of point C and D in this figure (**f**)

Figure 3.40 shows the tensile properties of Cu/Al/Cu laminates with 0.5 mm thickness with different intermediate annealing temperatures. The ultimate tensile strengths of laminates annealed at 350 °C, 450 °C and 550 °C are 256 MPa, 286 MPa and 283 MPa, with elongation of 6.2%, 9.4% and 8.5%, respectively. The results indicate that the laminates annealed at 450 °C can obtained the largest tensile strength and elongation, as shown in Fig. 3.40a. The chemical composition and

thickness of the intermetallic layer will significantly affect the mechanical performance of the Cu/Al/Cu laminates. In the tensile process, interface debonding occurs in the laminates annealed at 350 °C as a result of weak atomic diffusion (Fig. 3.40b and e). When the intermediate annealing temperature is increased to 450 °C, the plasticity of the laminate is further enhanced. The tensile fracture of the intermetallic layer is rugged (Fig. 3.40c and f), which can achieve collaborative deformation with the matrix metals to some extent. Moreover, the tight bonding between the intermetallic layer and the metal matrix and the formation of a complete and continuous IMC can contribute to the enhancement of the ultimate tensile strength of the laminates. As for those laminates annealed at 550 °C, the tensile fracture of the intermetallic layer is relatively smooth and exhibits a typical brittle fracture (Fig. 3.40d). Moreover, in the process of the tensile test, the thick intermetallic layer is destroyed by external force. The broken intermetallic layer will decrease the tensile strength and plasticity of the Cu/Al/Cu laminates synchronously. In addition, the thick brittle intermetallic layer can be easily debonded in the plastic deformation process, which can also be clearly observed in Fig. 3.40g.

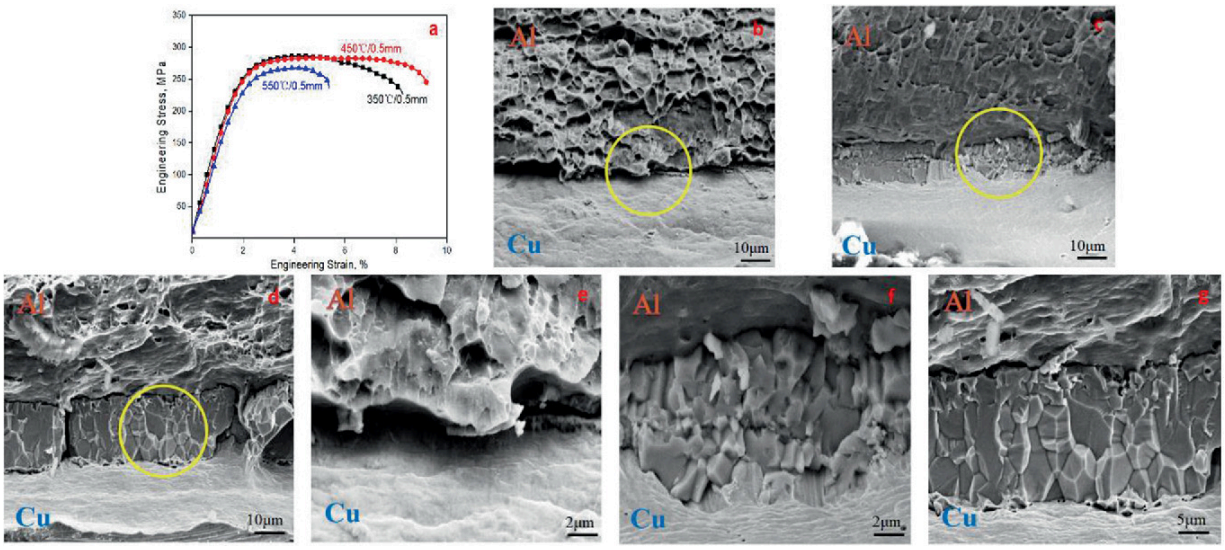


Fig. 3.40 Tensile properties of Cu/Al/Cu laminates with 0.5 mm thickness: **a** Engineering stress–strain curves and tensile fracture of laminates annealed at **b** 350 °C, **c** 450 °C, **d** 550 °C. **e**, **f**, **g** represent an enlarged images of the yellow circle zones in this figure (**b**), (**c**), (**d**)

3.3.3 Mechanism of Enhanced Bonding Strength of Cu/Al Laminates with SUS304 Interlayer

Table 3.2 lists the mechanical parameters of the SUS304 interlayers of different thicknesses [17]. The SUS304 foil used in specimen SR-30 exhibited the lowest yield strength but the largest elongation at fracture, implying better deformability than those used in specimens SR-10 and SR-20.

Table 3.2 Mechanical parameters of cold-rolled SUS304 foils

Laminates	Thickness of SUS304 foil (μm)	Yield strength of SUS304 foil (MPa)	Elongation of SUS304 foil (%)
SR-0	0	–	–
SR-10	10	1512	6.3
SR-20	20	1218	8.9
SR-30	30	1163	10.2

Figure 3.41 shows the SEM images of the bonding surface of Cu/Al laminates with the SUS304 interlayer. It can be seen from these images that the SUS304 foils were broken into fragments during the roll cladding process due to their limited deformability. Furthermore, the separation distance between fragments decreased with the increase of SUS304 thickness (Fig. 3.41a, c, e), reflected in the peeling surfaces of the laminates. Enlarged images (Fig. 3.41b, d, f) indicate that the flatness of the SUS304 interlayer improved with increasing thickness. This phenomenon was likely caused by the difference in deformability of SUS304 interlayers of different thicknesses. The thickest SUS304 interlayer achieved the largest thickness reduction during the roll cladding process, while the thinnest interlayer was more readily broken and displaced from the Cu/Al matrix, resulting in poor flatness. In contrast to the Cu/SUS304 interface, an obvious interfacial transition zone (ITZ) formed at the Al/SUS304 interface (Fig. 3.41g, h), which resulted from the formation of IMCs between Al and SUS304, while a solid solution (SS) was favored between Cu and SUS304.

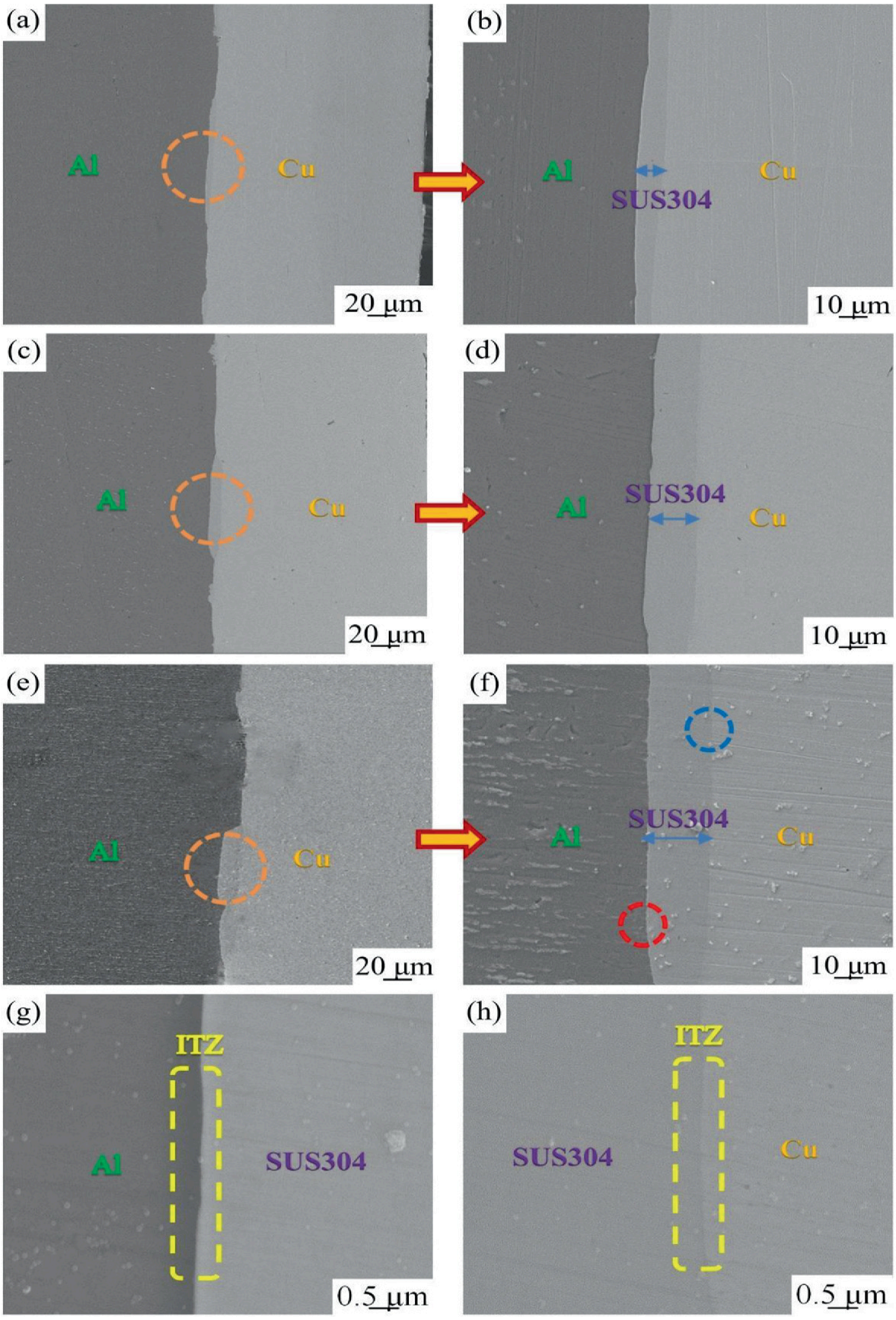

(a)
Al
Cu
20 μm
(b)
Al
SUS304
Cu
10 μm
(c)
Al
Cu
20 μm
(d)
Al
SUS304
Cu
10 μm
(e)
Al
Cu
20 μm
(f)
Al
SUS304
Cu
10 μm
(g)
ITZ
Al
SUS304
0.5 μm
(h)
ITZ
SUS304
Cu
0.5 μm

Fig. 3.41 SEM images of the bonding interface of Cu/Al laminates with an SUS304 interlayer: **a** SR-10, **c** SR-20, **e** SR-30; **b**, **d**, **f** Magnified images of orange circled zones in (**a**, **c**, **e**); **g**, **h** Magnified images of red (**g**) and blue (**h**) circled zones in (**f**)

To highlight the impact of the SUS304 foil on the bonding interface, SEM images of the interfacial microstructure and EDS mapping of the interface for specimens SR-0 and SR-30 are shown in Fig. 3.42. In SR-0, the serrated Cu-Al IMCs (circles in Fig. 3.42a) exhibited a discontinuous distribution at the bonding interface. In contrast, SR-30 demonstrated two different interfacial morphologies: one similar to that in Fig. 3.42a and the other as shown in Fig. 3.42b. At positions at which SUS304 fragments were present, a somewhat straight bonding interface without apparent IMCs was formed.

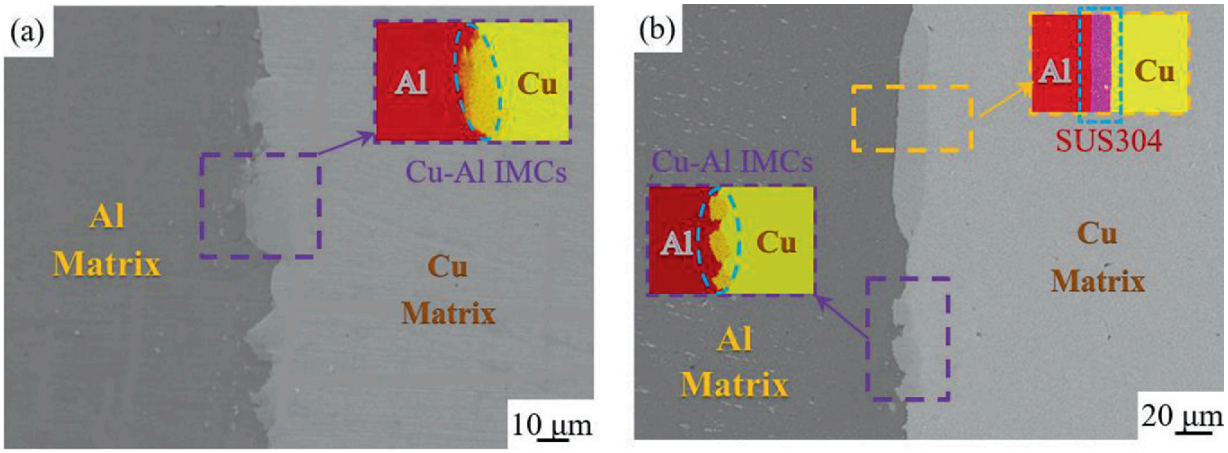


Fig. 3.42 Microstructure and EDS mapping of the bonding interface: **a** SR-0, **b** SR-30

The formation process of the bonding interface in Cu/Al laminates with an SUS304 interlayer is further illustrated in Fig. 3.43. During the initial rolling stage, intermittent cracks appeared in the SUS304 foil due to its limited plastic deformation capability. Meanwhile, Cu atoms and Al atoms were squeezed into the resulting gaps and then formed Cu-Al IMCs during the subsequent intermediate annealing process. Compared with the Cu and Al matrices, the SUS304 foil and Cu-Al IMCs demonstrated lower capacities for plastic deformation and thus were broken into pieces that were embedded into the Cu and Al matrices by the second rolling process.

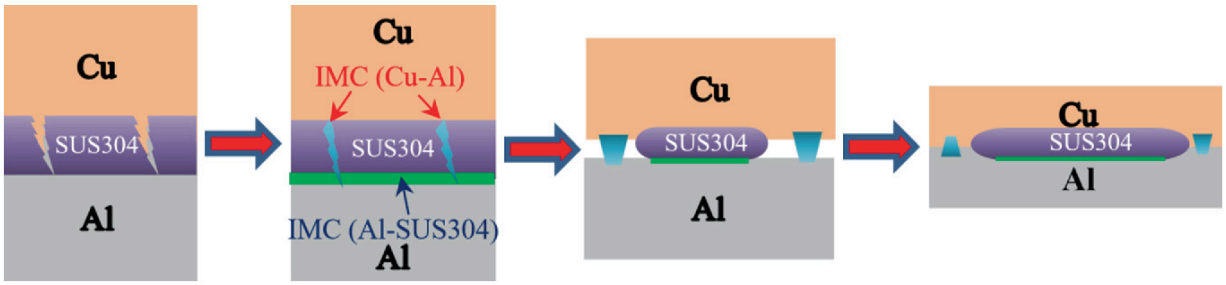


Fig. 3.43 Schematic of the formation of the bonding interface in Cu/Al laminates with an SUS304 interlayer

Figure 3.44 depicts the results of EDS line scans across the Cu/SUS304/Al interface in specimens with differing interlayer thicknesses. As shown in Fig. 3.44a–c, the EDS spectra were examined to determine the widths (thickness) of the ITZs at the Al/SUS304 and Cu/SUS304 interfaces, which measured 1.36 μm and 0.71 μm, respectively, in SR-10 (Fig. 3.44d). Larger ITZs were observed at the Al/SUS304 and Cu/SUS304 interfaces in SR-30, demonstrating widths of 2.24 μm and 1.13 μm, respectively, while intermediate widths were observed in SR-20. It is, thus, apparent that the width of the ITZ increases with the increase in SUS304 interlayer thickness.

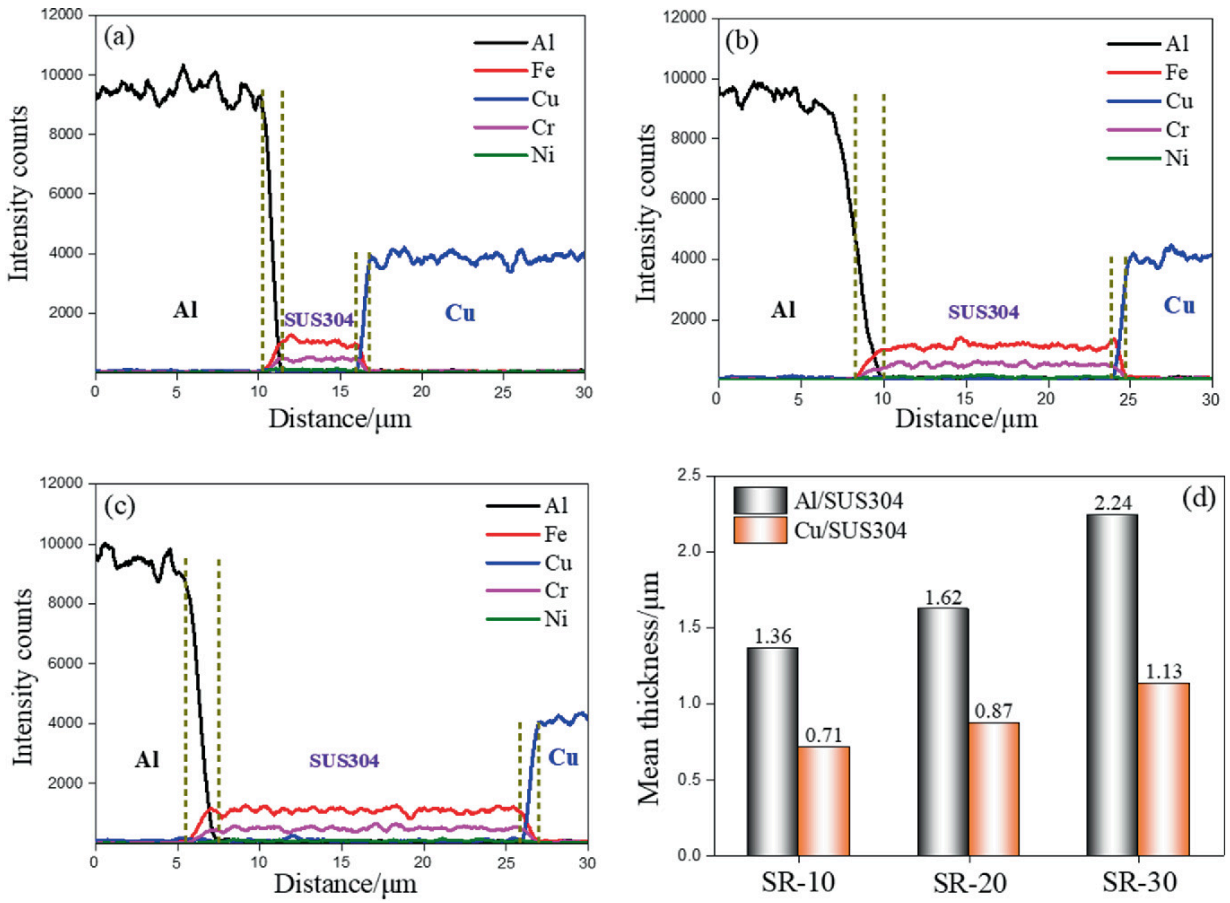


Fig. 3.44 EDS line scan analysis across the interface of Al/SUS304/Cu: **a** SR-10, **b** SR-20, **c** SR-30; **d** Thickness of ITZ at the bonding interfaces of Al/SUS304/Cu

The difference in elemental diffusion across the Al/SUS304/Cu interface is close to the variation in the thickness of the SUS304 interlayer during the roll cladding process, which is shown in Fig. 3.45a. The roll cladding process led to reductions in the thickness of the SUS304 interlayer of 5.25 μm, 6.33 μm, and 11.65 μm, respectively, for SR-10, SR-20, and SR-30. In general, a larger reduction in the thickness of the interlayer induces a larger degree of shear deformation, which can promote elemental diffusion across the bonding interface. This effect will be verified through examination of the peeling surface of the laminates.

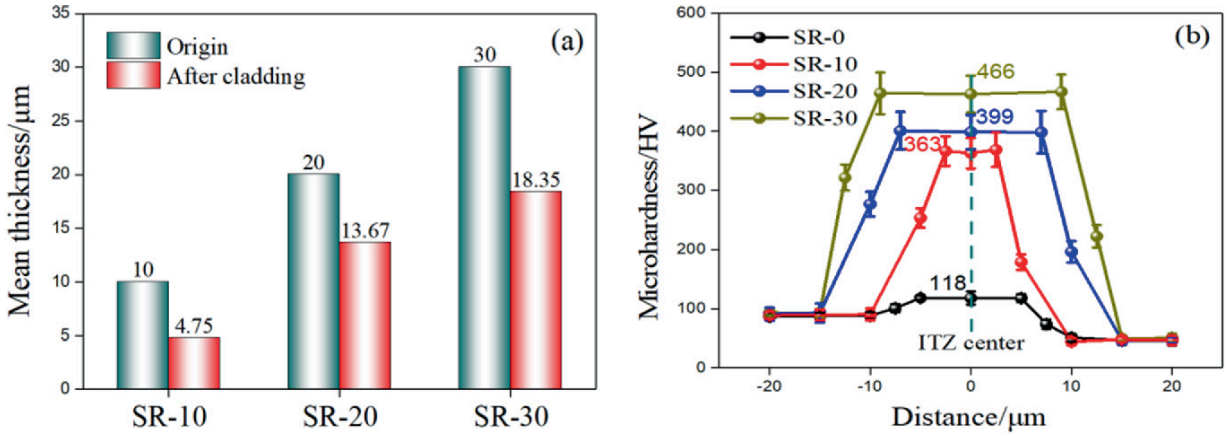


Fig. 3.45 Variations in **a** thickness of SUS304 interlayer and **b** microhardness around the bonding interface of the Cu/Al laminates

Microhardness data obtained near the bonding interface of Cu/Al laminates are shown in Fig. 3.45b. After cladding, the sheet possessing an SUS304 interlayer with a thickness of 30 μm exhibited the largest microhardness of 466 HV, resulting from severe work hardening. Furthermore, the microhardness of all sheets with SUS304 interlayers was much larger than that of the sheet with Cu-Al IMCs, which enhanced the shear deformation at the bonding interface.

Externally input energy can promote the formation of vacancies inside metals, allowing adjacent atoms to enter into these vacancies and facilitate diffusion. The diffusion process across a bimetallic bonding interface has been verified to conform with such a vacancy diffusion mechanism. In this study, the energy input for atomic diffusion had two sources: one was thermal energy from the intermediate annealing process; the other was shear strain energy provided by differences in deformability between the SUS304 interlayer and Cu/Al matrix. Thus, the diffusion area at the bonding interface can be divided into a thermal activation area and a shear strain induction area.

Prior research has indicated that a strong bonding interface for a bimetallic sheet can be obtained by cold rolling alone without heat input. This is because the energy barrier for diffusion can be significantly reduced by shear strain energy. Considering the effect of shear strain energy (E_S) on the diffusion process, the original formula for the diffusion coefficient (D) can be modified as follows:

$$D = \mathrm{D}_0 \exp\left(-\frac{Q - E_S}{\mathrm{R}T}\right) \tag{3.17}$$

where D_0 is the diffusion constant, Q is the diffusive activation energy, R is the molar gas constant, and T is the temperature. At a given intermediate annealing temperature, the larger the shear strain energy, the easier the interfacial diffusion. Thus, the widest ITZ was obtained in SR-30, benefiting from the largest degree of shear deformation induced by the largest reduction in thickness of the SUS304 interlayer.

The morphologies of the sheet surfaces and compounds from the interface of SR-10 after peeling are shown in Fig. 3.46. SEM images exhibit three different peeling morphologies on the Cu surface, comprising a smooth Cu matrix, reticulated Al matrix, and blocks of IMCs (Fig. 3.46a and b). This staggered distribution of three peeling morphologies was formed due to fracture of the SUS304 interlayer and IMC interlayer during the roll cladding process, which is consistent with the results shown in Fig. 3.43.

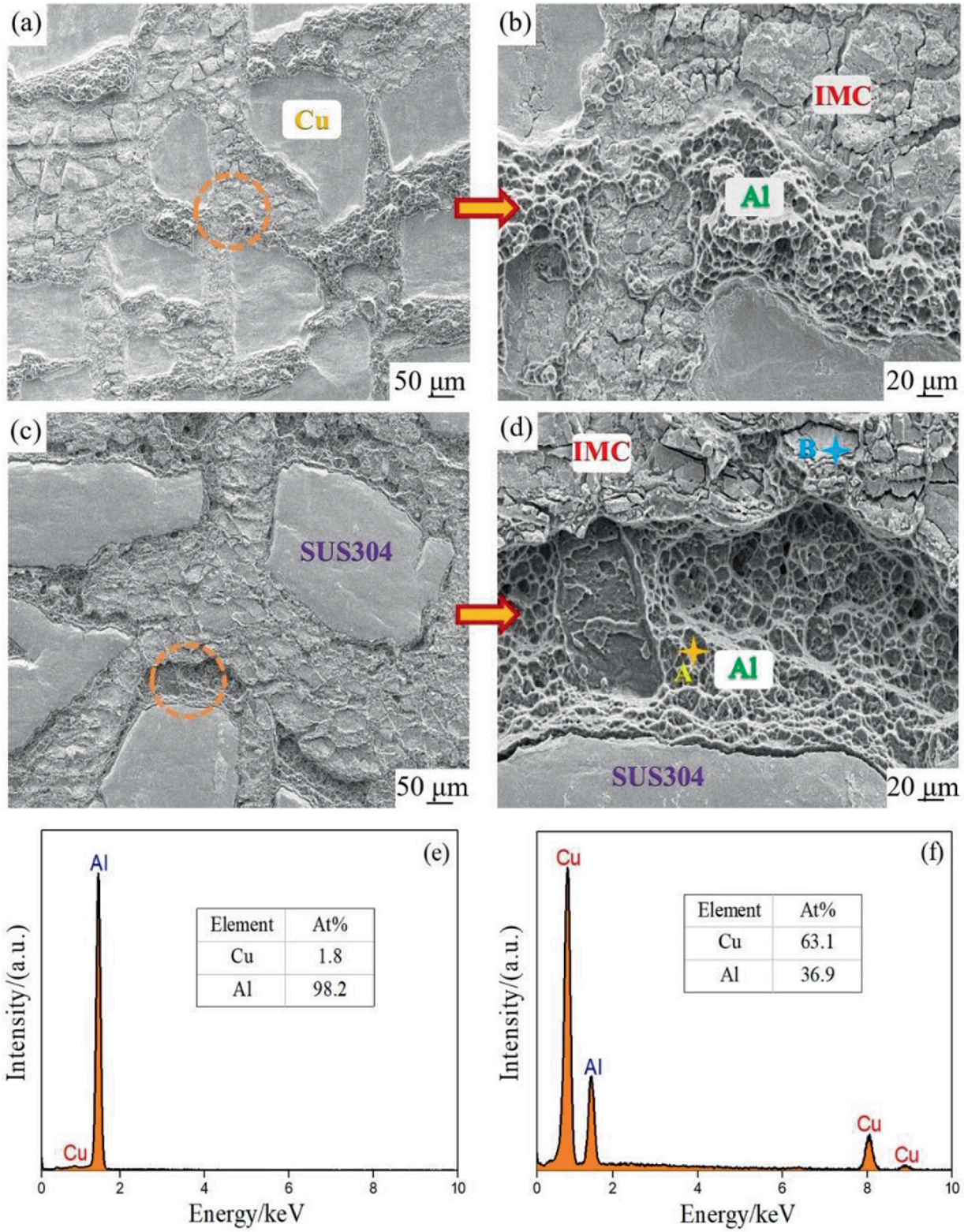


Fig. 3.46 Peeling surfaces of SR-10: **a** Cu surface, **c** Al surface; **b**, **d** Magnified images of orange circled zones in (**a**, **c**); **e**, **f** compositions at point A (**e**) and B (**f**) in (**d**)

The Al surface demonstrated SUS304 fragments embedded into a mixed matrix of Al and IMCs (Fig. 3.46c and d), as indicated by the EDS results (Fig. 3.46e and f). The surface depths of the IMCs, Al, and SUS304 fragments were almost equivalent, implying less deformation of the SUS304 interlayer.

The morphologies of sheet surfaces in SR-20 after peeling are shown in Fig. 3.47. With the increase in SUS304 interlayer thickness, the proportion of reticulated Al matrix and block IMCs observed on the Cu surface decreased apparently (Fig. 3.47a). Interestingly, a large amount of tiny wrinkles were clearly present in the Cu matrix (blue arrows in Fig. 3.47b), induced by the shear deformation of the SUS304 interlayer in contact with the Cu surface. Compared to SR-10, more SUS304 fragments remained embedded in the Al surface (Fig. 3.47c), and the edges of these fragments had been thinned (Fig. 3.47d). These two phenomena indicate that the elongation at fracture of the SUS304 interlayer was larger in SR-20 than in SR-10, which is consistent with the results shown in Fig. 3.45.

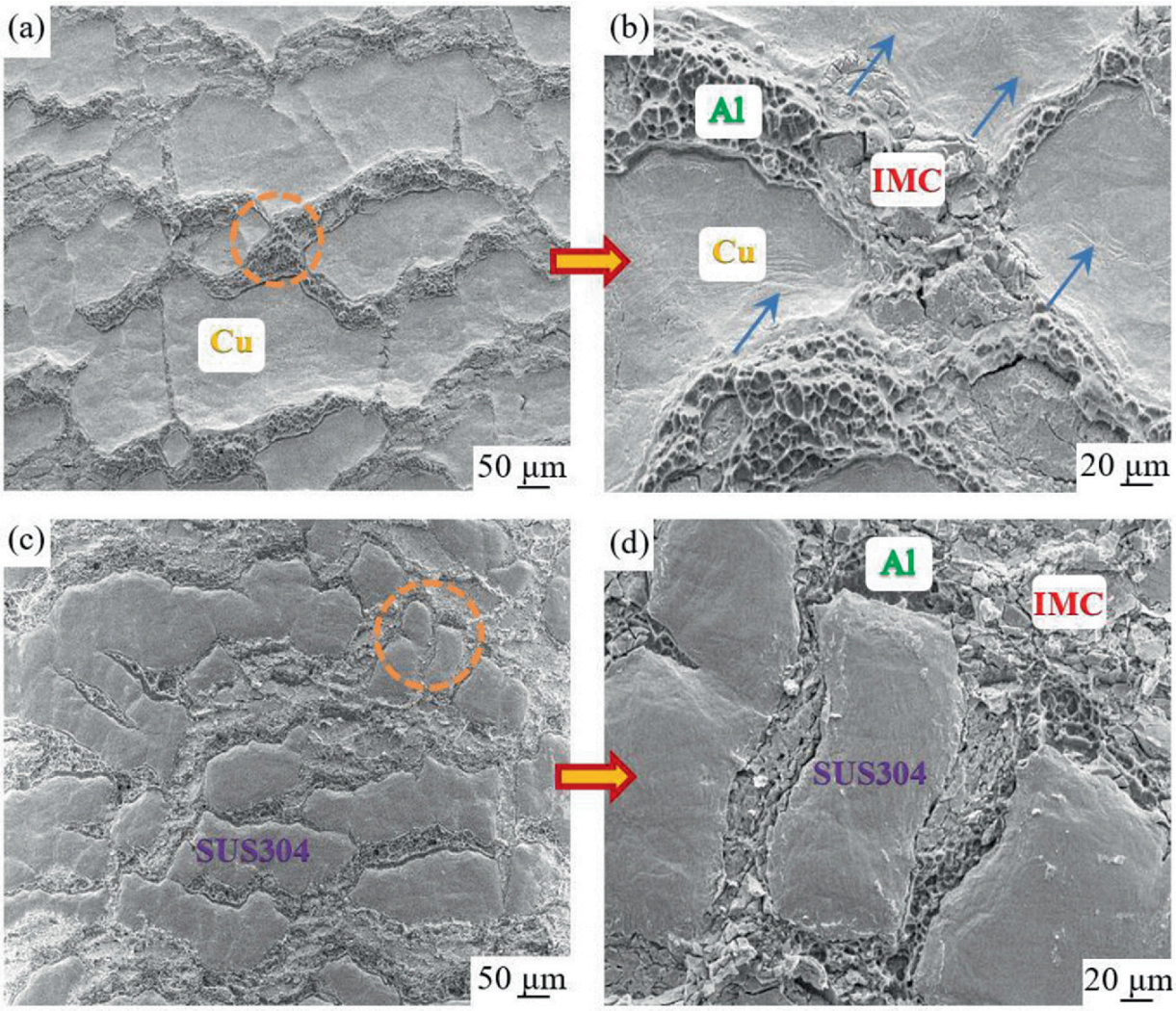


Fig. 3.47 Peeling surfaces of SR-20: **a** Cu surface, **c** Al surface; **b**, **d** Magnified images of orange circled zones in (**a**, **c**)

The morphologies of sheet surfaces in SR-30 after peeling are shown in Fig. 3.48. When the thickness of the SUS304 interlayer was increased to 30 μm, an obvious slope arose on the Cu surface after peeling, indicating strong adhesion between the SUS304 fragments and Cu matrix (Fig. 3.48a). In this specimen, few IMCs were observed, except for those embedded in small amounts of reticulated Al matrix. Moreover, apparent folds were induced in the Cu matrix, attributable to the large shear deformation of the adhered SUS304 interlayer (blue arrows in Fig. 3.48b), providing sufficient evidence for the formation of the widest ITZ in SR-30 (Fig. 3.44). Additionally, the proportion of SUS304 fragments embedded in the peeled Al surface demonstrated further increase with the increase in SUS304 thickness (Fig. 3.48c). The

relatively sufficient elongation of the SUS304 interlayer in SR-30 led to significant inhibition of direct contact between the Cu and Al matrices, resulting in reductions of exposed Al matrix and thus reduced formation of IMCs (Fig. 3.48d).

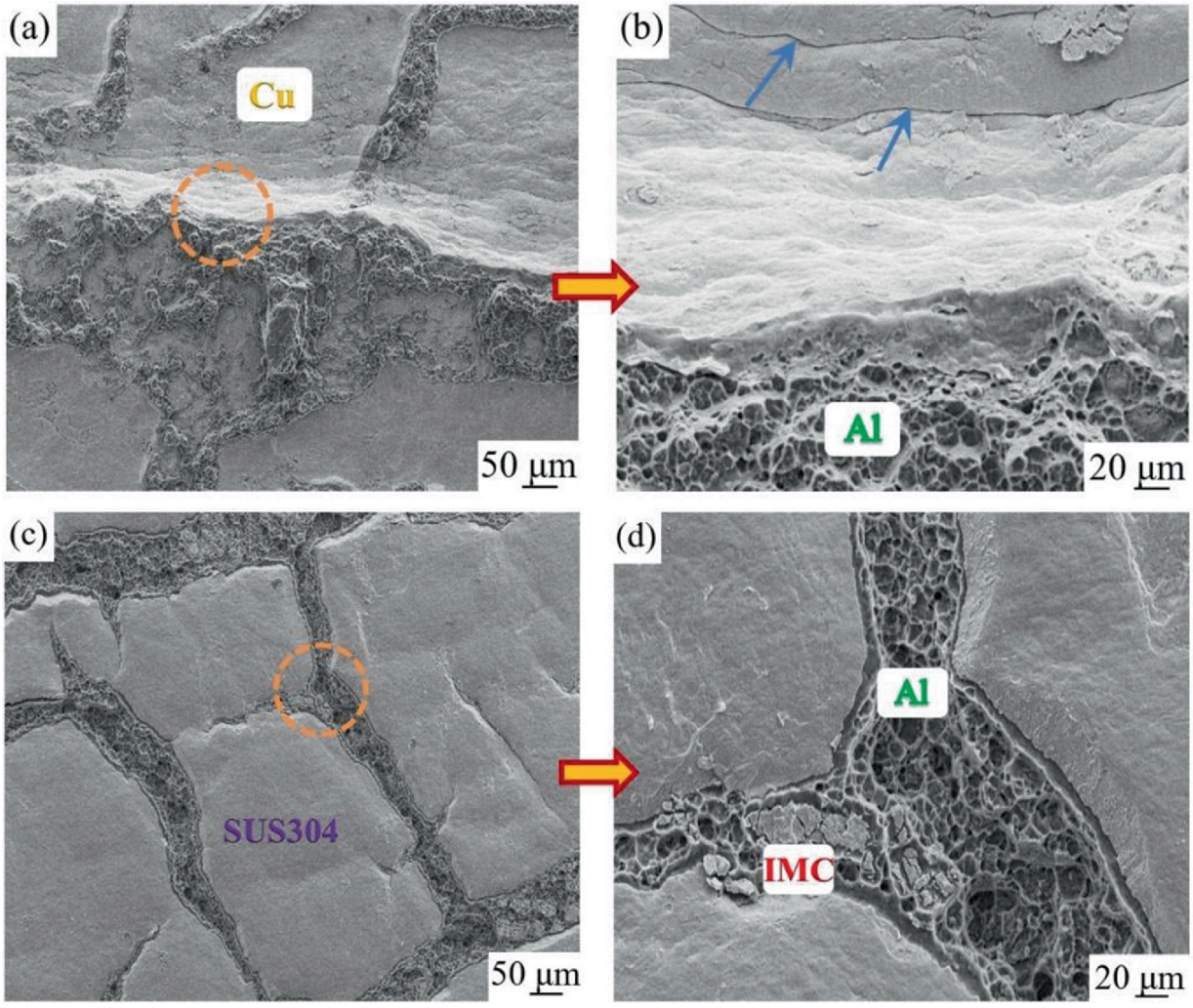


Fig. 3.48 Peeling surfaces of SR-30: **a** Cu surface, **c** Al surface; **b**, **d** Magnified images of orange circled zones in (**a**, **c**)

Based on observations of the peeling surfaces of the Cu/Al laminates with SUS304 interlayers (Figs. 3.46, 3.47 and 3.48), the fragmentation of SUS304, contact between Cu and Al matrices, and formation of IMCs, as well as the extent of shear deformation, could be controlled by changing the thickness of the SUS304 interlayer.

To further examine the influence of SUS304 thickness on the content of chemical compounds, XRD spectra of the peeling surfaces were obtained, as shown in Fig. 3.49. XRD identified the primary IMCs

observed on both Cu and Al peeling surfaces as Cu_9Al_4 and $CuAl_2$, with a significantly higher content of Cu_9Al_4. Chemical compounds present on the Cu surface included primarily Cu matrix, Al matrix, Cu_9Al_4, and $CuAl_2$. With increasing SUS304 interlayer thickness, the proportion of observable Cu matrix increased, accompanied by decreases in the presence of Al matrix and Cu-Al IMCs (Fig. 3.49a), which is consistent with SEM observations of the peeling surfaces. On the Al surface, a similar trend was demonstrated. Observed chemical compounds included SUS304 fragments, Al matrix, Cu_9Al_4, and $CuAl_2$. Higher contents of SUS304 fragments were present in samples with thicker SUS304 interlayer (Fig. 3.49b).

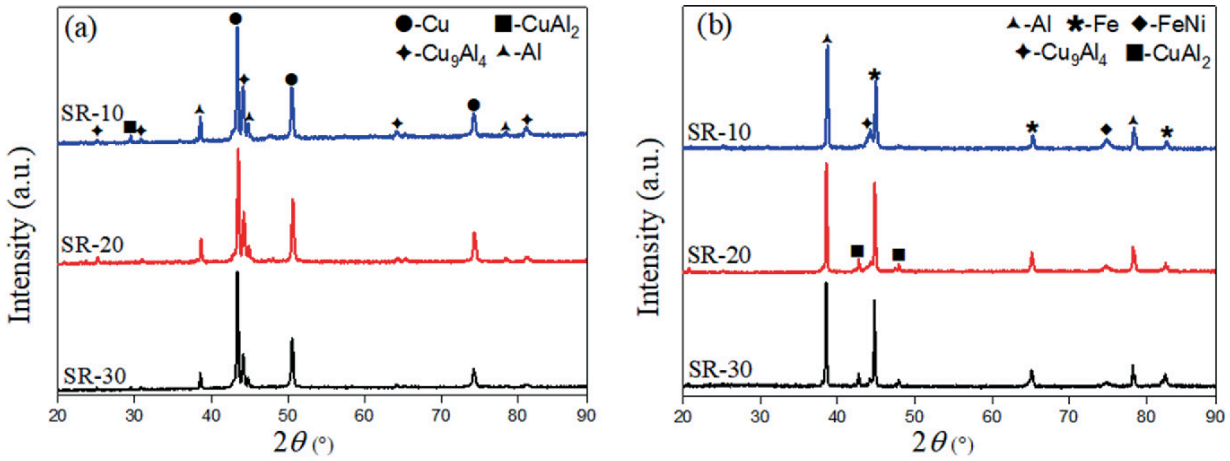


Fig. 3.49 XRD spectra of peeling surfaces: **a** Cu surface, **b** Al surface

Optimization of crack propagation paths significantly influences the bonding strength of laminates. The propagation paths of interfacial cracks through Cu/Al laminates with and without an interlayer are illustrated in Fig. 3.50. Cracks at the bonding interface of Cu/Al laminates without an interlayer are typically initiated in the soft Al matrix and then propagate along the layer of Cu-Al IMCs. Upon introducing an SUS304 interlayer, large proportions of Cu-Al IMCs were replaced by SUS304 fragments. The observed morphologies and XRD spectra of the peeling surfaces of Cu/Al laminates comprising an SUS304 interlayer (Figs. 3.46, 3.47, 3.48 and 3.49) indicate that interfacial cracks extended along the Al matrix, Cu/Al IMCs layer, and Cu/SUS304 interface.

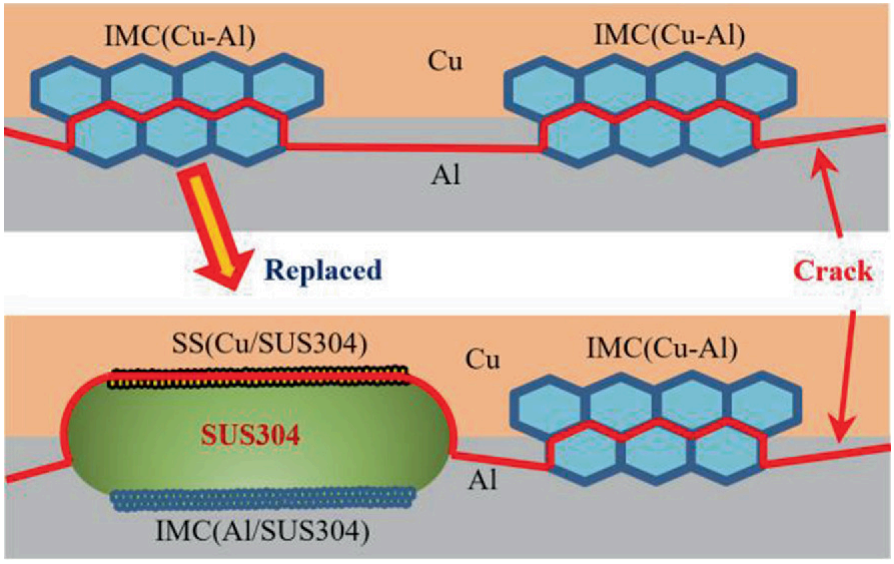


Fig. 3.50 Schematic diagram of crack propagation at the bonding interface

Figure 3.51 shows the peeling curves of Cu/Al laminates comprising SUS304 interlayers of different thicknesses. Introduction of different SUS304 foils improved the peeling strength of laminates by varying degrees: the thicker the SUS304 interlayer, the larger the peeling strength. Compared with SR-0, the peeling strength of SR-30 was improved by 73.6%, from 17.8 N/mm to 30.9 N/mm. This is likely related to the mechanism by which the SUS304 interlayer optimizes the propagation path of interfacial cracks (Fig. 3.50).

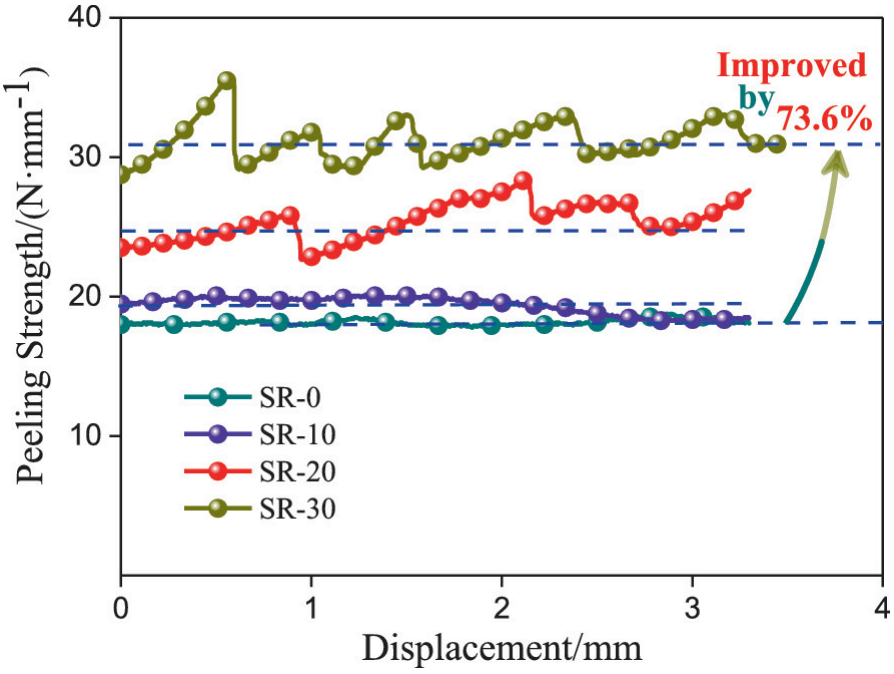


Fig. 3.51 Peeling curves of Cu/Al laminates

Based on the experimental results, the strengthening mechanism of SUS304 interlayer in the bonding strength of Cu/Al laminates can be concluded as three aspects: inhibiting the formation of Cu-Al IMCs with low bonding strength, enhancing the interfacial shear deformation and improving the interfacial mechanical joggle, as shown in Fig. 3.52.

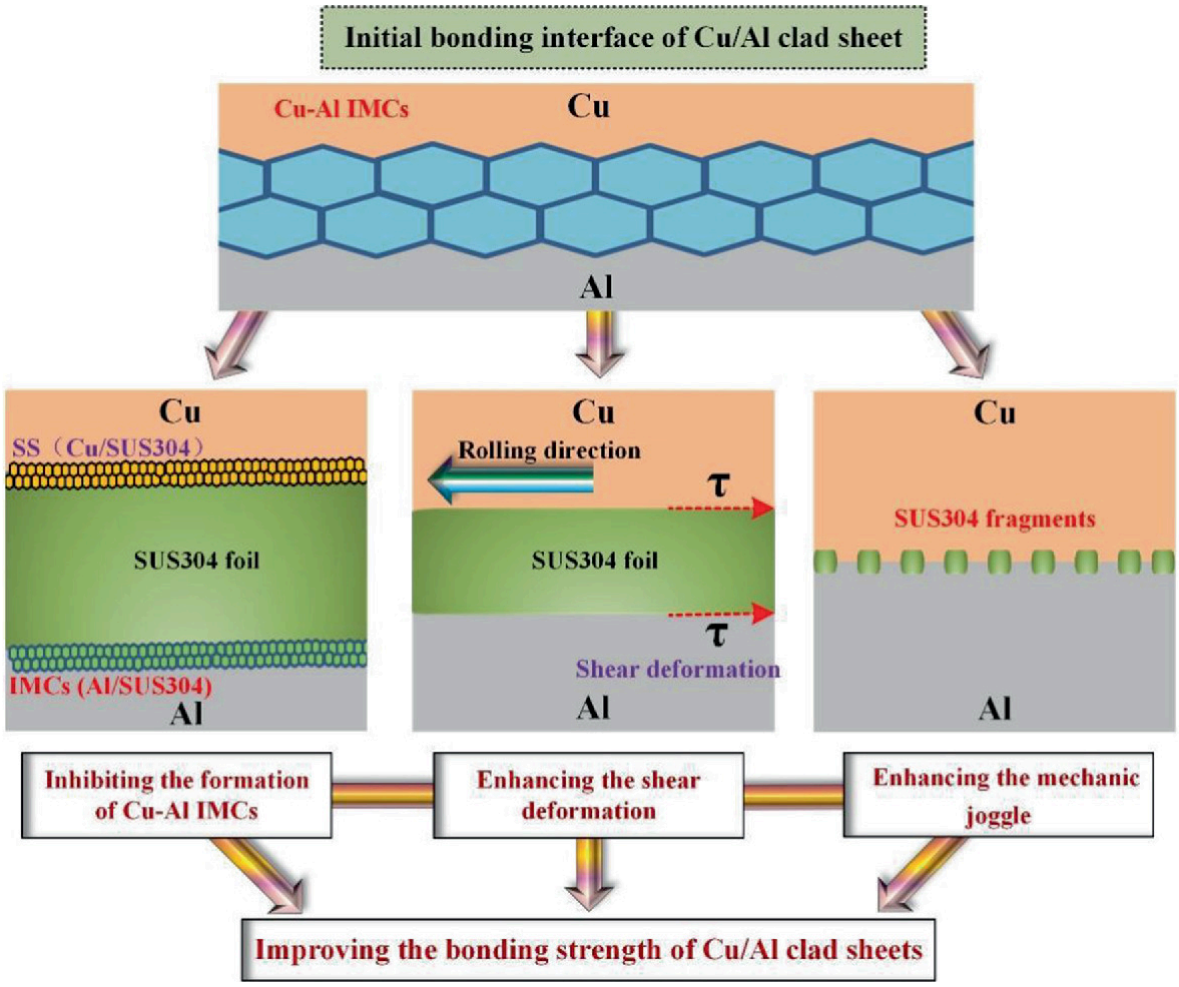


Fig. 3.52 Strengthening mechanism of SUS304 interlayer on bonding strength of Cu/Al laminates

Firstly, the types of IMCs are optimized. Czelej et al. [18] indicated that IMCs in the metallic laminates with high interfacial bonding interface usually exhibited large cohesive energy. According to the EDS line results across the interface of Al/SUS304/Cu, Cu/Fe/Al chemical compounds were examined as relevant to this study. Figure 3.53 depicts the cohesive energy of such chemical compounds at the bonding

interface of laminates, obtained from literature. These findings have shown that the absolute value of cohesive energy is much higher for chemical compounds that form between Cu/Fe and Al/Fe than that for Cu-Al IMCs [19–21]. This indicates that more energy is required to destroy (e.g., through crack propagation) the Cu/SUS304/Al interface than the Cu/Al interface.

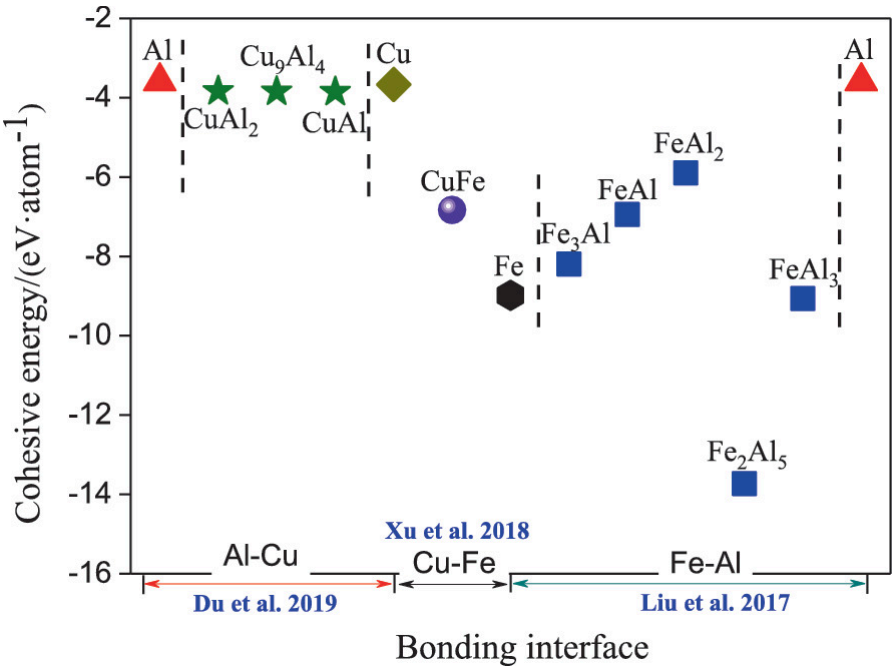


Fig. 3.53 Cohesive energy of chemical compounds at the bonding interface

Secondly, the introduction of shear deformation at the bonding interface by adding the SUS304 interlayer. Apart from the optimization of crack propagation path, the control of shear deformation between the SUS304 interlayer and Cu/Al matrix also contributes significantly to improvements in the peeling strength of laminates. Based on examinations of elemental diffusion across the bonding interface and of the peeling surfaces (Figs. 3.44, 3.46, 3.47 and 3.48), a thicker SUS304 interlayer can facilitate both larger shear deformation at the bonded surface and higher bonding strength.

Thirdly, the mechanical joggle of Cu/Al matrix is enhanced by the SUS304 fragments. Due to the weaker deformability than Cu/Al matrix, SUS304 foil is broken in the roll cladding and then embedded into the Cu/Al matrix. The microhardness of SUS304 interlayer is much higher than Cu-Al IMCs (Fig. 3.45b), resulting in the improvement of mechanical joggle of Cu/Al matrix.

Moreover, Fig. 3.51 shows that fluctuations in the peeling curve were more pronounced for laminates with greater interlayer thickness than for those with a thinner interlayer or no interlayer. The curve for SR-30, for example, indicates that the peeling strength initially increased under deformation, then decreased suddenly, and then increased again, continuing to oscillate about a mean peeling strength that was higher than that of the other specimens. Thus, the increased tolerance for deformation in thicker SUS304 interlayers resulted in higher bonding strength between thicker SUS304 fragments and the Cu/Al matrix, while thinner SUS304 interlayers and Cu-Al IMCs demonstrated much weaker adhesion.

References

1. Yu HL, Lu C, Tieu K, Li HJ, Godbole A, Kong C (2016) Annealing effect on microstructure and mechanical properties of Al/Ti/Al laminate sheets. Mater Sci Eng A 660:195–204 [Crossref]
2. Luo JG, Acoff VL (2004) Using cold roll bonding and annealing to process Ti/Al multi–layered composites from elemental foils. Mater Sci Eng A 379:164–172 [Crossref]
3. Yu HL, Tieu K, Lu C, Kong C (2014) Abnormally high residual dislocation density in pure aluminum after Al/Ti/Al laminate annealing for seven days. Philos Mag Lett 94:732–740 [Crossref]
4. Miyajima Y, Mitsuhara M, Hata S, Nakashima H, Tsuji N (2010) Document Quantification of internal dislocation density using scanning transmission electron microscopy in ultrafine grained pure aluminum fabricated by severe plastic deformation. Mater Sci Eng A 528:776–779 [Crossref]
5. Seitz F (1952) On the generation of vacancies by moving dislocations. Adv Phys 1:43–90 [Crossref]
6. Pines BY, Syrenko AF (1968) Change of dislocation density in aluminum and lithium fluoride after annealing near the melting point under hydrostatic pressure. J Mater Sci 3:80–88 [Crossref]
7. Yu HL, Tieu K, Lu C, Liu X, Godbole A, Li HJ, Kong C, Qin QH (2014) A deformation mechanism of hard metal surrounded by soft metal during roll forming. Sci Rep 4:5017 [Crossref][PubMed][PubMedCentral]
8. Mozaffari A, Danesh MH, Janghorban K (2010) Evaluation of mechanical properties and structure of multilayered Al/Ni composites produced by accumulative roll bonding (ARB)

process. J Alloy Compd 489:103–109
[Crossref]
9. Junqua N, Grilhé J (1995) Interface instabilities of multilayers and flat precipitates. Philos Mag A 71:1125–1134
[Crossref]
10. Junqua N, Grilhé J (1994) Instabilities of planar interfaces between two stressed materials. Philos Mag Lett 69:61–70
[Crossref]
11. Yu HL, Lu C, Tieu K, Li HJ, Godbole A, Kong C (2018) Nanoporous Al sandwich foils by using size effect of Al layer thickness during Cu/Al/Cu laminate rolling. Philos Mag 98:1537–1549
[Crossref]
12. Ervasti E, Ståhlberg U (2005) Void initiation close to a macro–inclusion during single pass reductions in the hot rolling of steel slabs: a numerical study. J Mater Process Tech 170:142–150
[Crossref]
13. Kadkhodapour J, Butz A, Ziaei RS (2011) Mechanisms of void formation during tensile testing in a commercial, dual–phase steel. Acta Mater 59:2575–2588
[Crossref]
14. Langdon TG (1979) A microscopic examination of void formation in superplastic materials. J Microscopy 116:47–54
[Crossref]
15. Srivatsan TS, Sriram S, Veeraraghavan D, Vasudevan VK (1997) Microstructure, tensile deformation and fracture behavior of aluminum alloy 7055. J Mater Sci 32:2883–2894
[Crossref]
16. Gao HT, Liu XH, Qi JL, Ai ZR, Liu LZ (2018) Microstructure and mechanical properties of Cu/Al/Cu clad strip processed by the powder–in–tube method. J Mater Process Tech 251:1–11
[Crossref]
17. Gao HT, Wang L, Liu SL, Li J, Kong C, Yu HL (2021) Effects of a stainless steel interlayer on the interfacial microstructure and bonding strength of Cu/Al clad sheets prepared via the powder–in–tube method. J Mater Res Tech 15:3514–3524
[Crossref]
18. Czelej K, Kurzydłowski KJ (2020) Ab initio prediction of strong interfacial bonding in the Fe|Al bimetallic composite system. Scr Mater 177:162–165
[Crossref]
19. Du JL, Zhang A, Zhang L, Xiong SM, Liu F (2019) Quantitative and qualitative correlations by atomistic determination for the precipitated phases in Al–Li–Cu system. Intermetallics 112:106551
[Crossref]

20. Xu PY, Wang YF, Gao HY, Wang J, Sun BD (2018) First–principles study of effects of alloying elements on Cu/γ–Fe interfacial properties. Chin J Nonfer Met 28:38–45
21. Liu YH, Chong XY, Jiang YH, Zhou R, Feng J (2017) Mechanical properties and electronic structures of Fe–Al intermetallic. Phys B 506:1–11
[Crossref]

© The Author(s), under exclusive license to Springer Nature Singapore Pte Ltd. 2024
H. Yu et al., *High-Performance Metallic Composites Fabricated by Advanced Rolling Techniques*
https://doi.org/10.1007/978-981-97-4331-5_4

4. Fabricated Metal Laminates via Cryorolling

Hailiang Yu[1] ✉, Haitao Gao[1] ✉ and Zhou Li[1]
(1) Central South University, Changsha, China

✉ **Hailiang Yu (Corresponding author)**
Email: yuhailiang@csu.edu.cn

✉ **Haitao Gao**
Email: gaohaitao@csu.edu.cn

Cryogenic roll bonding technique is an emerging technology to fabricate metal laminates, which can significantly improve the overall performance of composite strip, especially the interfacial bonding quality [1]. The microstructure, texture and mechanical properties of the AA1060 sheets processed by ARB at cryogenic temperature were investigated by Wang et al. [2]. Du et al. [3] indicated that the subsequent cryorolling process could further refine the grains in the ARB-processed AA1060 sheets. Takagawa et al. [4] successfully improved the tensile properties of the Cu-2.0 mass%Ni-0.5mass%Si-0.1mass%Zr alloy without reducing its electrical conductivity by combining both ARB and cryorolling with aging treatment. Yu et al. [5] found that the edge cracks appeared in the cold roll bonding of Al/Ti/Al laminates could be avoid by the cryogenic roll bonding process, as shown in Fig. 4.1. Furthermore, the ultimate tensile stress of laminates by cryogenic roll bonding increased up to 36.7% compared to that by cold roll bonding. On this foundation, the bonding strength of Al/Ti/Al laminated composites fabricated through the cryorolling, cold rolling

and hot rolling were compared by Liu et al. [6]. They thought that the bonding strength of Al/Ti/Al laminated composites depended on the mechanical locking strength, metallurgical bonding strength, and tensile strength of the Al layer.

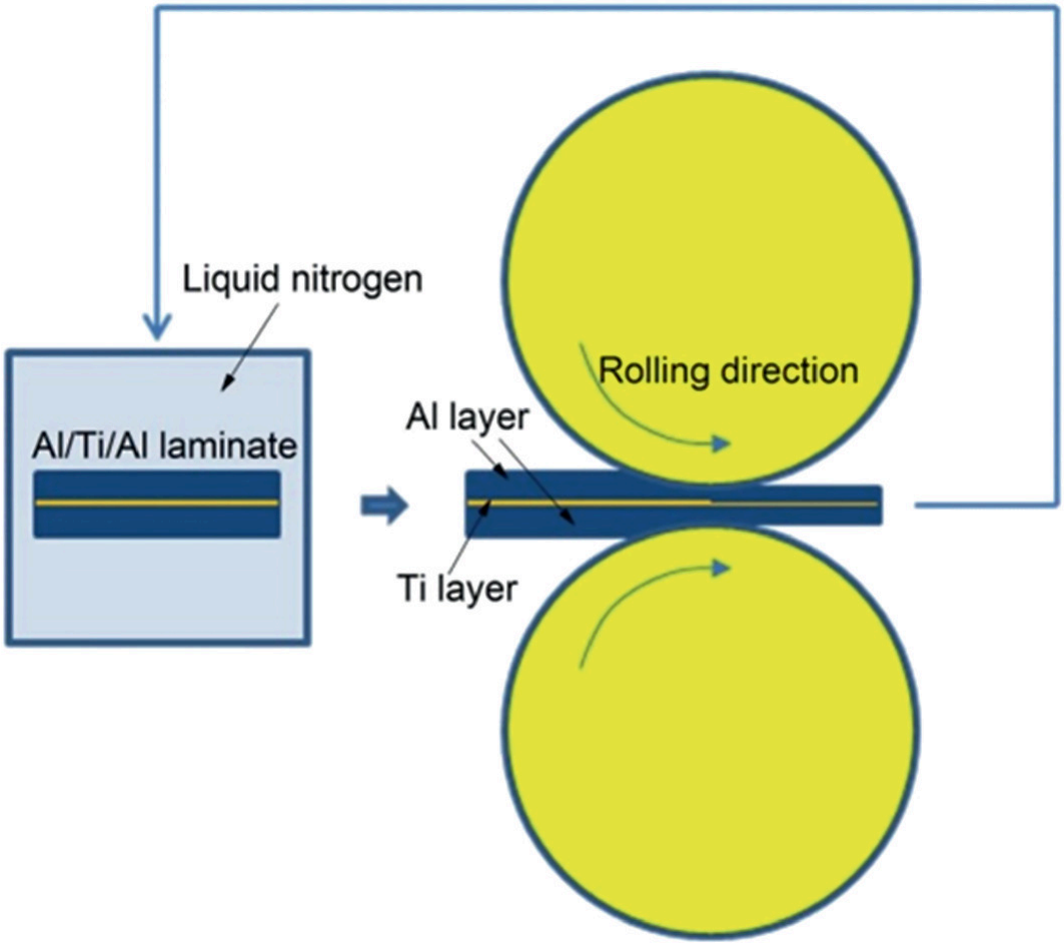


Fig. 4.1 Schematic diagram of laminate cryorolling process

The microstructure evolution and mechanical performance of Cu/Al/Cu laminates fabricated by hot rolling, cold rolling and cryorolling were compared by Wang et al. [7]. Results revealed that the highest ultimate tensile strength and the best ductility of the composites were achieved by cryorolling at −100 °C. Compared with the room temperature rolling process, the increments value of yield strength ($\triangle\sigma_{\mathrm{Y}}$) for AA3003 sheets in the cryogenic rolling process were characterized as Eq. (4.1) [8]:

$$\Delta\sigma_{\mathrm{Y}} = \Delta\sigma_{\mathrm{P}} + \Delta\sigma_{\mathrm{dis}} + \Delta\sigma_{\mathrm{gb}} \tag{4.1}$$

where $\Delta\sigma_{\mathrm{P}}$, $\Delta\sigma_{\mathrm{dis}}$ and $\Delta\sigma_{\mathrm{gb}}$ were the strengthening increments in the yield strength between the cryogenic rolling and room temperature rolling conditions resulted from the precipitation strengthening, dislocation strengthening, and grain refinement strengthening, respectively.

4.1 AA1050/AA5052 Laminates via Cryorolling

Two rolling schemes were used to prepare AA1050/AA5052 laminates. The present investigation aims to fabricate laminates with excellent properties by combining ARB and cryorolling, and to systematically analyze the relationship between the mechanical properties and microstructure [9].

4.1.1 Mechanical Properties of AA1050/AA5052 Laminates

Figure 4.2b indicates the engineering stress–strain curves of the laminates subjected to three ARB passes. In the first three ARB passes, as the applied strain increases, the UTS of the laminates increases continuously, which is the result of grain refinement and increased dislocation density. Figure 4.2c and d show the variation of UTS and elongation of the laminates vs the equivalent strain. The UTS reaches its maximum in the third pass and then decreases significantly during ARB. It can be considered that the fracture of the hard layer and poor interface bonding are the reasons for the decrease of UTS (Figs. 4.3d and 4.4b). However, UTS can be improved by cryorolling. Cryorolling obtains the highest strength for three reasons: suppresses dynamic recovery and accumulates higher dislocation density; delays the onset of necking and fracture; refines the grain size significantly. The variation of elongation is almost the same (Fig. 4.2d).

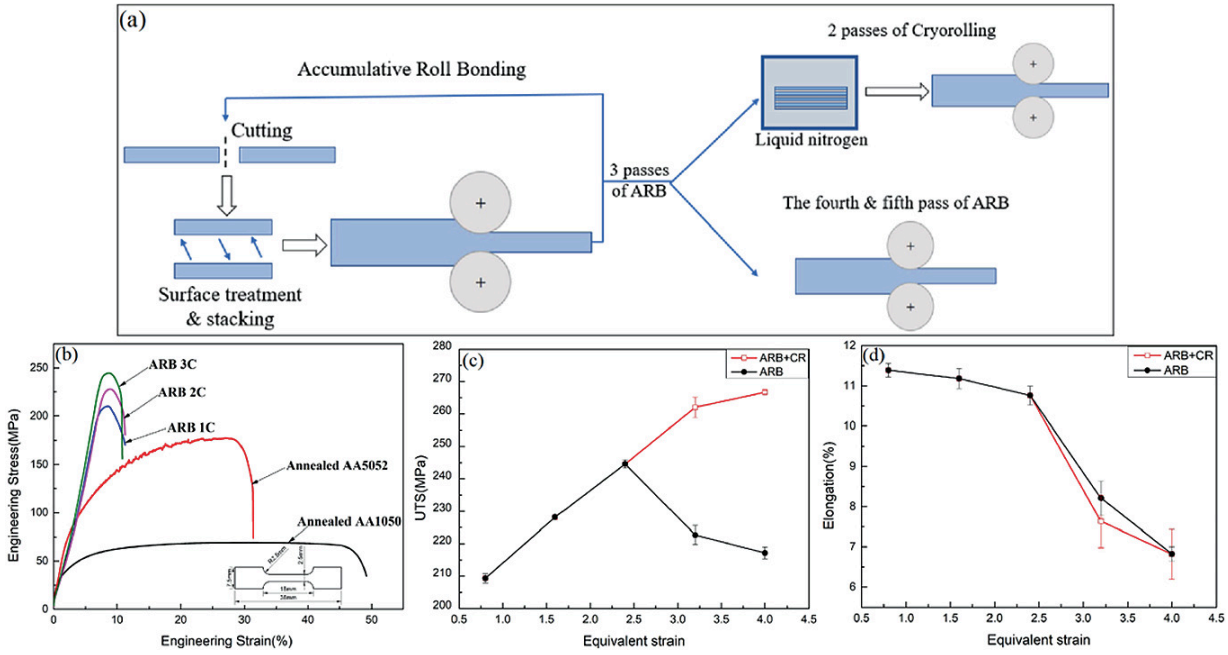


Fig. 4.2 **a** Illustration of fabrication of AA1050/AA5052 laminates. **b** Engineering stress–strain curves, variation in **c** UTS and **d** elongation versus equivalent strain after rolling

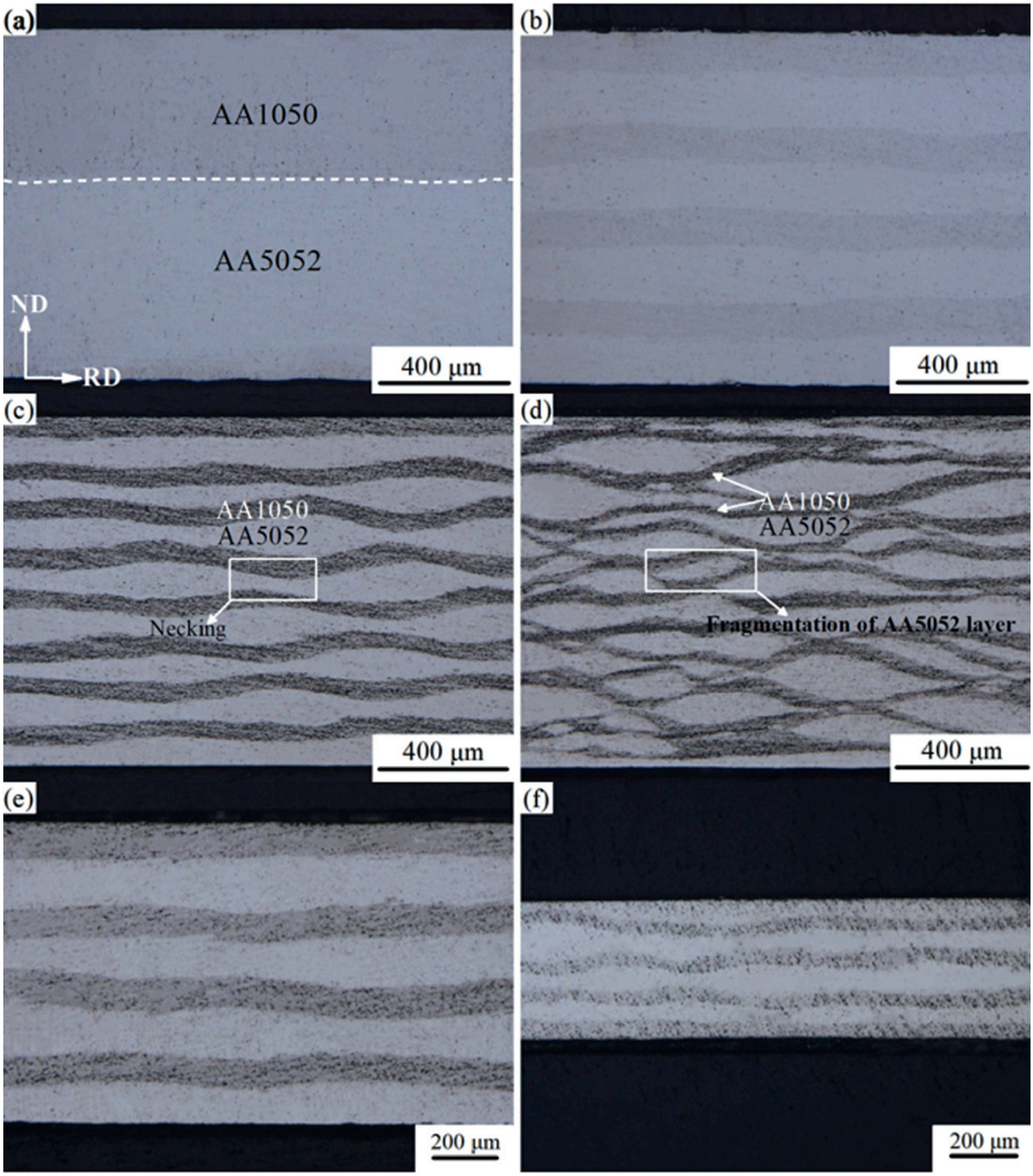


Fig. 4.3 Structure of AA1050/AA5052 laminates subjected to **a** the first, **b** third, **c** fourth, and **d** fifth ARB pass, and **e** the first and **f** second cryorolling pass

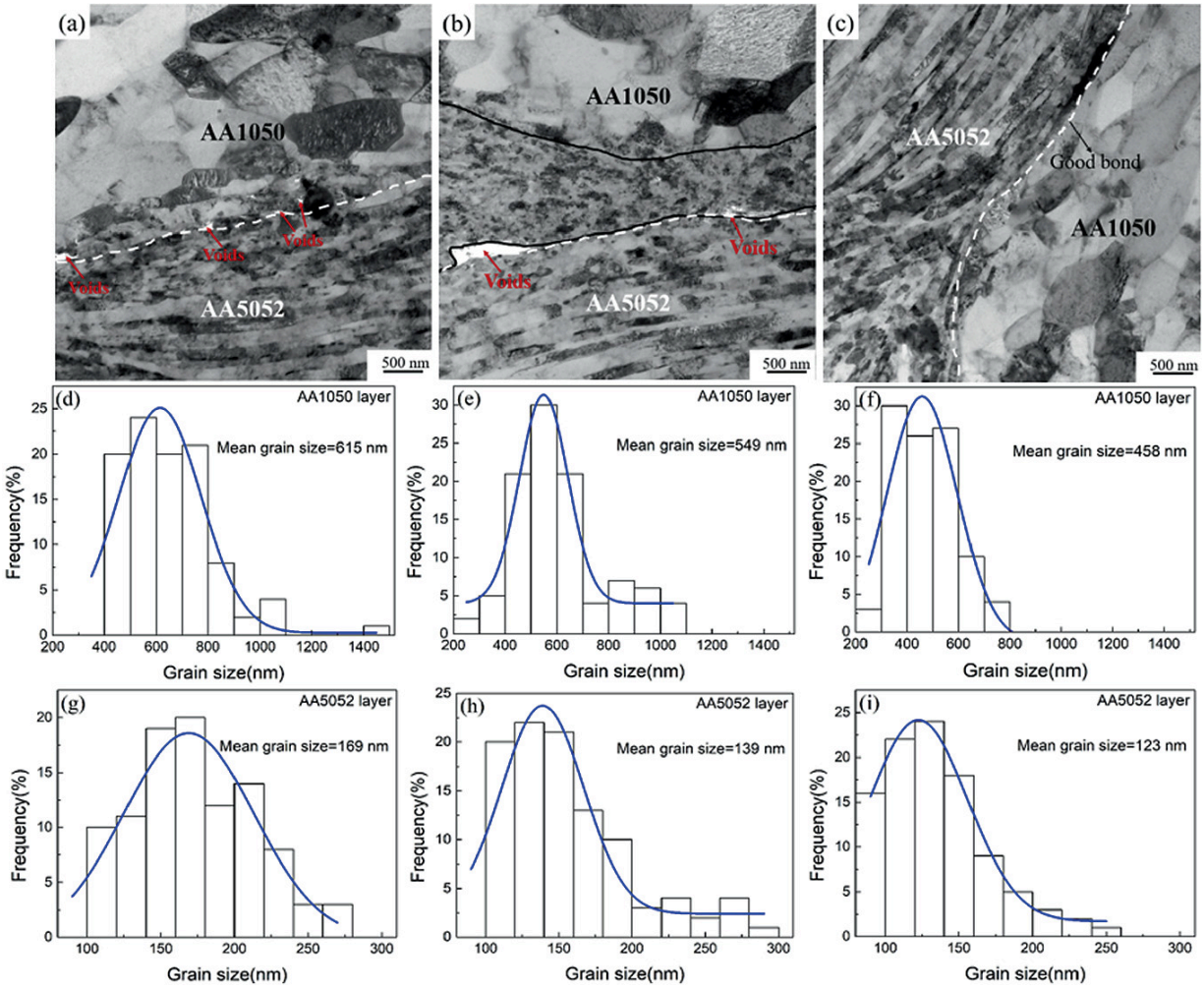


Fig. 4.4 TEM images of the AA1050/AA5052 laminates: **a** third and **b** fifth ARB pass, and **c** second cryorolling pass. Grain size distribution of AA1050 layer after **d** third and **e** fifth ARB pass, **f** second cryorolling pass, and AA5052 layer after **g** third and **h** fifth ARB pass, and **i** second cryorolling pass

4.1.2 Microstructure Evolution of AA1050/AA5052 Laminates

Figure 4.3 shows the optical micrographs of AA1050/AA5052 laminates. Figure 4.3a–d represent the layer structure of ARB processing. The two layers are bonded together. Up to the third pass, the two layers still maintain uniform co-deformation. And the hard layer (AA5052 layer) remains flat and continuous, which indicates that almost no plastic instability happens. However, the hard layer occurs necking after the fourth pass. In addition, as the applied strain increases, AA5052 layer appears fracture. It is generally believed that the plastic instability is caused by the different flow properties of the

two constituent layers. For the cryorolled samples after three ARB passes, no obvious necking occurs in the hard layer (Fig. 4.3e and f), indicating that cryorolling can delay the onset of necking and fracture and thus improve the mechanical properties of the laminates.

Figure 4.4a–c show TEM images of the laminates with different processes. After the third pass, a few small voids are observed at the interface, but after the fifth pass, due to the hard layer fractures (Fig. 4.3d), some fragmentations will be squeezed into the interface (in the black line area in Fig. 4.4b), which significantly reduces the interface bonding quality, and we can notice that the interface appears big voids. This causes a decrease in strength after the fifth ARB pass. In contrast, the sample interface of cryorolling is very well bonded (Fig. 4.4c), indicating that cryorolling can significantly improve the interface bonding quality, thus improving the mechanical properties of the laminates.

In Fig. 4.4d–i, the grain sizes of AA1050 and AA5052 layers are the smallest in the second cryorolling pass. Therefore, cryorolling can obtain finer grain size. According to Hall–Petch formula, the yield strength of materials increases with reduced grain size. Therefore, the strength of the laminates by three ARB passes plus two subsequent cryorolling passes is much higher than that by five ARB passes (Fig. 4.2c).

4.1.3 Fracture Morphology of AA1050/AA5052 Laminates After Tensile Testing

Figure 4.5 exhibits the fracture morphologies after tensile test. The bonding of the two constituent layers is poor in the early ARB (Fig. 4.5a). In these weak bonding positions, the initiation and propagation of microcracks will occur, which will lead to the fracture of the sample. As the imposed strain increases, the interface quality is improved, which can be confirmed by the improvement of UTS. Figure 4.5b and d show the tensile fracture at enlarged magnification, many dimples can be observed, indicating that the fracture mode of the laminates is ductile fracture. With increasing in rolling passes, the depth, size and number of dimples are decreasing (Fig. 4.5b and d), which reflects the decreasing of elongation (Fig. 4.5d). The tensile fracture of the samples via cryorolling are shown in Fig. 4.5e and f. The

interface bonding quality is significantly improved under cryorolling, which is consistent with TEM results.

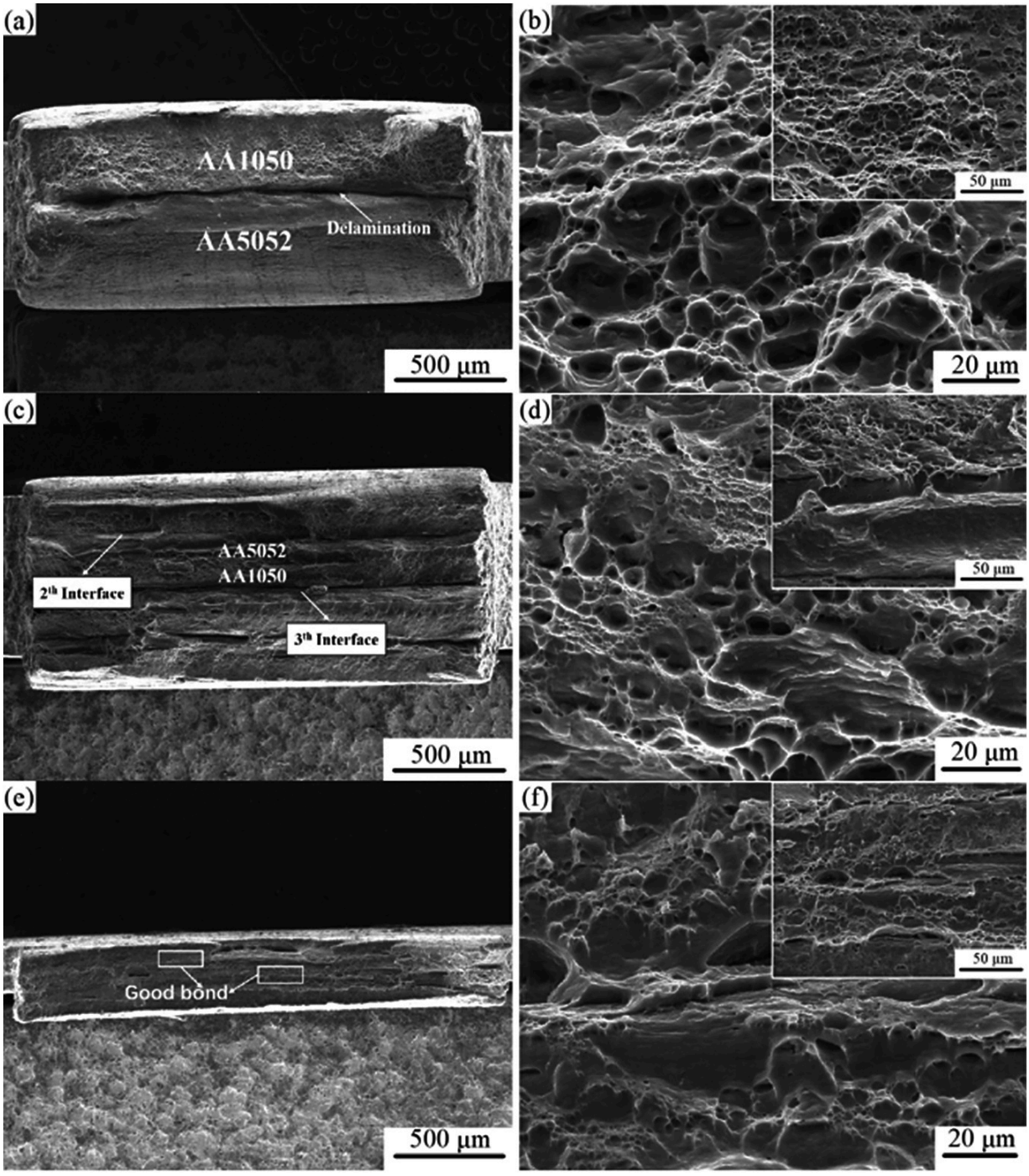


Fig. 4.5 SEM images of the tensile fracture subjected to **a**, **b** first pass and **c**, **d** third ARB pass, and **e**, **f** second cryorolling pass

4.2 AA1050/AA6061 Laminates via Cryorolling

Furthermore, AA1050/AA6061 laminates were designed and processed by combining ARB and cryorolling, followed by aging [10]. The effects of rolling and subsequent aging treatment on the mechanical properties and microstructure of the laminates were studied. The reasons for the improvement in UTS by cryorolling and aging treatment were also analyzed. The present study provides a clear insight for the fabrication of laminates with excellent comprehensive properties.

AA1050/AA6061 laminates were fabricated by ARB and subsequent cryorolling. The two metallic sheets were then stacked in the sequence AA1050 to AA6061. Subsequently, rolling was carried out at room temperature with a reduction of 50% in thickness. The rolled composites were cut in half, and then the surface cleaning, stacking, rolling process were repeated three times to obtain a three-cycle ARB multilayer laminates with a total of 8 layers. The three-cycle ARB laminates were then used for subsequent two kinds of rolling processes: (1) The ARB process continued for two cycles, eventually reaching five cycles, resulting in a total of 32 layers of the laminates; (2) Two-pass cryorolling was performed to obtain the laminates with a total of 8 layers, with a 50% reduction in thickness per pass to maintain the same equivalent strain as the laminates fabricated by four- and five-cycle ARB processes. Before each pass of cryorolling, the samples were immersed in liquid nitrogen (−196 ℃) for 30 min. These rolled samples were defined as A1–A5 (one to five-cycle ARB), C1 (three-cycle ARB + one-pass cryorolling), C2 (three-cycle ARB + two-pass cryorolling). The A5 and C2 samples were used in subsequent aging treatment. The samples were aged at 90, 100, 110 and 120℃ at various times (hardness tests for the samples aged for 6–78 h, and tensile tests for the samples aged for 24–60 h/78 h).

4.2.1 Mechanical Properties of AA1050/AA5061 Laminates

The engineering stress–strain curves of AA1050/AA6061 laminates prepared by ARB with different cycles are presented in Fig. 4.6a. The

tensile properties of annealed AA1050 sheet and solution treated AA6061 sheet are used as the initial state for comparison. Figure 4.6a shows that the mechanical properties exhibit the typical characteristics of laminates prepared by ARB, including an increase in UTS and a decrease in elongation with increasing ARB cycles. After three cycles, the UTS increases to 236 MPa, approximately 1.3 times the initial state samples. Figure 4.6b and c illustrate the variation of UTS and elongation of AA1050/AA6061 laminates fabricated only by ARB and ARB+ cryorolling, respectively. It is clear that in the subsequent ARB, the UTS increases slightly, only reaching 252 MPa after the fifth cycle. In comparison, the UTS exhibits significant improvement after cryorolling and achieves a maximum value of 310 MPa with two-pass cryorolling. These samples are all in the rolled state without heat treatment. Researchers proposed that several major factors affect the UTS of laminates processed through rolling, including strain hardening, grain refinement, interfacial bonding quality and the distribution of the constituent layers. At the initial stages of sample preparation, the strengthening is mainly due to strain hardening, increased dislocation density, and accumulation of internal stress. In the later stages, grain refinement has a significant contribution to the strength improvement.

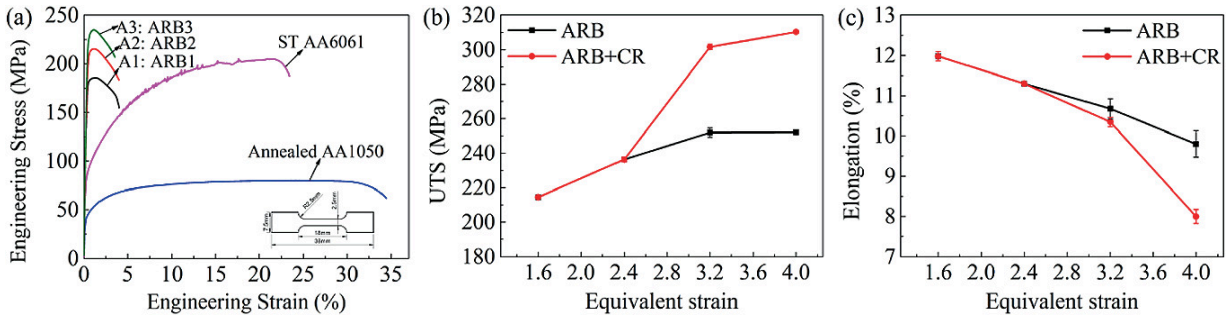


Fig. 4.6 Tensile properties of AA1050/AA6061 laminates. **a** Engineering stress–strain curves, **b** variation in UTS, **c** variation in elongation

The variation in the AA6061 layer hardness as a function of aging time and temperature is depicted in Fig. 4.7. The ST, A5, and C2 samples are aged for 1–78 h at different temperatures (90, 100, 110 and 120 ℃) to determine the optimal aging process. The aging hardening curves of the AA6061 layer in the composites are measured because it is a heat-treatable strengthened Al alloy that can further improve the material properties through precipitation strengthening. The hardness of the

AA6061 layer in the ST, A5, and C2 samples is 57 HV, 132 HV, and 138 HV, respectively. Under aging temperatures of 90 and 100 ℃, the hardness of ST samples increases consistently with aging time, with no discernible peak. After 60 h of aging at 110 and 120 °C, the hardness tends to be stable. By comparing the aging hardening response of as-rolled samples, it can be seen that under all artificial aging conditions, the peak hardness of the C2 sample is slightly higher than that of the A5 sample, and the aging time for the C2 sample to obtain peak hardness is significantly shorter, due to its high solute supersaturation. The hardness of rolled samples exhibits a fluctuating trend throughout four aging temperatures, which is mainly related to the competitive relationship among the change in dislocation density, precipitation of the second phase, and increase in grain size during aging. It can be found from the aging hardening curves of the C2 sample that the highest peak hardness is 145 HV after 54 h aging at 100 ℃. And the optimal peak aging condition of the A5 sample is 100 ℃ for 57 h. The aging-induced increase in hardness implies that precipitation strengthening can overcome recovery softening.

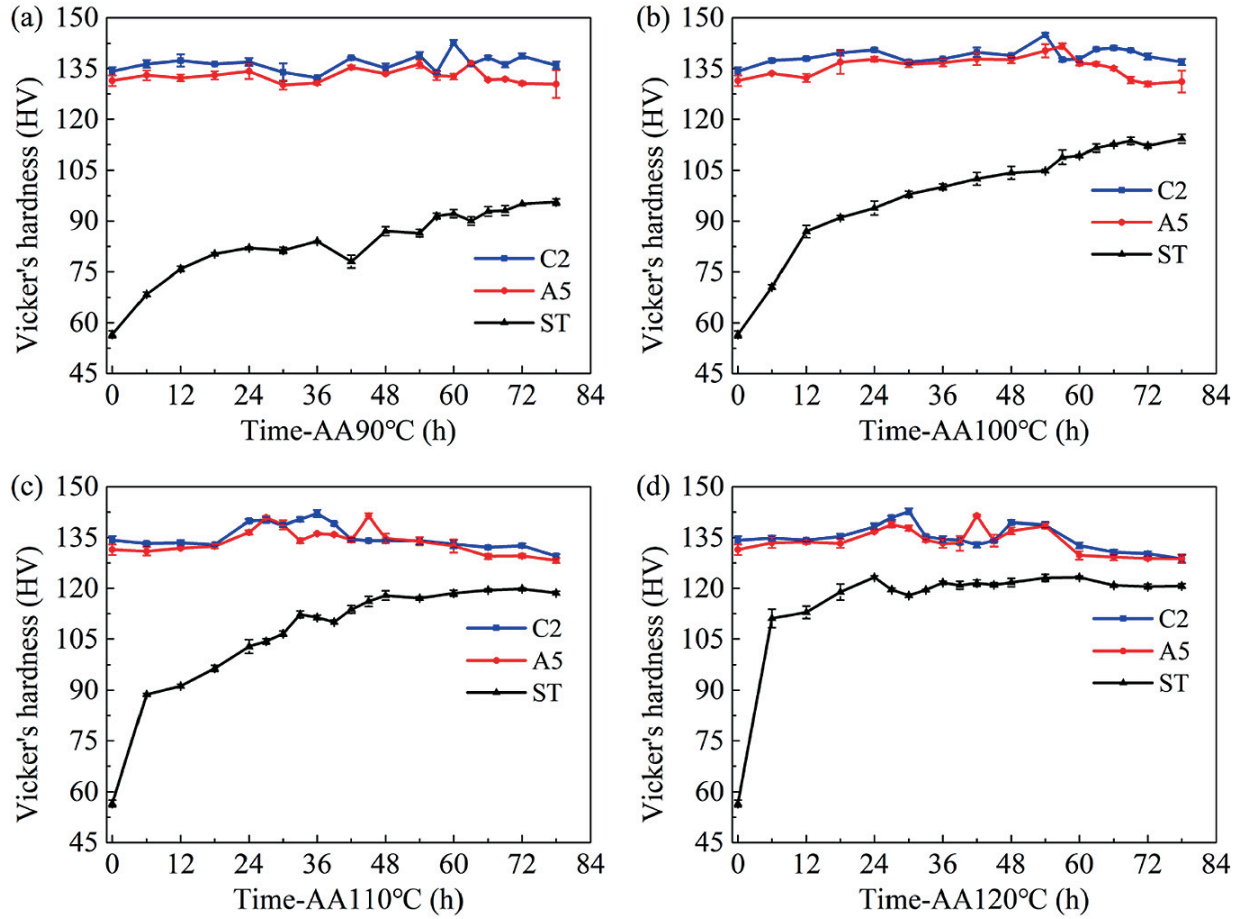


Fig. 4.7 The variation of Vicker's hardness with aging time of ST and rolled samples at different aging temperatures: **a** 90 ℃, **b** 100 ℃, **c** 110 ℃, **d** 120 ℃

Figure 4.8 illustrates the influence of aging temperature and time on the tensile properties of rolled samples. Under all four aging conditions, the UTS of the C2 sample is higher than that of the A5 sample, and the UTS of these samples also shows a fluctuating trend. The competition between second-phase precipitation and recovery during aging can explain this variation trend. Recovery and precipitation may occur simultaneously during aging. In the early stages of several aging treatments, the drop in UTS may be attributed to the domination of recovery, whose effect is pronounced, resulting in a reduction of defect density. The subsequent increase in UTS is related to the enhancement of the precipitation strengthening effect. Obviously, the contribution of precipitation to strength is higher than the strength loss caused by recovery; hence UTS improves overall. With an increase in aging temperature, the time to peak aging of rolled samples is observed to decrease. Using the test results presented in Table 4.1 and comparing

the UTS of the four aging conditions, the two rolled samples exhibit the highest peak strength at 100 °C. After 54 h and 57 h of aging at this temperature, the UTS of the C2 and A5 samples is 328 MPa and 265 MPa, respectively. These results are in good agreement with the aging hardening response.

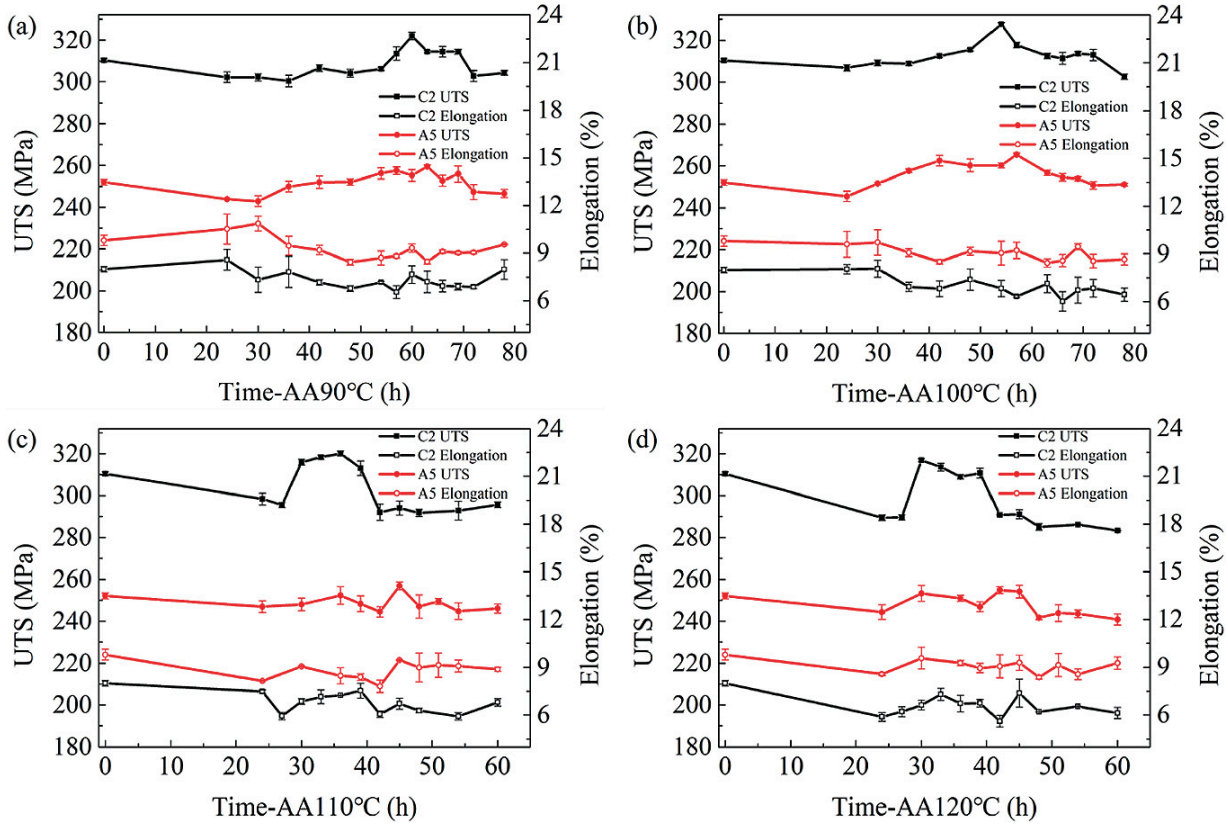


Fig. 4.8 Tensile properties of AA1050/AA6061 laminates varying versus aging time with aging temperatures of **a** 90 ℃, **b** 100 ℃, **c** 110 ℃, **d** 120 ℃

Table 4.1 Peak aging UTS of the A5 and C2 samples at different aging temperatures and times

Aging temperature (℃)	Sample via five-cycle ARB		Sample via three-cycle ARB+ two-pass cryorolling	
	Time (h)	UTS (MPa)	Time (h)	UTS (MPa)
90	63	259 ± 1	60	322 ± 2
100	57	265 ± 1	54	328 ± 1
110	39	257 ± 2	36	320 ± 1
120	36	255 ± 2	30	317 ± 1

4.2.2 Microstructure Evolution of AA1050/AA5061 Laminates

Figure 4.9 shows SEM images of AA1050/AA6061 laminates in the as-rolled condition, where the bright layer and dark layer represent AA6061 and AA1050 layers, respectively. There is no delamination at the interface between layers, indicating that the composites achieve good bonding after rolling. In Fig. 4.9a–c, with increasing in ARB cycles, the number of constituent layers increases while the thickness of layers decreases. The reduction in thickness of the soft layer (AA1050 layer) is more significant than that of the hard layer (AA60601 layer), which is mainly attributed to the different deformation of the two metals. At the initial stages of ARB, both the AA1050 and AA6061 layers deform homogeneously, and the interfacial flatness and interlayer continuity are maintained up to the third cycle (Fig. 4.9b). However, with a further increase to the fifth ARB cycle, the phenomenon of necking and fracture in the AA6061 layer can be obviously observed. And the adjacent AA1050 layer protrudes and fills in the fracture regions. Necking occurs when the shear stress is greater than the yield strength of the hard layer. Compared to A5 sample (Fig. 4.9c), the interfacial flatness is significantly improved after two-pass cryorolling with the same equivalent strain in which there are almost no necking in the C2 sample (Fig. 4.9d). It is obvious that cryorolling can effectively delay the onset of plastic instability and significantly enhance the uniform deformation between the constituent layers.

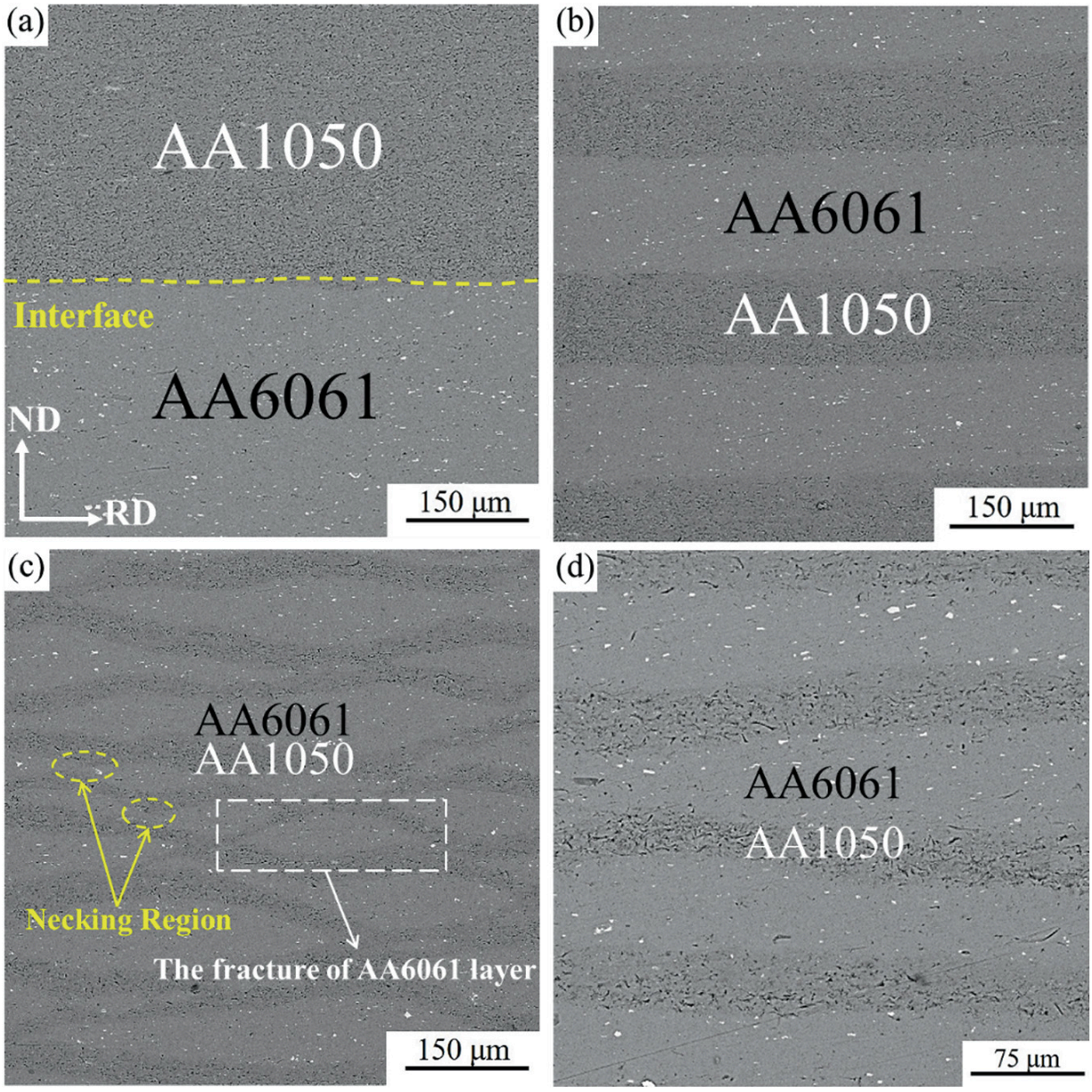


Fig. 4.9 SEM micrographs of AA1050/AA6061 laminates: **a** A1 sample, **b** A3 sample, **c** A5 sample, **d** C2 sample

Figure 4.10 shows the TEM micrographs and corresponding grain size distribution of rolled samples. Due to the relatively uniform microstructure of the constitute layers, TEM observations of the laminates are more concentrated near the interface. Figure 4.10a–c displays the morphology of the AA1050 layer, the AA6061 layer, and the bonding interface. The interfacial flatness of the C2 sample is better than that of the A5 sample, confirming that the cryorolling process can effectively improve the deformation incompatibility between the constituent layers, enhancing the mechanical properties of

AA1050/AA6061 laminates. The statistical results of the grain size distribution of the AA1050 layer and the AA6061 layer of the A3, A5, and C2 samples are shown in Fig. 4.10d–f and g–i, respectively. In conjunction with the TEM micrographs, the grains of the AA6061 layers of the three rolled samples exhibit evident elongation and refinement, with the C2 sample displaying the smallest grain size. For the AA1050 layer, the majority of grains in the A3 and C2 samples are elongated in the rolling direction. Equiaxed grains in the A5 sample suggest that dynamic recrystallization of the AA1050 layer has occurred, as the temperature and energy storage required for this process is attained after five-cycle ARB. In contrast, the AA1050 layer in the C2 sample still maintains the elongated grain morphology, which further illustrates that dynamic recovery is significantly inhibited during cryorolling.

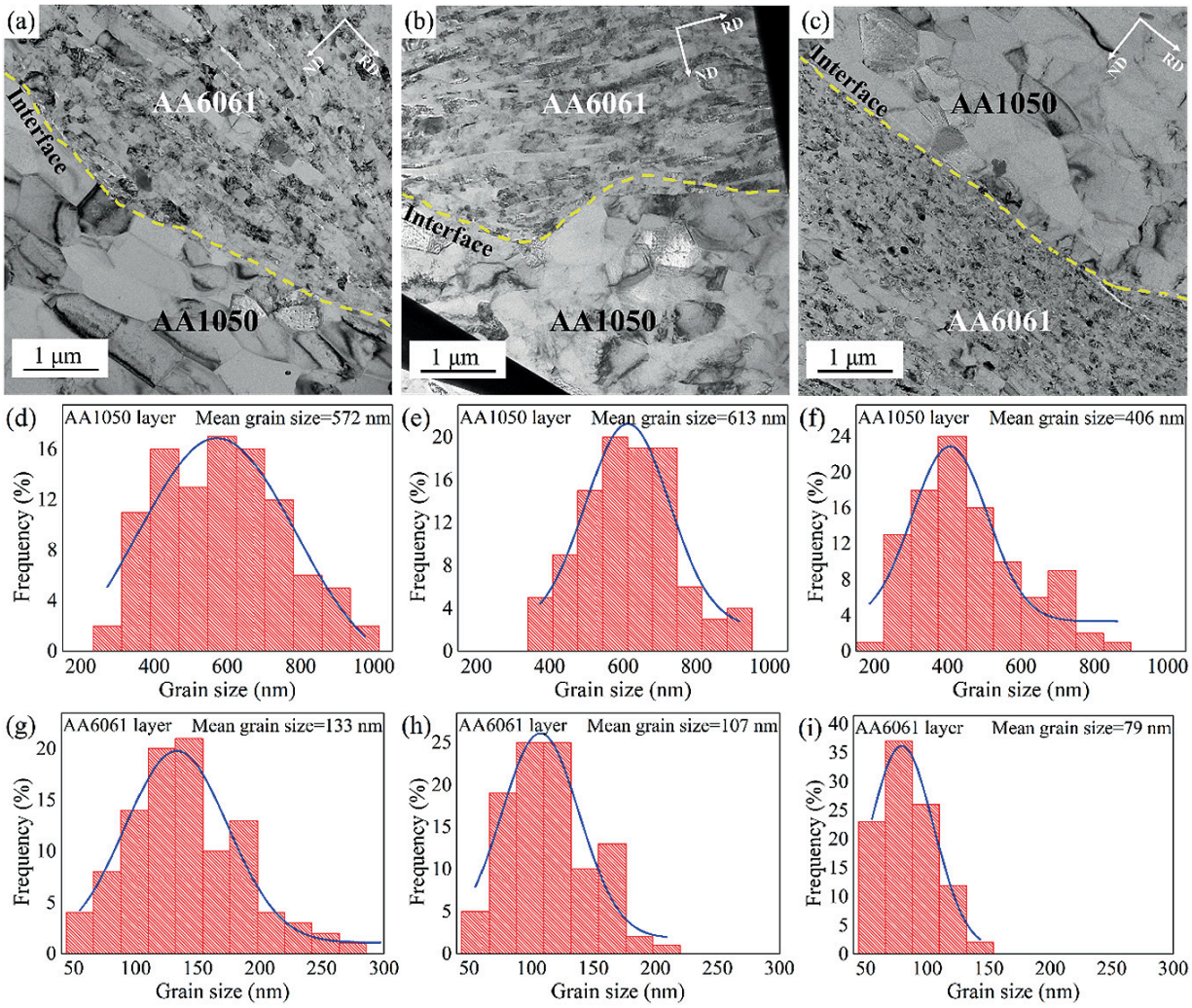


Fig. 4.10 TEM images of rolled samples: **a** A3 sample, **b** A5 sample, **c** C2 sample and corresponding grain size distribution: **d–f** AA1050 layer, **g–i** AA6061 layer

Figure 4.11a shows the XRD patterns of the samples with different rolling conditions. The (200) crystal plane parallel to the rolling surface is observed to be preferable to the other crystal planes. The intensity of the diffraction peak varies with the degree of deformation, which is closely related to texture evolution. Furthermore, the dislocation density of the samples is quantitatively analyzed using the XRD data in conjunction with the modified Williamson-Hall method to analyze the macroscopic trend of the dislocation density changes in the samples under different rolling states. The specific model equation is given below:

$$\Delta K \cong \frac{0.9}{D} + \left(\frac{\pi M^2 b^2}{2}\right)^{\frac{1}{2}} \rho^{\frac{1}{2}} K\overline{C}^{\frac{1}{2}} + O\left(K^2\overline{C}\right) \tag{4.2}$$

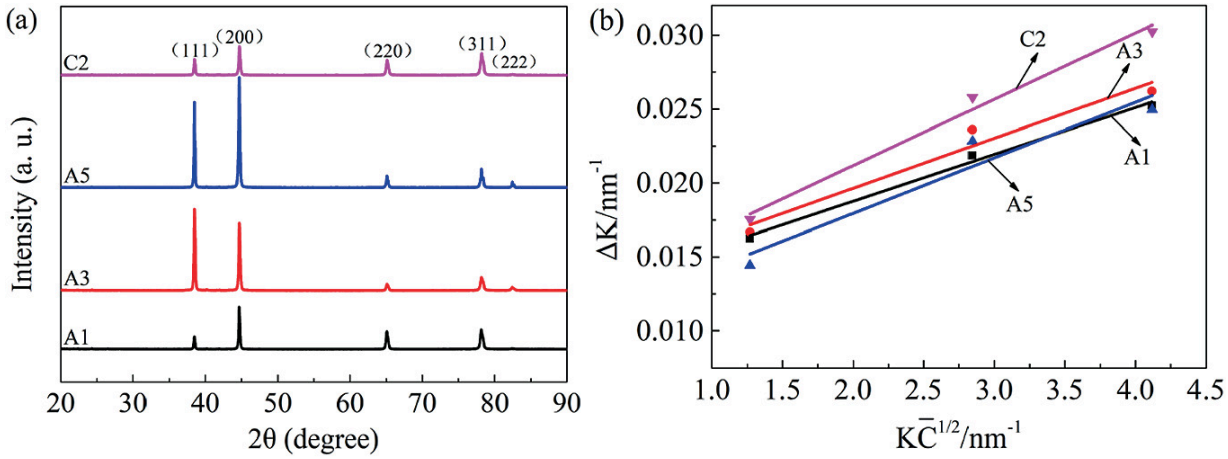


Fig. 4.11 **a** XRD diffraction patterns of AA1050/AA6061 laminates, **b** The modified Williamson–Hall plot of the corresponding rolled samples

where D is the grain size, b is the Burgers vector (0.286 for aluminum), M is the constant related to the effective truncation radius of the dislocation (generally M = 1–2, and the value of M in this investigation is taken as 1), ρ is the dislocation density, and $\overline{C}$ s the average contrast coefficient.

In Eq. (4.2), $K = \frac{2\sin\theta}{\lambda}$ $\Delta K = \frac{\cos\theta[\Delta(2\theta)]}{\lambda}, \overline{C} = \overline{C}_{hoo}\left(1 - q\frac{h^2l^2+h^2k^2+k^2l^2}{(h^2+l^2+k^2)^2}\right)$ θ and $\Delta(2\theta)$ are the

diffraction angle and the half-height breadth of the diffraction peak, respectively, and λ is the wavelength of χ ray. The following equation can be obtained by sorting out:

$$\frac{\cos\theta[\Delta(2\theta)]}{\lambda} \cong \frac{0.9}{D} + \left(\frac{\pi M^2 b^2}{2}\right)^{\frac{1}{2}} \rho^{\frac{1}{2}} \frac{2\sin\theta}{\lambda} \sqrt{\overline{C}_{hoo}\left(1 - q\frac{h^2l^2 + h^2k^2 + k^2l^2}{(h^2 + l^2 + k^2)^2}\right)} \quad (4.3)$$

It can be seen, after simplification, that the dislocation density is proportional to the slope of $\Delta K - K\overline{C}^{\frac{1}{2}}$ Fig. 4.11b depicts the relationship diagram after fitting. Dislocation density for samples A1, A3, A5 and C2 computed using corresponding equations is 7.82×10^{13}, 8.89×10^{13}, 1.10×10^{14} and 1.57×10^{14} m^{-2} respectively. The comparison reveals that the dislocation density rises with an increase in cycles, with the highest dislocation density accumulated in the two-pass cryorolled sample.

Figure 4.12 displays the TEM images of the A5 and C2 samples after rolling and peak aging treatment at 100 ℃. Figure 4.12a and b reveal that the AA6061 layer of the rolled laminates has an evident dislocation tangle, whereas the C2 sample exhibits the structure and morphology seen in Fig. 4.12b as a result of substantial grain refinement. According to A5 + PA (peak aging, 100 ℃/57 h) and C2 + PA (peak aging, 100 ℃/54 h) samples in Fig. 4.12c and d, the grain morphologies of the AA1050 and AA6061 layers are similar to the rolled state, indicating that only recovery occurs during the low temperature aging. In addition, although recovery occurs during this process, the formation of precipitates is also accompanied. A combination of dislocation annihilation during the recovery process and the impeding effect of precipitates on dislocation movement affects the defect density in the microstructure, and this is reflected in the variation of mechanical properties during the aging process (Figs. 4.7 and 4.8). The high dislocation density in the cryorolled sample can provide more heterogeneous nucleation sites for aging precipitates, causing the precipitates to nucleate near or on dislocation, and promoting the growth of precipitates through dislocation, a fast solute atom diffusion channel. Hence, high-density dislocation can facilitate the precipitation of strengthening phases and accelerate the aging precipitation process.

This is one of the reasons why C2 samples reach peak aging with a greater UTS and shorter aging time.

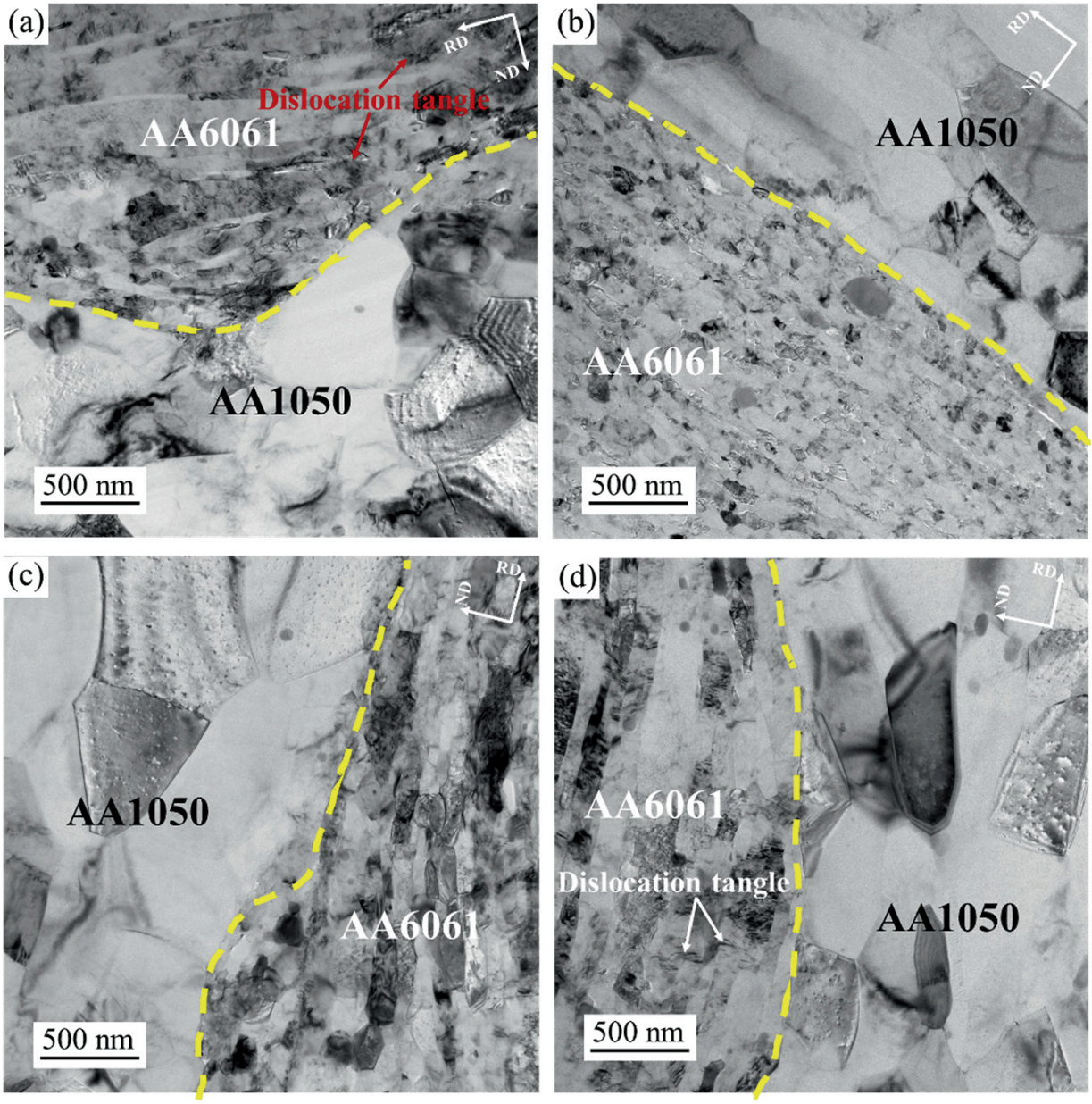


Fig. 4.12 TEM images of AA1050/AA6061 laminates: **a** A5 sample, **b** C2 sample, **c** A5 + PA sample, **d** C2 + PA sample

4.2.3 Fracture Morphology of AA1050/AA5061 Laminates After Tensile Testing

Figure 4.13 illustrates the fracture characteristics of rolled AA1050/AA6061 laminates after tensile deformation, where (a)–(c),

(d)–(f), and (g)–(i) correspond to the fracture morphologies of the A3, A5 and C2 samples, respectively. Macroscopic fractography of the composites reveals the overall morphology at the fracture, the interfacial bonding of the AA1050 and AA6061 layers (bonding and delamination), and the reduction in layer thickness. The delamination phenomenon between the constituent layers in the ARBed samples is illustrated in Fig. 4.13a and d, demonstrating that the interfacial bonding between component metals is relatively weak. During tensile deformation, the AA1050 layer exhibits more pronounced necking, indicating that it contributes more to the elongation of the laminates, while the interfacial delamination is one of the primary factors influencing the fracture of the composites. In contrast, there is no delamination at the tensile fracture of the cryorolled sample (see Fig. 4.13g), and the two metals have bonded so well that they can deform together, suggesting compatible deformation of the laminates. This phenomenon reveals that cryorolling can effectively improve the interfacial bonding strength, which is in good agreement with the UTS in mechanical properties. In the remaining microscopic tensile fractography, the composites display a ductile fracture mode characterized by dimples. As observed, the dimple size of the A3 sample is large and deep, and the fracture morphologies of the composites are primarily shallow shear dimples as the deformation progresses. This is owing to the performance difference between adjacent component metals and the “dragging” effect between the constituent layers, which causes the dimples of the AA1050 layer toward the AA6061 layer near the interface. The variation in dimple size and morphology is consistent with the tensile test results (Fig. 4.6).

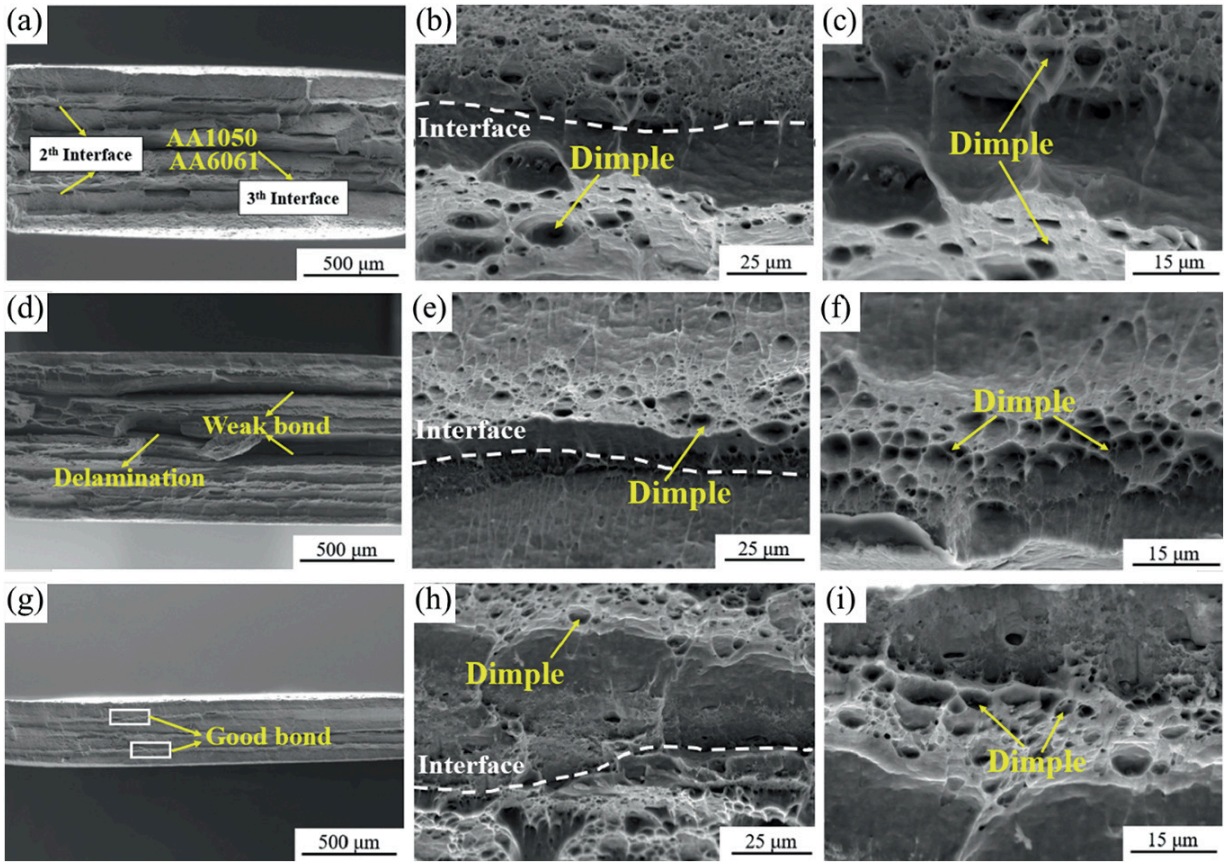


Fig. 4.13 SEM images of the tensile fracture surface of rolled samples: **a**–**c** A3 sample, **d**–**f** A5 sample, **g**–**i** C2 sample

Figure 4.14 depicts SEM images of the tensile fracture morphologies of the A5 + PA and C2 + PA samples. Compared to before aging, the interfacial bonding quality of the two rolled samples is enhanced after aging treatment, and no multiple delaminations are observed on the fracture surface at low magnification, as shown in Fig. 4.14a and d. It can be considered that this phenomenon has a positive effect on the strength improvement of the samples after peak aging. A number of dimples and tearing edges can be observed in the fractography at high magnification, indicating that the fracture mode of the laminates is still ductile fracture. The morphology and number of dimples are not significantly different from those before aging. In addition, precipitates form during the aging process; thus, the elongation of the samples is not high after peak aging. Dimple features not only correspond to the characterization of mechanical properties but their shapes and directions can also determine the type of load experienced during fracture and reveal the direction of crack propagation.

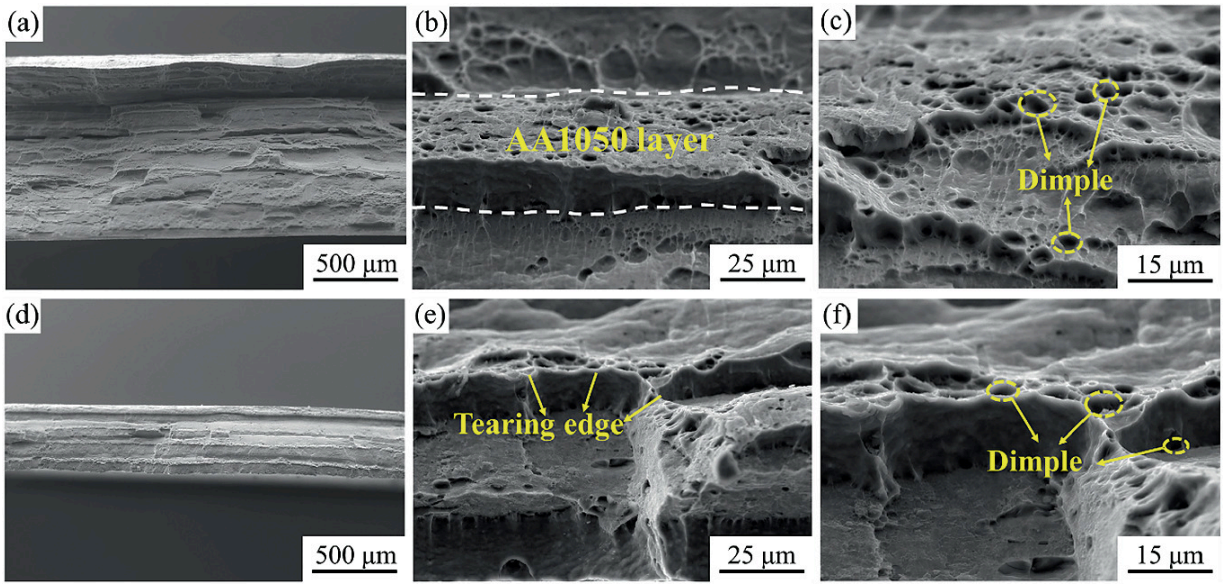


Fig. 4.14 SEM images of the tensile fracture surface of the samples: **a** A5 + PA sample, **b** enlarged image corresponding to (**a**), **c** enlarged image corresponding to (**b**), **d** C2 + PA sample, **e** enlarged image corresponding to (**d**), **f** enlarged image corresponding to (**e**)

4.2.4 Effect of Aging on Mechanical Properties of AA1050/AA5052 Laminates

Some studies on the preparation of laminates by ARB have demonstrated that after a certain number of cycles, the UTS hardly increases or even decreases as the number of ARB cycles increases. Similar results are observed in this research. As demonstrated in Fig. 4.6, after three-cycle ARB, the UTS growth rate of the laminates becomes relatively slow as deformation continues. This is mainly related to the plastic instability caused by the different flow characteristics between dissimilar metals during composite deformation. However, cryorolling can effectively overcome the deformation incompatibility between component metals and provide superior mechanical properties. After two-pass cryorolling, the UTS is significantly enhanced (by approximately 48% relative to the ARB of the initial cycle) without a notable decline in elongation (Fig. 4.6). Moreover, the contribution of cryorolling to strength improvement is also reflected in the following three facets. First, there is no delamination on the tensile fracture surface of the cryorolled sample, and good bonding is achieved between component metals. Second, the cryorolled sample has a higher dislocation density than the ARBed

samples, as calculated by the modified Williamson–Hall method. This is because the dynamic recovery is suppressed in the cryorolling process, leading to an increase in the number of dislocations and a decrease in the spacing between dislocations. As the deformation continues, the dislocation movement would be subjected to higher resistance, resulting in a rise in the stress required for composite deformation. Third, due to the refinement of grain size by cryorolling (Fig. 4.10), the relative area of grain boundaries increases, and the inhibiting effect of grain boundaries on dislocations is also enhanced. The stress required for further plastic deformation of the material increases, resulting in an increase in strength. According to the classic Hall-Patch equation, grain refinement has a significant effect on strength improvement. Although ARB, a severe plastic deformation process, is more effective in refining grains than conventional rolling, the grain refinement rate tends to saturate as strain increases. This saturation is attributed to the dynamic recovery growth rate caused by the accumulation of plastic deformation, and the dynamic recovery rate is inseparable from the deformation conditions. Therefore, the limited grain refinement can be overcome by changing the deformation conditions to suppress the dynamic recovery. In this way, cryorolling can increase both the rate and the limit of grain refinement, leading to composites with a finer grain size. According to the above analysis, the primary reasons for the UTS improvement of the cryorolled sample are to promote coordinated deformation, improve interfacial bonding quality, increase dislocation density, and further refine grains.

The mechanical properties of rolled samples can be further improved by undergoing an aging treatment at various temperatures. Figures 4.7 and 4.8 display the aging hardening response and tensile properties of the two rolled samples, respectively, and show that the optimal performance is attained at an aging temperature of 100 °C, where the peak strength of the C2 + PA sample is also at its highest. Figure 4.15 compares the strength and elongation of this research to that of previously reported Al/Al laminates. In Fig. 4.15, the black dot on the left represents AA1050/AA6061 laminates prepared by multi-cycle ARB, which have specific strength but low elongation. In contrast, this study shows that AA1050/AA6061 laminates exhibit high strength and good elongation following cryorolling and peak aging treatment.

Compared to other Al/Al laminates, its mechanical properties are significantly superior. The elongation of the samples exhibits a minor decreasing trend under multiple aging conditions. The authors studied the effect of aging treatment on the microstructure and properties of AA6061 prepared by cryorolling, and found that the strength of the material was significantly improved while its elongation was reduced. In this study, the high strength at the peak state of the laminates obtained by combining cryorolling with low temperature aging can be attributable to the three factors. First, residual dislocations also contribute to strength improvement. Second, the high dislocation density (compared with A5 sample) can provide more nucleation sites for the precipitation of strengthening phases. Finally, the size of precipitated particles does not increase obviously, and the interaction between precipitates and dislocations is also conducive to maintaining high strength.

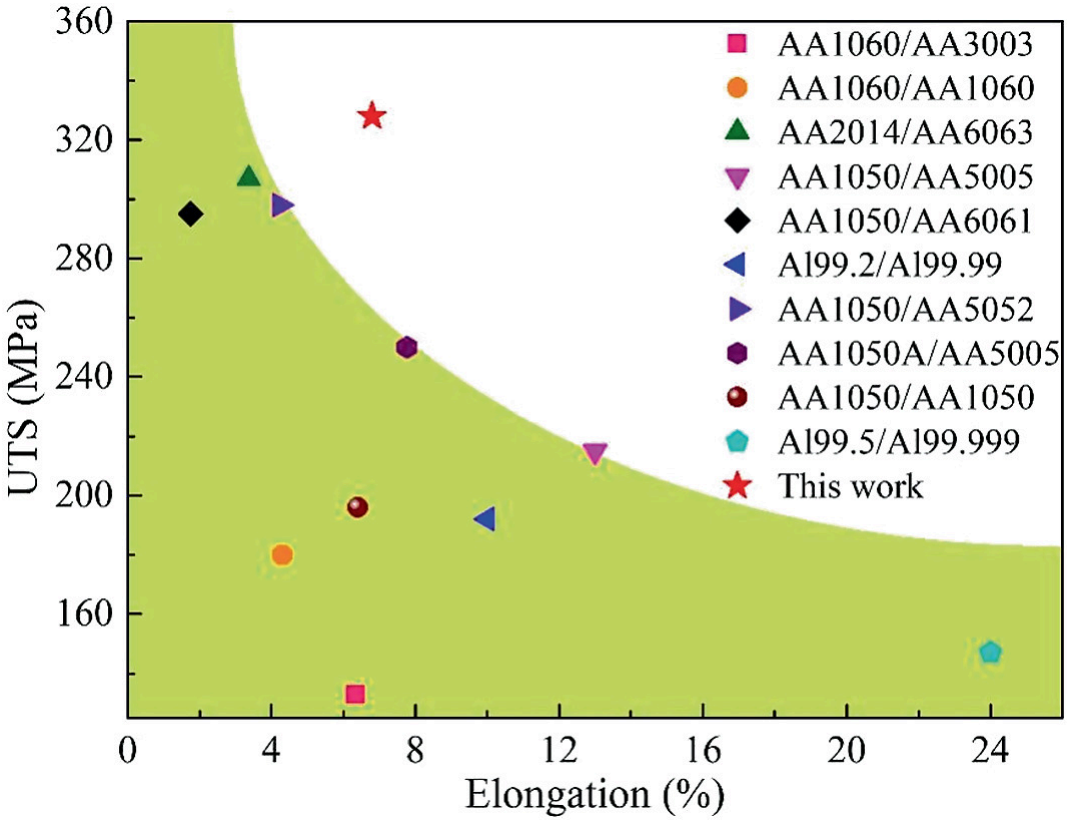


Fig. 4.15 Comparison of tensile properties with other Al/Al laminates

4.2.5 Microstructural Evolution Mechanism of AA1050/AA6061 Laminate During Aging

Figure 4.9c reveals a wavy and discontinuous laminated structure in the laminates after multi-cycle ARB, indicating that necking and fracture have occurred in the composites. During the co-deformation of dissimilar metals, the structural discontinuity is caused by the differences in the flow properties and mechanical properties of the constituent layers. Therefore, further deformation results in the AA6061 layer to neck and eventually fracture. The AA1050 layer requires further plastic deformation to accommodate the structural changes caused by the AA6061 layer. The plastic instability in the hard layer has also been reported in other bimetallic laminates. Many investigations have demonstrated that the phenomenon is influenced by several factors, including the initial thickness ratio, strain hardening index, and strength coefficient of the constituent layers of laminates prepared by ARB. In this research, the AA1050/AA6061 laminates with relatively flat and continuous lamellar structure are successfully fabricated utilizing cryorolling (as shown in Fig. 4.9d). This is consistent with the results of our prior study on optimizing the bonding interface and layered structure of laminates by changing the deformation temperature and reducing the formation of shear bands at the interface.

Figure 4.11 and the modified Williamson–Hall method show that the dislocation density of the cryorolled sample is higher than that of the ARBed sample. This is because cryorolling can produce higher dislocation storage in the samples by suppressing dynamic recovery and promoting dislocation generation. In addition, the plastic deformation at low temperature would restrict dislocation movement and lead to increased inhomogeneity in dislocation distribution. This non-uniform distribution means dislocation movement is more difficult to initiate during deformation and tends to be regionally dependent. However, the dislocation movement is impeded due to the incompatibility of adjacent regions, so a higher dislocation density is accumulated in the cryorolled sample. The high-density dislocation of rolled samples can promote the precipitation of strengthened phases during the aging process. Figure 4.16 depicts the TEM micrographs showing the microstructure evolution of the AA6061 layer in the A5 +

PA and C2 + PA samples. As illustrated in Fig. 4.16a and d, even if recovery has occurred after low temperature aging, the grain structure of rolled samples in the two peak aging states still maintains an elongated morphology with a certain number of dislocations. Moreover, the microstructure comprises fine spherical- and needle-shaped precipitates (depicted with purple and yellow arrows, respectively). Some studies believed that these fine precipitates in the matrix can hinder dislocation movement during tensile deformation, hence enhancing the strengthening effect of the dislocation shear mechanism on the samples. Thus, after reaching peak age, the UTS of both rolled samples increased (see Fig. 4.8). Figure 4.16b and e demonstrate high-resolution transmission electron microscopy (HRTEM) images of the peak aging samples. The diffraction spots patterns obtained by fast Fourier transform (FFT) of the marked dashed square are inserted in the figure, and the corresponding inverse fast Fourier transform (IFFT) is shown in Fig. 4.16c and f, respectively. In the IFFT figures, the dislocation (indicated by the yellow T) density in the C2 + PA sample is higher than that of the A5 + PA sample (The analysis of dislocation density was conducted at a significant number of randomly selected locations in the samples which show the same conclusion). This is because a high dislocation density in the cryorolled sample can facilitate the formation of precipitates during aging, and the precipitates can then pin dislocation, so there is still a certain amount of dislocations accumulation in the C2 + PA sample.

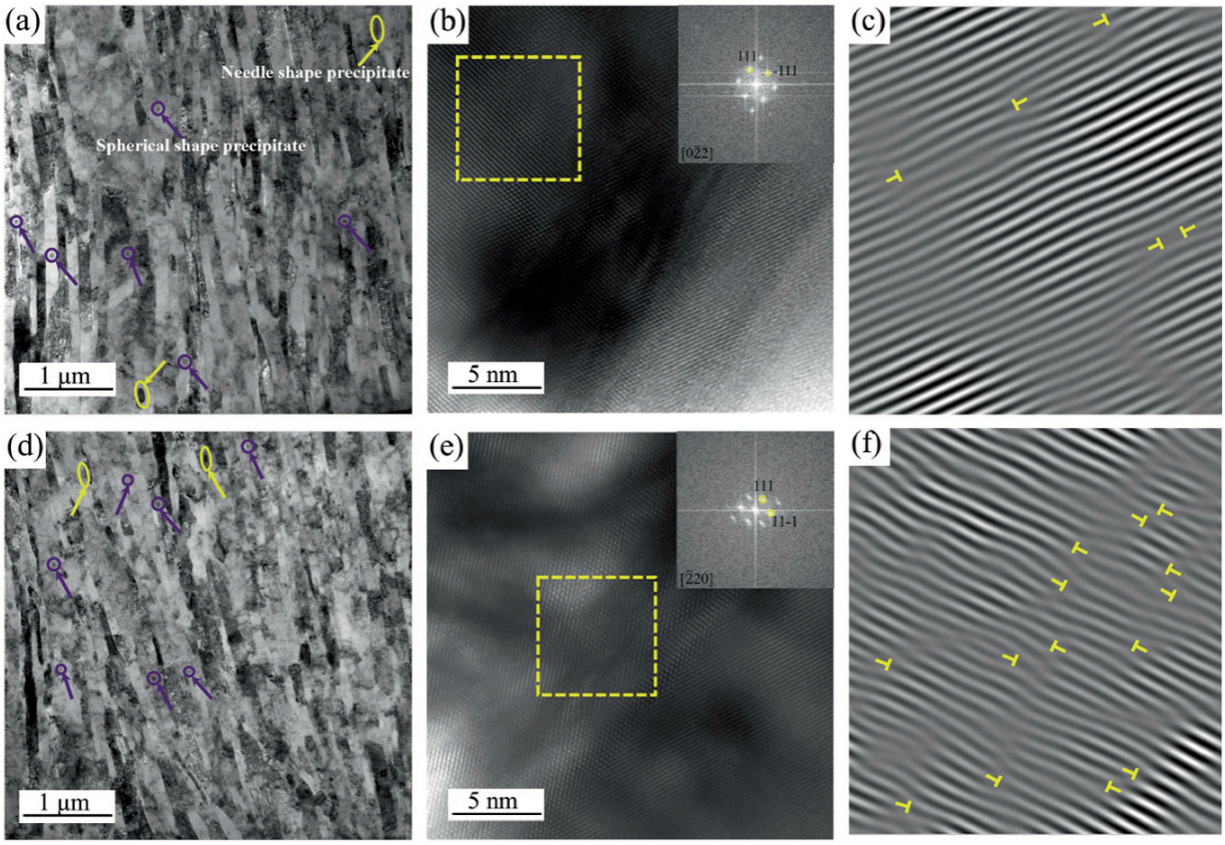


Fig. 4.16 TEM micrographs of AA6061 layer: **a** A5 + PA sample, **b** HRTEM images corresponding to (**a**), **c** corresponding IFFT pattern of the dashed square in (**b**), **d** C2 + PA sample, **e** HRTEM images corresponding to (**d**), **f** corresponding IFFT pattern of the dashed square in (**e**). The insets in (**b**) and (**e**) present the FFT pattern of selected areas marked with dashed squares

The tensile fracture surface analysis of rolled samples reveals that the bonding quality between the constituent layers of the cryorolled sample is better than that of the ARBed sample, and the interfacial bonding is weakest in the last cycle of ARB, as shown in Fig. 4.13. Interfacial delamination has been linked to two factors: (i) The inhomogeneous deformation between the constituent layers may generate strain gradients near the interface, thereby weakening the interface; (ii) In the process of deformation, the glide of dislocations on the two constituent layers would be constrained by the interface, causing them to accumulate at the bonding interface. This will cause the stress concentration at the interface, resulting in the interface is prone to debonding. In contrast, according to Fig. 4.13g, the cryorolled sample exhibits higher bonding strength, which is one of the key factors to enhance the comprehensive performance of the laminates. In addition, the interfacial bonding quality of the two rolled samples

under peak aging conditions has been improved (Fig. 4.14). Both rolled and aged samples show ductile fracture related to the nucleation, growth, and coalescence of microvoids in the microzone. Similar dimple-type fracture modes have been proposed in AA1100/AA7075 and AA1050/AA5052 laminates.

The microstructure evolution of AA1050/AA6061 laminates subjected to rolling and aging conditions is schematically explained in Fig. 4.17. Due to the severe plastic deformation process after three-cycle ARB, a certain number of dislocations are accumulated in the constituent layers of the composites (Fig. 4.17a). And the incompatible mechanical deformation characteristics of dissimilar metals would result in the accumulation of dislocations at the bonding interface and its adjacent areas. After cryorolling, the deformation at liquid nitrogen temperature inhibits the dynamic recovery of the material, leading to dislocation entanglement and accumulation to form a high dislocation density (Fig. 4.17b). The graphical model shown in Fig. 4.17c illustrates the microstructure variation of the C2 + PA sample. During the aging process, the high dislocation density of the cryorolled sample not only promotes the diffusion of Mg and Si atoms but also provides more heterogeneous nucleation sites for the aging precipitates. The precipitates, however, act as an obstacle to hinder the dislocation movement. They cause the forward-moving dislocations to bend through the pinning effect, resulting in the interaction between precipitates and dislocations. In addition, owing to the effective pinning effect, the entangled precipitates and dislocation structures are more stable than the microstructure without precipitates, enhancing the mechanical properties of the composites.

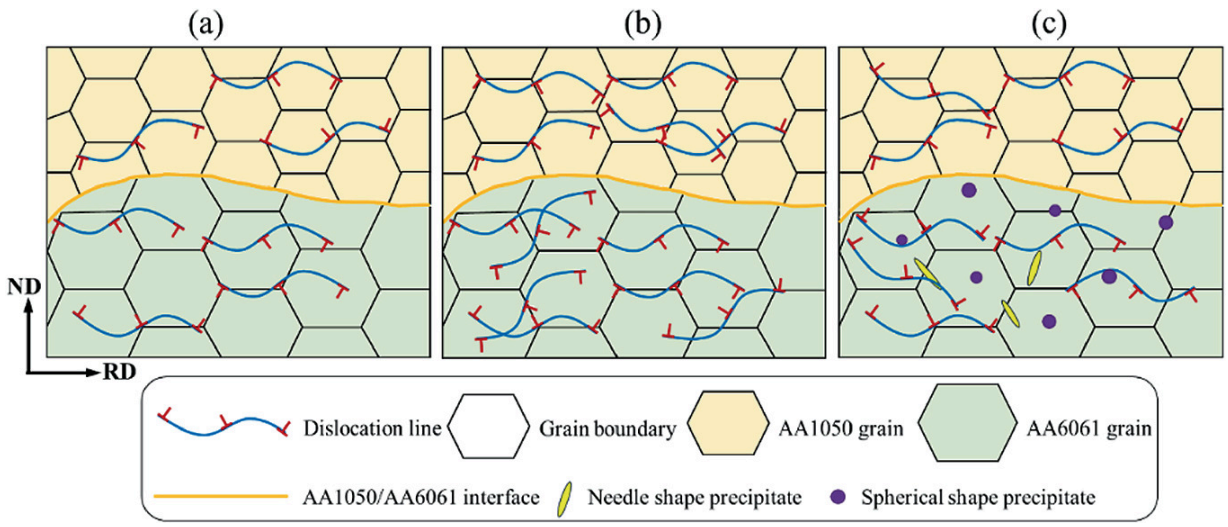


Fig. 4.17 Schematic illustration of microstructure evolution of AA1050/AA6061 laminates: **a** A3 sample, **b** C2 sample, **c** C2 + PA sample

4.3 Al/Ti/Al Laminates via Cryorolling

The Al/Ti/Al laminates were fabricated by using cryogenic roll bonding for first time [11]. The quality of laminates by cryogenic roll bonding such as edge cracks, mechanical properties, and interface bonding were compared with these by cold roll bonding. Finally, we discussed the improvement in edge quality and mechanical properties as well as the mechanism of interface bonding of Al/Ti/Al laminates during cryogenic roll bonding.

4.3.1 Edge Crack-Free Al/Ti/Al Laminates via Cryorolling

Figure 4.18a1–c1 show the Al/Ti/Al laminates produced by cold roll bonding. In the figure, there are some edge cracks which occur in the laminates after rolling. However, there are no edge cracks in the laminates produced by cryogenic roll bonding, as shown in Fig. 4.18a2–c2. It is obvious that the cryogenic roll bonding can enhance the quality of laminate edge compared to that by cold roll bonding.

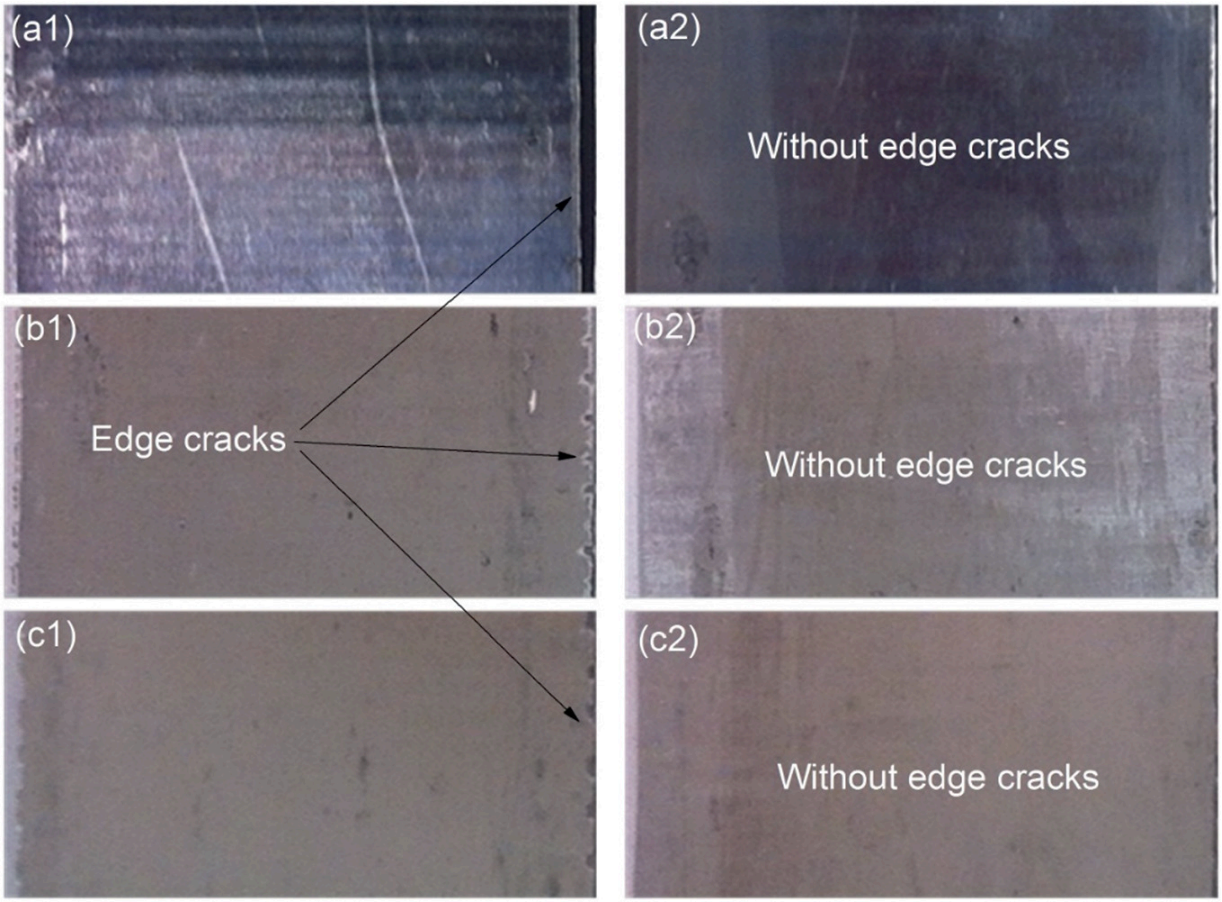


Fig. 4.18 **a1**, **b1** and **c1** for room-temperature roll bonded sheets, **a2**, **b2**, and **c2** for cryogenic roll bonded sheets. **a1**, **a2** the second pass; **b1**, **b2** the third pass; **c1**, **c2** the fourth pass

Edge cracks are the main defects in laminate products. These edge cracks must be trimmed before subsequent processing. For some metals such as Mg and steel, the ductility decreases at lower temperature. However, the ductility of Al alloys at cryogenic temperature is higher than that at room temperature.

4.3.2 Mechanical Properties of Cryorolled Al/Ti/Al Laminates

Figure 4.19 shows the engineering strain versus engineering stress curves of Al/Ti/Al laminates after the fourth pass subjected to cold roll bonding and cryogenic roll bonding respectively. For the laminates subject to room temperature rolling, the ultimate tensile stress is 150 MPa, which reaches 205 MPa for the laminates subject to cryogenic roll bonding. The ultimate tensile stress increases 36.7% by cryogenic roll bonding compared to that by cold roll bonding.

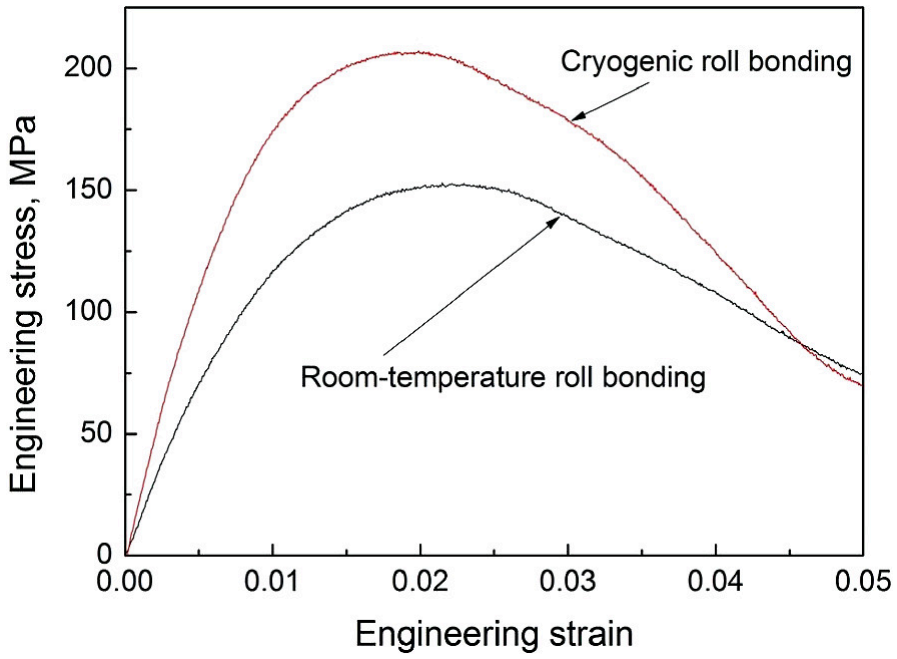


Fig. 4.19 Engineering strain versus stress of Al/Ti/Al laminates by cryogenic roll bonding and cold roll bonding

4.3.3 Microstructure Evolution of Al/Ti/Al Laminates

Figure 4.20a and b show the TEM images of the interface between the Ti and Al layers after the second and the fourth pass of cold roll bonding. After the second pass, some small voids are visible at the interfaces, although over most of the interface, the Al and Ti layers bond well. After the fourth pass, the interface between Ti and Al layer shows good bonding. Figure 4.20c and d show TEM images of the interface between the Ti and Al layers after the second and the fourth passes of cryogenic roll bonding. Compared to the samples produced by cold roll bonding, the residual voids are much larger at the interface and the grain sizes of Ti and Al layers near the interface are much finer after the second pass of cryogenic roll bonding. This is relevant to the finding that the bonding between interfaces becomes difficult with reduced temperature. With a higher number of rolling passes, the grains near the interface grow during rolling, and then the interface between Al and Ti layers also shows a good bond, as seen in Fig. 4.20d.

Figure 4.21a and b show the TEM images of the microstructure of Al layers after the fourth pass subjected to cryogenic roll bonding and cold roll bonding respectively. In Fig. 4.21a, there are no voids in the sample. However, there are a number of nanoscale voids in the sample

subjected to cold roll bonding, as shown in Fig. 4.21b. This means that the Al layer will have higher ductility during cryogenic roll bonding compared to that during cold roll bonding. Thus it suggests that a much lower deformation temperature can potentially be applied to reduce the edge-cracking tendency of Al laminates, as shown in Fig. 4.18.

Cryorolling has been reported that it can improve the mechanical properties of single metal sheets. In this study, we also believe that the finer grain size by cryogenic roll bonding improves the mechanical properties of laminates compared to that by cold roll bonding. In Fig. 4.21, we can find the grain size of Al layer subjected to cryogenic roll bonding is much finer than that subjected to cold roll bonding. Figure 4.22a and b show the TEM images of microstructure of Ti layer after the fourth pass subjected to cryogenic roll bonding and cold roll bonding respectively. In Fig. 4.22, it is obvious that the grain size of Ti layer subject to cryogenic roll bonding is much finer than that subjected to cold roll bonding. According to Hall–Petch formula, the yield strength of metal materials improves with finer grain size. Thus the strength of Al/Ti/Al laminates by cryogenic roll bonding is much higher than that by cold roll bonding, as shown in Fig. 4.19.

4.3.4 Interface Bonding Mechanism of Al/Ti/Al Laminates During Cryorolling

Interface bonding is one of the important factors that determine the final quality of product. There are many factors that determine the bonding quality such as rolling temperature, reduction ratio. In this study, the rolling reduction ratio per pass by cryogenic roll bonding is the same as that by cold roll bonding. Thus, the rolling temperature results in the difference of interface bonding behavior as shown in Fig. 4.20.

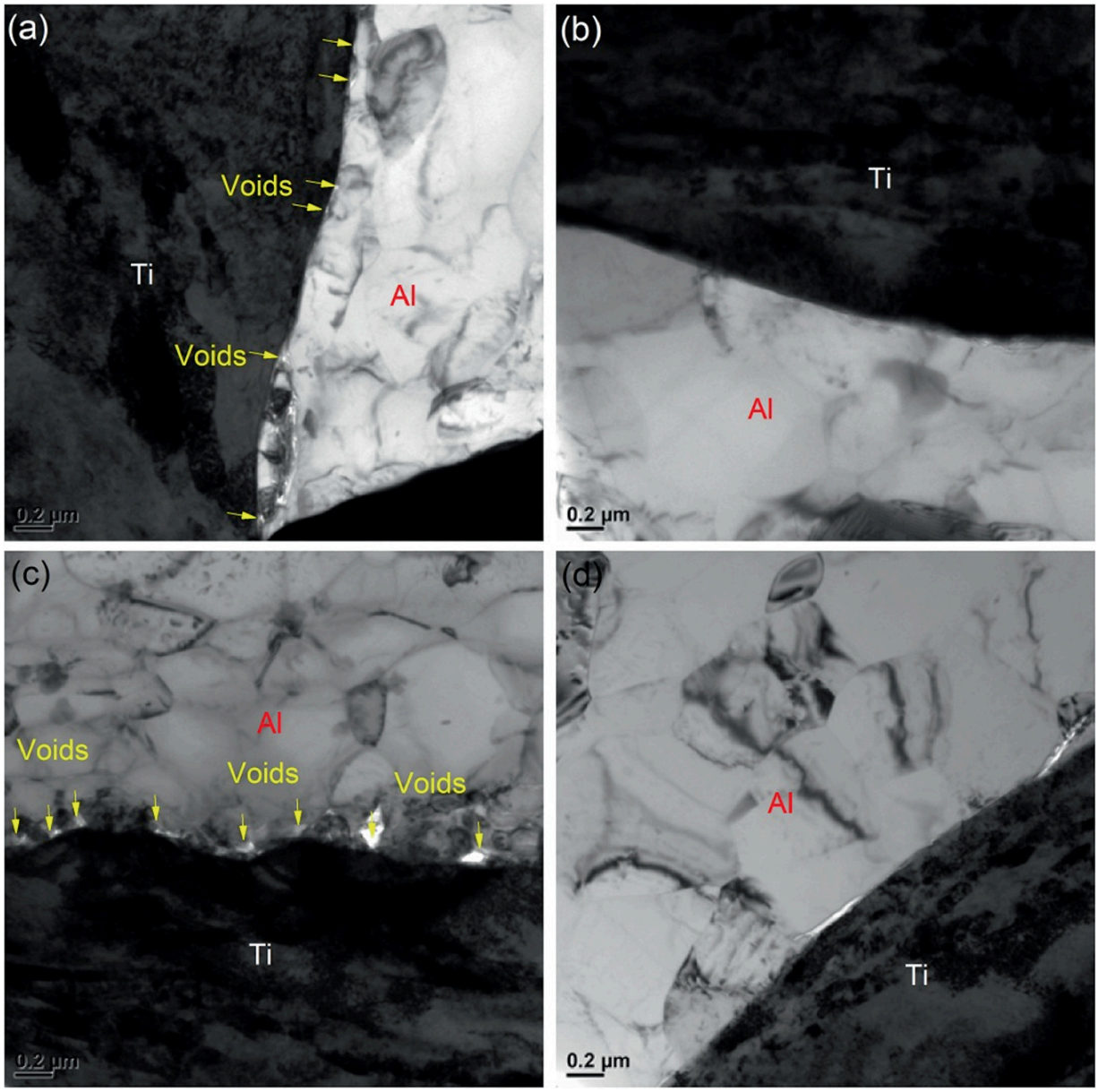


Fig. 4.20 TEM images of the microstructure near interface between Al and Ti layers. **a** and **b** for cold roll bonding after the second and fourth passes, **c** and **d** for cryogenic roll bonding after the second and fourth passes

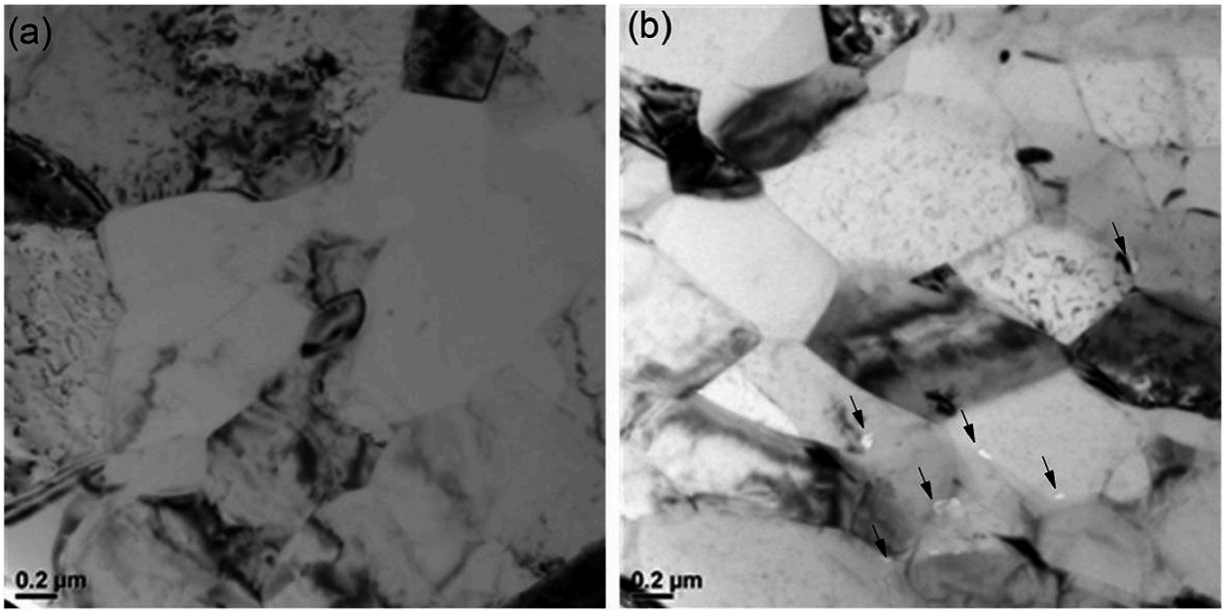


Fig. 4.21 TEM image of microstructure of Al layers after the fourth pass of **a** cryogenic roll bonding and **b** cold roll bonding. Arrows show nanoscale voids

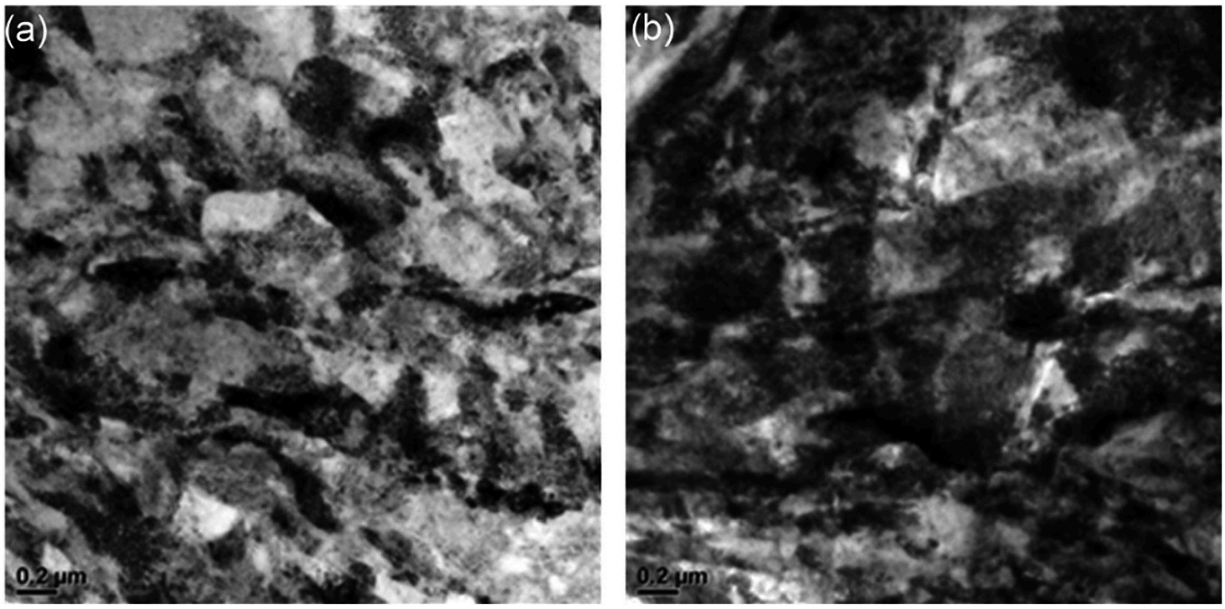


Fig. 4.22 TEM image of microstructure of Ti layers after the fourth pass of **a** cryogenic roll bonding and **b** cold roll bonding

Figure 4.23 shows the distribution of grain size of Al layer and Ti layer after different processing. As shown in Fig. 4.23a, the grain size of Al near the Al/Ti interface is 186 nm for samples rolled at room temperature, while the grain size is refined to 48 nm for the cryorolled samples as shown in Fig. 4.23b. In addition, the grains in the Al layer near the interface grow significantly under the action of stress. As

shown in Fig. 4.23c and d, the grain size increases to 398 nm and 386 nm after the fourth pass of cold roll bonding and cryogenic roll bonding respectively. It is obvious that the grain growth affects the bonding between the Al and Ti interfaces.

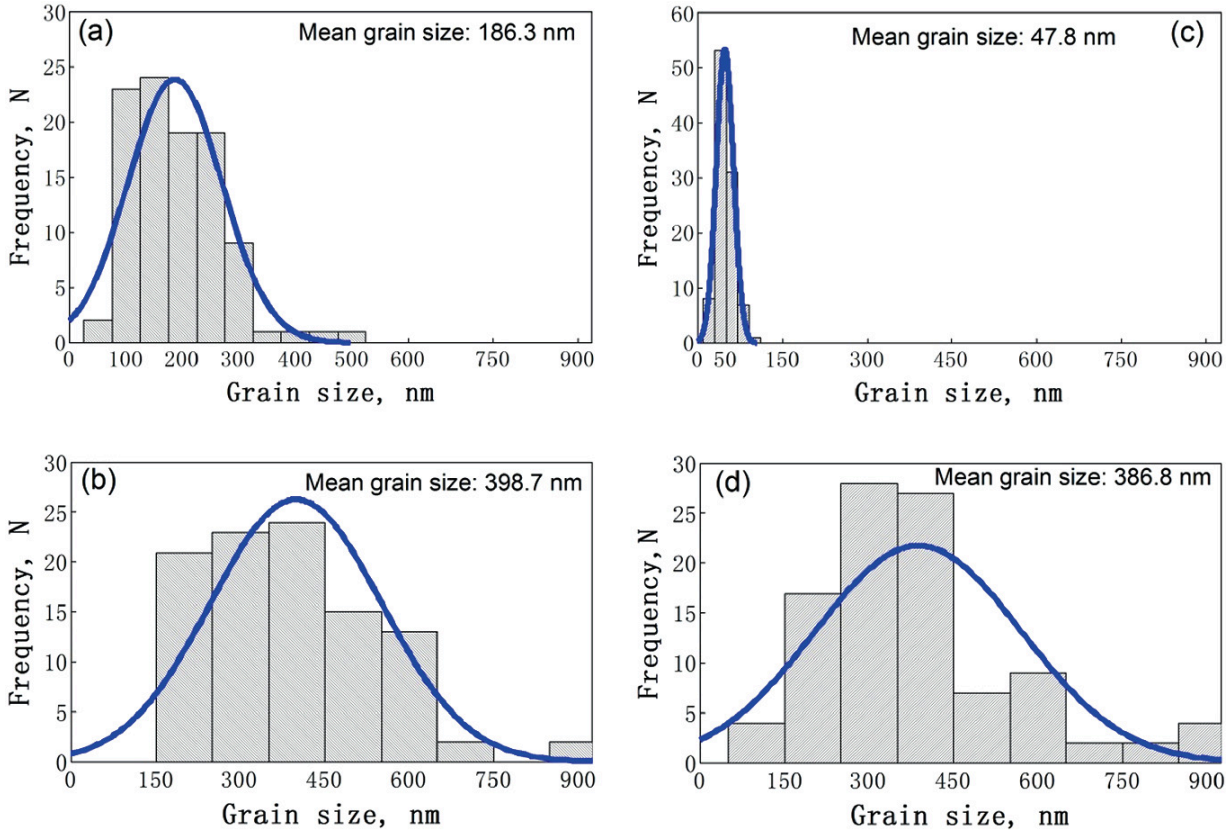


Fig. 4.23 Grain size distribution in Al layer. **a** and **b** for cold roll bonding after the second and fourth pass; **c** and **d** for cryogenic roll bonding after the second and fourth pass

To date, some mechanisms for cold roll bonding have been presented, such as the film theory, energy barrier theory, and diffusion bonding theory. Here, we propose a new bonding mechanism based on grain refinement and grain growth of soft layer. Figure 4.24 shows the mechanisms of interface bonding between Al and Ti layer subjected to cold roll bonding and cryogenic roll bonding. Before rolling, the Al and Ti surfaces are separate, and the grains are coarse, as shown in Fig. 4.24a. During rolling, firstly, the surfaces come into contact and the grains near the interface are refined greatly. There is a great deal of sliding between the Al and Ti sheets before the bond begins to form. The difference in mechanical properties results in a severe shear deformation in the surface layers, and then the grains are refined

greatly. Due to the suppression of the dynamic recovery behavior at cryogenic temperature, compared with cold roll bonding, cryorolling is more conducive to grain refinement, as illustrated in Fig. 4.24b and d. In addition, during sliding, the underlying regions of fresh metal are exposed, firming additional bonds. Rolling with greater reduction in thickness, results in the growth of ultrafine grains / nano grains. This facilitates the interfacial bond, as shown in Fig. 4.24c and e. With further reduction in thickness, most regions of the interfaces bond and there is no sliding between the layers. The ultrafine grains/nano grains near the interface grow under shear stress. There are many reports that ultrafine grains/nano grains grow during room-temperature deformation. For ARB-processed Al sheets, abnormal grain growth during asymmetric rolling can result in elimination of the interface between layers. Here, it is seen that the grains grow in the soft layer under severe shear stress both at room temperature and cryogenic temperature, which also contributes to the interfacial bonding.

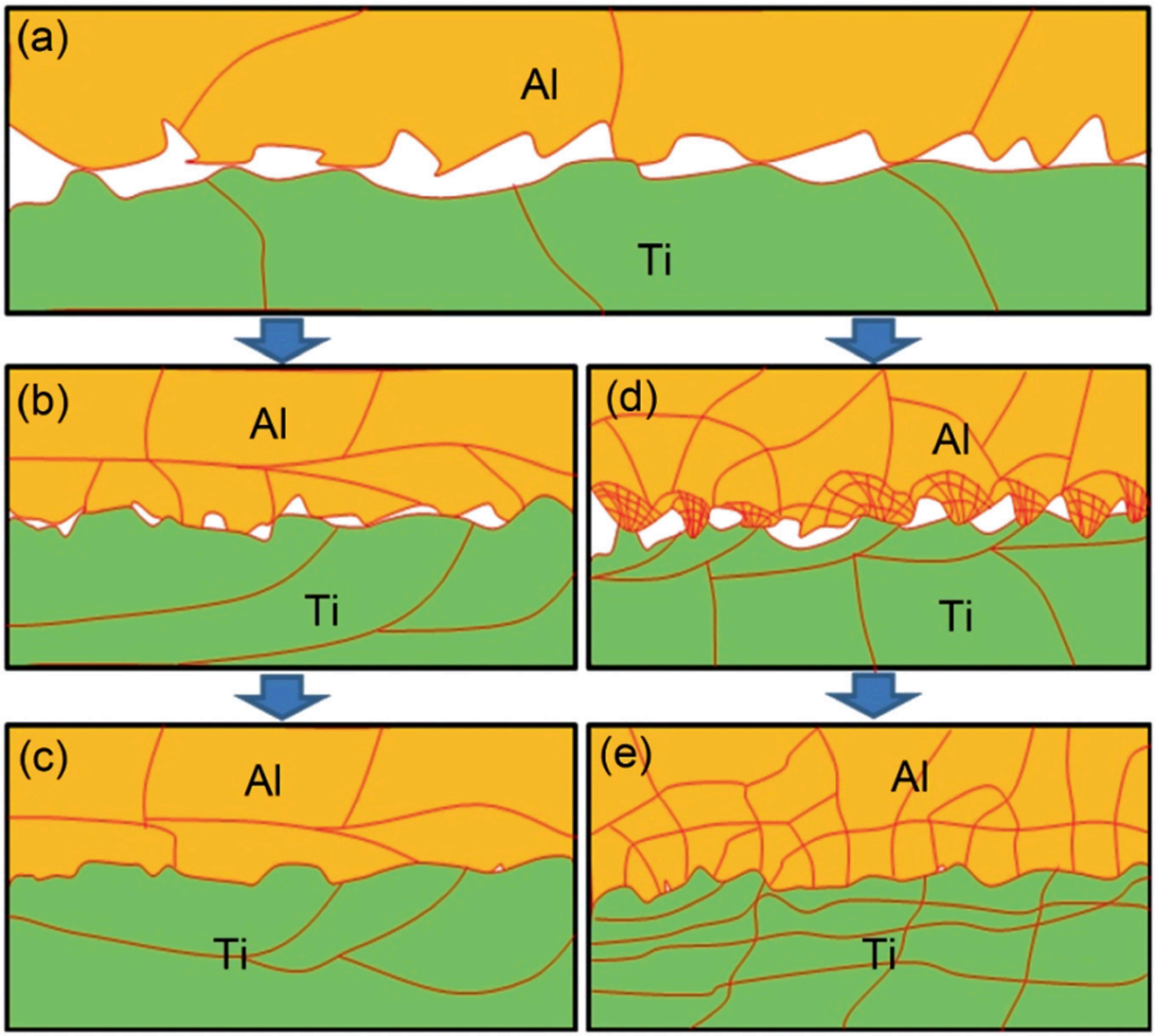


Fig. 4.24 Illustration of the interface bonding during rolling. **a** before rolling; **b** and **c** for the interface with higher reduction by cold roll bonding; **d** and **e** for the interface with higher reduction by cryogenic roll bonding

4.3.5 Effect of Cryorolling Temperatures on Peeling Strength of Al/Ti/Al Laminates

Al/Ti/Al laminates were fabricated by hot roll bonding combined with cryorolling (−190 °C and −100 °C, respectively), cold rolling, or hot rolling [6]. Their mechanical properties and bonding strength were studied and discussed. The results show that the cryorolling at −100 °C results in excellent bonding strength and mechanical properties of Al/Ti/Al laminates.

Figure 4.25 shows the morphology of the Al/Ti/Al laminates interface after rolling. In this figure, the Ti/Al interface is serrated due to Al squeezing into the Ti layer. Figure 4.25a and b shows the interface morphology of the Al/Ti/Al laminates by cryorolling. The interface is rough and jagged, and the interface is wide and deep in the Ti layer. The interface becomes smooth and straight as the rolling temperature rises (Fig. 4.25c). However, the interface becomes wider with the further temperature increases; the flatness of the interface decreases (Fig. 4.25d).

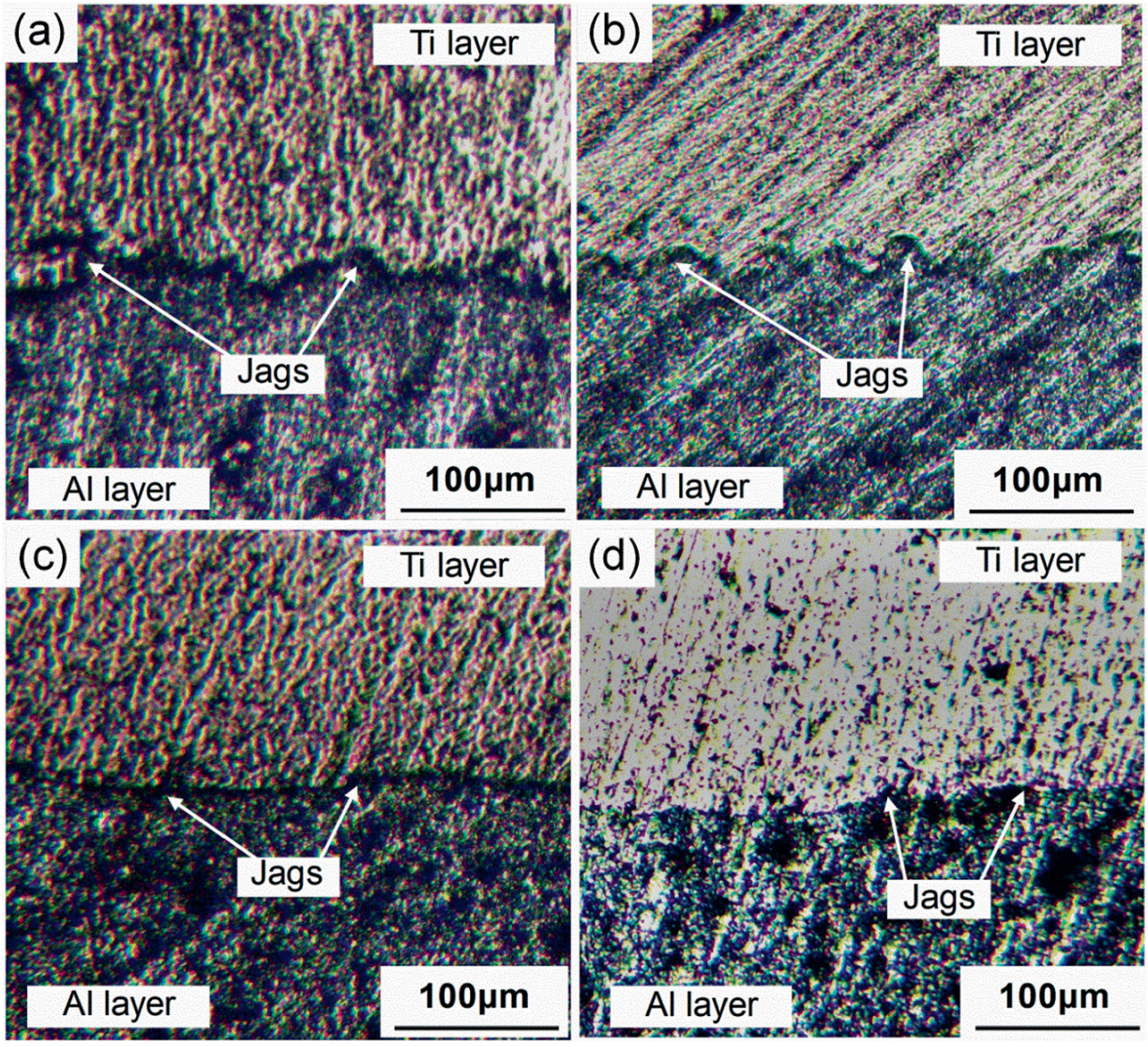


Fig. 4.25 Morphology of interface of an Al/Ti/Al laminated composite subjected to cryorolling: **a** −190 °C, **b** −100 °C, **c** cold rolling, or **d** hot rolling

Figure 4.26a illustrates the EDS line scan across the Ti/Al interface. Figure 4.26b–e shows the element distribution of Al and Ti atoms near the Ti/Al interface for different rolling processes. During rolling, the elemental interdiffusion occurs near the Ti/Al interface forming an intermetallic diffusion layer. The width of the intermetallic diffusion layer increases with rolling temperature. For the Al/Ti/Al laminates subjected to cryorolling, the width of the intermetallic diffusion layer ranges from 2.2 to 2.4 μm, but it increases to 2.7 μm for the Al/Ti/Al laminates subjected to hot rolling.

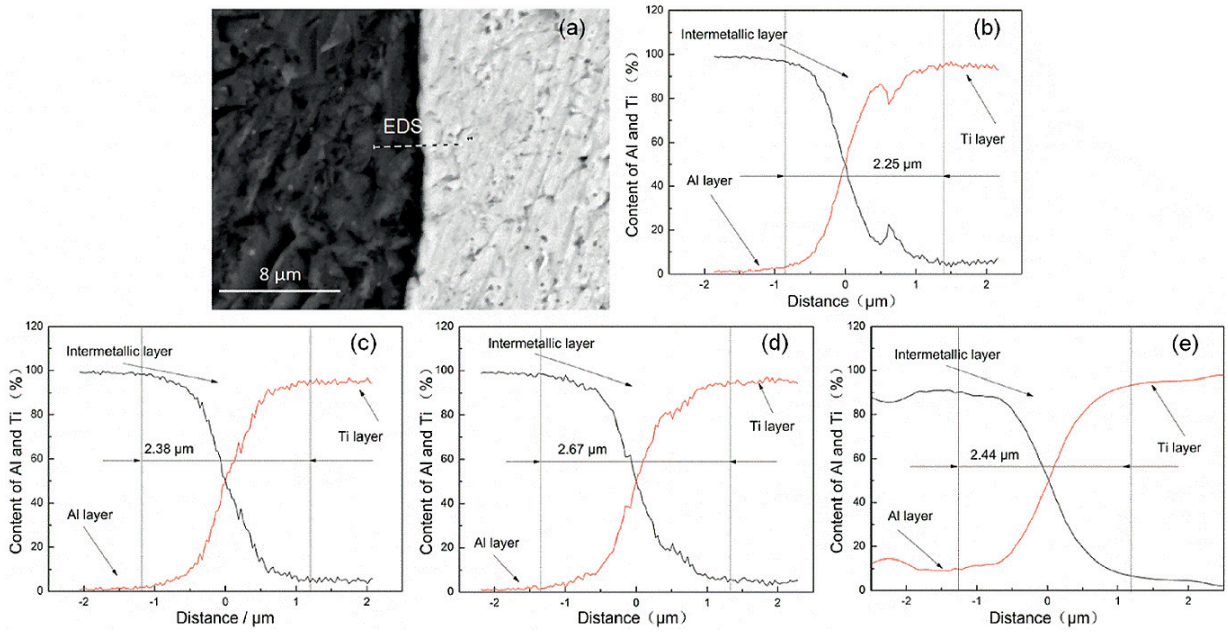


Fig. 4.26 **a** Illustration of the EDS analysis of the Al/Ti/Al laminates. Elemental distribution near the interface in the rolled specimens: **b** cryorolling at −190 °C, **c** cryorolling at −100 °C, **d** cold rolling, and **e** hot rolling

Figure 4.27a shows the peeling strength curves between the Ti layer and Al layer. The interface bonding strength improves with higher reduction regardless of the rolling temperature. The peeling strength curves gave the average peeling strength of the Al/Ti/Al laminates with different processing (Table 4.2**)**. The variation in the average peeling strength with rolling temperature is shown in Fig. 4.27b. The bonding strength of the Al/Ti/Al LC subjected to cold rolling has the lowest value of 6.4 $N{\cdot}mm^{-1}$. This is slightly lower than the sample subjected to hot rolling. The bonding strength of the Al/Ti/Al laminates sample prepared by cryorolling increases versus the samples subjected to cold

rolling. The bonding strength is highest in the −100 °C cryorolled samples—this strength is 7.2 N·mm^{-1} and is 12.5% higher than the sample subjected to cold rolling.

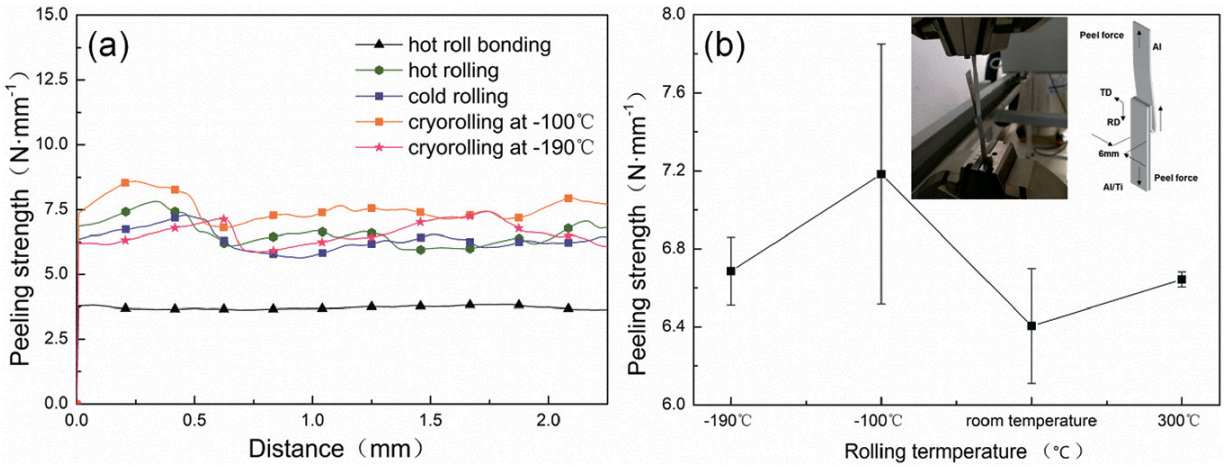


Fig. 4.27 **a** Peeling strength-distance curves of Al/Ti/Al laminates, **b** peeling strength versus the rolling temperature of the Al/Ti/Al laminates with the thickness of 0.42 mm. The illustration in (**b**) shows the schematic diagram of the peeling test

Table 4.2 Peeling strength and tensile properties of Al/Ti/Al laminates with the thickness of 0.42 mm

Rolling temperature	σ_p (N·mm^{-1})	σ_b (MPa)	δ_s (%)	Nanohardness (GPa)	
				Ti layer	Al layer
−190 °C	6.7 ± 0.2	234.8 ± 8.5	10.4 ± 0.1	2.8 ± 0.1	0.50 ± 0.04
−100 °C	7.2 ± 0.7	261.4 ± 1.6	12.4 ± 0.4	2.9 ± 0.1	0.55 ± 0.01
25 °C	6.4 ± 0.3	215.2 ± 2.9	9.4 ± 1.1	2.7 ± 0.02	0.48 ± 0.02
300 °C	6.6 ± 0.1	219.4 ± 0.3	13.2 ± 0.2	2.6 ± 0.1	0.43 ± 0.03

Figure 4.28 shows the SEM morphology of the Ti and Al surface after peeling tests for the specimens prepared after hot roll bonding. There are many cracks on the surface of the Ti side perpendicular to the rolling direction. In addition, there are few residual Al chips on the Ti surface: These are characterized by the bonding mode studied via mechanical locking.

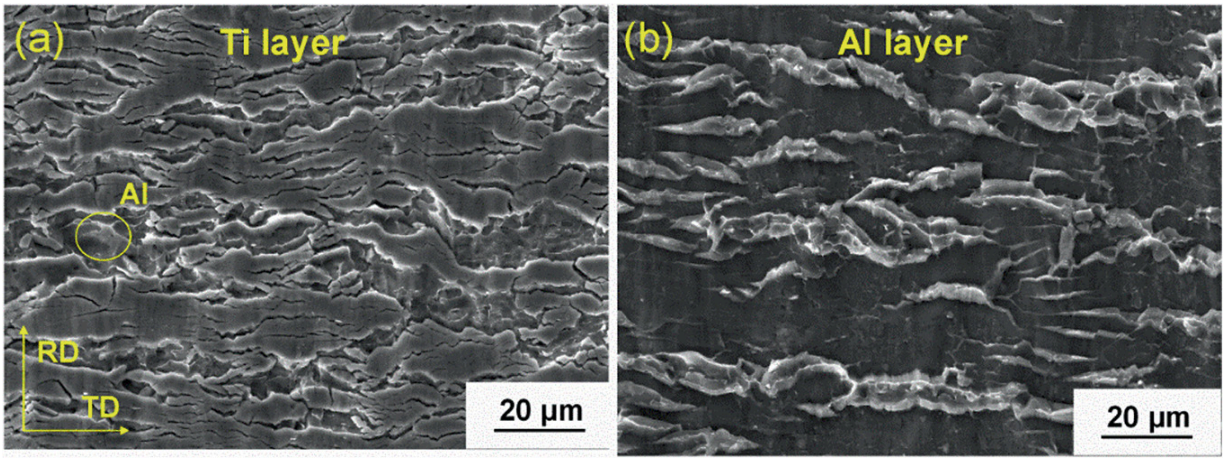


Fig. 4.28 SEM image of surfaces after peeling testing for hot roll bonded specimen: **a** Ti layer and **b** Al layer

The morphologies of the Ti surfaces and Al surfaces after further rolling processing are shown in Fig. 4.29. The cracks on the Ti surface are wider than those on hot roll bonded. the residual Al chips increase like a “ridge”—the ridge width is much wider for the specimen subjected to cryorolling. The formation of this “Al ridge” is because the bonding strength between the Ti and Al layers is higher than the tensile strength of the Al layer. The Al is necked and fractured, and the “Al ridge” forms during peeling. The width of the cracks on the Ti surface first decreases and reaches the minimum value at 25 °C as rolling temperature increases (Fig. 4.29a, c, e, and g). It then widens with increasing rolling temperature. The area fraction of the bond-well area between Ti and Al after peeling tests is shown in Fig. 4.30.

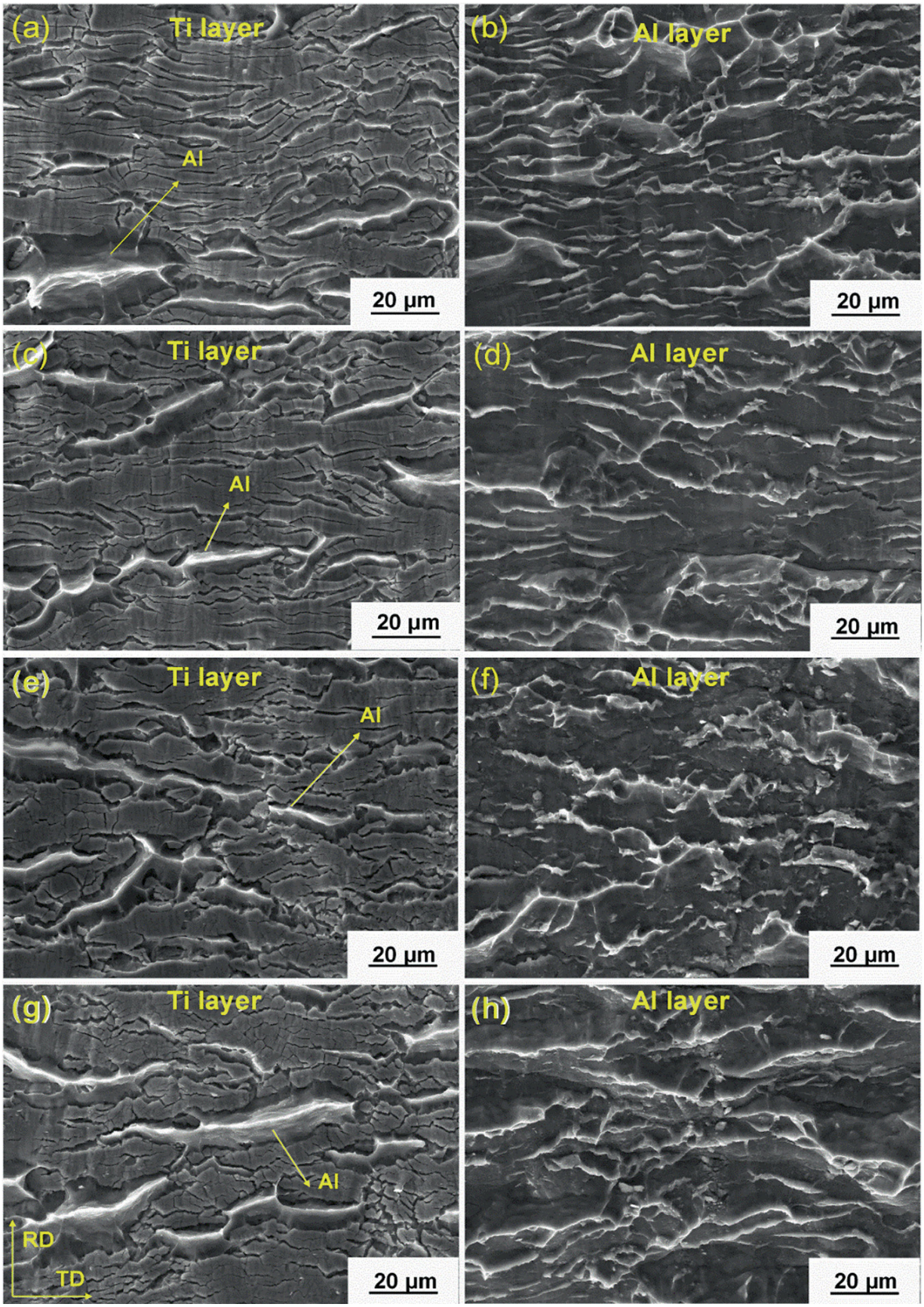

(a)
Ti layer
Al
20 μm
(b)
Al layer
20 μm
(c)
Ti layer
Al
20 μm
(d)
Al layer
20 μm
(e)
Ti layer
Al
20 μm
(f)
Al layer
20 μm
(g)
Ti layer
Al
RD
TD
20 μm
(h)
Al layer
20 μm

Fig. 4.29 SEM images of Ti and Al surface after peeling tests for the specimens subjected to cryorolling at **a**, **b** −190 °C and **c**, **d** −100 °C, **e**, **f** cold rolling, or **g**, **h** hot rolling

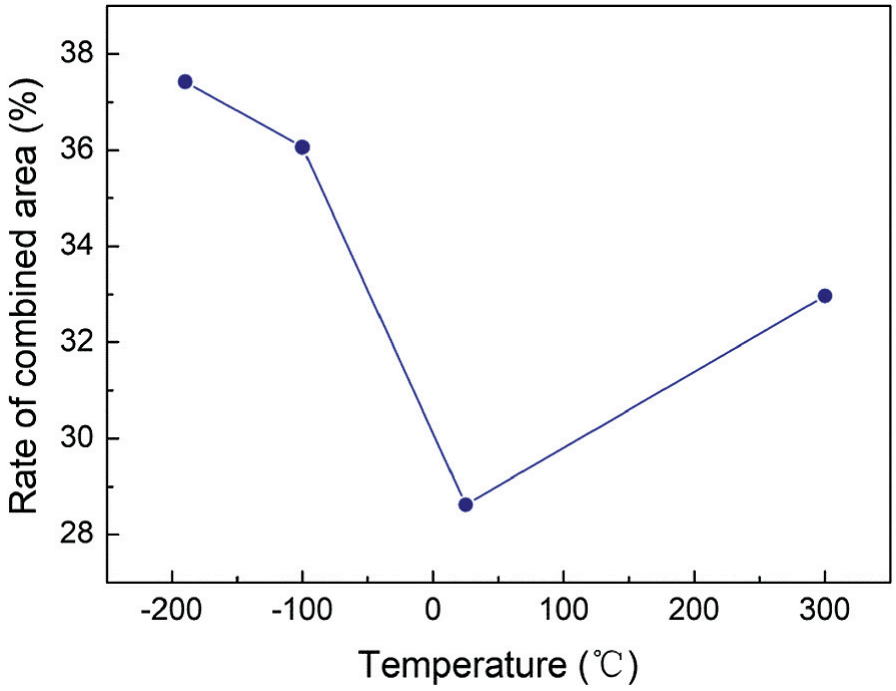


Fig. 4.30 Area fraction of the combined area between Ti and Al after peeling testing

The tensile curves and mechanical properties of the Al/Ti/Al laminates are shown in Fig. 4.31 and Table 4.2, respectively. The results indicate that both cryorolling and hot rolling can improve the tensile strength and ductility of the Al/Ti/Al laminates versus samples subjected to cold rolling. In addition, the Al/Ti/Al laminates subjected to cryorolling at −100 °C have the best properties with a tensile strength of 260 MPa; the failure strain is 12.4%.

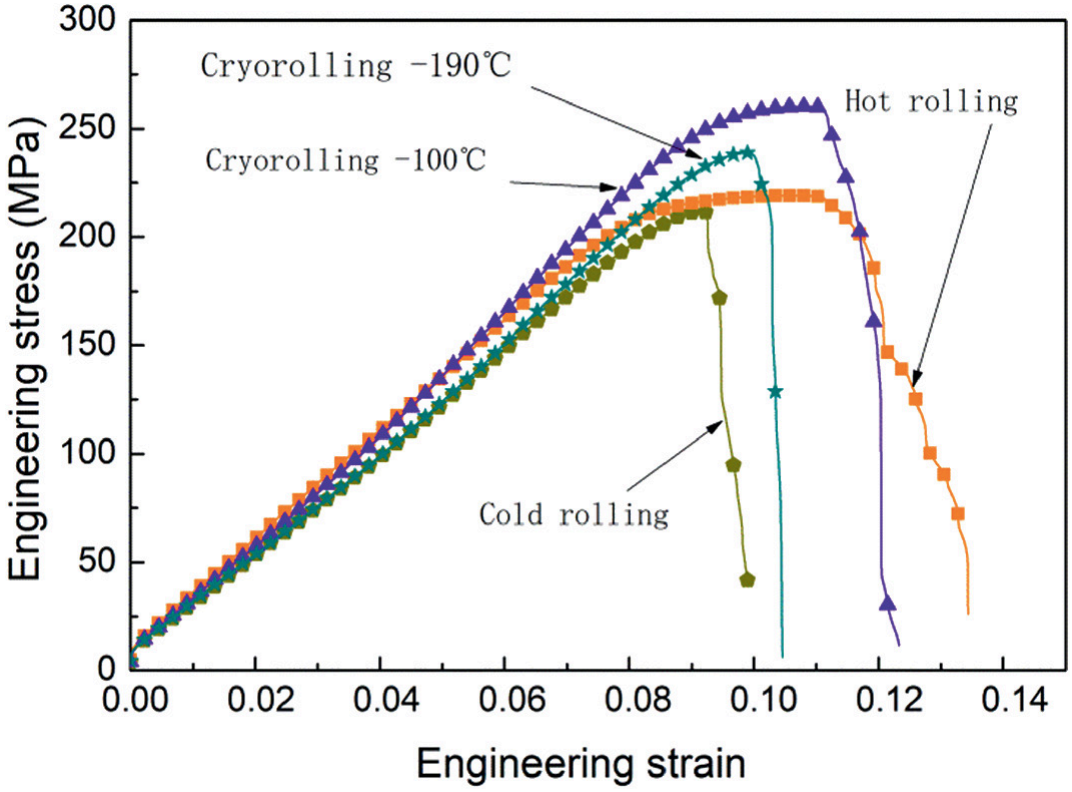


Fig. 4.31 Engineering stress–stain curves of Al/Ti/Al laminates subjected to different rolling processes

Figure 4.32 shows the SEM morphology of the tensile fracture surface. The interface delamination of the Al/Ti/Al laminates can be seen in the tensile fracture. The Al/Ti/Al laminates subjected to cryorolling at −100 °C have obvious dimples in both Al and Ti layers, and the dimples in the Ti layer are nearly the same size. The hot rolled Al/Ti/Al laminates have dimples that appear in the Ti layer and the Al layer; the Al has a ridge-like fracture due to the strong necking. Both the Al/Ti/Al laminates subjected to cryorolling at −100 °C and hot rolling show a plastic fracture with good ductility. However, the Al/Ti/Al laminates subjected to cryorolling at −190 °C or cold rolling have very few dimples on the Al layers and only a few shallow dimples on the Ti layer. There are also a few flat areas on the fracture surface, and thus, the ductility of the Al/Ti/Al laminates decreases.

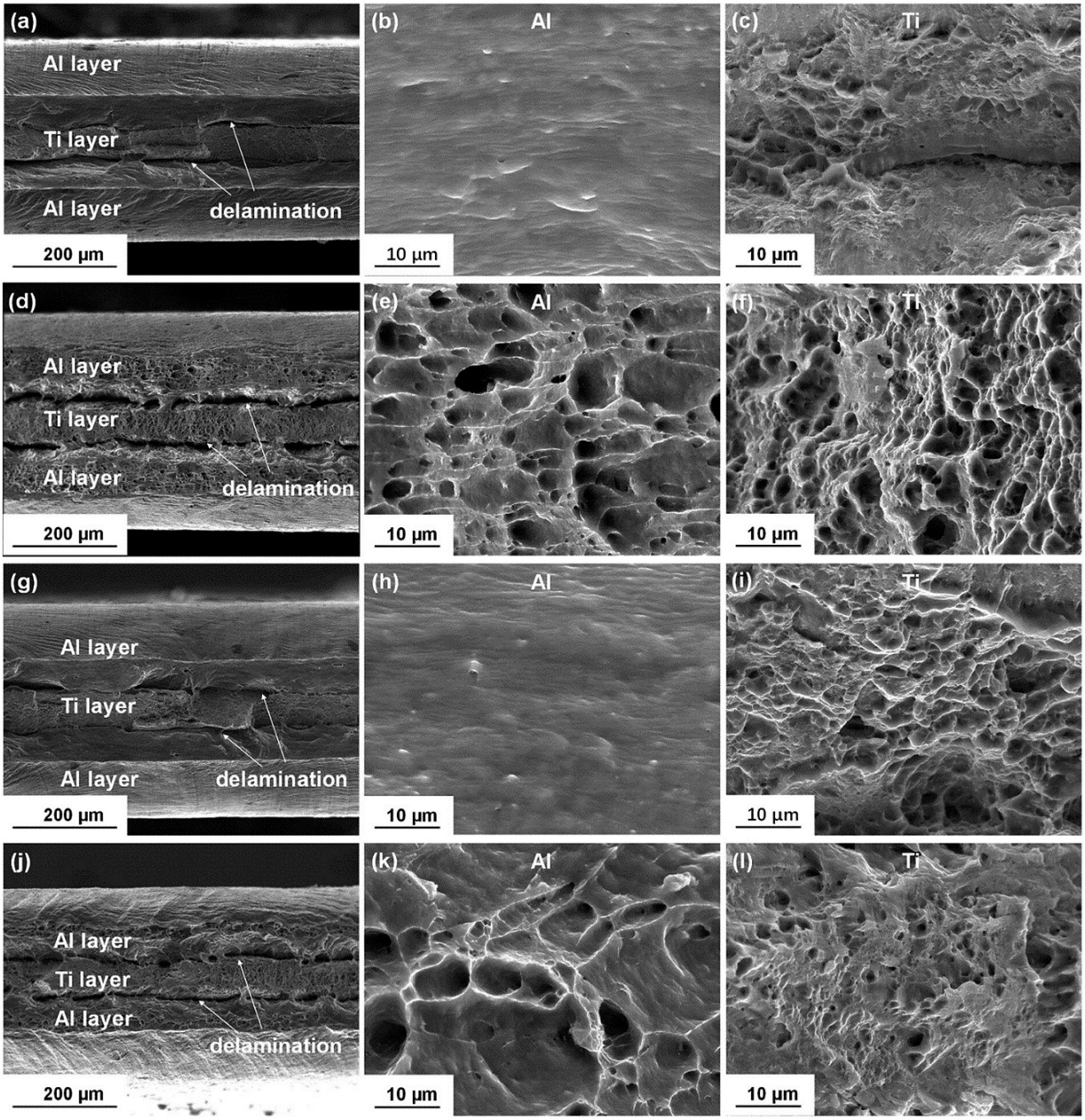


Fig. 4.32 SEM images of fracture surfaces of Al/Ti/Al laminates subjected to cryorolling at −190 °C (**a**, **b**, **c**), −100 °C (**d**, **e**, **f**), cold rolling (**g**, **h**, **i**), or hot rolling (**j**, **k**, **l**)

The nanohardness values of the Ti layer and Al layer of Al/Ti/Al laminates are listed in Table 4.2. The change in the nanohardness of the Al layer and the Ti layer with temperature is shown in Fig. 4.33. The nanohardness value of the Ti layer by cryorolling is lower than 3.25 GPa reported by Fomenko—this is likely because their test load was much smaller than 30 N. In Fig. 4.33, the Al layer and Ti layer have the maximum nanohardness values for the Al/Ti/Al laminates subjected to

cryorolling at −100 °C; these decrease with increasing rolling temperature.

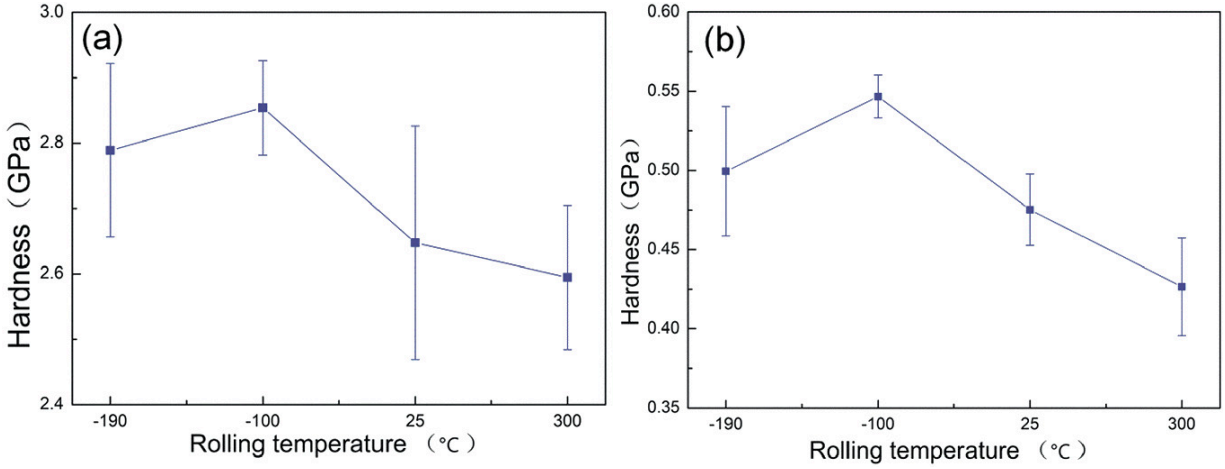


Fig. 4.33 Nanohardness of **a** Al layer and **b** Ti layer subjected to different rolling temperatures

4.3.6 Mechanism of Enhanced Peeling Strength of Al/Ti/Al Laminates via Cryorolling

Severe shear deformation occurs on the surface of Ti and Al layers during Al/Ti/Al laminates rolling due to the different deformation capacity of Ti and Al layers and the difference in friction between the contact surfaces. The cracks first appear on the surface of Ti layer due to its poor deformation ability (Fig. 4.28). The Al will be squeezed into those cracks under the action of the rolling force, which leads to mechanical locking. Generally, the LC bonding mode in the early rolling stage is mechanical locking. Here, the deformation capacity of the Ti layer might decrease with decreasing rolling temperature; the number of cracks increase and the crack size becomes wider (Fig. 4.29a, c, e, and g). More Al squeeze into the cracks, which leads to wider cracks; the mechanical bonding strength is then improved with increasing contact area between the two metals. In addition, cryorolling results in grain refinement, which can improve the strength of the materials (Fig. 4.30). The peeling strength is depended on the strength of Al layer, when the bonding strength is greater than the tensile strength of the Al layer. Thus, the higher tensile strength of the Al layer can increase the bearing capacity of the transverse load at the interface and improves the peeling strength due to improved mechanical locking strength.

In addition, with the formation of the Ti/Al interface, the Ti and Al layers form a solid diffusion system during rolling. Under the action of different atomic concentration, the active Ti (Al) atoms in Ti(Al) layer diffuse into the Al (Ti) layer leading to an intermetallic diffusion layer. The rearrangement of the atoms near the interface results in solution strengthening, and the interface bonding mode changes to metallurgical bonding. Over a certain range, the interfacial bonding strength increases as the intermetallic diffusion layer widens. The width of the interfacial diffusion layer is related to the atomic diffusion rate during rolling. The diffusion modes of the Ti and Al during rolling included atomic displacement, pipe diffusion along dislocations, and plastic deformation-induced vacancies. The energy inside an atom determines whether it can be diffused or not, and the diffusion rate is related to the number of atoms in the activated state. The diffusion rate of atoms in the diffusion system can be characterized by the diffusion coefficient as shown in Eq. (4.4):

$$D = D_0 exp\left(-\Delta E_a / RT\right) \tag{4.4}$$

Here, *D* is the diffusion coefficient, D_0 s the diffusion constant, ΔE_a s the diffusion activation energy (J·mol^{-1}), *R* is the gas constant with a value of 8.31 J·mol^{-1}·k^{-1}, and *T* is the absolute temperature (K). Temperature is the main factor affecting the diffusion coefficient. A higher temperature leads to more energetic atoms, higher frequency of their vibrations, and a greater chance that the energy of the atoms will exceed the barrier. Therefore, the atomic diffusion rate and the width of the diffusion layer at the Ti/Al interface will significantly increase as the temperature increases. The width of the interfacial diffusion layer increases with higher rolling temperature (Fig. 4.26). However, the high temperature may result in Kirkendall voids near the Al/Ti interface, which also affect the bonding strength. Thus, the high metallurgical bonding quality will directly affect the peeling strength.

In conclusion, both mechanical locking and metallurgical bonding determine the bonding strength (σ_B), as expressed in Eq. (4.5):

$$\sigma_B = \alpha\sigma_C + \beta\sigma_M \tag{4.5}$$

Here, the contribution of mechanical locking strength (σ_C) and metallurgical bonding strength (σ_M) are controlled respectively by α and β parameter. On the other hand, σ_C is related to the combined area, and σ_M is related to the width of the interfacial diffusion layer. According to the results in Figs. 4.26, 4.27 and 4.30, it can be known that the mechanical locking plays a key role in the enhancement of bonding strength. And the highest bonding strength was earned by cryorolling (Fig. 4.27).

In Fig. 4.30, the tensile curves of Al/Ti/Al laminates vary in stages. The tensile curves show that the tensile progress of the Al/Ti/Al laminates can be divided into three stages. First, the Ti and Al undergo elastic–plastic deformation, and the stress is maximized. Strain localization and the strain redistribution appear in the specimens due to the change of deformation coordination between Al and Ti. Here, Ti is the main bearing layer, and the existence of the interface on both sides of Ti restricts the deformation behavior of Ti and transfers the strain to the Al layer—this strain transfer improves the bearing capacity of Ti. The constraining effect of the interface changes the deformation behavior of the Ti so that the higher bonding strength can enhance the tensile strength of the laminates.

The second step is a drop in stress, crack initiation and propagation, and interface delamination. When the local stress at the interface exceeds the bonding strength, microcracks will be generated at the weak interface. There will be more cracks as the deformation continues. However, the constraining effect prevents lateral extension of cracks. These can only expand along the interface and will eventually delaminate (Fig. 4.32a, d, g and j). Furthermore, the constraining effect of the interface disappears due to delamination and the rapid decrease in strain.

Third, the Ti layer and Al layer successively fracture. The disappearance of the interfacial constraining effect forms cracks at the interface, and the Ti and Al layers can then expand rapidly; the laminates then fracture. Coarse grains can stop the propagation speed of cracks, and thus the third stage of the laminates subjected to hot rolling is more obvious than those subjected to cryorolling.

In addition to the plastic deformation characteristics and fracture modes, the grain size characteristics of the specimens are another important factor affecting the properties of the laminates. Cryorolling inhibits the occurrence of the dynamic recovery process—it enhances the dislocation accumulation and grain refinement to improve the strength of the Al layer and the Ti layer. For example, the tensile strength and elongation of commercially pure Al were improved by cryorolling. In another example, the grain size of commercial pure Ti cryorolled at −196 °C reached 80 nm with improved microhardness. In addition, some researchers validated the cryorolled metals have finer grains compared to hot rolled sheets with the same rolling reduction ratio. Figure 4.33 shows higher microhardness of Ti and Al prepared by cryorolling. According to the relationship between hardness and yield strength, the strength of single-layer Ti or Al by cryorolling is higher than that subjected to cold rolling and hot rolling. Data on the rule of mixture can be expressed by Eq. (4.6):

$$\sigma = \sigma_{Ti} \cdot V_{Ti} + \sigma_{Al} \cdot V_{Al} \tag{4.6}$$

Here, σ is the strength of the composite, σ_{Ti} and σ_{Al} are the strength of the Ti and the Al layers, and V_{Ti} and V_{Al} are the volume ratio of the Ti and the Al layers. When the volume ratio of each component remains the same, the hardness of singer-layer increases, its strength increases, and the strength of laminate will increase. Thus, cryorolling can improve the strength and ductility of Al/Ti/Al laminates.

4.4 Al/Mg/Al Laminates via Cryorolling

We proposed a two-step rolling process. The present study involved processing the well-assembled Al/Mg-Li laminates using hot rolling (HR), followed by room temperature rolling (RTR) and cryorolling to further improve their mechanical properties. It was observed that, compared to RTR, CR resulted in higher ductility in the laminates. In the end, the mechanisms underlying the enhanced ductility of the laminates were explored [12].

4.4.1 Microstructure Evolution of the Al/Mg/Al Laminates During Rolling

Figure 4.34a depicts the SEM image of the annealed LZ91 alloy. The alloy exhibited a typical dual-phase structure comprising the α-Mg phase distributed uniformly across the β-Li matrix. According to previous studies, the light "islands" are the α-Mg phases, which represent the solid solution phase of the hcp structure with Li soluble in Mg, while the gray regions are the β-Li phases, which represent the solid solution phase of the bcc structure with Mg soluble in Li.
Figure 4.34b–f present the SEM images of the Al/Mg-Li laminates. No evident voids and IMCs could be observed at the bonding interface. In addition, the interfaces in the HR + RTR laminates had become wavy. As the rolling reduction increased, the wavy trend became further evident (Fig. 4.34d), finally leading to the formation of shear bands (Fig. 4.35c and d). However, the flatness of the interface in the HR laminates and HR + CR laminates was relatively good and did not decrease with the increase in rolling reduction. Moreover, the dual-phase structure of the Mg-Li layers in the Al/Mg-Li laminates differed under different rolling processes.

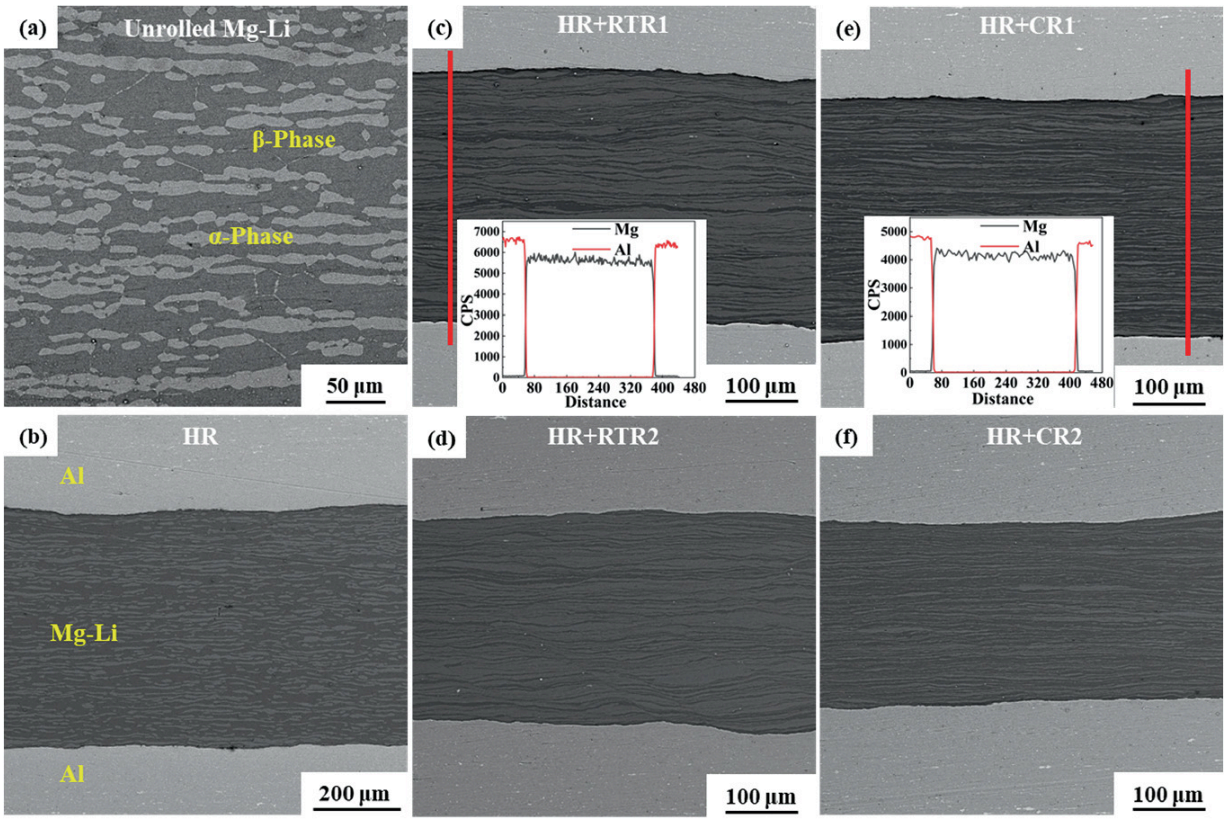


Fig. 4.34 The SEM images of the unrolled Mg-Li alloy and the Al/Mg-Li laminates: **a** the unrolled Mg-Li alloy, **b** the HR laminate, **c** the HR + RTR1 laminate, **d** the HR + RTR2 laminate, **e** the HR + CR1 laminate, and **f** the HR + CR2 laminate

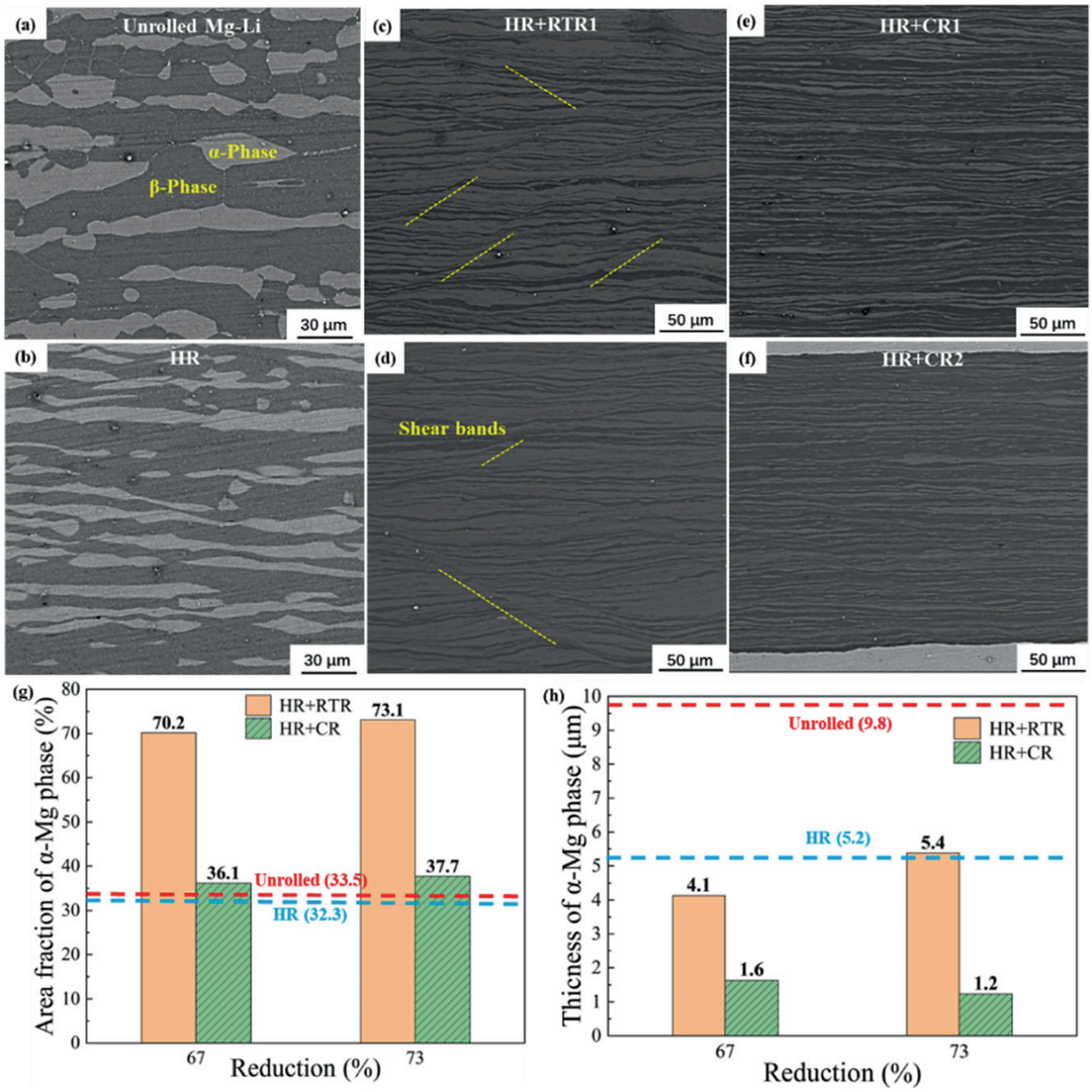


Fig. 4.35 **a**–**f** The morphology of the Mg-Li layer in the Al/Mg-Li laminates under different processes. **g** The volume fraction of the α-Mg phase. **h** The thickness of the α-Mg phase

Figure 4.35 depicts the area proportion of α-Mg phases and the morphology of the Mg-Li layer in the laminates. To facilitate comparison, the subsequent hot-rolled thinned laminates were prepared with the same reduction as that of HR + CR laminate and were designated as HR + HR1 laminate and HR + HR2 laminate. The area

proportion of α-Mg phases in the unrolled Mg-Li alloy was 33.5%, and it was reduced to 32.3% in the HR laminate (Fig. 4.35g), indicating only a slight change in the proportion of α-Mg phases compared to the former. However, the α-Mg phases were stretched into a slender strip structure, with a thickness decrease of 9.8–5.2 μm (Fig. 4.35h). After the HR + HR process, the content of α-Mg phases exhibited no change compared to the HR laminate, although the phase continued to be stretched into a slimmer strip structure with a thickness of 4.6 μm and 3.0 μm for the HR + HR1 laminate and HR + HR2 laminate, respectively. In the HR + RTR processing, the dual-phase structure of the Mg-Li layer changed evidently, and shear bands appeared, indicating great shear deformation. The thickness of the α-Mg phases was 4.1 μm and 5.4 mm, and the area proportion of the α-Mg phases increased significantly with the reduction rate to 70.2% and 73.1% for the HR + RTR1 laminate and HR + RTR2 laminate, respectively (Fig. 4.35c and d). This indicated that the intense strain-induced phase transformation from the β-Li phase to the α-Mg phase occurred during RTR. In the HR + CR process, the area proportion of the α-Mg phase was 36.1% and 37.8% for the HR + CR1 laminate and HR + CR2 laminate, respectively (Fig. 4.35e and f). Compared to HR + HR laminates, the area proportion of the α-Mg phase in the Mg-Li layer under the same strain increased slightly, and the α-Mg phase was stretched into a further slender strip lamellar structure with the thickness of 1.6 μm and 1.2 μm for the HR + CR1 laminate and HR + CR2 laminate, respectively (Fig. 4.35h). This indicated that only a small amount of strain-induced phase transformation could occur during CR.

Figure 4.36 depicts the inverse pole figure (IPF) diagram of the α-Mg phase in the Mg-Li layer and the Al layer. In the IPF diagram, the high-angle grain boundaries (HAGBs) with an angle of over 15° are indicated by black lines, while the low-angle grain boundaries (LAGBs) with angles ranging between 2 and 15° are indicated by gray lines. Figure 5 depicts the grain size distribution and the disorientation angle distribution (DAD) of the α-Mg phases and the Al layer. Regarding the Mg-Li layer, the β-Li phase was not displayed due to a low recognition rate, which was mainly because the β-Li phase was oxidized within a short duration after polishing, and its diffraction pattern was weak.

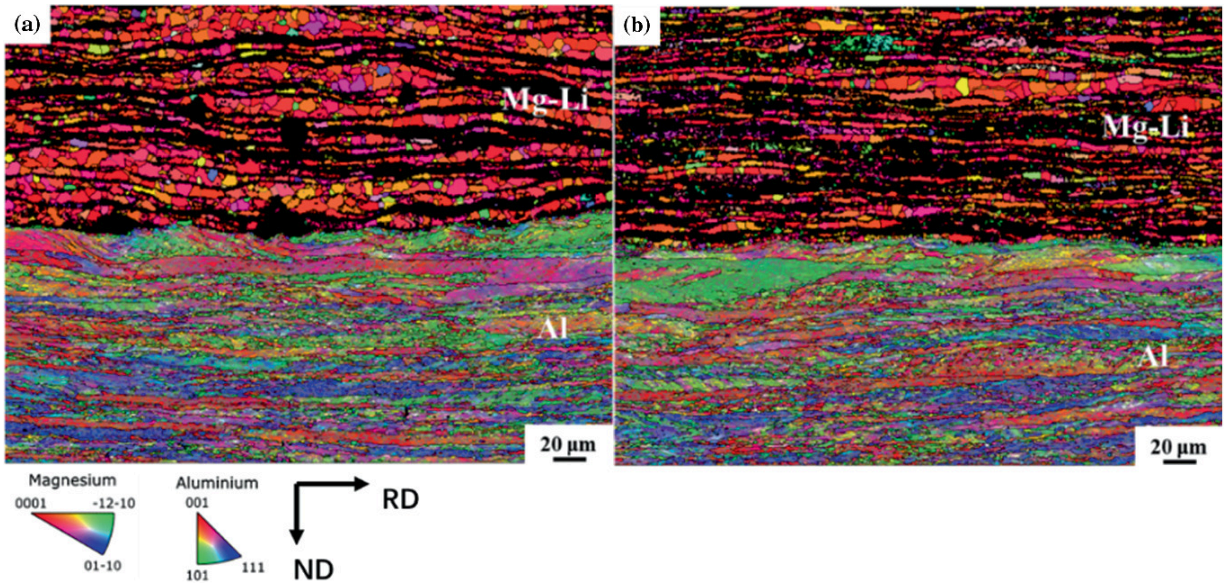


Fig. 4.36 The EBSD-IPF images of the Al layer and the α-Mg phase in the Mg-Li layer. **a** HR + RTR1 laminate. **b** HR + CR1 laminate

For the Mg layers, in the HR + RTR1 laminate, most of the α-Mg phases in the Mg-Li layer comprised multiple and elongated grains (Fig. 4.36a). However, in the HR + CR1 laminate, the distribution of the α-Mg phases was dispersed, with most of them comprising a single tiny grain of α-Mg phase (Fig. 4.36a). In addition, compared to the HR + RTR1 laminate, RTR + CR1 laminate presented a less volume fraction of the α-Mg phase, with their distribution further uniform. When analyzed together with Fig. 4.35, these results indicated that the strain-induced phase transformation from the bcc structure to the hcp structure during CR was less than that during RTR. As depicted in Fig. 4.37a and c, the average grain size of the α-Mg phase in HR + RTR1 laminate and HR + CR1 laminate was 5.14 μm and 4.52 μm, respectively. This indicated that the grain refinement effect of the α-Mg phase was further evident during CR. The proportions of HAGB and LAGB are presented in Fig. 4.37e and g, respectively. Greater LAGBs were observed in the HR + CR1 laminate (38.8%) compared to the HR + RTR1 laminate (18.6%), indicating that CR inhibited the transformation from LAGBs to HAGBs. For the Al layers, as visible in Fig. 4.36a and b, the Al layers were composed of both coarse elongated grains and fine equiaxed grains, with the fine grains distributed among the large deformed grains. This indicated refinement of the partial grains in the Al layers under large plastic deformation. Moreover, it was inferred from Fig. 4.37c, d, f, and h

that the average grain size and the DAD difference in Al layers between HR + RTR1 laminate and HR + CR1 laminate were small.

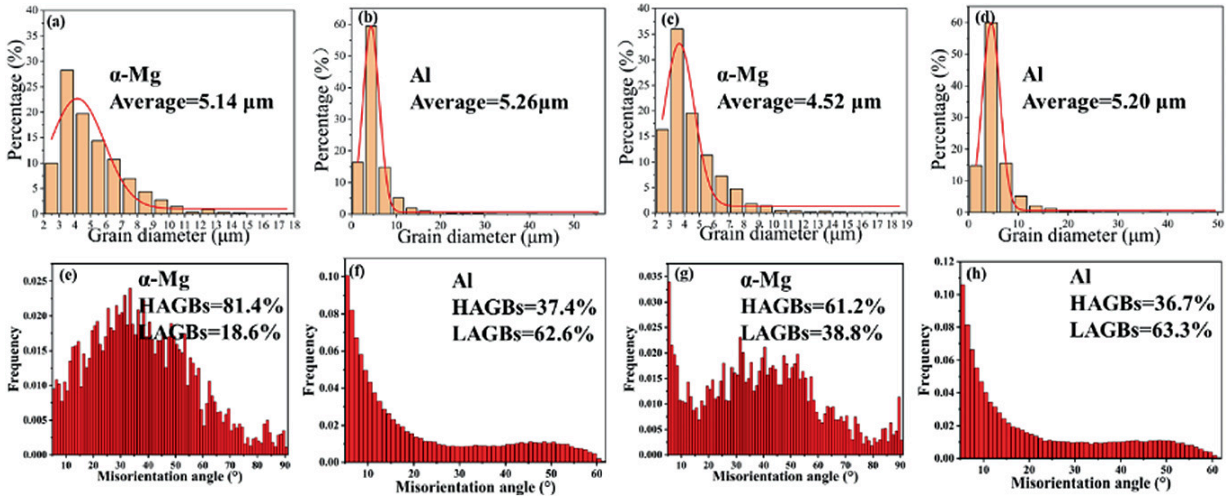


Fig. 4.37 The grain size distribution of the α-Mg phases and the Al layer: **a**, **b** HR + RTR1. **c**, **d** HR + CR1. The DAD of the α-Mg phases and the Al layer: **e**, **f** HR + RTR1. **g**, **h** HR + CR1

Figure 4.38a–d depict the Kernel average misorientation (KAM) diagram and the KAM value distribution. Figure 4.38e and f depict the geometrically necessary dislocation (GND) density map for the red rectangle indicated in Fig. 4.38a and b, which was derived from the KAM diagram and reflected the degree of homogenization of the ductile deformation of the material. A higher GND indicated a greater degree of ductile deformation and a higher dislocation density. As visible in Fig. 4.38a and e, the higher the KAM value, the higher the GND density. The average KAM values of the α-Mg phase in the Mg-Li layer were 0.52° and 0.63° for HR + RTR1 laminate and HR + CR1 laminate, respectively. These data implied that the strain of the α-Mg phase was less during RTR, which further indicated that the β-Li phase bears most of the strain in the Mg-Li layer. Furthermore, as visible in Fig. 4.38f, the fine α-Mg grains surrounded by the β-Li phase had a higher GND density. The average KAM values of the Al layers were 1.35 and 1.45° for HR + RTR1 laminate and HR + CR1 laminate, respectively. When analyzed together with Fig. 4.37, these results indicated that the degree of ductile deformation of the Al layers during the rolling process was larger than that in Mg-Li layers.

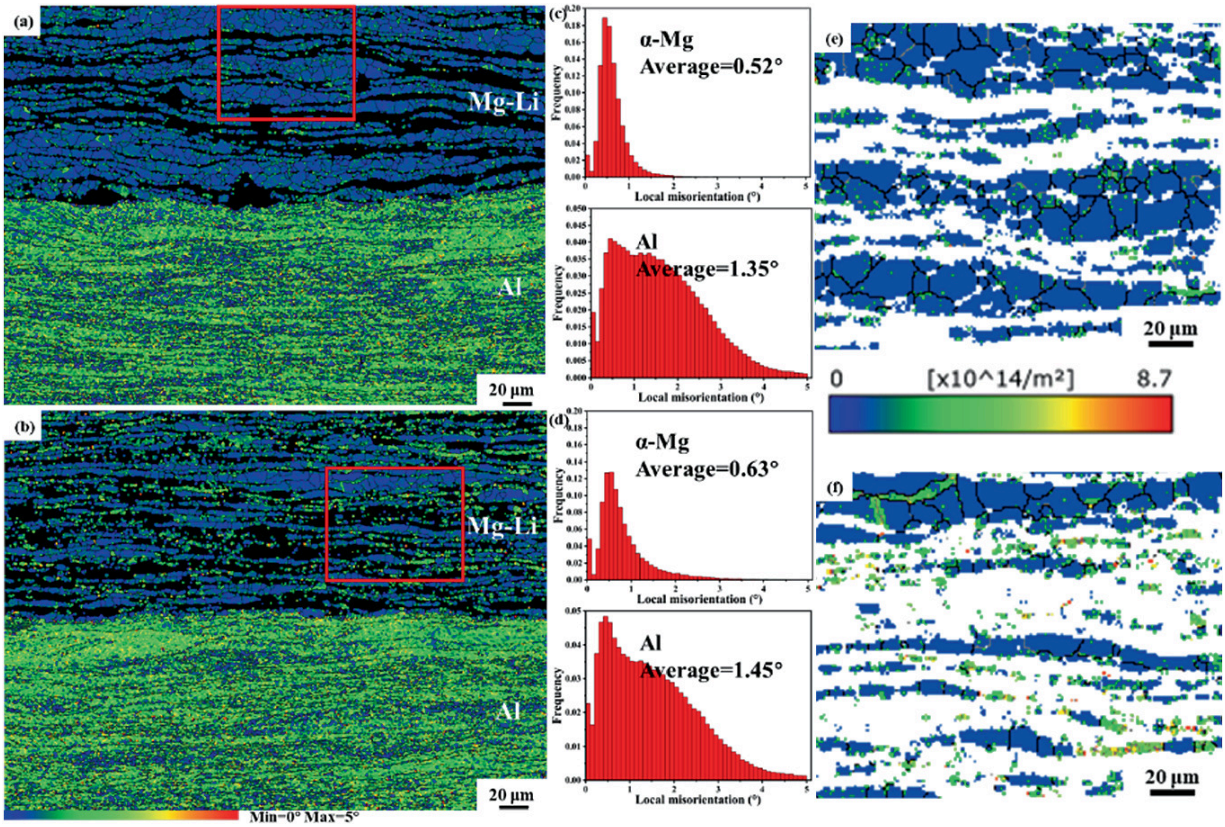


Fig. 4.38 The KAM maps and the distribution maps for the Al layer and the α-Mg phases, respectively: **a**, **c** HR + RTR1. **b**, **d** HR + CR1. **e**, **f** The GND maps for the red rectangles indicated in (**a**) and (**b**), respectively

Figure 4.39 depicts the TEM bright-field diagram for the Al/Mg-Li laminates. In the Al layer, a small number of dislocation tangles were observed under RTR, as visible in Fig. 4.39a and c, while many dislocation tangles appeared at the grain boundaries under CR. It was inferred that a higher accumulating dislocation density improved the mechanical properties of the material. Furthermore, small cracks appeared at the bonding interface under RTR (Fig. 4.39b), while the bonding interface was good under CR (Fig. 4.39d). It could be concluded that CR facilitated the mechanical locking of the laminates.

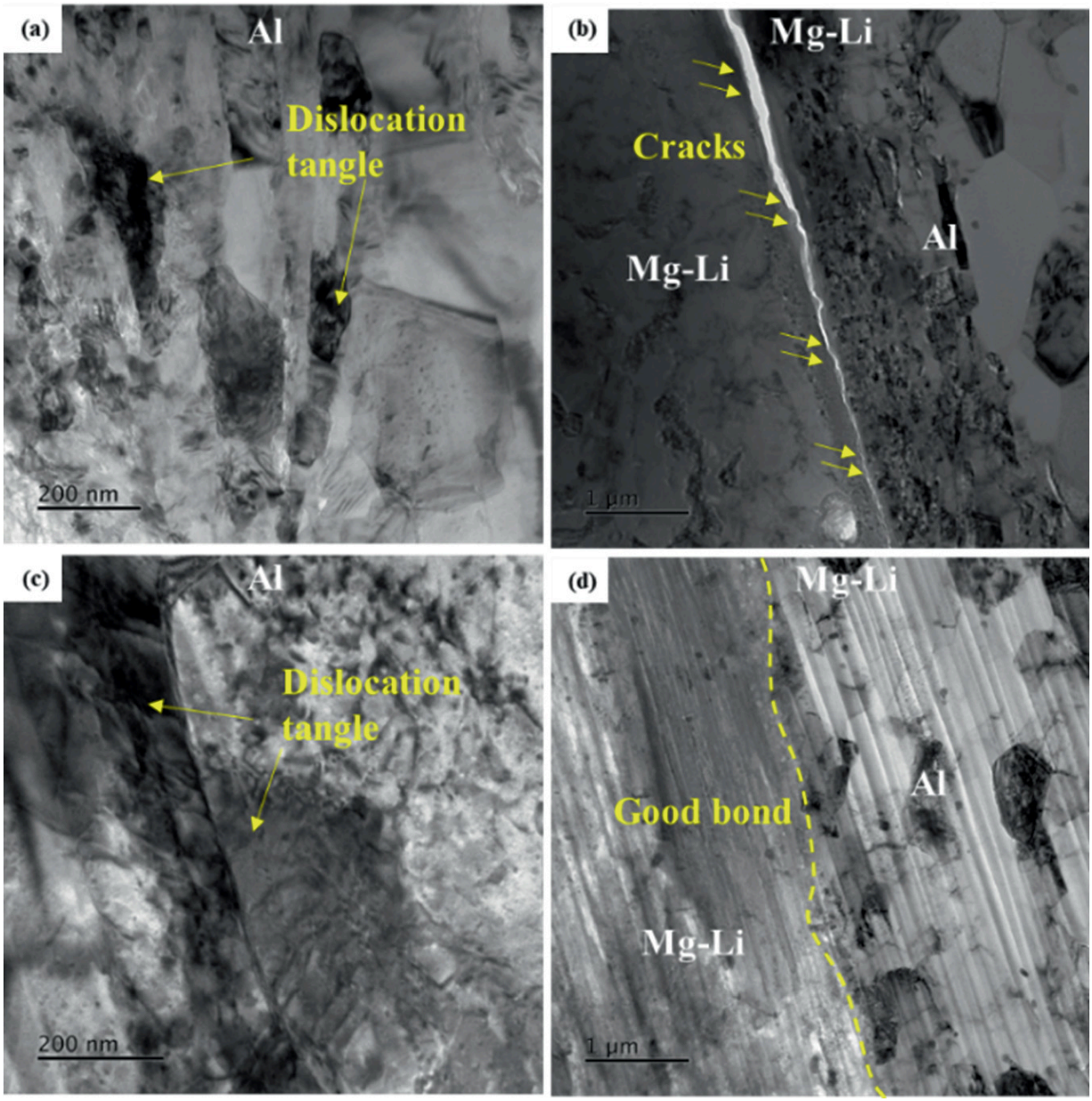


Fig. 4.39 The TEM bright-field images for the Al layers, Mg-Li layers, and the bonding interface of Al/Mg-Li laminates: **a**, **b** HR + RTR1. **c**, **d** HR + CR1

Figure 4.40a and b depict the pole figures of the β-Li phase of the Mg-Li layer in the HR + RTR1 and HR + CR1 laminates, respectively. In order to quantitatively analyze the texture evolution, sections of the orientation density functions (ODF) and evolution of the texture intensity of the β-Li phase, aligned in the α-fiber and γ-fiber, as depicted in Fig. 4.40c–g, were calculated. In the bcc structures, the $\varphi 2 = 0°$ and $\varphi 2 = 45°$ sections were selected for analysis, while the α-fiber and γ-fiber on the $\varphi 2 = 45°$ section were used for demonstrating the changes

of the rolling texture In the φ2 = 0° section, a stronger {001} <110> texture (R-cube) was obtained after both RTR and CR. The {112} <110> texture (R-copper) and the {111} <110> texture (E component) also appeared in the φ2 = 45° section. When analyzed together with the α-fiber depicted in Fig. 4.40f, these results indicated that the strength of the above-stated three rolled textures was higher in CR than in RTR under the same reduction. However, in the γ-fiber, the {111} <112> texture (Y component) of the β-Li phase in HR + RTR1 laminate was stronger than that in HR + CR1 laminate.

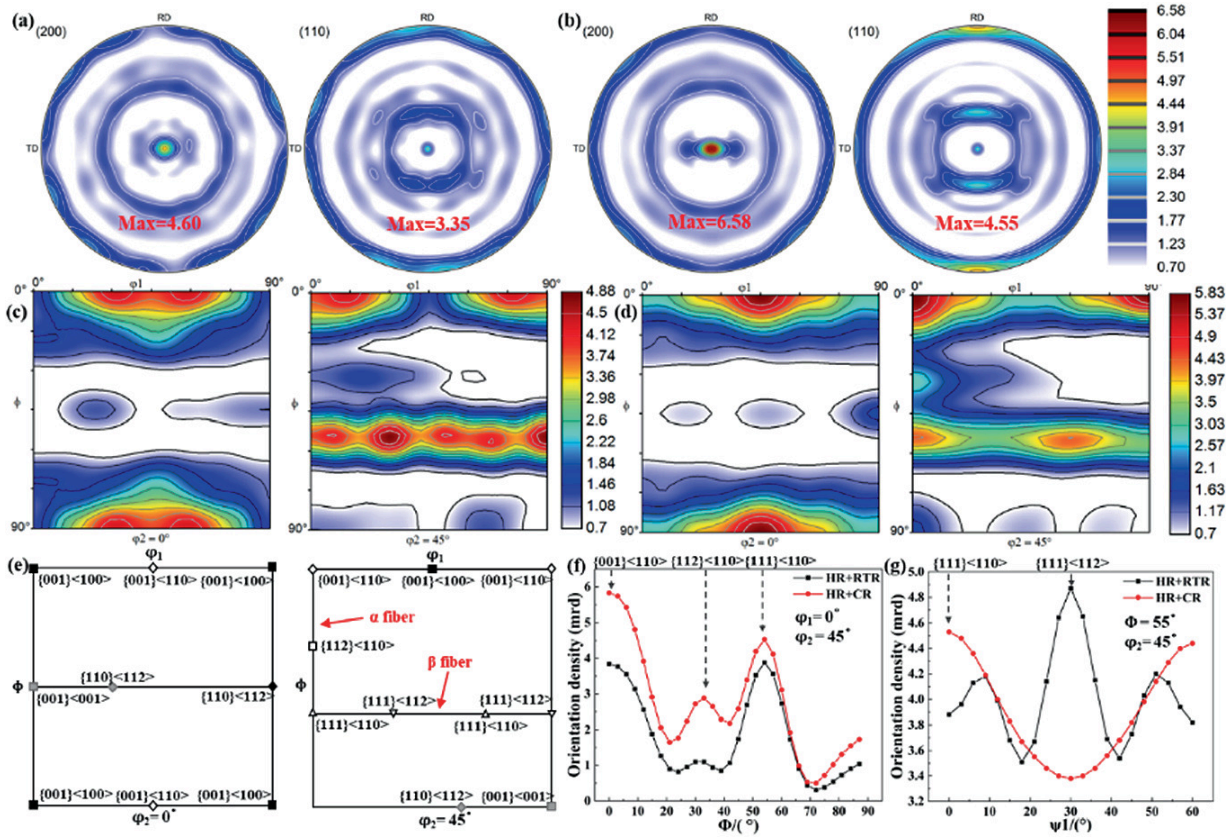


Fig. 4.40 The (200) and (110) pole figures of the β-Li phase: **a** HR + RTR1 laminate. **b** HR + CR1 laminate. The φ2 = 0° and φ2 = 45° sections of the ODF of β-Li phase: **c** HR + RTR1 laminate. **d** HR + CR1 laminate. **e** The schematic figures of the typical texture components of the bcc structure phases in the φ2 = 0° and φ2 = 45° section. The evolution of the texture intensity of the β-Li phase aligned in **f** the α-fiber and **g** γ-fiber

Figure 4.41 depicts the pole figure and the sections of the ODF of the α-Mg phase in the Mg-Li layer. In the HR + RTR1 laminate and HR + CR1 laminate, the α-Mg phase exhibited an evident double peak texture as the basal pole tilt ± (23–40)° from the ND toward the RD and ±(28–40)° from ND toward TD, while the density of the double peak texture

pole in the CR was stronger than that in RTR. The combined analysis of the pole figures and ODF sections led to the conclusion that the main textures of α-Mg phase in HR + RTR1 laminate and HR + CR1 laminate were {11$\bar{2}$0} <0001> prismatic texture and {11$\bar{2}$0} <10$\bar{1}$0> prismatic texture, The densities of the above-stated texture components were higher after CR. This indicated that a greater number of slips were activated during CR. In addition, the α-Mg phases in HR + CR1 laminate exhibited a stronger {10$\bar{1}$0} <0001> prismatic texture and {11$\bar{2}$2} <10$\bar{1}$ $\bar{1}$> pyramidal texture (Fig. 4.41d) than that in HR + RTR1 laminate These results indicated that more prismatic <a> slips, compared to basal slips, were initiated in the Mg-Li layer under the rolling process of laminate.

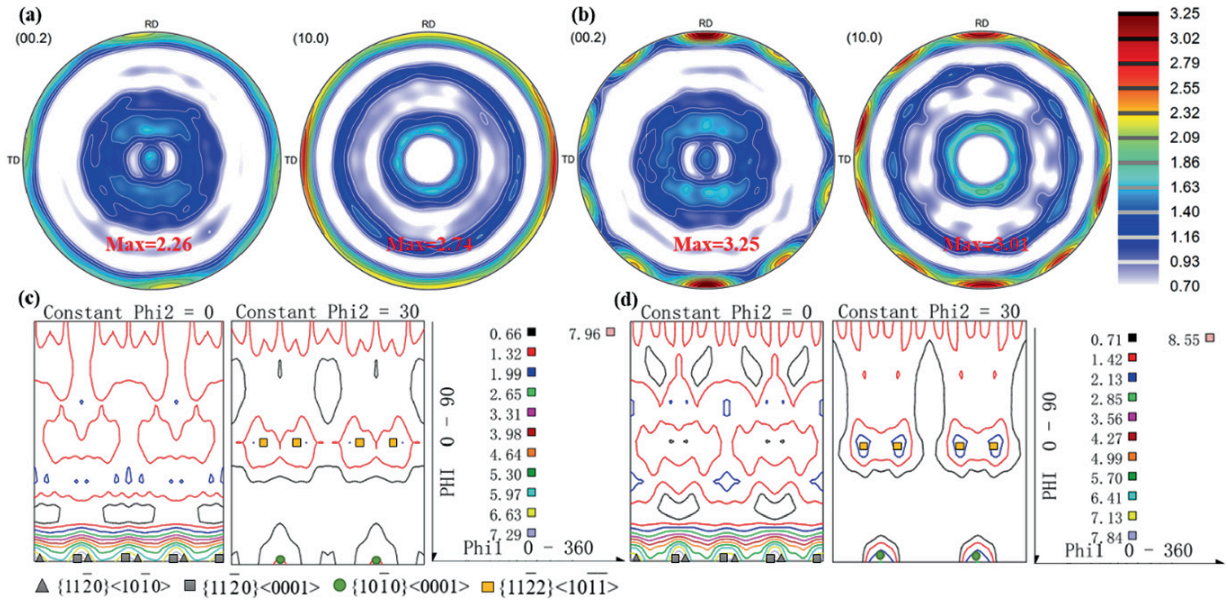


Fig. 4.41 The (0002) and (10 $\bar{1}$ 0) pole figures and the φ2 = 0° and φ2 = 30° sections of the ODF of the α-Mg phase: **a**, **c** HR + RTR1 laminate. **b**, **d** HR + CR1 laminate

4.4.2 Mechanical Properties of the Al/Mg/Al Laminates During Rolling

Figure 4.42 depicts the stress–strain curves, the tensile properties comparison image, and the strain hardening curves. According to the classical rule of mixing (ROM), the strength calculation formula for an laminate composed of two materials is as follows:

$$\sigma = f_{Al}\sigma_{Al} + f_{Mg-Li}\sigma_{Mg-Li} \tag{4.7}$$

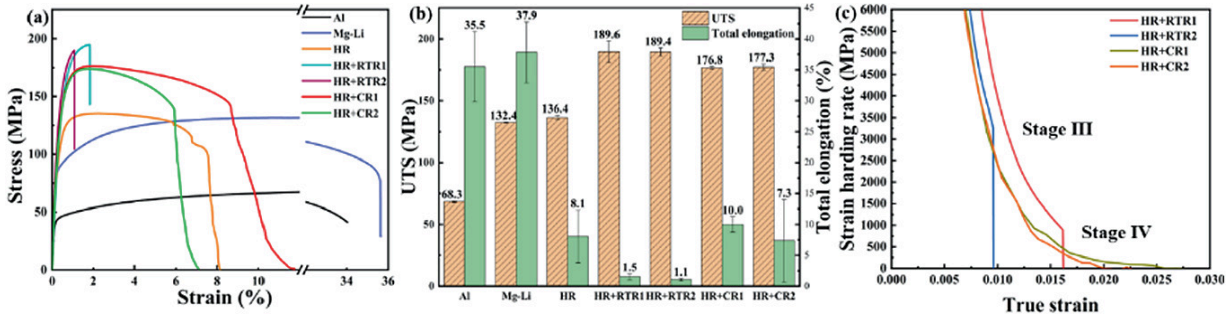


Fig. 4.42 **a** The engineering stress–strain curves. **b** The tensile properties comparison diagram. **c** The strain-hardening curves for the laminates obtained after different rolling processes

where, f and σ denote the volume fraction and the strength of the component layer, respectively. It is generally assumed that the thickness of each layer is distributed uniformly during the rolling process and, therefore, the ratio of the layer thickness represents the volume fraction ratio. Accordingly, the equivalent ultimate tensile strength (UTS) of the laminate without rolling was determined to be 89.7 MPa. After a single hot rolling with a 50% reduction, the UTS of the HR laminate reached 132.4 MPa, which was an increase of 48%, while the elongation decreased to 8.1%. The UTS of HR + RTR1 laminate and HR + CR1 laminate reached 189.6 MPa and 176.8 MPa, respectively, indicating corresponding increases of 111% and 97%. Although the UTS of HR + RTR1 laminate reached the highest value, its total elongation decreased sharply to 1.5%, while the total elongation of HR + CR1 laminate increased to 10%, exhibiting the best comprehensive performance. The UTS of HR + RTR2 laminate and HR + CR2 laminate, on the other hand, remained unchanged compared to HR + RTR1 laminate and HR + CR1 laminate, respectively. However, the total elongation decreased in both. As visible in Fig. 4.42a, the HR + CR laminates exhibited slightly lower UTS compared to HR + RTR, while their total elongation was significantly higher. The tensile curve of the former exhibited a necking stage, while the curve of the latter exhibited direct breaks after reaching the highest point, resulting in low ductility (Fig. 4.42a). This was also visible in the strain-hardening curves (Fig. 4.42c)

Figure 4.43a presents the peeling curves of the laminates. The peel strength is calculated by dividing the average peel force by the width of the specimen. The dotted line in Fig. 4.43a represents the peel strength.

The peel curve of the HR + RTR laminates fluctuated greatly, while the peel curve of the HR + CR laminates was stable, indicating a further uniform mechanical combination between the layers in HR + CR laminates. In addition, the peel strength increased with the increase in the reduction rate, and the maximum peel strength of 5.3 N/mm was exhibited by HR + CR2 laminate, which also had the best smoothness.

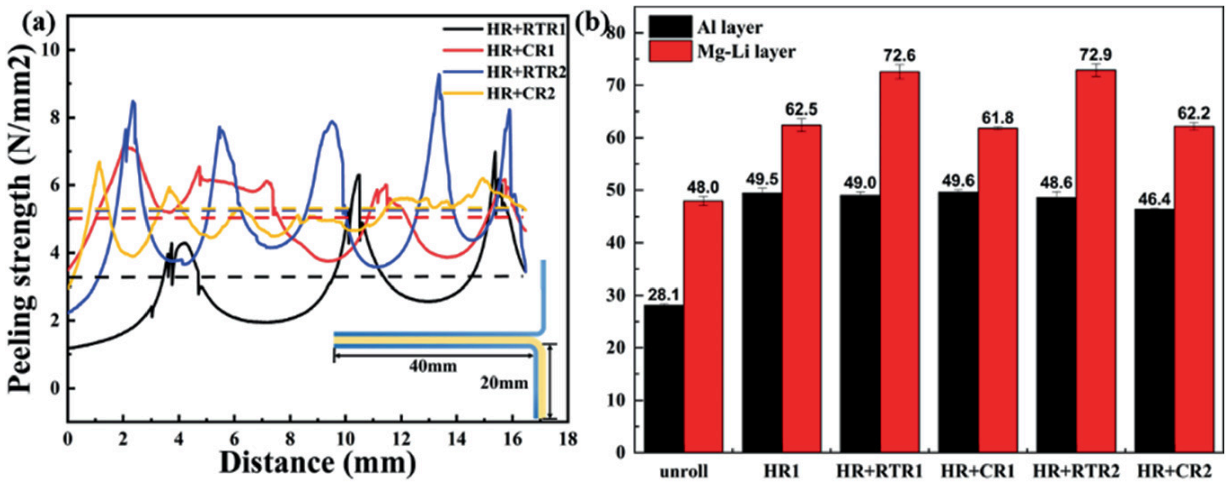


Fig. 4.43 Thw **a** peeling curves and **b** the microhardness of the Al and Mg-Li layers of laminates under different processes

Figure 4.43b presents the microhardness of each matrix layer in the Al/Mg-Li laminates. After HR, the hardness of the Mg-Li layer and the Al layer increased by 30% and 75%, to 62.3HV and 49.5HV, respectively. The microhardness of the Al layer exhibited a little change after the subsequent rolling at different temperatures and different reductions. The reduction also exerted little effect on the microhardness of the Mg-Li layer. However, the microhardness of the Mg-Li layer increased by 50% to 72.6 HV and 72.9 HV after RTR1 and RTR2, respectively. In comparison to the HR laminate, HR + CR laminates exhibited no evident change after CR. According to previous studies, the microhardness of the β-Li phase is lower than that of the α-Mg phase in Mg-Li alloys. The microhardness of HR + RTR laminates was higher than that of HR + CR laminate under the same reduction. When analyzed together with Fig. 4.35g, these results were inferred to be a result of greater β-Li phases in HR + CR laminates compared to HR + RTR laminates. Therefore, it was concluded that, whether the elongation of laminates during the HR + CR process is higher and the tensile strength is slightly

lower than that after the HR + RTR process, would depend on the Mg-Li layer.

Figure 4.44 depicts the tensile fracture morphology of Al/Mg-Li laminates. The interface delamination was observed to occur in all laminates, although the gap between the layers in the fracture morphology decreased with the increase in the reduction rate. As visible in Fig. 4.44a, d, j and g, all the Al layers under the four processes exhibited severe necking and a ridge shape, which indicated a ductile fracture. In the HR + RTR1 laminate, the Mg-Li layer exhibited a relatively smooth brittle fracture with cleavage and quasi-cleavage fracture characteristics, while the Al layer exhibited a ductile fracture with greater dimples on the fracture surface. In the HR + RTR2 laminate, a large cleavage was observed in the Mg-Li layer, and only a few dimples were present in the Al layer. The overall fracture mode of HR + RTR2 laminate was a brittle fracture. In contrast, the HR + CR1 laminate contained uniform dimples in the Mg-Li layer and large and deep dimples in the Al layer. The HR + CR2 laminate exhibited fewer dimples in the Mg-Li layer and shallower dimples in the Al layer compared to HR + CR1. The overall fracture mode in both HR + CR1 laminate and HR + CR2 laminate was a ductile fracture.

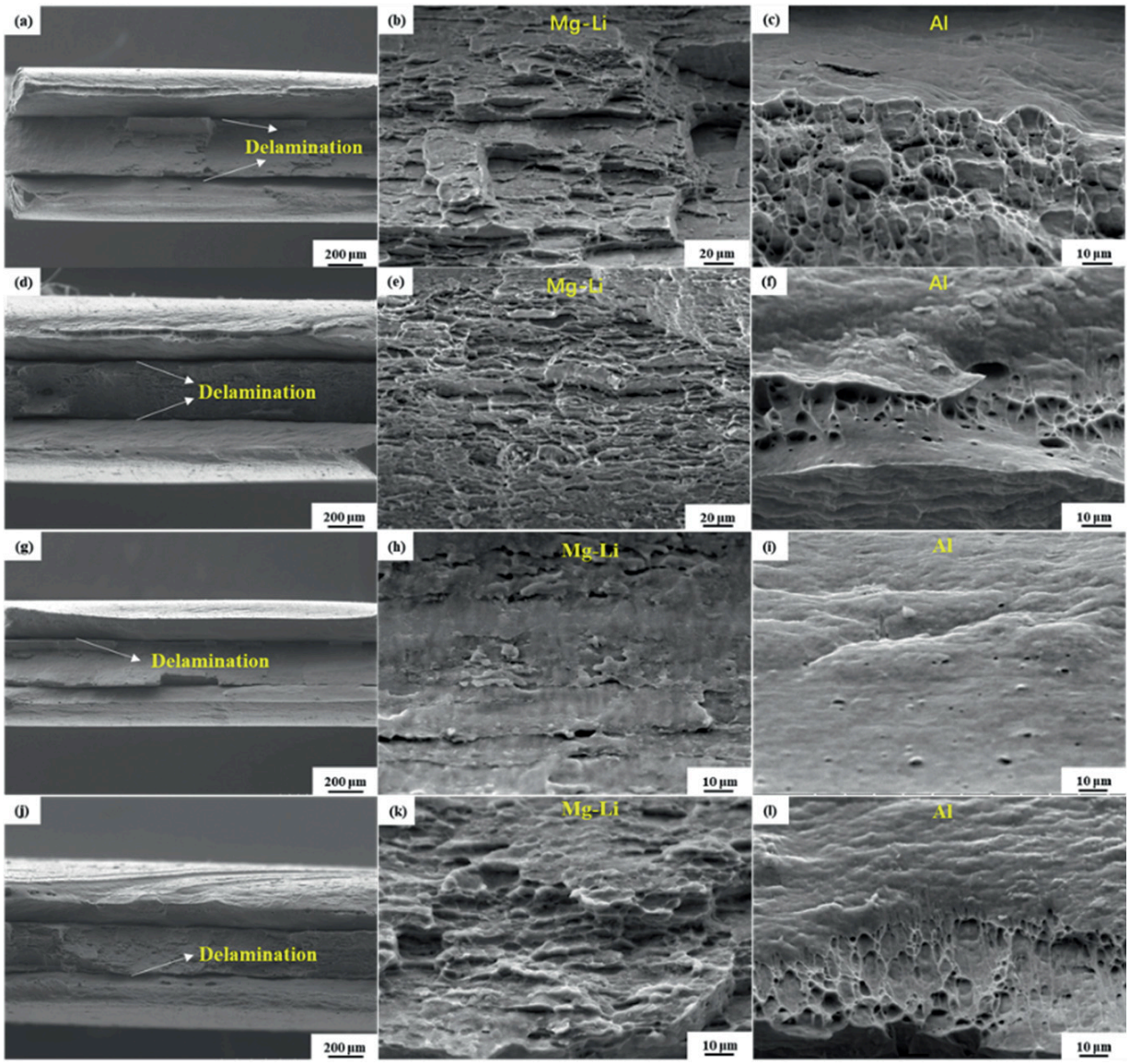


Fig. 4.44 The tensile fracture morphology of Al/Mg-Li laminates: **a**, **b**, **c** HR + RTR1 laminate. **d**, **e**, **f** HR + CR1 laminate. **g**, **h**, **i** HR + RTR2 laminate. **j**, **k**, **l** HR + CR2 laminate

Figure 4.45 exhibits the SEM-BSD and SEM–EDS images of the Mg-Li interface of Al/Mg-Li laminates after peeling. As visible in Fig. 4.45a and d, the Al matrix adhered to the Mg-Li layer of HR + RTR1 laminate was less and aggregated, while the Al matrix adhered to the Mg-Li layer of HR + CR1 laminate after stripping was greater and dispersed. The EDS images revealed that the Al element did not exhibit diffuse distribution in the Mg-Li layer, which implied that the combination kind in the Al/Mg-Li laminates was mainly mechanical bonding. The distribution characteristics of the Al element at the peeling interface of the Mg-Li layer could explain the peeling curves of the laminates. The

mechanical bonding between the Al layer and the Mg-Li layer was further uniform under CR, causing the peeling curve to fluctuate little. However, the distribution of the Al matrix thickness embedded into the Mg-Li matrix under RTR was not uniform, resulting in the peeling curve fluctuating greatly. It indicates that CR promoted the mechanical bonding of laminates.

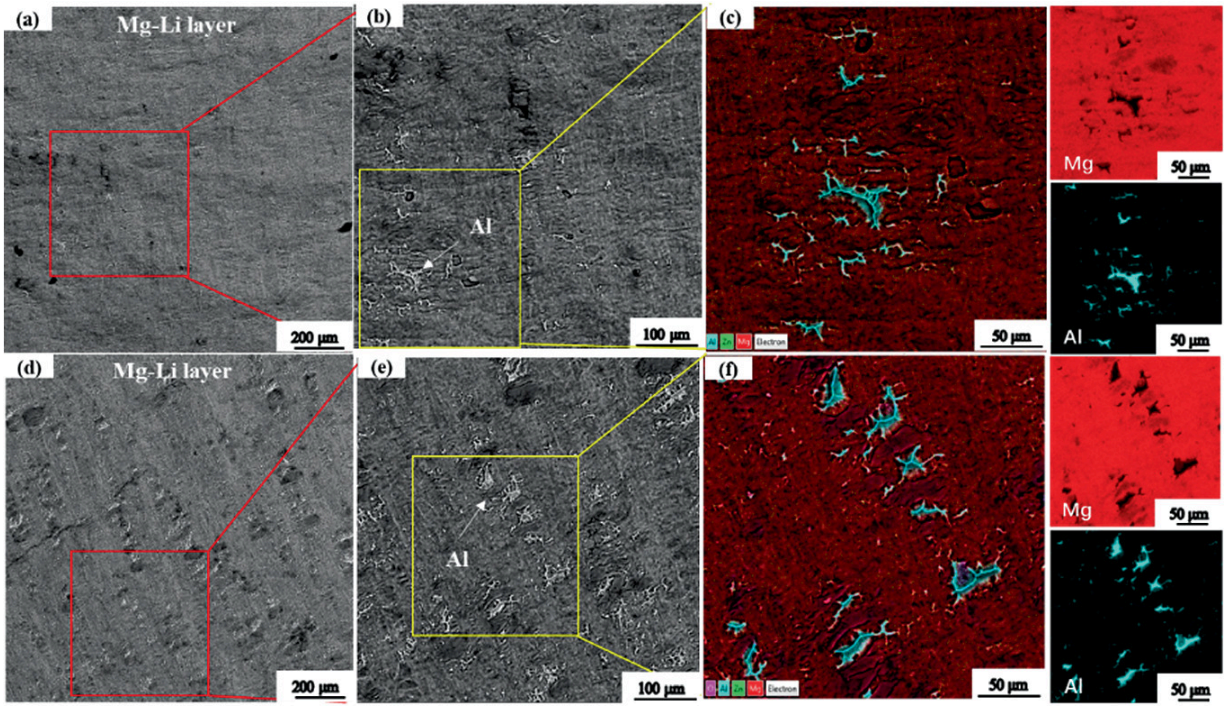


Fig. 4.45 The SEM-BSD and SEM–EDS images of the Mg-Li interface of Al/Mg-Li laminates after peeling: **a**, **b**, **c** HR + RTR1 laminate. **d**, **e**, **f** HR + CR1 laminate

The results of the present study revealed that the ductility of the HR + RTR Al/Mg-Li laminates was low (Fig. 4.42), while the ductility and the tensile strength of the HR + CR laminates were improved significantly. In addition, the dual-phase structure of the Mg-Li layers exhibited evident differences at different rolling temperatures (Fig. 4.35). The grain morphology and the texture strength of the HR + RTR1 laminates and HR + CR1 laminates were also different, which exerted a certain impact on the mechanical properties of laminates. Therefore, it was inferred that the dual-phase structure in the Mg-Li layer, the grain morphology of the laminates, and the texture of the Mg-Li layer contributed to the enhanced ductility.

4.4.3 Microstructure Evolution Mechanism of the Mg-Li Layer During Cryorolling

As visible in Fig. 4.35, the numbers of strain-induced phase transformation in the Mg-Li layer were evidently different. According to previous studies, when the reduction of RTR is over 30%, the strain-induced phase transformation from the β-Li phase into the needle-shape or massive α-Mg phase occurs in the dual-phase LZ91 alloy. In the present study, compared to unrolled Mg-Li (Fig. 4.46a), no phase transformation occurred under 473 K rolling (Fig. 4.46b), while different degrees of strain-induced phase transformation occurred under rolling at 298 K and 77 K (Fig. 4.46c and d, respectively). According to previous studies, the phase transformation is mostly attributed to the reduced deformation temperature, which decreases the Gibbs free energy difference between the β-Li phase and the α-Mg phase ($\Delta G_{(\beta\text{-Li}\rightarrow\alpha\text{-Mg})}$) and the atomic diffusion rate. The phase transformation occur only when $\Delta G_{(\beta\text{-Li}\rightarrow\alpha\text{-Mg})}$ is less than 0.

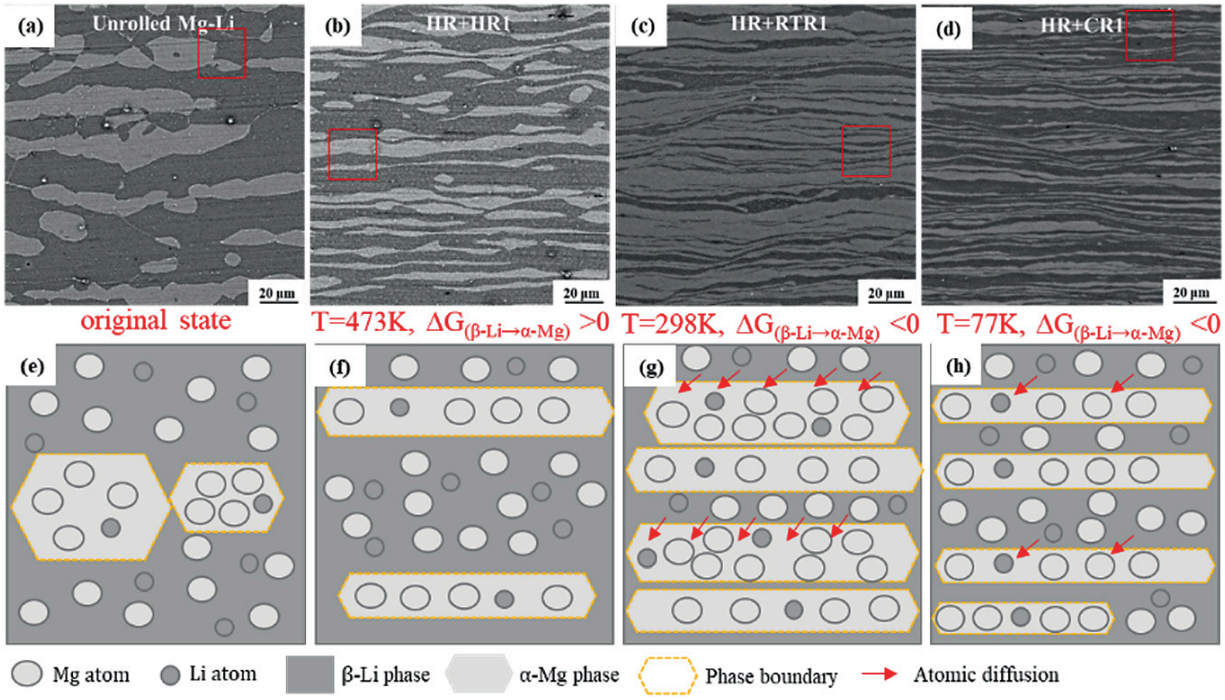


Fig. 4.46 The SEM-BSD image and the phase transformation mechanism of the Al/Mg-Li laminates rolled at different temperatures: **a**, **e** Images for the original Mg-Li alloy. **b**, **f** Images for HR + HR1 laminate. **c**, **g** Images for HR + RTR1 laminate. **d**, **h** Images for HR + CR1 laminate

Figure 4.46e and f illustrate the phase transformation mechanism under different rolling temperatures. HR + HR1 laminate (Fig. 4.46f) exhibited no phase transformation, probably because the chemical driving force $\Delta G_{(\beta\text{-Li}\rightarrow\alpha\text{-Mg})}$ was greater than 0 as the temperature increased. In the case of HR + RTR1 laminate (Fig. 4.46g), the α-Mg phase fraction increased sharply to 70%, which implied that many phase transformations occurred in the Mg-Li layer. Figure 14c depicts that the morphology of a portion of the α-Mg phase changed from strips to chunks under RTR, probably because a large amount of shear stress and compression stress was generated in the intermediate Mg-Li layer under the laminate rolling process with a high reduction. As visible in Fig. 4.38, due to the difference in the yield stress between the two phases, a large number of dislocations accumulated at the phase boundary, which resulted in a large number of lattice defects and sufficient driving energy to promote the phase transformation. According to previous studies, the Mg and Li atoms could also diffuse in a short range at room temperature under severe deformation. Consequently, the volume fraction of the α-Mg phase increased rapidly, and shear bands were formed due to the ductile difference between the two phases. In conclusion, the phase transformation could be promoted by the increased atomic diffusion rate and enough driving energy. HR + CR1 laminate (Fig. 4.46h) presented no shear band and a certain degree of strain-induced phase transformation in the Mg-Li layer, which indicated that the phase transformations were reduced during CR. The element transfer and crystal structure change require sufficient driving force when phase transformation occurs. While the deformation energy promotes the nucleation of the new α-Mg phase at a defect, the insufficient driving force and gradual atomic diffusion rate in the cryogenic environment led to the formation of only a few new phases. Therefore, the α-Mg phases were distributed uniformly throughout the β-Li matrix, and the β-Li phase fraction did not decrease dramatically in the HR + CR1 and HR + CR2 laminates. In Mg-Li alloy, the β-Li phase is a soft phase, which preferentially bears the deformation pressure during the deformation process. In addition, the bcc structure could initiate many slip systems in the deformation (Fig. 4.40), thereby leading to good ductility. This could be one of the reasons why the elongation of HR + CR laminate was greater than that of HR + RTR laminate.

The fraction and morphology of the α-Mg phase in the Mg-Li layers exert significant influence on the plasticity of laminates. According to the tensile fracture of the Al/Mg-Li laminates, as depicted in Fig. 4.44, necking occurred at the fracture stage of the Al layer under the four processes, leading to good ductility, while the Mg layers presented ductile fracture and brittle fracture under RTR and CR, respectively, indicating that the elongation of the laminates relied mainly on the ductility of the Mg layers. Figure 4.42c depicts the strain hardening rate curves of the samples rolled under different processes. The total elongation of the HR + CR laminates was much higher than that of the HR + RTR laminates (Fig. 4.42a and b) due to the appearance of Stage IV in the strain hardening curves (Fig. 4.42c). According to previous studies, the strain hardening curves of the HR + CR laminates may be divided into two stages, with the following two observations: a linear decrease in the strain hardening rate (Stage III), a low and stable strain hardening rate (Stage IV). The low strain hardening rate in Stage IV reportedly occurs more in dual-phase structural materials. Stage IV development is significantly influenced by the strain that passes from the "hard phase" (the α-Mg phase) to the "soft phase" (the β-Li phase). In the present study, the proportion of the β-Li phase in the Mg layers in HR + CR laminates was higher because the strain-induced phase transformations were reduced under CR (Fig. 4.35g). Studies have demonstrated that the plasticity of the Mg-Li dual-phase alloy relies mainly on the proportion of the soft phase. Since a greater proportion of the soft phase is favorable to bearing strain and a refined hard phase could bear strain simultaneously (Fig. 4.38b), continuous Stage IV appeared in the strain hardening curves of HR + CR laminates, increasing the ductility of the Mg-Li layer and delaying the overall fracture of the laminates. No Stage IV appeared in the strain hardening rate curve of HR + RTR laminates. The fraction of hard phases increased sharply in HR + RTR1 laminate and HR + RTR2 laminate (Fig. 4.35g). In particular, the width of hard phases was huge, and their KAM value, particularly for the interior phase, was low, which led to low ductile deformation. Therefore, the strain incompatibility between the phases was poor and the ductility difference of Al and Mg layers is large. As tension strain increased, cracks were more likely to be initiated at the

phase boundary and the interface of layers, which led to a fracture in the HR + RTR1 laminate after a short duration of Stage III.

The grain morphology of the laminates rolled at different temperatures was different. In the Mg-Li layers, as depicted in Fig. 4.37a and c, the average grain size of the α-Mg phase in HR + RTR1 laminate was coarser than that in the HR + CR1 laminate. In addition, as depicted in Fig. 4.35f, the β-Li phase was further abundant in the Mg-Li layer of HR + CR1. Strain and stress are more likely to accumulate in the β-Li phase due to its more slip systems than the α-Mg phase, indicating that the α-Mg grains surrounded by β-Li phases have less deformation energy for grain growth. Therefore, the refined α-Mg grains of the Mg-Li layer in HR + CR1 laminate were mostly distributed adjacent to the β-Li phase. HR + CR1 laminate has a greater fraction of LAGBs compared to HR + RTR1 laminate (Fig. 4.38e and g), indicating that the transformation from LAGBs to HAGBs are inhibited in α-Mg phases due to the lack of driving energy. In Fig. 4.38f, the higher GND density of the α-Mg grains surrounded by β-Li phases in HR + CR1 laminates indicated that fine α-Mg grains could undergo greater strain which improved the ductility of the laminate. In the Al layer, under high-reduction deformation, the grains were elongated into strip-like coarse grains, and many LAGBs were formed due to the rearrangement of dislocations. Unlike CR, RTR generated the heat of deformation that promoted dislocation migration, resulting in the transformation of partial LAGBs into HAGBs with dislocation migration. In summary, the average KAM value of the Al layer and the Mg-Li layer under CR was greater than that under RTR, indicating thatCR could significantly reduce the the thermal activation recovery process, thereby increasing the dislocation density and the refined grains.

The ductility of the Mg-Li alloy is also affected by its texture. While slip and twinning affect the grain orientation, since the twinning behavior of the Mg-Li alloy is limited, the effect of slip on the texture holds greater significance. In the β-Li phase of the bcc structure (Fig. 4.40), {110} <111>, {112} <111>, and {123} <111> were the main slip systems in most of the bcc structural material. In the present study, the HR + RTR1 had {110} <111> and {123} <111> as the main activated slip systems. Therefore, a strong Y component appeared. On the other hand, in HR + CR1, a greater {112} <111> slip was activated addition to

the {110} <111> and {123} <111> slip systems, which led to the strong R-cube and E components. In summary, more slip systems were activated in the β-Li phase of HR + CR laminates. In the case of α-Mg phases with an hcp structure (Fig. 4.41). Evidence suggests that the rolling temperature and the axial size (c/a) exert significant influence on the slip behavior of α-Mg. When c/a <1.633, the prismatic <a> slip replaces the basal slip to become an important slip system in the α-Mg phase. As depicted in Fig. 4.41, prismatic slip plays a leading role in the deformation of α-Mg in the Mg-Li layer, which usually leads to the expansion of the basal axis along TD. In addition, the expansion of the basal axis along RD is usually attributed to the activation of the pyramidal <c + a> slip system. As visible in Fig. 4.40c and d, the prismatic texture and pyramidal texture of HR + CR1 laminate was stronger than that of HR + RTR1 laminate, indicating that cryogenic temperature is conducive to initiating the prismatic <a> slip and pyramidal <c + a> slip systems. It was concluded that, under CR, the α-Mg phase and the β-Li phase of the Mg-Li layer in laminates exhibited more activated slip systems. Furthermore, α-Mg phases were distributed evenly in the β-Li matrix in HR + CR laminates. Compared to the HR + RTR laminates, the narrow α-Mg phase enclosed in the β-Li phase produced internal stress along the phase boundary, which activated more slip systems to share the strain for the α-Mg phase. As visible in Fig. 4.38b, in the Mg-Li layer of the HR + CR1 laminate, the KAM value of the refined α-Mg phases surrounded by the β-Li matrix was larger, which indicated that the α-Mg phases also bear a portion of the stress and strain. Therefore, in the HR + CR laminates, both α-Mg and β-Li phases bear the stress and strain together, which delays the initiation of cracks in the Mg-Li layer and causes it to co-deform with the Al layer, thereby improving the overall ductility of the laminates.

4.5 Cu/Al/Cu Laminates Subjected to Cryorolling

We investigated the mechanical properties and the microstructure evaluation of sandwich-like Cu/Al/Cu composites subjected to hot rolling, cold rolling and cryorolling respectively. We found that grain

size, bonding strength, and thickness of intermetallic layer have significant effects on both the ductility and the tensile strength of the sandwich-like Cu/Al/Cu composites [13].

4.5.1 Microstructure and Mechanical Properties of Cu/Al/Cu Laminates

Figure 4.47a shows the mechanical properties of the sandwich-like Cu/Al/Cu composites. After hot roll bonding, the ultimate tensile strength and the max failure strain of the sandwich-like Cu/Al/Cu composites are 207 MPa and 0.137 respectively. It is obvious that the Young's modulus of the composites subjected to further rolling are steeper compared to that subjected to hot roll bonding, which can be contributed to the refined grains during rolling. The Young's modulus of the samples subjected to hot rolling and cold rolling are steeper than the ones subjected to cryorolling duo to the increased thickness of AlCu intermetallic layer. Compared to the Young's modulus of the cryorolled composites (−190 °C), the Young's modulus of the cryorolled composite (−100 °C) is small resulting from the different bonding quality and the mean grain size. After further rolling, the highest ultimate tensile stress and the max failure strain were obtained for the composites subjected to cryorolling at rolling temperature −100 °C, as shown in Fig. 4.47b, which are 355 MPa and 0.096 respectively. When the rolling temperature is −190 °C, the ultimate tensile stress decreases slightly to 350 MPa, but the max failure strain decreases to 0.079. When using cold rolling or hot rolling, the mechanical properties drop greatly, and the ultimate tensile stress and the ductility decrease to 340 MPa, 0.073 and 304 MPa, 0.069 respectively. In addition, the non-uniform deformation of the composites subjected to cryorolling is lower than that subjected to hot rolling.

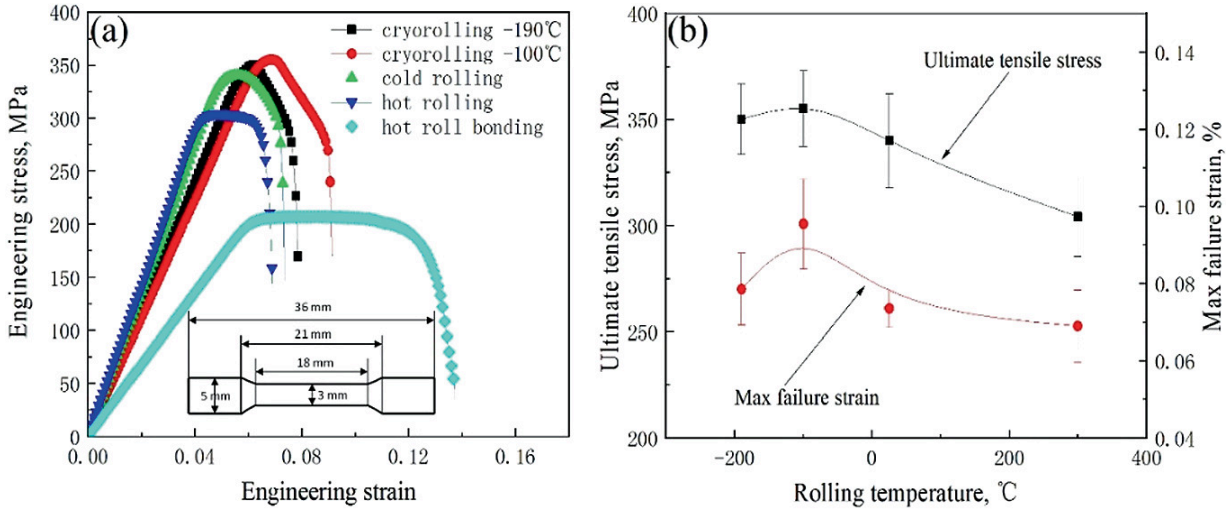


Fig. 4.47 Mechanical properties of the sandwich-like Cu/Al/Cu composites. **a** Engineering stress–strain curves. **b** Ultimate tensile stress and max failure strain as a function of rolling temperature

Figures 4.48 and 4.49 show the microstructure of the Cu layer and Al layer respectively. The grains in Cu and Al are typical laminated structures after rolling processing. When using the cryorolling at −190 ºC, the average Cu grain size and Al grain size are 0.8 μm and 2.1 μm respectively. With increasing the rolling temperature, the grain sizes (thickness of elongated grain) increase, and the average grain size of Cu layer are 1.2 μm, 3.5 μm, 7.1 μm and the average grain size of Al layer are 2.6 μm, 6.2 μm, 7.5 μm for the sandwich-like Cu/Al/Cu composites subjected to cryorolling at −100 °C, cold rolling and hot rolling, respectively.

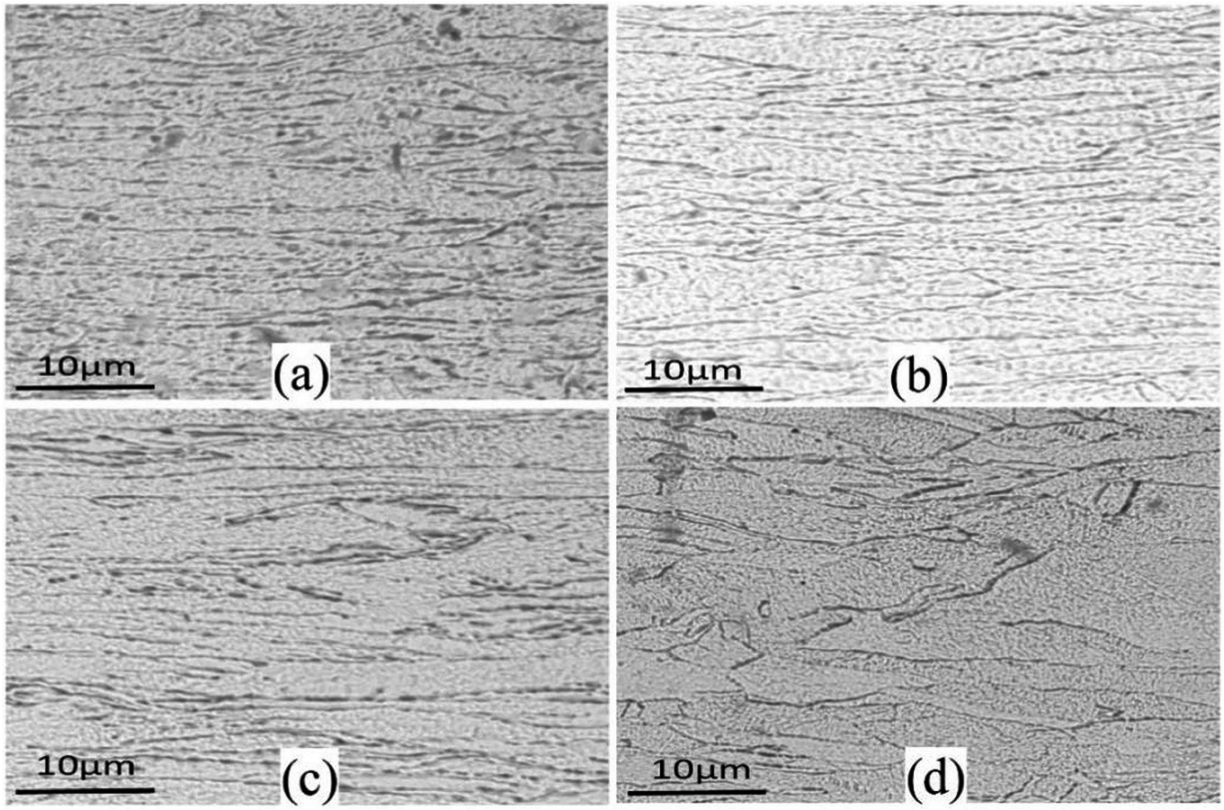


Fig. 4.48 SEM images of the microstructure in Cu layer, **a** cryorolling −190 °C; **b** cryorolling −100 °C; **c** cold rolling and **d** hot rolling

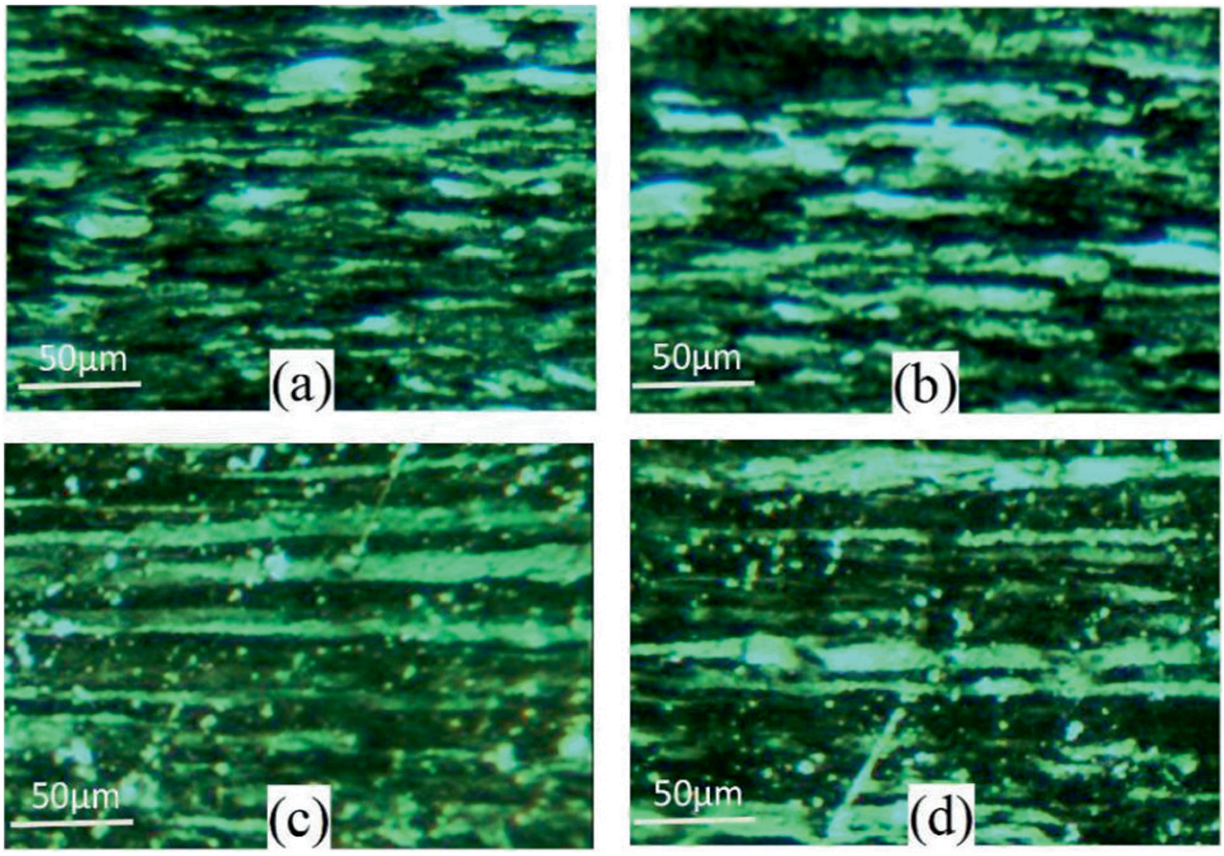


Fig. 4.49 Optical microscopy images of the microstructure in Al layer, **a** cryorolling −190 °C; **b** cryorolling −100 °C; **c** cold rolling and **d** hot rolling

Figure 4.50 shows the SEM images of the microstructure near the interface between Cu layer and Al layer. When using cryorolling at −190 °C, the interlayer became serrated obviously and there are some broken zones along the AlCu intermetallic layer. With increasing in the rolling temperature, the serrated shape becomes flattened gradually. When using hot rolling, there is no broken zone along the AlCu intermetallic layer. The relationship between the interface characterization and rolling temperature is similar to the Al/Ti composite rolling.

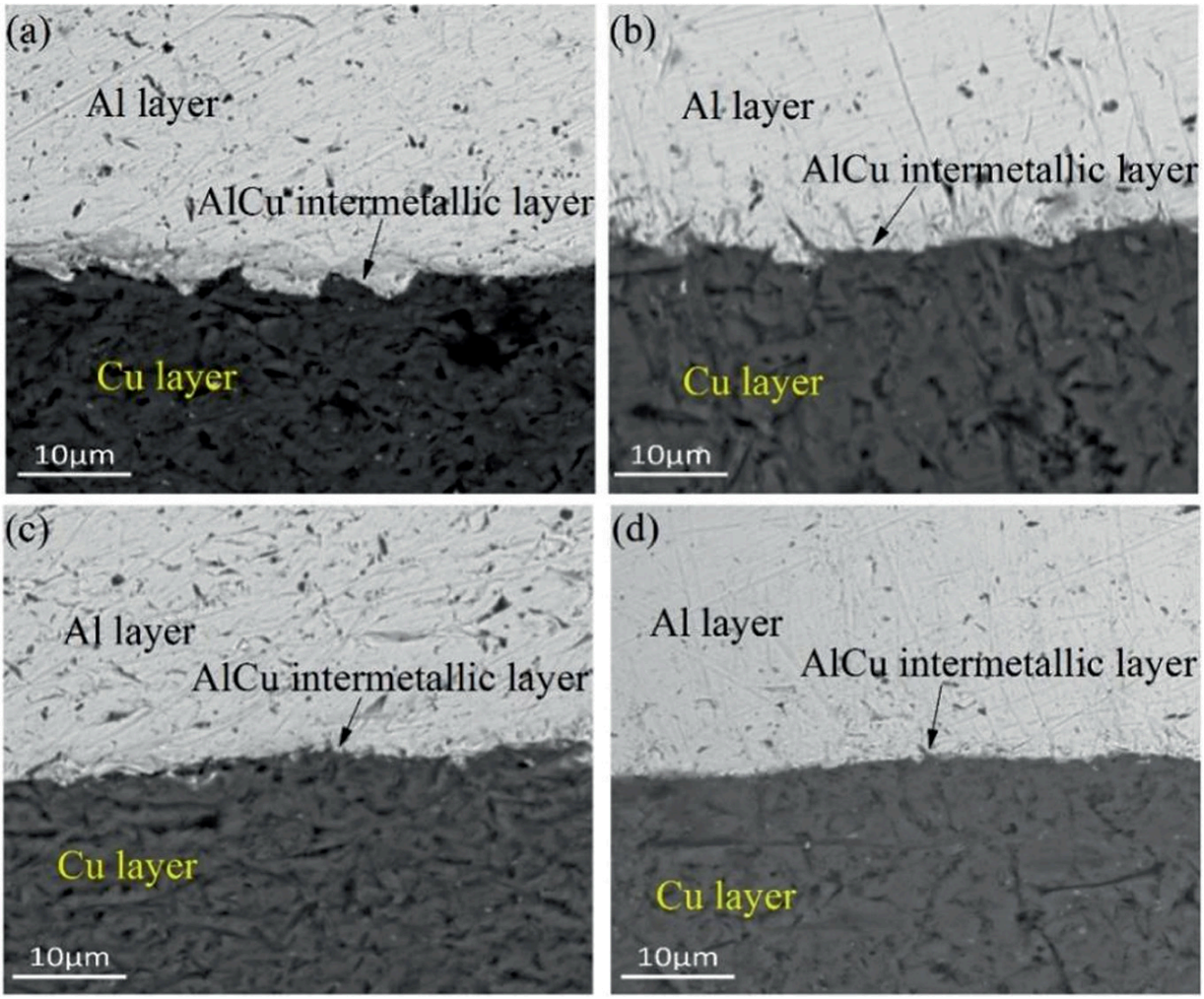


Fig. 4.50 SEM images of structure near the interface between Cu layer and Al layer, **a** cryorolling −190 °C; **b** cryorolling −100 °C; **c** cold rolling and **d** hot rolling

Figure 4.51 shows the EDS mapping of Al and Cu element distribution and the element distribution near the interface between Cu layer and Al layer. With increasing in rolling temperature, the thickness of AlCu intermetallic layer increases. The average thickness of AlCu intermetallic layer is 2.61 μm for cryorolling at −190 °C, which increases to 5.97 μm for hot rolling. The average thickness of AlCu intermetallic layer and rolling temperature are exponentially related which has been certificated. The change in the thickness of AlCu intermetallic layer is also related with the mechanical properties.

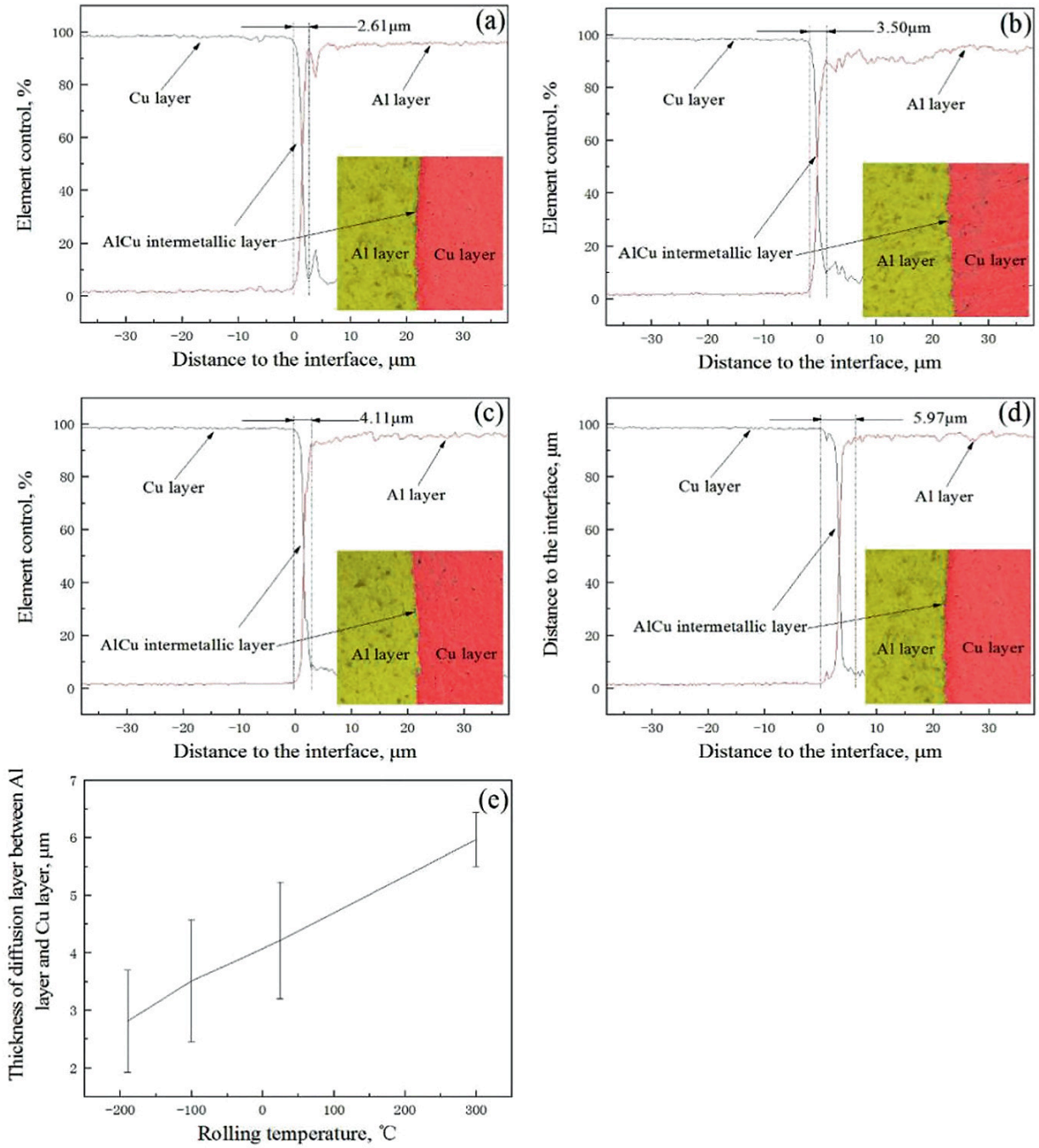


Fig. 4.51 Cu and Al element distribution near Cu/Al interface by EDS, **a** cryorolling −190 °C; **b** cryorolling −100 °C; **c** cold rolling and **d** hot rolling. **e** Thickness of intermetallic layer versus rolling temperature

Figure 4.52 shows the SEM images of fracture surface near the interlayer of the sandwich-like Cu/Al/Cu composites after tensile tests. The bonding between layers is very clearly when using cryorolling at −190 °C (Fig. 4.52a), and these extensive voids between the Cu and Al layer indicate that the bonding strength is low. With the increasing in

rolling temperature, the bonding quality between layers become better (as shown in Fig. 4.52b–d), which means that the bonding strength increases sharply with higher rolling temperature. With higher rolling temperature, the residual stress near the AlCu intermetallic layer reduces, and its distribution becomes more uniform. According to the film theory, the brittle surface layer is broken due to the rolling pressure. In addition, the brittle surface layer is easier to broken with lower rolling temperature. Thus, the serrated shape is formed at interface for the samples subjected to cryorolling.

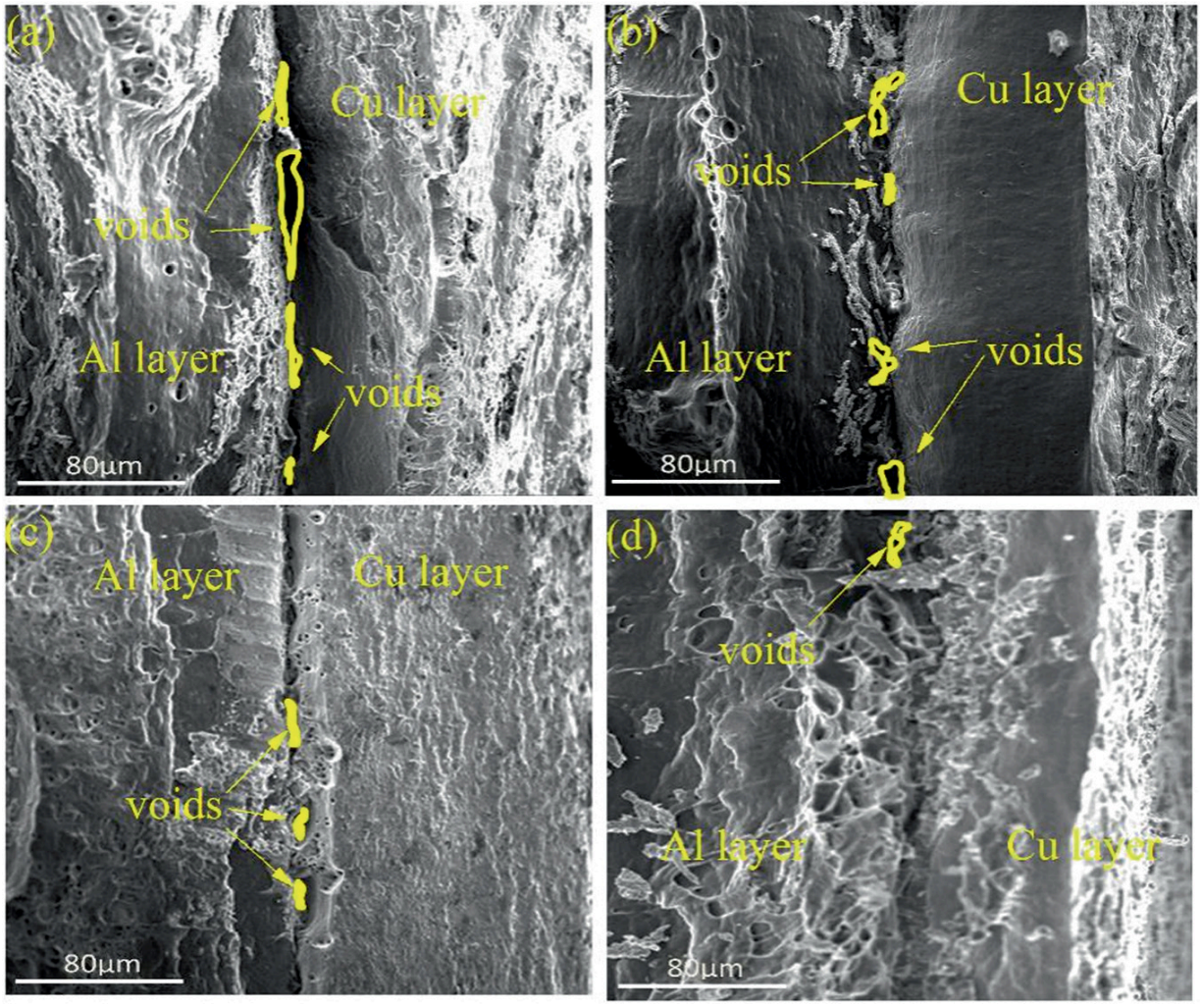


Fig. 4.52 SEM images of fracture surface, **a** cryorolling −190 °C; **b** cryorolling −100 °C; **c** cold rolling and **d** hot rolling

4.5.2 Fracture Mechanism of Cryorolled Cu/Al/Cu Laminates

In Fig. 4.47, both the ultimate tensile stress and the max failure strain are the best for the sandwich-like Cu/Al/Cu composites subjected to cryorolling at −100 °C. Here we think that the grain size, the thickness of intermetallic layer, the interface bonding characterization and quality determine the mechanical properties of the composites.

According to Hall–Petch equation, with finer grain size, the yield stress of metals and alloys increases. In this study, the rolling processing parameters are the same except for the rolling temperatures. It is obvious that the rolling temperatures significantly determine the grain sizes of Cu layer and Al layer. When the temperature is higher than the room temperature, the dislocation density in metals will reduce dramatically with increasing in the rolling temperature. Especially, dynamic recrystallization of grains occurs at higher temperatures during deformation, which will result in coarse grain in the rolled products, as shown in Figs. 4.48 and 4.49, the mean grain size in Cu layer and Al layer are 7.1 μm and 7.5 μm respectively. In contrast, when the temperature is lower than the room temperature, the dislocation density will sharply increase with the decrease of the deformation temperature. when the rolling temperature is −100 °C or −190 °C, the movement of the dislocation and dynamic recovery are depressed, resulting in finer grain sizes. The similar results have been reported in Al and Cu alloys. Grain refinement appears in the composites lamellar with the decrease of the rolling temperature. In Figs. 4.48 and 4.49, after rolling, the grain size increases dramatically with the rolling temperature increasing from −190 to 300 °C. This can explain the decrease of yield stress of the sandwich-like Cu/Al/Cu composites rolling processed at the temperatures of −100, 25 and 300 ºC.

The Cu/Al interlayer bonding quality affected by the rolling temperature is also a significant factor on the mechanical properties. It has been extremely reported that the deformation parameters, such as rolling reduction, rolling temperature, the friction condition, heat treatment, rolling strain rate, etc., have great effects on the bound quality. However, there are few reports about the investigation on the mechanical properties of Cu/Al composites subjected to cryorolling, which have a broad application prospect as potential structure materials. In this study, the AlCu interface became serrated when the

Cu/Al/Cu composites were cryorolled. These serrated interfaces are channels for the virgin metals that are exposed to the opposite sides. During rolling, the two materials near the interface begin to bond in a mechanical locking that enters into each other's bite, as distinguished from diffusion bonding which is the main bonding mechanism during hot rolling. The main bonding mechanisms of Cu/Al/Cu composites subjected to cryorolling are mechanical bonding, while the main bonding mechanisms for hot rolling at high temperature are diffusion bonding. Different bonding mechanisms result in different fracture modes during tensile tests as shown in Fig. 4.53, which result in different mechanical properties of composites along the rolling direction. The best evidence is the variation of interface morphology before and after tensile experiments in Fig. 4.52.

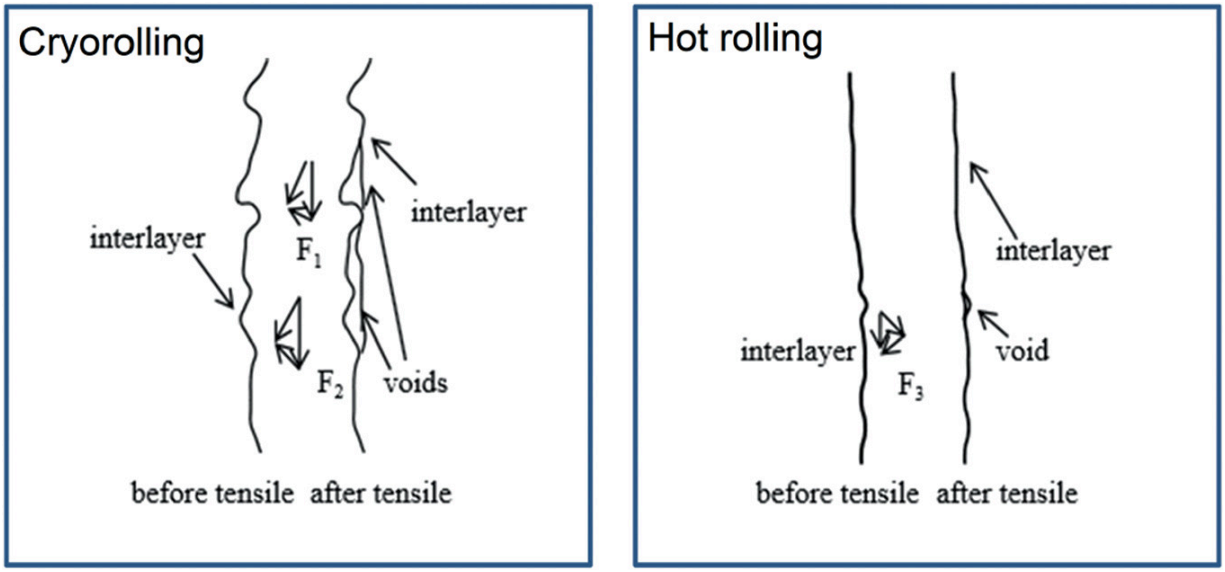


Fig. 4.53 Different fracture models near the AlCu intermetallic layer during tensile testing

The interface diffusion happened during both heating and rolling and its influence cannot be ignored. In Fig. 4.51, the thicknesses of AlCu intermetallic layer in the sandwich-like Cu/Al/Cu composites change as rolling temperature varies, which affects the mechanical properties of composites. During hot roll bonding, Al_2Cu, AlCu, Al_3Cu_4 and Al_4Cu_9 form near the Cu/Al interlayer. In Fig. 4.47, the similar result that the ductility of Cu/Al composites rolling at 300 °C decreased compared to at 25 °C although grains growth was obtained.

In Fig. 4.50a, necking appears in the AlCu intermetallic layer during cryorolling at −190 °C, resulting from local plastic heterogeneities associated with the different plastic characteristics of the Cu and Al composites, which is similar observed in Al/Ni composite during accumulative roll bonding. This indicates that the AlCu intermetallic layer reaches the condition for strain instability considerably earlier than the Al layer for the composites subjected to cryorolling at −190 °C. The phenomenon of necking becomes slight with increasing in the rolling temperature. In Fig. 4.47, the yield stress of laminates increases as the rolling temperature increases from −190 °C to −100 °C although the grain size of laminates increases, which is mainly resulted from the numerous voids around necking regions. Increasing the rolling temperature might lead to higher bonding strength through the reduction of the necking behavior of intermetallic layer. In Fig. 4.52, the bonding quality between Cu layer and Al layer is the best when the Cu/Al laminates is fabricated at 300 °C. There are extensive researches on the evaluation of the interlayer of the composites, but the relationship between the bonding strength and mechanical properties of laminates is still under debate. The tensile properties of the sandwich-like composites can be predicted by the rule of mixtures, an average of component properties weighted by the cross-sectional area fractions, as follows,

$$X = f_a X_a + f_b X_b + f_c X_c + f_d X_d \tag{4.8}$$

where, *f* is the cross-sectional area fraction, *X* is the property value of the relevant component, subscripts *a b c* and *d* represent Cu layer, Al layer, intermetallic layer and equivalent voids layer. Assuming that the thickness of each constituent layer is homogeneous in the tensile direction, the cross-sectional area fraction *f* can be substituted by the thickness ratio of individual layer. Obviously, the strength of the voids is zero. So, with the fraction raising of the equivalent voids layer, the strength will reduce sharply which is the reason for the ultimate tensile stress decreasing of the composites subjected to cryorolling at −100 °C and at −190 °C.

Multilayered Cu/Al laminates have been successfully fabricated by ARB technique [14]. The effect of subsequent cold-rolling and cryorolling on the microstructure and mechanical properties of Cu/Al

laminates are compared. More importantly, the influence mechanism of cryorolling in improving the tensile strength and thermal stability of Cu/Al laminates is also elaborated.

4.5.3 Microstructure Evolution of Cu/Al Laminates Subjected to ARB and Cryorolling

Figure 4.54 shows the SEM micrographs of Cu/Al laminates processed by different ARB cycles. In the first ARB cycle, well-defined lamellar structures with flat Cu/Al interface are formed (Fig. 4.54a). As the ARB cycles increase, the harder Cu layers are prone to necking and even rupturing, marked by the arrows in Fig. 4.54b and c, resulting from the difference in flow stress and hardening rate of Cu/Al metals. Similarly, the preferential necking and rupturing of harder layers have also been found in other MMCs. Shear bands induced by the interfacial shear stress can be clearly observed and form an angle of ~25° to the RD direction. Furthermore, the shear bands become more evident as the ARB cycles increasing, marked by the dashed lines in Fig. 4.54b–d.

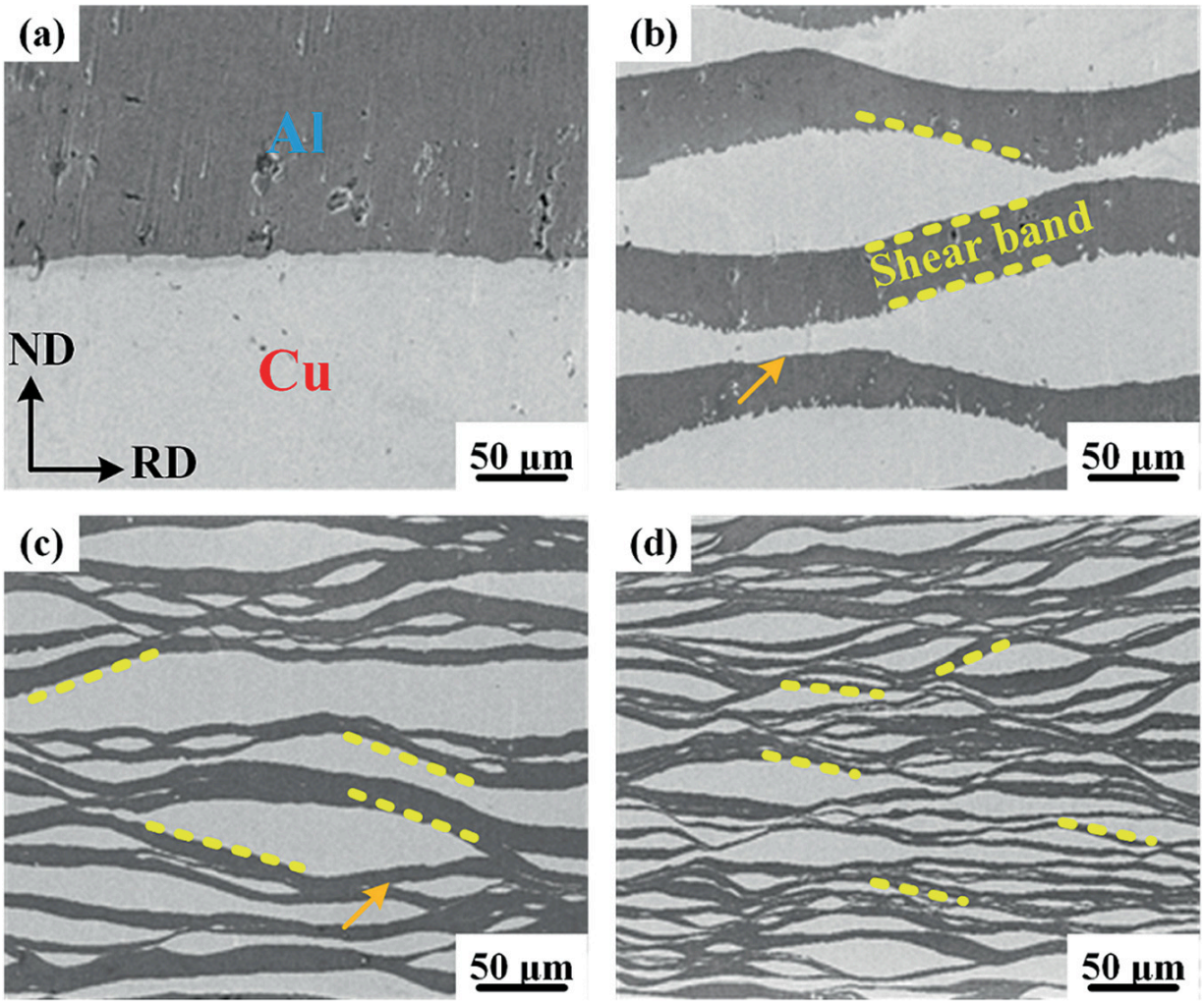


Fig. 4.54 SEM micrographs of Cu/Al laminates processed by different ARB cycles: **a** one, **b** three, **c** five, **d** seven

The microstructure of Cu/Al laminates processed by subsequent rolling is exhibited as Fig. 4.55. It can be seen that the subsequent rolling process can improve the interfacial flatness. Moreover, the shear bands in the cryorolled sample are much less than those in the cold-rolled sample. This result is consist with our previous research. The detailed microstructure difference between cold-rolled sample and cryorolled sample will be further characterized by TEM.

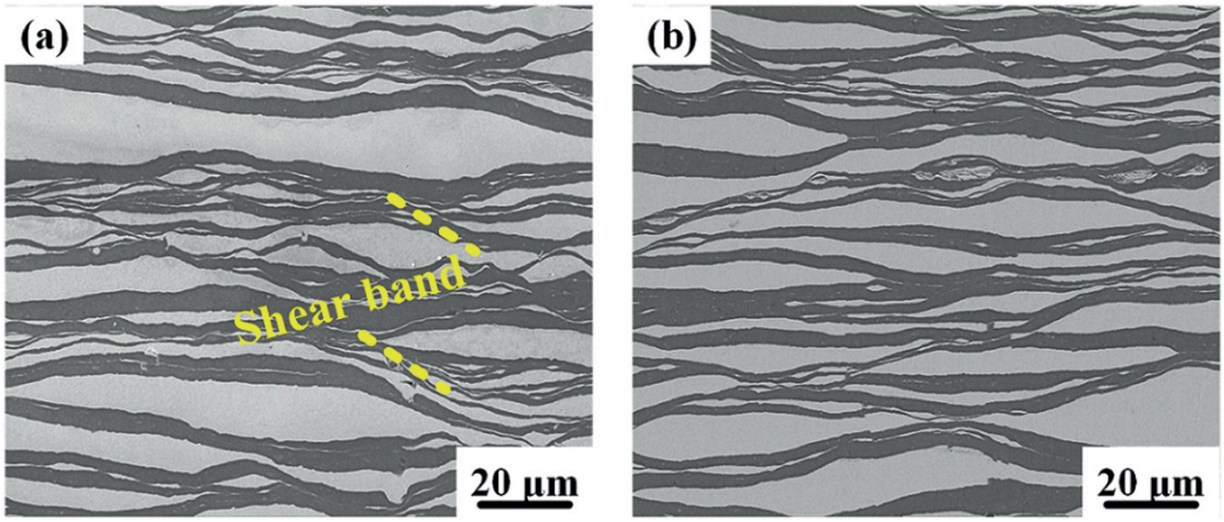


Fig. 4.55 SEM micrographs of Cu/Al laminates processed by subsequent rolling: **a** cold rolling, **b** cryorolling

Figure 4.56 shows the TEM micrographs of Cu/Al layers processed by subsequent cold rolling and cryorolling. For Al layer, it can be observed that the grain size in the cryorolled sample (Fig. 4.56b) is smaller than that in the cold-rolled one (Fig. 4.56a), due to the formation of more micro-shear bands in the cryorolling process. As to Cu layer, only a few dislocation tangles can be observed for cold-rolled sample (Fig. 4.56c). Nevertheless, large amounts of stacking faults with high density are formed in the cryorolled sample (Fig. 4.56d), which can significantly enhance the mechanical properties of metallic materials.

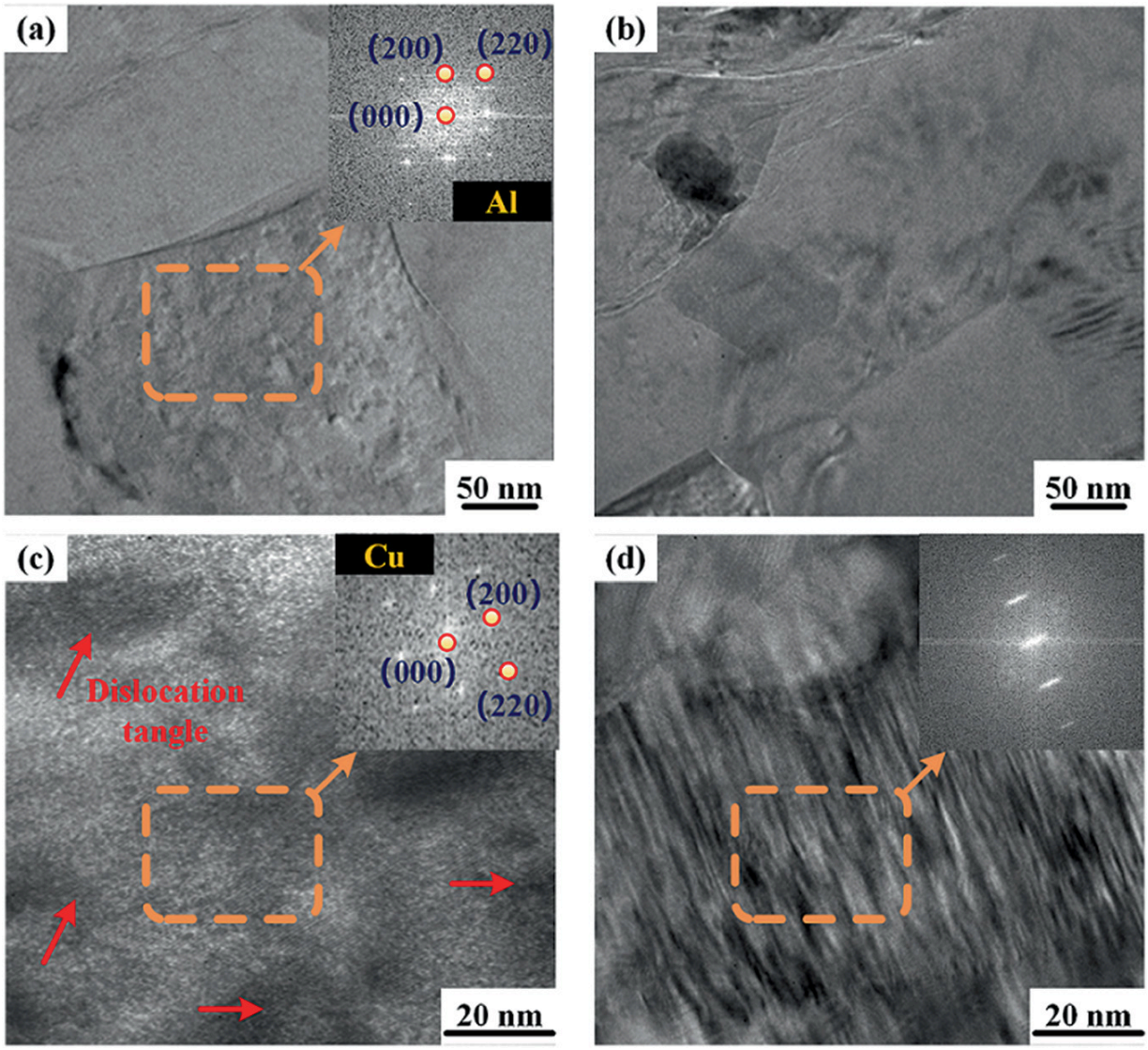


Fig. 4.56 TEM micrographs of Cu/Al matrix. Cold rolling: **a** Al, **c** Cu and cryorolling: **b** Al, **d** Cu. Insets are the fast Fourier transform patterns (FFT) in selected areas marked by dashed squares

Moreover, the TEM images of Cu/Al interface are provided as Fig. 4.57. According to the diffraction spots, Cu-Al IMCs are detected, revealing the diffusion of Cu and Al atoms across the interface. The input energy for the interfacial diffusion comes from two aspects: deformation heat in the ARB process and shear strain energy induced by the plastic mismatch between Cu and Al. For the cold-rolled sample, $CuAl_2$ and CuAl crystalline phases are detected around the Cu/Al interface (Fig. 4.57a), while only $CuAl_2$ phase is determined for the cryorolled sample (Fig. 4.57b). The above results prove that the cryorolling process can effectively inhibit the formation of brittle Cu-Al

IMCs, which may also make contribution to the mechanical improvement of Cu/Al laminates.

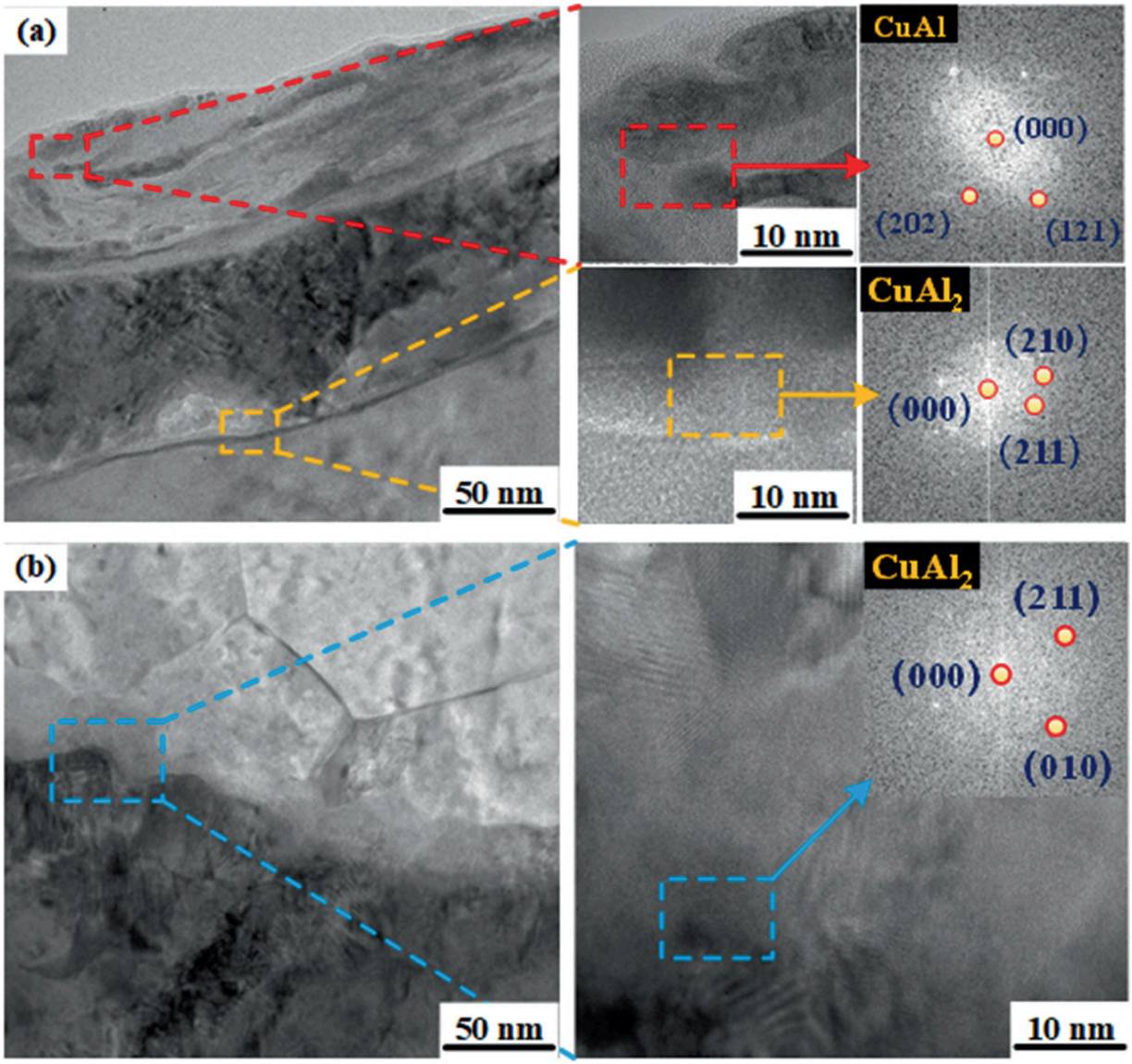


Fig. 4.57 TEM micrographs of Cu/Al interface: **a** cold rolling, **b** cryorolling. The corresponding enlarged images are provided and insets are FFT in the selected areas marked by dashed squares

4.5.4 Tensile Properties of Cu/Al Laminates Subjected to ARB and Cryorolling

Figure 4.58a shows the engineering stress–strain curves of Cu/Al laminates, as well as the initial Cu and Al. Compared with the soft Cu/Al matrix, the composites exhibit the much higher strength but less

ductile, which is the typical characteristics of MMCs fabricated by ARB technique. The total elongation of the composites gradually decreases and finally stabilizes at ~10% (Fig. 4.58b). The tensile strength increases with the ARB cycle, from 222 MPa in 1st cycle to 269 MPa in 7th cycle, resulting from the grain refinement and accumulation of dislocation. Furthermore, the subsequent rolling process can further enhance the tensile strength of the composites through modifying the local necking and making Cu/Al layers thinner (Figs. 4.54 and 4.55). Benefiting from the high-density stacking faults and less Cu-Al IMCs (Figs. 4.56 and 4.57), cryorolled sample exhibits the higher tensile strength than the cold-rolled sample.

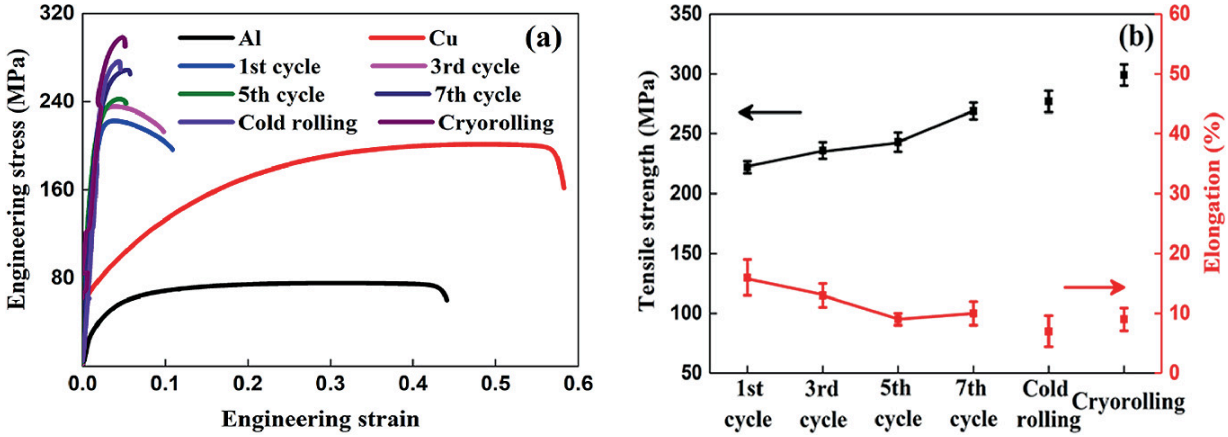


Fig. 4.58 Tensile properties of Cu/Al laminates: **a** engineering stress–strain curves, **b** variation in tensile strength and elongation

Figure 4.59 shows the tensile fracture of Cu/Al laminates. For both samples, brittle fracture is the dominant fracture mode duo to the few dimples. An obvious lamellar structure can be still observed for the cold-rolled sample and crevice type cracks propagate the Cu/Al interface (Fig. 4.59a), indicating the weak interfacial bonding quality. On the contrary, the lamellar structure in the tensile fracture of cryorolled sample becomes ambiguous (Fig. 4.59b), implying the compatible deformation of Cu/Al metals. This phenomenon also proves that cryorolling process can enhance the interfacial bonding strength of MMCs.

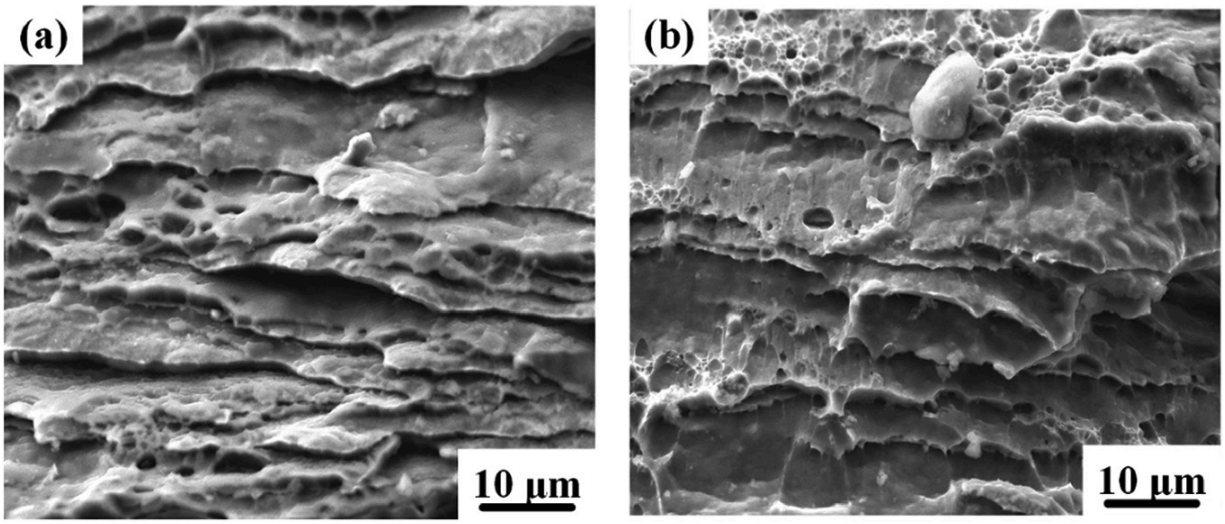


Fig. 4.59 Tensile fracture of Cu/Al laminates processed by subsequent rolling: **a** cold rolling, **b** cryorolling

4.5.5 Thermal Stability of Cu/Al Laminates Subjected to ARB and Cryorolling

The microstructure of the composites processed by the subsequent rolling and annealed at different temperature is presented as Fig. 4.60. In order to make the analysis more accurate, the corresponding EDS mapping for the cryorolled sample at different annealing temperature is also provided as Fig. 4.61. There is the minimal difference for the cold-rolled sample and cryorolled sample in the cross-sectional morphologies characterized by SEM, which will be further determined by EBSD and tensile fracture. For the samples annealed at 473 K, seldom Cu-Al IMCs are detected and obvious lamellar structure is remained (Fig. 4.60a and d), which can also been proved by the corresponding EDS mapping (Fig. 4.61a and d). When the annealing temperature increases to 573 K, a thin and fluffy Cu-Al IMCs layer is formed (Fig. 4.60b and e), which is promoted by the more energy input and results in the appearance of obscure bonding interface (Fig. 4.61b and e). The relationship between the diffusion coefficient D and temperature T can be expressed as Eq. (4.9):

$$D = \mathrm{D}_0 \exp\left(-\frac{\mathrm{Q}}{\mathrm{R}T}\right) \tag{4.9}$$

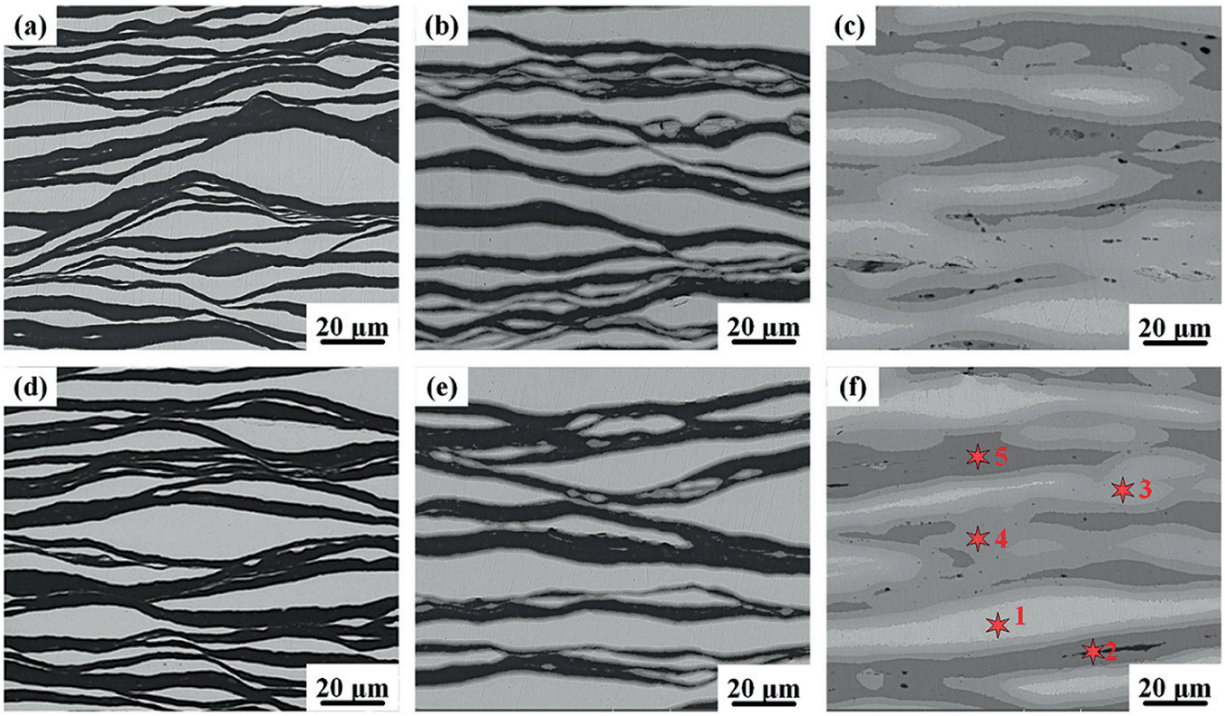


Fig. 4.60 SEM images of the composites processed by cold rolling and cryorolling at different annealing temperature: **a**, **d** 473 K, **b**, **e** 573 K, **c**, **f** 673 K

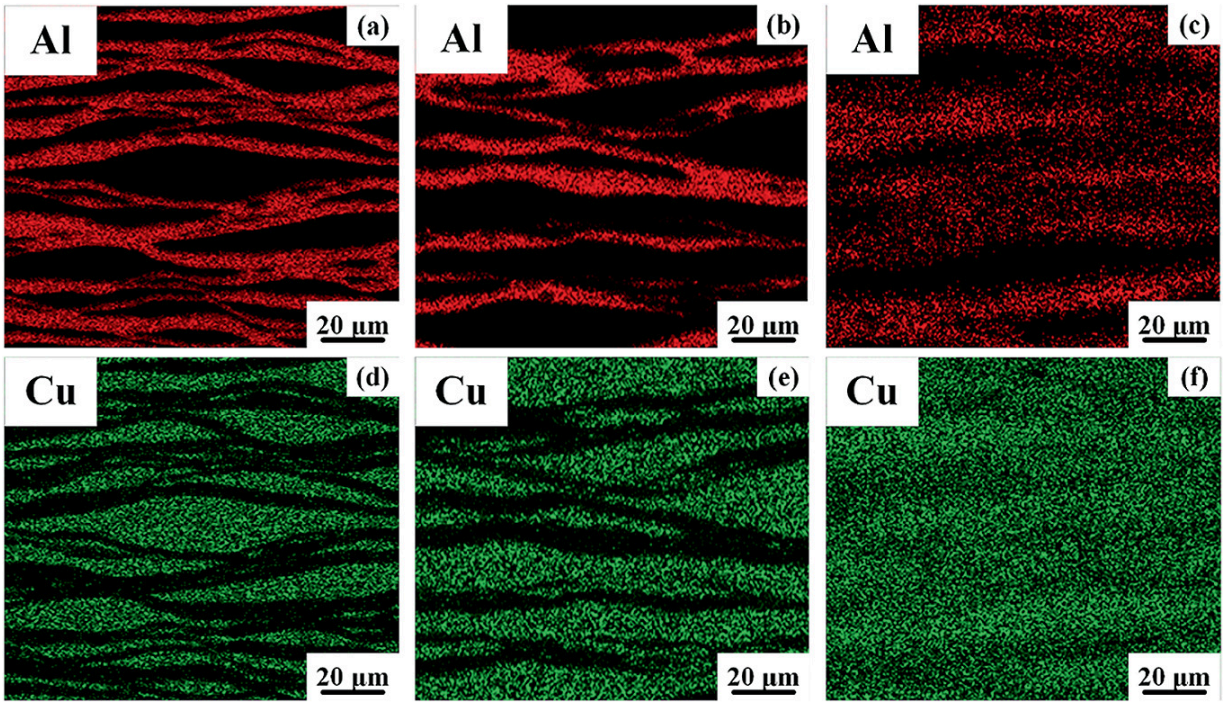


Fig. 4.61 The corresponding ESD mapping for the cryorolled sample at different annealing temperature: **a**, **d** 473 K, **b**, **e** 573 K, **c**, **f** 673 K

where D_0 represents the diffusion constant, Q represents the activation energy (a constant for a specific material), R represents the universal gas constant. A slight increase in annealing temperature may lead to a significant increment of mutual diffusional intensity of Cu/Al.

When the annealing temperature reaches 673 K, large amounts of Cu-Al IMCs are formed, as indicated in Fig. 4.60c and f. Interestingly, there is more Cu matrix is remained than Al matrix. According to the EDS results in Table 4.3, the distribution of crystalline phases around the bonding interface is in the order of α-Cu, Cu_9Al_4, CuAl, $CuAl_2$ and α-Al. Furthermore, the obvious lamellar structure of the sample annealed at low temperature is changed into the serious mixing (Fig. 4.61c and f). The excessive formation of brittle Cu-Al IMCs may decimate the mechanical properties of Cu/Al laminates.

Table 4.3 The EDS results of the points in Fig. 4.60f

Point	Al (at.%)	Cu (at.%)	Phase
1	0.62	99.38	Cu
2	99.75	0.25	Al
3	36.38	63.62	Cu_9Al_4
4	49.85	50.15	CuAl
5	67.27	32.73	$CuAl_2$

For the MMCs without the formation of IMCs, their thermal stability can be determined by the variation of micro-hardness. Nevertheless, this method will not be suitable to evaluate the thermal stability of MMCs containing IMCs any more. It is indisputable that the micro-hardness of MMCs can be enhanced via forming the IMCs and achieving the interface alloying. Herein, the thermal stability of Cu/Al laminates is reflected by the variation in tensile strength. Previous researches indicated that the Cu and Al metals with ultra-fine grains processed by SPD technique can exhibit excellent thermal stability when the annealing temperature was below 423 K. Figure 4.62 presents the changeable rule in the tensile strength of the samples annealed at 473–673 K. It can be seen that the tensile strength of all samples shows a gradual decline with the increment of annealing temperature, revealing the occurance of thermally-induced instability. Especially, the serious

degradation of the tensile strength (below 100 MPa) occurs for these samples annealed at 673 K. Furthermore, the cryorolled samples exhibits the higher thermal stability (~10%) than the cold-rolled samples. For MMCs without the IMCs, grain coarsening is the major incentive of thermal instability. While for MMCs containing IMCs, the thermal instability is induced by the comprehensive effect of grain coarsening and formation of brittle IMCs.

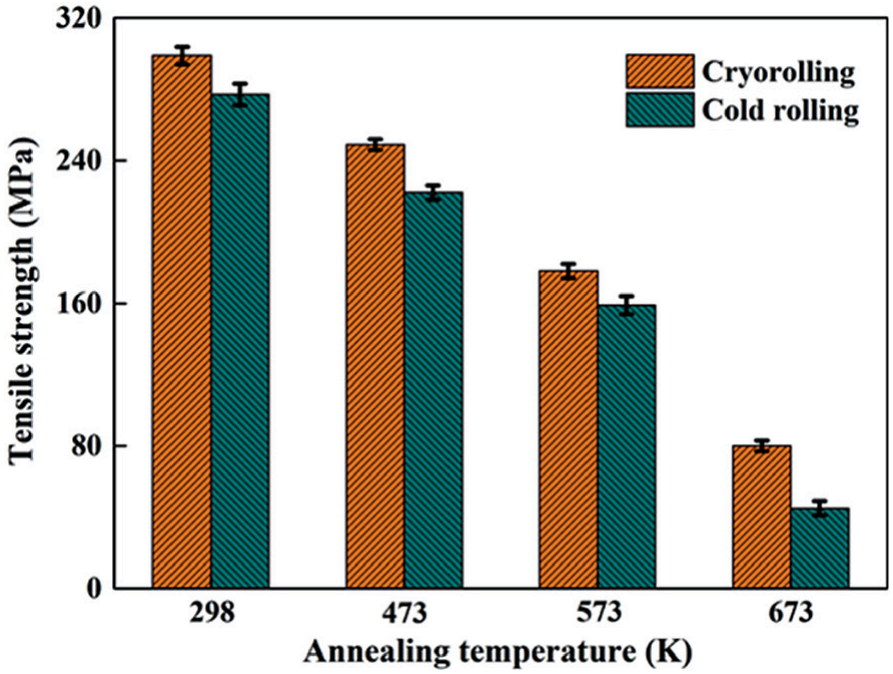


Fig. 4.62 Variation of the tensile strength for the samples annealed at different temperature

At low annealing temperature (473 K), there are few IMCs formed at the Cu/Al interface (Fig. 4.60). In this case, the decline in the tensile strength of the Cu/Al laminates is mainly caused by the grain coarsening. Figure 4.63 shows the EBSD maps, grain size diagram and misorientation angle of the samples processed by the subsequent rolling. For the cold-rolled sample, obvious deformed elongated grains in Cu matrix exhibiting the rolling orientation are still kept (Fig. 4.63a) and the average grain diameter is 697 nm (Fig. 4.63c).

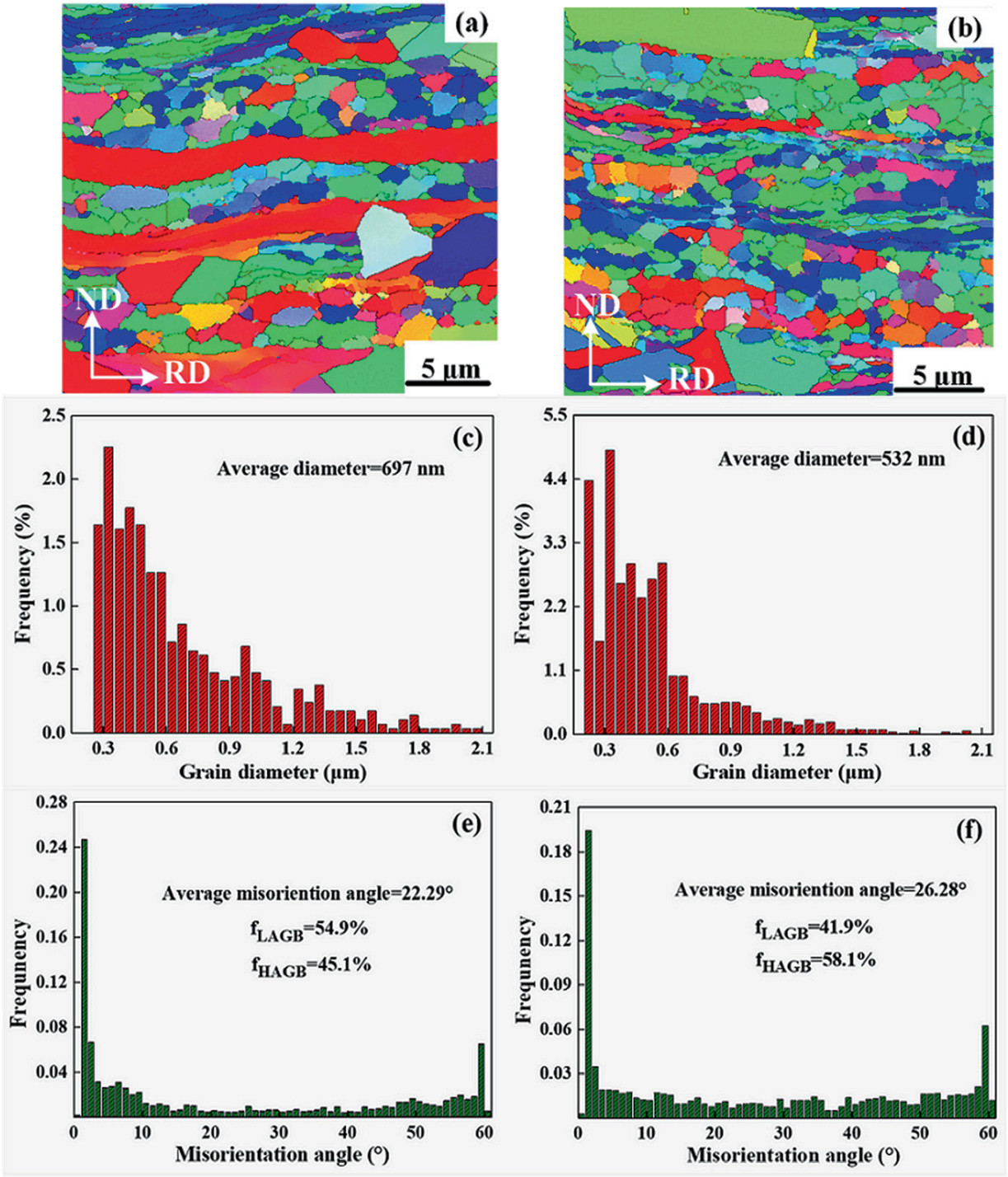


Fig. 4.63 EBSD maps, grain size diagram and misorientation angle of the composites: **a**, **c**, **e** cold rolling, **b**, **d**, **f** cryorolling

As to the cryorolled sample, most of the deformed elongated grains in Cu matrix are transferred into the equiaxed grains (Fig. 4.63b) with the smaller size of 532 nm (Fig. 4.63d). Furthermore, the proportion of high angle grain boundaries (HAGB) and low angle grain boundaries

(LAGB) is tallied as Fig. 4.63e and f. There are more HAGBs in the cryorolled sample than the cold-rolled sample with the average misorientation angle of 26.28°. The above results indicate that the high-density stacking faults in Cu matrix formed in the cryorolling process can facilitate the transition from LAGBs to HAGBs and formation of ultra-fine recrystallized grains in the low-temperature annealing process.

When the annealing temperature is above 473 K, abundant Cu-Al IMCs will be formed at the bonding interface (Fig. 4.60). At this time, the formation and growth of Cu-Al IMCs become the dominant factors of the decrease in tensile strength of Cu/Al laminates. The tensile fracture of cold-rolled sample and cryorolled sample annealed at different temperature is presented as Fig. 4.64. For the samples annealed at 473 K (Fig. 4.64a and d), there are more Cu-Al IMCs particles appeared at the tensile fracture of the cold-rolled sample than the cryorolled one (marked by the red ovals). As the annealing temperature reaches 573 K, the Cu-Al IMCs particles are transformed into Cu-Al IMCs layer, as indicated by Fig. 4.64b and e. Furthermore, the width of Cu-Al IMCs layer is larger for the cold-rolled sample than cryorolled one (marked by the yellow arrows). When the annealing temperature is up to 673 K, the tensile fracture is full of the Cu-Al IMCs with typical crystallographic characteristics. Compared with the cold-rolled sample, the grain size of Cu-Al IMCs in cryorolled sample is much smaller. And some unreacted Cu matrix can be determined on the tensile fracture of cryorolled sample (Fig. 4.64c and f), which is consist with the result in Fig. 4.60f. The above results imply that the cryorolling process can significantly delays the formation and growth of Cu-Al IMCs, leading to the better thermal stability. According to the TEM micrographs of Cu/Al interface (Fig. 4.57), there are more nanoscale Cu-Al IMCs formed in the cold rolling process than the cryorolling process, which becomes the nucleation sites of new Cu-Al IMCs. Under the same heat input, the new Cu-Al IMCs for cold-rolled sample are easier to form and grow than the cryorolled one.

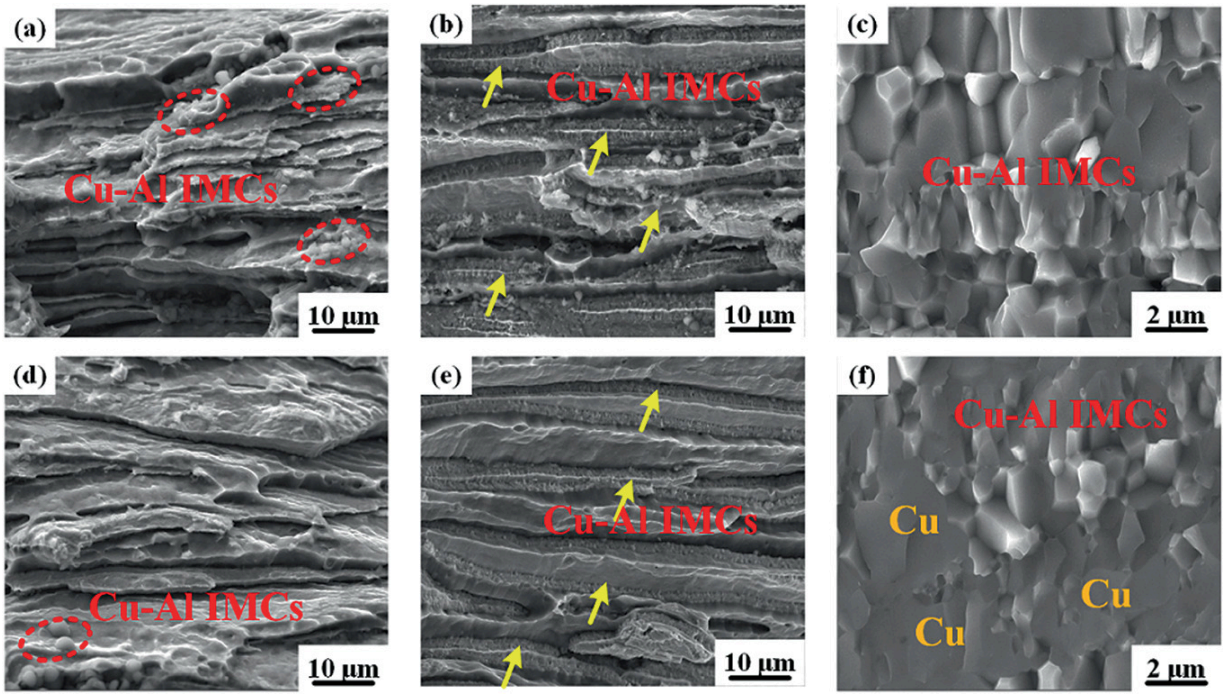


Fig. 4.64 Tensile fracture surface of cold-rolled sample and cryorolled sample annealed at different temperature: **a**, **d** 473 K, **b**, **e** 573 K, **c**, **f** 673 K

4.6 Cu/Nb Laminates Subjected to Cryorolling and Annealing

To investigate the effect of deformation temperature on the mechanical properties and thermal stability of Cu/Nb laminate, the composites were processed by 9-cycle ARB followed by cryorolling and cold rolling, respectively [15].

4.6.1 Mechanical Properties of Cu/Nb Laminates

After 9-ARB cycles, the ultimate tensile strength (UTS) of the Cu/Nb laminates was 575 MPa (Fig. 4.65a), who reported that the UTS of Cu/Nb laminates after 9-cycle ARB reached 550 MPa. As Fig. 4.65a shows, the UTS of the Cu/Nb laminates increases to 645 MPa after cold rolling, which decreases after annealing with increasing annealing temperature, while the elongation is recovered well. After annealing at 773 K, the UTS decreased to 537 MPa, and the elongation increased to 6.2%. The UTS of the cryorolled laminate is 683 MPa, which is 5.9% higher than that of cold rolled samples (Fig. 4.65b). After annealing at

773 K, the UTS of the cryorolling composite decreases to 545 MPa, which is similar to that of the cold rolled samples. However, the elongation of the cryorolled Cu/Nb laminates increased to 8.3% after annealing, which is higher than that of the cold rolled samples. As Fig. 4.65c shows, with the same annealing temperature, the strength of the cryorolled Cu/Nb laminates is always higher than that of the cold rolled samples, and the trend is the same for the elongation. When annealed in the range of 623 K and 973 K, the hardness values of the cryorolled Cu/Nb laminates are higher than cold rolled samples (Fig. 4.65d). The hardness values of the composites prepared by both cryorolling and RTR show a linearly decreasing trend with annealing temperature, but the rate of decrease in the case of the cryorolled composites is slower than that of the RTR composites, implying that the cryorolled composites have better thermal stability.

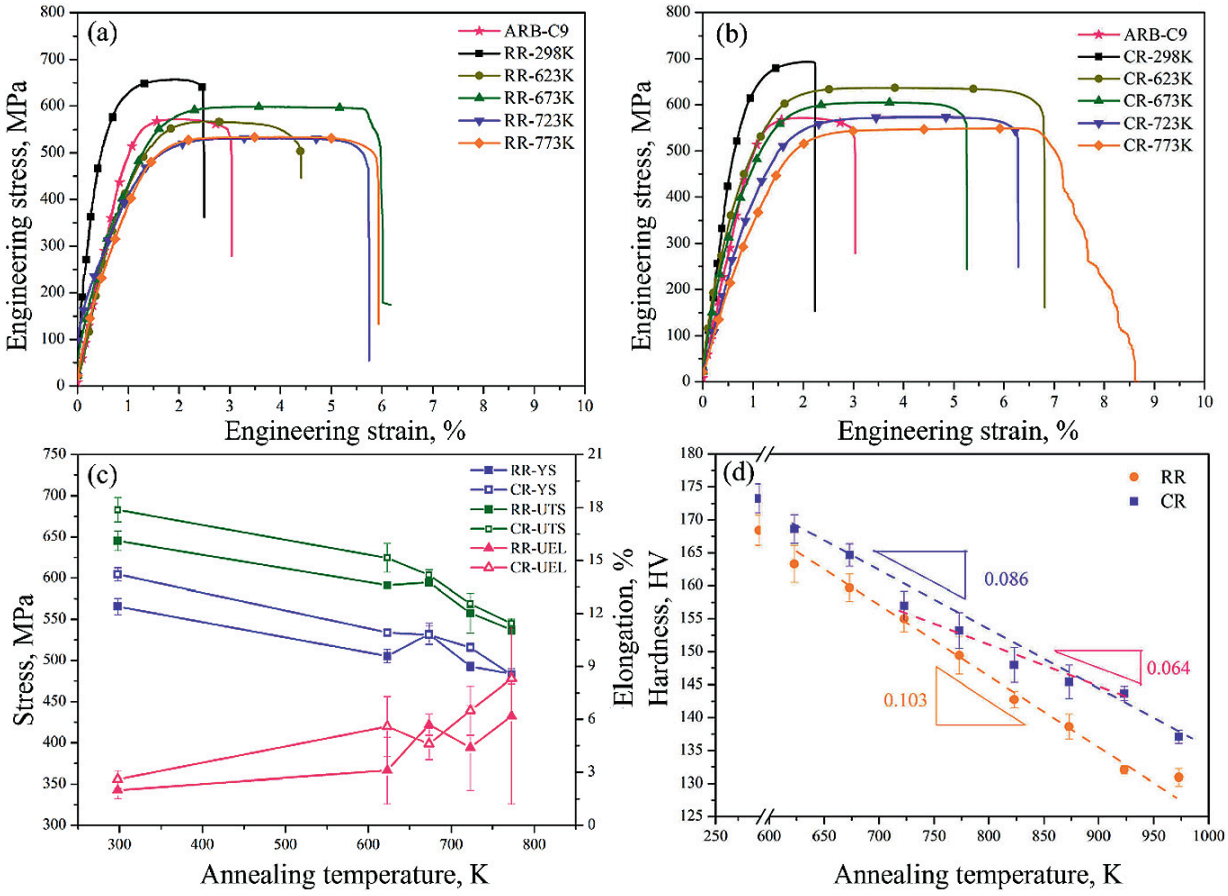


Fig. 4.65 Mechanical properties of the Cu/Nb laminates under various annealing temperatures. Engineering stress–strain curves of **a** cold rolled and **b** cryorolled samples. **c**

Tensile properties of samples at different annealing temperature. **d** Hardness of samples at different annealing temperature

4.6.2 Microstructural Evolution of Cu/Nb Laminates

Figure 4.66 shows TEM images of the microstructure of the Cu/Nb laminates. The average layer thickness of the RTR Cu/Nb laminates is 37 nm, and there are no twins in the Cu layer (Fig. 4.66a). While the cryorolled Cu/Nb laminates has an average layer thickness of 35 nm, and twins are found in the Cu layer (Fig. 4.66c). Dislocation slip is the main deformation mechanism of FCC metals at room temperature, and twinning deformation is more likely to occur when deformation occurs at temperatures below 103 K. When deformed at cryogenic temperatures, the grain boundaries with excess energy and energy relax, which improves the formation rate of twins. After annealing at 773 K, the average layer thickness of cryorolled and cold rolled Cu/Nb laminates increases to 45 nm and 51 nm (Fig. 4.66b and d), respectively. The highly entangled dislocations in the Cu layer were alleviated after annealing at 773 K for the cold rolled Cu/Nb laminates (Fig. 4.66c), and there was some formation of annealing twins. However, there are more annealing twins in the Cu layer of the cryorolled Cu/Nb laminates after annealing (Fig. 4.66d). This may be due to the formation of high-density stacking faults and deformation twins during cryorolling, which promotes the formation of twins during the crystallization process.

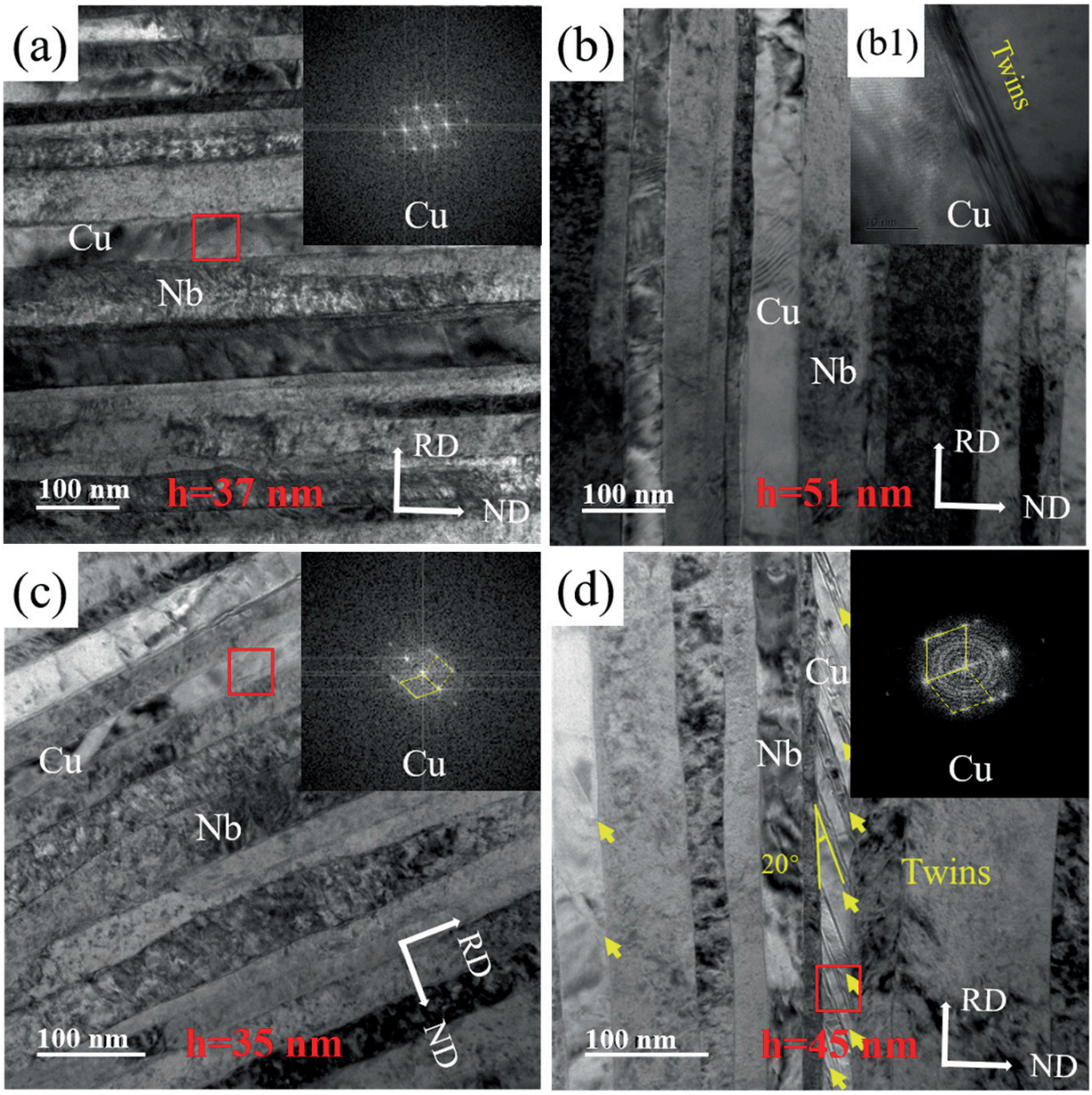


Fig. 4.66 TEM images of microstructure of Cu/Nb laminates. **a** cold rolled sample, inset is a fast Fourier transform patterns (FFT) in selected areas marked by red squares **b** Sample subjected to cold rolling and subsequent annealing at 773 K, inset is a high resolution transmission electron microscopy (HRTEM) images of twins found in Cu layer. **c** cryorolled sample, inset is a FFT in selected areas marked by red squares. **d** Sample subjected to cryorolling and subsequent annealing at 773 K, inset is a FFT in selected areas marked by red squares

In Fig. 4.65d, the hardness values of cryorolling composites after annealing at 723, 773 and 823 K have large deviation from the fitted straight line, and the rate of decrease in these temperature ranges (show in Fig. 4.65d with the pink line) is slower than that in the whole annealing ranges, indicating that the thermal stability of cryorolling

Cu/Nb laminates is high in this temperature range. To further study the effect of cryorolling and cold rolling on the thermal stability of Cu/Nb laminates, the inverse fast Fourier transform (IFFT) (Fig. 4.67) and HRTEM images (Fig. 4.68) were used to analyze the interface structures of Cu/Nb laminates samples as rolled, annealing at 723 K and 773 K, respectively. The IFFT images of Nb and Cu layers were used to evaluate the dislocation density by the average number of dislocations per unit area. Due to the high melting point of Nb (2741 K), the Nb layers in the Cu/Nb laminates via both cold rolling and cryorolling retain many dislocations after annealing at 723 and 773 K (Fig. 4.67c–f). In the case of the Cu layer, the dislocation density of the cryorolling (3.594×10^{17} m^{-2}) is higher than that of the cold rolled sample (2.316×10^{17} m^{-2}) **(**Fig. 4.67a and b). This can be attributed to the suppression of dynamic recovery and recrystallization during cryorolling, allowing a high density of dislocations to be retained. After annealing at 723 K, the dislocation density of cold rolled samples (1.278×10^{17} m^{-2}) decreased by 44.8% (Fig. 4.67c), while that of cryorolling (3.354×10^{17} m^{-2}) decreased by only 6.3% (Fig. 4.67d). This indicates that cryorolled composites can inhibit the occurrence of recovery during the annealing. After annealing at 773 K, annealing twins were formed in the Cu layers of both cold rolled and cryorolled composites **(**Fig. 4.66), indicating that recrystallization occurred in the Cu layers of both cold rolled and cryorolled composites. However, the dislocations in the Cu layer of the sample subjected to RR + annealing at 773 K were nearly consumed (Fig. 4.67e), and the dislocation density is 3.194×10^{16} m^{-2}, decreased 86.2% than that of cold rolled composites. In Fig. 4.67f, the dislocation density of Cu layer of the sample subjected to cryorolling + annealing at 773 K is 9.583×10^{16} m^{-2}, decreased 73.3% comparing to the cryorolled sample. It is obvious that the consumption rate of dislocations in the cryorolled Cu/Nb laminates is slowed down during the annealing, resulting in improved thermal stability.

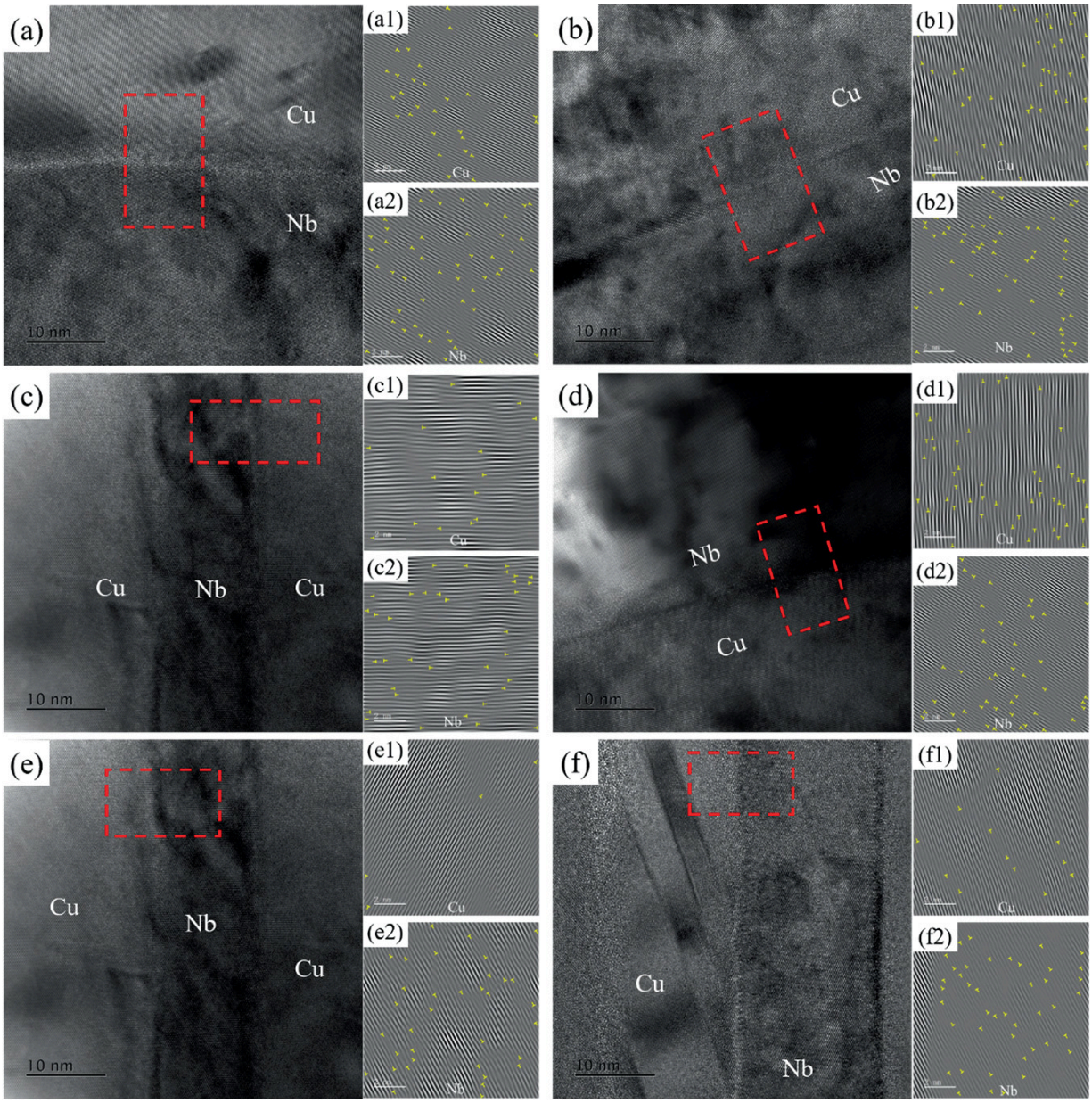


Fig. 4.67 HRTEM images of the Cu/Nb laminates subjected to cold rolling and cryorolling and subsequent annealing, and the inset images are the inverse fast Fourier transform (IFFT) obtained from selected areas marked by dashed squares. **a** RR, **a1** IFFT of Cu layer, **a2** IFFT of Nb layer. **b** cryorolling, **b1** IFFT of Cu layer, **b2** IFFT of Nb layer. **c** cold rolling + annealing at 723 K, **c1** IFFT of Cu layer, **c2** IFFT of Nb layer. **d** cryorolling + annealing at 723 K, **d1** IFFT of Cu layer, **d2** IFFT of Nb layer. **e** cold rolling + annealing at 773 K, **e1** IFFT of Cu layer, **e2** IFFT of Nb layer. **f** cryorolling + annealing at 773 K, **f1** IFFT of Cu layer, **f2** IFFT of Nb layer

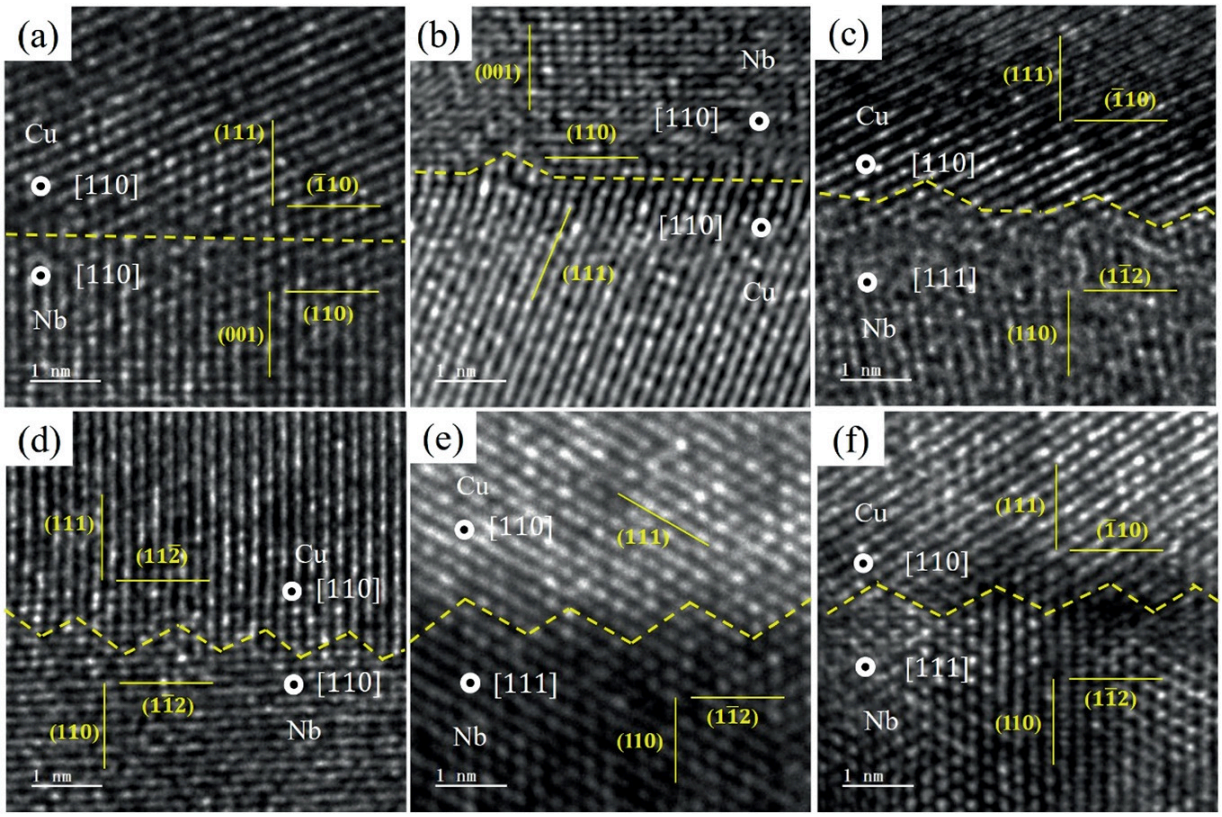


Fig. 4.68 HRTEM images interface structures of the Cu/Nb laminates. **a** cryorolled sample, **b** cryorolled sample after annealing at 723 K, **c** cryorolled sample after annealing 773 K, **d** cold rolled sample, **e** cold rolled sample after annealing at 723 K, **f** cold rolled sample after annealing at 773 K

The cryorolled Cu/Nb laminates shows a flat interface with a {110} <111> Cu||{001} <110> Nb orientation relationship (Fig. 4.68a), which has the same Nishiyama-Wasserman (N–W) orientation relationship as that seen in PVD Cu/Nb laminates. The Cu/Nb laminates prepared by cross ARB also have {110} <111> Cu||{001} <110> Nb interfaces. The interface orientation relationship has changed slightly after annealing at 723 K, but the interface is still straight (Fig. 4.68b). After annealing at 773 K, the straight interface has been transformed into a zigzag interface, and the interface relationship has become {110} <111> Cu|| {112} <110> Nb (Fig. 4.68c). The transformation of the interface structure of the cryorolled Cu/Nb laminates during annealing may be caused by the formation of twins (Fig. 4.67f). The formation of twins would trigger the interfacial structural reorientation of Cu/Nb. The Cu/Nb interface structure of the cold rolled sample retains the interface structure characteristics of ARB, and the interface structure is {112} <111> Cu||{112} <110> Nb zigzag interface (Fig. 4.68d). After

annealing, it is found that the interface of the cold rolled samples always maintains the zigzag features (Fig. 4.68e and f).

Unlike the cold rolled samples, the cryorolled Cu/Nb laminates have large numbers of deformation twins (Fig. 4.68a and c). This shows that the deformation mechanism of the Cu layer has changed during cryorolling. According to the Zener-Hollomon relationship, the lower the deformation temperature, the larger the parameter Z, and the more difficult it is for plastic deformation to occur in the Cu layer. Thus, the dislocation slipping and climbing in the Cu layer with moderate stacking fault energy is severely inhibited during cryorolling, which results in some incomplete dislocations. As the deformation continues, a large number of incomplete dislocations accumulate and expand in the lattice to form stacking faults, providing favorable conditions for the formation of twins (Fig. 4.66c). Studies have shown that the presence of twins has a strong hindering effect on dislocation motion. The dislocation can pass through the twin boundary by cross-slip, or a full dislocation can be decomposed into two Shockley incomplete dislocations on the twin boundary and then propagate along with it. However, these two transmission methods are driven by additional stress, improving the strength and hardness of the Cu layer. Thus, the presence of deformation twins contributes to the improved strength of the Cu/Nb laminates.

The thermal stability of Cu/Nb laminates is related to grain size, interfacial density (single layer thickness), and interface structure. In this study, the difference between the average layer thicknesses of the cryorolled and cold rolled Cu/Nb laminates is slight and can have only a negligible effect on their thermal stabilities. Thus, the difference between the interface structures of the cryorolled and cold rolled samples is the key factor that leads to the differences in thermal stability between the cryorolled and cold rolled Cu/Nb laminates. Misra and Hoagland found that PVD Cu/Nb laminates with a flat interface could maintain the layered structure after annealing at 973 K, while the ARB Nb layer was spheroidized. This means that a {110} <111> Cu|| {001} <110> Nb interface has better thermal stability than a {112} <111> Cu||{112} <110> Nb interface. In this study, the recovery of the cryorolled Cu/Nb laminates ribbon is also delayed. This means that the flat interface of the cryorolled Cu/Nb laminates has a better ability to

inhibit the recovery of the Cu layer than the zigzag interface of cold rolled composites, resulting in better thermal stability. In addition, the formation of deformation twins could change the Cu/Nb interface structure and result in a lower energy Cu/Nb interface. The formation of deformation twins in cryorolled Cu/Nb laminates reduces the local interfacial energy and reduces the occurrence of Rayleigh instability. Thus in Fig. 4.66b and d, after annealing at 773 K, the cryorolled Cu/Nb laminates showed less increase in layer thickness and better thermal stability.

As Fig. 4.65 shows, the strength of the cryorolled Cu/Nb laminates after annealing is similar to that of cold rolled samples, but the hardness values are higher. Zheng et al. [16] also reported that the Cu/Nb laminates with {110} <111> Cu||{001} <110> Nb interfacial orientation relationship prepared by cross-rolling after annealing at 873 K had the same strength of samples subjected to ARB + annealing, but the hardness of cross-rolled samples is higher than that of the ARB samples. The semi-coherent Cu/Nb interface has a strong hindering effect on dislocation transmission across interface. During deformation, the Cu/Nb interface with low shear strength inhibits the transport of dislocation motion across the interface, confines dislocations within the layer and forms stacking at the interface, and causes local flow at the interface to induce stress concentrated. This local flow will lead to the generation of micropores and cracks at the interface, thus limiting the overall deformability of the Cu/Nb laminates. As the deformation increases, the dislocations interact with each other so that the dislocations become evenly distributed in each layer, thereby alleviating stress concentration. The zigzag Cu/Nb interface has greater Misfit dislocations can stimulate more slip systems during deformation, thereby reducing stress concentration more effectively. Therefore, in Fig. 4.65, the hardness values of the cryorolled Cu/Nb laminates after annealing are higher, but the strength is similar to that of cold rolled samples. After annealing at 773 K, interface structures of cryorolled and cold rolled samples have the same zigzag interface (Fig. 4.68f). For the cryorolled Cu/Nb laminates, the effect of twins needs to be considered in the deformation processing. Under the action of twinning, the total dislocations in the Nb layer can be demarcated as Shockley incomplete dislocations at the Cu/Nb interface and then

transferred to the Cu layer along the twin boundaries. Thus, the presence of twinning provides more dislocation paths, improves the deformation ability of Cu/Nb laminates, and further alleviates stress concentration during stretching. Twinning during stretching could absorb dislocations, thereby improving the plasticity of Cu. Therefore, the cryorolled Cu/Nb laminates after annealing shows better ductility.

4.7 Cu/Brass Laminates Subjected to Cryorolling

In addition, the cryorolling process is introduced to achieve the synergetic enhancement in strength and ductility of heterostructured Cu/brass laminates. Furthermore, the role of cryorolling on the formation of shear bands and nano twins, recrystallization, interface shape, and HDI stress is also investigated [17].

4.7.1 Microstructural Evolution of Cu/Brass Laminates

Figure 4.69 exhibits the EBSD and TEM results of cold rolled and cryorolled samples. The distinct lamellar structure with an average layer thickness of approximately 62.5 μm can be observed in the Cu/brass laminate (Fig. 4.69a). After ARB and subsequent rolling, the nanoscale fibrous elongated grains are formed in the Cu layer due to the large equivalent strain (ε = 3.2), which is obtained by:

$$\varepsilon = \frac{2}{\sqrt{3}} \ln\left(\frac{H_0}{h}\right) \tag{4.10}$$

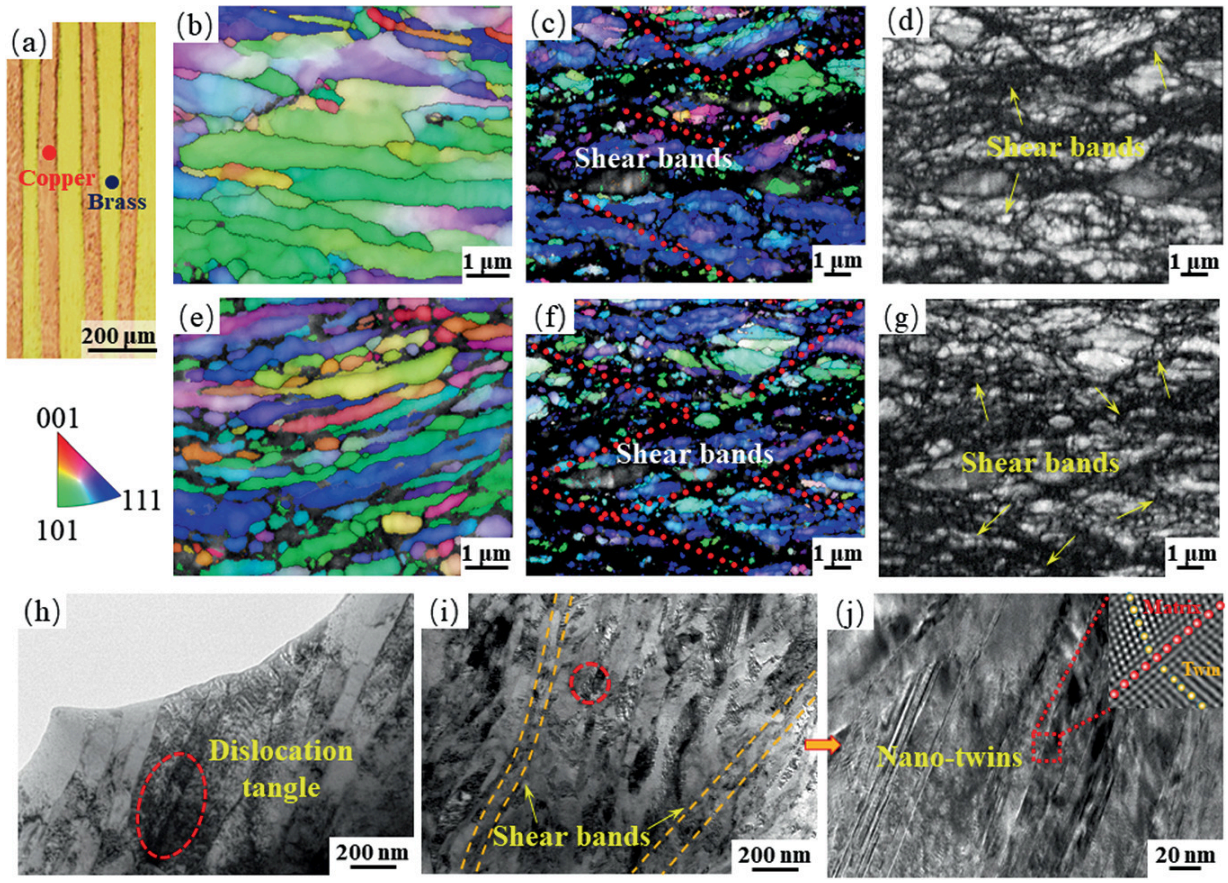


Fig. 4.69 Microstructure of rolled samples: **a** Optical image of Cu/brass laminates; inversed pole figure maps of Cu layer and brass layer in **b**, **c** cold rolled and **e**, **f** cryorolled samples; image quality maps and TEM images of brass layer in **d**, **h** cold rolled and **g**, **i** cryorolled samples, **j** enlarged image of the red circle in (**i**), the inset is the magnified image of nanotwin

where H_0 and h are the initial layer thickness of 1 mm and the final layer thickness of 62.5 μm, respectively. The average grain size of the Cu layer in cryorolling sample is 236 nm, much smaller than that of 503 nm in cold rolled sample (Fig. 4.69b and e), benefiting from the suppression of dynamic recovery and increase of dislocation density during cryorolling.

Different from the microstructure of Cu layer, randomly distributed shear bands surrounded by large amounts of low-angle boundaries appear at the brass layers (Fig. 4.69c and f). The solid solution of Zn element in Cu matrix makes the lattice distorted, reduces the stacking fault energy (SFE) (78 mJ/m^2 for Cu and 35 mJ/m^2 for brass) and suppresses the dynamic recovery of brass. The above factors significantly enhance the probability of local shear deformation (shear

bands) as a result of further grain refinement and dislocation multiplication. Moreover, the density of shear bands in brass layer of cryorolled sample is much higher than that in cold rolled sample (Fig. 4.69d and g).

According to the TEM images of brass layer in cold rolled sample, obvious dislocation tangles and sub-grains are observed, implying that dislocation slip is the dominant deformation mode for brass layer in cold rolled sample with an average grain size of ~156 nm (Fig. 4.69h). In contrast, much finer grains (~82 nm) containing high-density deformation twins (DTs), ranging from 2 to 30 nm, can be identified for brass layer in cryorolled sample (Fig. 4.69i and j). According to the transition state theory, the σ-dependent thermal activation energy Q(σ) for the nucleation of DT is 0.62 eV at room temperature (298 K) and 0.16 eV at liquid-nitrogen temperature (77 K), which can be calculated by:

$$\mathrm{Q}(\sigma) = -k_{\mathrm{B}} T \ln\left(\frac{f}{f_0}\right) \tag{4.11}$$

where k_{B} is the Boltzmann constant (1.38×10^{-23} J/K), T is the deformation temperature, f_0 is the typical experimental frequency (10^{11} s^{-1}) and f is the thermal activation frequency of DT (set as 1 s^{-1}). Besides, the decline of deformation temperature can further decrease the SFE of brass, which obviously enhances the generation of nano twins to hinder the dislocation slip. The dislocation pile-up around the twin boundary (Fig. 4.69j) results in the local stress concentration, as well as the nucleation of shear bands. Therefore, the amounts of shear bands in the cryorolled sample are much larger than those in the room-temperature rolled sample. Furthermore, the shear bands are shown to be less thermal stability and potent nucleation sites for the recrystallized grains, which dramatically affect the microstructure and mechanical properties of annealed samples.

Figure 4.70 displays the EBSD maps of annealed of the room-temperature rolled (A-RTR) and annealed cryorolled (A-CR) samples. For Cu layer, the initial fibrous elongated grains are completely transformed into equiaxed grains under the action of recrystallization containing considerable Σ3 [111] annealing twins (ATs) (red line in

Fig. 4.70a and d). The ratio of twin boundaries in the Cu layer of A-RTR sample is 41.6%, slightly lower than that of 45.2% in A-CR sample. More importantly, the average twin width in Cu layer of A-RTR sample is 1.37 μm, 2.9 times of that in A-CR sample. The large amounts of deformation energy storage and high-density defects produced by cryorolling make a great contribution to the formation of ultrafine ATs, which enhances the strength-ductility combinations of Cu layer.

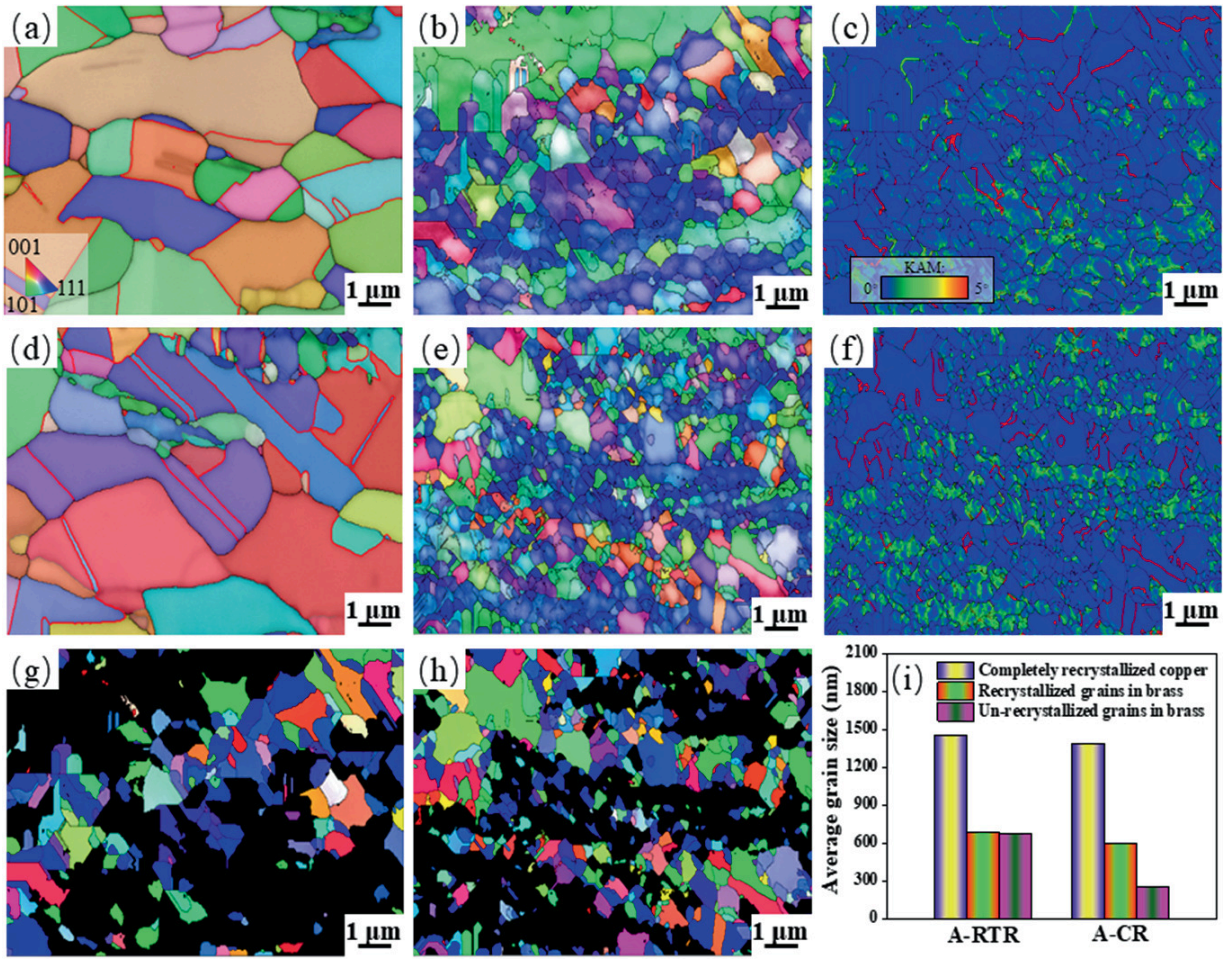


Fig. 4.70 Inversed pole figure maps of Cu layer and brass layer in **a**, **b** A-RTR and **d**, **e** A-CR samples; kernel average misorientation maps with Σ3 twin boundaries and recrystallized grain maps of brass layer in **c**, **g** A-RTR and **f**, **h** A-CR samples; **i** average grain size of A-RTR and A-CR samples

As to brass layer, the partial recrystallization structure can be observed (Fig. 4.70b and e). Statically recrystallized grains with low density of geometrically necessary dislocations (GNDs) are formed at the expense of the deformation structures (Fig. 4.70c and f). The recrystallization fraction of brass layer in A-RTR sample is 42.2%, much

lower than that of 54.2% in A-CR sample (Fig. 4.70g and h). The large amounts of shear bands formed in the cryorolling process significantly promote the nucleation of the recrystallized grains, which contributes to the ductility of brass layer. Interestingly, the average size of recrystallized grains (690 nm) in brass layer of A-RTR sample is close to the un-recrystallized grains (670 nm). In contrast, the recrystallized grains (603 nm) of brass layer in A-CR sample are much larger than the un-recrystallized grains (252 nm), resulting in the formation of extra heterogeneous structure in brass (Fig. 4.70i). This multistage heterostructure (consisting of coarse grains in Cu layer, medium-sized recrystallized grains and ultrafine un-recrystallized grains in brass layer) is beneficial to enlarging strain gradient, producing extra HDI strengthening and enhancing work hardening ability of A-CR sample. The lengths of total twin boundaries and grain boundaries in brass layer of A-CR sample are 54.7 and 576.4 μm, much larger than those in A-RTR sample of 20.9 and 303.7 μm. The larger grain boundary length implies the smaller average grain size. The yield strength of materials can be improved by refining the grain size to reduce the free-path of dislocations. Furthermore, more twins obviously enhance the stain hardening ability of brass layer in A-CR sample attributed to the twinning-induced plasticity effect.

Figure 4.71a and b show the representative Cu/brass interfaces in A-RTR and A-CR, revealing a transition from coarse-grained (CG) Cu to nanostructured (NS) brass. The formation of Cu/brass bonding interface is divided as four stages, which is consist with the Bay theory. Firstly, the oxidation film and work hardening layer on the surface of Cu and brass sheets are broken under huge rolling pressure. Secondly, the expansion of broken surface makes the matrix metal exposed. Thirdly, matrix metals are squeezed into the cracks in the oxidation film and work hardening layer. Finally, dissimilar metal atoms at the bonding interface are activated to form metallurgical bonding. Obviously, the recrystallized grains in the Cu layer are much larger and exhibit less dislocation than those in the brass layer. Interestingly, the flat bonding interface is formed in A-RTR sample contracts the curved bonding interface in A-CR sample. The high density dislocations resulted from the cryorolling process are blocked by the Cu/brass interfaces and thus cause the local stress concentration to form the curved interface.

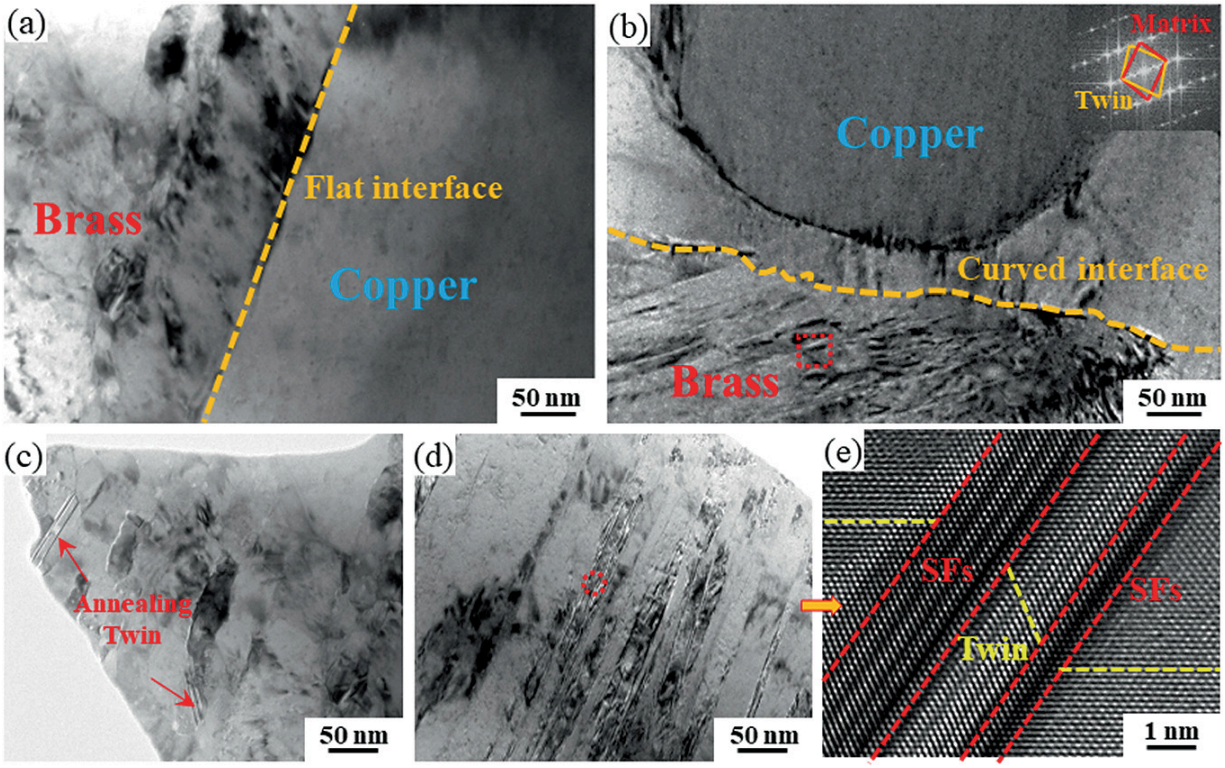


Fig. 4.71 TEM results of annealed samples: Bonding interface and brass layer of **a**, **c** A-RTR and **b**, **d** A-CR samples, **e** enlarged image of red circle in (**d**) containing nanotwins and SFs

Based on the dislocation ledge source model, the ledges on the Cu/brass interfaces can act as sources to emit dislocations, which are defined as the interface-affect-zone (IAZ). The number of dislocations (n) induced by the interfacial ledges can be expressed as:

$$n = \frac{\pi(1-\nu)\sigma}{\mu b} \cdot W \tag{4.12}$$

where v is the Poisson's ratio, σ is the applied stress, μ is the shear modulus, b is the burgers vector and W is the width of IAZ. Clearly, the wider IAZ induces the more dislocations. The width of IAZ in A-CR sample is much larger than that in A-RTR sample due to the formation of curved interface. The more emitted dislocations around the interface of A-CR sample promote the nucleation of DTs, as shown in Fig. 4.71b. Furthermore, the wider IAZ leads to the higher strain gradient between CG-copper/NS-brass and more HDI strengthening, associated with the increment of GNDs density. Figure 4.71c and d show more microstructural details in the brass layers of two samples. Nanocrystalline, dislocation cells and dislocation-free ATs are formed in

brass layer of A-RTR sample (Fig. 4.71c). In contrast, high density DTs are maintained in brass layer of A-CR sample (Fig. 4.71d). Furthermore, the boundary of nano twins is decorated by thick stacking faults (SFs) (Fig. 4.71e). The nano twins and SFs hinder the motion and glide of dislocations, resulting in more dislocation accumulation and improved work hardening.

4.7.2 Mechanical Properties of Cu/Brass Laminates

Figure 4.72a shows the engineering stress–strain curves containing strain hardening rate (SHR) curves of A-RTR and A-CR samples. For these samples processed by severe plastic deformation, the ultimate tensile strength (UTS) of CR sample reaches 582 MPa, 21.5% higher than that of 479 MPa for cold rolled sample. The enhanced strength is attributed to the formation of finer grains, dislocation blockage, and nano twins during cryorolling. After annealing, the UTS and uniform elongation of A-RTR sample is 409 MPa and 7.7%, while the corresponding values of A-CR sample are synergistically improved to 456 MPa and 8.2%, respectively. Furthermore, the SHR capability of Cu/brass laminate is enhanced by the decline of deformation temperature, implying that the cryorolling process can delay the occurrence of necking to retain ductility.

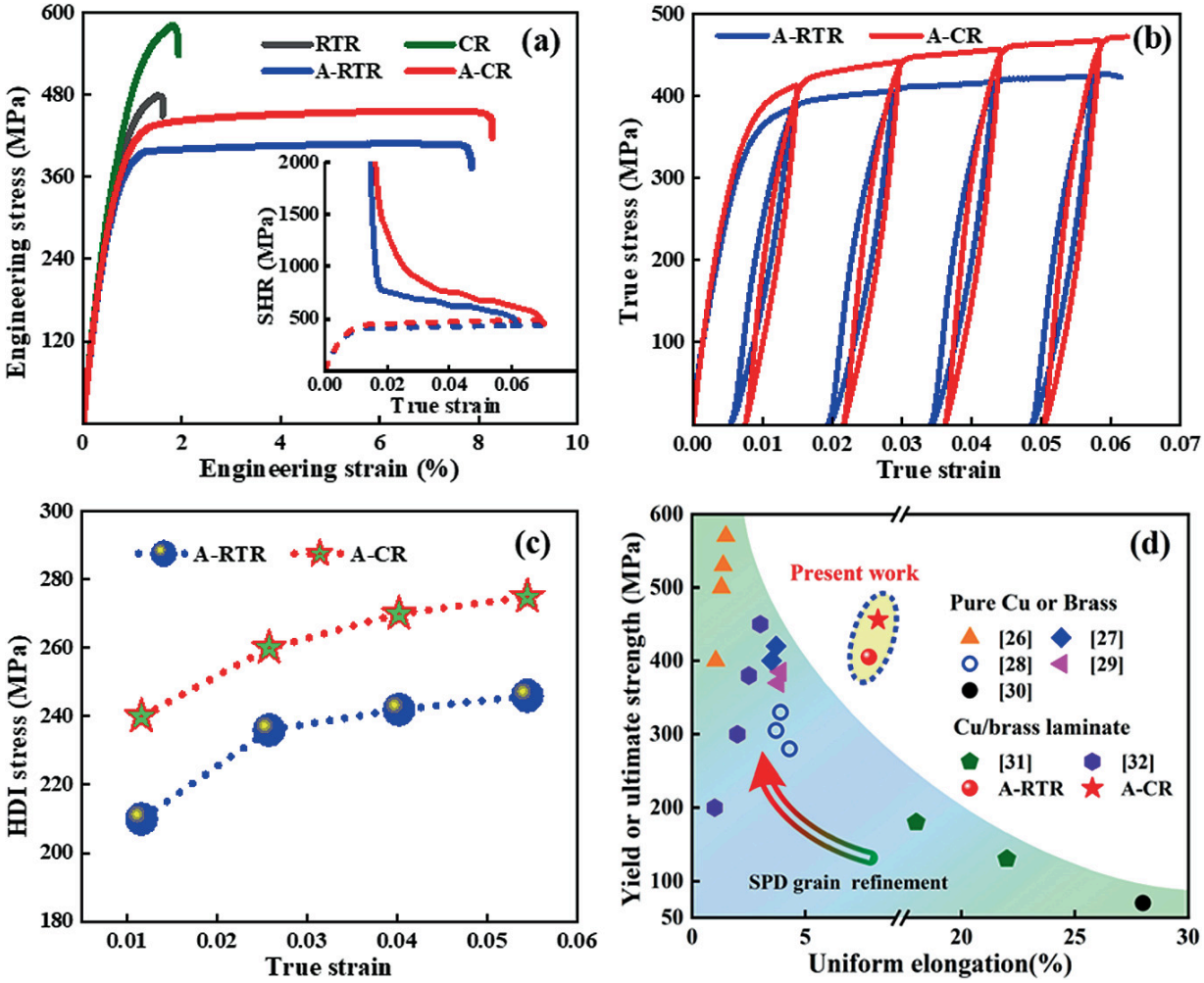


Fig. 4.72 Tensile properties of Cu/brass laminates: **a** Engineering stress–strain curves of the laminates, **b** unloading–reloading curves and **c** HDI stress evolution of A-RTR and A-CR samples, **d** comparison of tensile properties between A-series samples and other materials

The bonding interfaces between CG-Cu and NS-brass are expected to produce strong HDI stress, which is proved by the appearance of hysteresis loops (Fig. 4.72b) and determined by unloading–reloading experiments. As shown in Fig. 4.72c, the HDI stress for A-RTR sample increases linearly with the increased loading strain, ranging from 210 to 246 MPa. While the HDI stress for A-CR sample is nearly 30 MPa higher than A-RTR sample at the same strain. Figure 4.72d compares the strength and ductility of A-series samples with those homogeneous Cu and brass, which strongly demonstrates the performance advantages of LHMM. Besides, the introduction of intermediate thinning rolling process, especially cryorolling, between ARB and annealing (A-series samples) achieves further enhancement in the mechanical properties of Cu/brass laminates.

During the tensile deformation of Cu/brass laminates, the plastic deformation occurs firstly in soft CG-copper, while the hard NS-brass deforms elastically. Accordingly, the strain gradient, the pile-up of GNDs and HDI stress are induced by mechanical incompatibility. Compared to A-RTR sample, the better enhancement effect of strength-ductility synergy is obtained by A-CR sample through the following mechanisms: (1) Large amounts of ultrafine un-recrystallized grains in the brass layer of A-CR sample (Fig. 4.70e) reduce the average grain sizes of Cu/brass laminate, which enhances the grain boundary hardening. Furthermore, the multistage heterostructure (Fig. 4.70i) and wider IAZ around the boding interface (Fig. 4.71b) in A-CR sample produce the extra HDI strengthening, leading to the higher strength. (2) The higher HDI stress in A-CR sample also obviously improves the strain hardening ability of Cu/brass laminates (Fig. 4.72a) through suppressing the appearance of necking. Besides, the more defect-free recrystallized grains (Fig. 4.70h) and higher density of nano twins (twinning-induced plasticity effect) (Figs. 4.70d, f and 4.71d) in A-CR sample contributes to retaining the ductility of Cu/brass laminates.

References

1. Yu HL (2020) Progresses in fabrication of high–performance metals by using cryorolling. China Mech Eng 31(1):89–99
2. Wang ZJ, Ma M, Qiu ZX, Zhang JX, Liu WC (2018) Microstructure, texture and mechanical properties of AA 1060 aluminum alloy processed by cryogenic accumulative roll bonding. Mater Charact 139:269–278 [Crossref]
3. Du QL, Li C, Cui XH, Kong C, Yu HL (2021) Fabrication of ultrafine–grained AA1060 sheets via accumulative roll bonding with subsequent cryorolling. Trans Nonfer Met Soc China 31:3370–3379 [Crossref]
4. Takagawa Y, Tsujiuchi Y, Watanabe C, Monzen R, Tsuji N (2013) Improvement in mechanical properties of a Cu–2.0 mass% Ni–0.5 mass% Si–0.1 mass% Zr alloy by combining both accumulative roll–bonding and cryo–rolling with aging. Mater Trans 54:1–8 [Crossref]
5. Yu HL, Lu C, Tieu K, Li HJ, Godbole A, Liu X (2017) Enhanced materials performance of Al/Ti/Al laminate sheets subjected to cryogenic roll bonding. J Mater Res 32:3761–3768 [Crossref]

6. Liu J, Wu YZ, Wang L, Wang H, Kong C, Pesin A, Zhilyaev AP, Yu HL (2020) Fabrication and characterization of high-bonding-strength Al/Ti/Al laminated composites via cryorolling. Acta Metall Sin Eng Lett 33:871–880
[Crossref]
7. Wang L, Liu J, Kong C, Pesin A, Zhilyaev AP, Yu HL (2020) Sandwich–like Cu/Al/Cu composites fabricated by cryorolling. Adv Eng Mater 22(10):2000122
[Crossref]
8. Yang QY, Zhou YL, Tan YB, Xiang S, Ma M, Zhao F (2021) Effects of microstructure, texture evolution and strengthening mechanisms on mechanical properties of 3003 aluminum alloy during cryogenic rolling. J Alloy Compd 884:161135
[Crossref]
9. Song LL, Xie ZB, Gao HT, Kong C, Yu HL (2022) Microstructure and mechanical properties of ARB–processed AA1050/AA5052 multilayer laminate sheets during cryorolling. Mater Lett 307:130998
[Crossref]
10. Song LL, Gao HT, Bhatt L, Kong C, Yu HL (2023) Microstructure and mechanical properties of AA1050/AA6061 multilayer composites via accumulative roll bonding and cryorolling and subsequent ageing. Mater Sci Eng A 874:145069
[Crossref]
11. Yu HL, Lu C, Tieu K, Li HJ, Godbole A, Liu X, Kong C (2017) Enhanced materials performance of Al/Ti/Al laminate sheets subjected to cryogenic roll bonding. J Mater Res 32:3761–3768
[Crossref]
12. Li HL, Guo AH, Kong C, Yu HL (2024) Mechanical properties and microstructure evolution of Al/Mg–Li/Al laminate composites via hot rolling and subsequent cryorolling. Mater Sci Eng A 891:146007
[Crossref]
13. Wang L, Liu J, Kong C, Pesin A, Zhilyaev AP, Yu HL (2020) Sandwich–like Cu/Al/Cu composites fabricated by cryorolling. Adv Eng Mater 22:2000122
[Crossref]
14. Gao HT, Li J, Lei G, Song LL, Kong C, Yu HL (2022) High strength and thermal stability of multilayered Cu/Al composites via accumulative roll bonding and cryorolling. Metall Mater Trans A 53:1176–1187
[Crossref]
15. Liu J, Wu YZ, Gao HT, Kong C, Yu HL (2023) Enhanced mechanical properties and thermal stability of accumulative roll bonded Cu/Nb multilayer composites via cryorolling. Metall Mater Trans A 54:16–22
[Crossref]
16. Zheng S, Beyerlein IJ, Carpenter JS, Kang K, Wang J, Han W, Mara NA (2013) High-strength and thermally stable bulk nanolayered composites due to twin-induced interfaces. Nat Commun 4:1696

17. Gao HT, Liu SL, Song LL, Kong C, Yu HL (2023) Enhanced strength–ductility synergy in heterostructured copper/brass laminates via introducing cryorolling. Mater Sci Eng A 878:145239
[Crossref]

© The Author(s), under exclusive license to Springer Nature Singapore Pte Ltd. 2024
H. Yu et al., *High-Performance Metallic Composites Fabricated by Advanced Rolling Techniques*
https://doi.org/10.1007/978-981-97-4331-5_5

5. Fabricated Al/Particle Composites via Cryorolling

Hailiang Yu[1] ✉, Haitao Gao[1] ✉ and Zhou Li[1]
(1) Central South University, Changsha, China

✉ **Hailiang Yu (Corresponding author)**
Email: yuhailiang@csu.edu.cn

✉ **Haitao Gao**
Email: gaohaitao@csu.edu.cn

Particle-reinforced Al matrix composites (AMC) are the most famous metal matrix composites which find wide applications in aerospace [1] and automotive industries [2]. This demand specifically arises from their high specific strength [3], excellent stiffness [4], and good wear resistance [5]. Ceramic particles with high outstanding strength and elastic moduli, such as SiC and TiC particles, are often used in AMCs nowadays [6]. However, the ductility of such AMCs decreases significantly owing to the poor deformation ability of ceramic particles. Additionally, the secondary processing of such AMCs is challenging due to the discordant deformation of ceramic particles and the Al matrix [3]. Therefore, it is of real importance to seek new kinds of reinforcing particles and processing technology to develop PAMC sheets.

In recent years, high-entropy alloys (HEAs) have high strength, good plasticity, and excellent cryogenic-temperature mechanical properties [7], which make them excellent candidates to act as reinforced particles in AMCs. Li et al. [8] prepared AMCs reinforced by $Al_{0.8}CoCrFeNi$ high-entropy alloy particles (HEAp) through friction stir processing and

found that the average hardness was remarkably enhanced from 80.5 (Al matrix) to 125.7 HV (AMCs). Attributed to the good bonding ability between the HEAp and Al matrix, the ultimate tensile strength (UTS) of the AMCs was 371 MPa. Yuan et al. [9] fabricated AMCs reinforced with $Al_{0.6}$CoCrFeNi HEAp by a vacuum hot-pressing sintering process. Post annealing at 773 K for 12 h, the hardness of the AMCs could be enhanced from 136 to 178 HV. A continuous interfacial layer was generated, which could transfer more loads from the Al matrix to the HEAp. Liu et al. [10] applied spark plasma sintering to prepare AlCoCrFeNi-reinforced AMCs and found that both the yield strength and ductility were enhanced with sintering temperature. Luo et al. [11] compared the deformation behavior of Al/HEAp MMCs under room temperature rolling and cryorolling. After cryorolling, the mechanical properties got better, and a low density of defects was observed compared to those obtained via room temperature rolling. Li et al. [12] prepared Al/HEAp MMCs by powder metallurgy. The nanohardness and elastic modulus at the interface was 1245 MPa and 72 GPa, respectively, which points toward an excellent interfacial bonding strength. However, for Al/HEAp MMCs, defects such as microcracks were easily generated when deformed at room temperature. This, in turn, has a deteriorating effect on the bonding ability of the HEAp and Al matrix [11]. In addition, the mismatch between the coefficient of thermal expansion of the HEAp reinforcement and Al matrix may also accelerate the generation of micropores [13]. Therefore, it is necessary to develop new techniques that would strengthen Al/HEAp MMCs.

Asymmetric rolling (AR) can reduce the rolling force, improve sheet forming performance and mechanical properties [14, 15]. Asymmetric cryorolling (ACR) is considered a severe plastic deformation process that benefits from the advantages of both AR and cryorolling [16]. The cryogenic environment in the ACR can effectively inhibit dynamic recovery, accumulate more dislocations, and promote grain refinement, resulting in higher tensile strength [17]. Yu et al. [18] prepared AA6061 sheets by ACR and observed that the hardness and tensile strength were improved, and the grain size was refined to 235 nm after 7 ACR cycles. Zhang et al. [19] observed that the grains became finer, and the deformation twins appeared in CoCrNi sheets after 77 K ACR processing, which resulted in excellent mechanical properties.

However, there are only few studies on the development of Al/HEAp MMCs by using ACR. The deformation behavior of HEAp during shear deformation by ACR greatly affected the mechanical properties of AMCs. At present, the strengthening mechanism of Al/HEAp MMCs by the ACR process was not clear. Therefore, it was very significant to explore the relationship between mechanical properties and microstructure of AMCs during ACR.

5.1 Fabrication of AA1050/HEAp MMCs via Cryorolling

AA1050/HEAp MMCs strips were prepared by stir-casting and subsequent rolling. The microstructure and mechanical properties of cold rolled and cryorolled AA1050/HEAp MMCs were studied. The AA1050/HEAp MMCs strips have fewer defects and higher mechanical properties by cryorolling. Also, we discuss the mechanism of improving mechanical properties by cryorolling [11].

The AA1050/HEAp MMCs were prepared by a stir casting method. The schematic representation of the stir casting process is shown in Fig. 5.1a. The AA1050 ingot was melted at 1093 K with a resistance furnace. After the alloy was completely melted, HEAp wrapped with high-purity Al foil were added, and then mechanical stirring was carried out for 3 min. The mixed molten AA1050/HEAp MMCs was poured into the preheated mold to obtain the ingots. AA1050/HEAp MMCs ingots with HEAp mass fractions of 0, 1, 3, and 6 wt% were prepared.

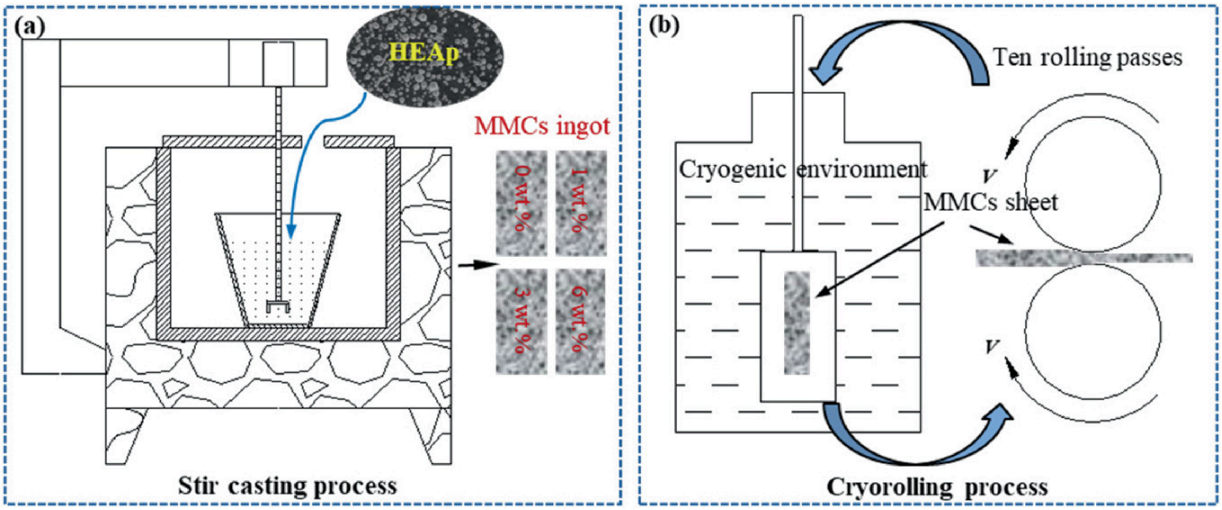


Fig. 5.1 Schematic illustrations of the AA1050/HEAp MMCs: **a** stir casting process and **b** cryorolling process

The AA1050/HEAp MMCs ingots were cut into sheets with thicknesses of 2.00 mm using wire-cut electrical discharge machining. And then the sheets were processed by cold rolling and cryorolling respectively. The cold rolling temperature was 298 K, and the cryorolling temperature was 77 K (Fig. 5.1b).

5.1.1 Microstructure Evolution of AA1050/HEAp Composites

Figure 5.2 shows the XRD spectra of the $Al_{0.5}CoCrFeNi$ HEAp and AA1050/HEAp MMCs. In Fig. 5.2a, the $Al_{0.5}CoCrFeNi$ HEAp possessed a face-centered cubic (FCC) + body-centered cubic (BCC) two-phase structure. The FCC structure mainly has (111), (200), and (220) crystal plane diffraction peaks. The diffraction peaks of the BCC structure were concentrated on the (110), (200), and (211) crystal planes. $Al_xCoCrFeNi$ HEA have FCC and BCC two-phase structures when x is 0.3–0.8. $Al_{0.5}CoCrFeNi$ HEA is a typical two-phase-structure alloy with excellent strength and good ductility. The XRD results when different mass fractions of HEAp were added to the AA1050 matrix are shown in Fig. 5.2b. After the addition of HEAp, the special (211) crystal plane of the $Al_{0.5}CoCrFeNi$ HEA was found in the XRD spectrum of the AA1050/HEAp MMCs, which proved that the HEAp were presented in the AA1050 matrix. With the increase in the mass fraction of the HEAp,

the diffraction peak intensity of the BCC phase increased gradually, which was not found in the AA1050 without HEAp.

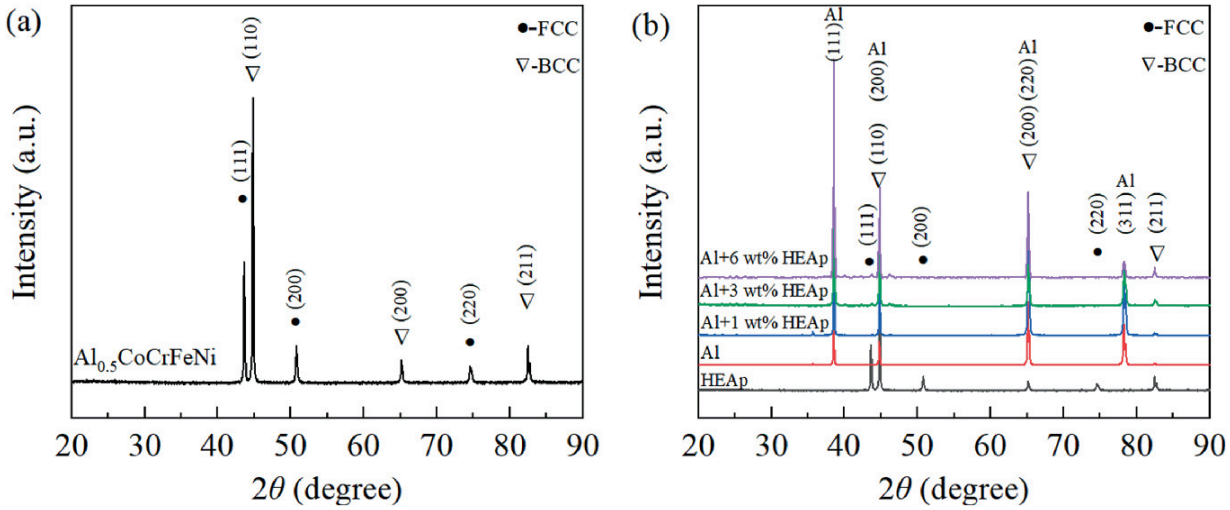


Fig. 5.2 X-ray diffractograms of **a** HEAp and **b** AA1050/HEAp MMCs with different mass fractions of HEAp

Figure 5.3 shows the SEM image of the HEAp in as-cast AA1050/HEAp MMCs and the surface scanning results of the corresponding area. The HEAp were composed of five elements, Al, Co, Fe, Cr, and Ni. The distribution of the above five elements can be clearly observed in the surface scanning results in Fig. 5.3.

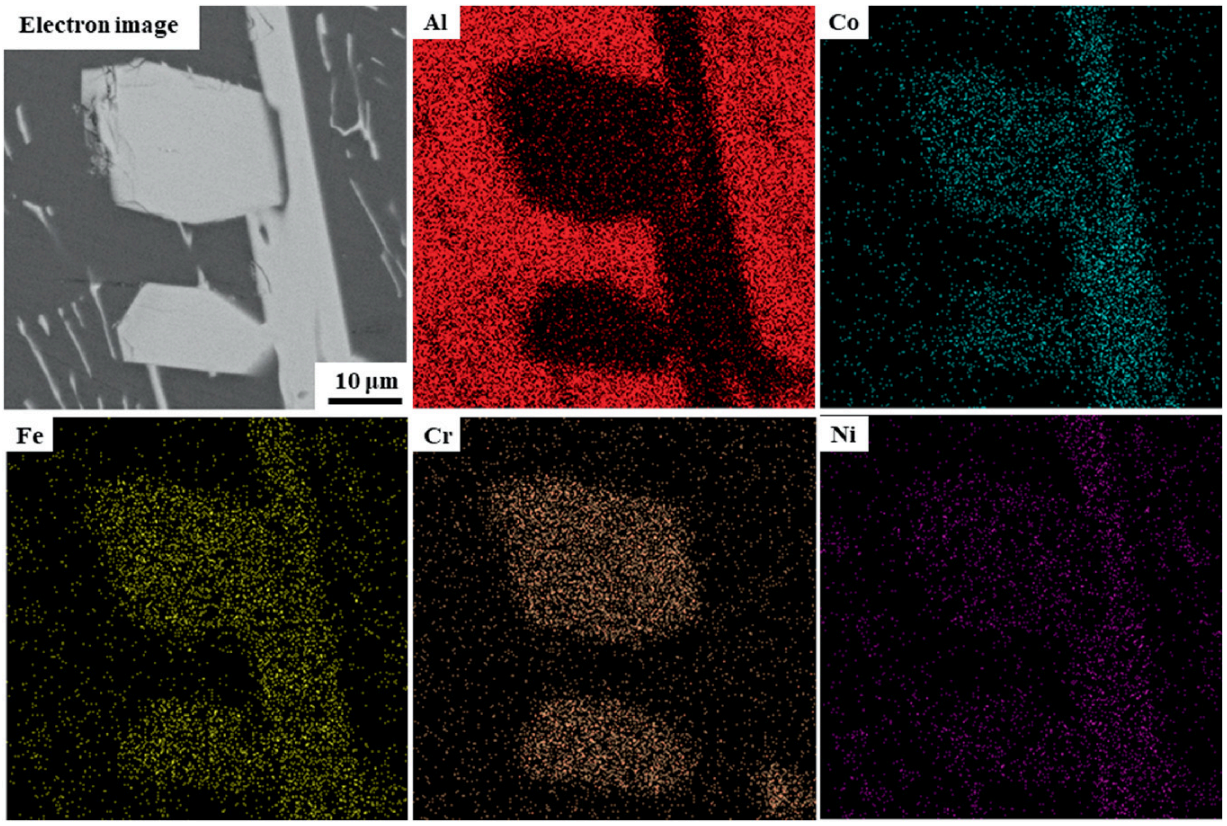


Fig. 5.3 SEM image and element distribution of HEAp in as-cast AA1050/HEAp MMCs

Figure 5.4 shows the SEM images of the AA1050/HEAp MMCs with different rolling deformation. As shown in Fig. 5.4a–d, cold rolling and cryorolling were carried out with reduction ratios of 50% and 95%, respectively. After cold rolling, there are many microvoids in the AA1050/HEAp MMCs. With the increase of deformation from 50 to 95%, the number of microvoids increased rapidly. However, no defects such as microvoids and fractures were found in the cryorolled AA1050/HEAp MMCs. The cryorolling temperature was very low, which inhibited the dynamic recovery during rolling and made the material structure more uniform. In addition, comparing Fig. 5.4a and c, although the rolling deformation of the cold rolling and cryorolling were identical, their deformed microstructures were significantly different. The reinforcement phase of the HEAp became more uniform and elongated after the cryorolling than after the RTR.

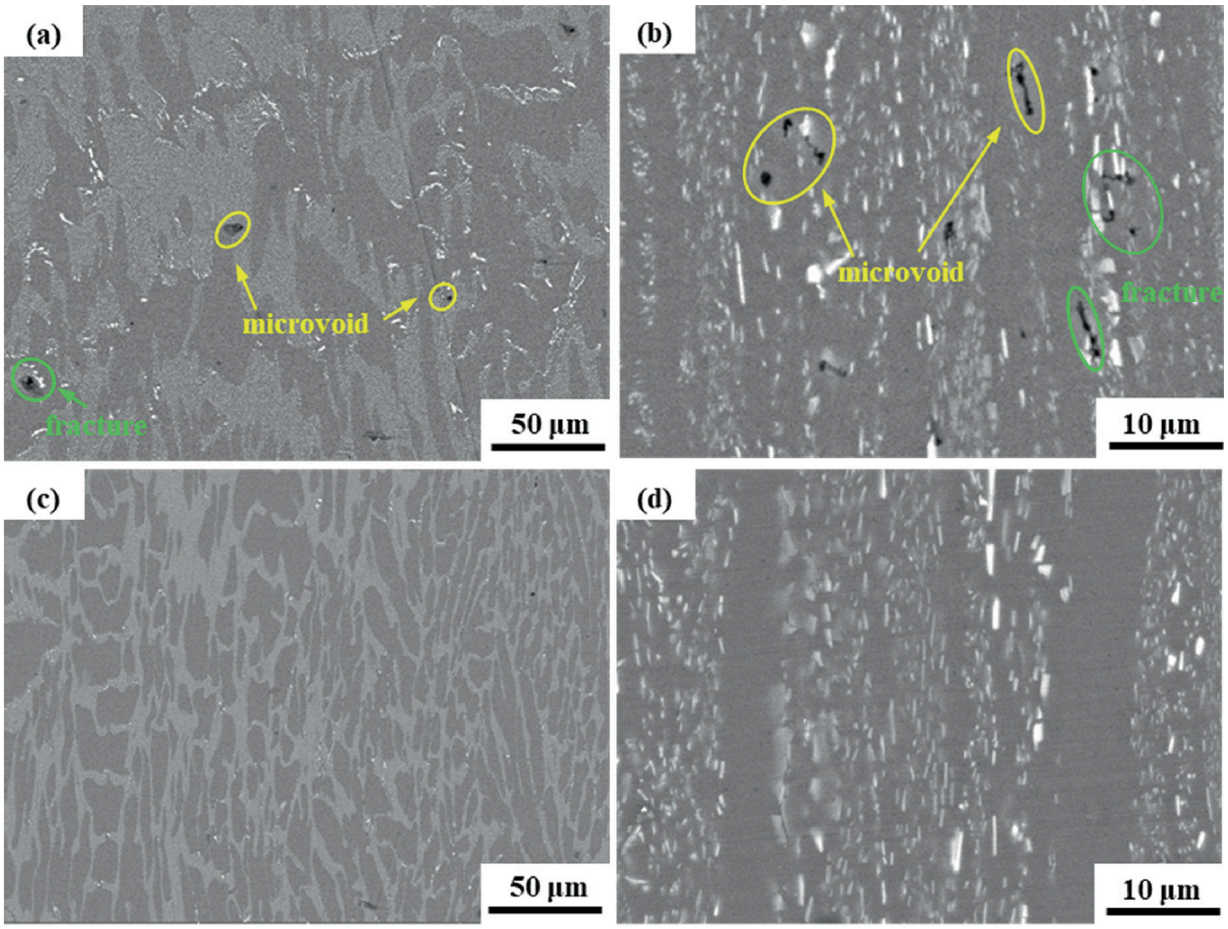


Fig. 5.4 SEM images of AA1050–3 wt% HEAp MMCs after cold rolling and cryorolling: cold rolling with rolling reduction of **a** 50% and **b** 95%; cryorolling with rolling reduction of **c** 50% and **d** 95%

5.1.2 Mechanical Properties of AA1050/HEAp MMCs

Figure 5.5 shows the microhardness values of the AA1050/HEAp MMCs in the casting state and after rolling. As shown in Fig. 5.5a, the hardness values of the AA1050/HEAp MMCs were significantly improved after the addition of HEAp. The microhardness values were 26.3, 40.7, 55.2 and 69.2 HV when four kinds of mass fraction HEAp were added. The microhardness values of the AA1050/HEAp MMCs increased by 163.1% after adding 6 wt% HEAp. Figure 5.5b–d show the microhardness values of the AA1050/HEAp MMCs obtained by cold rolling and cryorolling with different deformation. The microhardness values of the cryorolled AA1050/HEAp MMCs were generally higher than those of the RTR. Under the same deformation conditions, the increase of microhardness value of the A1050 – HEAp MMCs was

higher than that of the AA1050. This result was also confirmed in the ultimate tensile strength in Fig. 5.6.

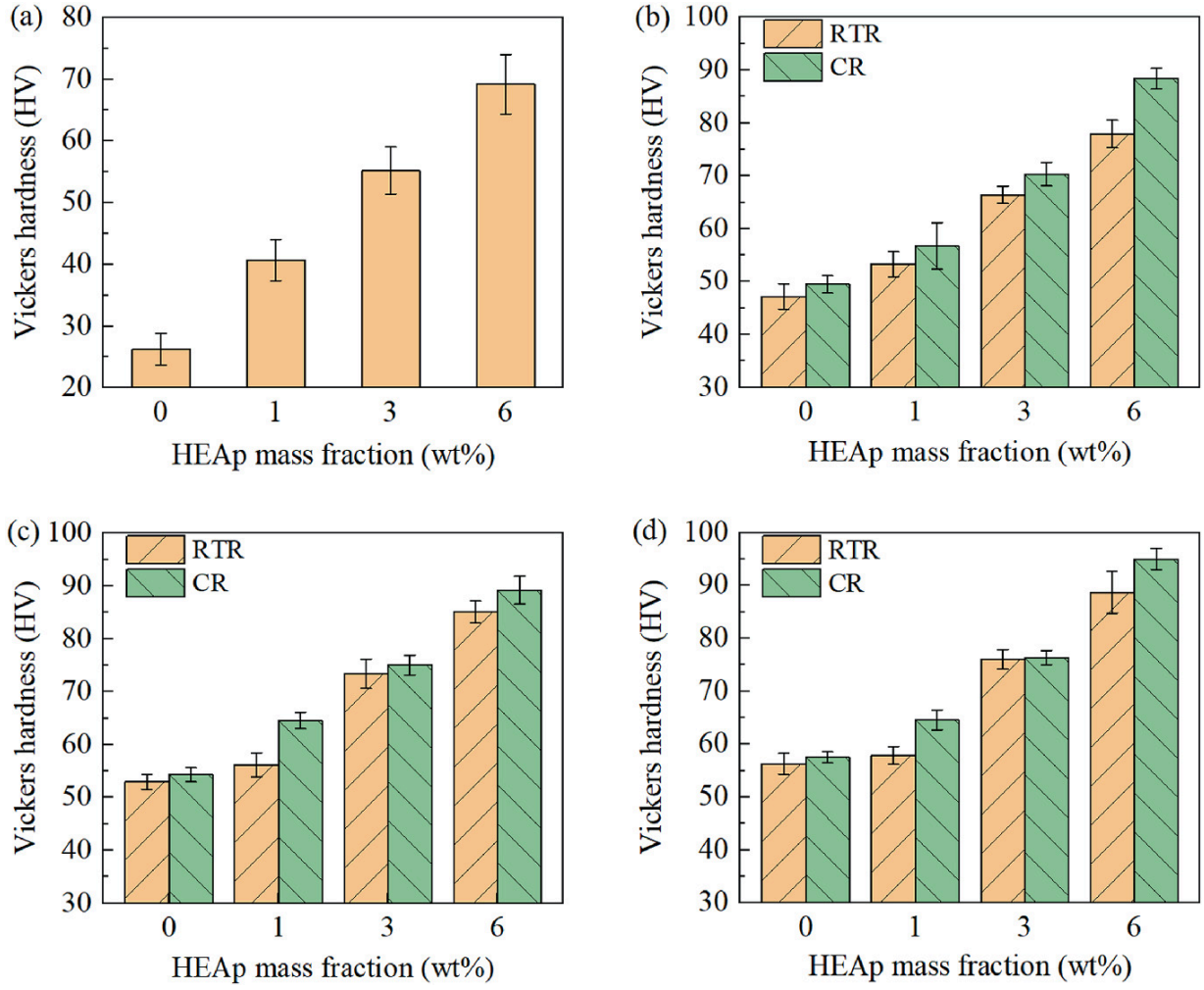


Fig. 5.5 Vickers hardness histogram of **a** as-cast AA1050/HEAp MMCs; rolled AA1050/HEAp MMCs at reduction ratio of **b** 50%, **c** 80%, and **d** 95%

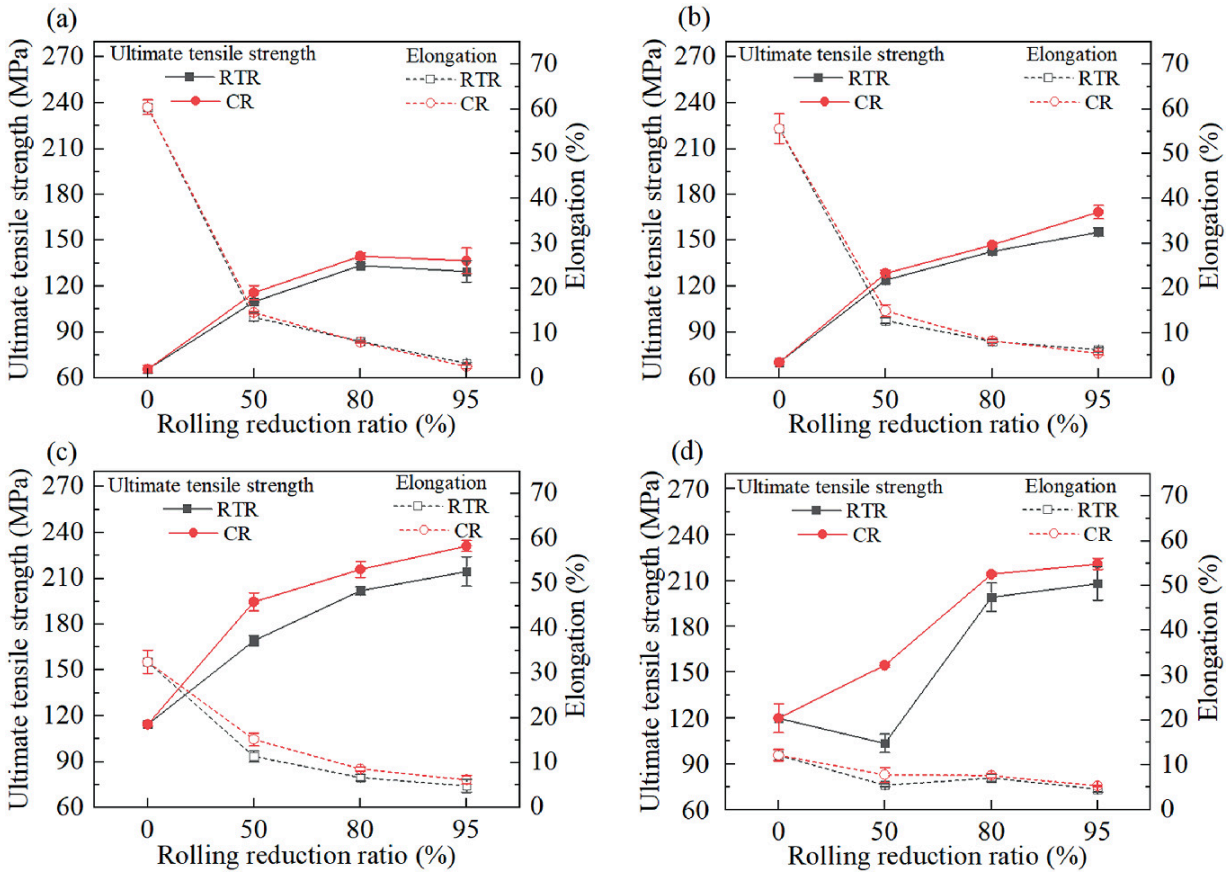


Fig. 5.6 Mechanical properties of AA1050/HEAp MMCs rolled at 298 and 77 K **a** without HEAp and with **b** 1 wt% HEAp, **c** 3 wt% HEAp, and **d** with 6 wt% HEAp

Figure 5.6 shows the tensile mechanical properties of the AA1050/HEAp MMCs in different states. It can be seen that the mechanical properties of the AA1050/HEAp MMCs in the as-cast state were improved with the increase of the HEAp. The ultimate tensile strength of AA1050 was 65 MPa. When 3 wt% HEAp were added, the ultimate tensile strength of the AA1050 MMCs reached 115 MPa. At the same time, the elongation reached 32.1%. However, the improvement of ultimate tensile strength was limited when the mass fraction of HEAp was increased to 6 wt%. This is consistent with the results of Vickers hardness. As shown in Fig. 5.6a–d, the comprehensive mechanical properties of the materials after cryorolling were better than those after RTR. Taking Fig. 5.6c as an example, the ultimate tensile strength and elongation of cryorolled AA1050 – 3 wt% HEAp MMCs were 195 MPa and 15.2% at 50% deformation, while the cold rolled MMCs were 169 MPa and 11.4%. The ultimate tensile strength of the cryorolled AA1050 – 3 wt% HEAp MMCs was 15.4% higher than that of

RTR, and the elongation of the cryorolled MMCs were 33.3% higher than that of the cold rolled MMCs. In addition, when the mass fraction of HEAp was low, the differences in the mechanical properties of the cold rolled and cryorolled samples were small. With the mass fraction of HEAp increased to 3 wt%, the improvement of the mechanical properties of the cryorolled samples became more significant. When 6 wt% HEAp was added, the mechanical properties of the rolled MMCs were generally lower than that of AA1050 – 3 wt% HEAp MMCs.

Figure 5.7 shows the tensile fracture morphologies of the AA1050 – 3 wt% HEAp MMCs after cold rolling and cryorolling. The elongation of composites were closely related to the fracture morphology. The number of dimples in the fracture significantly decreased with the increase in the rolling deformation. In addition, the dimple size decreased, the depth decreased, and the dimple tearing edges began to appear. This was consistent with the general rule that the elongation of the AA1050/HEAp MMCs decreased with the increase in the deformation. However, many interesting phenomena can be found by observing the tensile fracture of the cold rolling and cryorolling with the same deformation in Fig. 5.7. According to the results of the mechanical properties, the elongation properties of the cryorolled AA1050/HEAp MMCs were better than those of the cold rolled MMCs. As shown in Fig. 5.7a and d, the number of dimples in the cryorolled MMCs was significantly greater than that in the cold rolled MMCs. This was the microstructural reason that the elongation of the cryorolled MMCs was better than that of cold rolled MMCs. As shown in Fig. 5.7c and f, a large number of tearing edges and quasi-cleavage fracture features appeared in the cold rolled MMCs, however, the number and widths of the tear edges in the cryorolled MMCs were far lower than those of the cold rolled MMCs, which further proved that the elongation of the cryorolled MMCs was better. It was also noteworthy that the HEAp were found to fall off at the cold rolled MMCs tensile fracture. This phenomenon was not found in the cryorolled MMCs tensile fracture. It was proved that the HEAp and Al alloy matrix in the cryorolled MMCs have better bonding ability and were not easy to fall off.

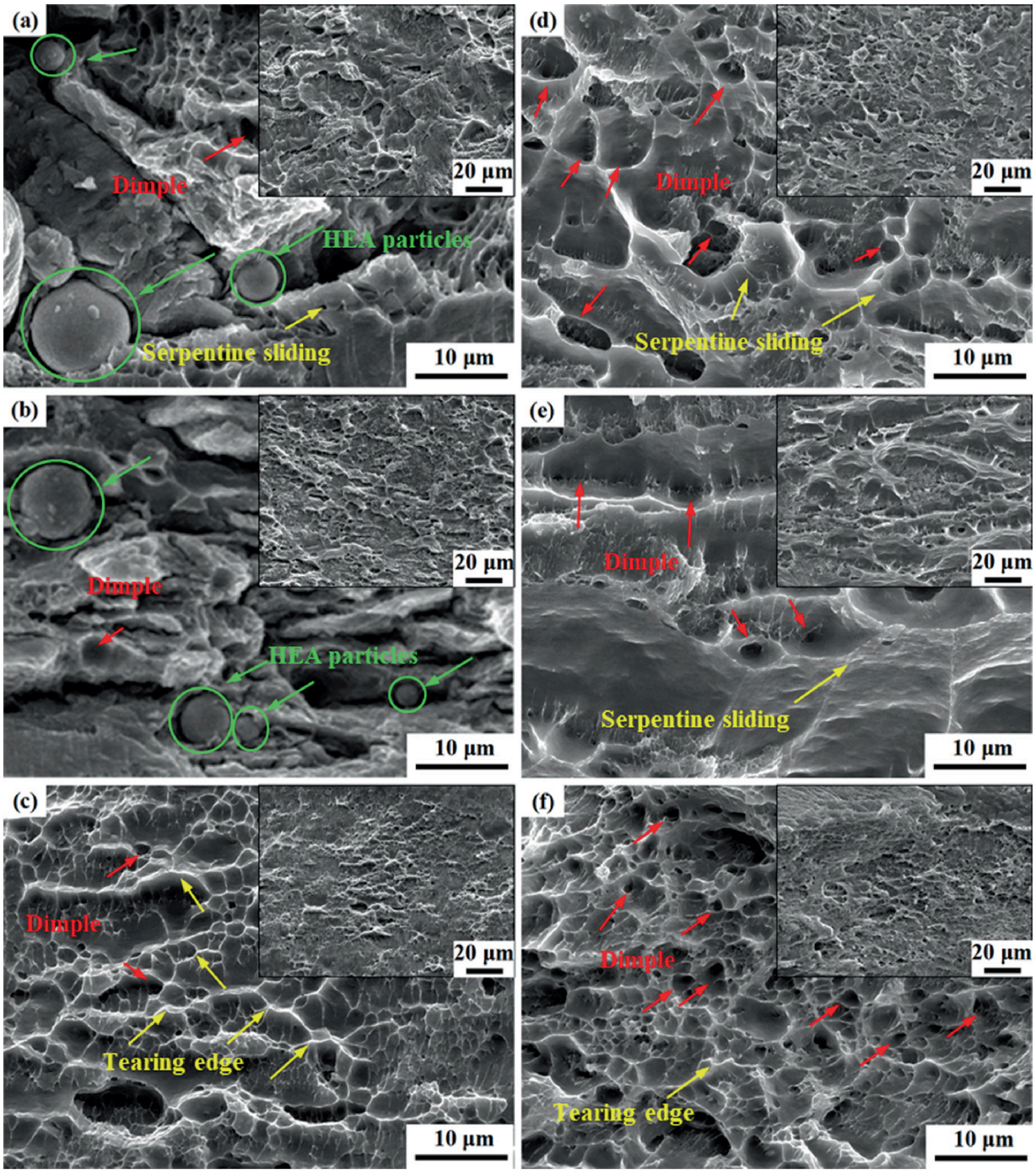


Fig. 5.7 Fracture morphologies of rolling AA1050 − 3 wt% HEAp MMCs: cold rolling with rolling reduction ratio of **a** 50%, **b** 80%, and **c** 95%; cryorolling with rolling reduction ratio of **d** 50%, **e** 80%, and **f** 95%

5.1.3 Mechanism of Suppression of Microvoid and Fracture in AA1050/HEAp MMCs During Cryorolling

In Fig. 5.7, the phenomenon of HEAp fell off was observed at the tensile fracture of the cold rolled MMCs, but not in the cryorolled MMCs. At the same time, it was found in Fig. 5.4 that the cold rolled MMCs have more defects, while the cryorolled MMCs have obvious improvement.

When the cryorolling temperature was 77 K, volume shrinkage of the AA1050/HEAp MMCs occurred, which can be expressed as follows:

$$V_T = V_0 e^{\alpha(T-T_0)} \tag{5.1}$$

where α is the coefficient of thermal expansion (CTE). When the temperature changes from T_0 to T, the corresponding volume changes from V_0 to V_T, respectively. It can be seen from the above formula that the change of temperature has a great influence on the volume of solid materials. Cryorolling is carried out at −77 K, and a large temperature difference (221 K) will produce a strong volume shrinkage effect. The volume shrinkage will have an important effect on the microstructures and mechanical properties of materials. The volume shrinkage of cryorolling includes the shrinkage of Al alloy matrix and the shrinkage of HEAp. Because the thermal expansion coefficient of Al alloy matrix (68.1×10^{-6} K^{-1}) was higher than that of HEAp (11.7×10^{-6} K^{-1}), the volume shrinkage degree of Al alloy matrix and HEAp matrix was different. The stronger volume shrinkage of Al alloy makes the Al alloy matrix bond with the HEAp more firmly. The stronger bonding makes the HEAp less likely to fall off during tensile fracture. In the absence of this effect in RTR, the HEAp is more likely to fall off from the Al alloy matrix. It can also be seen from Fig. 5.8a and b that fracture was also found near HEAp in the cold rolled MMCs. However, these defects could be avoided by cryorolling because of the volume shrinkage effect, which resulted in the better mechanical properties of the cryorolled materials. According to Fig. 5.7c and d, fractures and other defects are not observed in cryorolling. This defect in microstructure can also be confirmed by the SEM results in Fig. 5.4a–d.

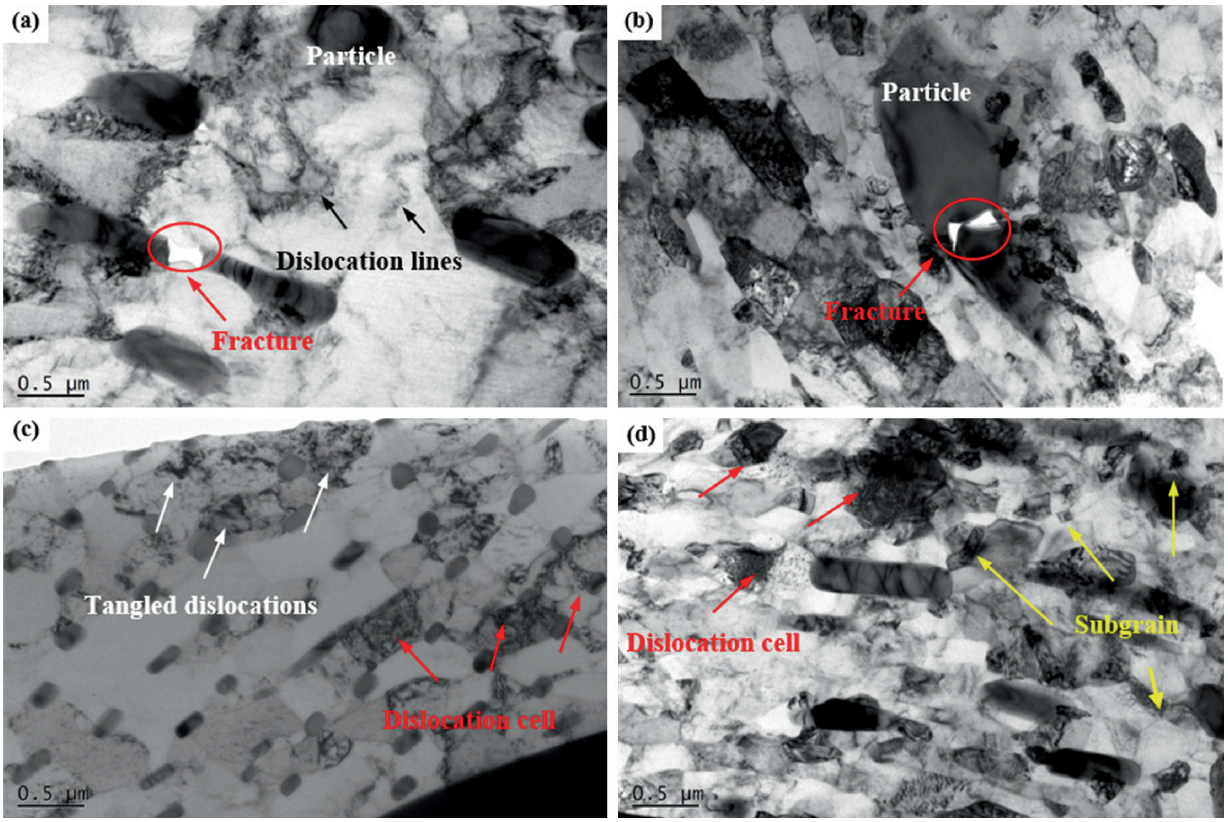


Fig. 5.8 TEM images of the cold rolled AA1050–3 wt% HEAp MMCs at **a** 50% deformation and **b** 95% deformation and the cryorolled AA1050–3 wt% HEAp MMCs at **c** 50% deformation and **d** 95% deformation

In addition, Al alloys and HEA have better ductility in cryogenic environment compared to that in room temperature environment. These enhanced deformation performance in cryogenic environment may also contribute to the defect-free MMC strips after cryorolling.

In the cryogenic environment, a large number of dislocations and substructures are produced. During cryogenic deformation, the atomic energy is low and the dynamic recovery is severely inhibited. These dislocations are unrecoverable and difficult to cancel and rearrange. Dislocations are constantly entangled and accumulated, and finally a cellular structure appears. In Fig. 5.8c, dislocation cells formed by high-density dislocation tangles are evident for the cryorolled materials. When the deformation of cryorolling was further increased, the extremely high dislocation density generated subcrystalline structures, which are evident in Fig. 5.8d. The high-density dislocations and substructures can improve the comprehensive mechanical properties of the AA1050/HEAp MMCs.

5.1.4 Mechanism of Cryorolling on Enhanced Mechanical Property of AA1050/HEAp MMCs

In the cryogenic environment, materials could accumulate a large amount of storage energy with high density dislocations, which could refine the grains during rolling. Figure 5.9 shows the statistical results of AA1050/HEAp MMCs grain size after rolling deformation. As can be seen from the comparison of Fig. 5.9a–d, under the same rolling deformation condition, the grain size of AA1050/HEAp MMCs obtained by cold rolling and cryorolling is significantly different. At 50% rolling deformation, the grain size of the AA1050/HEAp MMCs obtained by cold rolling is 592 nm, while the grain size of the AA1050/HEAp MMCs obtained by cryorolling is 340 nm. The mean grain size is reduced by 42.6%. The grain refinement of the AA1050/HEAp MMCs obtained by cryorolling is obvious. According to the Hall–Petch formula, grain refinement can improve the strength of the material. The grain size of cryorolled MMCs is significantly smaller than that of cold rolled samples, so the strength is higher.

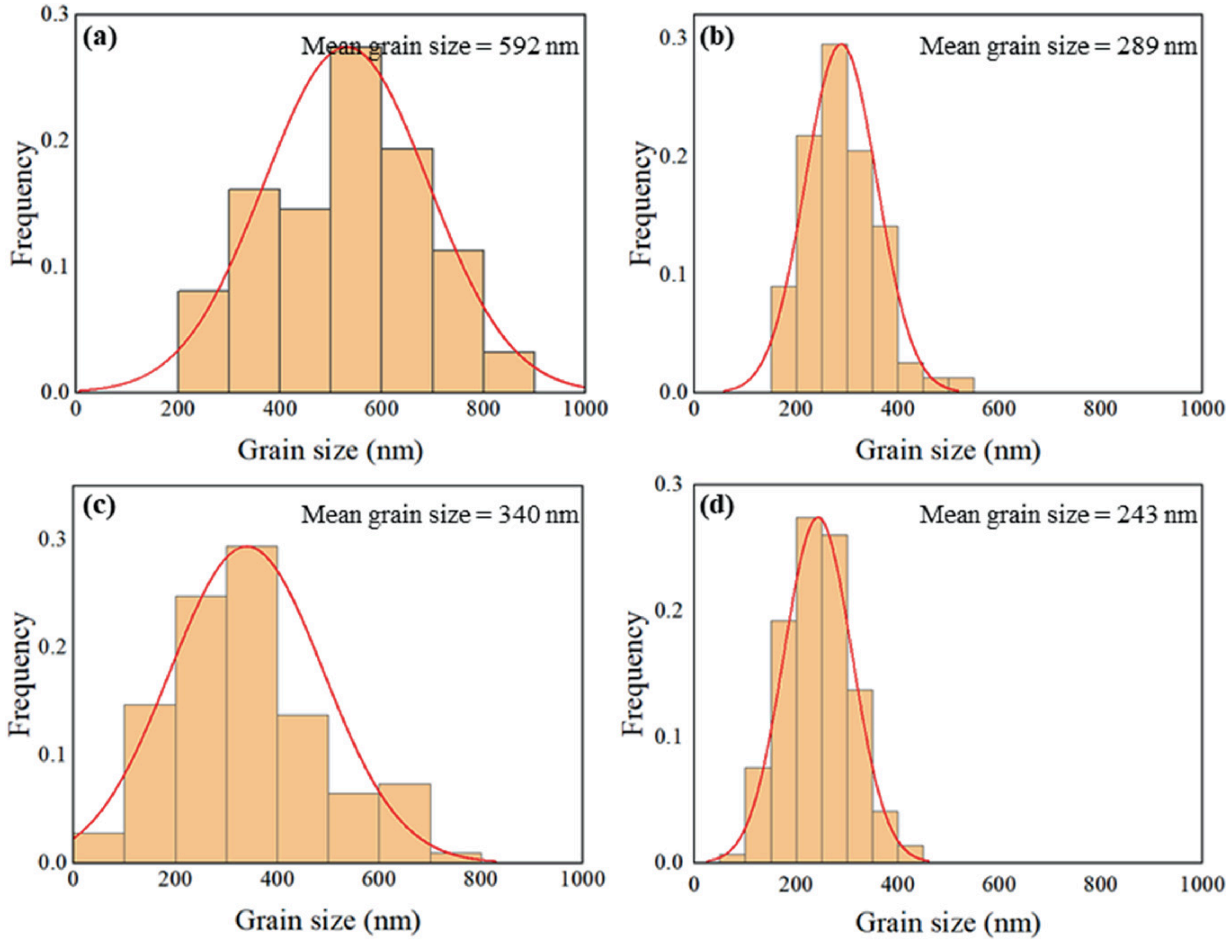


Fig. 5.9 Statistical results of grain size at cold rolled AA1050–3 wt% HEAp MMCs with rolling reduction ratio of **a** 50% and **b** 95%; cryorolled AA1050–3 wt% HEAp MMCs with rolling reduction ratio of **c** 50% and **d** 95%

In Figs. 5.4 and 5.8, the cryorolled MMCs strips have fewer defects, so the elongation is better than that of cold rolled MMCs. Also, volume shrinkage will lead to greater internal stress in the material and then induce the generation of dislocations. According to dislocation strengthening theory, when a dislocation contacts other dislocation on the slip plane in the process of dislocation movement, the dislocation will deliver, thus increasing the resistance to dislocation movement. Therefore, volume shrinkage plays a positive role in the strengthening of the material.

5.2 Fabrication of AA2024/HEAp MMCs via Cryorolling

The HEAp reinforced AA2024 matrix composite were prepared through conventional casting technology to facilitate their industrial mass production [20]. This technology can be applied with minor improvements to the existing production equipment. We introduced HEAps during the Al casting process and adopted mechanical stirring to make the particles uniformly distributed. The HEAp reinforced AA2024 matrix composite were successfully prepared via this method, and the HEAp addition had a significant grain refinement effect. Second, to investigate the strengthening methods of the HEAp reinforced AA2024 matrix composite and their machinability, they were rolled at different temperatures. Both the tensile strength and elongation of the HEAp reinforced AA2024 matrix composite subjected to cryorolling (−100 °C) increased, and the composites exhibited good comprehensive properties.

5.2.1 Microstructure Evolution of AA2024/HEAp MMCs

The microstructures of the $Al_{0.5}$CoCrFeNi AA2024/HEAp MMCs are displayed in Fig. 5.10. The specimens with 0 weight percent, 1 weight percent and 3 weight percent HEAp contents had equiaxed grains (Fig. 5.10a–c). The average grain sizes of the three specimens were 77.9 μm, 56.4 μm and 53.4 μm, respectively (Fig. 5.10d). With the addition of 1 weight percent HEAp content to the composite, the average grain size of the specimen was significantly reduced by 28%. When the HEAp content was increased to 3 weight percent, the grain size was further reduced, but the reduction effect was not significant.

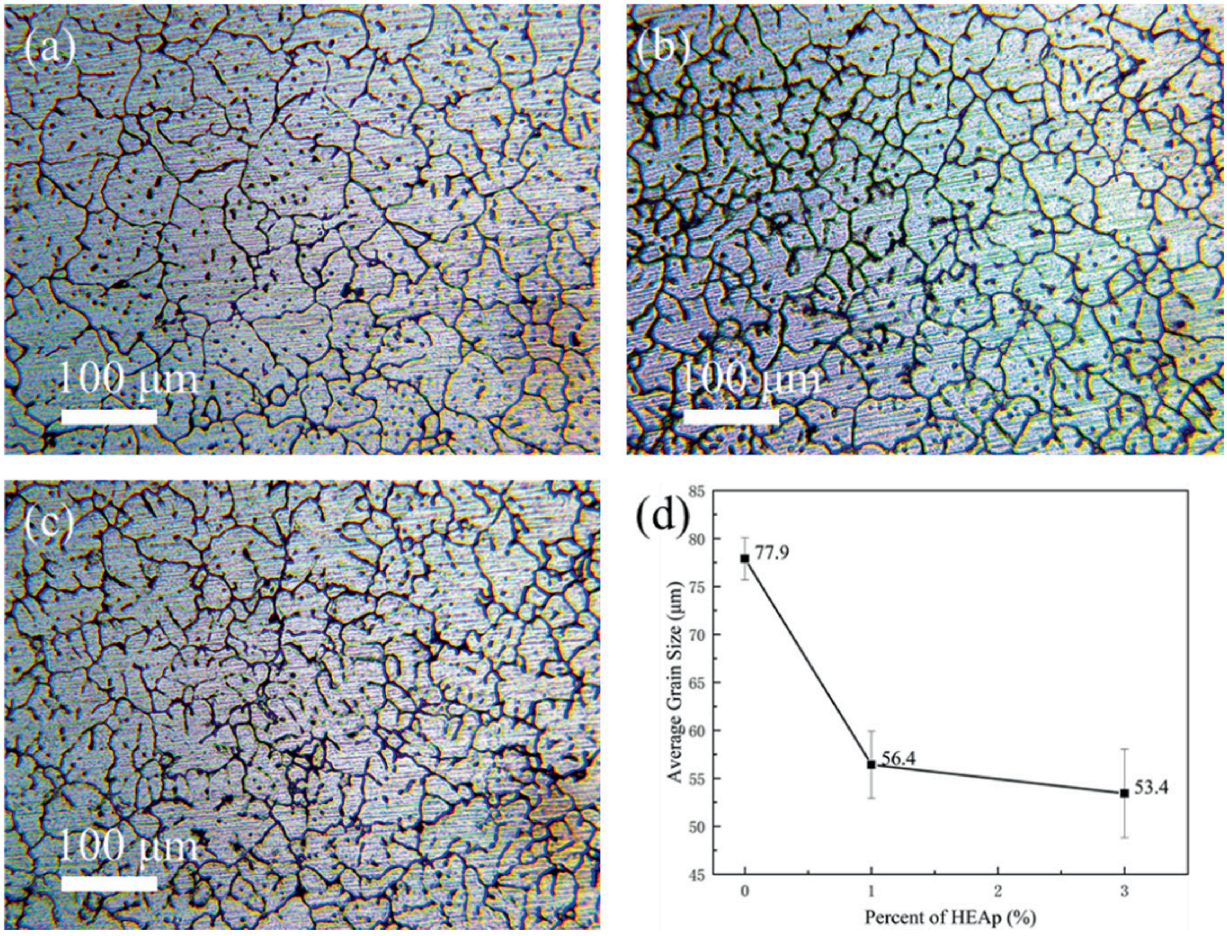


Fig. 5.10 Microstructure of AA2024/HEAp MMC with **a** 0 weight percent, **b** 1 weight percent, **c** 3 weight percent, and **d** average grain sizes

The scanning electron microscopy images of AA2024/HEAp MMCs are shown in Fig. 5.11. One of the main solute elements in AA2024 is Cu, which can easily combine with Al atoms and to form the Al_2Cu phase. That was a key mechanism for the excellent strength. With an increase in the HEAp content, the number of crystalline phase particles in the material significantly increased, and the distribution become diffused (Fig. 5.11a, c and e). The areas marked with red boxes in Fig. 5.11a, c and e are enlarged in Fig. 5.11b, d and f, respectively. As shown in the figures, the crystalline phase particles in AA2024 and the composites were distributed as a network. This may be due to an enrichment of the crystalline phase particles in the high energy microstructural regions such as grain boundaries and subgrain boundaries. As shown in Fig. 5.11b, the alloy without HEAps had fewer crystalline phase particles and a larger size than the alloys with HEAps. After the addition of 3 weight percent HEAp content (Fig. 5.11f), the

enrichment of the crystalline phase particles at the microstructural regions of the composite significantly increased; however, its size decreased, and the morphology presented significant discontinuity. The addition of HEAps did not only cause a grain refinement effect (Fig. 5.10), but also caused the generation more subgrain boundaries, which may improve the alloy performance.

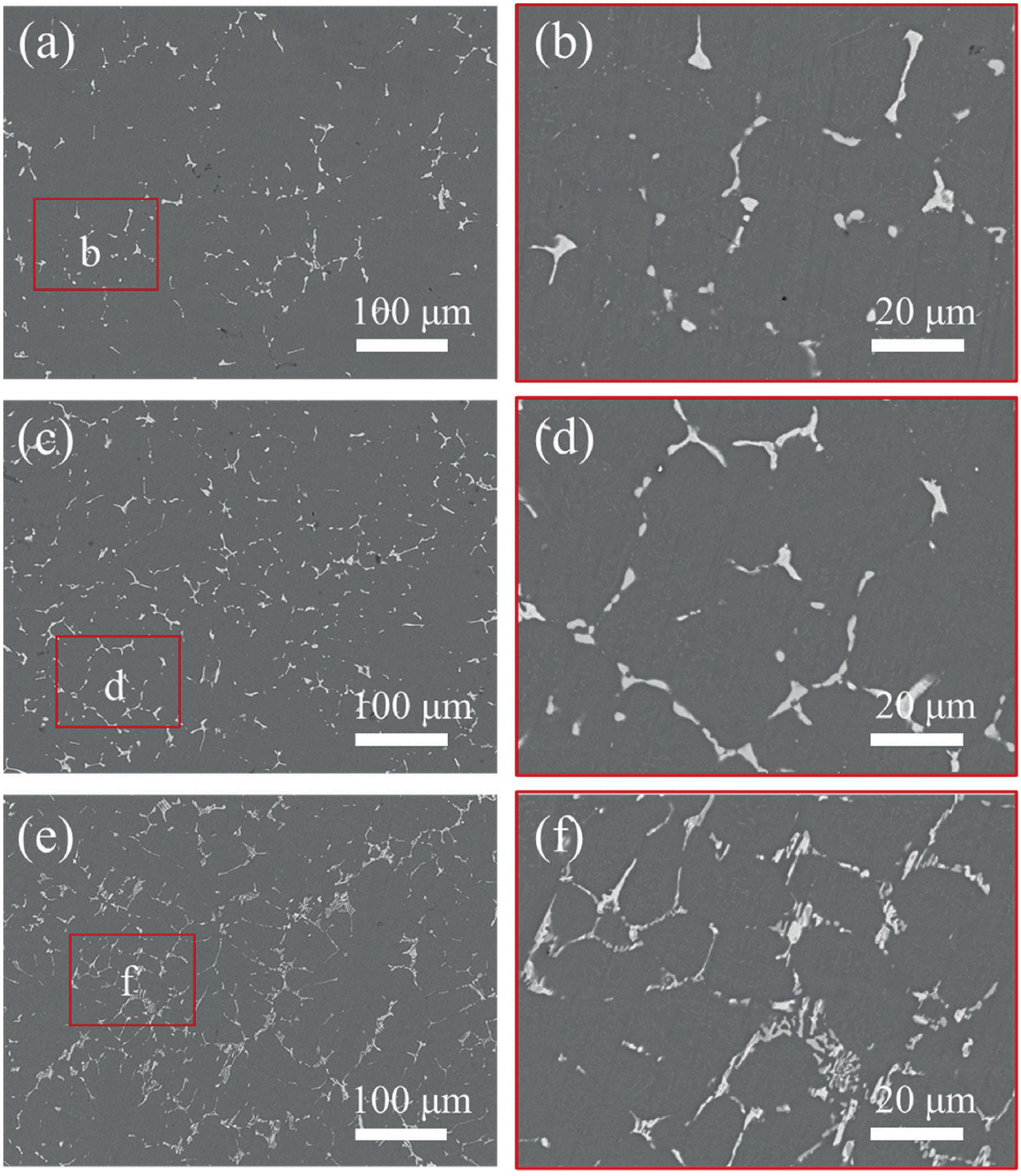


Fig. 5.11 Scanning electron microscopy microstructure of as-cast AA2024/HEAp MMCs, with different HEAp contents: **a**, **b** 0 weight percent, **c**, **d** 1 weight percent, **e**, **f** 3 weight percent

5.2.2 Mechanical Properties of AA2024/HEAp MMCs

The hardness and tensile strength of the as-cast AA2024/HEAp MMCs are illustrated in Fig. 5.12a and b, respectively. The hardness of the samples improved upon HEAp addition, however, the hardness of the 3 weight percent specimen was lower than that of the 1 weight percent specimen. Moreover, with the HEAp addition, the tensile strength of the 1 weight percent sample hardly increased, while that of the 3 weight percent sample decreased to some extent, and the elongation decreased (Fig. 5.12b).

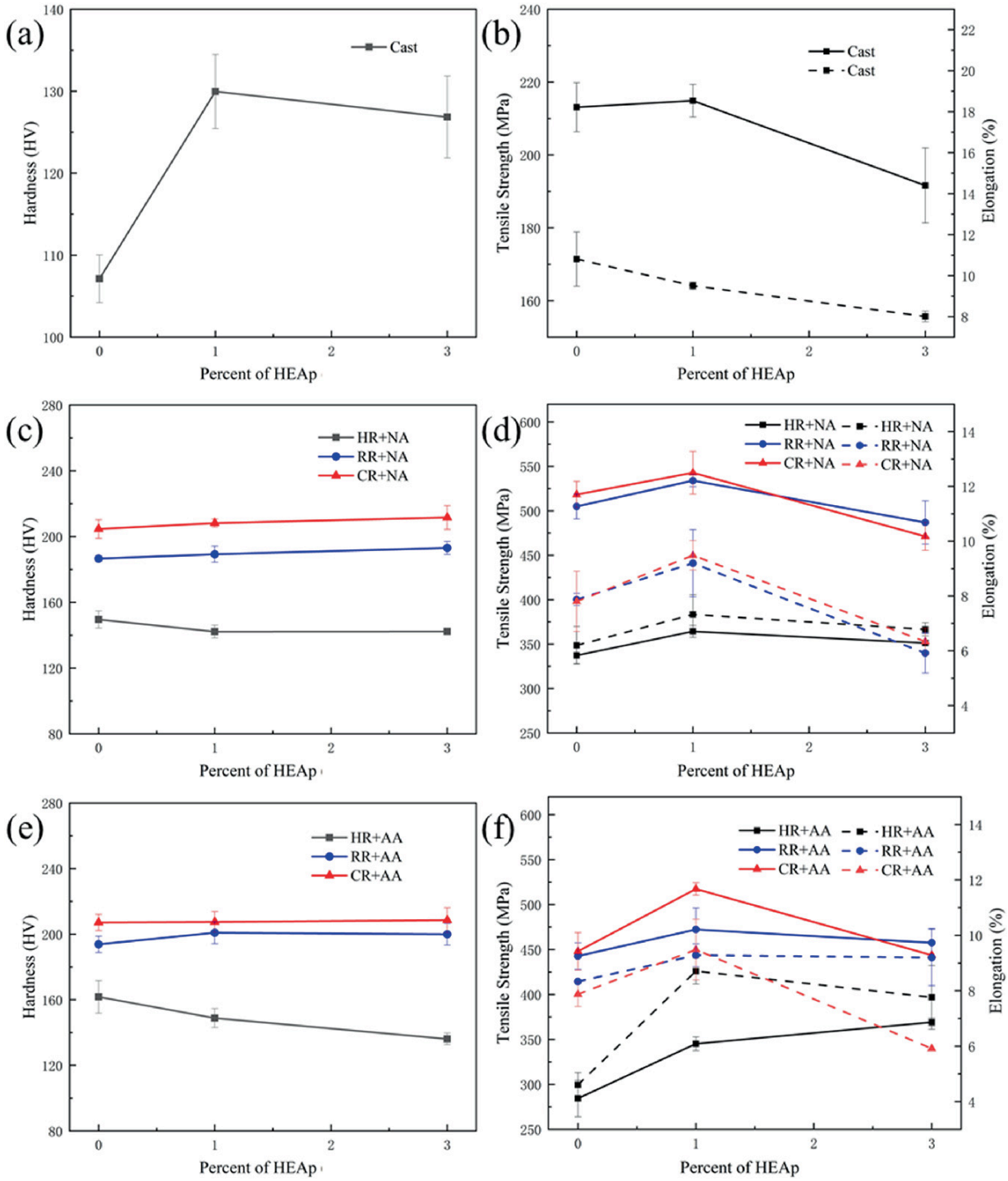


Fig. 5.12 Hardness and tensile strength of as-cast and rolled AA2024/HEAp MMCs: **a**, **b** as cast; **c**, **d** natural aging after rolling; **e**, **f** artificial aging after rolling; the solid line corresponds to the tensile strength, and the dashed line represents the elongation

The hardness and tensile results of the specimens subjected to natural aging after hot rolling (HR + NA), natural aging after rolling at room temperature (RR + NA), and natural aging after cryorolling (CR +

NA) are shown in Fig. 5.12c and d, respectively. The hardness and tensile results of the specimens subjected to artificial aging after hot rolling (HR + AA), artificial aging after rolling at room temperature (RR + AA), and artificial aging after cryorolling (CR + AA) are shown in Fig. 5.12e and f, respectively. The results in Fig. 5.12c and e reveal that the hardness of the specimens subjected to cryorolling and room temperature rolling was significantly higher than that of the hot-rolled specimen. The HEAp addition had a slight effect on the hardness after rolling at different temperatures. As deduced from Fig. 5.12d and f, the tensile strength of the rolled specimen was somewhat lower than those of the as-cast specimens, while the elongation of the as-cast specimen was slightly higher than those of the rolled specimens, owing to the occurrence of dislocation recovery in the heat preservation process. The tensile strength and elongation of the 1 weight percent AA2024/HEAp MMC was higher than those of AA2024 under different rolling temperatures; however, the tensile strength and elongation of the 3 weight percent AA2024/HEAp MMC was significantly lower than those of AA2024. After natural aging, the tensile strength of the 1 weight percent AA2024/HEAp MMC reached 543 MPa. The tensile strength of the artificially aged MMC specimen (518 MPa) was 70 MPa higher than that of AA2024, and the specimen exhibited 10 percent elongation.

5.2.3 Mechanism of Enhanced Mechanical Properties of AA2024/HEAp MMCs

As shown in Fig. 5.10, the HEAp addition had a significant influence on the grain refinement of the AA2024/HEAp MMC. This may be because the HEAps served as excellent sites for heterogeneous grain nucleation during the melt solidification and because the melting point of HEAps is much higher than of AA2024. According to the scanning electron microscopy results (Fig. 5.11), the HEAp addition had significant effect on the crystalline phase formation during solidification of AA2024/HEAp MMC. The crystalline phase particles became smaller in size and their distribution was more discrete.

Energy dispersive spectrometry detection was performed for the crystalline phase particles and the results are presented in Fig. 5.13. The results showed the bright white crystalline phase particles in the

scanning electron microscopy images to be rich in Cu, which is a common thick crystalline phase particle in AA2xxx sheets. However, with the increase in the HEAp content, the Cu content of the crystalline phase particles decreased, and the color of the energy spectrum of Cu darkened is shown in Fig. 5.13. The quantitative element contents in the right section of Fig. 5.13 show the same result. The decrease in the Cu content may be because with HEAp addition, the Cu in the crystalline phase particles was replaced by cobalt, iron, and nickel. The energy dispersive spectrometry result of crystalline phase particles in 3 weight percent AA2024/HEAp MMC is shown in Fig. 5.13c. Owing to the low contents of cobalt, iron, and nickel, their contributions were not clear from the energy dispersive spectrometry plane sweep results. The use of dotted lines with different colors can enable better data analysis. It is supposed that the addition of cobalt, iron and nickel may be the reason for the decrease in the average grain size and the discontinuity of the crystalline phases.

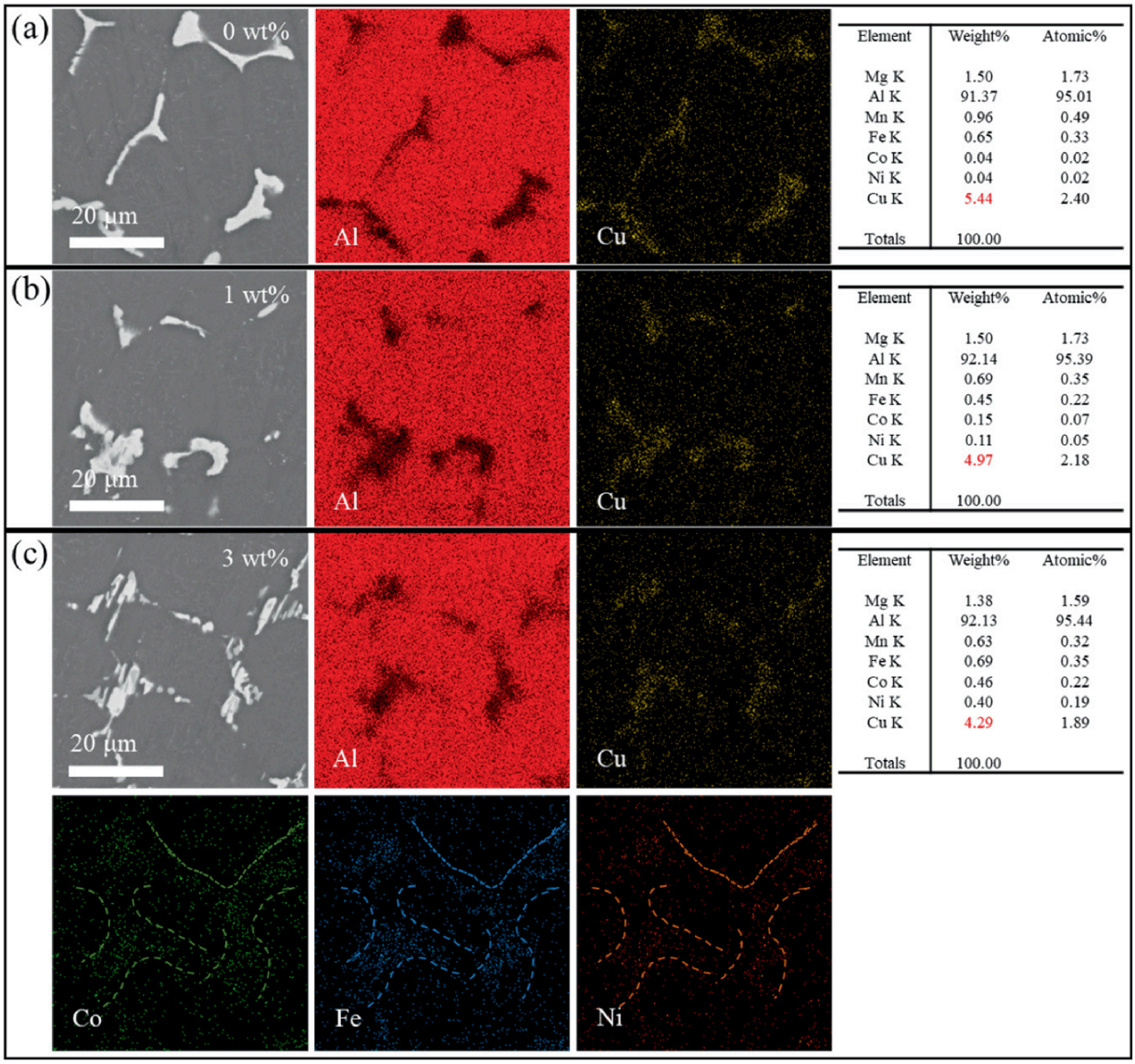


Fig. 5.13 Energy dispersive spectrometry results of the crystalline phase particles in AA2024/HEAp MMC: **a** 0 weight percent, **b** 1 weight percent, **c** 3 weight percent

As demonstrated in Fig. 5.12a and b, the HEAp addition improved the microhardness of the as-cast specimen; however, the addition of 3 weight percent HEAp content to AA2024 decreased the alloy tensile strength. This may be because more defects were produced in the ingot when an excessive HEAp amount was added. These defects will cause the formation of microscopic cracks during the tensile procedure and cause the specimen to break prematurely. This also explains the decrease in elongation with increasing HEAp content. For the 1 weight percent AA2024/HEAp MMC specimens, there were few defects, but this had an insignificant effect on the increase in tensile strength and

decrease in elongation. The defects in 1 weight percent HEAp-AMC specimens can be effectively eliminated by the rolling process, especially cryorolling, which may be why the rolled AA2024/HEAp MMC had better properties than AA2024. In particle-reinforced Al matrix composites, the rolling process eliminated the pores and cracks between the reinforced particles and the matrix and resulted in a more uniform dispersion of the reinforced particles within the matrix, which could improve the tensile strength of Al matrix composites. Al-4%Cu-3%TiB2 in situ composites obtained good comprehensive properties of high strength and high elongation after cryorolling. The greatest contribution to the strength was the strengthening of fine grains via cryogrolling. The grain elongation of Al matrix composites was blocked in the rolling direction due to the existence of reinforced particles. This hindrance of the reinforcing particles resulted in the surrounding grains to experience large strains and accumulate many dislocations near the grains. Eventually, this created a large strain at the reinforcing particles, causing them to break up.

The strong dislocation strengthening of particle reinforced Al matrix composites after cryorolling was mainly caused by two factors. First, compared with other deformation processes, the dislocation recovery of the material was inhibited in the cryogenic environment; therefore, more dislocations accumulated during deformation. Second, due to the deformation mismatch between the reinforcement particles and the matrix material during rolling, a large number of dislocations are produced. The accumulation of more dislocations will increase the deformation resistance during cryorolling and stronger work hardening, thus improving the material strength. In this study, there was slight difference between natural aging and artificial aging, indicating that in Al matrix composites, dislocation strengthening was the main strengthening mechanism, and precipitation strengthening effect was not obvious. The strengthening effect of precipitation and the softening effect caused by dislocation recovery in the aging process offset each other, so that the strengthening effect of precipitation was not obvious, and even the strength decreased after artificial aging. The scanning electron microscopy results of the 1 weight percent AA2024/HEAp MMC specimens after cryorolling and room temperature rolling are shown in Fig. 5.14a and b. The crystalline phase

particles after cryorolling had smaller size and featured diffuse distribution. The specimens also had better surface quality on the rolled surface, as indicated by the red arrows in Fig. 5.14. Owing to an increase in material strength during cryorolling, a greater rolling force than that in conventional rolling was required for the same deformation amount; therefore, the material had higher internal stress, which was adequate to break up the thicker crystalline phase particles that were produced during the casting process. During cryorolling, the material toughness was enhanced, with an improvement in deformation capability. Compared to hot rolling, cryorolling improves the deformation performance of the rolled sheet, inhibits recovery, and makes the rolled sheet maintain a good forming surface coupled with excellent properties. This may be why properties of the 1 weight percent specimen after cryorolling were better than those after rolling at room temperature. The tensile fracture morphology of the artificially aged 1 weight percent AA2024/HEAp MMC specimens after cryorolling is shown in Fig. 5.14c–e. As shown in Fig. 5.14c and d, the fracture was relatively flat, with a large number of small dimples, indicated by yellow arrows in Fig. 5.14e. The specimens featured a typical plastic fracture morphology. Additionally, many particles were stuck to the surface of the fracture particles, as indicated by the yellow circles in Fig. 5.14e. No gaps around the particles, which demonstrates good interfacial bonding.

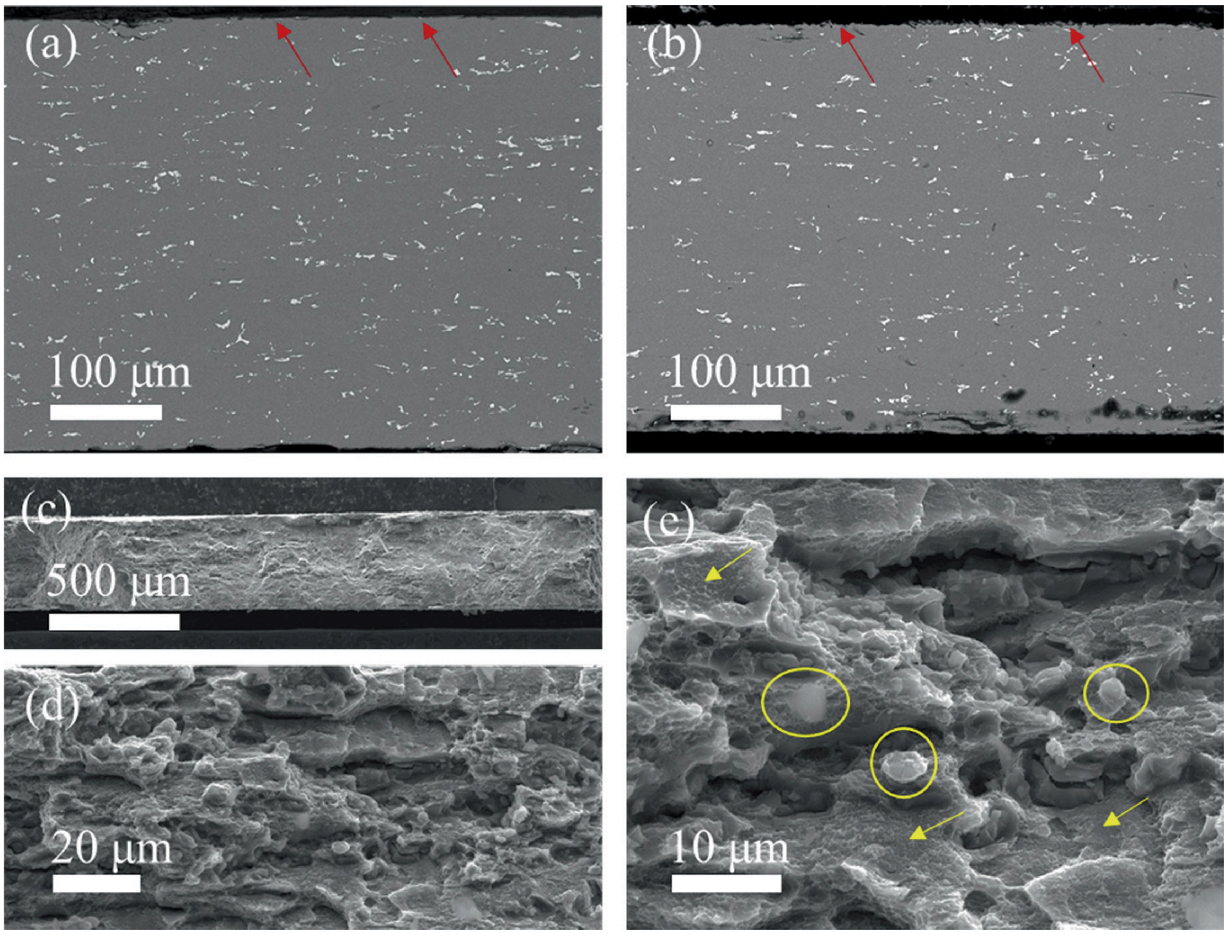


Fig. 5.14 Scanning electron microscopy results of 1 weight percent AA2024/HEAp MMC specimens after rolling, **a** cryorolling, and **b** room temperature rolling; **c**, **d**, **e** tensile fracture surface of specimens subjected to artificial aging after cryorolling

The results of the rolled sheet performance after artificial aging and natural aging are shown in Fig. 5.12d and f. As shown in the figures, the strength of the artificially aged sheet was lower than that of the naturally aged sheet, and the elongation of the artificially aged specimen was not significantly improved. Regarding the comprehensive properties of the material, it is necessary to perform artificial aging treatment. The tensile strength and elongation results in our study and others studies on particle reinforced AA2024MMC are summarized in Fig. 5.15. The figure shows that the AA2024/HEAp MMC in this study had excellent combination properties. Our follow-up research will focus on other mechanical properties of AA2024/HEAp MMCs.

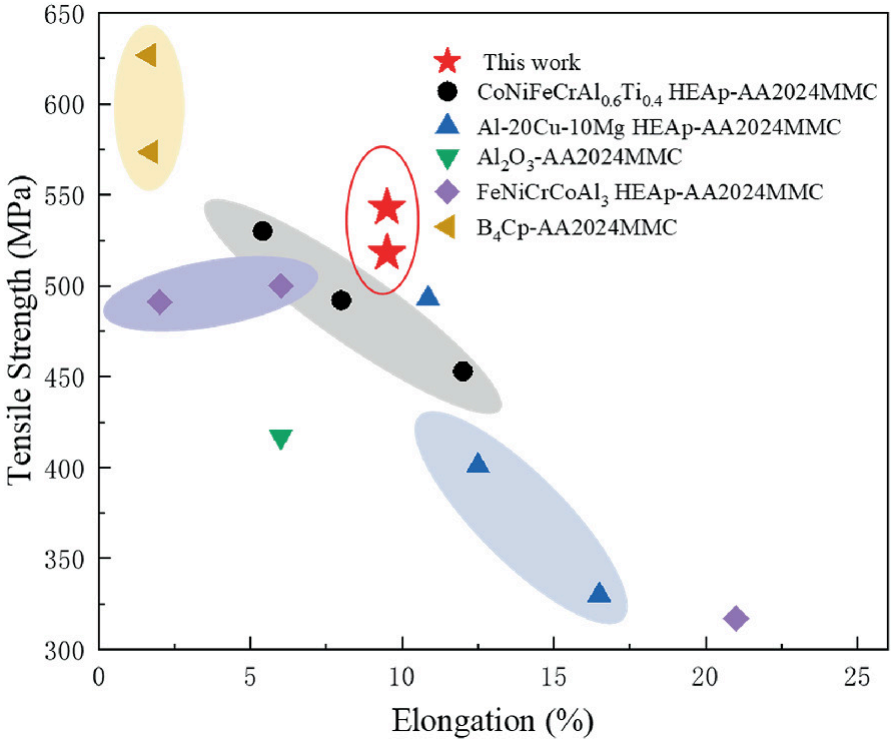


Fig. 5.15 Comparison of the results of this study with those of other studies on particle reinforced AA2024 MMCs

5.3 Fabrication of AA5083/HEAp MMCs During Cryorolling

$Al_{0.5}$CoCrFeNi HEAps were added as reinforcing particles to the AA5083 matrix by using casting, and subsequently rolled at 573 K and 77 K. Moreover, the microstructural evolution of the AA5083/$Al_{0.5}$CoCrFeNi HEAps MMCs sheets was analyzed, and the mechanical properties of the samples after hot rolling (HR) and cryorolling were also investigated [21].

5.3.1 Microstructure Evolution of AA5083/HEAp MMCs

Figure 5.16 illustrates the element distribution of the AA5083/$Al_{0.5}$CoCrFeNi HEAps MMC with 3 wt% HEAps. There are many bumps on the sample surface because that Ar ion milling was used in the sample preparation process. The dark gray area is mainly composed of the Al matrix, while the light gray area in the middle is HEAps. The distribution of Co, Cr, and Fe elements is consistent with

HEAps in the SEM image. The distribution of Ni elements shows uniform characteristics because that Ni occupies a diffusion channel under the action of the temperature field of casting, whose diffusion in the Al matrix is more sufficient than other elements.

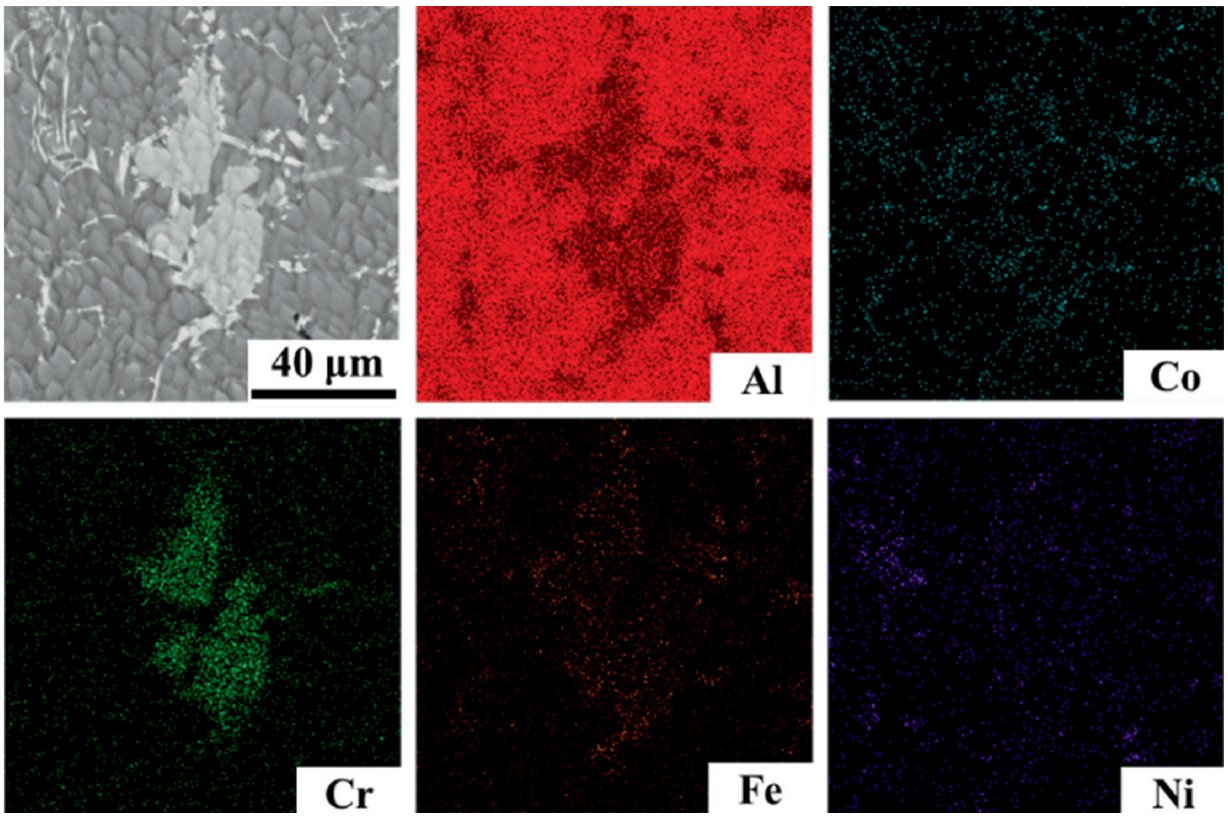


Fig. 5.16 SEM–EDS spectrum of AA5083/$Al_{0.5}$CoCrFeNi HEAps MMCs with 3 wt% HEAps

Figure 5.17 shows the SEM images of the microstructure and the grain sizes distribution of as-cast MMCs. For the grain size, at least 100 grains were counted for every sample. The grain refinement is promoted with more HEAps. The average grain size decreases from 76 to 69 μm when 1 wt% HEAps were added in the MMC. After introduced 3 wt% HEAps, the average grain size sharply decreases to 33 μm. In addition, some casting defects such as voids can be seen in Fig. 5.17a and c from the AA5083 and the MMC with 3 wt% HEAps, which may result in the loss of mechanical properties. It can be seen that the HEAps are unevenly distributed in the matrix in Fig. 5.17c. Furthermore, the agglomeration of eutectic phase at grain boundary is more obvious with increasing the HEAps.

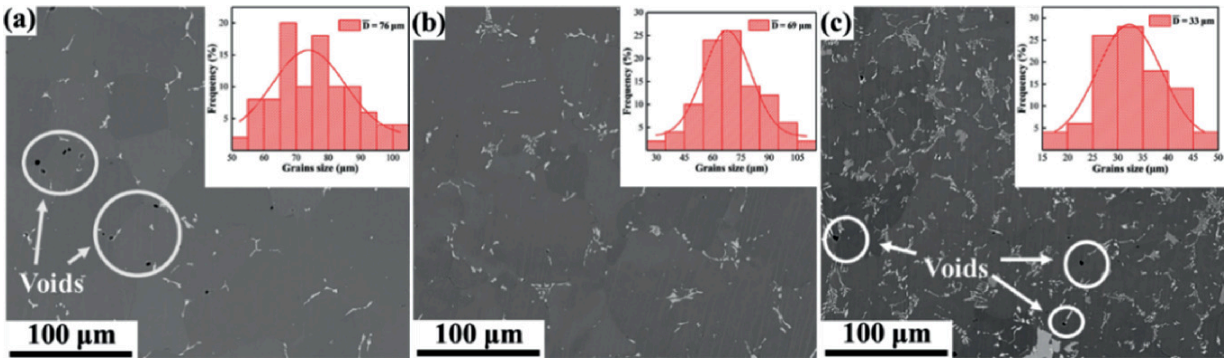


Fig. 5.17 SEM images and grain size distribution of as-cast **a** AA5083 and AA5083/$Al_{0.5}$CoCrFeNi HEAps MMCs with **b** 1 wt% and **c** 3 wt% HEAps

The microstructures of HEAps in as-cast and rolled MMCs with 3 wt% HEAps are shown in Fig. 5.18. The dark gray phase is the AA5083 matrix and the yellow arrow refers to the HEAps reinforcements with a diameter of about 15–20 μm. After rolling, the diameter of the HEAps is reduced to 5–10 μm. Some crashing positions were also observed in HEAps, as the white circle marked in Fig. 5.18b.

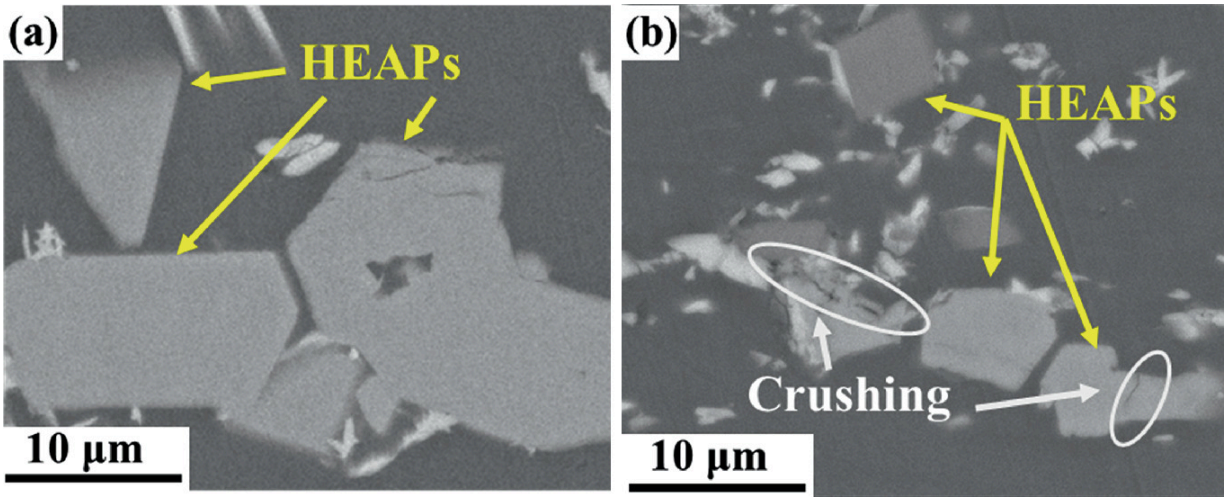


Fig. 5.18 SEM images of HEAps in **a** as-cast and **b** cryorolling-0.4 mm AA5083/$Al_{0.5}$CoCrFeNi HEAps MMCs with 3 wt% HEAps

5.3.2 Mechanical Properties of AA5083/HEAp MMCs

The tensile properties of as-cast AA5083 and the AA5083/$Al_{0.5}$CoCrFeNi HEAps MMCs are listed in Table 5.1. It is obvious that the mechanical properties of MMCs are promoted by adding different content of HEAps. The YS of the AA5083 is 120 MPa, which increases to 207 MPa for the MMC with 3 wt% HEAps. And, the

UTS of the AA5083 is 203 MPa, which shows a small increment after adding 1 wt% HEAps, but increases by 26.6% as the mass fraction of HEAps increased to 3 wt%. However, the addition of HEAps has a certain influence on elongation to fracture. The elongation to fracture of AA5083 is 23.0% and then decreases to 15.0% and 11.7% after adding 1 wt% and 3 wt% of HEAps, respectively.

Table 5.1 Tensile mechanical properties of as-cast materials

Materials	σ_{YS} (MPa)	σ_{UTS} (MPa)	El (%)
AA5083	120 ± 6	203 ± 13	23.0 ± 1.7
MMCs with 1 wt% HEAps	146 ± 7	218 ± 9	15.0 ± 0.9
MMCs with 3 wt% HEAps	207 ± 11	257 ± 14	11.7 ± 1.9

The mechanical properties of AA5083 and AA5083/HEAp MMCs after HR and cryorolling are shown in Fig. 5.19. The UTS varies with reduction and addition of HEAps (Fig. 5.19a). Compared to the as-cast samples, the UTS of the rolled composites considerably improved. After 50% rolling reduction ratio, the UTS of AA5083 via HR and cryorolling are 323 ± 4 MPa and 363 ± 3 MPa, respectively. The UTS of composites with 3 wt% HEAps via HR and cryorolling both reached over 380 MPa. Similar results have been reported in the study of A356/Al_2O_3 composites. When the rolling reduction ratio reached 80%, the UTS was further improved. The UTS of AA5083 and the composites with 3 wt% HEAps are up to 396 ± 7 MPa and 429 ± 9 MPa after cryorolling, respectively. The elongation to fracture in the tensile test is shown in Fig. 5.19b. The value of elongation to fracture decreases with increasing the HEAps and the rolling reduction ratio. Figure 5.19c depicts the variation of microhardness of the MMCs. For the as-cast samples, the microhardness improves from 82.7 ± 3.3 HV to 111.1 ± 5.1 HV (35% increment) after adding 3 wt% HEAps. Besides, the microhardness increases with an incremental rolling reduction ratio due to the work hardening effect. Also, the hardness of the cryorolled samples is generally higher than the HR samples.

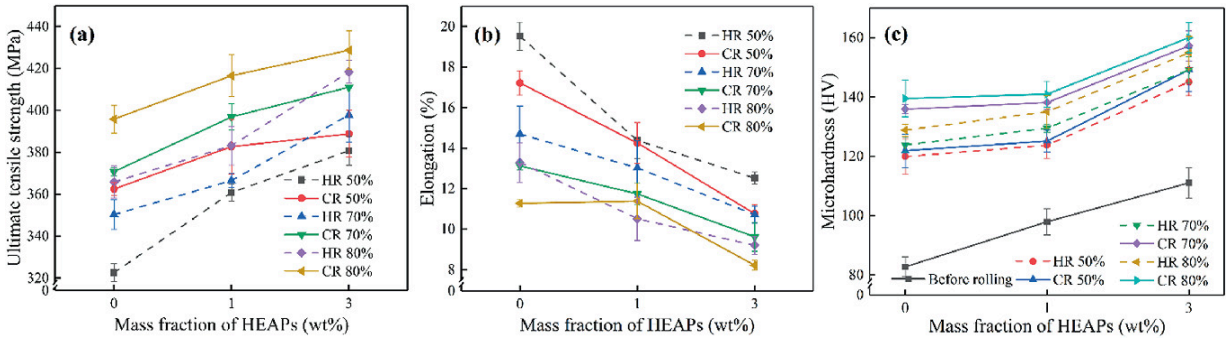


Fig. 5.19 Mechanical properties of AA5083 and AA5083/$Al_{0.5}$CoCrFeNi HEAps MMCs via HR and cryorolling. **a** UTS, **b** elongation to fracture and **c** microhardness of the MMCs with different mass fraction of HEAps

The representative SEM fractographies of the AA5083 and AA5083/$Al_{0.5}$CoCrFeNi HEAps MMCs are shown in Fig. 5.20. For the as-cast AA5083, large and deep dimples in combination with a number of small dimples and tearing edges distribute on the fracture surface, indicating ductile fracture. Addition of 3 wt% HEAps in the MMC narrows down the size and density of the dimples. And few HEAps are present on the fracture surface as the yellow circle in Fig. 5.20b. Therefore, the fracture of the MMC (3 wt% HEAps) sheets may be extended continuously along the crack between the particles and the matrix. In addition, the white circles marked in Fig. 5.20a and b indicate that there are some casting defects such as voids. So, the influence of voids in Fig. 5.17 on tensile properties is inevitable.

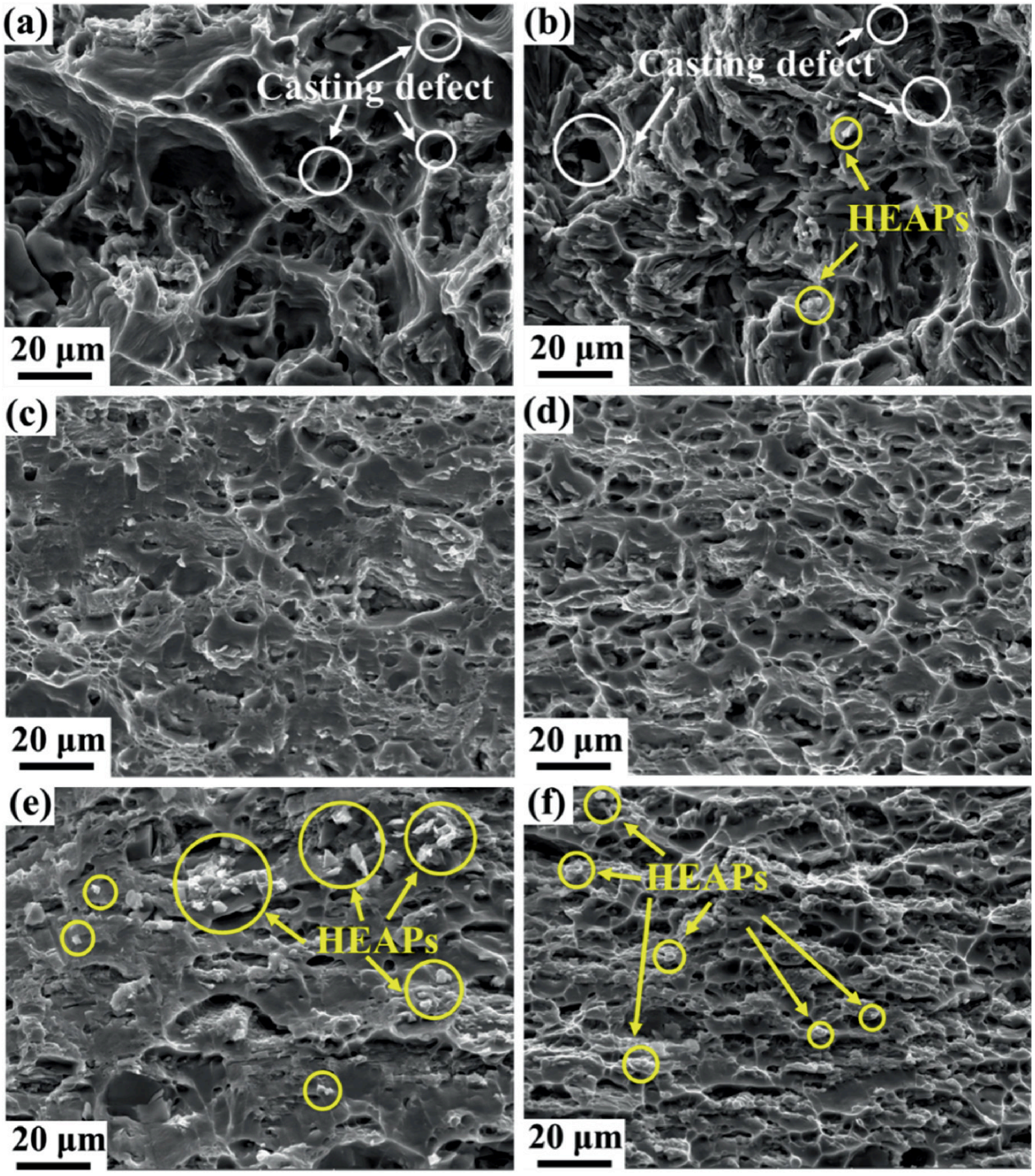


Fig. 5.20 Fracture surface of as-cast **a** AA5083 and **b** AA5083/$Al_{0.5}$CoCrFeNi HEAps MMCs with 3 wt% of HEAps, and AA5083 subjected to **c** HR and **d** cryorolling with 80% rolling reduction ratio, and the MMCs with 3 wt% HEAps subjected to **e** HR and **f** cryorolling with 80% rolling reduction ratio

The void defects generated during casting have been eliminated after rolling as shown in Fig. 5.20c and d. Comparing with cryorolled samples, the fracture surface of HR samples exhibits relatively finer,

denser, and deeper dimples. Additionally, high-density larger and deeper dimples are observed in the samples rolled 80% thickness instead of as-cast samples. It can be seen that the fractures of HR samples with 3 wt% HEAps rolled 80% thickness are different from that of the AA5083, as shown in Fig. 5.20e. A few dimples are observed on the fracture surface of the composite. A cleavage fracture as well as a stepped cleavage plane with a large area is observed in Fig. 5.20e. The depth of dimples is relatively shallow. This can be attributed to the interface fracture between the matrix and the particles. Ductility decreases with an incremental rolling reduction percentage, which is consistent with the results of the tensile test. At the same time, a lot of HEAps are unexpectedly observed in the fracture morphology (Fig. 5.20e and f). During the HR process, although the distribution of these particles is generally uniform, some local clusters are also evident. However, the HEAps are more evenly distributed in the AA5083 matrix after cryorolling.

5.3.3 Mechanism of Enhanced Mechanical Properties of AA5083/HEAp MMCs During Cryorolling

It can be seen from Figs. 5.17 and 5.18 that the HEAps uniformly distribute in the AA5083 matrix with an irregular shape. This is attributed to the diffusion of the elements of HEAps in the matrix under a long period high temperature during casting. It is difficult to identify the grain boundary of the AA5083/$Al_{0.5}$CoCrFeNi HEAps MMCs with 3 wt% HEAps (Fig. 5.17c), which is the same as the previous studies by introducing TiC or TiB_2 particles into Al matrix. An 80% thickness reduction of the MMCs by rolling resulted in a 3–5 folds reduction in the size of HEAps (Fig. 5.18a and b). The results indicate that the strain applied by the rolling process is adopted by the dislocation slip of the AA5083 matrix and the HEAps.

The relationship between the UTS and elongation to fracture of AA5XXX after the addition of reinforced particles is shown in Fig. 5.21. GNPs were added into the annealed AA5052 matrix. As a result, the UTS increased from 206 to 244 MPa, and the elongation to failure was 20.1%. The maximum UTS of MMCs reinforced by HEAps in this work is 205 MPa higher than that in literature. While the AA5052/GNPs MMCs

obtain the utmost elongation. Other non-metallic reinforcing particles, e.g. alumina powders, SiC/CNTs, and CNTs, and carbon fiber were introduced into AA5XXX matrix, but their UTS was lower than this work.

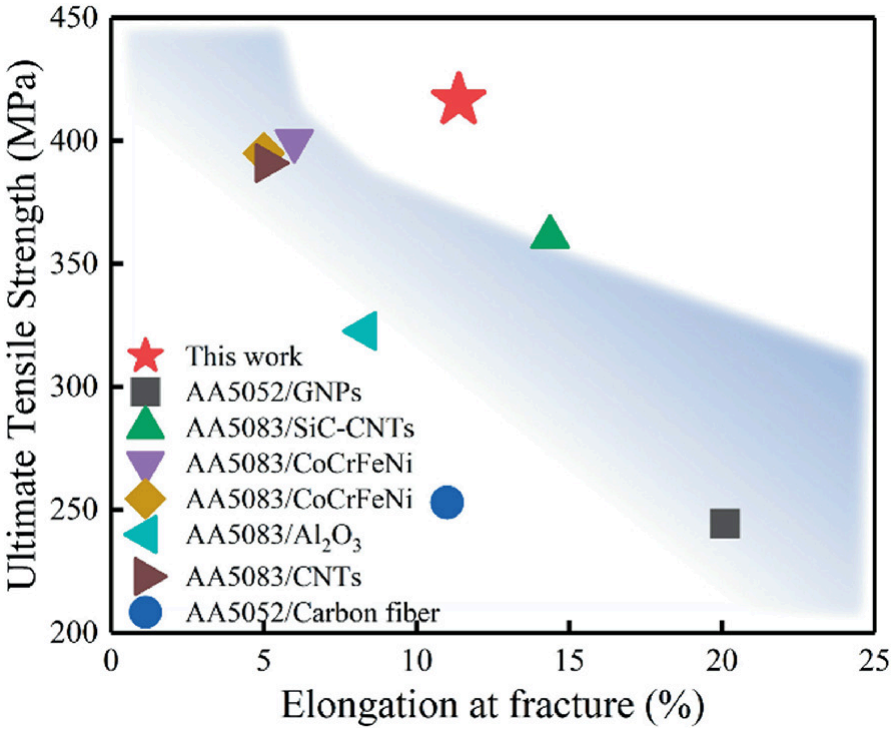


Fig. 5.21 Mechanical properties of AA5xxx metal matrix composites

Figure 5.22 illustrates the strengthening mechanism and microstructural evolution of AA5083 and AA5083/HEAps MMCs. In Table 5.1, the YS of the as-cast AA5083 is 120 MPa, and it increases to 146 MPa and 207 MPa, respectively after adding 1 wt% and 3 wt% HEAps in the AA5083 matrix. It is obvious that the additional HEAps are helpful to the improvement of YS of the AA5083 MMCs. Similar to other types of reinforcement particles, there are three primary strengthening mechanisms of HEAps in the Al matrix.

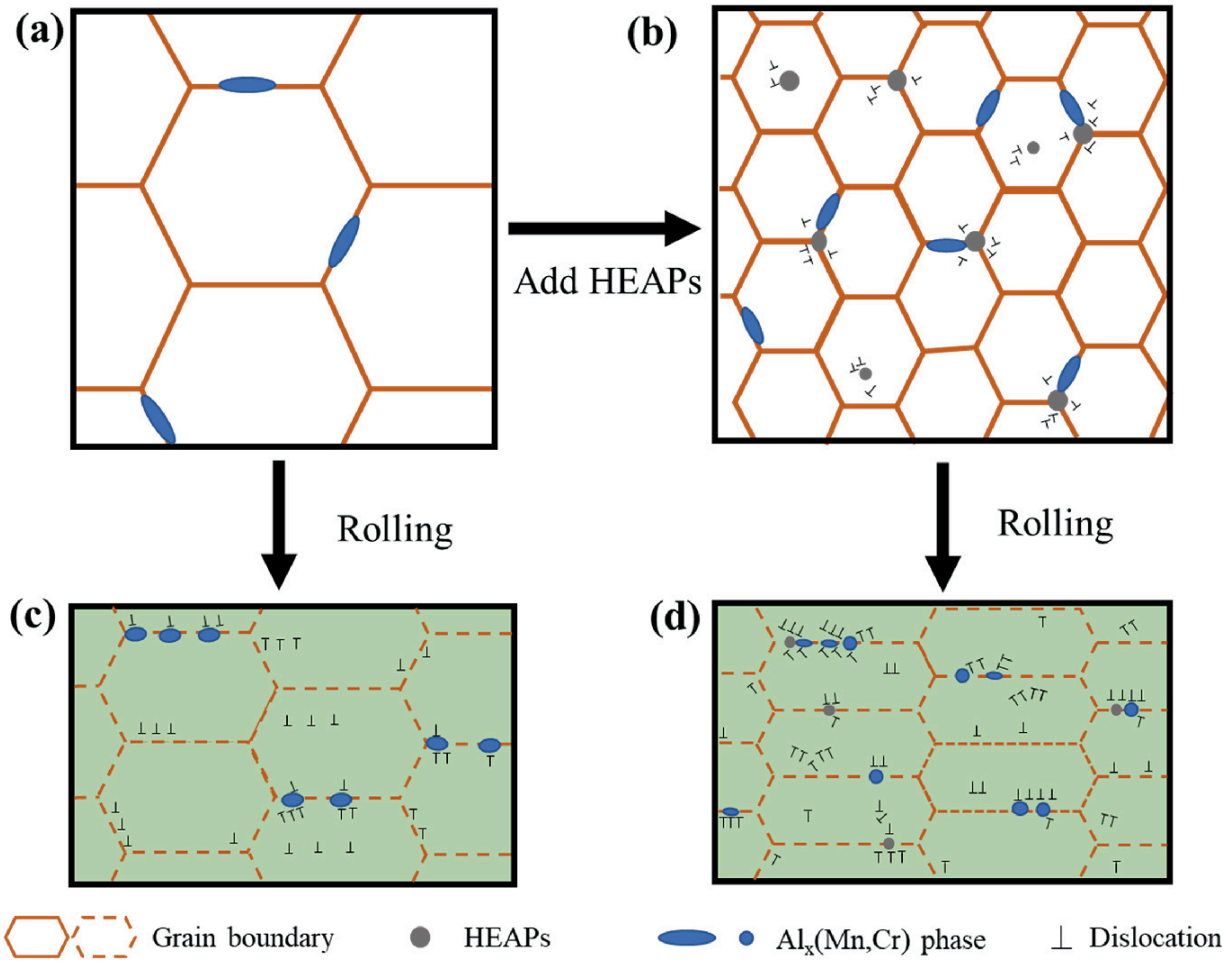


Fig. 5.22 Illustration of strengthening mechanism and microstructural evolution of materials during rolling. As-cast. **a** AA5083 and **b** AA5083/HEAps MMCs, rolled **c** AA5083 and **d** AA5083/HEAps MMCs

(I) Grain refinement strengthening. Grain refinement strengthening is based on the promotion of crystallization nucleation and Hall–Petch relationship ($\Delta\sigma_{HP}$). HEAps act as nucleating agents in the casting process. Therefore, the grain size of the MMCs is smaller than that of AA5083, as shown in Fig. 5.17. Smaller grain size of the MMCs leads to a higher strength. The contribution of grain refinement to YS can be denoted as:

$$\Delta\sigma_{HP} = K\left(d_{AMC}^{-1/2} - d_{AA}^{-1/2}\right) \tag{5.2}$$

where K is the Hall–Petch coefficien, d_{AMC} (μm) is the average grain size of the MMCs, and d_{AA} (μm) is the average grain size of as-cast AA5083. A smaller grain size of the MMCs leads to a greater $\Delta\sigma_{HP}$. The

$Al_{0.5}$CrCoFeNi HEAps are multi-element metal alloy. Comparing to other reinforced particles such as SiC and CNTs, the $Al_{0.5}$CrCoFeNi HEAps have better wettability with AA5083 matrix during casting. More crystal embryos transform into crystal nuclei in the molten alloy, improving the nucleation rate. HEAps could promote the heterogeneous nucleation of AA5083 matrix and play a major role in grain refinement. In this study, the average grain size of AA5083 matrix is 76 μm, and it decreases by 9.2 and 56.6% after adding 1 wt% and 3 wt% HEAps. It is obvious that the adding HEAps results in finer grains and improved the mechanical properties of MMCs.

(II) Geometric necessary dislocation (GND) strengthening. GND strengthening can be caused by two situations. One is due to the difference in coefficient of thermal expansion (CTE) between the matrix and the HEAps. There is a thermal mismatch during casting, resulting in large thermal stress. Then the softer matrix will deform to form the geometric necessary dispositions for adapting the thermal mismatch. The GNDs are generated to hinder the dislocation migration in the deformation process, promoting the strength. This enhancement can be expressed as follows:

$$\Delta\sigma_{\mathrm{CTE}} = \beta \mathrm{Gb}\sqrt{\rho_{\mathrm{CTE}}} \tag{5.3}$$

here, β is a strengthening constant; G and b are the shear modulus of the matrix and the Burgers vector respectively. ρ_{CTE} is the dislocation density induced by the CTE mismatch, which can be estimated by Eq. (5.4):

$$\rho_{CTE} = \frac{12\Delta\alpha\Delta T V_p}{bD\left(1 - V_p\right)} \tag{5.4}$$

where $\triangle\alpha$ is the CTE mismatch between the matrix and the $Al_{0.5}$CoCrFeNi HEAps; $\triangle\mathrm{T}$ (K) is the difference between the pouring temperature and the test temperature; $\mathrm{V_p}$ is the volume fraction of the HEAps; and D (μm) is the diameter of the HEAps. In addition, the elastic modulus mismatch (EMM) between matrix and HEAps also causes the GNDs in the matrix during casting to accommodate this mismatch. Similar to the thermal mismatch, GNDs caused by EMM (ρ_{EMM}) can be calculated by Eqs. (5.5) and (5.6):

$$\Delta\sigma_{\mathrm{EMM}} = \sqrt{3}\beta \mathrm{Gb}\sqrt{\rho_{\mathrm{EMM}}} \tag{5.5}$$

$$\rho_{\mathrm{EMM}} = \frac{6\mathrm{V_p}}{\mathrm{bD}}\varepsilon \tag{5.6}$$

where ε is the plastic strain of MMCs. Thus, as shown in Fig. 5.22b, the GNDs are generated in the as-cast MMCs for achieving reinforcement. In the loading process, the strength of the MMCs depends on the inhibition effect on the movement of dislocation. The dislocation stops moving and stores inside the matrix, generally increasing the strength of MMCs. Additionally, it may be blocked in the process of slipping and bending when the reinforcement particles uniformly distributed in the materials with a relatively smaller size. Thus, a dislocation loop is eventually generated. Besides, the reinforcing particles can also form a nailing effect on the dislocation. The crushed HEAps in Fig. 4.22b might accumulate a high density of dislocations. It is obvious that both the $\Delta\sigma_{\mathrm{CTE}}$ and the $\Delta\sigma_{\mathrm{EMM}}$ increase with higher V_p.

(III) Load transfer strengthening. During rolling, the reinforcement particles turn into the main load bearer for the interface friction and a certain degree of strain mismatch leading to a load transfer from matrix to the reinforcement. HEAps have higher strength, hardness, and elastic modulus. Thus, the load will be transferred from the matrix to HEAps when the stress is applied. As a result, the reinforcing particles bear most of the load. Compared to AA5083, it is necessary to apply a greater load to the MMCs during deformation because there are more dislocations around the HEAps (Fig. 5.22c and d). This strengthening effect is a major mechanism when the diameter of the high-strength reinforcement is over 10 μm. The YS of the MMCs mainly depends on the YS of matrix and the volume ratio of reinforcements, the greater the YS of the MMCs can be predicted by Eq. (5.7):

$$\Delta\sigma_{\mathrm{Load}} = 0.5\mathrm{V_p}\sigma_{\mathrm{AA}} \tag{5.7}$$

here, σ_{AA} is the YS of the AA5083 matrix, $\mathrm{V_p}$ is the particle volume fraction in the MMCs. As the $\mathrm{V_p}$ increases, the contribution of $\Delta\sigma_{\mathrm{Load}}$ to the MMCs increases. In addition, more dislocations may generate near the HEAps for the local stress concentration during deformation

process, which is attributed to the strengthening effect of the MMCs after deformation.

Furthermore, HEAps will reduce the stacking fault energy, which is not conducive to dynamic recovery. Work hardening and dynamic recovery/dynamic recrystallization occur at the same time in the rolling process. The dynamic recovery of AA5083 with a high stacking fault energy is apparent. In this process, the climbing of edge dislocations and the cross slipping of the screw dislocation significantly offset the dislocation, leading to decrease of dislocation density. The extended dislocation width of the AA5083 is so narrow that the cross-slipping and climbing are easy to occur, allowing the dislocation to escape from the node or dislocation network and offset other dislocations. Because of the addition of HEAps, the dynamic recovery is difficult to occur in composites. As a result, the strength and hardness of the MMCs remain higher than that of AA5083 under the same deformation. In the heat treatment before rolling, the MMCs and AA5083 have distinct differences. The addition of the reinforcing particle impedes the nucleation and growth of recrystallized grains, thus delaying the recrystallization process and increasing the recrystallization temperature. Therefore, the recrystallization degree of the MMCs must be significantly lower than the AA5083 at the same temperature and period.

Currently there are few researches on the rolling deformation of aluminum/HEAps MMCs at liquid nitrogen temperature. Figure 19a compares the UTS of the MMCs prepared under various technological conditions and different rolling reductions. Under the same deformation, the UTS of cryorolled samples is higher than HR samples, which is obvious for AA5083 and MMCs with HEAps. At 50% reduction of AA5083, the UTSs of cryorolling and HR samples are 363 ± 3 MPa and 323 ± 4 MPa, respectively. The UTS of the AA5083 under cryorolling exceeds the UTS of the MMCs with 1 wt% HEAps under HR. The UTS of the cryorolled MMCs with 1 wt% HEAps is similar to that of the HR MMCs with 3 wt% HEAps, indicating that the impact of cryorolling on the UTS is significant. Geometric necessary dislocation strengthening mechanism is related to the loading temperature, because more dislocations will be generated at cryogenic temperatures.

Therefore, it also highlights the advantages of cryorolling technology, which is also confirmed in the experimental results.

The UTS of MMCs substantially increases after 50% rolling reduction. However, a further reduction does not result in the same increase in UTS, indicating that the deformation strengthening of the MMCs is close to the threshold. The grain size and dislocation accumulation are up to the limit. Therefore, the strengthening mechanism of HEAps may change after deformation. When the MMCs is subjected to a larger load accompanied with more tiny HEAps, the strengthening mechanism may be transformed from the load transfer strengthening to the pinning strengthening of fine particles i.e., the strengthening effect of HEAps still exists.

In addition to generating deformation heat, there is also ample energy stored in the material such as lattice distortion energy and grain defect distortion energy, which served as the driving force for recrystallization. Although the HR temperature is higher than the recrystallization temperature of AA5083, the incubation period is long enough that the recrystallization does not occur quickly. According to the Johnson-Mehl equation, only dynamic recovery occurs in HR process due to short heating period. Hardening and softening behaviors occur simultaneously under the combined effect of temperature and stress field. The dynamic recovery is weakened by the addition of HEAps. Therefore, the MMCs by HR remain a higher strength, as well as a good elongation to fracture.

Both recovery and recrystallization are inhibited when a strain field of dislocation is introduced in the cryogenic environment. Comparing Fig. 5.20e with Fig. 5.20f, the number of HEAps on the fracture surface indicates that the matrix and HEAps in the MMCs have a better interfacial bonding strength through cryorolling than HR. Figure 5.23 shows the TEM image of the 0.4-mm MMC sheets with 3wt % HEAps by cryorolling. A HEAp with a diameter of about 2 μm can be seen in Fig. 5.23a. Also, the interfaces between the matrix and HEAp bond well after cryorolling. A large number of dislocation tangles are gathered in the matrix. Dislocations are retained and entangled in the matrix under cryorolling (Fig. 5.23b). Besides, the SAED pattern shows a typical characteristic of deformed polycrystalline structure. Some grains marked with dotted lines can be seen in the matrix from Fig. 5.23b. It

can be concluded that the dislocation strengthening caused by such high-density dislocation is the main reason that UTS is higher after cryorolling. With increasing the rolling reduction, dislocations accumulate and their density increases sharply, making the recovery and recrystallization more difficult. As a result, the UTS of the cryorolled specimens is higher than that of HR specimens. These beneficial effects of cryorolling were also demonstrated in rolled AA6XXX and titanium alloy.

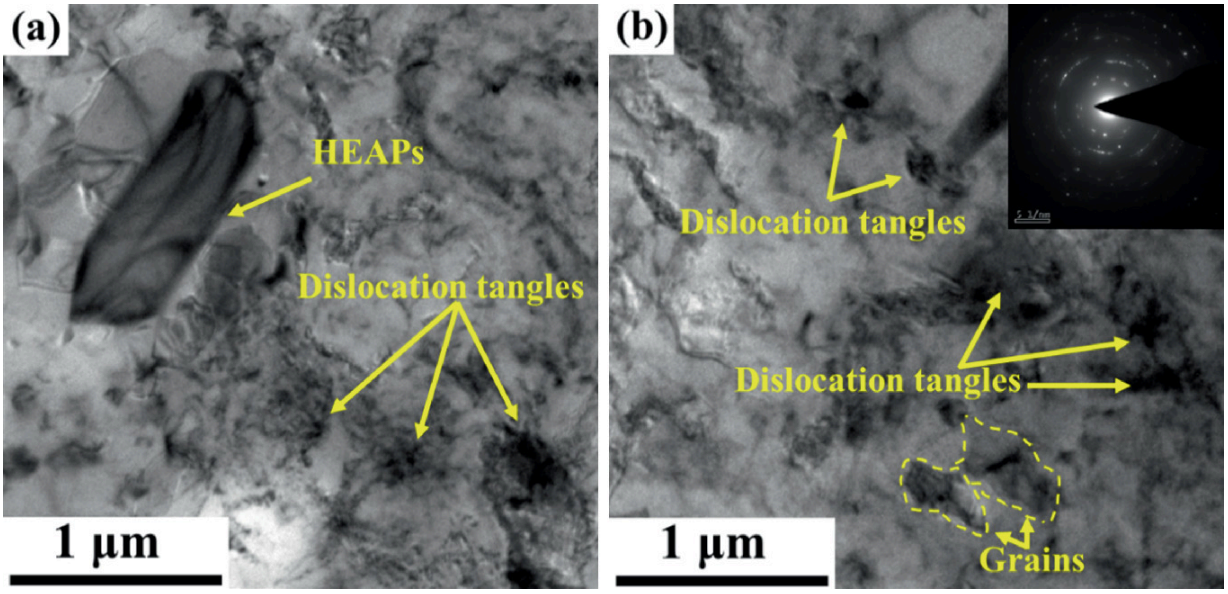


Fig. 5.23 TEM image of the 0.4-mm AA5083/$Al_{0.}$5CoCrFeNi HEAps MMCs with 3wt % HEAps by cryorolling. **a** microstructure near a HEAp and **b** Al matrix

5.4 Fabrication of AA1050/HEAp Composites Subjected to Asymmetric Cryorolling

The Al/HEAp MMC sheets were processed by ACR (77 K) and AR (293 K), respectively. The mechanical properties and microstructure evolution of the Al/HEAp MMC sheets after rolling were analyzed. Finally, the effect of plastic deformation in a cryogenic environment on the microstructure and mechanical properties of Al/HEAp MMCs was discussed [22, 23].

5.4.1 Microstructure Evolution of AA1050/HEAp Composites During Asymmetric Cryorolling

The HEAp and AMCs were characterized using SEM. Figure 5.24a shows the morphology of HEAp. EDS was used to characterize the elements constituting HEAp. The distributions of Al, Fe, Co, Cr, and Ni elements in HEAp were relatively uniform without any impurity elements, as depicted in Fig. 5.24b–f. The particle size distribution of HEAp is shown in Fig. 5.24g, and no obvious oversized particles were observed. The average particles size of HEAp was 4.5 μm.

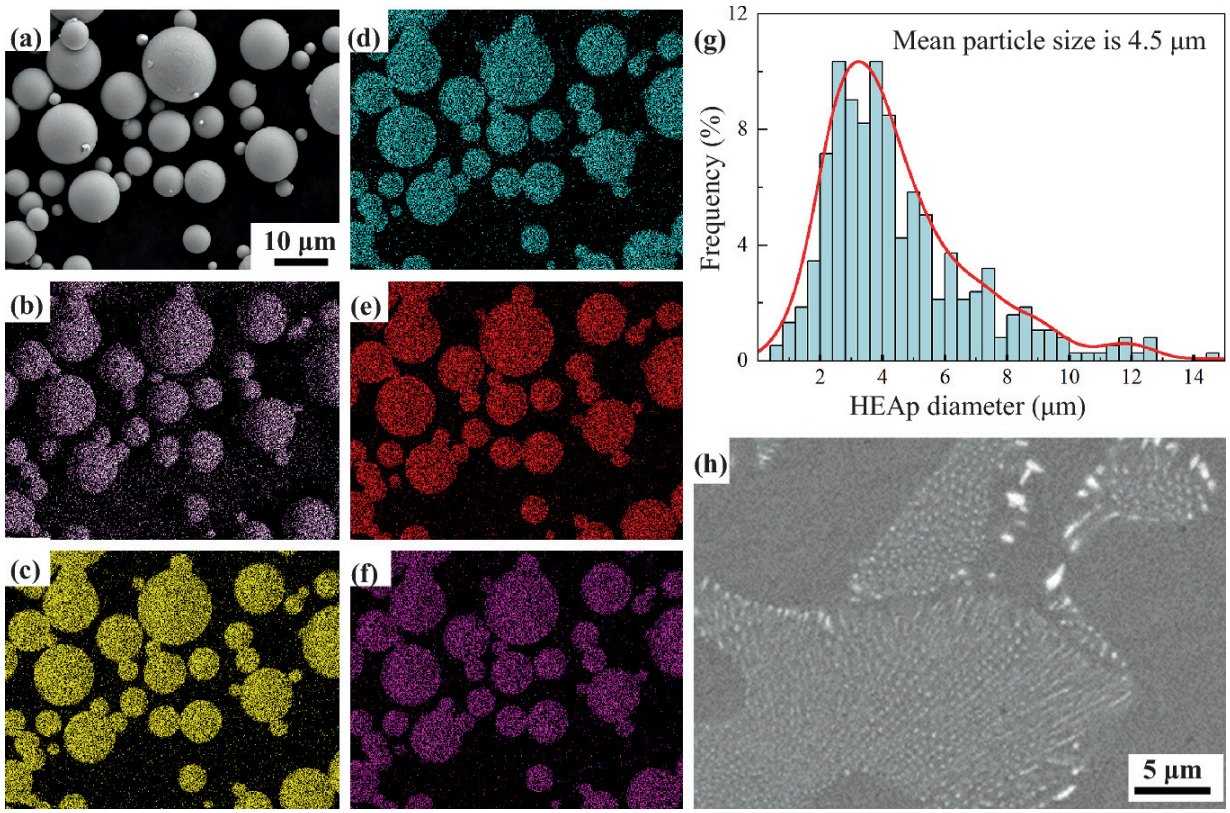


Fig. 5.24 **a** SEM image of HEAp; EDS results of **b** Al, **c** Fe, **d** Co, **e** Cr, and **f** Ni distribution; **g** HEAp size distribution; **h** SEM image of 3 wt% Al/HEAp MMCs before rolling

The XRD results are shown in Fig. 5.25. Only the α-Al phase existed in pure Al. A typical dual-phase structure of FCC + BCC was characterized for the HEAp. In the range of 82–83°, the peak intensity of pure Al was lower, while a relatively strong BCC phase peak from HEAp was detected in this range. In addition, the FCC phase corresponding to HEAp was also detected in the range of 43–44° from

the 3 wt% Al/HEAp MMCs. However, due to a low mass fraction of HEAp, the peak intensities were generally low. The XRD results were also utilized to quantitatively calculate the dislocation density of the composites by the Williamson Hall formula.

$$\frac{\beta \cos\theta}{\lambda} = \frac{1}{D_v} + 2e\left(\frac{2\sin\theta}{\lambda}\right) \tag{5.8}$$

$$\rho = (\rho_D \times \rho_s)^{1/2} \tag{5.9}$$

$$\rho_D = 3/D_v^2 \tag{5.10}$$

$$\rho_s = K\left(e^2\right)/b^2 \tag{5.11}$$

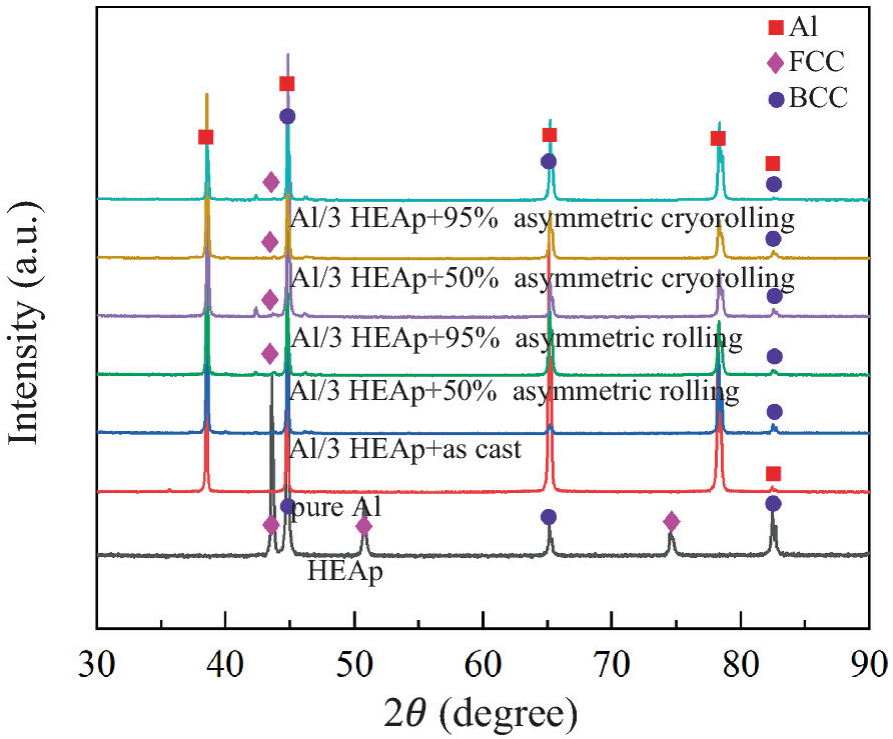


Fig. 5.25 XRD patterns of the HEAp and MMCs

where $K = 6\pi$, and b is the Burgers vector for the FCC structure. Although the dislocation density measured by XRD was not precise, this method was reasonably good to evaluate the variation of dislocation density in Al/HEAp MMCs under different rolling processes. The calculated results are listed in Table 5.3, and the data suggests that

under the same rolling deformation, the dislocation densities of the AMCs obtained via the ACR process were higher than that of AR.

Table 5.3 Calculation results of crystallite size and dislocation density of AMCs under different rolling processes

Process condition (%)	Crystallite size (nm)	Dislocation density (m^{-2})
AR-95	237	1.94×10^{14}
ACR-95	179	2.61×10^{14}

The microstructure of the 3 wt% Al/HEAp MMCs after 95% reduction via AR and ACR processes was characterized by SEM. Figure 5.26a and c demonstrate the HEAp reinforcement phase in the AMCs distributed along the rolling direction. The HEAp size after ACR was significantly smaller than that after the AR process, which could be intuitively observed from the higher magnification image in Fig. 5.26b and d. Additionally, more microvoids and microcracks can be observed near the HEAp reinforcement phase corresponding to AR Al/HEAp MMCs. In contrast, none was found in ACR Al/HEAp MMC samples. The microvoids in Fig. 5.26b and d for AR and ACR processes have been quantitatively evaluated. In the AR process, 39 micropores were identified in a 588 square micron range, while only 11 micropores were observed in the corresponding ACR process. The number density of micropores in the AR process was 3.5 times that in the ACR process. In addition, the HEAp reinforcement phase was smaller in the AMCs, and more particles appeared.

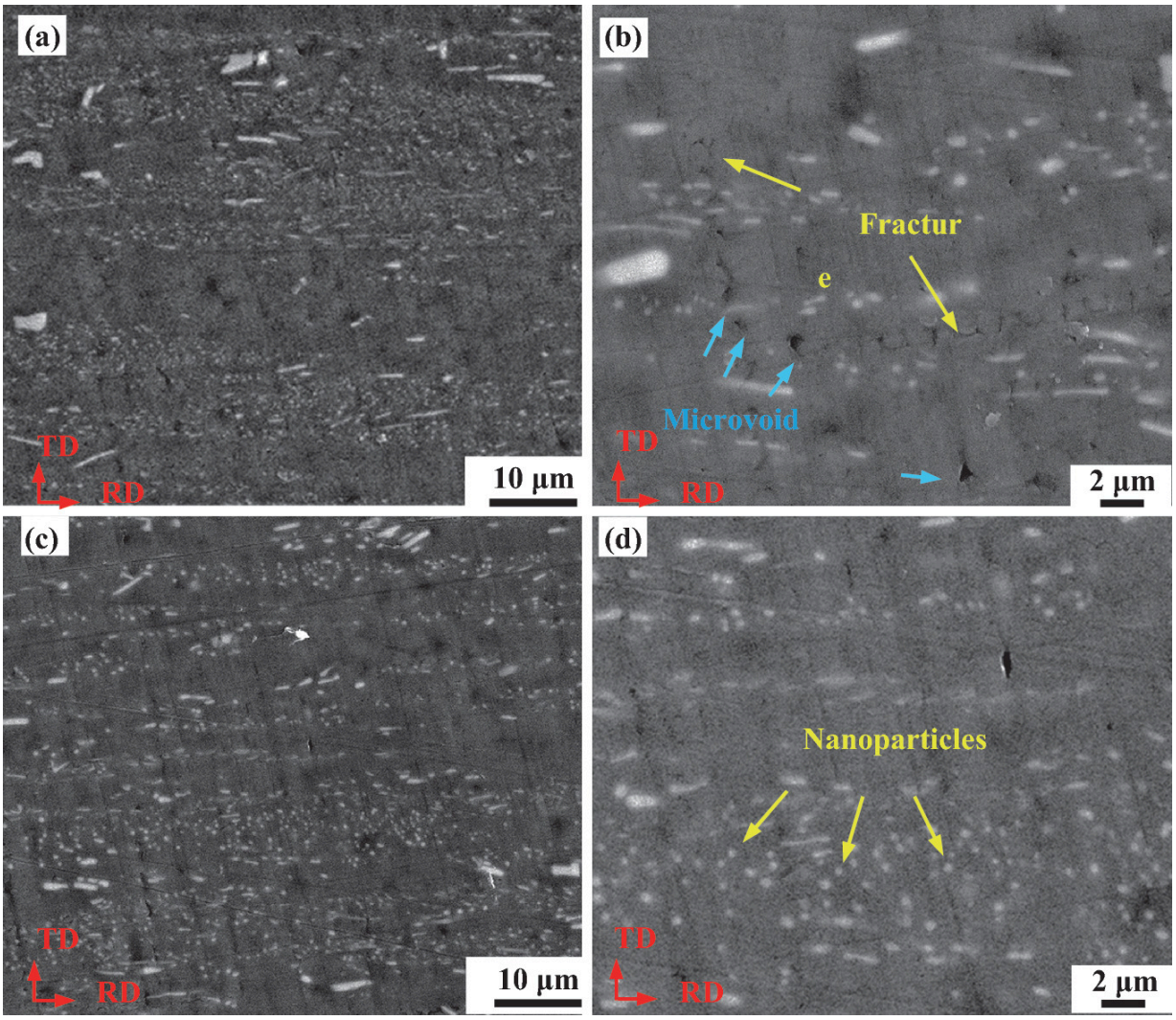


Fig. 5.26 SEM images of 3 wt% Al/HEAp MMCs after 95% rolling reduction by **a**, **b** AR, and **c**, **d** ACR processes

Figure 5.27 illustrates the TEM images of the 3 wt% Al/HEAp MMCs after AR and ACR with a 95% reduction. Many dislocation lines appeared in the microstructure of the AR Al/HEAp MMCs. Several microvoids were observed around the HEAp during AR (Fig. 5.26a), which also appeared in the room temperature-rolled sheets. Compared to the microstructure of AR Al/HEAp MMCs, the grains of ACR Al/HEAp MMCs were significantly refined. The grain structures below 100 nm dimension appeared locally in the ACR Al/HEAp MMCs, while it was absent in the AR ones. Many tangled dislocation regions were generated in the ACR samples. Due to the high density of tangled dislocations, dislocation cell structures were observed along with subgrain structures. The HEAp size of ACR Al/HEAp MMCs was also

remarkably smaller than that of AR, which is evident from the SEM result in Fig. 5.26. These special structures were significantly different from the AR Al/HEAp MMCs, showcasing the unique advantages of the ACR process. No microvoids were detected in the ACR Al/HEAp MMCs, which demonstrated a positive effect of the ACR process in avoiding defects in AMCs sheets.

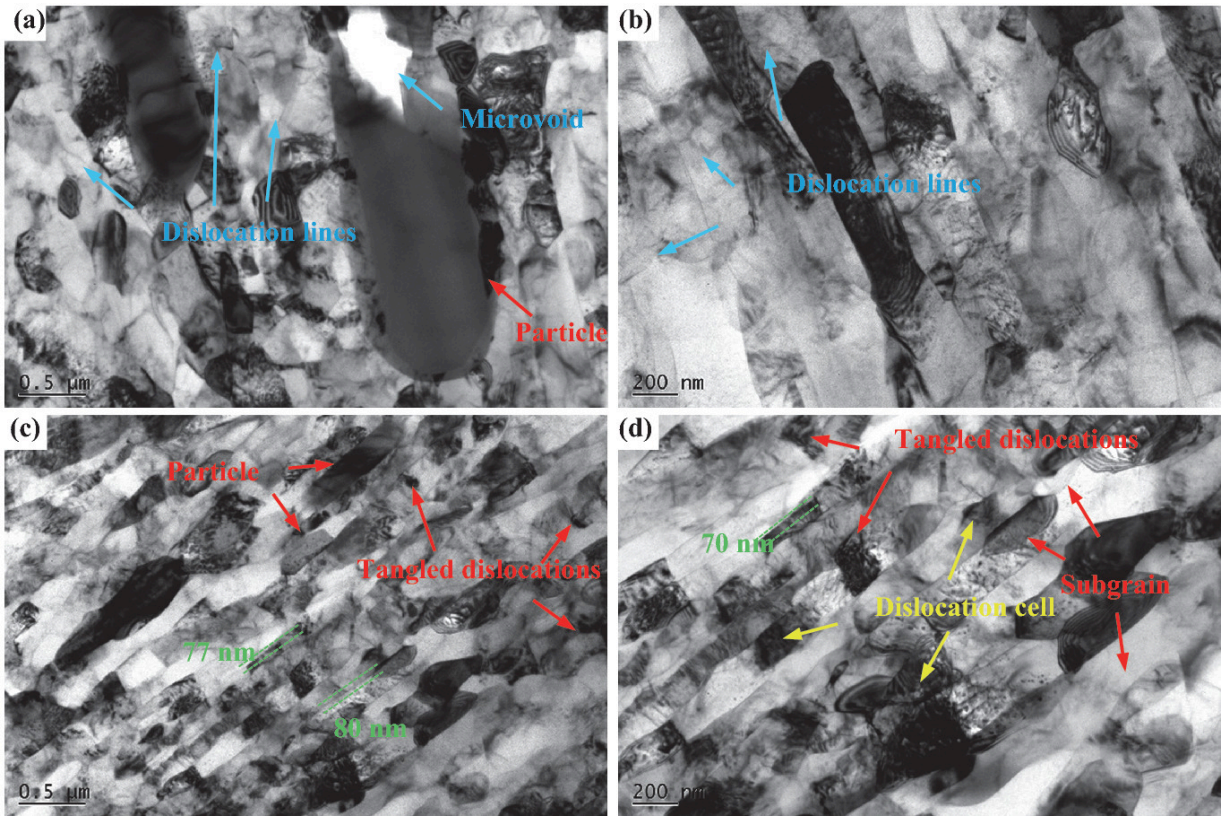


Fig. 5.27 TEM images of 3 wt% Al/HEAp MMCs with 95% rolling reduction via **a**, **b** AR and **c**, **d** ACR processes

The grain sizes of AR and ACR Al/HEAp MMCs were statistically analyzed and are presented in Fig. 5.28. The average grain size of the AR Al/HEAp MMCs was 237 nm (Fig. 5.28a), and that of ACR was 179 nm (Fig. 5.28b). This result was also intuitively reflected in the TEM images in Fig. 5.27, which further affirmed that the grain size of 3 wt% Al/HEAp MMCs was refined by the ACR process.

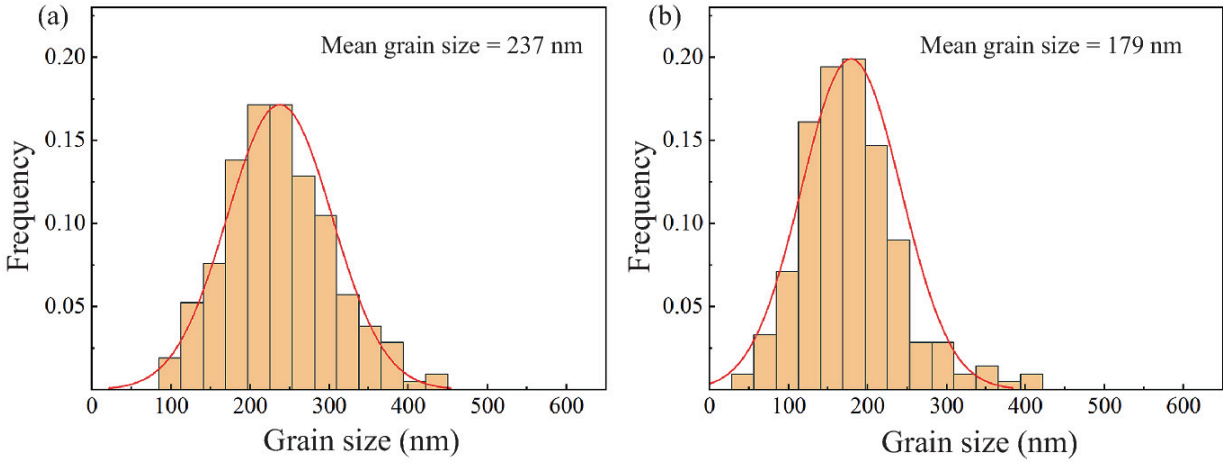


Fig. 5.28 Grain size distribution of 3 wt% Al/HEAp MMCs after a 95% rolling reduction ratio via **a** AR and **b** ACR

5.4.2 Mechanical Properties of Asymmetrical Cryorolled AA1050/HEAp Composites

Figure 5.29 shows the microhardness values of Al/HEAp MMCs under different rolling processes. With increasing rolling reduction, the microhardness value of Al/HEAp MMCs gradually increases. The microhardness of ACR Al/HEAp MMCs was higher than that of AR Al/HEAp MMCs under the same rolling reduction. In Fig. 5.29a, ACR shows a slight increase in the microhardness value of pure Al. With the increase in the mass fraction of HEAp, ACR markedly improves the microhardness of the Al/HEAp MMCs. Taking 3 wt% Al/HEAp MMCs as an example, under 50% rolling reduction, the microhardness of ACR Al/HEAp MMCs was 74 HV, and that of AR was 69 HV. The microhardness of ACR Al/HEAp MMCs was increased by 7.2% compared with that of AR Al/HEAp MMCs. When the rolling reduction is increased from 80 to 90%, the microhardness value of the Al/HEAp MMCs also increases from 76 to 84 HV. These results suggest that the ACR process can significantly improve the microhardness of Al/HEAp MMCs.

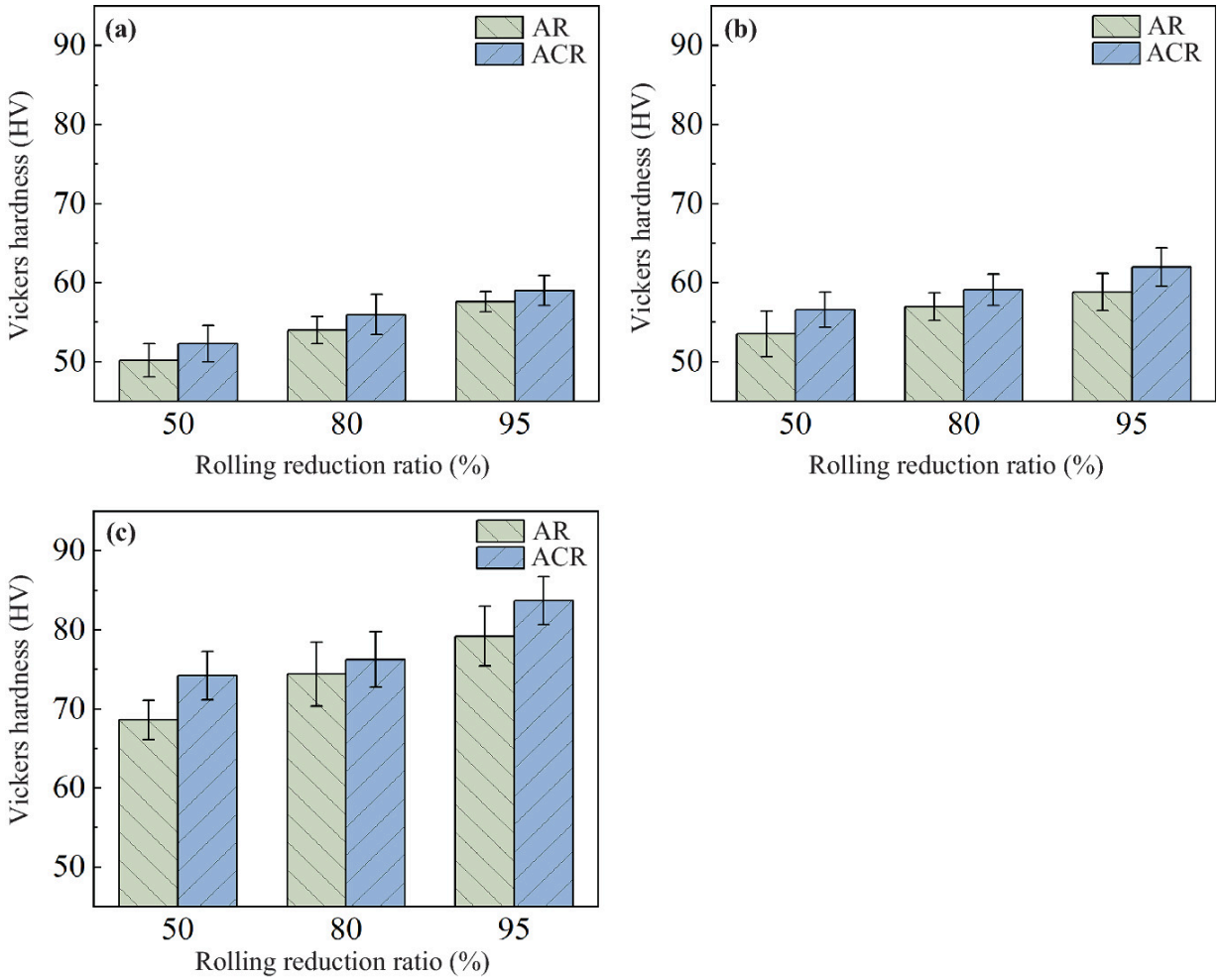


Fig. 5.29 Microhardness of the **a** 0 wt% **b** 1 wt% **c** 3 wt% Al/HEAp MMCs

Figures 5.30 and 5.31 show the yield strength, ultimate tensile stress, and elongation values of the Al/HEAp MMCs sheets after rolling. After rolling deformation, the mechanical properties of the ACR Al/HEAp MMCs got better than those of the AR Al/HEAp MMCs. Considering 3 wt% Al/HEAp MMCs as an example, the yield strength of ACR samples was improved by 10.5% compared to AR. The yield strength was 195 MPa for AR samples, which increased to 213 MPa for ACR samples at a rolling reduction ratio of 80%. Similarly, the yield strength increased from 200 to 221 MPa when the rolling reduction ratio was increased to 95%. The UTS of the ACR Al/HEAp MMCs was 10.2% higher than that of the AR samples. The UTS of the initial Al/HEAp MMCs was 115 MPa, which was markedly increased to 207 MPa for AR Al/HEAp MMCs and 231 MPa for ACR Al/HEAp MMCs at a rolling reduction ratio of 80%. After 95% rolling reduction, the UTS

was 223 MPa for AR samples, while it reached 253 MPa in ACR sheets, approximately a 13.5% increase. Meanwhile, the elongation of the Al/HEAp MMCs was 4.3% and 7%, respectively, in AR and ACR samples. Thus, it became obvious that both the strength and elongation were further enhanced by ACR.

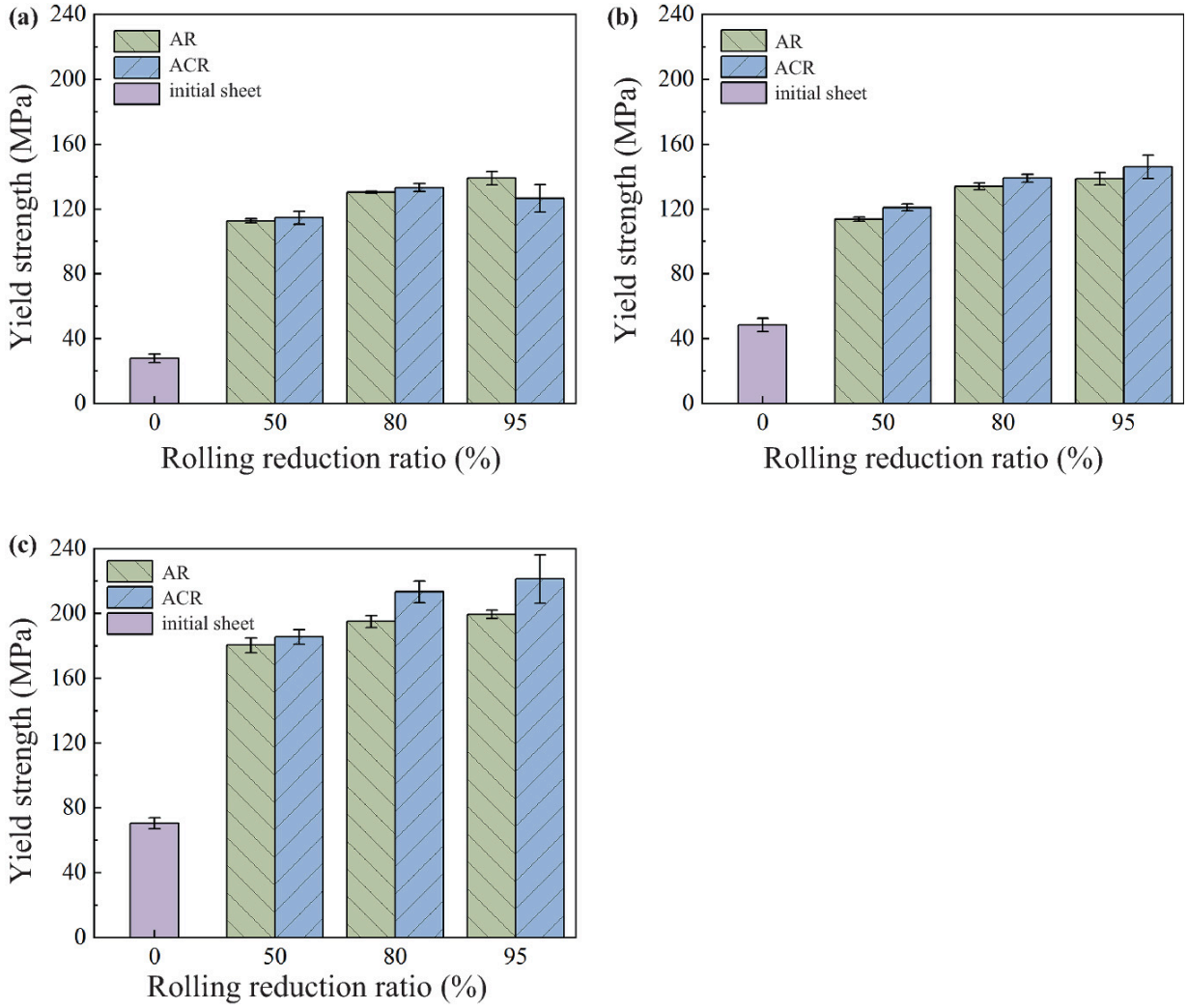


Fig. 5.30 Yield Strength of the **a** 0 wt% **b** 1 wt% **c** 3 wt% Al/HEAp MMC sheets via AR and ACR at different rolling reductions

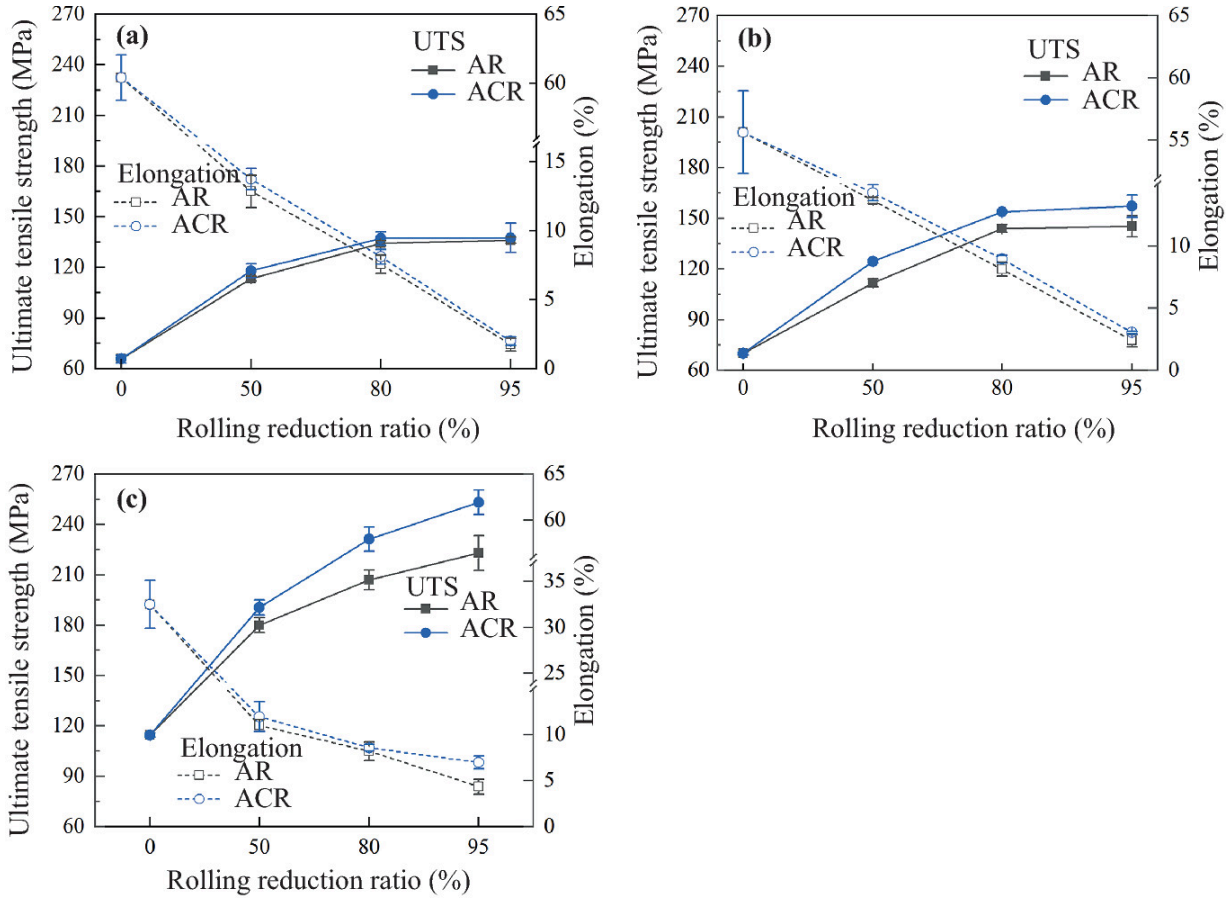


Fig. 5.31 Ultimate tensile strength and elongation of the **a** 0 wt% **b** 1 wt% **c** 3 wt% Al/HEAp MMC sheets via AR and ACR at different rolling reduction ratios

Figure 5.32a–c show the tensile fracture morphology of 3 wt% Al/HEAp MMC samples with different rolling reduction ratios post the AR and ACR processes. Under 50% rolling reduction, some dimples were generated on the tensile surface of the AR Al/HEAp MMCs (Fig. 5.32a). However, a larger number of dimples with enlarged dimensions could be observed in the ACR samples (Fig. 5.32d). Meanwhile, more evident tearing edges were observed in the AR Al/HEAp MMC tensile fracture morphology, unlike in the ACR samples. Figure 5.32b and e demonstrate an interesting phenomenon. Large areas of cleavage surface appeared in the tensile fracture of AR Al/HEAp MMCs, but the number of dimples was small and with shallow depth. This reflected that the AR Al/HEAp MMCs exhibited a brittle fracture mode at 80% rolling reduction. However, under the same deformation, the surface of tensile fracture in ACR Al/HEAp MMCs showed great differences. A great density of dimples with a relatively large area was observed on the fracture surface. Every single dimple

was deeper, and only a few tearing edges appeared on the surface, suggesting a mix-mode fracture characteristic. Such a fracture morphology reflected that ACR Al/HEAp MMCs still have a good elongation at 80% rolling reduction, which was in sharp contrast with AR samples. Under 95% rolling reduction, the tensile fracture morphology image shows that the large cleavage surface along with some small-sized dimples was very vague; in fact, it was almost invisible (Fig. 5.32c), which reflected the cleavage fracture characteristics. However, only a small cleavage surface in the tensile fracture of ACR Al/HEAp MMCs, and a certain number of dimples (Fig. 5.32f), confirmed that the ACR AMCs still possess a certain ductility. The differences in the tensile fracture morphology are reflected in the mechanical properties as well. It was further confirmed that ACR could improve the elongation of Al/HEAp MMCs compared to AR (Fig. 5.31).

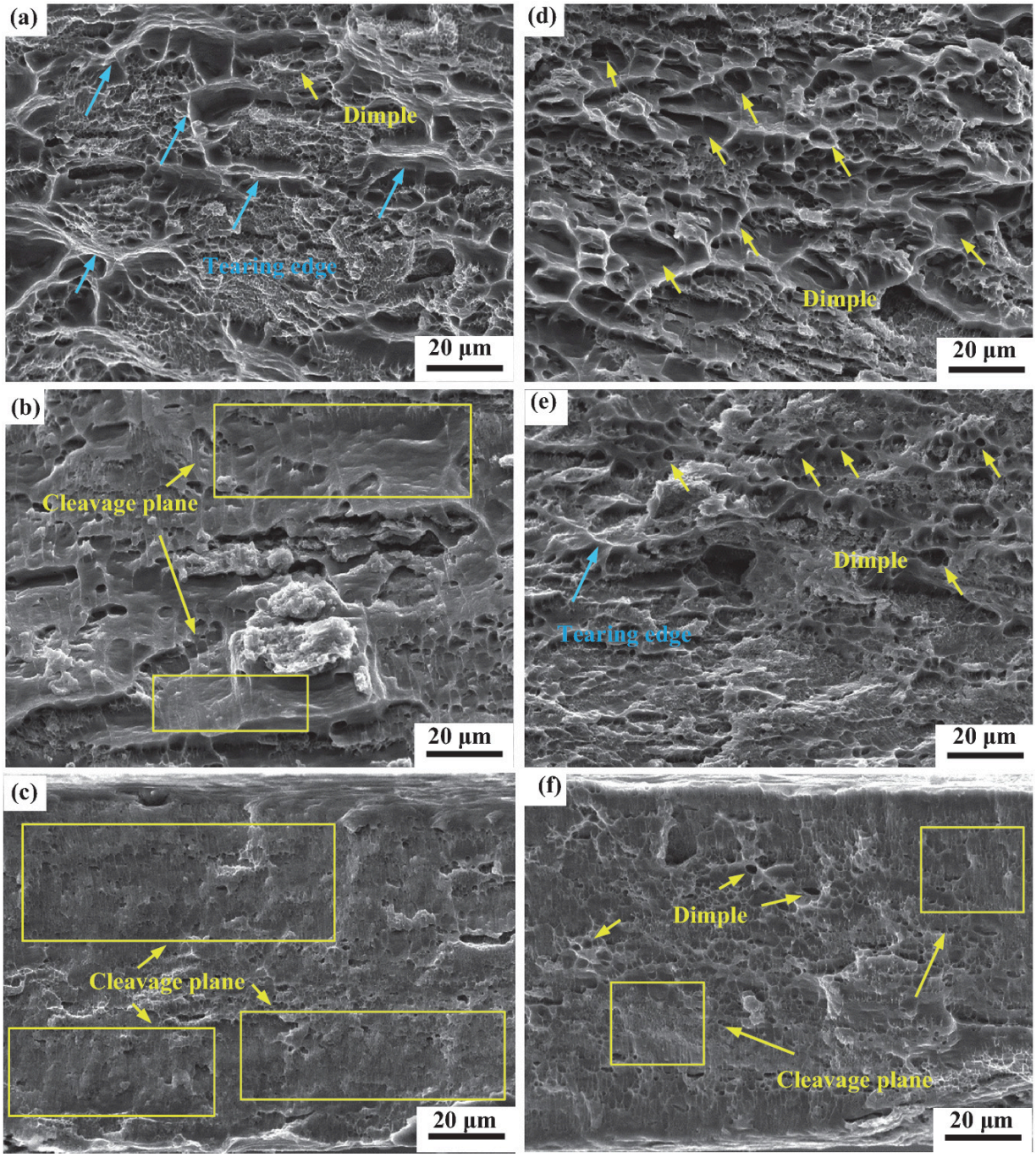


Fig. 5.32 Fracture morphologies of AR 3 wt% Al/HEAp MMCs at **a** 50%, **b** 80%, and **c** 95%; ACR 3 wt% Al/HEAp MMCs at **d** 50%, **e** 80%, and **f** 95% rolling reduction ratios

5.4.3 Mechanism of Enhanced Mechanical Properties of AA1050/HEAp Composites via Asymmetric Cryorolling

Compared with the AR Al/HEAp MMCs, the mechanical properties of ACR were quite improved, and the change in the micro defects played

an important role. As evident from Figs. 5.26b and 5.27a, the AR Al/HEAp MMCs possessed microvoid and fracture phenomena. The AR process can refine the size of HEAp reinforcement to a certain extent by introducing shear deformation. However, if the shear deformation becomes too strong, then it makes it more difficult to coordinate the deformation between HEAp and the Al matrix. Therefore, microvoids and other defects might appear around the HEAp. The HEAp reinforcement in ACR Al/HEAp MMCs, on the other hand, has an improved microstructure without obvious microvoids. This phenomenon is a result of the volume shrinkage effect. The volume shrinkage of the Al/HEAp MMCs occurred at 77 K and could be expressed by Eq. (5.12):

$$V_T = V_0 e^{\alpha(T-T_0)} \tag{5.12}$$

where α is the coefficient of thermal expansion (CTE), V is the volume, and T is the temperature. The volume shrinkage effect significantly influences the microstructure and mechanical properties of Al/HEAp MMCs. When the Al/HEAp MMCs are rolled at room temperature, the deformation of HEAp and matrix will not be coordinated due to the large difference in elastic modulus between the HEAp and Al matrix, and hence defects might occur around the HEAp. It is worth noting that the volume shrinkage effect of the Al matrix is different from that of the HEAp reinforcement in the cryogenic environment (77 K). The CTE of Al alloy is larger, and the volume shrinkage effect becomes more significant. The HEAp has a low CTE and a weak volume shrinkage effect. The larger the volume shrinkage effect of the Al alloy, the more tightly the Al will wrap the HEAp reinforcement. This will strengthen the bonding between the matrix and HEAp. Due to the volume shrinkage effect in a cryogenic environment, ACR plays a significant role in avoiding such defects that were caused by the large plastic deformation of Al/HEAp MMC sheets. In addition, the ductility of Al and HEA at cryogenic temperatures is higher than that at room temperature. The enhanced ductility will also contribute to reduced defects in ACR Al/HEAp MMC sheets, which in turn enhances their elongation during tensile testing.

The mechanical properties of the Al/HEAp MMCs improved obviously after ACR, as presented in Figs. 5.30 and 5.31. In addition to

the reduced defects, it was reported that CTE mismatch strengthening, fine grain strengthening, and Orowan strengthening also play important roles in the enhanced mechanical properties of ACR processed Al/HEAp MMC sheets.

CTE mismatch strengthening is a special strengthening method observed in composites. The CTE of HEAp is different from that of the Al matrix, and the temperature of the composites will change from preparation to processing. Therefore, a residual plastic strain will be generated in the composites, causing an increase in dislocation density. In this study, the deformation temperature of ACR was 77 K, while that of AR was 298 K. The temperature difference between them was about 221 K, which led to a higher dislocation density of ACR Al/HEAp MMCs.

The finer grains tend to enhance the mechanical properties. In the cryogenic environment, the lattice of the material will also shrink. As the lattice shrinks, the spacing between the atoms in the material decreases. According to the Peirls–Nabarro equation,

$$\tau_{P-N} = [2G/(1-\gamma)] \exp[-2\pi a/(1-\gamma)b] \tag{5.13}$$

where a is the distance between slip planes, γ is Poisson's ratio, and b is the Burgers vector. When the atomic spacing decreases due to lattice shrink, correspondingly, the lattice resistance to slip dislocations increases. In other words, lattice shrinkage will inhibit dislocation slip, and dislocation pinning will improve the strength of the composite material. In addition, the lattice distortion caused by the huge compressive stress during the process of cryogenic temperature will also promote an increase in dislocation density. Thus, during ACR, dynamic recovery is severely inhibited. Consequently, a large number of dislocations are irretrievable and difficult to cancel or rearrange. Dislocations are constantly entangled and accumulate, resulting in cellular structures, as shown in Fig. 5.27d. A large number of dislocation cells are formed due to the high-density dislocation entanglement in the ACR process, and this extremely high dislocation density will generate subgrains. In cryogenic environments, composites can accumulate a large amount of stored energy with high-density dislocations, which can refine grains during rolling. In short, ACR can form high-density dislocations and substructures in Al/HEAp MMCs, thus, improving the comprehensive mechanical properties. The grain

size of the ACR Al/HEAp MMCs was refined to 179 nm, while that of the AR Al/HEAp MMCs was 237 nm, as presented in Fig. 5.28. Grain boundaries can inhibit dislocation movement, so the stress required for plastic deformation of materials increases, which is reflected in the improvement of the mechanical properties of Al/HEAp MMCs during the process of tensile fracture.

Orowan strengthening is a mechanism to enhance the mechanical properties of materials by the hindering effect of dislocations while passing through nanoscale particles. In the present study, it could be observed that the HEAp in the composites was remarkably refined, and more particles appeared after the asymmetric cryorolling process, as shown in Fig. 5.26d. Therefore, the Orowan strengthening mechanism still exists in ACR Al/HEAp MMCs.

In summary, the grain size of the Al/HEAp MMCs is significantly refined after ACR, and the dislocation density is higher than that of AR Al/HEAp MMCs. The plastic deformation during ACR reduces the microvoids and other defects. These factors enhance the comprehensive mechanical properties of the ACR Al/HEAp MMCs. Figure 5.33 presents comparisons of the mechanical properties of ACR Al/HEAp MMCs with those of pure Al matrix composites enhanced by some other particles. Such a comparative study reassures that the ACR Al/HEAp MMCs obtained in the present study have excellent mechanical properties.

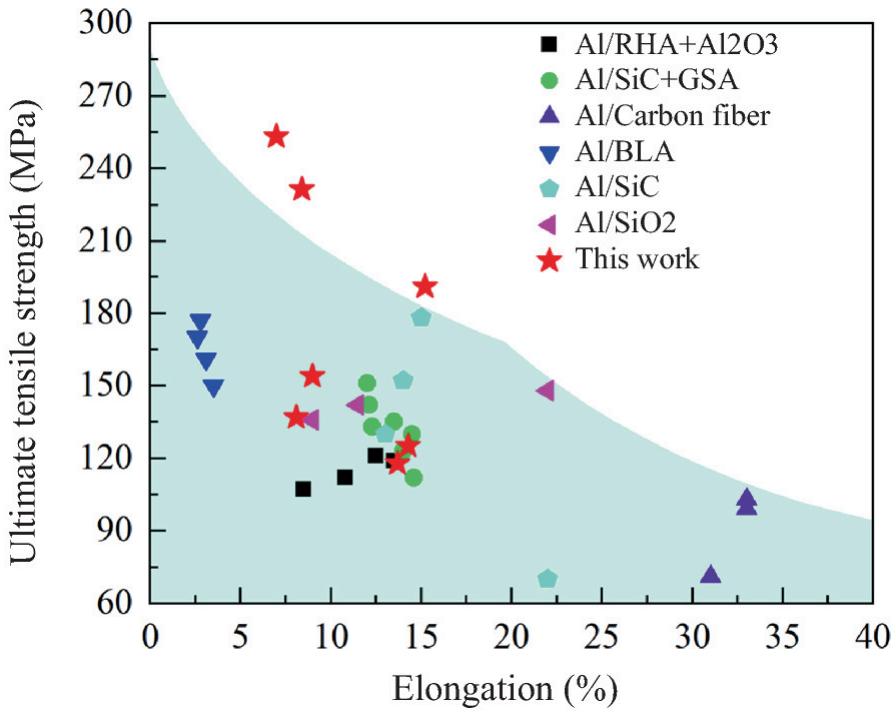


Fig. 5.33 Comparison of the mechanical properties in this study with other reported values

5.5 Mechanical Properties of Al/HEAp Composites at Extreme Environments

In present study, the mechanical properties of cryorolled Al/HEAp MMCs sheets at cryogenic temperatures were investigated. The deformation mechanism of the AMCs at different temperatures was discussed by examining the difference in microstructures of the Al/HEAp MMCs deformed at 298 K and 173 K. The microscopic mechanism of the large increase in strength and elongation of the Al/HEAp MMCs at cryogenic temperature was confirmed [24].

Figure 5.34a shows the SEM image of HEAp. Figure 5.34b illustrates the distribution of particle sizes of HEAp, and the average particle size is 3.8 μm. The HEAp is a typical single-phase BCC alloy, which has been confirmed by XRD analysis (Fig. 5.34c). Figure 5.34d and e show the EDS diffraction and surface scanning results of elements in AlCoCrFeNi HEAp. It can be speculated that the atomic percentage of the five elements resembles the equal atomic ratio and the distributions of the elements in the HEAp were relatively uniform.

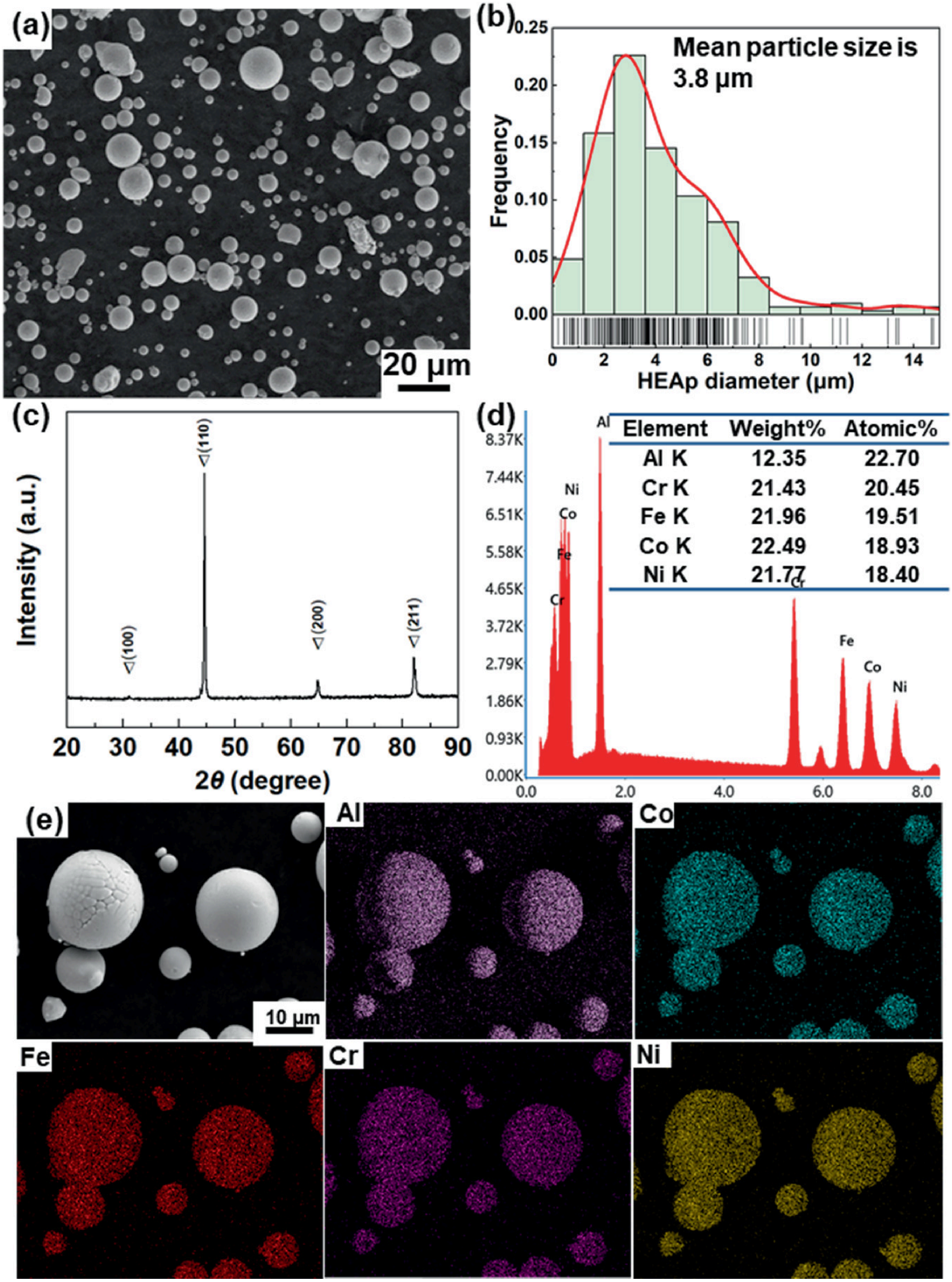

(a)
20 μm
(b)
Mean particle size is
3.8 μm
Frequency
HEAp diameter (μm)
(c)
Intensity (a.u.)
(100)
(110)
(200)
(211)
2θ (degree)
(d)
Element Weight% Atomic%
Al K 12.35 22.70
Cr K 21.43 20.45
Fe K 21.96 19.51
Co K 22.49 18.93
Ni K 21.77 18.40
(e)
10 μm
Al
Co
Fe
Cr
Ni

Fig. 5.34 **a** SEM image of AlCoCrFeNi HEAp, **b** statistical distribution of particle size, **c** XRD diffraction pattern of HEAp, **d** diffraction intensity of elements in HEAp, **e** EDS surface scanning images of element distribution in HEAp

Figure 5.35a and b show the TEM images of the 3 wt% Al/HEAp MMCs before cryorolling. In Fig. 5.35a, a higher dislocation density was observed around the HEAp, and more dislocation entanglement regions were formed. The dislocation cell structure was gradually shaped with the upsurge of dislocation entanglement regions. Figure 5.35b shows the interfacial bonding between HEAp and the Al alloy matrix at high magnification. A uniformly distributed interface was formed without microvoid generation. Figure 5.35c shows the HAADF image of Al/HEAp MMCs. It has been observed that bright white particles are found in the Al alloy matrix. To determine the elemental distribution, the yellow rectangle area in Fig. 5.35d was analyzed using EDS scanning, as shown in Fig. 5.35e. The major peak in EDS spectra depicts the abundance of Al in the matrix of AMCs. However, the EDS peaks of Cr, Co, Fe, and Ni elements were also detected. The peak intensities of Co, Fe, and Ni were similar and higher than those of Cr. Further, EDS line scanning analysis was carried out on the labeled straight-line area in Fig. 5.35d, and the results are shown in Fig. 5.35f. The black curve represents the intensity of the HAADF diffraction peak, whose intensity increased significantly when passing through the particle. The red curve shows the diffraction intensity of the Al element, which decreased slightly as it passed through the particle. In addition, diffraction peaks of Cr, Co, Fe, and Ni elements were also found, which belong to HEAp.

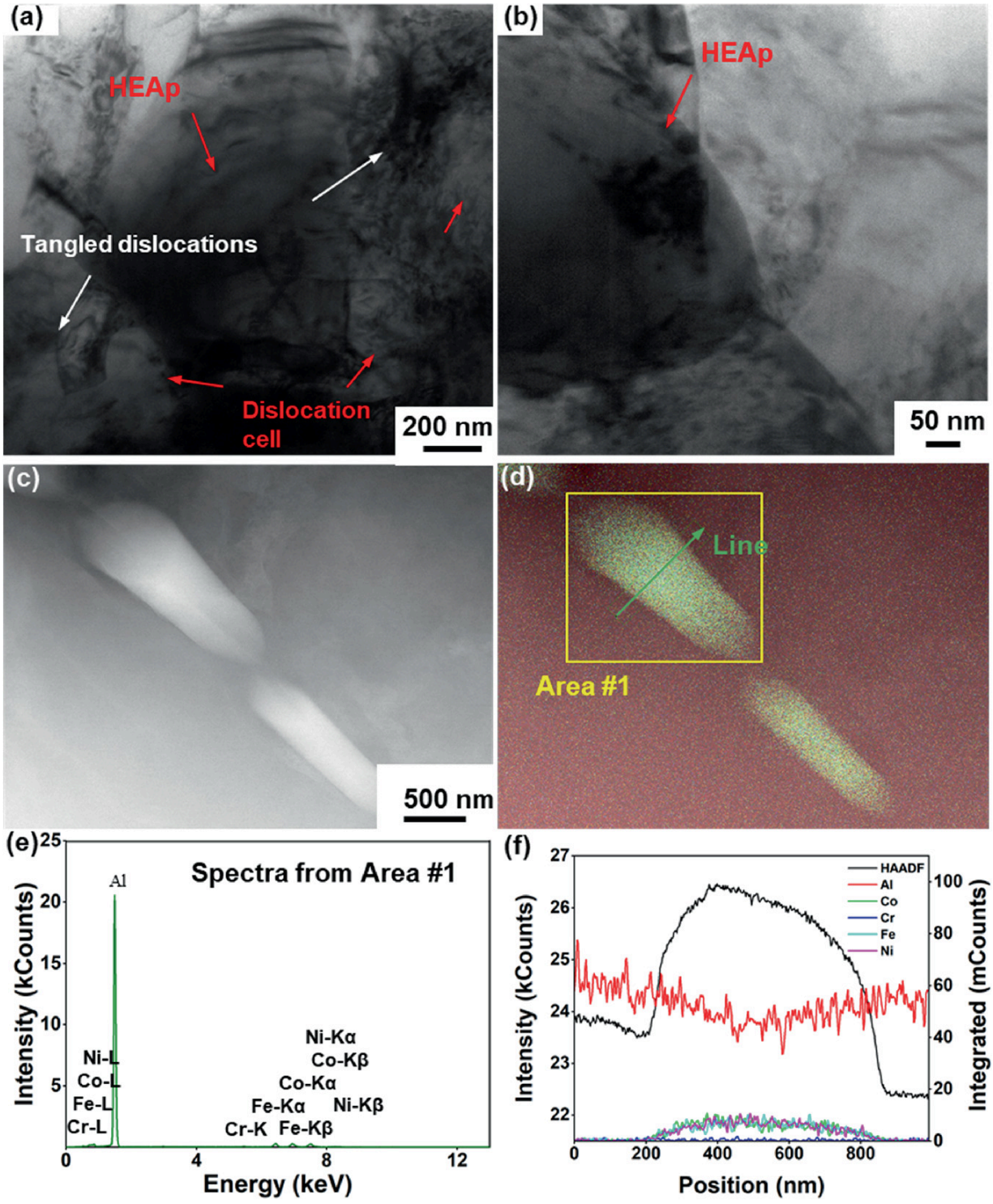


Fig. 5.35 **a** and **b** TEM images of 3 wt% Al/HEAp MMCs, **c** HAADF images of Al/HEAp MMCs, **d** EDS spectrum analysis, **e** EDS for Area #1, **f** EDS line scanning results in (**d**)

Figure 5.36 shows the SEM images of 3 wt% Al/HEAp MMCs. As shown in Fig. 5.36a, before deformation, the HEAp has a net-like structure that is uniformly distributed in the Al alloy matrix. At 30%

rolling reduction, the reinforcement of HEAp in the Al alloy matrix was aligned along the rolling direction in a streamlined strip (Fig. 5.36b). With a further increase in rolling reduction, the spacing between the reinforcements decreases further. At 90% rolling reduction, the reinforcement was evenly distributed in the Al alloy matrix, as shown in Fig. 5.36d. This is the same with the previous study that the cryorolling could avoid the void appearance near the interface between particles and matrix.

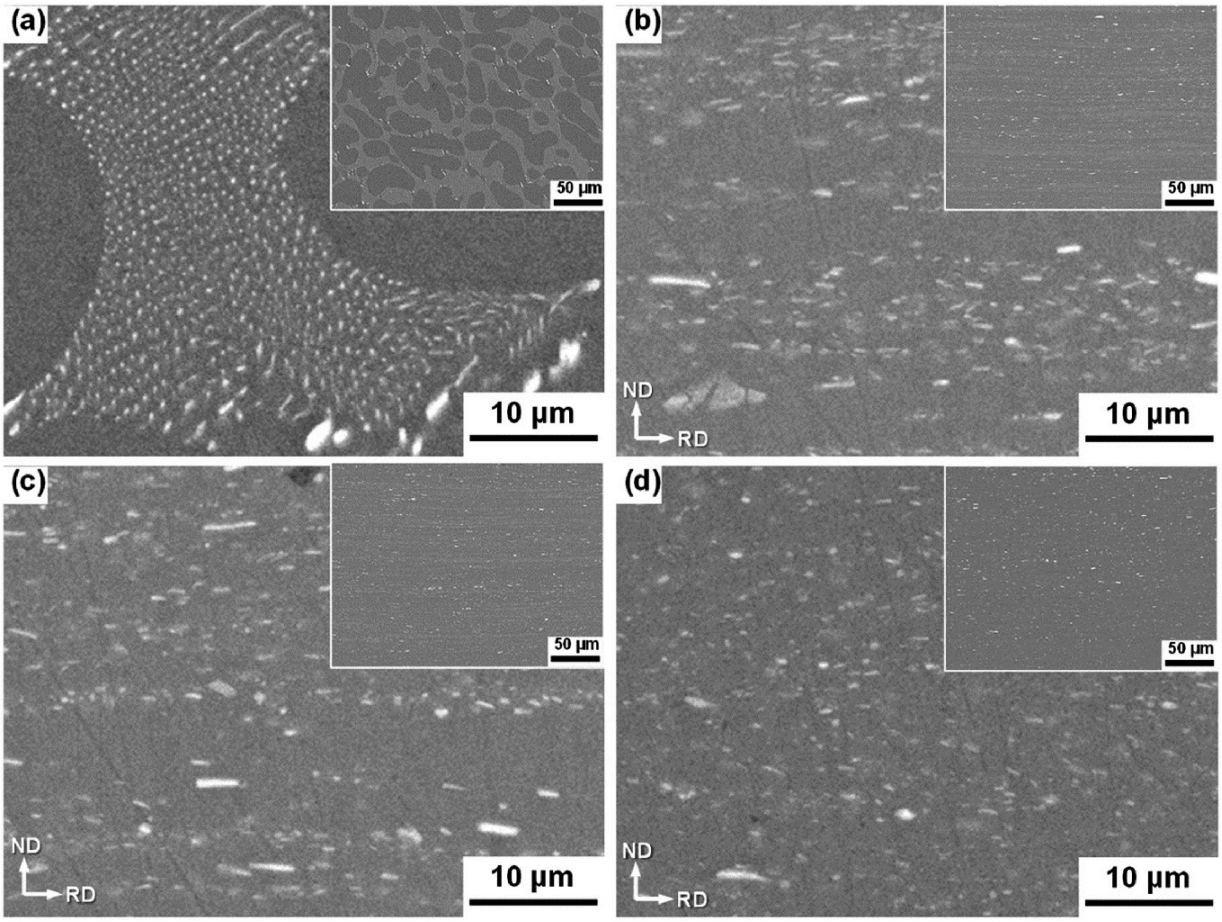


Fig. 5.36 SEM images of 3 wt% Al/HEAp MMCs samples **a** before rolling, and **b** 30%, **c** 60%, and **d** 90% rolling reductions

5.5.1 Mechanical Properties of Al/HEAp MMCs in a Cryogenic Environment

The mechanical properties of pure Al and Al/HEAp MMCs after different rolling reductions at room and cryogenic temperatures were further studied. Figure 5.37 shows the tensile stress–strain curves of

the Al/HEAp MMCs after different rolling reductions at room temperature (298 K) and cryogenic temperature (173 K). The blue curve shows the stress–strain curve of the materials after different rolling reductions at cryogenic temperature. Under 30% rolling reduction, the tensile strength of pure Al (Fig. 5.37a) was 68 ± 2.6 MPa at room temperature and 72 ± 1.3 MPa in a cryogenic environment. Compared with room temperature, the cryogenic mechanical properties of pure Al had a certain degree of improvement (5.9%), but the improvement was small. However, the cryogenic mechanical properties of the Al/HEAp MMCs were much better than pure Al. The tensile strengths of 3 wt% Al/HEAp MMCs (Fig. 5.37c) after 30%, 60%, and 90% rolling reduction were 154 ± 0.9 MPa, 179 ± 0.4 MPa, and 204 ± 3.2 MPa at room temperature, respectively. While, as the decrease of temperatures, the tensile strengths were 185 ± 0.4 MPa, 219 ± 0.9 MPa, and 251 ± 4.0 MPa respectively at cryogenic temperature. The mechanical properties of the Tensile-173 Al/HEAp MMCs were greatly improved in cryogenic temperature, with an average increase of 21.8%. After adding 4.5 wt% HEAp, the cryogenic tensile strength of the Al/HEAp MMCs (Fig. 5.37d) at different rolling reductions increased from 175 ± 2.5 MPa, 198 ± 1.6 MPa, 216 ± 3.6 MPa to 209 ± 1 MPa, 241 ± 2.3 MPa, and 263 ± 1.8 MPa, respectively. The cryogenic mechanical properties of 4.5 wt% Al/HEAp MMCs increased by 21% on average under the three rolling reduction conditions. With the addition of HEAp, the cryogenic mechanical properties of the AMCs were greatly improved. In addition, for the AMCs with the same HEAp mass fraction, the failure strain of the Al/HEAp MMCs sheets tensile tested at the same temperature decreases with increasing in the rolling reduction. For 3 wt.% Al/HEAp MMCs samples, the failure strains decrease from 12.2% ± 0.3%, 9.8% ± 0.2% to 4.9% ± 0.2% at 298 K with increasing in rolling reduction from 30, 60 to 90%. Therefore, the Al/HEAp MMCs still had a good ductility even after a large rolling reduction. Also, the increase of HEAp particles contents had a limited effect on the strain of AMCs. When the rolling reduction was 60%, the failure strains of the 1.5 wt%, 3 wt% and 4.5 wt% Al/HEAp MMCs were 12.3% ± 3.5%, 11.3% ± 0.9% and 10.0% ± 0.2%, respectively. The failure strain of the Al/HEAp MMCs did not significantly decrease with the increase of HEAp contents with the same rolling reduction.

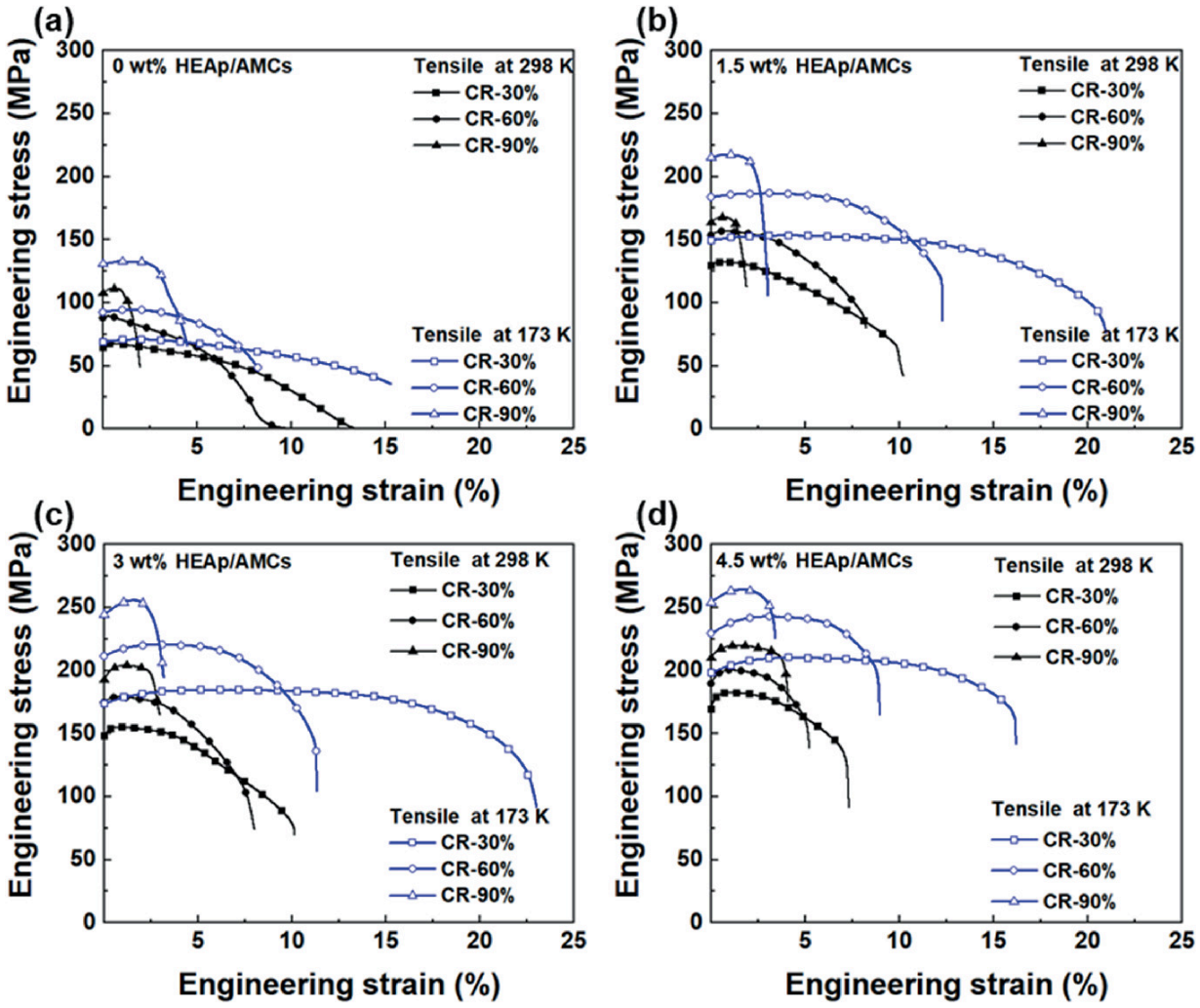


Fig. 5.37 The stress–strain curves of the **a** pure Al and AMCs with **b** 1.5 wt% **c** 3 wt% **d** 4.5 wt% HEAp at room and cryogenic temperature

The fracture morphology can reveal the influence on the fracture mechanism and elongation of Al/HEAp MMCs. Figure 5.38 shows the fracture morphology of the Tensile-298 and Tensile-173 Al/HEAp MMCs, respectively, indicating that the fracture mode of both was a ductile fracture. In the case of Tensile-298 Al/HEAp MMCs, they contained a large area of dimple-free regions (Fig. 5.38a_2 and c_1) with more tearing edges (Fig. 5.38a_1), which depicted the low fracture elongation. Tensile-173 AMCs/HEAp contained dense dimples with a higher depth (Fig. 5.38d_1 and d_2) than that of Tensile-298 samples. The illustration in Fig. 5.38d_1 shows the presence of HEAp at the bottom of the dimples, which depicts the improved uniform deformation capacity of Tensile-173 Al/HEAp MMCs. The area and depth of individual

dimples in Tensile-173 Al/HEAp MMCs were significantly larger than those in Tensile-298 Al/HEAp MMCs. In addition, uniformly and densely distributed dimples were observed in larger rolling reduction (Fig. 5.38e_1 and f_1) Tensile-173 Al/HEAp MMCs, indicating its excellent deformation ability at cryogenic temperature. The results demonstrated the higher elongation of the cryogenic temperature Al/HEAp MMCs compared to the room temperature.

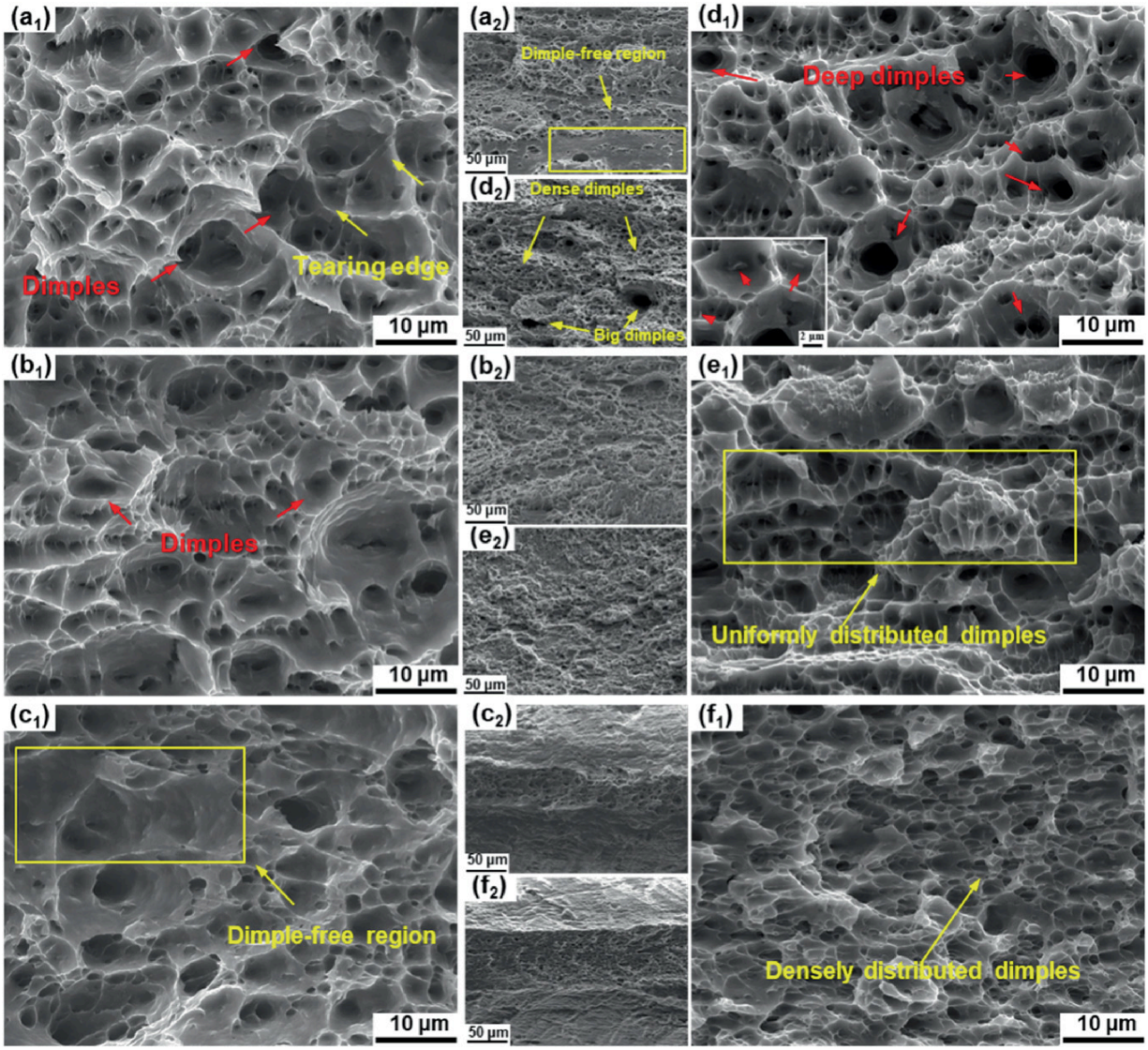


Fig. 5.38 Tensile fracture morphology of **a** 30% rolling reduction, **b** 60% rolling reduction and **c** 90% rolling reduction 3 wt% Al/HEAp MMCs at 298 K; **d** 30% rolling reduction **e** 60% rolling reduction and **f** 90% rolling reduction 3 wt% Al/HEAp MMCs at 173 K

5.5.2 Microstructure Evolution of Al/HEAp MMCs During Cryogenic Tensile Testing

Figure 5.39 illustrates the EBSD results of 3 wt% Al/HEAp MMCs samples after cryorolling and tensile testing at different temperatures. Commonly, grain boundary angles in the range of 2–15° are called low-angle grain boundaries (LAGB), and that >15° are called high-angle grain boundaries (HAGB). In Fig. 5.39a–c, LAGB and HAGB are represented by white and black curves, respectively. The proportional statistics of LAGB and HAGB in Al/HEAp MMCs are shown in Fig. 5.39d–f. The ratio of LAGB in the Al/HEAp MMCs with no tensile deformation was only 16.8%. After being deformed at room temperature, the ratio of LAGB was 36.7% in Tensile-298 Al/HEAp MMCs. Also, a higher density of LAGB was formed in the case of Tensile-173 Al/HEAp MMCs, and the proportion increased to 37.7%. The dynamic recovery of AMCs was inhibited at cryogenic temperature, so the dislocation elimination of AMCs was suppressed. As a result, more substructures were formed in the grains, increasing the proportion of LAGB. Therefore, the proportion of LAGB in Tensile-173 Al/HEAp MMCs was higher than Tensile-298 Al/HEAp MMCs.

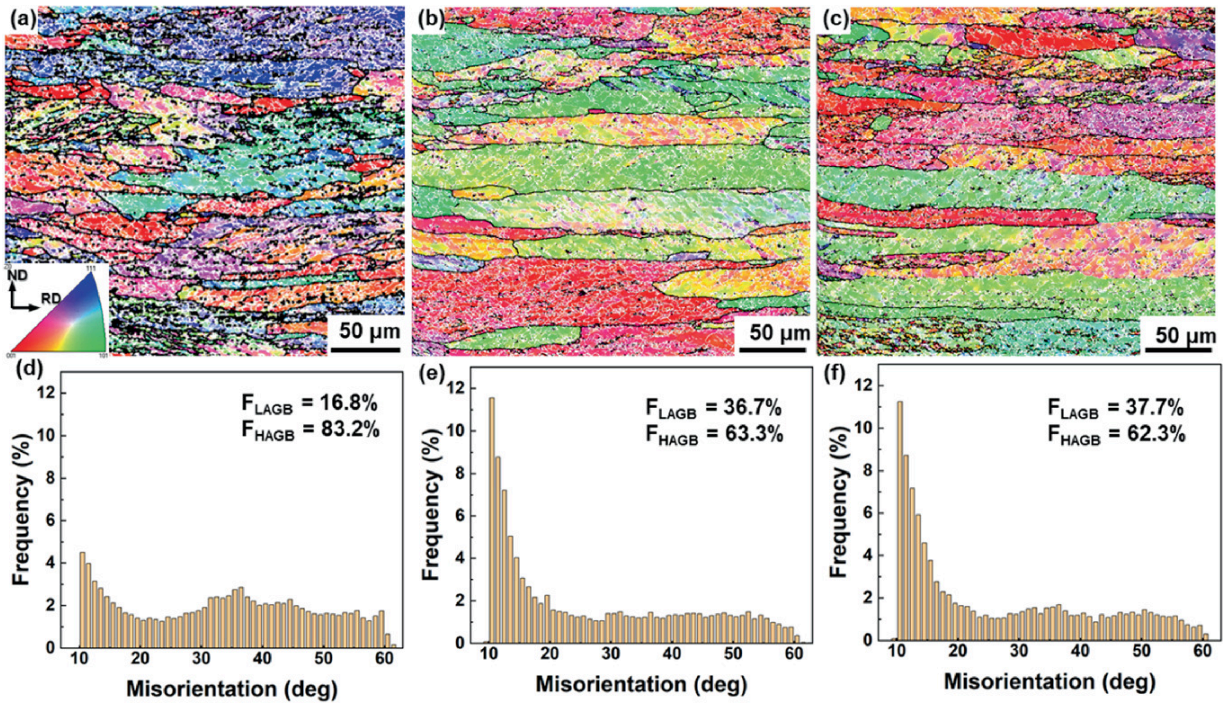


Fig. 5.39 IPF images and the corresponding misorientation distribution of **a** and **d** cryorolled, **b** and **e** Tensile-298, **c** and **f** Tensile-173 3 wt% Al/HEAp MMCs

Furthermore, the Schmid factor images of the Al/HEAp MMCs under three states were used to analyze the deformation behavior. The {111} <110> slip system of Al alloy was used to calculate the Schmid factor, and the results are shown in Fig. 5.40a and b. The Schmid factor varies in the range of 0.25–0.5 for the grains of the Al/HEAp MMCs in different states. Areas with larger values are marked with a deep orange color, and areas with smaller values are marked with a turquoise color. The Schmid factors of the Al/HEAp MMCs were used to plot Fig. 5.40c, which can be divided into three stages. The percentage of grains with a Schmid factor of <0.42 was small for all states of the AMCs. The percentage of grains with a Schmid factor between the interval of 0.42–0.47 in Tensile-298 Al/HEAp MMCs was higher than in Tensile-173 Al/HEAp MMCs. The percentage of grains with a Schmid factor between the interval of 0.47–0.5 in Tensile-173 Al/HEAp MMCs was higher than in Tensile-298 Al/HEAp MMCs. In the slip system of AMCs, grains with a higher Schmid factor were more likely to be activated. Therefore, the deformability of the lattice planes of the Tensile-173 Al/HEAp MMCs was improved.

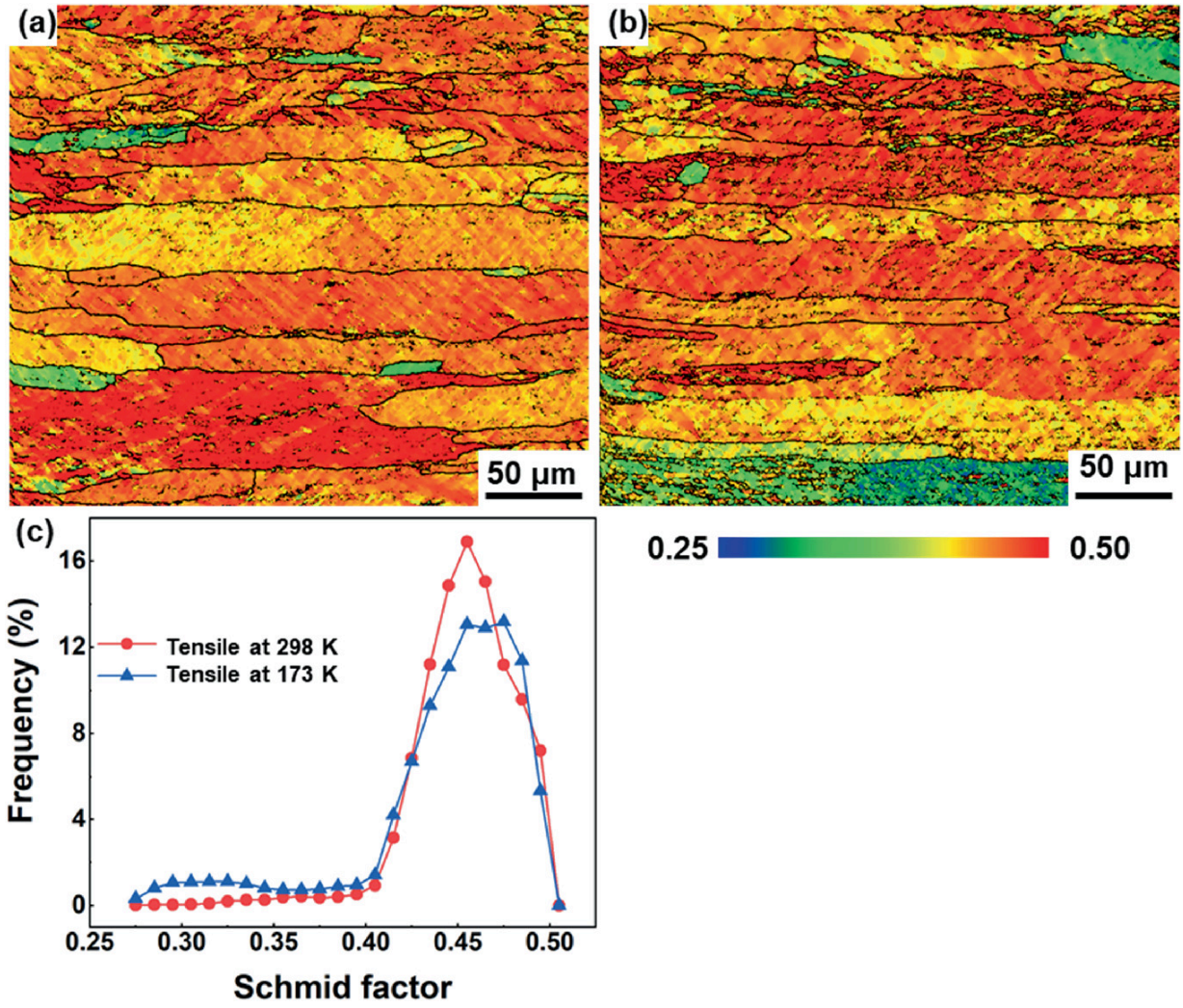


Fig. 5.40 Schmid factor images of **a** Tensile-298 **b** Tensile-173 3 wt.% Al/HEAp MMCs, **c** statistical results of Schmid factor for 3 wt% Al/HEAp MMCs

Figure 5.41a and c show the kernel average misorientation (KAM) distribution of the Al/HEAp MMCs. The Tensile-298 Al/HEAp MMCs have a larger area in the blue region, representing their lower KAM values, while the Tensile-173 Al/HEAp MMCs show a higher KAM distribution. Typically, a higher KAM value in a local area represents a greater orientation difference and lattice distortion. The KAM values were calculated as a function of distance by selecting the red dashed line in Fig. 5.41a and c. This method can also be used to evaluate the KAM difference between different grains, as shown in Fig. 5.41b and e. It can be speculated that the orientation difference between the grains of Tensile-298 and Tensile-173 Al/HEAp MMCs was significant. The KAM values vary between different grains, with a difference of 49.5° in

Tensile-298 Al/HEAp MMCs. While the KAM values of the Tensile-173 Al/HEAp MMCs vary slightly as they pass through the different grains, with a maximum difference of 40.3°. And the inhomogeneity of the difference in orientation between the different grains in Tensile-173 Al/HEAp MMCs decreased significantly. The KAM values for the whole region of the Al/HEAp MMCs were calculated, as shown in Fig. 5.41c and f. The average KAM value of the Tensile-298 Al/HEAp MMCs was 1.17, and that of the Tensile-173 samples was 1.19. The Al/HEAp MMCs show a higher KAM value in a cryogenic environment.

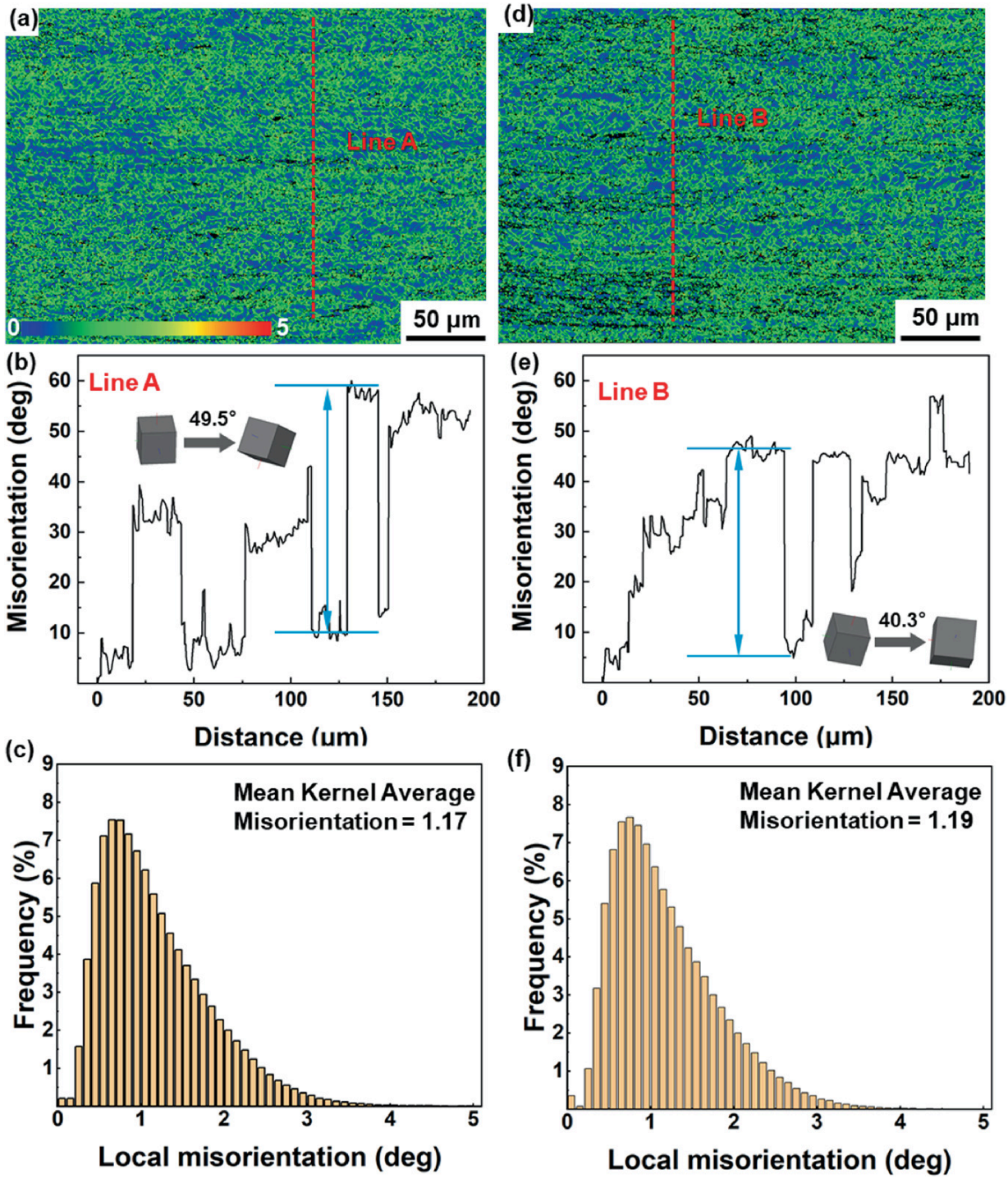


Fig. 5.41 KAM images of **a** Tensile-298 and **d** Tensile-173 3 wt% Al/HEAp MMCs; the curve of KAM value changing with distance of **b** Tensile-298 and **e** Tensile-173 3 wt% Al/HEAp MMCs; KAM statistics result of **c** Tensile-298 and **f** Tensile-173 3 wt% Al/HEAp MMCs

Figure 5.42 shows the TEM images of the 3 wt% Al/HEAp MMCs after tensile fracture at 298 K and 173 K. Only a few dislocation lines existed in the vicinity of particles in the Al/HEAp MMCs after tensile at

room temperature (Fig. 5.42a). However, a large number of dislocation tangles were observed after tensile at cryogenic temperature (Fig. 5.42c), and dislocation cells were formed in some regions. Dislocation cells can promote the deformation of Al/HEAp MMCs, and higher dislocation density makes Al/HEAp MMCs have higher tensile strength. TEM results show that the Tensile-173 samples had higher dislocation density, which was consistent with EBSD results.
Figure 5.42b and d show the length-diameter ratio of the particles in Tensile-298 and Tensile-173 Al/HEAp MMCs. In Tensile-298 Al/HEAp MMCs, the particles length-diameter ratio was 1.9, but increased to 3.8 in Tensile-173 samples. The particles in Al/HEAp MMCs had a higher length-diameter ratio along the tensile direction at cryogenic temperature. The results show that the Al/HEAp MMCs underwent higher plastic deformation, that is, higher elongation, before tensile fracture at cryogenic temperature.

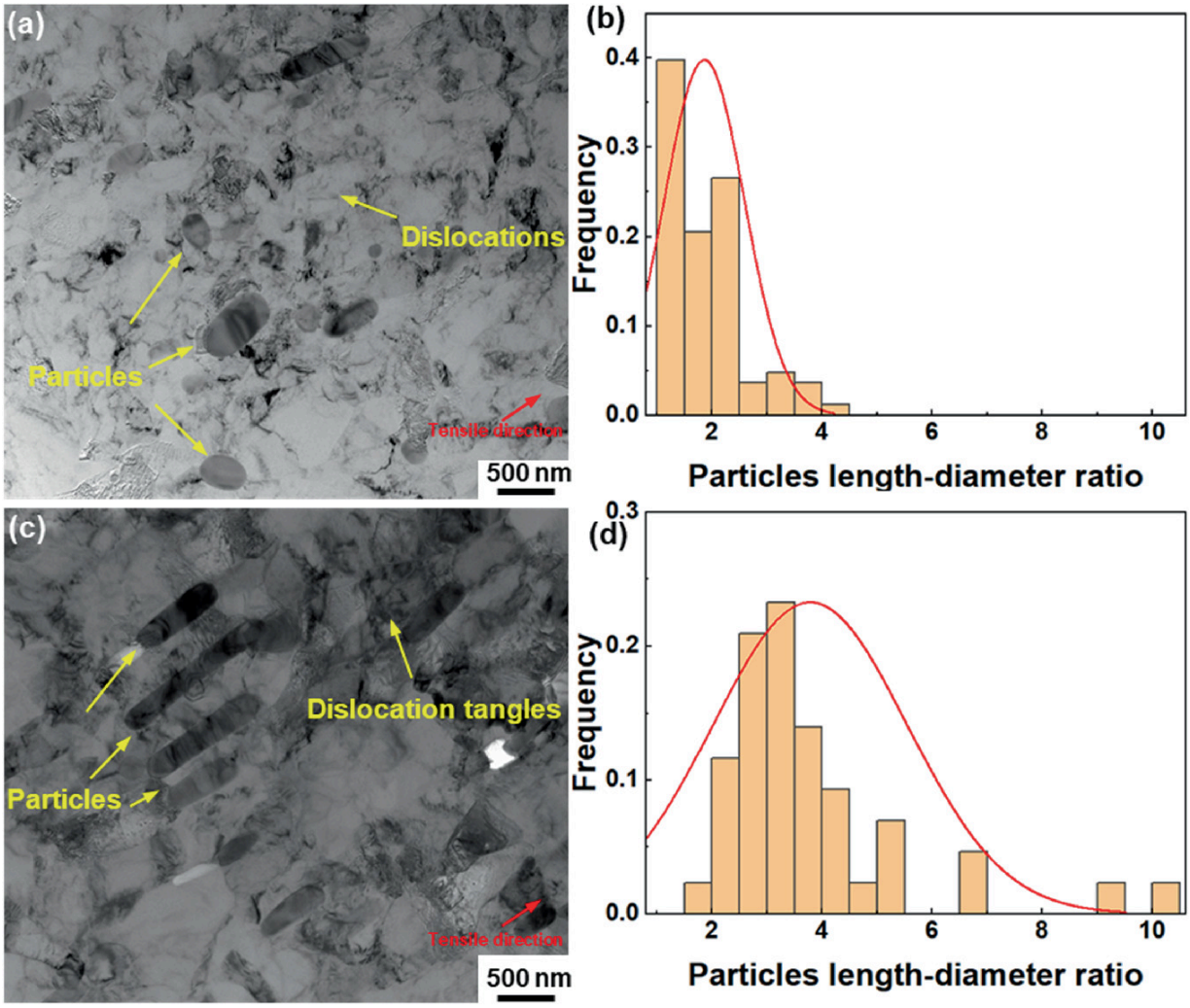


Fig. 5.42 TEM images of **a** Tensile-298 and **c** Tensile-173 3 wt% Al/HEAp MMCs with 30% rolling reduction; Statistical results of particles length-diameter ratio in **b** Tensile-298 and **d** Tensile-173 AMCs

The microstructure of the 3 wt% Al/HEAp MMCs with larger rolling reduction was further observed after tensile fracture at 298 K and 173 K. There were many dislocation lines in Al/HEAp MMCs at 298 K, and the dislocations began to tangle (Fig. 5.43a and b). However, the distribution of dislocations was not uniform. There were a lot of dislocation tangles in the local regions, but only a few dislocation lines in some regions. However, the dislocation density of Al/HEAp MMCs increased significantly at cryogenic temperature and its distribution became more uniform (Fig. 5.43c and d). Higher dislocation density resulted in a large number of dislocation walls and dislocation cells, thus improving the strength of the Al/HEAp MMCs. The uniformly distributed dislocation cell also reduced the local deformation.

Therefore, the stress concentration in the Al/HEAp MMCs was reduced and the occurrence of necking and fracture can be delayed at cryogenic temperature. As a result, the elongation of the Tensile-173 Al/HEAp MMCs was significantly improved.

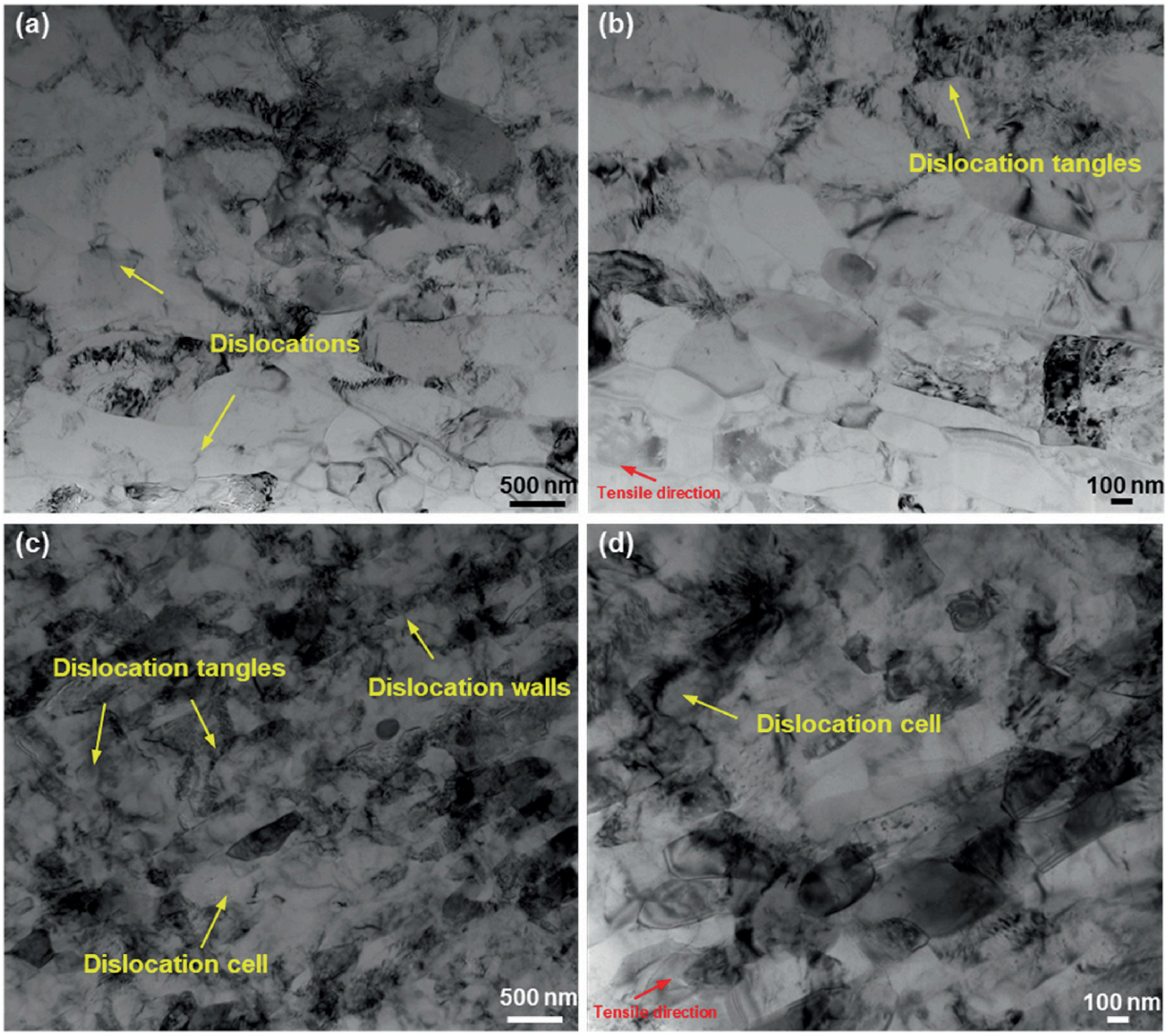


Fig. 5.43 TEM images of 3 wt% Al/HEAp MMCs after 90% rolling reduction tensile at **a** and **b** 298 K, **c** and **d** 173 K

5.5.3 Mechanism of Al/HEAp MMCs Strength Enhancement in a Cryogenic Environment

According to Fig. 5.37, the ultimate tensile strength (UTS) and elongation of Al/HEAp MMCs at cryogenic temperature were higher than room temperature. Figure 5.44 shows the comparison of UTS of

pure Al and Al/HEAp MMCs at different temperatures and rolling reduction ratio. The UTS of pure Al at cryogenic temperature was increased by only 5.9% compared with room temperature at 30% rolling reduction (Fig. 5.44a). The mechanical properties of pure Al had been improved to a certain extent in the cryogenic temperature, but the improvement was not large. When 1.5 wt%, 3 wt%, and 4.5 wt% HEAp (Fig. 5.44b–d) were added to prepare the AMCs, the mechanical properties in cryogenic temperature increased by 20.8%, 21.8%, and 21% on average under different rolling reductions, respectively.

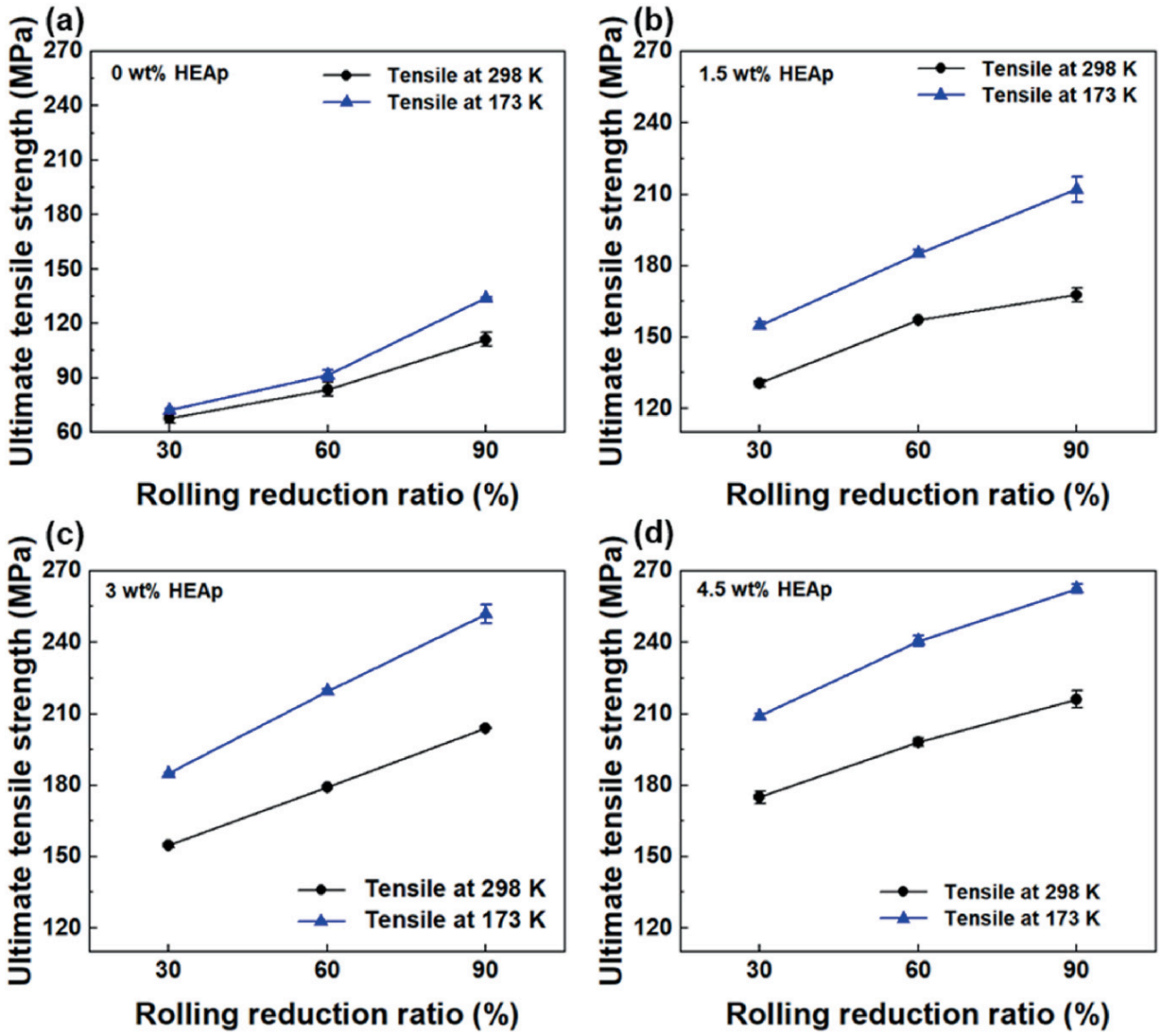


Fig. 5.44 Comparison of ultimate tensile strength of **a** pure Al and AMCs with **b** 1.5 wt% **c** 3 wt% **d** 4.5 wt% HEAp at room and cryogenic environment

The tensile strength of Al alloy can be improved in a cryogenic environment. The tensile strength of the AA2060 alloy at 153 K was higher than at 298 K. Similarly, AA6061 and Al-Cu-Mn alloys show higher tensile strength at cryogenic temperature (173 K and 143 K) than room temperature. The tensile strengths of Al alloys and the Al/HEAp MMCs at different temperatures were compared, as shown in Table 5.4. It has been observed that the strength of the four materials was improved to some extent at cryogenic temperature. The cryogenic tensile strengths of different kinds of Al alloys were improved by 11% on average. However, the cryogenic tensile strength of the Al/HEAp MMCs increased by 23%. The enhancement of the cryogenic tensile strength of Al/HEAp MMCs was significantly higher than Al alloys.

Table 5.4 Comparison of room and cryogenic temperature tensile strength of Al alloy and Al/HEAp MMCs

Alloy	Room temperature (K)	UTS (MPa)	Cryogenic temperature (K)	UTS (MPa)	Improvement (%)
AA2060	298	436	153	481	10.3
AA6061	298	316	173	345	9.2
Al-Cu-Mn	293	148	143	168	13.5
Al/HEAp MMCs	298	204	173	251	23

In addition to the common strengthening mechanism of Al alloy in a cryogenic environment, there must be a unique strengthening mechanism for Al/HEAp MMCs. The reasons for the significant improvement in mechanical properties of Al/HEAp MMCs in a cryogenic environment have been discussed below.

(1) Mismatch in coefficient of thermal expansion (CTE) reinforcement:

The residual plastic strain is generated at a cryogenic temperature due to the difference in CTE of HEAp (9.03×10^{-6} K^{-1}) and Al alloy matrix (23.4×10^{-6} K^{-1}). This strain is responsible for a further increase in the dislocation density of the Al/HEAp MMCs, resulting in enhanced strength. There is a greater temperature difference (125 K) between

cryogenic environments (173 K) and room temperature environments (298 K); thus, the Tensile-173 Al/HEAp MMCs show a higher CTE mismatch reinforcement effect. In the Tensile-173 Al/HEAp MMCs (Figs. 5.42c and 5.43c), we found a significant increase in dislocation density around the particles. The strength increase caused by the CTE mismatch can be calculated using Eqs. (5.14) and (5.15).

$$\rho^{\mathrm{CTE}} = \frac{A\Delta\alpha\Delta T V_p}{bd_p\left(1 - V_p\right)} \tag{5.14}$$

$$\Delta\sigma_{\mathrm{CTE}} = \beta G_m b\sqrt{\rho^{\mathrm{CTE}}} \tag{5.15}$$

where ρ^{CTE} is the increase of dislocation density caused by the difference in CTE, G_{m} is the shear modulus of Al alloy, A is a constant of 12, $\Delta\alpha$ is the difference of CTE between Al alloy and HEAp, ΔT is the difference between room temperature and cryogenic temperature, d_{p} is the average particle size of the reinforcement, V_{p} is the volume fraction of the reinforcement, β is a constant, and b is the Burgers vector. As a result, the strength increase caused by CTE mismatch is a function of temperature difference. According to Eqs. (5.14) and (5.15), the strength increase caused by CTE reinforcement was 4.7 MPa. Thus, the Al/HEAp MMCs will have a higher CTE mismatch strengthening effect in a cryogenic temperature.

(2) Dislocation strengthening:

Higher lattice distortion boundaries occurred near the grains of the Tensile-173 Al/HEAp MMCs and the planar slip mode is effectively curbed at cryogenic temperatures. According to Fig. 5.41f, the volume shrinkage effect is responsible for the high local orientation difference in a cryogenic temperature. The temperature difference between the cryogenic temperature and room temperature (125 K) leads to different volume shrinkage effects due to the difference in CTE of the HEAp and Al matrix. Figure 5.45a and d show the high-resolution TEM (HRTEM) results of the Al/HEAp MMCs tensile at 298 K and 173 K. A Fast Fourier Transform (FFT) of the rectangular region in Fig. 5.45a and d identified the presence of reinforcement particles (Fig. 5.45b and e).

According to the inverse FFT (Fig. 5.45c and f), the microstructure and dislocation accumulation of the particles at the two temperatures were significantly different. There were only a few dislocations in the Tensile-298 samples (Fig. 5.45c). However, the Tensile-173 ones showed obviously higher density of dislocations (Fig. 5.45f). Moreover, due to the inhibition of dynamic recovery at cryogenic temperature, the reinforcement particles can store a higher density of dislocations, thus resulting in higher tensile strength. A significant volume shrinkage occurred in the cryogenic environment, resulting in a greater geometrically necessary dislocation (GND) density. The KAM method based on strain gradient theory can be used to compute GND density values, which are linearly related to the KAM value. KAM value reflects the degree of plastic deformation homogenization. Larger KAM value represents greater plastic deformation and dislocation density. The KAM values obtained from the EBSD data (Fig. 5.45c and f) can be used to calculate the GND density in the material and the formulae used (Eqs. 5.16 and 5.17) are as follows.

$$\mathrm{KAM}_{\mathrm{ave}} = \exp\left[\frac{1}{N}\sum_{1}^{i}\ln\mathrm{KAM}_{L,i}\right] \tag{5.16}$$

$$\rho^{\mathrm{GND}} = 2\mathrm{KAM}_{\mathrm{ave}}/\mu b \tag{5.17}$$

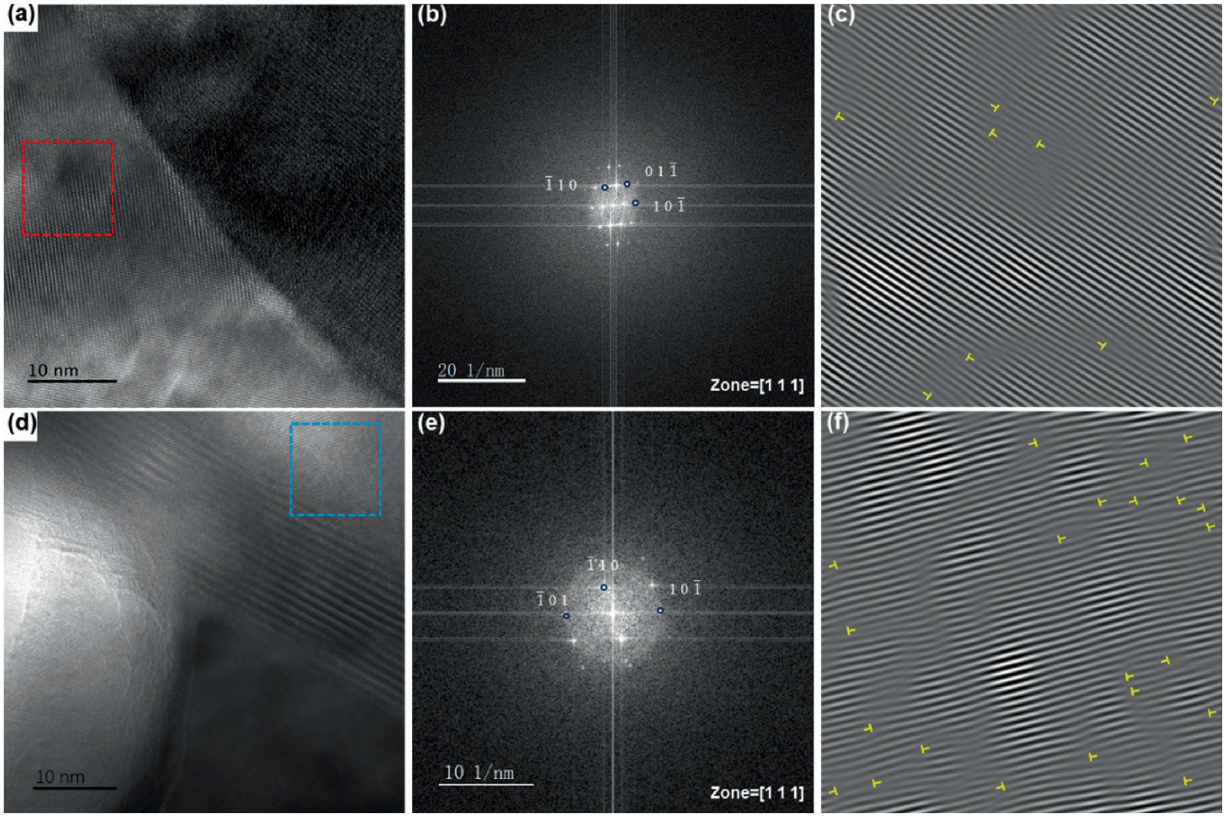


Fig. 5.45 HRTEM images of the interface in **a** Tensile-298 and **d** Tensile-173 Al/HEAp MMCs; **b** Fast Fourier Transform (FFT) and **c** Inverse FFT of the red rectangular region in (**a**); **e** Fast Fourier Transform (FFT) and **f** Inverse FFT of the blue rectangular region in (**d**); The dislocations are marked by '⊥' symbol

where KAM_{ave} is the average KAM value of the AMCs, ρ^{GND} is the GND density value, μ is the step size of EBSD (0.4 μm), b is the Burgers vector (0.286 nm). The GND density is proportional to KAM value, and the Al/HEAp MMCs have a higher KAM value in a cryogenic environment. Thus, the higher GND density in a cryogenic environment will improve the mechanical properties of the Al/HEAp MMCs. The difference in the dislocation density of the Al/HEAp MMCs at 298 K and 173 K was calculated to be 6.1×10^{12} m^{-2} and the strength increase was 23.2 MPa. And the tensile strength of the Tensile-173 Al/HEAp MMCs will also be increased due to the stronger bonding between the reinforcement particles and the Al alloy matrix in a cryogenic temperature via the volume shrinkage effect.

In a cryogenic environment, the lattice of materials will shrink to a certain extent. The Peirls-Nabarro stress represents the resistance of

the lattice to dislocation motion. The Peirls-Nabarro formula can be expressed as Eq. 5.18.

$$\tau_{P-N} = [2G/(1-\gamma)] \exp[-2\pi\omega/b] \tag{5.18}$$

where γ is Poisson's ratio, ω is the dislocation width, a quantity related to the lattice parameters.

As the lattice shrinks, the atomic spacing decreases, and the resistance of the lattice to dislocations increases. Therefore, the slip dislocation is suppressed, and the entanglement and pinning of dislocations further increase the strength of the Al/HEAp MMCs. ω is a temperature-related parameter that can be expressed as Eq. 5.19.

$$\frac{\omega}{b} = \left(\frac{\omega}{b}\right)_0 \exp\left[\frac{T}{3T_m}\right] \approx \omega_0 \left(1 + \frac{T}{3T_m}\right) \tag{5.19}$$

where α is a positive number, T_m is the melting temperature.

According to the above formula, the dependence of the Peirls-Nabarro stress on temperature is expressed as Eq. 5.20.

$$\tau_{P-N} = [2G/(1-\gamma)] \exp[-2\pi\omega_0/b] \exp[-2\alpha T\pi\omega_0/b] \tag{5.20}$$

Therefore, the Peirls-Nabarro stress is a parameter having a high dependency on temperature. This could be the explanation for the increase in strength due to the volume shrinkage effect that occurs in a cryogenic environment. In addition, the generated high frictional stress also limits the movement of dislocations under the action of large lattice distortion caused by rolling deformation. The deformation process is usually accompanied by dislocation multiplication and movement. And the motion of dislocations is suppressed due to the lower dynamic recovery and atomic migration in the cryogenic environment. The multiplication of dislocations will increase, resulting in further accumulation of higher dislocation densities (Fig. 5.45f) and an increase in the strength of the Al/HEAp MMCs. In the present experimental results, the tensile strength of the Al/HEAp MMCs increased by 21.8% in the cryogenic environment. The results show that CTE reinforcement and dislocation strengthening were the key factors to enhance the strength of Al/HEAp MMCs in a cryogenic environment.

5.5.4 Mechanism of Al/HEAp MMCs Elongation Enhancement in Cryogenic Environment

Figure 5.37b–d show that the elongation of the Al/HEAp MMCs was greatly improved at cryogenic temperature (173 K) compared to room temperature (298 K). Also, both the characterization of tensile fracture morphology (Fig. 5.37) and the microstructure characterization (Fig. 5.42) reflect the enhanced ductility of Al/HEAp MMCs at cryogenic temperature. To reveal the evolution process of microstructure during tensile deformation at cryogenic temperature, the molecular dynamics model tensile at 173 K and 298 K was built, which revealed the nucleation and growth of voids during tensile fracture at different temperatures.

Figure 5.46a and b show the evolution process of the voids in the model at cryogenic temperature (173 K) and at room temperature (298 K). According to Fig. 5.46, the atoms around the voids contain high potential energy ranging from −2.1 eV to −1.5 eV. The circles marked in magenta color depict the nucleation and growth of the voids. The number of voids in the model at 173 K was significantly less than at 298 K under the same strain. Figure 5.46c demonstrates the evolution of void volume fraction (VVF) in the model at 173 K and at 298 K. The atoms were disordered by tensile in the first stage ($\varepsilon < 9.60 \times 10^{-2}$), and vacancies were uniformly distributed in the model. However, the strain did not reach the threshold of void nucleation, and these vacancies could not be upgraded to voids. When the strain increased to the nucleation point (9.84×10^{-2} at 173 K, 9.60×10^{-2} at 298 K), the voids began to grow with a rapid increase in the VVF, and during this stage, the VVF at 173 K was always less than at 298 K. According to the failure criterion of VVF ≥ 25%, the deformation of model failure at 173 K was greater than that at 298 K. The third stage was the void coalescence stage, and the VVF at two temperatures almost coincided with each other and increased linearly. It has been observed that the nucleation threshold at 173 K was higher than at 298 K, and the growth rate was lower at 173 K than at 298 K. Therefore, the tensile deformation performance of the model at cryogenic temperature was better than that at room temperature due to inhibition or delay in the failure of the

material caused by the voids. Thus, the elongation of the material at cryogenic temperature was greater than that at room temperature.

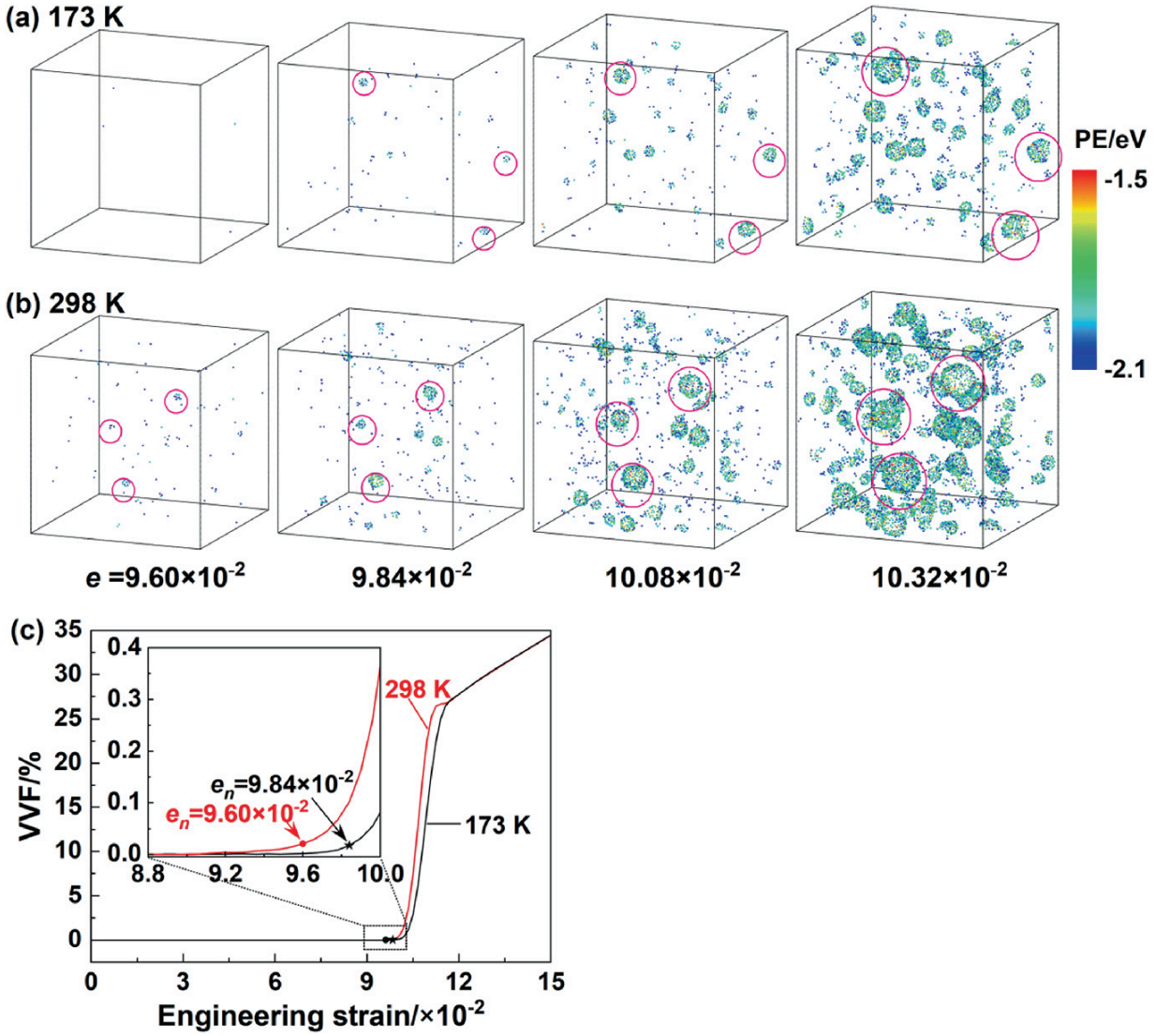


Fig. 5.46 Snapshots of void nucleation and growth in simulation model at **a** 173 K, and **b** 298 K; **c** evolution of void volume fraction

Figure 5.47 shows the surface morphology on the lateral view of the Tensile-298 (Fig. 5.47a) and Tensile-173 (Fig. 5.47d) Al/HEAp MMCs. The shrinkage length of the Tensile-298 Al/HEAp MMCs was 2055 μm, while the Tensile-173 samples decreased to 1722 μm at cryogenic temperature. Therefore, Al/HEAp MMCs had a higher reduction of area in cryogenic environment. Moreover, it can be found in the local enlarged view of Fig. 5.47b that the tensile fracture at room temperature was relatively straight and almost broke along a straight

line. However, the cryogenic tensile fracture (Fig. 5.47e) shows a zigzag morphology. In addition, there were more slip bands in the Tensile-173 Al/HEAp MMCs than Tensile-298 samples. Furthermore, the slip bands angles of Al/HEAp MMCs at different temperatures were obviously different. In Tensile-298 Al/HEAp MMCs, the slip band angle was 12–29°, while was 45–48° in Tensile-173 samples. At room temperature, the nucleation rate of microvoids in the Al/HEAp MMCs was higher. The strain value was lower when the Al/HEAp MMCs reached the fracture limit. At the beginning of plastic deformation, the stress increased rapidly, and the dislocation began to proliferate and the dislocation density increased rapidly. When the plastic strain reached the limit, the local stress concentration of the Al/HEAp MMCs was too high, and the slip in tensile deformation cannot be further extended. Therefore, the Al/HEAp MMCs were more prone to fracture during the tensile process at room temperature, resulting in a low slip angle. As a consequence, the elongation of Al/HEAp MMCs at room temperature was lower than that at cryogenic temperature. The tensile fracture morphology proved that the simulation results were consistent with the experimental results.

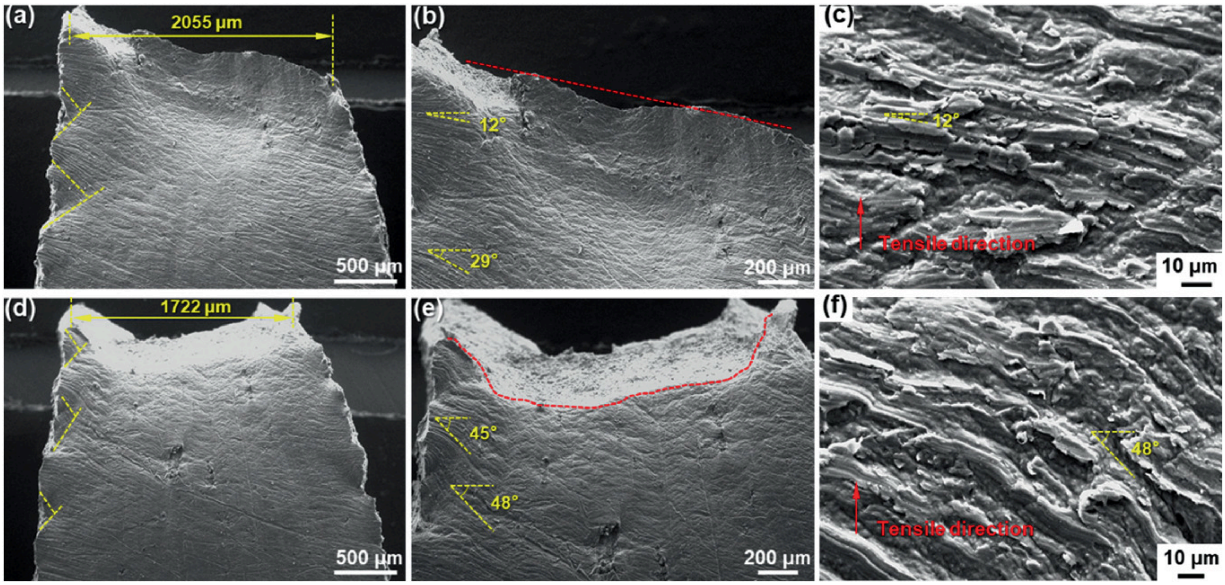


Fig. 5.47 SEM images of lateral view tensile fracture. Tensile-298 samples: **a** full-view, **b** and **c** local enlarged view of the area in (**a**); Tensile-173 samples: **d** full-view, **e** and **f** local enlarged view of the area in (**d**)

In addition, the crack growth rate of the Tensile-173 Al/HEAp MMCs is a linear function of the temperature. According to the Arrhenius

equation model, the crack growth rate can be expressed as Eq. 5.21.

$$\eta = CN\exp\left(-\frac{Q}{KT}\right) \tag{5.21}$$

where C is a constant related to temperature (which decreases sharply with the decrease of temperature), N is the crack growth coefficient, Q is the activation energy of low-temperature deformation, and K is the Boltzmann constant (1.38×10^{-23} J/K).

It has been observed that the crack growth rate decreases with the decrease in temperature. The formation and growth of cracks in the Tensile-173 Al/HEAp MMCs were inhibited in cryogenic environment, resulted in the increased elongation. The cutting on the Al alloy matrix was weakened, and the extension of cracks was further reduced when the formation and growth of cracks were inhibited.

Dislocation and other substructures become unstable before tensile fracture, forming larger and deeper dimples. As mentioned above, higher dislocation density and more LAGB are gathered in the cryogenic environment, and these characteristics of Al/HEAp MMCs promote uniform deforming at cryogenic temperatures. As shown in Fig. 5.38d, the tensile fracture morphology of the Tensile-173 Al/HEAp MMCs was more prone to forming deeper dimples. Large dimples were positively correlated with the tensile stress of the Al/HEAp MMCs and exhibited higher plastic deformation, i.e., higher elongation, before fracture, whereas the small dimple morphology indicated low resistance to plastic deformation. Therefore, the elongation of Al/HEAp MMCs in a cryogenic environment is higher than at room temperature. According to the Schmid factor determined by grain orientation, the higher the Schmid factor, the larger the grain strain in the corresponding region and the easier the dislocation slip. Figure 5.40 shows that the plastic strain of the Al/HEAp MMCs at different temperatures was quite different. The Tensile-173 Al/HEAp MMCs have more dislocation accumulation, so they have a higher Schmid factor, resulting in easier production of larger plastic deformation. The morphology of particles in Al/HEAp MMCs reflected the degree of plastic deformation before tensile fracture. Significant differences in particles morphology at different temperatures were observed in TEM images of Al/HEAp MMCs after tensile fracture shown in Fig. 5.42a and

c. The length-diameter ratio of the particles in Tensile-298 Al/HEAp MMCs was 1.9, whereas this value reached 3.8 in Tensile-173 samples. This implies that the Al/HEAp MMCs have larger plastic deformation along the tensile direction at cryogenic temperatures, i.e. the Al/HEAp MMCs have a higher elongation at cryogenic temperatures.

In addition, due to the low CTE of HEAp, the shrinkage ratio of Al alloy is large when the volume shrinkage effect occurs in cryogenic environment. Therefore, the Al alloy matrix can be more tightly coated with HEAp when tensile tests are carried out on the AMCs in a cryogenic environment, which further enhances the interfacial bonding between the Al alloy matrix and HEAp. In the fracture morphology, as shown in Fig. 5.38, it has been observed that the Tensile-298 Al/HEAp MMCs locally cracked, and the dimple distribution was significantly uneven. However, a lot of dimples with a large area and deep depth were evenly distributed in the fracture of the Tensile-173 Al/HEAp MMC, indicating uniform cracking. During the tensile process, the soft Al alloy matrix gradually deforms, while the HEAp deformation lags. As a result, the GND accumulates and concentrates at the interface between the HEAp and the Al alloy. The crack will develop rapidly and eventually lead to fracture with the increase in stress. The strain during tensile fracture can be evenly distributed around the HEAp due to the more significant volume shrinkage effect of Al alloy in a cryogenic environment, which helps to suppress crack extension. Macroscopically, this will also enable the Al/HEAp MMCs to have higher elongation in cryogenic environments. Figure 5.48 summarized the mechanical properties of different AMCs with the data. The Al/HEAp MMCs have advantages compared to SiC and Al_2O_3 particles, which have high strength and good elongation.

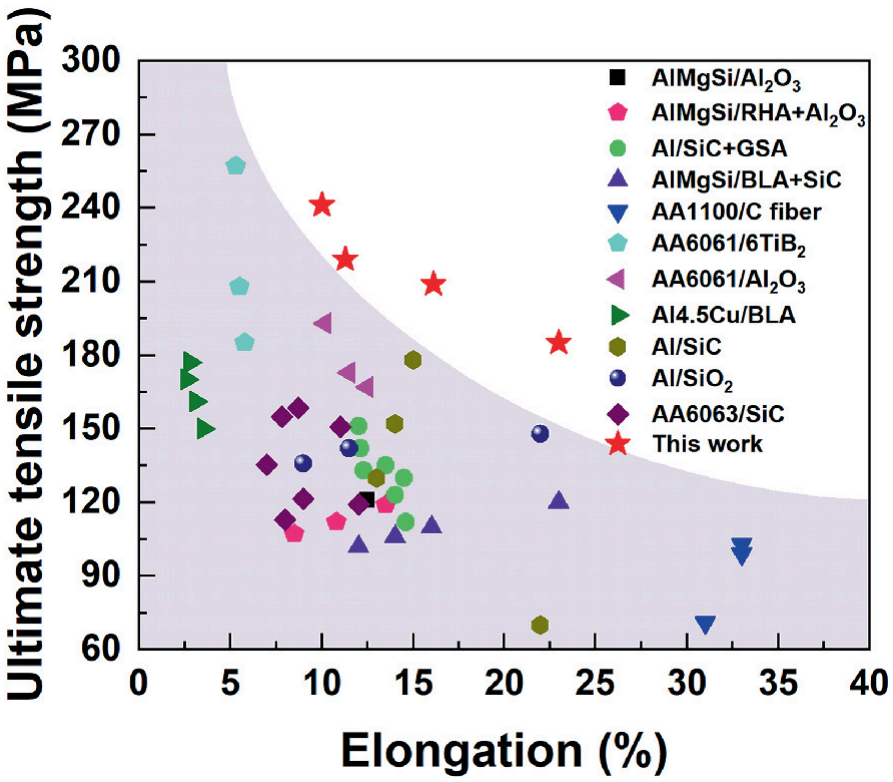


Fig. 5.48 Comparison of the mechanical properties in this study with the data

5.6 Al/TiC Composites via ARB and Cryorolling

According to the literature, although some works have been done on the mechanical properties of Al matrix composites (AMCs) reinforced with TiC utilizing various Al matrixes and fabrication processes, none of the researchers used AA1050 laminate composite reinforced with TiC by a combination of advanced way of ARB with cryorolling. In this study, the experiments were designed to make research on the feasibility to fabricate Al/TiC AMC [25]. A novel design method approach is sketched. The novel contribution of this research is in its endeavor to choose a better techniques combination by comparing the results of each technique individually, which facilitates industrial persons and academic users to select appropriate parameters and methodology for manufacturing metal matrix composites (MMCs). As the ARB has been used to produce Al matrix reinforced nano-particles before but the cryorolling process has never been used. To study the

effect of Nano TiC and as its novelty, the cryorolled samples after the third cycle guarantee a uniform distribution of reinforcement particles through the Al matrix. In addition, this research work possesses significant novelty in fabricating that offer better tensile and hardness properties. We investigated the mechanical characterization of the matrix by improved methodology. We studied the mechanical and microstructure properties of (AA1050 + 2.0 wt% TiC) reinforced AMCs. The Al/TiC AMC mechanical properties enhanced significantly. The microstructure shows uniform TiC particles distribution in Al matrix after the third cryorolling cycle.

5.6.1 Microstructural Evolution of Al/TiC AMCs During ARB

The SEM images of Al/TiC AMCs after various rolling steps are shown in Fig. 5.49. Figure 5.49a shows TiC particles layers between three Al sheets after ARB-1. TiC particles were clustered during the initial ARB process stages, and appeared the TiC particles free zones area. The TiC clustering particles disappeared with increasing the number of cycles. The impact of cryorolling after the advanced ARB processing results in the laminated shape of the Al/TiC AMC transformed into more uniform particles distributed composite (Fig. 5.49d). The element mapping and micrograph by EDS was utilized to understand better TiC particle dispersion in the composite after cryorolling-3, as shown in Fig. 5.50. The white particles that were uniformly distributed throughout Al matrix are reinforcement of TiC particles, as seen in Fig. 5.50a. Moreover, the green spots in Fig. 5.50b, yellow spots in Fig. 5.50c, and white spot in Fig. 5.50d reflect the element mapping of Al, Ti, and C, which is particles distribution representation in Al/TiC AMCs. It has been discovered that it's difficult to disperse nanoparticles across the sheets. Although it's a challenge to disperse particles uniformly on sheets, but some reports show well dispersed uniformly particle distribution achieved by more rolling cycles.

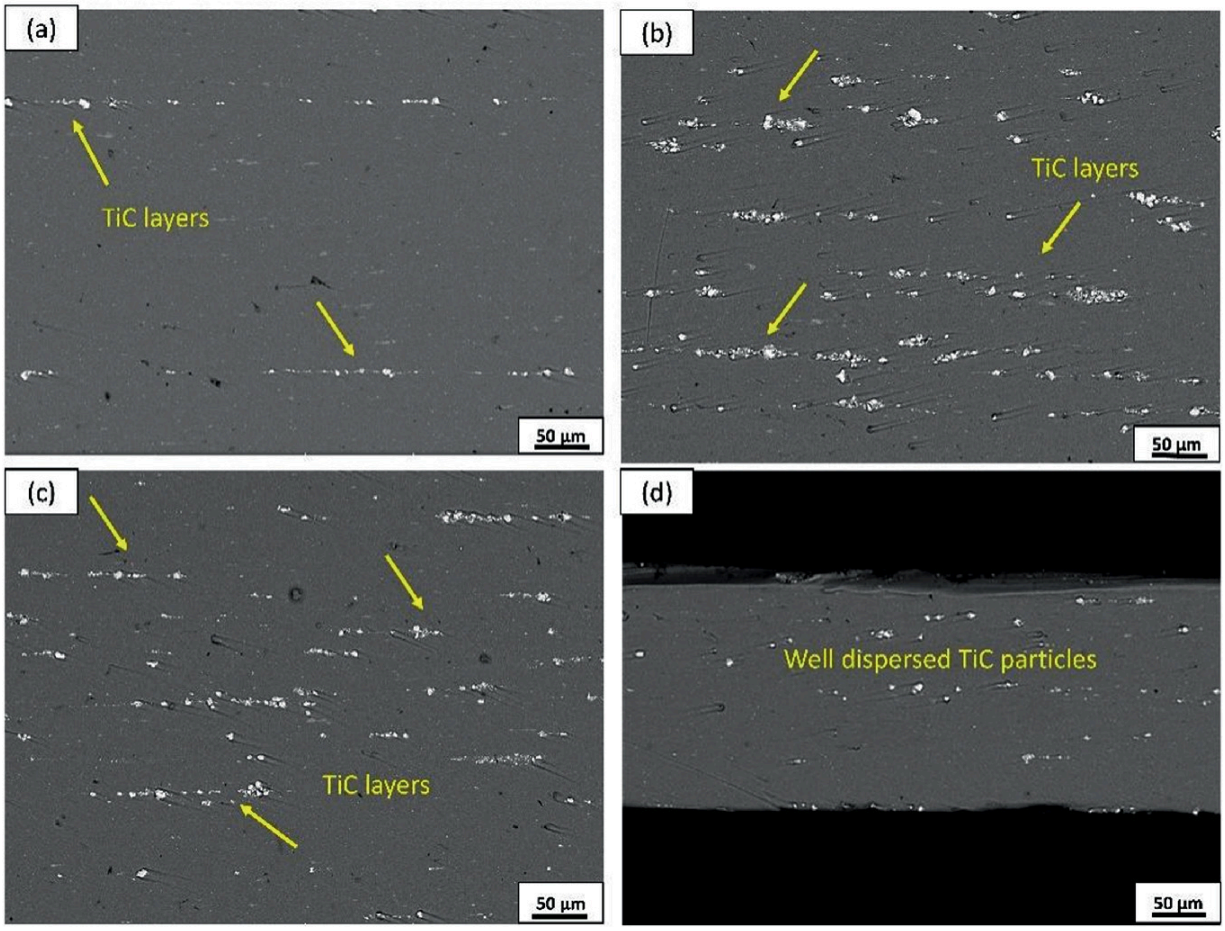


Fig. 5.49 SEM micrographs of Al/TiC AMC after **a** ARB-1, **b** ARB-3, **c** ARB-5, and **d** cryorolling-3

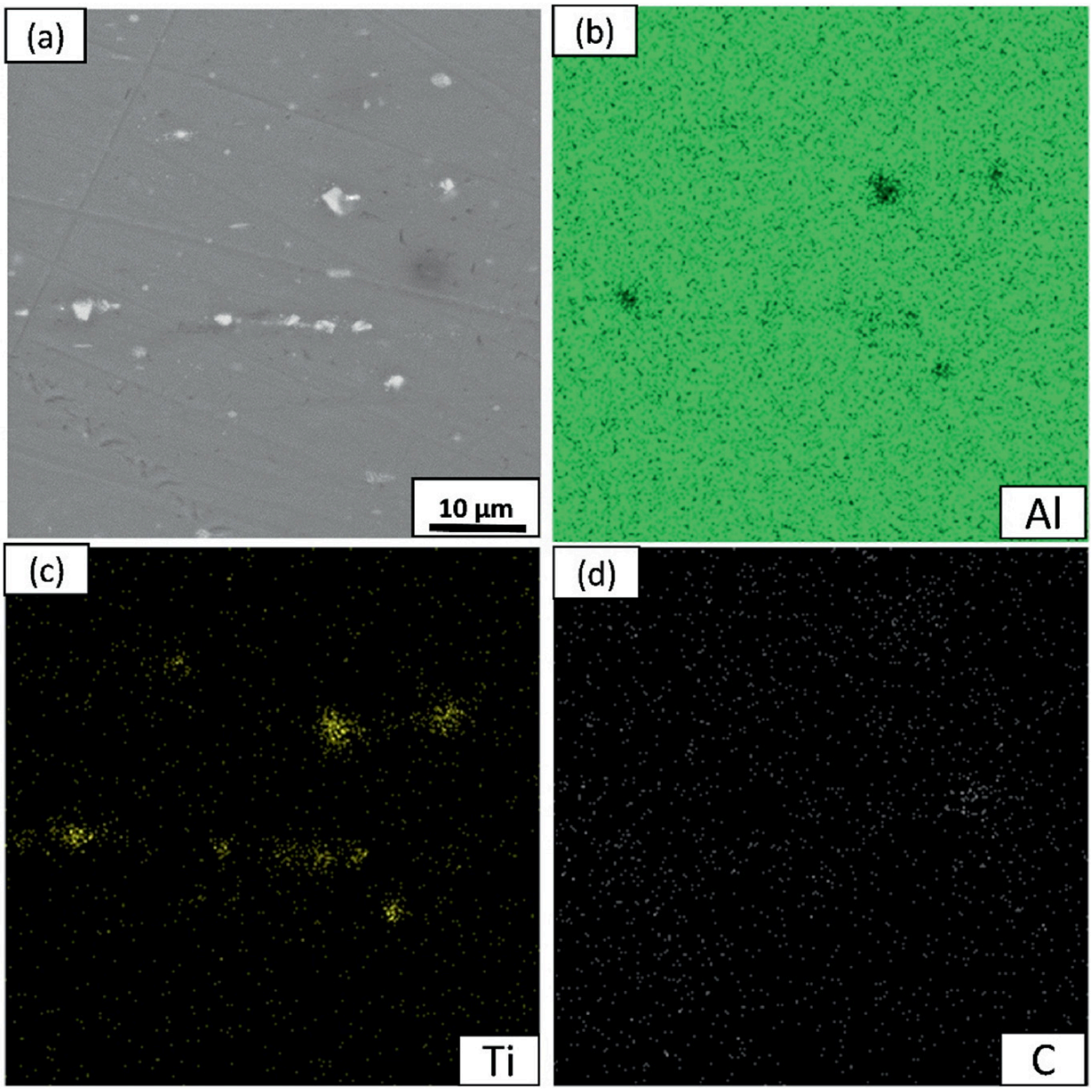


Fig. 5.50 Element distribution in cryorolling-3 AMC by EDS. **a** micrograph, **b** Al, **c** Ti, and **d** C element

The grain size, misorientation angle, and EBSD maps of the processed samples are shown in Fig. 5.51. The prominent, elongated, and deformed grains that indicated the rolling processed orientation were retained in the Al matrix for the ARB sample (Fig. 5.51a), with a 1020 nm mean grain size (Fig. 5.51e). After cryorolling, the deformed elongated grains were changed to finer grains with an 833 nm (Fig. 5.51b and f). Figure 5.51c and d shows the fractions of low-angle grain boundaries (LAGB) and high-angle grain boundaries (HAGB). Furthermore, in theory, random pairs and adjacent (neighbor) pairs

represent the theoretical random distribution (TRD), pairs of non-contacting grains and physical contact in pairs of grains respectively. It illustrates deviation from the predicted curve and the distribution of random pairs for a lower misorientation angle. When transitioning from coarse to fine-grained, the deviation decreases. Based on the misorientation angle shown in Fig. 5.51, the ARB-5 sample has more HAGBs than the cryorolling-3 sample. These findings show that grains with more HAGBs have an advantage over grains with LAGBs, because they have more energy which favors the dispersion and formation of precipitates near grain boundaries as the material process.

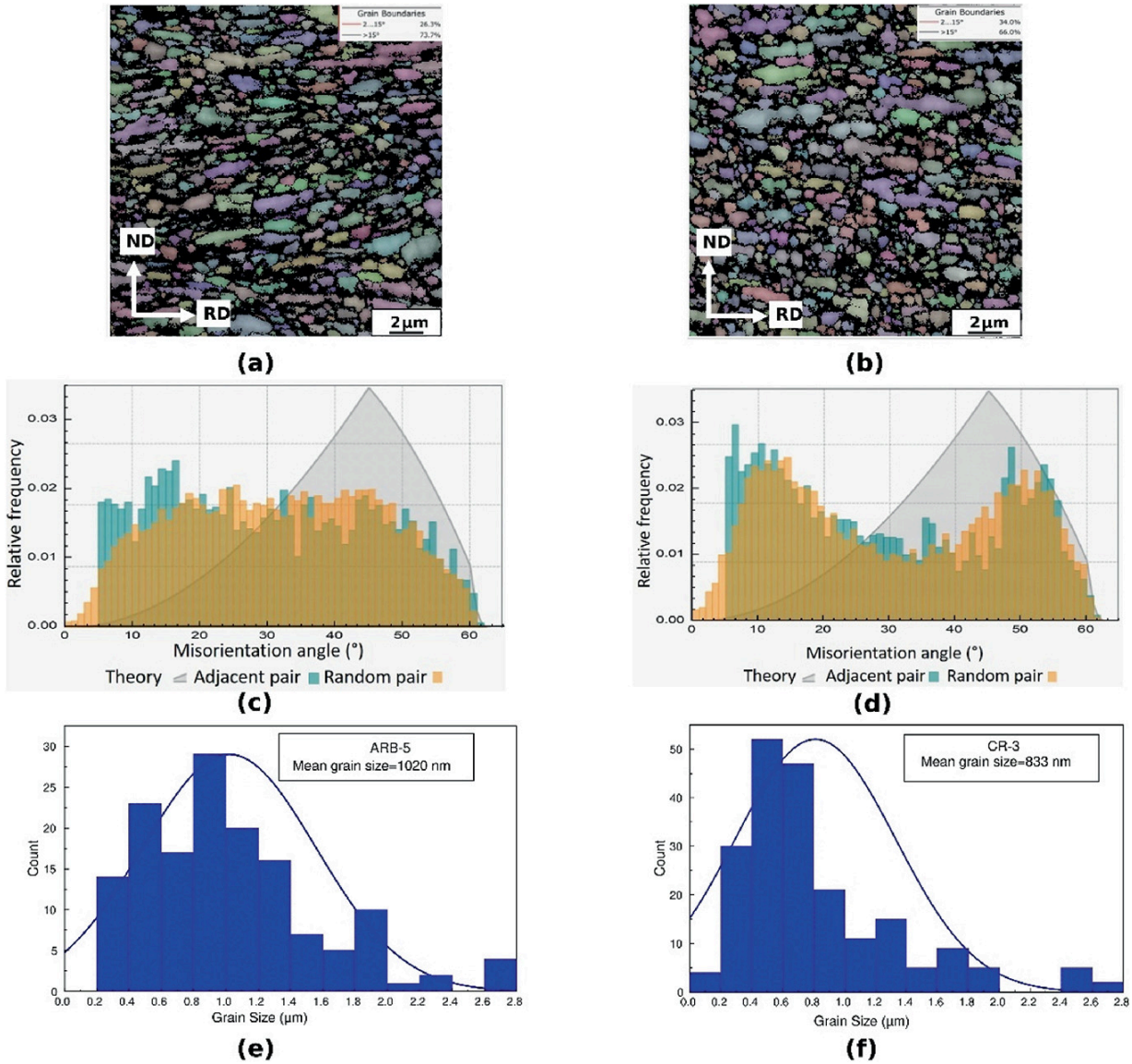


Fig. 5.51 EBSD maps, misorientation angle and grain size diagram of Al/TiC: **a**, **c**, and **e** ARB-5 and **b**, **d**, and **f** cryorolling-3

5.6.2 Mechanical Properties of ARB-Processed Al/TiC AMCs

The engineering stress–strain curves for partially annealed as-starting AA1050 sheets and the impact of ARB with cryorolling on composites are shown in Fig. 5.52a. The Al/TiC AMC variations and comparisons in elongation, yield, and ultimate tensile strength during ARB with cryorolling cycles are shown in Fig. 5.52b. The elongation, hardness, and ultimate tensile strength of AA1050 sheet were 6%, 41 HV and 135 MPa respectively. Each cycle by this methodology significantly impacts on generated sheet's mechanical properties. The high strengthening in current study is attributed to this methodology and uniformly reinforced TiC particles in the matrix. The strain hardening during the initial ARB cycles plays a crucial role in strengthening, the TiC particles have also a large impact on strain hardening since they are not entirely disseminated within Al matrix, causing in big layers. TiC particles cause the Al matrix to slip, resulting in increased dislocation density and strain hardening in these zones. The TiC particles in the Al matrix were dispersed, refined, and extended by the increased number of cycles. As a result, the strengthening may occur in the higher rolling processes due to refined TiC particles. Furthermore, as the increased number of rolling cycles, the reinforcement particles distribution in Al matrix improved and quality of the bond between sheet and reinforced particles improved, resulting in a significantly higher tensile strength. The Al/TiC AMC yield and ultimate tensile strength continuously increased, reaching a peak at the cryorolling-3 (Fig. 5.52a). The tensile strength of the composite reached 308 MPa after cryorolling-3, which was 2.5 times higher than the material supplied.

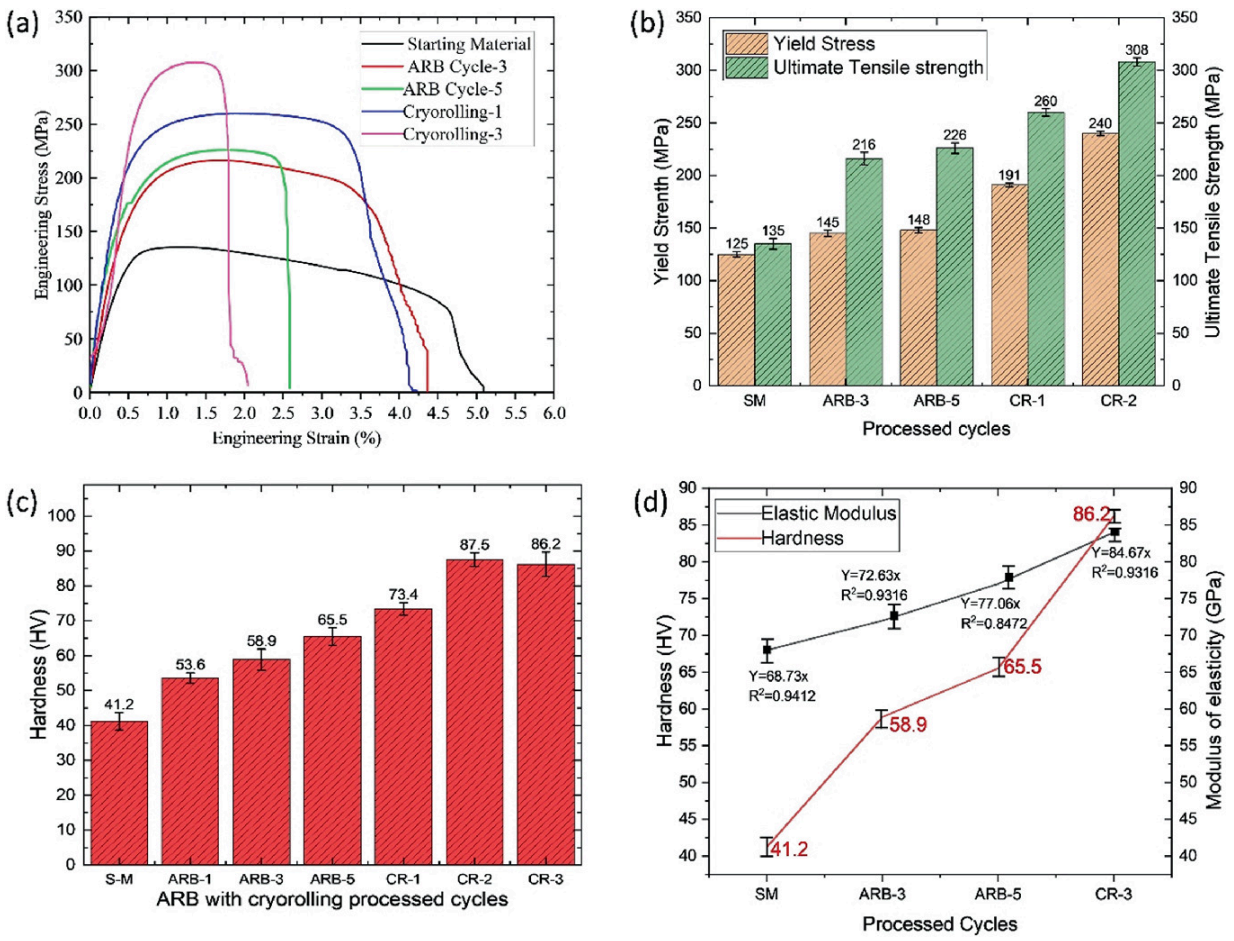


Fig. 5.52 Al/TiC AMCs with 2.0 wt% TiC. **a** Engineering stress versus strain curves. **b** Ultimate tensile strength and yield strength, **c** hardness (HV) values, and **d** Young modulus and hardness relationship with respect to processed cycles

During ARB processing, the Al/TiC AMC tensile strength increased while its elongation decreased (Fig. 5.52a). After the ARB-5 cycles, the tensile strength increased to 226 MPa. On the other hand, applying cryorolling cycles after ARB increased both tensile strength and elongation (Fig. 5.52a). Composites' strength and elongation are expected to rise simultaneously. Cryorolling processes rapidly increased the strength to its maximum strength level (Fig. 5.52a and b**).** As compared to base material, yield and tensile stress increased to 240 MPa and 308 MPa respectively, as shown in Fig. 5.52b. Eventually, macroscopic necking and tensile fracture occur. It can be seen that the layers of TiC between sheets are merged and mixed with sheet after the final cycle. Two strengthening mechanisms have been accounted for improving its tensile properties, which are grain refinement and TiC nano-particle content. Strain hardening plays a significant role in

increasing strength in the initial stages of the cycle. By contrast, if the rolling passes are increased, grain refinement becomes more effective. The ARB with cryorolling processes promoted grain refinement in the Al matrix, which enhanced tensile strength in the Al metal. Due to their higher strength, these particles can withstand higher tensile strains than Al, resulting in enhanced strength of the produced nanocomposites. The rising quantity of misoriented grain boundaries and ultra-fine grains has been proven to cause this impact. The elastic modulus is determined by the graphical technique as shown in Fig. 5.52d. The obtained value of elastic modulus for pure Al was about 68GPa. During different cycles for ARB and cryrolling cycles, the elastic modulus values were achieved at about 72GPa, 77GPa, and 84GPa for ARB-3, ARB-5 and cryorolling-3 respectively as shown in Fig. 5.52d. For Al/TiC composites, the modulus changes at variant cycles. Improvements of modulus 20% on the base material were attained with a reinforcement addition of 2.0 wt. % for cryorolling-3.

Additionally, it has been analyzed that in ARB and cryorolled samples, the failure strain is less in the initial Al matrix due to grain refinement and high angles in the sub-grains, which reduce the deformation capability of these grains. A large part of this improvement may be attributed to the formation of low-angle sub-grains and grain refinement. The Al/TiC AMC elongation reaches 2.7% after ARB-3 (Fig. 5.52a). Because the grain elongation in the rolling direction is more significant, preventing the grains from slipping off each other. As a result, the TiC particles penetrate the Al grains and reduce their deformability. This composite exhibits a lower elongation than as received Al at same ARB cycle. Furthermore, the particles of TiC on Al grain boundaries reduce their ability to slip between each other. A previous study has made similar observations. During ARB, Al stacking defects might contribute to elongation improvement. Elongation of samples is influenced by sheets of the proper connection in presence of proper reinforcement particle distribution and by the reduction of porosity. The existence of porosity has an impact on the composite sample's characterizations. The porosity found near the reinforcing particles results in a rapid reduction in elongation. The cryorolling cycles subjected to ARB result in the improved elongation to 4.3%. This is due to the formation of sub-grains, which allow the material to slip

between sub-grains more easily. The elongation of Al cryorolled samples is likely related to grain refinement during plastic deformation. Due to the presence of TiC particles, dislocations are prevented, and ductility is reduced.

Figure 5.52c shows how the ARB and cryorolling cycles impact the hardness. It shows the micro-hardness of Al reinforced with TiC increases with the number of cycles. Micro-hardness of the phases shows a rapid increase from 41 to 88HV after ARB and cryorolling cycles. The high strain hardening rate is responsible for the enhanced rate of micro-hardness in the primary cycles (based on the interactions between them and the density of dislocations). The micro-hardness increases gradually as the number of cycles increases until it reaches the highest value in cryorolling-2. The hardness increases rapidly after the initial two cryorolling passes due to the refinement of grain and based on strengthening mechanisms that are likewise to the tensile properties (in Fig. 5.52). However, the increasing hardness rate is very low during the ARB process for Al/TiC nanocomposites. TiC particles are the key reason for dislocation strengthening and facilitating grain refinement of the Al/TiC AMCs. Based on the previous findings, the ARB with cryorolling technique appears to be the most successful method for producing well-distributed, high-strength, and uniform Al/TiC AMCs.

Figure 5.53 shows lower and higher magnification images of the analyzed fractured surfaces. The red dotted area from Fig. 5.53a–f of lower magnification were analyzed by higher magnification images in Fig. 5.53a–f (1–2). The good bonding strength of the composite was confirmed by the tensile test method as shown in Fig. 5.53f. For the pure Al sheet without reinforced TiC particle sheet, the size and deepness of dimples in the tensile specimen are more prominent, which causes an increase in ductility, which in turn influences the plastic deformation (Fig. 5.53a). A ductile fracture appears as hemispheroidal or equiaxed dimples (Fig. 5.53a(1–2)). Fractures of this type are caused by the conjunction of cracks, formation of microvoids, and shear fracture. Figure 5.53b–d show the delamination at the fracture surfaces middle layer (Al/TiC/Al interface) for different ARB cycles. There are two de-bonded areas in the 3-layer sample (Fig. 5.53b), where the layers are interconnected. The fracture occurred during ARB passes

(Fig. 5.53b–d) as a result of poor-quality bonds between the AA1050/AA1050 interfaces and the deposition of TiC particles. After a higher number of rolling cycles, equiaxed and elongated dimples are created by dynamic shear loads, non-uniform tensions, and plastic strain in three directions (Fig. 5.53d-2, e-1). Increasing the number of passes improves bonding quality at interfaces (Fig. 5.53f). When stretched, the 108-layers sheet (Fig. 5.53f) is barely visible de-bonded. As previously stated, the growth of these de-bonded zones directly impacts elongation reduction and increased strength at higher cycles. The condition of stresses and direction of fracture expansion can also be determined by examining the shape and direction of the dimples. Micro voids tend to elongate in shear loads. The initial ARB cycles revealed large clusters of reinforcement particles (Fig. 5.53b, c-2). Upon increased the number of processes cycles, the clusters particles of TiC broke up into further particles due to the metal being extruded through the clusters (Fig. 5.53f(1–2)), which subsequently caused the particles to become uniform dispersion within the Al matrix. By increasing the rolling passes, the TiC particles were dispersed **(**Fig. 5.53f(1–2)). Due to the increased rolling pressure applied, the level of porosity in the Al/TiC interfaces was reduced. Ductile rapture and dimple creation were discovered to be the most prominent failure mechanisms of AA1050/TiC; both the reinforcement (TiC particles) and rapture surface of Al material remained ductile having dimples.

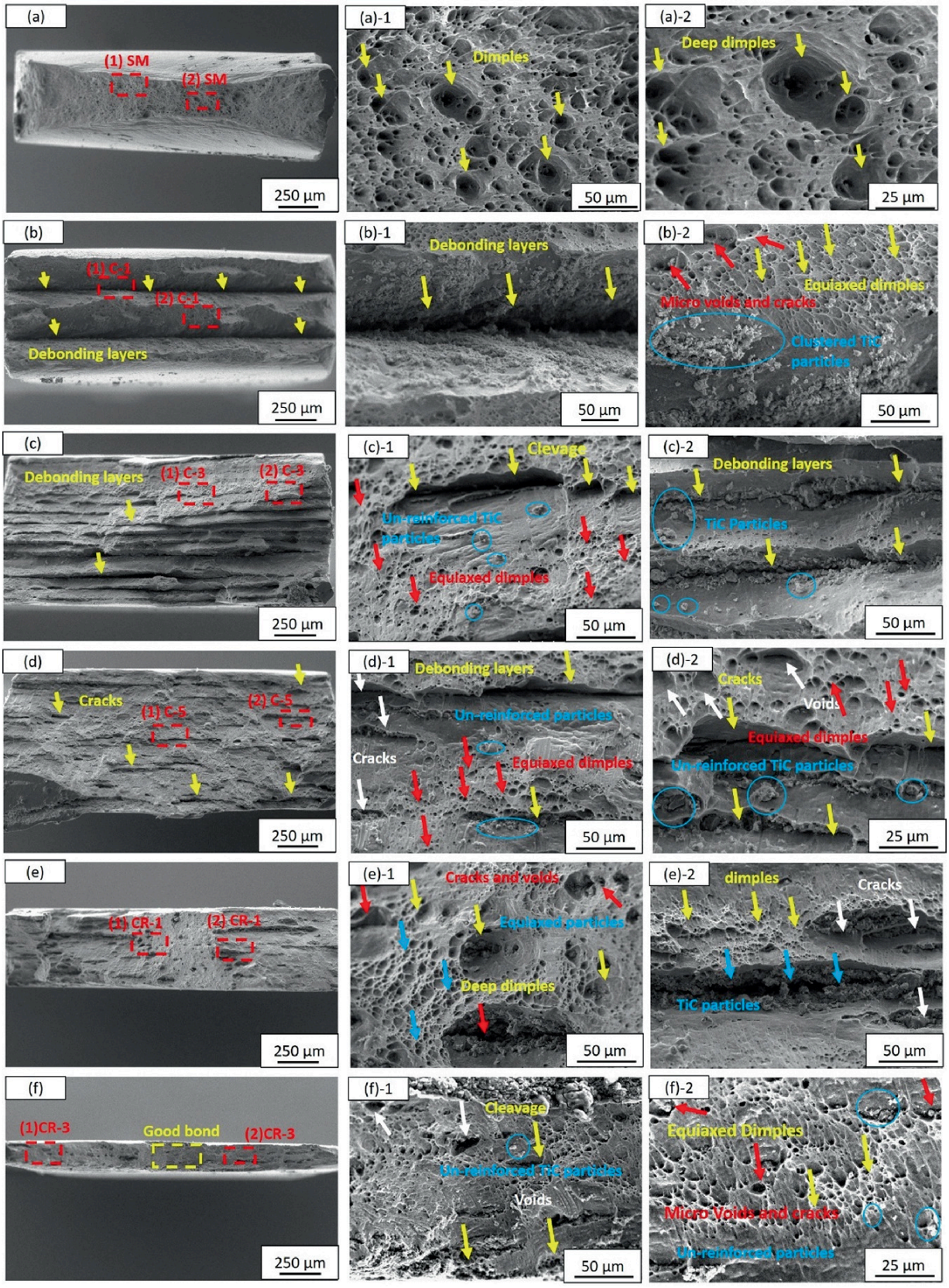

(a)
(1) SM
(2) SM
250 µm
(a)-1
Dimples
50 µm
(a)-2
Deep dimples
25 µm
(b)
(1) C-1
(2) C-1
Debonding layers
250 µm
(b)-1
Debonding layers
50 µm
(b)-2
Equiaxed dimples
Micro voids and cracks
Clustered TiC particles
50 µm
(c)
Debonding layers
(1) C-3
(2) C-3
250 µm
(c)-1
Cleavage
Un-reinforced TiC particles
Equiaxed dimples
50 µm
(c)-2
Debonding layers
TiC Particles
50 µm
(d)
Cracks
(1) C-5
(2) C-5
250 µm
(d)-1
Debonding layers
Un-reinforced particles
Cracks
Equiaxed dimples
50 µm
(d)-2
Cracks
Voids
Equiaxed dimples
Un-reinforced TiC particles
25 µm
(e)
(1) CR-1
(2) CR-1
250 µm
(e)-1
Cracks and voids
Equiaxed particles
Deep dimples
50 µm
(e)-2
dimples
Cracks
TiC particles
50 µm
(f)
(1)CR-3
Good bond
(2)CR-3
250 µm
(f)-1
Cleavage
Un-reinforced TiC particles
Voids
50 µm
(f)-2
Equiaxed Dimples
Micro Voids and cracks
Un-reinforced particles
25 µm

Fig. 5.53 SEM images of tensile fracture surface of samples subjected to **a**-(1–2) Starting Material, **b**-(1–2) ARB-1, **c**-(1–2) ARB-3, **d**-(1–2) ARB-5, **e**-(1–2) cryorolling-1, and **f**-(1–2) cryorolling-3

The formation of Al/TiC AMC by this methodology enhanced the material's properties, significantly increasing the hardness, yield and tensile strength. In general, strength enhancement results in some reduction of ductility. It is found that the strength of Al alloy was increased, however, the ductility was decreased with the addition of nano-particles. Lower elongation may also occur due to defects in the Al/TiC interface bonding and particle-cluster distribution. After the ARB-5 processed Al/TiC AMC, the ductility in the cryorolling-1 increased significantly. As shown above in the microstructure in Figs. 5.49 and 5.50, at the beginning of processed cycles, there were many clustered particles; as the number of cycles increased to cryorolling-3, the TiC particles were dispersed throughout the Al matrix quite uniformly. From the lower magnification images in Fig. 5.53, it can be noticed that the bonding energy was not very good at the starting cycles. The layers and voids can be seen clearly. As processed cycles increased, layers of TiC between sheets disappeared and the bonding strength is enhanced as shown in Fig. 5.53f. The enhanced properties of the material composite were achieved after the cryorolling-3 cycle. The grain refinement strengthening significantly improves the strength of the processed composite. Adding TiC particles further retard the migration of sub-grain and grain boundaries, resulting in further reduction in grain size processed composite after several ARB and cryorolling processes cycles. Figure 5.54 shows the change in grain size with an increasing number of rolling cycles. It can be noticed that the material grain size reduced notably after applying the advanced way of rolling cycles. It can be noticed that after the impact of ARB processes cycles on the grain size reduction significantly, the grain size reduced to 1.02 μm and then after cryrolling cycles, the grain size further reduced to 0.83 μm. Our results indicate the stable grain refinement of the composites at the final cryorolling cycle.

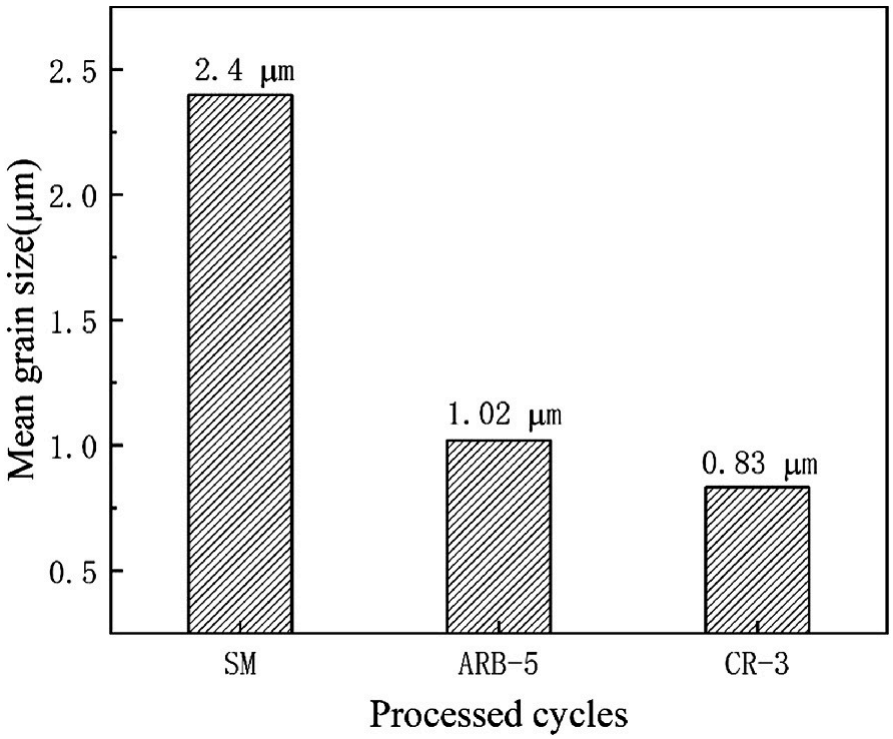


Fig. 5.54 Change in grain size with processed rolling cycles (CR-3 for cryorolling-3)

In the ARB+ cryorolled sheets, there was a significant improvement in grain refinement (cryorolling-3) versus only ARB-5 sheets. The sheets in both cases were strained in a similar manner (equivalent strains 2.5 and 2.2 in the ARB and cryorolling processes, respectively). Cryorolled Al sheets exhibit different deformation mechanisms than ARB processed sheets. It could be caused by a variation in deformation temperatures. To qualify as an actual grain structure submicron, two criteria must be met: the distance between the HAGBs must be below 1 μm and the fraction of these boundaries must be above 70%. These parameters are fulfilled by Al sheets processed via five ARB cycles and three cryorolling cycles, as shown in this work. Different mechanisms are involved in this unique technique process feature.

The grain refinement mechanisms are influenced by strain levels in this research. The main mechanism during the beginning cycles of ARB is grain subdivision. At this strain level, subgrains are formed that are surrounded by a number of low-angle grain boundaries. The grain subdivision ratio falls after the ARB-5, as shown in Fig. 5.51e and f, and the change in grain thickness after the cryorolling-3 is significant. Figure 5.51c and d show the HAGBs increases at the expense of LAGBs and the propensity for a Mackenzie distribution to be misaligned with

the lamellar structure. Therefore, the process causing a lamellar structure at these strain levels may be the LAGBs undergo a strain-induced conversion to HAGBs. On the other hand, as can be seen in Fig. 5.51, almost no structural change occurs at the higher strains, except for an increase in grain length. Using liquid nitrogen in rolling Al is highly likely to obtain a work-hardened Al with a sufficiently higher dislocation density relative to that of Al rolled at room temperature or even higher. This rolled Al with high energy stored is expected to give higher strength but low ductility and lower the set temperature of recrystallization.

The Al/TiC AMC mechanical properties were investigated in this work, and it was discovered that sheets strength increases with increased rolling cycles. Figure 5.52 illustrates the deviation and comparison of elongation, yield and tensile properties during material processing ARBed and cryorolled cycles. An enhancement in strength could be observed as the rolling cycle increases. As the strength increases, it is hypothesized that (i) dislocation strengthening contributes to the enhancement and (ii) grain boundary strengthening contributes to the enhancement. Among the most accurate and quick ways to assess the mechanical behavior of composites is through the measurement of hardness. The hardness results of the matrix vs composites with Modulus of elasticity are shown in Fig. 5.51d. In comparison to a base metal, the composite exhibits increased hardness and modulus. In our investigation, we estimated the elastic modulus, which in our case study is 84 GPa for cryorolling-3. A material's stiffness can be determined by looking at its elastic modulus. It determines how easily a material bent or stretched. It's the slope of the stress and strain diagram up to the proportionality limit. As shown in Fig. 5.55, cryorolling improved the mechanical properties compared to similar Al/TiC alloy systems subjected to various other severe plastic deformation techniques. The Al/TiC composite has substantially better hardness and ultimate tensile strength than the Al matrix, as shown in Fig. 5.55a and b. The ARBed sheets were subsequent cryorolled, and the maximum increase in strength was around 308 MPa. Dynamic recrystallization occurs during SPD processing in all other SPD processes, resulting in fine/UFG microstructure. Thus, all the other

processed materials are also strengthened by grain boundary strengthening.

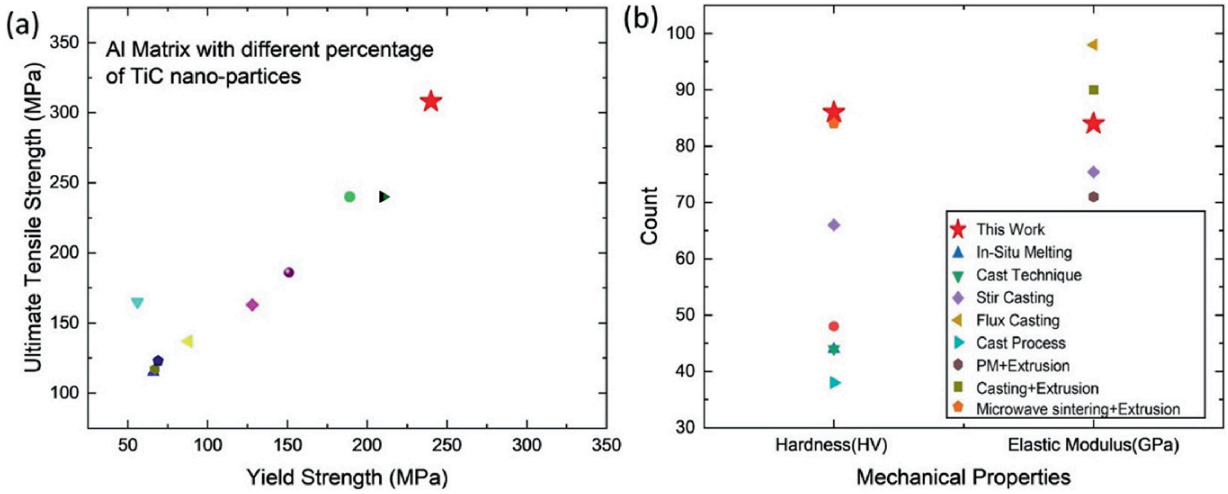


Fig. 5.55 Comparison of different properties of Al/TiC composites. **a** Ultimate tensile strength vs yield Strength **b** Hardness and elastic modulus

During ARB and cryorolling, non-uniform strain causes the spherical and co-axial dimples were distorted in various directions. The split layers have a sharp interface, indicating low bonding strength during ARB process. Cryorolling significantly enhanced bonding strength of laminate interface with no gap. This indicates that the advanced metholdolgy to produce UFG of Al sheets improved ductility. For the material ductility optimization, the methods of cryogenic deformation should be investigated further, compared with other processes. The fracture mechanism is influenced by the reinforcing TiC particles as well. In SEM microstructure, the reinforcing particles can be seen at the middle of dimples and et al. surface, resulting in crack propagation. A ductile fracture with deep holes is present on the surface of the fracture, while the matrix exhibits a gray surface with nearly spherical holes as well. Initially, the micro void formation leads to fracture, then emissions and micro-cracks join and eventually cause failures at tension angles. Particle-free zones and clustered TiC particles decreased after eight cycles, as observed by SEM microstructure. In the microstructures, there was also a relatively homogenous hybrid particle dispersion and good bonding. The ARB with cryorolling technology has an advantage over different methods in which a nanoscale initial reinforcement, as the TiC particles become nano-sized. Reinforcement clustering/accumulation is difficult to eradicate in such

a procedure when reinforcement volume fractions are large through the final cycle, the composite was loaded uniformly with small particle reinforcement. Because there are no voids or porosity in the sample, it implies excellent bonding between TiC/Al1050 matrixes. Due to the obvious reduction in porosities, the density of the composite increases as the number of cycles passes increases. This conclusion is consistent and in accordance with what has been found in the literature. The authors of this papers also showed that the methodology of ARB + cryorolling improved uniformity. Furthermore, uniform particle reinforcement dispersion in the matrix improved the composite materials' properties. In the SEM images of the tensile fracture surfaces, micro-pores and dimples are evident in all samples, indicating that ductile fracture dominates. The Al sheets strength by this method is nearly as good as Hall–Petch relations, even for the structure's submicron grain. By lowering the grain size, we can make materials stronger beyond their theoretical limit. As grain size decreases, its strength increases until it reaches a maximum value. The current investigation also reveals that the following yielding, the quantity of work hardening is relatively minor, and necking happens abruptly, resulting in restricted uniform elongation. However, future works should elaborate on the material formation by the advanced methodology of ARB with cryorolling relationship and strengthening mechanisms.

5.6.3 Various Ceramic Nano-particles Reinforced AMCs via ARB

Commercially pure Al AA1050 sheets of a thickness of 0.80 mm, and SiCp and TiCp particles were used as the starting materials to prepare good-strength AMCs [26]. The SEM images of TiCp and SiCp and particle size are shown in Fig. 5.56. The optical microscope (OM) image of AA1050 and grain size are shown in Fig. 5.57.

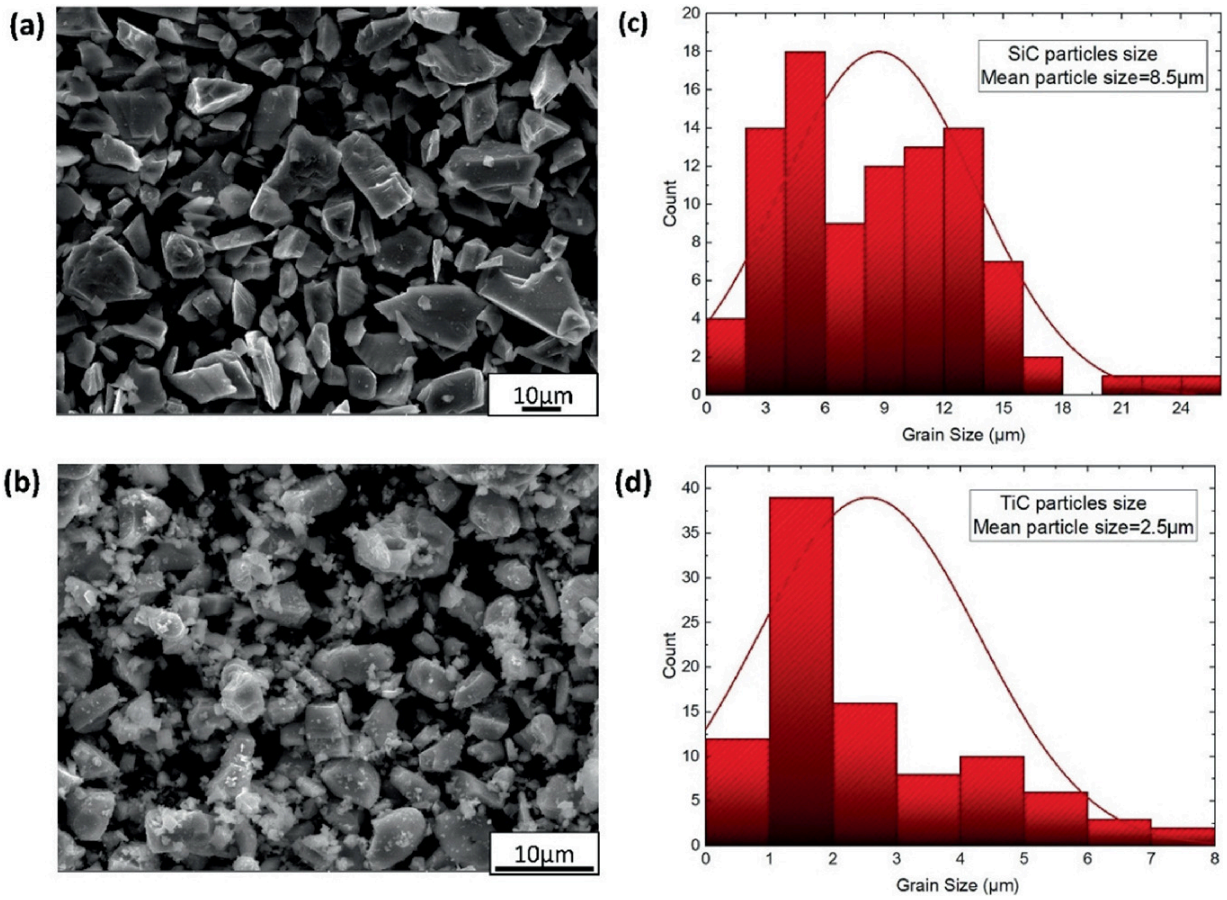


Fig. 5.56 SEM image and grain size of **a** SiCp; **b** TiCp; **c** and **d** particles size respectively

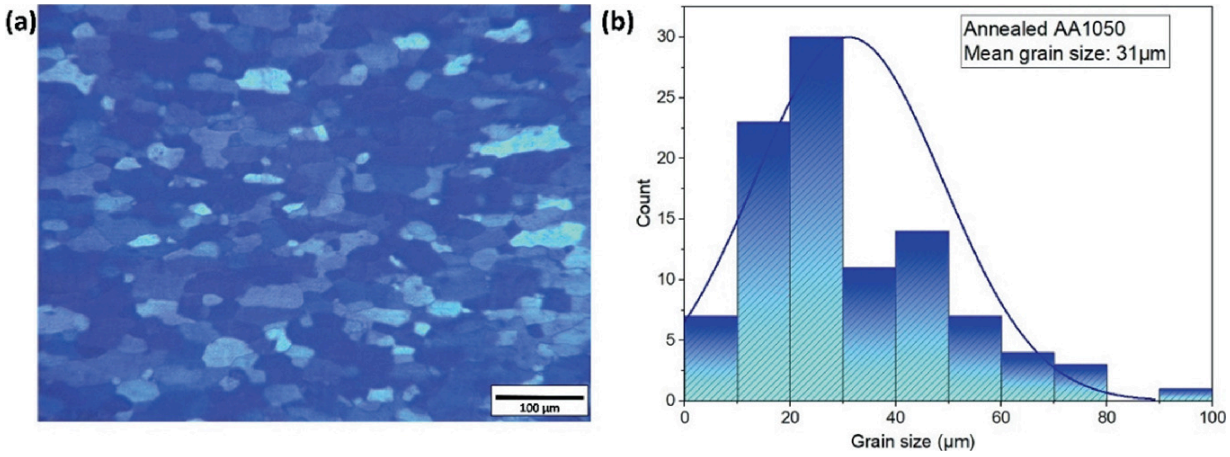


Fig. 5.57 Optical microscope (OM) **a** AA1050 and **b** grain size

Figures 5.58 and 5.59 show the SEM images of the Al/SiCp, Al/TiCp and Al/TiCp-SiCp AMCs after various rolling steps. Figure 5.58a, d, and g show two layers of SiCp, TiCp and SiCp particles respectively, between three Al sheets after the ARB-1. The initial stages of the process cycles

led to the clustering of the nano-sized particles, which resulted in free zones of the nano-particles. The clustering of the nano-particles disappeared with increasing the number of processes up to cryorolling-3, and the laminated shape of the Al/SiCp, Al/TiCp and Al/TiCp-SiCp composites transformed into more uniform particles distributed composites, as shown in Fig. 5.59b, d and f respectively. The latest research work suggests that incorporating nano-sized reinforcement particles into metal matrices can significantly enhance the mechanical and physical properties of the resulting composites, such as stiffness, and strength. The ARB process is an effective method to fabricate bulk AMCs with improved properties, and it involves the repetitive folding and rolling of alternating layers of metal and reinforcement particles. The present study investigated the effects of the number of ARB processes on the clustering behavior of nano-sized reinforcement particles in Al-based AMCs reinforced with SiCp, TiCp, and a combination of both.

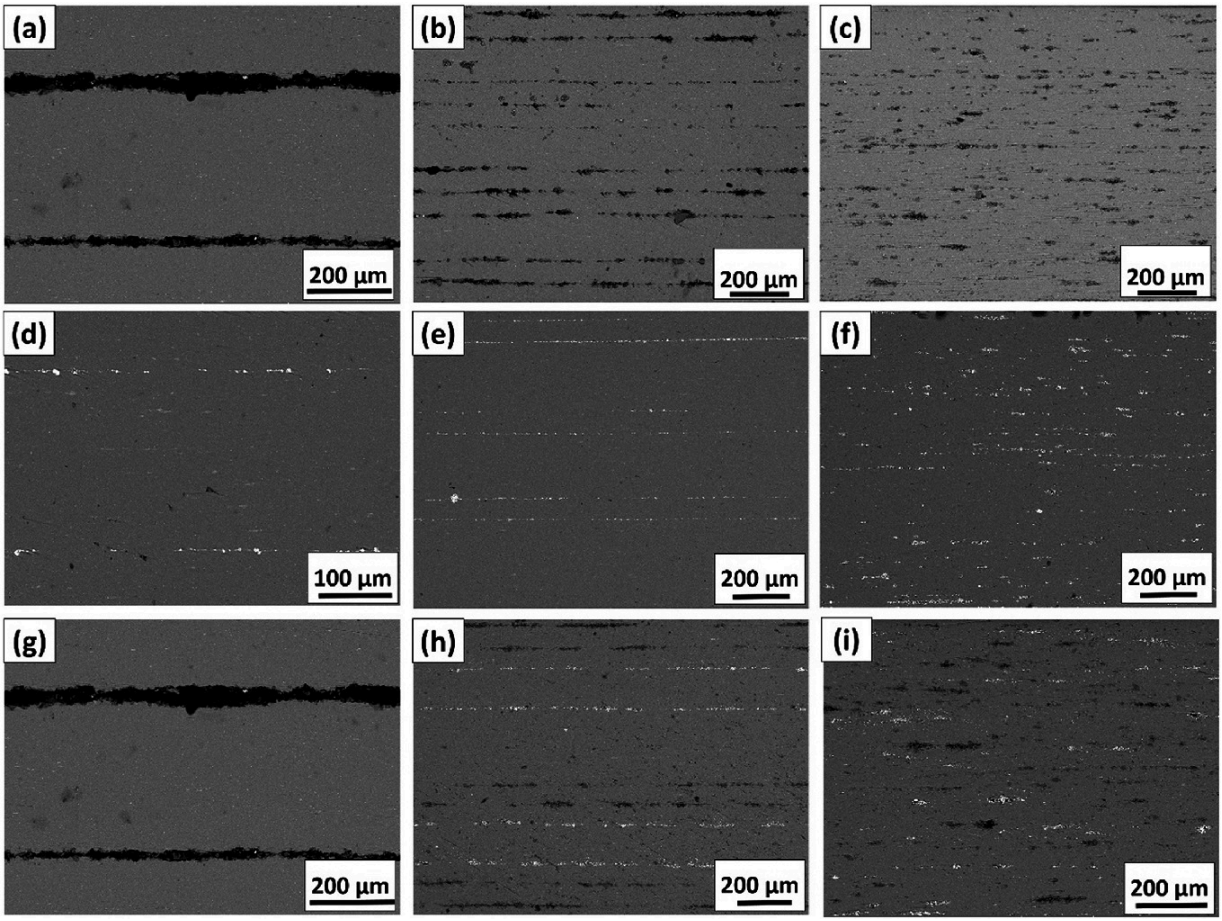


Fig. 5.58 SEM micrographs of ARB-1, ARB-3, ARB-5 from **a–c** Al/SiCp **d–f** Al/TiCp and **g–**i Al/SiCp-TiCp composite respectively

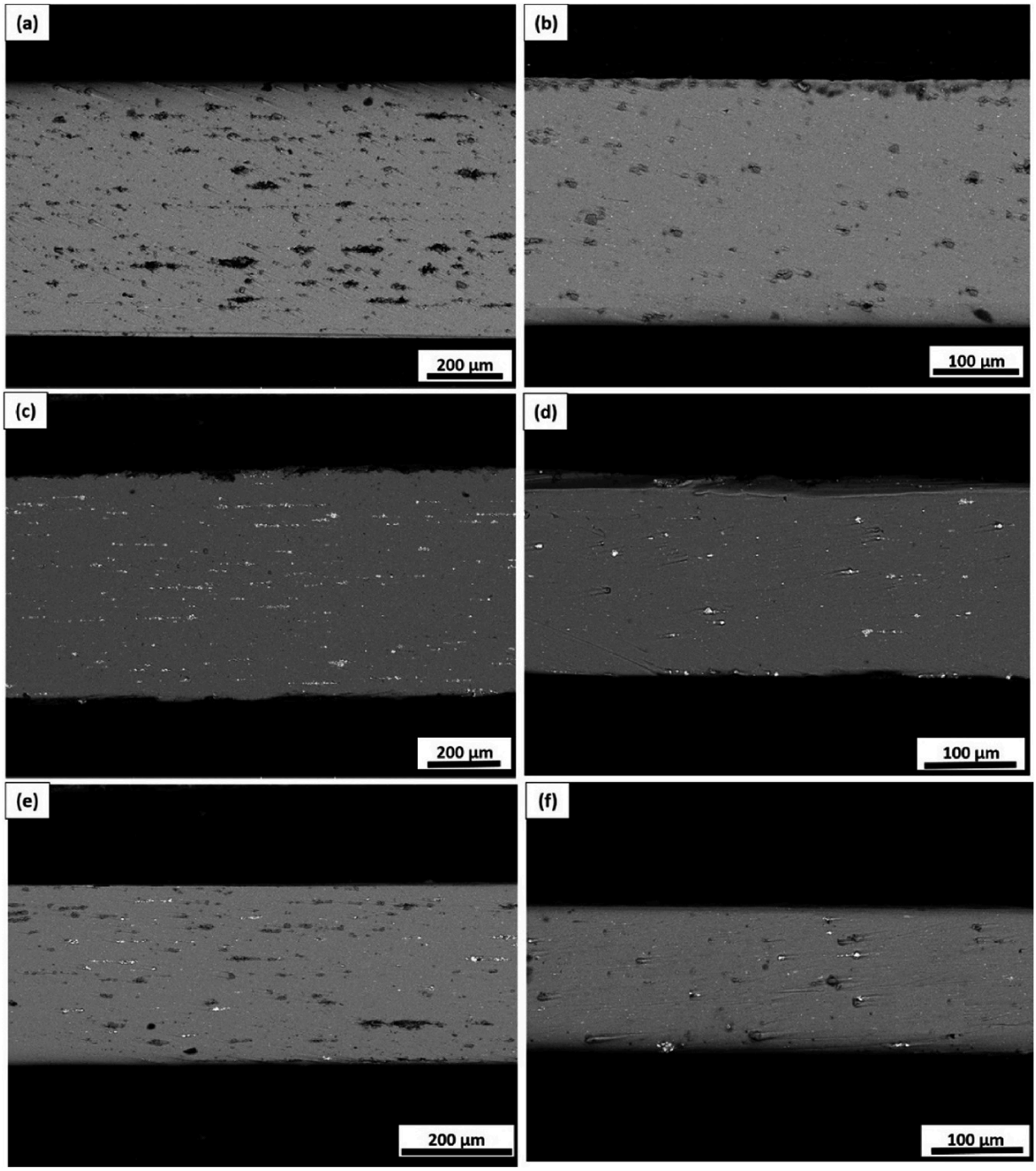


Fig. 5.59 SEM micrographs of cryorolling-1 and cryorolling-3 **a**, **b** Al/SiCp **c**, **d** Al/TiCp and **e**, **f** Al/SiCp-TiCp composite respectively

The distribution of particles in the composites, FESEM was performed to analysis the samples surface, and the EDX images are shown in Figs. 5.60 and 5.61. The interface on which the surface

scanning was performed was used to take a FESEM microphotograph of the nanocomposite sample examination, and results findings are provided by EDX of the different particles mixed with Al matrix samples. The results of surface scanning show a homogeneous distribution of elements in the structure. The element mapping and micrograph by EDS were utilized to understand better the Ti, Si and C particles dispersion in the composites after cryorolling-3, as shown in Fig. 5.60a–d, e–h and Fig. 5.61a–e show Al/SiCp, Al/TiCp and Al/SiCp-TiCp composites particles distribution respectively. The nano-particles that were uniformly distributed throughout the Al matrix are the reinforcement TiCp and SiCp nano-particles. The distribution of Al, C, Si and Ti Nano-particles in all these composites are uniformly distributed as seen in Fig. 5.60. Moreover, the green spots in Figs. 5.60c, g, 5.61c, yellow spots in Figs. 5.60d, 5.61d and red spots in Figs. 5.60b, 5.61b reflect the element mapping of Al, Si, and C, respectively, while blue and yellow spots in Fig. 5.60h, 5.61e**,** and white spots in Fig. 5.60f reflect the element mapping of Ti and C respectively, which are Al/SiCp, Al/TiCp and Al/SiCp-TiCp composites particles distribution representation. The distribution of particles in composites has been investigated extensively in recent research using various analytical techniques such as SEM and EDS. A study by Saha used ARB to fabricate Al reinforced TiCp and SiCp based composites and characterized their microstructure and properties using FESEM and EDS. The authors found that the TiCp and SiCp particles were uniformly dispersed in the Al matrix, as observed in the element mapping and micrograph by EDS. The EDX images also showed a homogeneous distribution of elements, including Al, carbon, silicon, and titanium, in the composites.

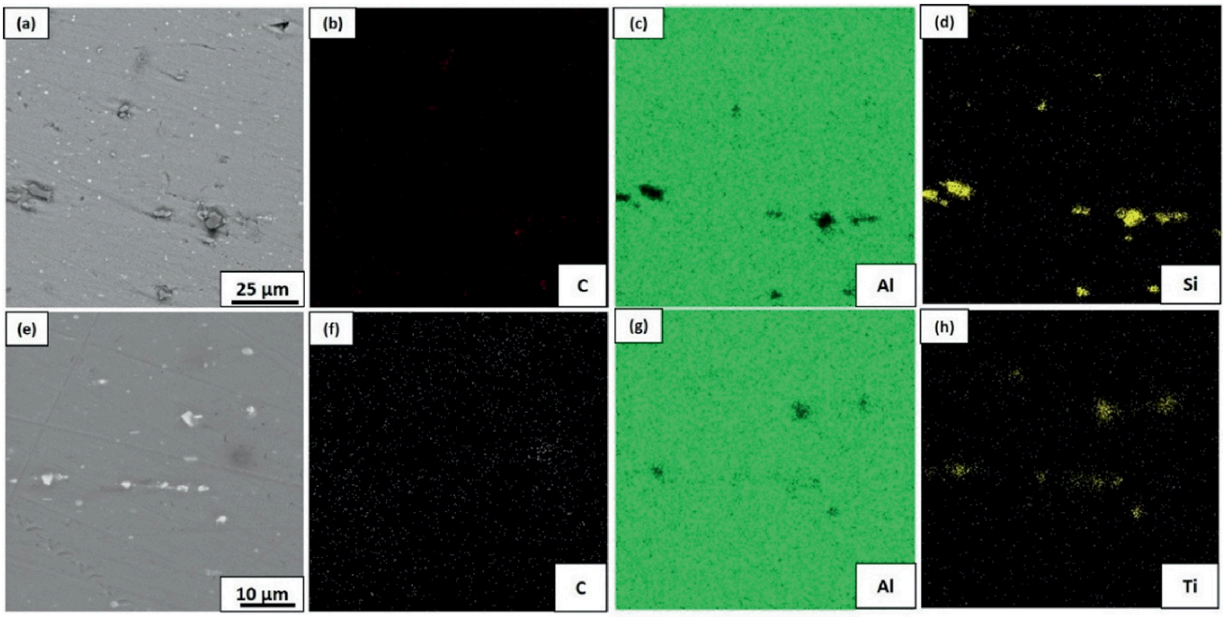


Fig. 5.60 Element distribution in cryorolling-3 AMC by EDS micrograph of **a–d** Al/SiCp **e–h** Al/TiCp and the elements **c**, **g** Al. **h** Ti, **d** Si and **b**, **f** C

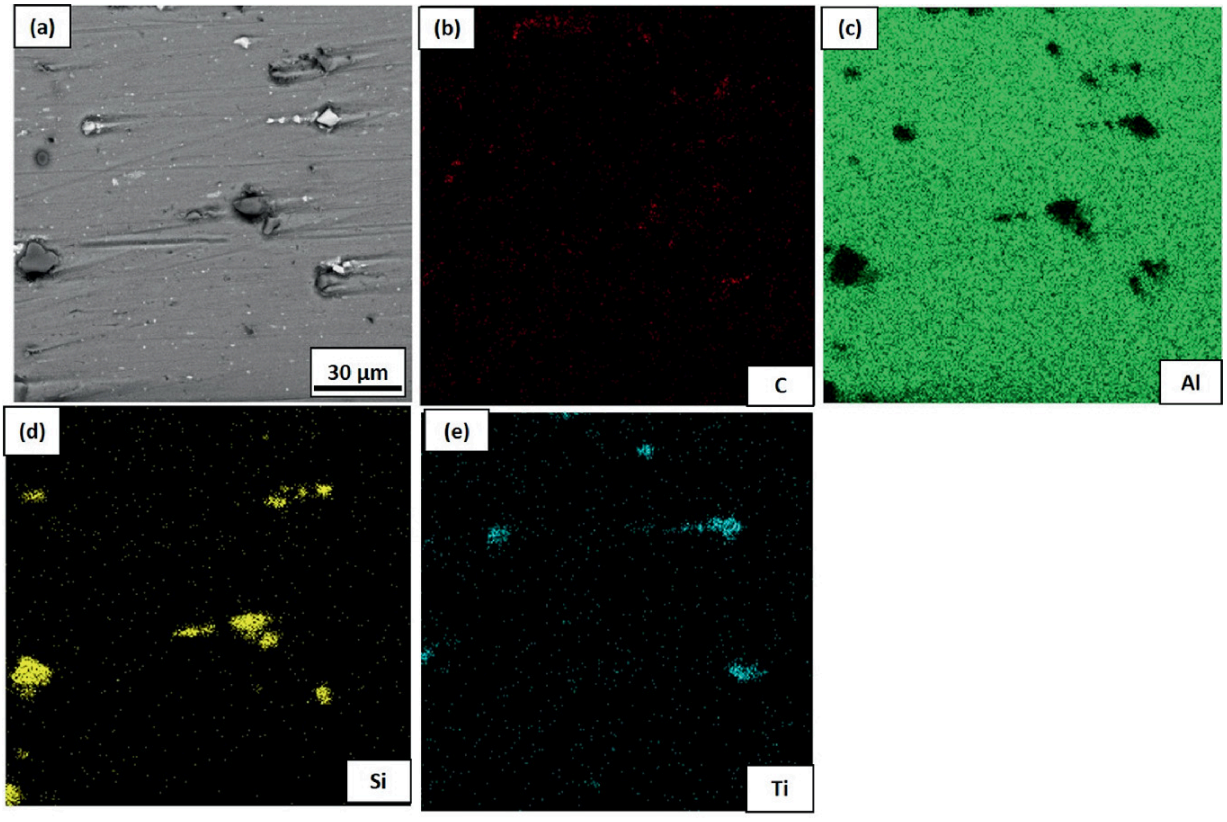


Fig. 5.61 Element distribution of Al/SiCp-TiCp at cryorolling-3 AMC by EDS micrograph of the elements **c** Al. **e** Ti, **d** Si and **b** C

The stress–strain curves for annealed Al samples in their as-received condition and the ARBed with cryrolled processed of Al/SiCp,Al/TiCp and Al/TiCp-SiCp hybrid composites with 4.0 wt.% SiCp, 2.0 wt.% TiCp and the (2 + 4) wt.% TiCp and SiCp after ARBed with cryorolled cycles are compared in Figs. 5.62 and 5.63a. The creation of the composites through the ARB+ cryorolling method results in an increase in tensile strength. The findings indicate that the strength of the hybrid composites after processing surpasses that of the annealed Al strip. Particularly, the Al/TiCp-SiCp hybrid composite achieved the highest tensile strength of 361 MPa after undergoing ARB and cryorolling cycles, which is 5.2 times greater than the initial strength of the as-received material (70 MPa). The hybrid composite of Al/TiCp-SiCp highest yield stress which was 310 MPa noticed **(**Fig. 5.63b**)** as compared to other composites. Also, the combination of SiCp and TiCp ceramic particles as compared to individual particles with Al matrix enhanced the tensile strength significantly, while the elongation decreased. Plastic instabilities are indeed responsible for this trend. The occurrence and characteristics of these plastic instabilities are influenced by various factors such as the initial thickness, work hardening exponent, and strength coefficient of the individual constituents. However, Al with TiCp particles composite resulted in lower strength as compared to other composite. Significant enhancements in the tensile strength of all composites were observed after the third cryorolling cycle. This increase in strength in severely deformed materials can be attributed to two primary strengthening mechanisms. During the initial stages of the ARB process, strain hardening plays a crucial role in augmenting the strength. However, at higher cryorolling cycles, grain refinement becomes the dominant strengthening mechanism as the number of processed cycles increases. This effect has been substantiated by the presence of a greater number of ultra-fine grains and misoriented grain boundaries in the material. This study revealed that in each cycle, the ARB-ed with cryorolled composites Al/TiCp-SiCp tensile strength was more than that for other composite samples (Figs. 5.62 and 5.63a). Also, compared to other composites, its strength was increased in most cryorolling cycles. To further evaluate bonding between SiCp,TiCp with Al matrix, the tensile

fracture surface of the ARBed with cryrolled composites was examined by SEM.

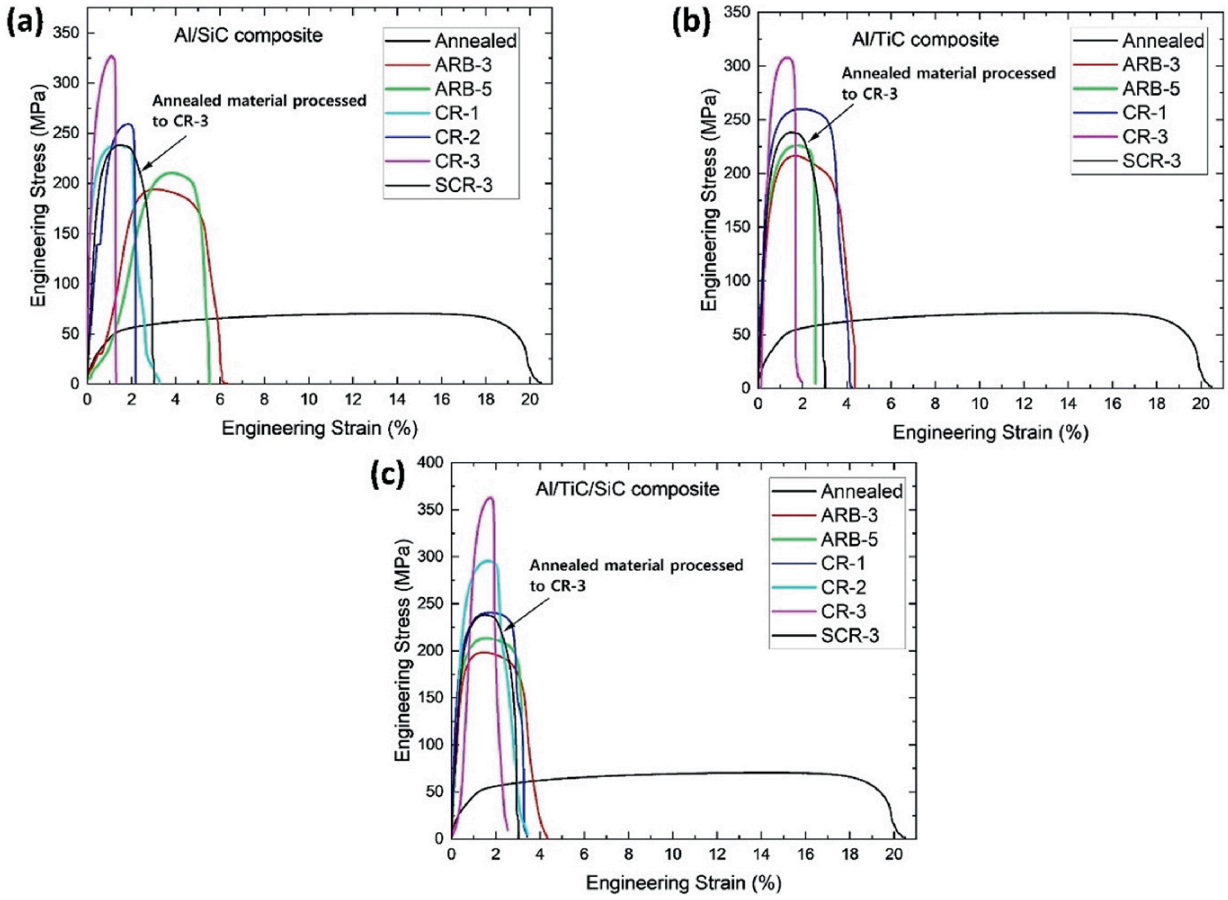


Fig. 5.62 Engineering stress–strain curves of the AMCs ARBed with cryrolled processed cycles **a** Al/SiCp composite **b** Al/TiCp composite **c** Al/SiCp-TiCp composite

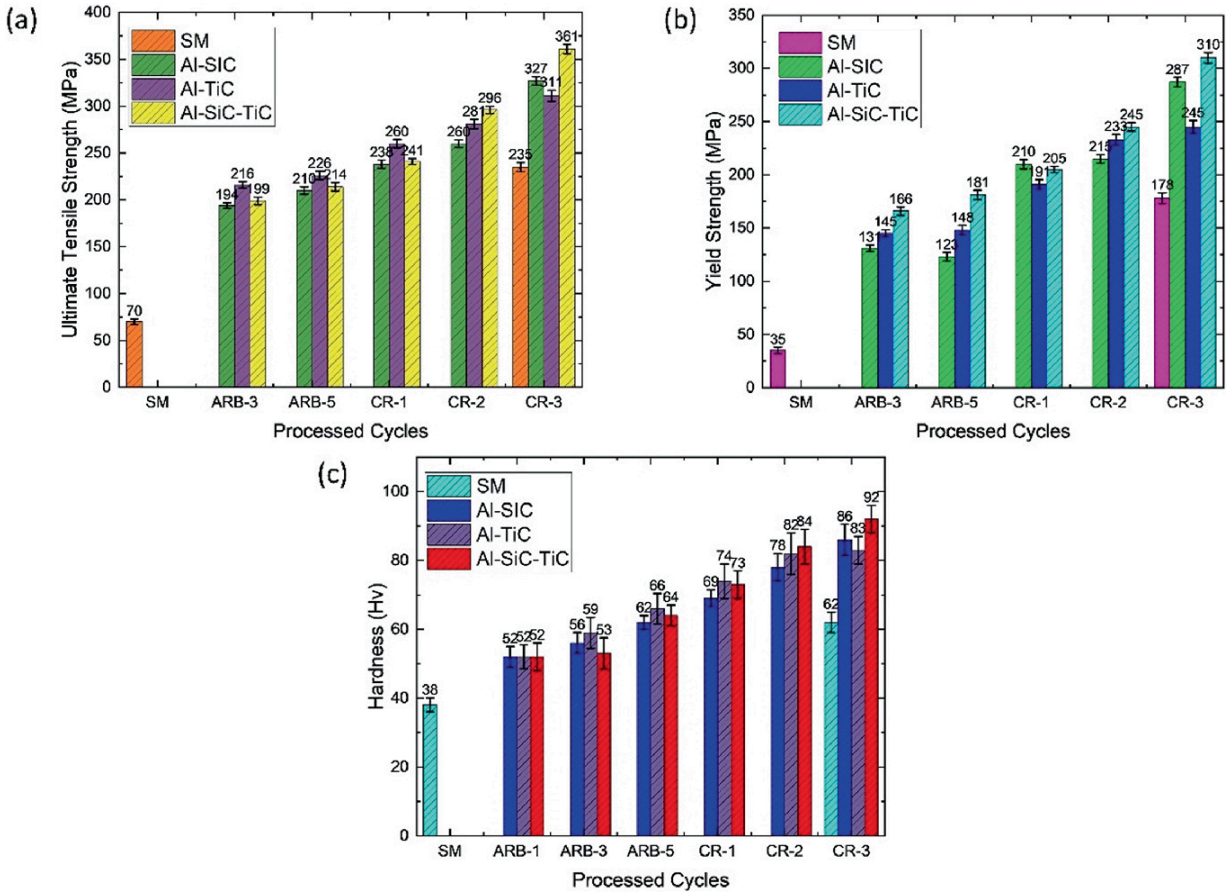


Fig. 5.63 Mechanical properties comparison between annealed Al, Al/SiCp,Al/TiCp and Al/TiCp-SiCp hybrid composites processed ARBed with cryorolled cycles of **a** ultimate tensile strength **b** Yield strength and **c** Hardness (HV) values

Figure 5.63c illustrates how the AMCs ARBed with cryrolled processed cycles of Al/SiCp, Al/TiCp composite, and Al/SiCp-TiCp composites impact the micro-hardness. It shows that the micro-hardness of Al reinforced with ceramic particles increases with the number of cycles. It was noticed that the composite micro-hardness of the phases shows a rapid increase as compared to an annealed Al matrix with processed cycles. While the highest hardness value was noticed in the case of Al/SiCp-TiCp hybride composites which was 92Hv. The high strain hardening rate is responsible for the enhanced rate of micro-hardness in the primary cycles (based on the interactions between them and the density of dislocations). The composite's hardness increases rapidly after the initial cryorolling passes due to the refinement of grain and based on strain hardening strengthening mechanisms which are in accordance with the tensile properties (in Fig. 5.63a). However, the increasing hardness rate is very low during

the ARB process for composites. Ceramic particles were the key reason for dislocation strengthening and facilitating grain refinement of the composites. The modulus of toughness is calculated mathematically using the integral method by finding the area under the stress–strain curve. The composites comparison of modulus of toughness are shown in Fig. 5.64a. The area integration percentage is calculated by dividing the area under the curve by the total area under the curve and multiplying by 100%. The row index is the index of the data point where the maximum stress is reached. The FWHM is the width of the stress–strain curve at half of its maximum stress value. It can be noticed that, the highest toughness achieved in Al-SiCp-TiCp composite as compared to other composites. The elastic modulus is determined by the graphical technique as shown in Fig. 5.64b–d. Each data point presented in Fig. 5.64b, c, and d represents the average of three tests conducted on separate samples, and the standard deviation is indicated by the error bars on the graphs. The obtained value of elastic modulus for pure Al was about 69GPa. During different cycles for ARB and cryrolling cycles, highest elastic modulus values were achieved in Al/SiCp-TiCp composite at cryorolling-3 which were 90GPa as shown in Fig. 5.64d. For different composites at various nano-particles, the modulus changes at variant cycles. It can be noticed that, hardness value increased normally during ARB cycles. But during the final cryorolling cycle, its hardness and elastic modulus value enhanced effectively especially in Al/SiCp-TiCp case.

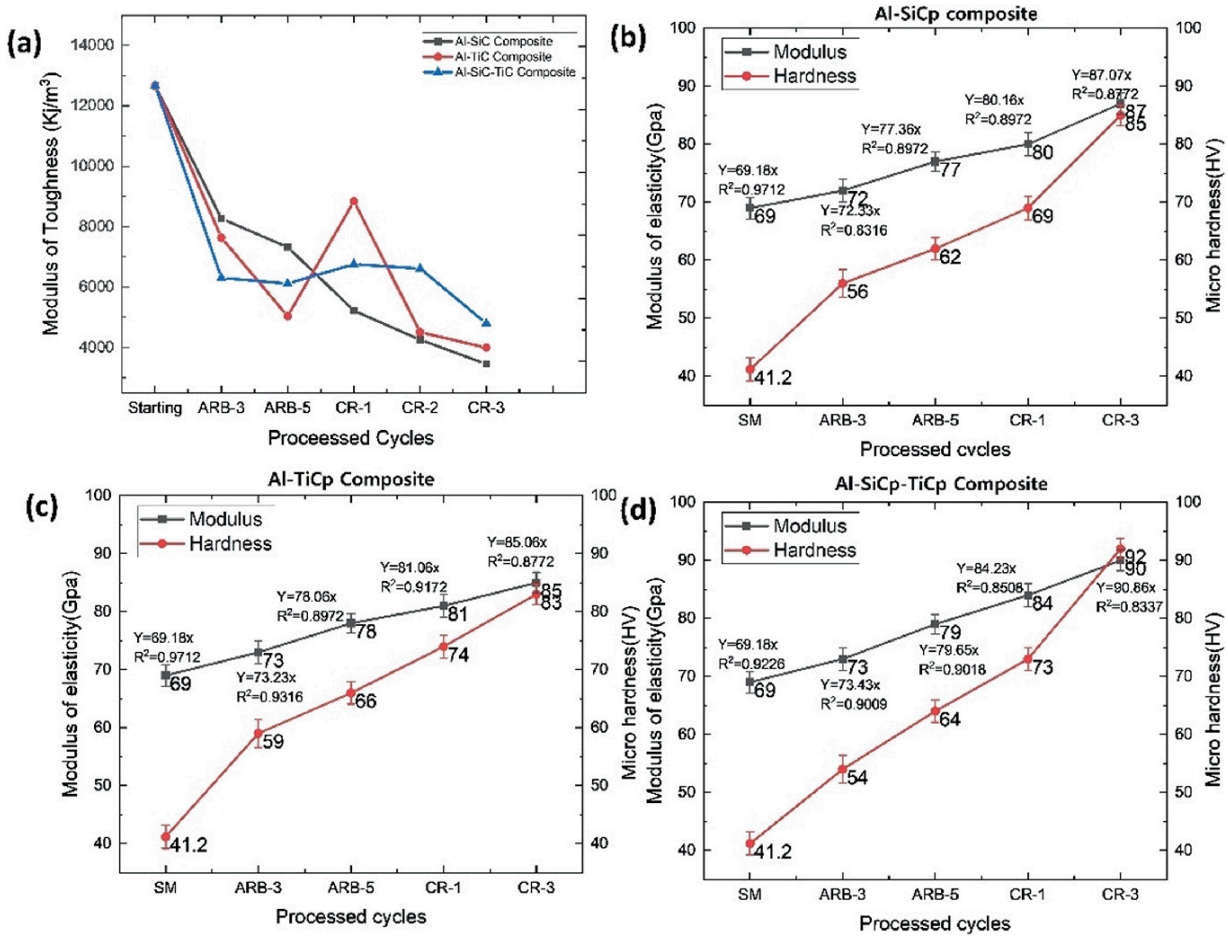


Fig. 5.64 AMCs mechanical properties comparison of Al, Al/SiCp,Al/TiCp and Al/TiCp-SiCp hybrid composites with respect to processed cycles **a** modulus of toughness **b**, **c** and **d** young modulus vs micro hardness

References

1. Zhang X, Li S, Pan D, Pan B, Kondoh K (2018) Microstructure and synergistic–strengthening efficiency of CNTs–SiCp dual–nano reinforcements in aluminum matrix composites. Comp P A 105: 87–96
2. Zhang Y, Li X, Gu H, Li R, Chen P, Kong C, Yu HL (2021) Insight of high–entropy alloy particles–reinforced 2219 Al matrix composites via the ultrasonic casting technology. Mater Charact 182:111548
[Crossref]
3. Gupta R, Nanda T, Pandey OP (2021) Comparison of wear behaviour of LM13 Al–Si alloy based composites reinforced with synthetic (B4C) and natural (ilmenite) ceramic particles. Trans Nonfer Met Soc China 31:3613–3625
[Crossref]

4. Dey D, Bhowmik A, Biswas A (2021) Influence of TiB_2 addition on friction and wear behaviour of Al2024–TiB2 ex–situ composites. Trans Nonfer Met Soc China 31:1249–1261 [Crossref]
5. Toozandehjani M, Ostovan F, Jamaludin KR, Amrin A, Matori KA, Shafiei E (2020) Process–microstructure–properties relationship in Al–CNTs–Al_2O_3 nanocomposites manufactured by hybrid powder metallurgy and microwave sintering process. Trans Nonfer Met Soc China 30:2339–2354 [Crossref]
6. Monikandan VV, Rajendrakumap PK, Joseph MA (2020) High temperature tribological behaviors of aluminum matrix composites reinforced with solid lubricant particles. Trans Nonfer Met Soc China 30:1195–1210 [Crossref]
7. Gludovatz B, Hohenwarter A, Catoor D, Chang EH, George EP, Ritchie RO (2014) A fracture–resistant high–entropy alloy for cryogenic applications. Science 345:1153–1158 [Crossref][PubMed]
8. Li J, Li Y, Wang F, Meng X, Wan L, Dong Z, Huang Y (2020) Friction stir processing of high–entropy alloy reinforced aluminum matrix composites for mechanical properties enhancement. Mater Sci Eng A 792:139755 [Crossref]
9. Yuan Z, Tian W, Li F, Fu Q, Wang X, Qian W, An W (2020) Effect of heat treatment on the interface of high–entropy alloy particles reinforced aluminum matrix composites. J Alloy Compd 822:153658 [Crossref]
10. Liu Y, Chen J, Li Z, Wang X, Fan X, Liu J (2019) Formation of transition layer and its effect on mechanical properties of AlCoCrFeNi high–entropy alloy/Al composites. J Alloy Compd 780:558–564 [Crossref]
11. Luo K, Xiong H, Zhang Y, Gu H, Li Z, Kong C, Yu HL (2022) AA1050 metal matrix composites reinforced by high–entropy alloy particles via stir casting and subsequent rolling. J Alloy Compd 893:162370 [Crossref]
12. Li G, Wen H, Wang H, Ren W, Yan Y, Chen J, Wang C, Zhao Y (2021) Microstructural characteristics and mechanical behavior of microwave–assisted sintered ferromagnetic FeCoNi1.5CrCu HEAp/Al matrix composites. J Alloy Compd 861: 158439
13. Li Z, Zhang Y, Xiong H, Kong C, Yu HL (2022) Fabrication of particle–reinforced aluminum alloy composite: role of casting and rolling. Mater Manuf Process 37:90–98 [Crossref]
14. Zanchetta BD, Silva VKDA, Sordi VL, Rubert JB, Kliauga AM (2019) Effect of asymmetric rolling under high friction coefficient on recrystallization texture and plastic anisotropy of AA1050 alloy. Trans Nonfer Met Soc China 29:2262–2272

[Crossref]
15. Toth LS, Beausir B, Orlov D, Lapovok R, Haldar A (2012) Analysis of texture and R value variations in asymmetric rolling of IF steel. J Mater Process Tech 212:509–515 [Crossref]
16. Li C, Xiong H, Bhatta L, Wang L, Zhang Z, Wang H, Kong C, Yu HL (2020) Microstructure evolution and mechanical properties of Al–3.6Cu–1Li alloy via cryorolling and aging. Trans Nonfer Met Soc China 30:2904–2914 [Crossref]
17. Du Q, Li C, Cui X, Kong C, Yu HL (2021) Fabrication of ultrafine–grained AA1060 sheets via accumulative roll bonding with subsequent cryorolling. Trans Nonfer Met Soc China 31:3370–3379 [Crossref]
18. Yu H, Tieu AK, Lu C, Liu X, Godbole A, Kong C (2013) Mechanical properties of Al–Mg–Si alloy sheets produced using asymmetric cryorolling and ageing treatment. Mater Sci Eng A 568:212–218 [Crossref]
19. Zhang Z, Wu Y, Bhatta L, Li C, Gan B, Kong C, Wang Y, Yu HL (2021) Mechanical properties and microstructure evolution of a CrCoNi medium entropy alloy subjected to asymmetric cryorolling and subsequent annealing. Mater Today Comm 26:101776 [Crossref]
20. Li ZD, Zhang Y, Xiong HQ, Kong C, Yu HL (2022) Fabrication of high–entropy alloy particles reinforced AA2024 composites using casting and rolling. Mater Manuf Process 37:90–98 [Crossref]
21. Gu H, Li ZD, Luo KG, Bhatta L, Xiong HQ, Zhang Y, Kong C, Yu HL (2022) Enhanced mechanical properties of AA 5083 matrix composite via introducing Al0.5CoCrFeNi particles and cryorolling. Acta Metall Sin Eng Lett 35:879–889 [Crossref]
22. Luo KG, Liu SL, Xiong HQ, Zhang Y, Kong C, Yu HL (2022) Mechanical properties and strengthening mechanism of aluminum matrix composites reinforced by high–entropy alloy particles. Met Mater Int 28:2811–2821 [Crossref]
23. Luo KG, Wu YZ, Xiong HQ, Zhang Y, Kong C, Yu HL (2023) Enhanced mechanical properties of aluminum matrix composites reinforced with high–entropy alloy particles via asymmetric cryorolling. Trans Nonfer Met Soc China 33:1988–2000 [Crossref]
24. Luo KG, Lei G, Liu SL, Kong C, Yu HL (2023) Mechanical properties and microstructure evolution of cryorolled AlCoCrFeNi–reinforced aluminum matrix composites tensile tested at room and cryogenic temperatures. Metall Mater Trans A 54:2292–2310 [Crossref]
25. Farid W, Bah TA, Kong C, Yu HL (2023) A novel way to fabricate high elastic modulus and high strength of TiC reinforced aluminum matrix composite. Mater Manuf Process

38:1785–1797
[Crossref]
26. Farid W, Wang ZY, Cui HJ, Kong C, Yu HL (2023) Investigation on various ceramic nano–particles reinforced aluminum matrix composites via accumulative roll bonding and cryorolling. Adv Eng Mater 25:202300936
[Crossref]

© The Author(s), under exclusive license to Springer Nature Singapore Pte Ltd. 2024
H. Yu et al., *High-Performance Metallic Composites Fabricated by Advanced Rolling Techniques*
https://doi.org/10.1007/978-981-97-4331-5_6

6. Future Applications of High-Performance Metallic Composites

Hailiang Yu[1] ✉, Haitao Gao[1] ✉ and Zhou Li[1]
(1) Central South University, Changsha, China

✉ **Hailiang Yu (Corresponding author)**
Email: yuhailiang@csu.edu.cn

✉ **Haitao Gao**
Email: gaohaitao@csu.edu.cn

The new generation of high-end equipment, spanning fields such as defense, military, aerospace, deep-sea exploration, and new energy vehicles, is confronted with increasingly demanding service requirements. These demands include ultra-high speed, large-scale capabilities, ultra-lightweight construction, and high-performance attributes, among others. The application of advanced engineering materials in this context has become more critical than ever. To meet the needs of the high-end manufacturing industry and achieve specialized performance objectives, the utilization of new multifunctional metallic composites has emerged as a pivotal direction in the manufacturing of high-performance components. Consequently, these metallic composites offer a wide range of possible future applications across various industries, due to their unique combination of characteristics, such as high strength, lightweight, improved durability, impact-resistance and cost-effective [1–4]. Here are some potential future applications of high-performance metallic composites: aerospace and aviation, armor and protective gear, high-speed train,

chemical transport containers, mining equipment, energy storage and others, as shown in Fig. 6.1. The following subsections will detail the situation of metallic composites that are already being explored in the three areas of aerospace and aviation, defense industry and energy equipment, as well as potential possible future applications.

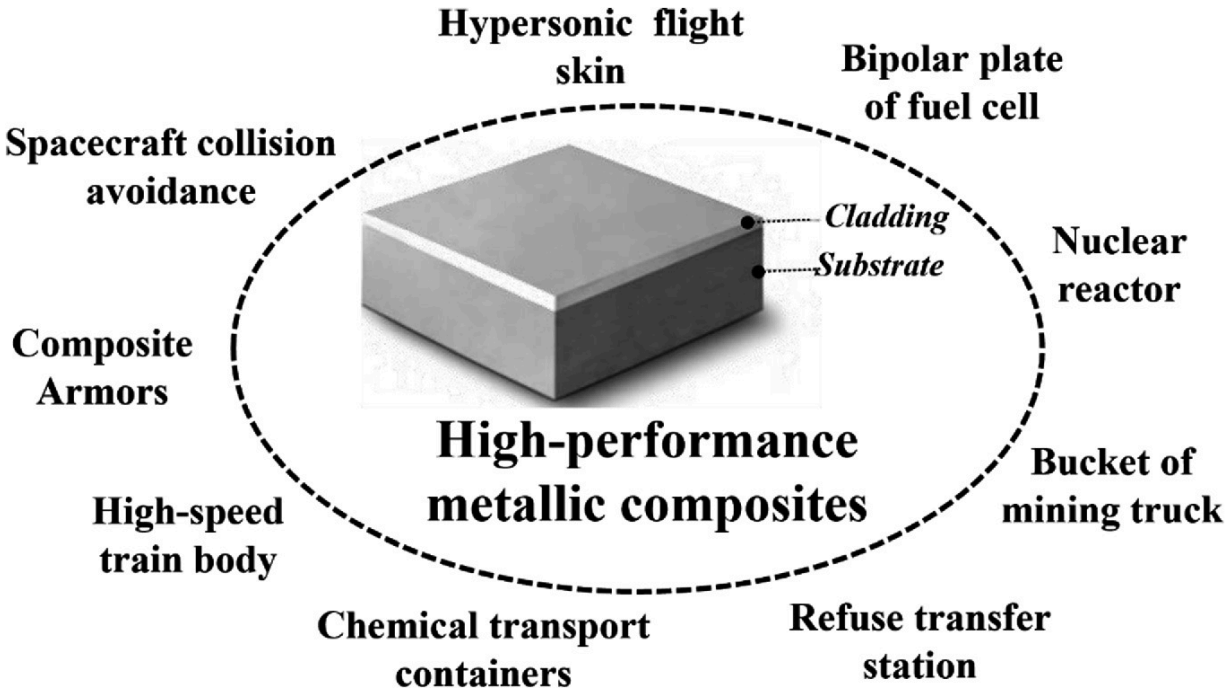


Fig. 6.1 Potential applications of high-performance metallic composites in various industries

6.1 Aerospace and Aviation

In the backdrop of the scientific and technological revolution, aerospace science and technology have emerged as one of the most rapidly advancing fields since the twentieth century, exerting a profound influence on both production and daily life. The aerospace industry has always been an industry that is closely linked to "high-performance," "cutting-edge technology," and "advanced manufacturing." This industry has always led the way in the technological development of advanced materials, and the composites revolution has occurred as a result of the extraordinary properties of their products and the technological developments of recent years.

In aircraft design, the shift from purely metallic materials to composites can result in a weight reduction of 10–40% and a reduction

in structural costs of 15–30%. Light weighting plays an important role in improving the performance of warplanes, civil passenger aircraft and spacecraft, and increasing the service life of warplanes. For instance, compared with fourth-generation fighters, a significant distinction lies in the extensive utilization of advanced composite materials for fifth-generation fighters. Future sixth-generation fighters, long-range bombers, large civil aircraft, etc. require further structural lightweight, aero-engine development requirements continue to improve the thrust-to-weight ratio also put forward the lightweight requirements, in addition to the further development of new metallic composite materials to enhance the high-temperature resistance, anti-icing capabilities, and stealth characteristics of these aircraft. Metallic layered composites are presently employed to manufacture crucial structural components such as spacecraft storage tanks, and Ti-based and Al-based layered composites are currently the most prevalent choices in the aerospace sector. In the future, Ti/Al alloy composites have the potential to supplant traditional Al alloys and Ti alloys, finding applications in areas such as satellite protective shells, detector outer covers and tail fins of fighter aircraft, as shown in Fig. 6.2.

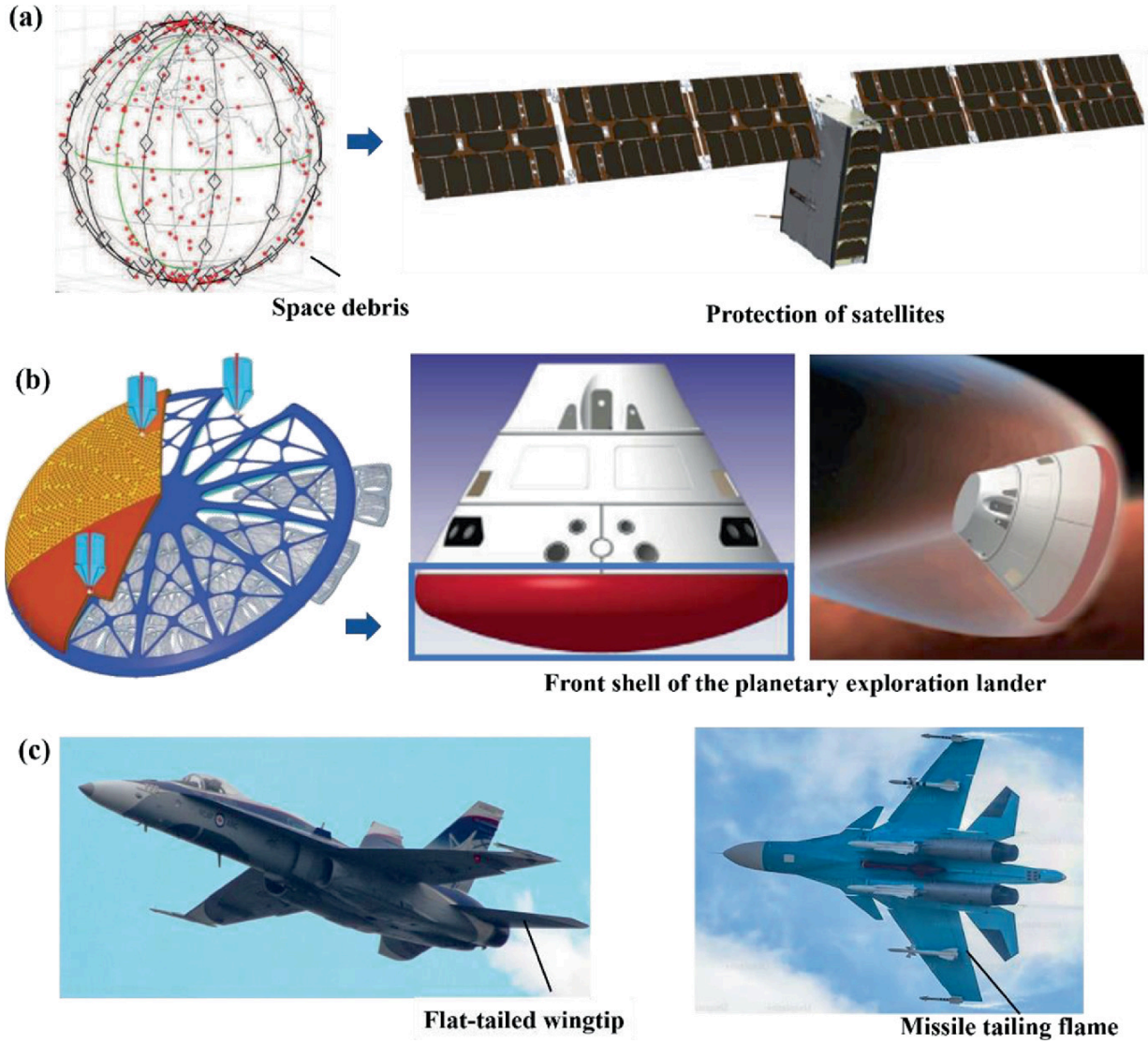


Fig. 6.2 **a** Space debris and satellite protective shells [5, 6]; **b** the front shell of a planetary exploration lander [7]; **c** the structure of a certain type of fighter aircraft and the tail flame of a launched missile

6.2 Defense and Military

Ballistic or armor protection materials play an important role in both defense and military applications, as shown in Fig. 6.3, and weight reduction and improved impact resistance have been the goal of research. Conventional armor typically consists of a single material, such as steel armor and Al alloy armor, known as homogeneous armor. With the increasing penetration of anti-tank artillery shells, missiles and rockets, homogeneous armor alone has struggled to withstand the

attack of such weapons. Continue to increase the thickness of the armor can certainly improve the protection of the tank, but increase the degree of armor is bound to increase the weight of the tank, affecting the mobility of the tank. Consequently, researchers and engineers have devised composite armor, which incorporates a range of materials, typically featuring multiple layers of both metallic and non-metallic components. These layers are strategically stacked, often forming a structure with four or five layers of alternating metal and non-metallic materials while maintaining an effective gap or space between them to absorb and dissipate the energy from incoming threats.

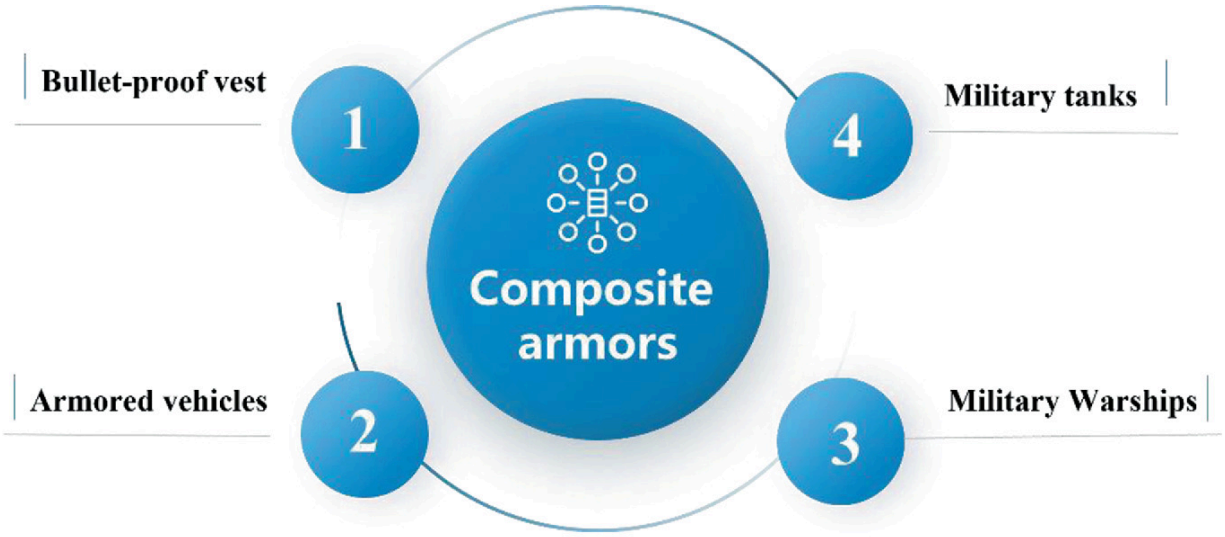


Fig. 6.3 Composite armors in military equipment of bulletproof vest, armored vehicles, tanks, and warships

Armor-piercing or armor-breaking rounds penetrate each layer to consume a certain amount of energy. Due to the different hardness of each layer of material, the core of the armor-piercing bullet or the metal jet of the armor-breaking bullet can be made to change the direction, or even break the core of the armor-piercing bullet. Therefore, the anti-penetration capability of composite armor is much higher than that of homogeneous armor. In the same weight per unit area of the armor, the ability of composite armor to resist armor-breaking bullets is two times higher than that of homogeneous steel armor. This kind of armor is divided into metal and metallic composite armor, metallic and non-metallic composite armor and spacer armor three kinds, they all have strong comprehensive protection performance.

The use of lightweight alloys combined with high toughness alloy composites can reduce the weight of the material while enabling improved performance. Vecchio et al. [8] found that laminates prepared by mixing 20% Ti-6Al-4 V with 80% Al_3Ti had excellent ballistic properties. Currently military laminated composites are not limited to pure metal-based, the use of glass fiber, epoxy resin, carbon fiber, ceramics and other materials and metallic composite can often play a better performance. For example, high-performance metal and high-strength ceramics prepared by the laminated composite materials can reduce the weight of armored vehicles, improve mobility and ballistic performance. Piezoelectric sensors embedded in the laminated metallic composite can also increase the sensing ability and promote the intelligence of armored vehicles in future.

6.3 Energy Applications

Proton exchange membrane hydrogen fuel cells (PEMFCs) are regarded as a promising avenue for advancing green aviation, and one of its core components is the microfluidic bipolar plate, as shown in Fig. 6.4a, which plays the roles of uniform gas distribution, current collection, cooling and support. The processing materials of bipolar plates are mainly graphite, metal and metallic composite materials, which account for 60–80% of the total weight, 30–40% of the cost and 60% of the volume of the cell, which is one of the main factors leading to the low volume/mass power density and high cost of the cell.

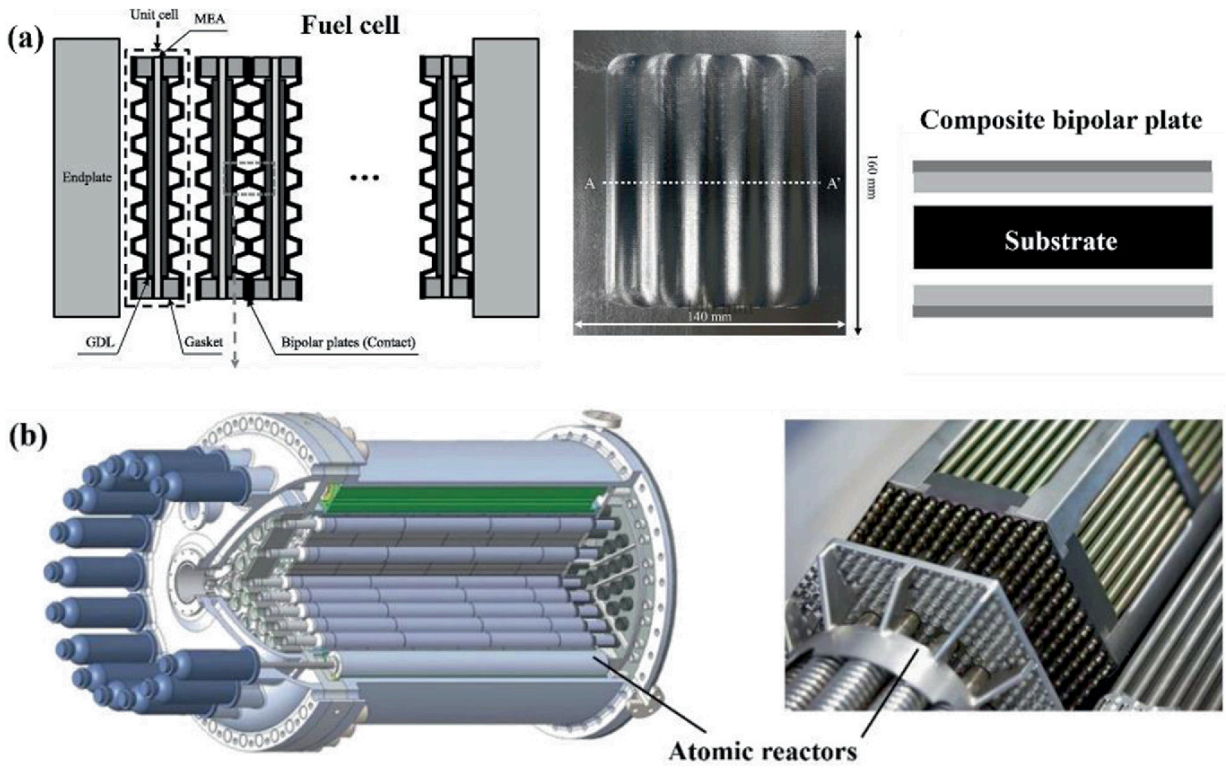


Fig. 6.4 **a** Composite bipolar plates of the fuel cell [9]; **b** composite pipes of the atomic reactor [10]

Composite bipolar plates combine the advantages of graphite bipolar plates and metallic bipolar plates, and at the same time have good electrical conductivity, mechanical strength, and corrosion resistance, as well as good processing performance and low cost, which has become the focus of research on bipolar plate materials for PEMFCs. At present, the composite bipolar plates have been used, including carbon matrix composite bipolar plates and metal matrix composite bipolar plates, although the electrical conductivity and thermal conductivity of the composite bipolar plates are lower than that of the pure graphite material and metal material bipolar plates, but by optimizing the composite material composition, proportioning and molding process, the performance of the bipolar plates will meet the requirements for the use of PEMFCs.

In addition, nuclear engineers have been actively exploring novel formulations, geometries, and dimensions for the radioactive fuel employed to drive the reactors within the world's nuclear power plants. These innovations represent a critical aspect of the energy landscape, as nuclear power remains one of the primary sources of zero-carbon

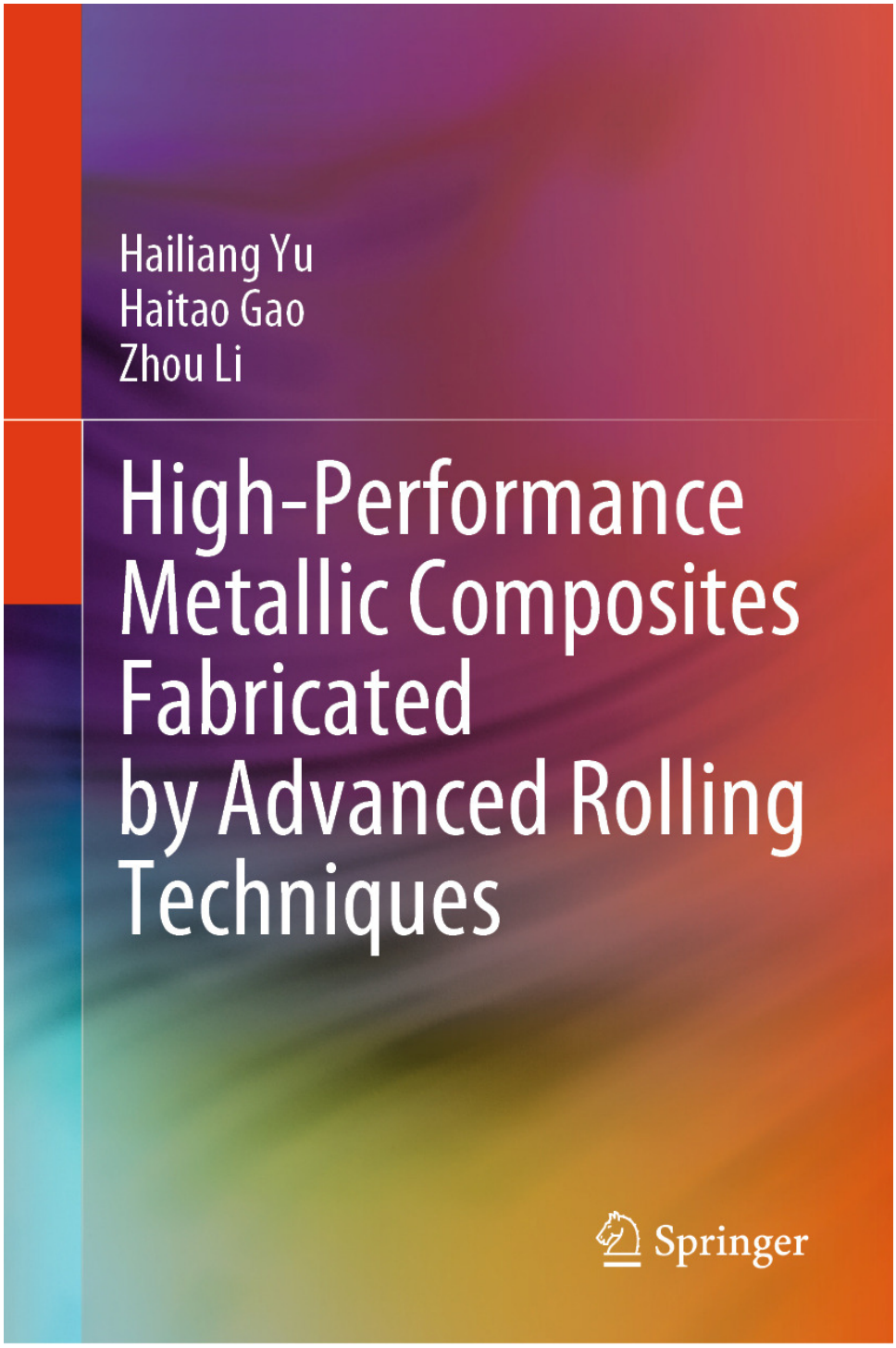
electricity generation. Fuel rods are integral components of nuclear reactors, serving as crucial functional units, as shown in Fig. 6.4b. They make direct contact with uranium fuel and play a pivotal role in regulating the intensity of the nuclear reactions within the reactor core. A unique sandwich steel-vanadium-steel composite was developed by the National University of Science and Technology “MISIS” (NUST MISIS) and this composite is able to withstand temperatures of up to 700 °C, hard radiation exposure, mechanical stress and chemical exposure for a long period of time. This new composite material holds the potential for applications in the containment shells of nuclear reactor cores. Moreover, ongoing research is likely to explore the development of additional metallic composites tailored for use in future nuclear reactor designs. These advancements in composite science are critical for enhancing the safety and efficiency of nuclear power generation.

In summary, metallic and other composites have served mankind well for thousands of years since their inception, and the quest for high-performance metallic composites remains ongoing. For composites tailored to specific working conditions, how to select the right materials and improve the preparation and processing process is still a formidable challenge. This effort relies not only on continued rigorous theoretical research but also demands substantial human and material resources to conduct extensive experimental investigations.

References

1. Li Z, Cao L, Huo M, Jiang Z (2023) Evidence–based uncertainty quantification for bending properties of bimetal composites. Appl Math Model 121:59–74 [Crossref]
2. Haoren W, Chaoyi Z, Kenneth SV (2020) Deformation and fracture evolution of FeAl–based metallic–intermetallic laminate (MIL) composites. Acta Mater 194:496–515 [Crossref]
3. Li Z, Lin YC, Zhang L, Zheng J, Zhao J, Wang R, Jiang Z, Jiao S (2022) In–situ investigation on tensile properties of a novel Ti/Al composite sheet. Int J Mech Sci 231:107592 [Crossref]
4. Li Z, Lin YC, Zhang L, Jia F, Jiang Z, Jiao S (2022) Investigation of compact tensile and fracture mechanical properties of a duplex stainless steel bimetal composite with the interfacial zone. J Mater Res Tech 19:809–820

[Crossref]
5. Anttonen A, Kiviranta M, Höyhtyä M (2021) Space debris detection over intersatellite communication signals. Acta Astronaut 187:156–166
[Crossref]
6. Barato F (2023) Optimal use of electric propulsion for drag compensation in very low earth orbit on satellites with deployable solar panels. Acta Astronaut 213:1–19
[Crossref]
7. Gu D, Shi X, Poprawe R, Bourell DL, Setchi R, Zhu J (2021) Material–structure–performance integrated laser–metal additive manufacturing. Science 372:1–15
[Crossref]
8. Vecchio K, Jiang F (2016) Fracture toughness of Ceramic–Fiber–Reinforced Metallic–Intermetallic–Laminate (CFR–MIL) composites. Mater Sci Eng A 649:407–416
[Crossref]
9. Lim JW, Lee D, Kim M, Choe J, Nam S, Lee DG (2015) Composite structures for proton exchange membrane fuel cells (PEMFC) and energy storage systems (ESS): review. Compos Struct 134:927–949
[Crossref]
10. Gustafson JL (2021) Space nuclear propulsion fuel and moderator development plan conceptual testing reference design. Nuclear Tech 207:882–884
[Crossref]


Hailiang Yu
Haitao Gao
Zhou Li
High-Performance Metallic Composites Fabricated by Advanced Rolling Techniques
Springer